

The background of the entire page is a photograph of the Fontana del Gallo in Rome, Italy. It features a large central statue of a bearded man (the Gallo) standing on a rocky base, surrounded by other statues including a winged horse and a winged figure. Water flows from the base of the fountain into a pool. The architecture behind the fountain includes classical columns and a large dome with a diamond-patterned facade.

BEI-2023

Bridge Engineering Institute Conference

July 17-20, 2023

Rome, Italy

Edited by
Yail J. Kim
Isamu Yoshitake
Vanissorn Vimonsatit
Xuhui He
Yongcheng Ji
Jun Wang

BEI

An International Technical Society



Bridge Engineering Institute Conference in 2023 (BEI-2023)

Rome, Italy

July 17 to 20, 2023

Edited by
Yail J. Kim
Isamu Yoshitake
Vanissorn Vimonsatit
Xuhui He
Yongcheng Ji
Jun Wang

ISBN: 978-1-7340386-1-3

The Bridge Engineering Institute
An International Technical Society
www.beibridge.org

Table of Contents

The Bridge Engineering Institute, An International Technical Society.....	9
Conference Organization.....	10
Plenary Speakers.....	11
Plenary Speeches	
A Review of 30 Years of Experience in Field Testing of Bridges.....	16
<i>Issam Harik</i>	
Performance-Based Electrochemical Analysis of an Innovative Magnesium Phosphate Cement Coating to Mitigate Mild Steel Bar Corrosion.....	19
<i>John J. Myers, Fan Zhang, and Hongyan Ma</i>	
Diagnostic Load Testing of a Bridge Before and After Rehabilitation.....	24
<i>Jiayi Ding, Nicolas Begasse, Adriana Toro, Francisco De Caso, and Antonio Nanni</i>	
Current State of Expressways and New Technologies for Bridge Deck Maintenance in Japan..	29
<i>Takashi Yamane</i>	
Materials and Performance	
Quality of Lamination Structure Made by 3D Printing under Different Lamination Conditions..	35
<i>Yuji Yamada, Tomoko Fukuyama, Yunmi Kim, Hiroharu Kamada, and Dhruva N. Katpady</i>	
Bond Strength Evaluation of Grout Materials for Closure Pour of Precast Concrete Bridge Deck Panels.....	39
<i>Zhifu Yang</i>	
Experimental Investigation of the Effect of Debonding on PSC Girders.....	44
<i>Shambhavi Dube and Durgesh C. Rai</i>	
Investigation of Nitrogen Oxide Removal of Cementitious Materials Containing TiO ₂	49
<i>Byoungsun Park, Suji Woo, Young Cheol Choi, and Sung-Won Yoo</i>	
The Diagnosis Method for Neutralization of Concrete Using Microorganisms.....	53
<i>China Kuratomi, Atsushi Teramoto, So Fujiyoshi, and Fumito Maruyama</i>	
Research on Fatigue Properties of Basalt Fiber Cement Stabilized Macadam.....	58
<i>Wei Li, Peifeng Cheng, Wenmei Zhao, and Zhanming Zhang</i>	
Wind, Vibration, and Aerodynamics	
Analysis of Dynamic Characteristics of Semi-Submersible Deep-Water Floating Foundation under Wind-Wave Coupling Actions.....	64
<i>Honggang Xu, Haiquan Jing, and Xuhui He</i>	

Field Measurement Study on Wind Characteristics at the Bridge Site of Plateau Deep-Cut Canyon.....	69
<i>Xinghui Kang, Yunfeng Zou, Xuhui He, and Longan Li</i>	
Dynamical Analysis of Vehicle-Bridge Interaction System under Ice and Wind Loads.....	74
<i>Tianyu Wu, Wenliang Qiu, Guowen Yao, and Zengwei Guo</i>	
Safety Analysis of Wind Barriers on the Bridge under the 400 km/h High-Speed Trains Loading of Slipstream.....	82
<i>Dianyi Guo, Yunfeng Zou, Xuhui He, and Haobo Liang</i>	
Fatigue Analysis of Anchored Concrete Structures of Catenary Induced by Train Wind Load Considering Different Bolt Pre-Tightening.....	87
<i>Zhuole Shu, Pengru Deng, Hanfeng Wang, and Xuhui He</i>	
Influence of Spacing on Aerodynamic Interference of Parallel Rail-Cum-Road Bridges with Twin Separated Parallel Girder.....	92
<i>Jing He, Yunfeng Zou, Xuhui He, and Lulu Liu</i>	
Monitoring	
A Trust-Based Approach for Resilient UAV Networks Monitoring Bridges.....	97
<i>Francesco Buccafurri and Francesca Scoleri</i>	
Evaluation Method for Grouting Condition in Post-tensioned PC Bridges Considering Directive Propagation Properties of Elastic Waves in the Wide-Range Ultrasonic Testing (WUT).....	101
<i>Takanori Kinoshita, Yoshino Sako, Kuniharu Fukushima, and Isamu Yoshitake</i>	
Detection of Defects in Prestressed Concrete Bridge Box Girders Using GPR Image Reconstruction.....	105
<i>Wael Zatar, Hien Nghiem, and Hai Nguyen</i>	
Prestressing Force Distribution in Post-Tensioned I-Girder Bridges Measured Using Smart Strands.....	110
<i>Se-Jin Jeon, Sang-Hyun Kim, Sung Yong Park, and Sung Tae Kim</i>	
Detection of Cable Section Loss in Cable-stayed Bridge with Electromagnetic Sensor.....	115
<i>Imjong Kwahk, Changbin Joh, Ji-Young Choi, Kwang-Yeun Park, and Joo-Hyung Lee</i>	
Evaluation of Salt Resistance of Three-Component Cement Concrete by Unsteady Electrophoresis Test.....	119
<i>Kohei Kanaoka and Tatsuya Nukushina</i>	
Field Testing	
Grating on Bridge Deck for Improving Flutter Performance: A Case Study of Cable-Suspended Bridge.....	125
<i>Zhen Wang, Xuhui He, Haiquan Jing, and Lulu Liu</i>	

Development of Elevated Road and Rail Projects in Singapore.....	129
<i>Hooi Leng Phua</i>	
Structural Behavior of a 40+ Year Old PSC-I Concrete Bridge According to its Internal Tendon Loss in the Central Part.....	133
<i>Yeonghun Seong and Hyunjoong Kim</i>	
The Use of Engineered Cementitious Composite (ECC) Deck Overlay at Curry Street Bridge, Windsor, Ontario, Canada : Lessons Learned and Challenges.....	134
<i>Don Gardonio, Steve Volpatti, Emad Booya, and Philip Loh</i>	
Transporting Heavy Weight Cargo, Diagnosis Philosophy, and a Case Study.....	143
<i>Daniel Elmaleh and Yehonatan Pestes</i>	
Development of Pre-Tension Method for On-Site Production of Prestressed Concrete Girders with Span Length between 20 m to 50 m.....	149
<i>Dong-Woo Seo, Sangki Park, Ki-Tae Park, Hyun-Ock Jang, and Yeon-Woo Shin</i>	
Environmental Effects	
Temperature-Induced Variation in Geometric Characteristics of Existing Cracks in Double-Box Girders of Concrete Cable-Stayed Bridge.....	155
<i>Xujia Liu, Youliang Ding, Hanwei Zhao, Chunfeng Wan, and Fangfang Geng</i>	
Utilizing Pressurized Injection of Lithium Nitrite in Treating Alkali-Silica Reaction and Salt Damage in Concrete Structures.....	160
<i>Shohei Notsu, Tatsuya Kitada, Son Van Nguyen, and Kazunori Era</i>	
Fatigue of Steel Anchor Box on Cable-Stayed Bridges Considering Thermal and Vortex-Induced Vibration under Random Traffic Flows.....	164
<i>Zhiwen Zhu, Shuang Yan, Federico Accornero, and Yichun Deng</i>	
Mechanism of Control Method for the Alkali-Silica Reaction and Delayed Ettringite Formation Expansion Using Artificial Lightweight Aggregate.....	170
<i>Atsushi Teramoto and Moka Tanabe</i>	
Repair and FRP Composites	
Electromechanical Response of Smart Repair Material with Carbon Black Based on Rapid Setting Cement.....	175
<i>Tae Uk Kim, Min Kyoung Kim, Lai Thanh Tu, and Dong Joo Kim</i>	
Bending Tests of GFRP Sandwich Panel Using a Rigid Polyethylene Core.....	179
<i>Hiroki Iwata, Sumitaka Inoue, and Masahide Matsumura</i>	
Analysis of Flexural-Bond Behavior of Beams Reinforced with CFRP.....	183
<i>Dongkyu Lim and Myoungsung Choi</i>	

Evaluation of Tensile Performance of CFRP Cable Anchorage System Using Non-Corrosive Steel Material.....	187
<i>Seung-Hyeon Hwang, Ji-Young Kim, Jin-Young Yoon, Tae-Kyun Kim, and Woo-Tai Jung</i>	
Failure Mode and Adhesive Strength of Single Lap Joint of GFRP Laminated Plates with Different Fiver Volumes Bonded by a Low Elastic Adhesive.....	191
<i>Masahide Matsumura, Sumitaka Inoue, Hiroki Iwata, and Yuto Anan</i>	
Ultra-High Performance Concrete	
Titanium Alloy Reinforced Ultra-High Performance Concrete (TARUHPC): A Next Generation of Advanced Materials for Civil Infrastructure.....	196
<i>Mahesh Acharya, Jared Cantrell, Luis Bedrinana, and Mustafa Mashal</i>	
Design of Ultra-High Performance Concrete Bridges.....	201
<i>Benjamin Graybeal and Rafic Helou</i>	
Axial Compression Performance of UHPC-Filled Square Duplex Stainless Steel Tube Short Columns.....	205
<i>Hongyuan Tang, Xiaowei Hu, Jinjun Liu, and Duan Hong</i>	
Seismic Retrofit of Precast and Cast-in-Place Piers Using Ultra High-Performance Concrete (UHPC).....	210
<i>Kathryn Hogarth, Manish Acharya, Arya Ebrahimpour, and Mustafa Mashal</i>	
Railway Bridges	
Numerical Investigation of Aerodynamic Characteristics of High-Speed Railway Train-Bridge System under Tornado-Like Winds.....	215
<i>Xuhui He and Simin Zou</i>	
Effects of Splitter Plates on the VIV Performances of Twin Separated Parallel Decks for a Rail-Cum-Road Bridge.....	219
<i>Lulu Liu, Xuhui He, Yunfeng Zou, and Zhen Wang</i>	
Aerodynamics of a High-speed Train Crossing the Wake of a Bridge Tower in Different Yaw Angles	224
<i>Zuyu Xie, Huan Li, Xuhui He, and Zhirui Huang</i>	
Concrete Structure Damage Analysis of the Anchoring End of Wind Barriers of High-Speed Railway Bridge under Wind Load of Train.....	225
<i>Haobo Liang, Yunfeng Zou, Xuhui He, and Dianyi Guo</i>	
Parametric Study on the Aerodynamic Characteristics of Wind-Guide Barriers for Train-Bridge System.....	230
<i>Shuo Jiang, Yunfeng Zou, Xuhui He, and Dianyi Guo</i>	

Earthquake and Dynamics

Experimental Evaluation on Seismic Behavior of Precast Concrete Walls with Developed Vertical Joints for Enhanced Shear Strength.....236
Kyo Young Moon, Sung Jig Kim, and Chunho Jang

Hybrid Testing of CFST Columns in Rigid-Frame Bridges Subjected to Horizontal and Vertical Ground Motions.....240
Riadh Al-Mahaidi, Javad Hashemi, and Ali Al-Attraqchi

Seismic Performance of Precast Segmental Bridge Columns with Resettable Sliding Joints: Joint Responses and Simulation244
Feng Liang, Yingqi Liu, and Francis T.K. Au

Effects of Vertical Ground Motions on the Response of Long-Span Prestressed Bridges.....249
Hsiao-Hui Hung, Chang-Wei Huang, and Yi-Hui Lu

Seismic Performance Assessment of Wall Piers Supported by Pile Foundation.....254
Shin-Tai Song and Wen-Li Huang

Experimental Techniques

Flexural Behavior of 3D-Printed Beam Members.....259
In-Hwan Yang, Quang-The Bui, Jihun Park, Jungwoo Lee, and Changbin Joh

ELSS Joint: Development of Semi-Rigid Joint for Joining Precast Prestressed Concrete Slabs in Japan.....264
Mohammad Emran Nasery, Tatsuhiko Mimoto, Nobuaki Sakurai

Horizontal-Vertical Ratio for Concrete Pumping Pipe268
Ki-Yeol Kim, Young-Jin Kim, and Myoung-Sung Choi

Over Torque Test Method to Assess the Concrete Strength.....273
Kenji Tada, Tatsuki Hatakeyama, and Tetsuya Ohmura

Application of Automatic Welding Robot in Integrated Construction of Bridge Pile Foundation.....277
Liangjun Hu, Xiaoli Sun, and Jun Yang

Structural Behavior of Precast Concrete Beam-Column Joints.....282
Jaehyung Heo, DongIk Shin, Yeon Je Choi, Dong-Hwan Kim, Hyeong-Gook Kim, Kil-Hee Kim, and Jung-Yoon Lee

Diaphragm Wall Mono-Shaft as an Economical Time Saving Bridge Deep Foundation.....286
Yoni Pestes and Daniel Elmaleh

Performance Comparison of Nonlinear Dampers for Suppressing Vortex-Induced Vibration of Flexible Bluff Structures.....	292
<i>Jingwei Zhang, Xiaojun Wei, and Xuhui He</i>	
Control the Torsional Flutter of a Rectangular Plate with Flexible Membrane at its Leading Edge	296
<i>Ziqiang Zhang, Hanfeng Wang, Zhiwei Liu, and Chi Zhang</i>	
Modeling and Advanced Analysis	
Unseating of Bridge Decks- Codal Provisions and Fragility Analysis.....	302
<i>Shambhavi Dube, Nirav Thakkar, and Durgesh C. Rai</i>	
Finite Element Modeling of Compressive Membrane Action in Transversely Prestressed Deck Slabs.....	309
<i>Amir Sana</i>	
Modelling of Bend Corners of FRP Reinforcement for Concrete Structures Considering Material Anisotropy.....	313
<i>Yuanzhang Yang and Weijian Zhao</i>	
Water Pressure Variation on Porous Calcium-Silicate-Hydrates Using Molecular Dynamics	318
<i>Shota Takinami, Ryo Yoshida, and Ryo Kobayashi</i>	
Real Imperfections of Longitudinally Stiffened Plates Compared to the Proposed Imperfections in EN 1993-1-5.....	323
<i>N. Thomas, A. Weinhuber, M. Mensinger, C. Holst, and J. Ndogmo</i>	
Structural Damage Prediction with Multi-Level Neural Networks Using Modal Group Response	327
<i>Yunfeng Zou, Xuandong Lu, Xuhui He, and Chenzhi Cai</i>	
Use of Steel Orthotropic Box Girders for Light Weight Long Span Bridges- Analysis and Design of Pedestrian Bridge in Dubai.....	331
<i>Tharun John Joseph, Anirudh Desai, Koyya Satyanarayana, Bogdan Barbulescu, and Kannaw Shrivatsa</i>	
Analytical Study of Fracture Behavior of Post-Tension Anchorage Zone Using FEM.....	336
<i>Kyun-Tae Lee, Jun-Mo Yang, and Jin-Kook Kim</i>	
Development of Shrinkage and Creep Prediction Model for SCC (B4-TW-SCC) and Implementation in Bridge Design Software.....	340
<i>Wen-Cheng Liao and Jenn-Chuan Chern</i>	

A Data-Driven Method for Predicting the Temperature Response of Composite Bridges Based on Deep Learning Technology.....	348
<i>Yanjia Wang, Dong Yang, and Francis T.K. Au</i>	
Topology Optimization of Concrete Bridges Prestressed with Shape Memory Alloys.....	353
<i>Minsoo Sung and Bassem Andrawes</i>	
A Mesoscale Probabilistic Fatigue Crack Initiation Model for Steel Bridges Based on the Modified Fine and Bhat Theory.....	358
<i>Fei Jiang, You-Liang Ding, Kang Yang, and Xiao-Nan Zhang</i>	
Tension Estimation Method for Linked Suspenders Based on Identified Mode-Shapes.....	363
<i>Chien-Chou Chen, Wen-Hwa Wu, and Yen-Chih Peng</i>	
Research on Crack Damage Model and Size Effect of Flexible Fiber Reinforced Recycled Concrete.....	368
<i>Yongcheng Ji, Yanmin Jia, Dayang Wang, Yanwei Jia, and Zhiyang Pei</i>	
Finite Element Analysis Model of Prestressed Concrete Girder through Nonlinear Material Properties Correction of Strand.....	373
<i>Do-Yeon Kim, Young-Ji Park, Jin-Woong Choi, Young-Jin Kim, Il-Young Jang, Seong-Kyum Kim</i>	
Corrosion and Durability	
Visualization of the Effect of Steel Corrosion Cracks on Shear Deformation inside Mortar Using X-ray CT.....	378
<i>Takayuki Fumoto, Koshiro Maekawa, Shintaro Kikuchi, and Yuta Yamada</i>	
A Change in the Failure Mode and Decrease in the Strength of RC Slabs due to the Progress of Frost Damage.....	382
<i>Hiroshi Hayashida</i>	
Experimental Performance of Lightweight Aggregate Concrete due to Freezing and Thawing	387
<i>Sangwoo Kim, Sardorbek Rustamov, and Jinsup Kim</i>	
Rust Evaluation of Weathering Steel Bridges by Optical Spectra in the Visible and Near-Infrared Regions.....	391
<i>Ryuichi Inoue, Rina Hasuike, Hirokazu Furuki, and Toshihiko Aso</i>	
Effect of Measures for Inhibiting Galvanic Corrosion in an Aluminum Alloy Bridge and Guard Railings.....	395
<i>Yoshito Itoh and Tatsuya Kawabata</i>	
Study of Water Absorption Properties in Actual Structure Concrete Based on Pore Structure.....	400
<i>N'da Yacoub Bouadou, Peter Kuira Macharia, Lai Lai Mon, and Ryo Yoshida</i>	

Performance Evaluation

Evaluation of the National Bridge Inventory (NBI) to Predict Bridge Deterioration in Missouri, USA.....405

Glenn Washer, John J. Myers, and Mohammed Hammed

Assessment of Live Load Carrying Capacity of Prestressed Concrete Bridge: a Case Study....409

Shin-Tai Song and Yiching Lin

Strategic Asset Management of Locally Owned Bridges.....413

Mi G. Chorzepa

Platform and Bigdata-Driven Bridge Smart Maintenance Techniques.....417

Ki-Tae Park, Kyusan Jeong, Jaehwan Kim, Kun-Soo Kim, Byeongcheol Kim, and Dongwoo Seo

The Bridge Engineering Institute, An International Technical Society

Executive Committee



Yail Jimmy Kim
President
University of Colorado Denver
USA



Isamu Yoshitake
Vice-President
Yamaguchi University
Japan



Vanissorn Vimonsatit
Director
Macquarie University
Australia



Xuhui He
Director
Central South University
China

Diversity, Equity, and Inclusion (DEI) Committee



Su Taylor
Queen's University Belfast
United Kingdom



Catherine Armwood-Gordon
Tennes. State Univ.
USA



Monique Head
University of Delaware
USA



Eva Lantsoght
Delft Univ. of Technology
Netherlands



Jun Wang
Univ. of Colorado
Denver USA

International Advisory Committee and Secretary



Riadh Al-Mahaidi
Swinburne University of
Technology, Australia



Brahim Benmokrane
University of Sherbrooke,
Canada



Steve C.S. Cai
Louisiana State
University, USA



Nien-Yin Chang
University of Colorado
Denver, USA



Mark F. Green
Queen's University,
Canada



Issam Harik
University of Kentucky,
USA



Venkatesh Kodur
Michigan State
University, USA



Urs Meier
EMPA,
Switzerland



Hiroshi Mutsuyoshi
Saitama University,
Japan



John Myers
Missouri University
of S. and T., USA



Antonio Nanni
University of Miami,
USA



Steve Nolan,
Florida Department of
Transportation, USA



Saiid Saiidi
University of Nevada
Reno, USA



Jim Shiau
University of Southern
Queensland, Australia



Johan L. Silfwerbrand
KTH Royal Institute of
Technology, Sweden



Jongsung Sim
Hanyang University,
Korea



Ertugrul Tacioglu
University of California
Los Angeles, USA



Dan Tobias
Illinois Department of
Transportation, USA



Mark Williams
Walter P. Moore
USA



Yongcheng Ji
Northeast Forestry
University, China

Conference Organization

Conference Chair

Yail Jimmy Kim
University of Colorado Denver (USA)

Organizing Committee

Isamu Yoshitake (Chair)
Yamaguchi University (Japan)

Vanissorn Vimonsatit
Curtin University (Australia)

Xuhui He (China)
Central South University (China)

International Scientific Committee

Riadh S Al-Mahaidi (Australia)
Toshihiko Aso (Japan)
Brahim Benmokrane (Canada)
Steve Cai (USA)
NY Chang (USA)
Mark Green (Canada)
Issam Harik (USA)
Tatsumasa Kaita (Japan)
Andreas Kappos (UAE)
Venkatesh Kodur (USA)
Urs Meier (Switzerland)
Hiroshi Mutsuyoshi (Japan)
John Myers (USA)
Hideaki Nakamura (Japan)

Antonio Nanni (USA)
Sriram Narasimhan (USA)
Steven Nolan (USA)
Saiid Saiidi (USA)
Xianming Shi (USA)
Jim Shiau (Australia)
Johan L Silfwerbrand (Sweden)
Jongsung Sim (Korea)
Ertugrul Taciroglu (USA)
Su Tylor (UK)
Dan Tobias (USA)
Mark Williams (USA)
Takashi Yamane (Japan)
Zhiwen Zhu (China)



Bridge Engineering Institute Conference 2023 (BEI-2023)
Rome, Italy, July 17-20, 2023



Plenary Speakers

(alphabetical order)



Professor Issam E. Harik, Ph.D.
University of Kentucky, USA

Since joining the University of Kentucky in August 1982, Dr. Harik has directed or codirected research on more than 120 funded projects. Dr. Harik has directed or is currently directing the research of 55 Post Docs/visiting professors/scholars, 100 graduate students, 70 undergraduate students, and 24 high school students. Dr. Harik currently serves as a member of engineering societies and 4 committees; he chaired the Transportation Research Board Committee on Structural FRP (AFF80) from 2009 to 2015 and is a Council Member of the International Institute for Fiber Reinforced Polymer Composites in Construction and a member of the International Advisory Committee - Bridge Engineering Institute. He has organized, co-organized, and chaired national and international conferences, workshops, and technical sessions. Dr. Harik has authored or co-authored more than 360 technical publications.



Bridge Engineering Institute Conference 2023 (BEI-2023)
Rome, Italy, July 17-20, 2023



Plenary Speakers

(alphabetical order)



Professor John J. Myers, Ph.D., P.E.
Missouri University Science and Technology, USA

Dr. John J. Myers is Professor of Structural Engineering in the department of Civil, Architectural and Environmental Engineering at Missouri University of Science and Technology and is Deputy Director of the Missouri Center for Transportation Innovation. He served as Associate Dean for Academic Affairs in the College of Engineering and Computing from 2015 to 2019. Dr. Myers has been a member of the Missouri S&T faculty since 1999. He holds Ph.D. and M.S. degrees in civil engineering from the University of Texas at Austin and a bachelor's degree in architectural engineering from Pennsylvania State University. He previously served as the college's acting vice provost and dean. Dr. Myers oversees all curriculum and instruction in the College of Engineering and Computing along with development and implementation of strategic planning related to academic programs. He establishes plans for faculty development and recruitment as well as program development and also leads efforts in the development and implementation of the college's recognition and award structure.



Plenary Speakers

(alphabetical order)



Professor Antonio Nanni, Ph.D., P.E.
University of Miami, USA

Dr. Antonio Nanni, President of the American Concrete Institute (ACI), is a structural engineer interested in construction materials, their structural performance, and field application. His interests are in the field of buildings and civil infrastructure sustainability, monitoring and renewal. He is the Co-Director of two federally funded centers: NSF Industry/University Cooperative Research Center (I/UCRC) for the Integration of Composites into Infrastructure (CICI); and, US DOT University Transportation Center on Research on Concrete Applications for Sustainable Transportation (RE-CAST). In the past 30 years, he has obtained experience in concrete and advanced composites based systems as the principal investigator of projects sponsored by federal and state agencies, and private industry. Over the course of this time, his constant efforts in materials and structures research have impacted the work of several technical committees in the US and abroad. Dr. Nanni is the Editor-in-Chief of the ASCE Journal of Materials in Civil Engineering and serves on the editorial board of other technical journals. He has advised over 60 graduate students pursuing MSc and PhD degrees, and published over 200 and 310 papers in refereed journals and conference proceedings, respectively, in addition two co-authoring two books. Dr. Nanni has maintained a balance between academic and practical experience and has received several awards including: 2014 IIFC Medal, International Institute for FRP in Construction; ASCE 2012 Henry L. Michel Award for Industry Advancement of Research; and, Engineering News-Record Award of Excellence for 1997, (Top 25 Newsmakers in Construction). He is a registered PE in Italy, FL, PA, MO, and OK.



Plenary Speakers

(alphabetical order)



Mr. Takashi Yamane, P.E.
Kyokuto Kowa Corporation, Japan

Takashi Yamane is the President of Kyokuto-Kowa Corporation, a prestressed concrete bridge construction company in Japan. He has been a registered Professional Engineer in Japan since 2006. He graduated from Kure National College of Technology and joined Kyokuto-Kogyo Corporation (formerly Kyokuto-Kowa Corporation) in 1980. Mr. Yamane earned a master's degree in civil engineering from the University of Nebraska, Lincoln, in 1995. His work experience includes design and construction of various types of prestressed concrete bridges, such as box girder bridges with a balanced cantilever construction, cast-in-place hollow slab bridges with span-by-span construction, and composite I-section girder bridges. Mr. Yamane led the engineering department and sales department of the company before becoming president. He had been a member of the Japan Prestressed Concrete Contractors Association, and chaired the committee on design guidelines for precast/prestressed concrete splice-girder bridges. He has published many technical papers and patents in the bridge engineering field.



Bridge Engineering Institute Conference 2023 (BEI-2023)
Rome, Italy, July 17-20, 2023



Plenary Speeches



A Review of 30 Years of Experience in Field Testing of Bridges

Issam Harik^{1*}

¹: University of Kentucky, Lexington USA; email: Harik@uky.edu

*: corresponding author

Keywords: Bridges, Steel, Truss, Concrete, Dynamic, Static, Rating

Abstract: A review is presented of the author and his team's experience with field testing of more than 30 bridges in Kentucky. From the late 1980s to late 1990s, long span bridges over the Ohio and other rivers were primarily tested to evaluate their seismic vulnerability when subjected to projected earthquakes. Two cable stay bridges were also tested prior to opening to traffic to capture their baseline dynamic properties for comparison with properties derived from future tests. From the mid-1990s to 2022, field tests were primarily conducted on short and medium span bridges to evaluate the effectiveness of Heavy bridge deck overlays, bridges with and without diaphragms, effectiveness of bridge retrofit, and load rating of bridges. Highlights of bridge testing and evaluation are presented.

1. Introduction

The 1989 Loma Prieta Earthquake highlighted the seismic risk to double deck highway bridges with the partial collapse of the San Francisco-Oakland Bay Bridge and the Cypress Viaduct. Following the earthquake, the Federal Highway Administration (FHWA) commissioned the seismic evaluation of all double-deck bridges located in seismically active regions. Two of the bridges over the Ohio River are double deck bridges, the Brent-Spence Bridge between Covington, Kentucky (KY) and Cincinnati, Ohio, and the Sherman-Minton Bridge between Louisville, KY and New Albany, Indiana. Both bridges fall under the category of non-regular bridges and could not be evaluated using the 1996 AASHTO Standard Specifications and the 1998 AASHTO-LFRD seismic design and analyses methods. Consequently, more rigorous assessment is required, and is dependent on the bridge as-built conditions and the creation of accurate finite element models to assess their behavior during projected seismic events. The process includes preliminary finite element (FE) modeling, followed by non-destructive dynamic field testing and calibration of the FE model. The Brent-Spence Bridge (Fig. 1a) is the author's first involvement with field testing and evaluation of bridges (Harik et. al., 1997).

In addition to dynamic field testing for seismic evaluation of several long span bridges over the Ohio, Cumberland, and Tennessee Rivers (e.g., Fig. 1b), dynamic field testing was carried out to capture the baseline dynamic properties of the Owensboro and Maysville (Fig. 1c) cable stay bridges. While, for the Roebling Bridge (Fig. 1d), dynamic field testing was carried out to calibrate the finite element model used for load rating.

Static load testing was carried out on more than twenty short and medium span bridges to evaluate the effectiveness of the deployment of new design and construction details, e.g., removal of intermediate diaphragms (Griffin and Harik, 1997), or load rate the bridge for load posting (Hutchinson et al., 2021).



(a) Brent-Spence Double Deck Bridge



(b) US51 Bridge



(c) Maysville Bridge



(d) Roebling Bridge

Fig. 1. Bridges over the Ohio River assessed using finite element models calibrated based on dynamic field testing

2. Dynamic Field Testing for Seismic Evaluation of Bridges

Long span bridges have limited access to the floor beams along the length of the bridge. Consequently, acceleration measurements are collected by placing accelerometers on the deck. Since these bridges are main thoroughfares and bridge closure is not an option, one lane of traffic is generally allocated for field testing, and for a brief period of 2 to 3 hours when traffic volume is low (e.g., Sunday morning). Ambient vibration measurements under traffic and wind induced excitations are recorded along the bridge at various locations preselected from the preliminary finite element model of the bridge.



Following testing, field data is analyzed to determine the natural frequencies and mode shapes of the bridge. The three-dimensional finite element model of the bridge is calibrated by adjusting the stiffness of the bridge members until an acceptable match is observed in few natural frequencies and mode shapes. Then, the calibrated finite element model is used for the seismic time history response analysis for projected earthquakes. The analysis reveals deficiencies requiring further evaluation to determine retrofit measures.

2. Static Field Testing for Load Rating

Field testing for load rating has generally been carried out on bridges whose structural plans are not available. The lack of information about the bridge often yields overly conservative theoretical load ratings leading to load postings that may exclude school buses and emergency vehicles from traversing the bridges.

Field testing is carried out using loaded trucks with measured axle weights. Strain gauges, and LVDTs where applicable, are placed at predetermined stations along the bridge. The data gathered during the positioning of the truck axles at designated locations along the bridge is used to load rate the bridge.

3. Conclusions

Field testing has been carried out on more than thirty bridges in Kentucky by the author and his team since the late 1980s. The primary advantage of testing and evaluation of bridges is the “accurate” determination of the as constructed or current condition of the bridges. Such knowledge is essential in the evaluation of seismic vulnerabilities, load posting, new materials, structural systems, etc., and in the decision making on whether to replace or strengthen a bridge, limit vehicle weights, etc. Such decisions are essential for the safety of the safety of the transportation system.

4. References

- Griffin, J.J. and Harik, I.E., 1997. Experimental Analysis and Analytical Modeling of Bridges with and Without Diaphragms, 14th International Bridge Conference, Pittsburgh, Pennsylvania, 122-127.
- Harik, I.E., D. L. Allen, R. L. Street, Guo, M.W., Graves, R.C., Harrison, J., and Gawry, M. J. 1997. Free and Ambient Vibration of Brent-Spence Bridge, ASCE Journal of Structural Engineering., 123(9), 1262-1268.
- Harik, I.E., D. L. Allen, R. L. Street, Guo, M.W., Graves, R.C., Harrison, J., and Gawry, M. J. 1997. Seismic Evaluation of Brent-Spence Bridge, ASCE Journal of Structural Engineering., 123(9), 1269-1277.
- Hutchinson, C., Peiris, A., and Harik, I.E., 2021. Load Testing and Rating of a Concrete Arch Bridge, International Conference on Structural Engineering and Construction Management (ICSECM 2021), Kandy, Sri Lanka, 16 pp.



Performance-Based Electrochemical Analysis of an Innovative Magnesium Phosphate Cement Coating to Mitigate Mild Steel Bar Corrosion

John J. Myers^{1*}, Fan Zhang, and Hongyan Ma

¹: Missouri University of Science and Technology, Rolla, Missouri, USA; email: jmyers@mst.edu

*: corresponding author

Keywords: magnesium potassium phosphate cement; ribbed steel bars; coating; anti-corrosion; double protection system.

Abstract: Corrosion of steel is the largest threat to concrete structures including bridges whether it is a superstructure element or substructure element. In the United States, the total direct cost of corrosion is estimated at \$276 billion per year, which is 3.1% U.S. gross domestic product (GDP). Preventing and mitigating steel corrosion is critical to ensure long service-life in a RC structure. This study engages in the investigation of the anti-corrosion performance of rebar in magnesium phosphate cement (MKPC) coating and ordinary Portland cement (OPC) coating detailed the electrochemical properties from the open-circuit potential (OCP), polarization resistance (PR) and electrochemical impedance spectrometer (EIS), and morphology from scanning electron microscope (SEM). While the MKPC coating holds promise for new construction, the focus of this paper will be to examine the laboratory results to date and how it may be most suitable for rehabilitation of corrosion damaged mild reinforcing steel often found in older bridge bridges and infrastructure elements exposed to harsh exterior environments. This study investigated how MKPC performed compared to traditional OPC and was benchmarked to black steel samples. The results show that the MPC coating layer offered far better corrosion protection than OPC coating and hold great promise for a new innovative coating technology to mitigate mild steel corrosion in an economical sustainable fashion.

1. Introduction

Currently, the most efficient and common method to protect mild steel bars in an external corrosive environment is by building a chemical or physical barrier between the steel and environment. Improving the anti-corrosion performance of reinforcement in concrete can be achieved by modifying the ordinary Portland cement's cementitious protective cover (i.e., using a specific type cement, adding a super-plasticizer or other admixtures [1] and changing the water-cement ratio, or by using the cathodic method to protect the bars (i.e., hot-dip galvanized coating [2] and magnesium alloy anode [3]) or by providing a special coating over bars before casting fresh concrete, such as fusion bonded epoxy and enamel coating [4]. In addition, another mechanism is to form a passive film on the steel surfaces to prevent the corrosion process. One of the most common is the passive film formed due to high alkalinity from the ordinary Portland cement system [5]. However, current methods of preventing corrosion have different limitations or flaws. Incomplete coating over the entire surface of the bars will lead to small pits by human error, which affects the long-term performance of corrosion resistance [6-8].

Magnesium potassium phosphate cement (MKPC) is made of dead-burned magnesium oxide (MgO), the calcination temperature is 1000-1500 °C (1832 to 2732 °F), and potassium dihydrogen phosphate, KH_2PO_4 (KDP) through an acid-based chemical reaction. Compared to traditional concrete, MKPC possess many beneficial characteristics, such as high early-strength, favorable bond strength to old concrete and steel, and a low permeability with good durability characteristics. Therefore, magnesium potassium phosphate cement holds great promise as a fast repair material for reinforcement concrete structures due to its fast-setting nature and good steel corrosion inhibition capacity.

2. Experimental Details

2.1 Materials

A dead burned magnesia (DBM) and a chemical reagent of 99% purity potassium dihydrogen phosphate (KH_2PO_4 , KDP) were supplied by Martin Marietta Magnesia Special Ties, LLC from Manistee MI, United States and ICL Specialty Fertilizers-Americas from Summerville SC, United States, respectively. The Type I Portland cement (PC) supplied by the LafargeHolcim Ltd building materials company was used to produce specimens coated with ordinary Portland cement paste as one comparison group. This group was compared with the specimens coated in magnesium potassium phosphate cement paste.

2.2 Specimen Types, Solution Exposure and Coating Process

In this research, three testing sample conditions were investigated: Group I (UN) is the bare mild steel bar without any surface treatment. The samples of Group II (OPC) were coated with ordinary Portland cement paste. Group III (MKPC) is mild steel bar coated with magnesium potassium phosphate cement paste. The MgO to KDP (M/P) mole ratios and water to binder (w/b) ratios of the MKPC paste using in the research are 6 and 0.18, respectively, and the retarder was not used in this research. Since the compressive strength of MKPC paste was about 27.58 MPa (4000 psi) at the seven days testing age, the same compressive strength for OPC paste was needed, thus, the 0.38 w/b ratio for OPC paste was used in this research.

The 3.5 wt.% NaCl corrosion solution was made by mixing purified sodium chloride with deionized water, so it means that the chloride concentration is about 0.6 mol/L. After magnetic stirring in an indoor environment [temperature is 20 ± 2 °C (64 to 72 °F) and air humidity is $55 \pm 10\%$], all samples were immersed into this solution. Before the electrochemical test, conductivity and temperature of the 3.5 wt.% NaCl corrosion solution were determined by a Hanna Instruments HI5522 Meter. These two values stabilize at 55.0 ± 5 mS/cm and 20 ± 2 °C (64 to 72 °F), respectively. During the entire EC test period, the conductivity and temperature of the corrosion solution was measured in the same way, the values kept stable, and no changes occurred. Furthermore, during the EC test, the pH value of corrosion solution also was monitored.

3. Test Methods

The electrochemical measurements and data were performed and collected by using a typical three-electrode setup. A 25.4 x 25.4 x 0.254 mm (1 x 1 x 0.01 in.) platinum sheet, a saturated calomel electrode (SCE) and the prepared specimens, as shown in Fig. 1, were used as counter electrode (CE), reference electrode (RE) and working electrode (WE), respectively. The EC test setup is shown in Fig. 2.

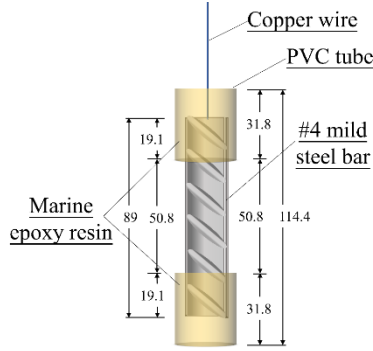


Fig. 1. Geometry of rebar samples (unit: mm)

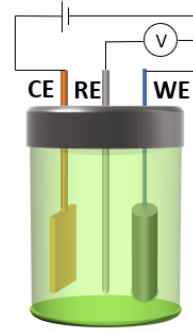


Fig. 2. Three-electrode setup

In addition to the EC testing, specimens underwent the SEM test using a Helios Nanolab 600 coupled to an energy dispersive X-ray spectroscopy (EDS), which was used to analyze the distribution of chemical elements of the cross section of specimens from the inner substrate mild steel part to outside coating part. The surfaces of substrate steel of MKPC specimens underwent the XPS test to analyze the chemical group formed due to the reaction between MKPC paste and mild steel rebar. The TG/DTA test was conducted on the prepared treated powder by using a TA instruments SDT Q600 under nitrogen atmosphere. To analyze the chemical composition of cementitious coating, X-ray diffraction (XRD) data of prepared specimens were collected by a Panalytical X'pert Pro MPD diffractometer.

4. Results and Discussion

Due to length requirements of the paper, highlights of the above-mentioned experimental tests will only be presented. Fig. 3 shows the corrosion maps of three sample types, which were immersed into 3.5 wt.% NaCl corrosion solution and tested under the same indoor environment, after the 5376 hours (224 days) electrochemical test. In these figures, the degree of corrosion trends to become weak from the samples without coating compared to the samples with ordinary Portland cement coating, and lastly, to the samples with magnesium potassium phosphate cement paste coating.

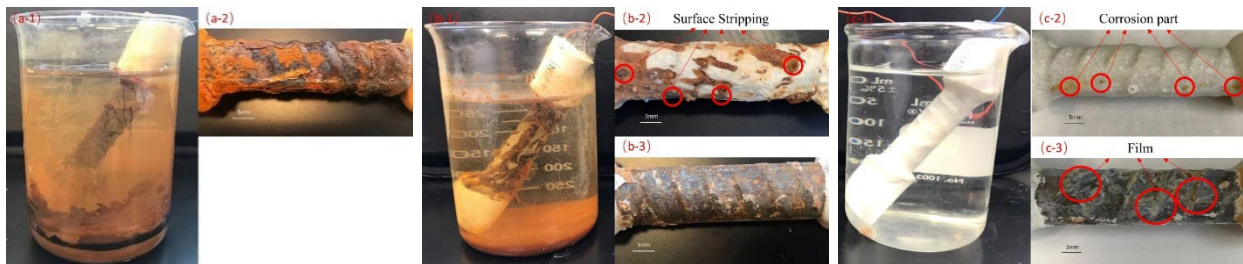


Fig. 3. Bar surface conditions of samples after 5376 hours EC test for: (a) UN, (b) OPC and (c) MKPC.

Table 1 shows the values of corrosion current density (I_{corr}) and corrosion potential (E_{corr}) which were extracted from potentiodynamic polarization plots, and the corrosion rate (CR) was calculated based on (1):

$$CR = \frac{I_c \cdot K \cdot EW}{d \cdot A} \quad (1)$$

where CR is corrosion rate, I_c is the corrosion current in Ampere, K is the constant that defines the units of the corrosion rate, EW is equivalent weight (in g/equivalent), d is the density, and A is the sample area. This shows the significant magnitude of order in corrosion rate reductions.

Table 1. Parameters from potentiodynamic polarization curves for OPC and MKPC specimens.

Time (hours)	E _{corr} (mV/SCE)		I _{corr} (μA/cm ²)		Corrosion rate (mm/year)	
	OPC	MKPC	OPC	MKPC	OPC	MKPC
5	-868.568	-997.484	14.763	7.903	0.17128	0.09169
1344	-953.089	-969.436	27.453	5.971	0.31851	0.06928
5376	-825.883	-999.615	27.051	2.051	0.31385	0.02379

5. Concluding Remarks

This study was developed to investigate and evaluate the steel bar anti-corrosion performance under the protection of the ordinary Portland cement paste and magnesium phosphate cement paste coating referred to as OPC and MKPC, respectively in this work.

- The MKPC coating impedance kept increasing until the 3369 hours (140 days) and maintained stability to the end of test in the corrosive environment-increasing around 7 times from the first test, supporting that the MKPC coating paste developed a far better excellent anti-corrosion performance than OPC coating.
- The MKPC samples' integral coating demonstrated no flaws after 5376 hours (224 days), therefore the magnesium potassium phosphate cement paste coating displayed strong robust properties to delay the corrosion rate.
- The MKPC material may be considered to be practical for repair as well some underwater construction and some traditional reinforcement concrete structures to reduce the corrosion rate and to eventually extend service life of the structure.

6. References

- ¹Shi, X., et al., *Strength and corrosion properties of Portland cement mortar and concrete with mineral admixtures*. Construction and Building Materials, 2011. **25**(8): p. 3245-3256.
- ²Sistonen, E., A. Cwirzen, and J. Puttonen, *Corrosion mechanism of hot-dip galvanised reinforcement bar in cracked concrete*. Corrosion Science, 2008. **50**(12): p. 3416-3428.
- ³Parthiban, G., et al., *Cathodic protection of steel in concrete using magnesium alloy anode*. Corrosion Science, 2008. **50**(12): p. 3329-3335.
- ⁴Tang, F., G. Chen, and R.K. Brow, *Chloride-induced corrosion mechanism and rate of enamel- and epoxy-coated deformed steel bars embedded in mortar*. Cement and Concrete Research, 2016. **82**: p. 58-73.
- ⁵Feng, X., et al., *The degradation of passive film on carbon steel in concrete pore solution under compressive and tensile stresses*. Electrochimica Acta, 2011. **58**: p. 258-263.



- ⁶Behzadnasab, M., S. Mirabedini, and M. Esfandeh, *Corrosion protection of steel by epoxy nanocomposite coatings containing various combinations of clay and nanoparticulate zirconia*. Corrosion Science, 2013. **75**: p. 134-141.
- ⁷Tang, F., et al., *Corrosion resistance and mechanism of steel rebar coated with three types of enamel*. Corrosion Science, 2012. **59**: p. 157-168.
- ⁸Etteyeb, N., et al., *Corrosion protection of steel reinforcement by a pretreatment in phosphate solutions: assessment of passivity by electrochemical techniques*. Corrosion engineering, science and technology, 2006. **41**(4): p. 336-341.



Diagnostic Load Testing of a Bridge Before and After Rehabilitation

Jiayi Ding¹, Nicolas Begasse², Adriana Toro³, Francisco De Caso⁴, and Antonio Nanni^{5*}

¹: HDR, Doral, FL, USA; email: jiayi.ding@hdrinc.com

²: HDR, Doral, FL, USA; email: nicolas.begassededhaem@hdrinc.com

³: Broward County, FL, USA; email: atoro@broward.org

⁴: University of Miami, Coral Gables, FL, USA; email: fdecaso@miami.edu

⁵: University of Miami, Coral Gables, FL, USA; email: nanni@miami.edu

*: corresponding author

Keywords: Sonovoid bridge; deterioration; load testing; rehabilitation technique; serviceability

Abstract: This paper provides the experimental results of two diagnostic load tests conducted on a Sonovoid® (i.e., prestressed concrete voided slab) bridge in Broward County, FL, which was built in the late 80's. Diagnostic load tests were conducted pre- and post-rehabilitation to evaluate the bridge's behavior and effectiveness of rehabilitation technique. The collected data was utilized to determine the lateral load distribution, both before and after rehabilitation. Actual live load distribution factors were calculated based on deflection and strain measurements. Among the data collected were: a) concrete longitudinal strains and vertical deformations of slab units within the tested span; and, b) strains in dowel bars forming part of the repairs. Diagnostic load testing also provides the decision-making tool for evaluating this repair technique for similar bridges in the future. Considering that most of this rehabilitation work was performed under the bridge, the need for lane closure is significantly reduced. Due to the novelty of the rehabilitation technique, load testing was necessary to evaluate its effectiveness.

1. Introduction

Diagnostic load tests (Olaszek et al., 2014) are the most common type of testing techniques used in new bridges as well as existing ones. The load test method can be used to check several in-situ parameters for a given bridge (Lantsoght et al., 2017) as well as the verification of the design assumptions and analytical models used for design (AASHTO 2017). The verification of the design assumptions can be carried out by comparing the measured structural response and the analytically determined response. Two diagnostic load tests were conducted on a Sonovoid® bridge to evaluate the behavior characteristics of the bridge under static and dynamic (moving) loads, both before and after rehabilitation. The load tests aimed to determine the load distribution between the Sonovoid® beam elements spanning a segment of the bridge and provide experimental data for modeling and verification purposes.

Sonovoid® bridge. The bridge, located in Broward County, FL, is a five-span structure, with north and south bound traffic and pedestrian sidewalks, where each span is 36-ft. (10.97-m) long as seen in Fig. 1(a). The spanning elements are prestressed concrete hollow Sonovoid® slab elements as seen in Fig. 1(b). The north and south bound superstructures are separate structures connected only by a raised median slab. At all other spans, the superstructure is one continuous structure. The test Span 4 (south bound) consists of a total of 12 Sonovoid® elements.

The rehabilitation technique utilizes transverse Near-Surface-Mounted (NSM) stainless steel dowels with Carbon-Fiber-Reinforced-Polymers (CFRP) laminates. Each dowel bar is inserted in a 1¼ x 1¼ in. (32 x 32 mm) groove and filled with epoxy. CFRP laminates are then provided on the bottom face of slab elements over the dowels. This technique was selected for further investigation because of its potential efficiency, lower cost, and minor impact to traffic during construction. The enhanced live load distribution would result in less flexural demand on the individual slab units. In addition, enhancing the interconnection between adjacent units would mitigate relative movement, and ultimately prevent the existing shear keys from further cracking and deterioration. Externally bonded CFRP laminates were applied to support the concrete cover against the peeling forces induced by the dowel steel bars. In addition, CFRP is intended to provide an enhanced level of protection against possible corrosion of the steel bars.

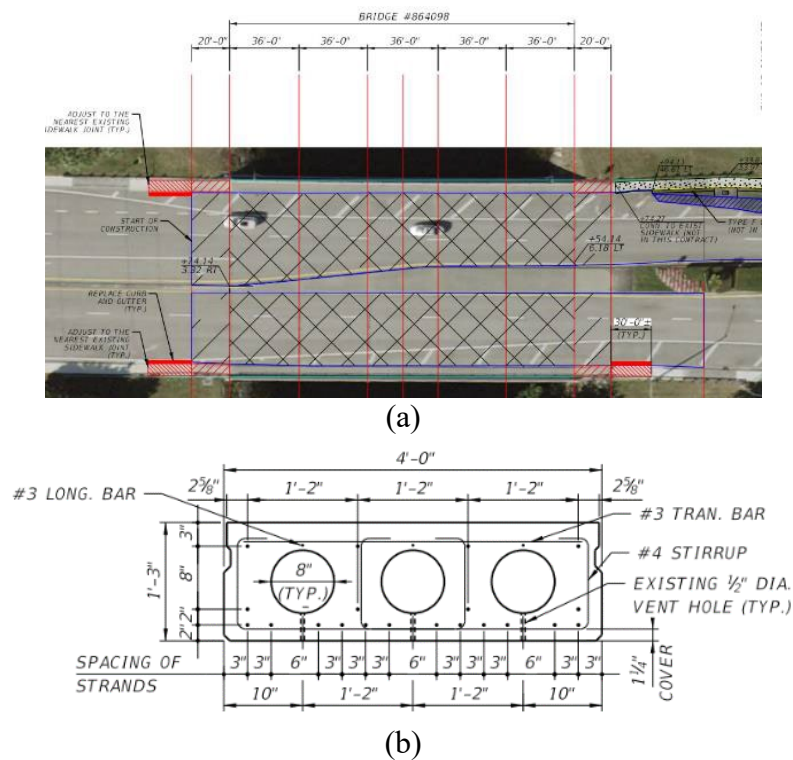


Fig. 1. Sonovoid® bridge, located in Broward County, FL: (a) aerial view, and (b) typical unit section (1 in.=25.4 mm; 1 ft. = 305 mm)

Instrumentation. Instruments used in the load tests were: four spring-loaded Linear Variable Differential Transformers (LVDTs); 12 spring-return linear potentiometers; eight spring-loaded dial gauges with an internal closed-circuit television (CCTV) used to visually monitor deflections real time; two inclinometers with integrated sensor electronics; 14 wire strain gauges bonded to concrete; 10 rosette gauges bonded to steel dowels. A dedicated suspended access scaffolding with a rigid support frame system was installed under the bridge to hold and secure all instruments during the load tests (See Fig. 2). The scaffolding system was fastened to the bent caps located on either side of Span 4, providing a means of accessing the underside of the bridge for instrument installation, maintenance, and removal before, during, and after testing. To enable this, a floating platform over the water was utilized.

Load Protocol. Six Load Cases (LCs) were considered as part of load protocol for the bridge Load Test 1 (pre-rehabilitation), while seven LCs were considered for Load Test 2 (post-rehabilitation). For each LC, the same fully-loaded truck with gross weight of 67,440 lb. (300 kN) was used. For the static load tests of each LC, the truck remained stationary on Span 4 with double rear axles placed on either side of the mid-span line. For the dynamic load tests, the truck moved over the bridge in the south bound direction at an approximate constant speed of 10 mph (16 kph), driving over a 4 x 4 in. (100 x 100 mm) piece of lumber placed perpendicular to the travel direction. Two load repetitions per each LC and load protocol were performed.



Fig. 2. Overall view of instruments on the scaffolding

2. Results

The results herein reported are based on average net values (absolute magnitude) for the two repetitions. The average net measurements are computed by the difference between the initial reading and the average maximum value recorded at the time of load application.

Linear Variable Displacement Transducers (LVDTs). Only LVDT readings for Load Test 1 (before repairs) are summarized in and Table 1 for the dynamic load protocol. LVDTs measured the vertical (LV2 and LV4) and horizontal (LV1 and LV3) mid-span displacements (deflections) of slab units No. 4 and No. 10, respectively (numbered from the west side).

Table 1. LVDT mid-span displacements for the dynamic load for Load Test 1(1 in.= 25.4 mm)

Equipment ID	Unit	Slab #	Dynamic Load Protocol					
			LC1D	LC2D	LC3D	LC4D	LC5D	LC6D
LV2 (Vertical)	in.	4	0.144	0.193	0.147	0.100	0.084	0.053
LV4 (Vertical)		10	0.025	0.050	0.087	0.134	0.182	0.219
LV1 (Horizontal)	in.	4	0.012	0.011	0.011	0.011	0.011	0.012
LV3 (Horizontal)		10	0.014	0.025	0.028	0.021	0.020	0.018

Potentiometer: Static Load Tests. Fig. 3 shows the vertical displacement differences between Load Test 1 and Load Test 2 under LC2 providing a representation of the relative shear transfer between the slab units.

Potentiometer: Dynamic Load Tests. Deformation results of dynamic load protocol were based on maximum readings of each Load Case. Results like those shown in Fig. 3 were obtained for vertical displacement differences between Load Test 1 and Load Test 2.

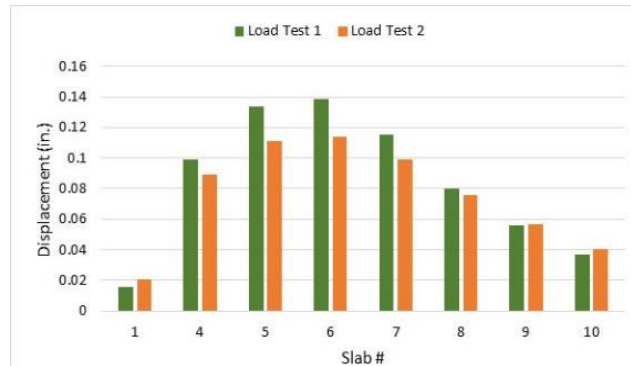


Fig. 3. Difference between Load Tests 1 and 2 for static LC2 (1 in. = 25.4 mm)

3. Discussion

- The results of the first and second repetitions across various LCs and load protocols demonstrated a high degree of repeatability with minimal differences.
- Dial gauges and CCTV effectively monitored the bridge responses and validated vertical displacements during load tests.
- Horizontal displacements were relatively constant and negligible, across the different Load Cases and load protocols. Vertical displacements correlated directly to the position of the truck and Load Case, where there was a relatively high transfer of shear load, based on net deflections (about 75% of the peak displacement) to the adjacent unloaded slab units.
- Dynamic loading imposed higher demand on slab units with varying levels of transfer depending on the location of the applied load.
- The dynamic load protocol resulted in higher peak displacements, on average 50% more than under static loads. Similarly, a relatively higher transfer of shear loads, based on net deflections to adjacent unloaded slab units were observed.
- Longitudinal concrete strain responses were effectively recorded. Strains measured under dynamic load protocol were on average 60% more than under static loads.
- Slab unit No. 4 rotations correlate closely to measured mid-span deformations. This indicates that the supports of Slab unit No. 4 have limited restraints.
- Composite action between the stainless-steel dowels and Sonovoid® elements was confirmed, with reduced total magnitude of deflections compared to pre-rehabilitation.

4. Conclusions

This paper provides the experimental results of the diagnostic bridge pre- and post- rehabilitation load tests conducted on a segment of the Sonovoid® bridge. Tests consisted of combining six to seven different Load Cases by positioning a fully loaded truck at different locations on bridge span No. 4 (South Bound) engaging different slab elements, with two repetitions for each load case, and two different load protocols (static and dynamic). Overall, the two diagnostic load tests proved to be a highly effective tool for assessing the degree of success of the chosen rehabilitation intervention. By providing the owner and design team with quantitative data and a benchmark for future evaluations.

5. Acknowledgements

The authors would like to thank NSF for partial financial support under grant No. 1916342.



Bridge Engineering Institute Conference 2023 (BEI-2023)
Rome, Italy, July 17-20, 2023



6. References

AASHTO. 2017. "Manual for Condition Evaluation of Bridges," AASHTO, 3rd Edition Washington, DC

Lantsoght, E., der Veen, C., de Boerd, A., Hordijk, D.A. 2017. Bridge engineering institute conference, Journal of Bridge Engineering Institute, 1(2), 36-45.

Olaszek, Z., Lagoda, M., and Casas, J.R. 2014. "Diagnostic Load Testing and Assessment of Existing Bridges: Example of Application," Structure and Infrastructure Engineering, 10, 834-842

Current State of Expressways and New Technologies for Bridge Deck Maintenance in Japan

Takashi Yamane^{1*}

¹: Kyokuto Kowa Corporation, Hiroshima, Japan; email: tyamane@kkn.co.jp

*: corresponding author

Keywords: Precast concrete slabs; Joint; Loop joint; ELSS joint; Productivity; Slab replacement

Abstract: This paper outlines the service and damage status of expressways in Japan, as well as repair and renewal technologies. The decks of expressway bridges in Japan have been found to be severely damaged, and major renewal projects centered on deck repair and renewal are therefore underway. One challenge in these projects is shortening the traffic restriction period. Therefore, this paper outlines three technologies that can shorten this period when repairing/renewing a bridge deck. The first is a technology for removing an existing deck; the second is a technology for bonding PC slabs when renewing a deck; and the third is a preventive maintenance technology that does not require any traffic restrictions.

1. Introduction

In Japan, where the popularization of the automobile occurred later than in the US and Europe, expressway construction also began later. The first expressway opened in Japan in 1963. Construction has progressed rapidly since then, and an expressway network extending over approximately 9000 km is in place today. Approximately 3700 km (roughly 40%) of this network consists of roads that have been in service for 30 years or more (Fig.1).

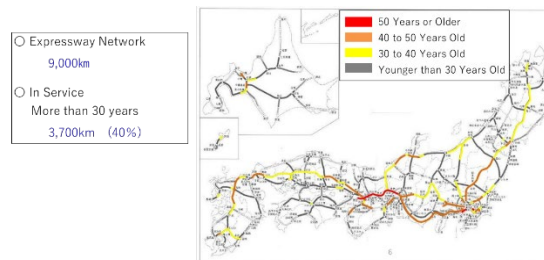


Fig. 1. Expressway network in Japan

When we look at the expressways by type of bridge structure, prestressed concrete bridges account for 35%, reinforced concrete bridges for 32%, and steel bridges for 33%.

Shifting our focus to the damage status of expressway bridges, the most severe damage is to the reinforced concrete decks of steel bridges. Survey results show that the prominent causes are salt damage and heavy traffic (Fig. 2).

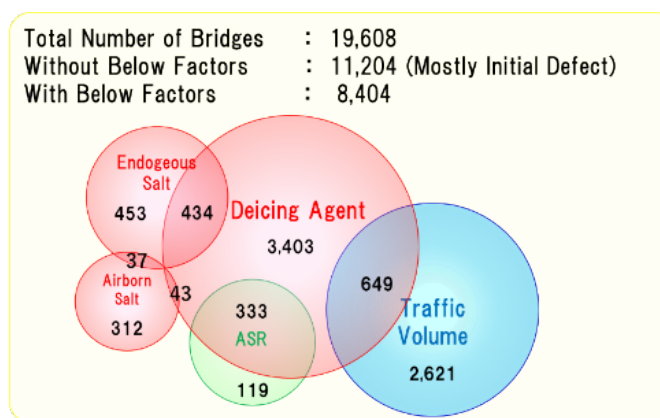


Fig. 2. Cause of damage of expressway bridges

2. Outline of Renewal Project

In 2014, the three companies that manage Japan's main expressway network (East Nippon Expressway Company Limited, Central Nippon Expressway Company Limited, and West Nippon Expressway Company Limited) designed major renewal and repair projects and embarked on their implementation. The scale of these projects is extremely large, with the combined cost of the major renewal and repair projects totaling \$22,271,000,000. Of this amount, deck slab replacement work accounts for approximately 55%, or \$12,170,000,000.

3. New Technologies for Bridge Deck Maintenance

3.1 Deck removal for composite girder bridge

Steel bridges include composite and non-composite structures. In composite structures, numerous studs are welded to the top flanges of the steel girders, making deck removal difficult and labor intensive. The technology introduced here is for removing the concrete deck slab of a composite steel girder bridge by cutting it into large blocks.

First, a cutter is used to divide the existing slab into blocks that can be lifted with a crane. Next, an electric wall saw is used to cut the middle of the studs from the top surface of the slab (Fig. 3).

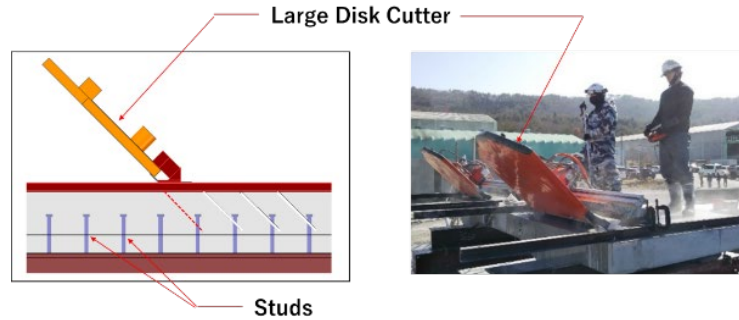


Fig. 3. Electric wall saw to cut the studs

This separates the stud heads from the steel girder, so there is very little resistance when the slab is pulled off the girder. Then, the slab is jacked up and removed in block units (Fig. 4). This technology can drastically reduce on-site labor and shorten the work period.

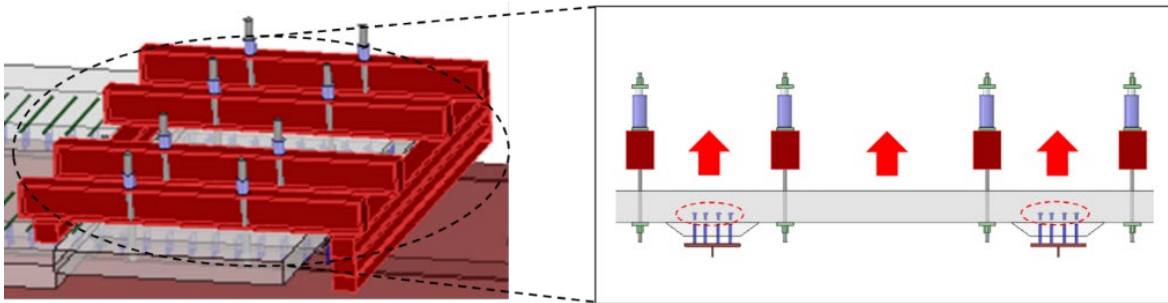


Fig. 4. Jack up block units

3.2 Panel to panel connection

This technology is applicable to works in which a bridge deck is constructed by connecting precast/prestressed concrete slabs on site. It enables connections between precast slabs, which conventionally have a reinforced concrete construction, to be made using only a filling material that is softer than the slab concrete (We call this system “ELLS Joint.”). Safety, durability, drivability, and economic efficiency were confirmed by analyses and full-scale experiments. The deck is supported continuously in the driving direction by the steel girders and the wall balustrades. When this kind of deck is constructed using precast slabs, a filling material that is less rigid than the main body is used to fill the joints, so that the deck becomes an anisotropic slab. As a result, the bending moment in the driving direction is reduced, while the bending moment in the road width direction is increased. In response to this, the required strength is secured by increasing the number of PC steel bars in the precast slab (Fig. 5). Employing this joint structure results in reductions of 10% or more in manpower, number of workdays, and cost.

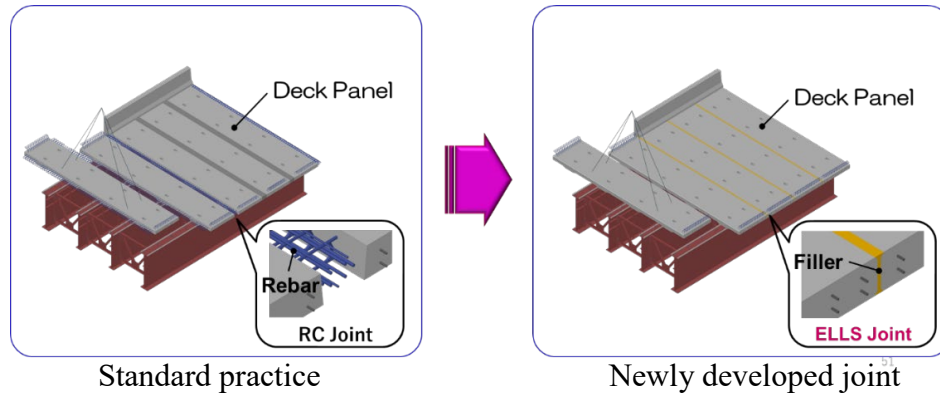


Fig. 5. Panel-to-panel connections

3.3 Lithium pressurized injection for preventive maintenance

Lithium pressurized injection is a technology that involves injecting a lithium nitrite solution at high pressure into the concrete. This technology was developed to inhibit internal expansion of concrete associated with the alkali-silica reaction by taking advantage of the nature of lithium ions. However, because the nitrite ions reach the rebar, this technology also has the effect of preventing rust on the reinforcing steel. Making use of the latter effect, rebar corrosion in the upper and lower surfaces of a deck slab can be prevented by injecting a lithium nitrite solution from the underside of the deck. Because all the work is done from the underside, this method does not involve traffic restrictions (Fig. 6). This is a very useful advantage in bridge maintenance, and we hope to expand the applications of this method in the future (Fig. 7).



Fig. 6. Lithium pressurized injection from underneath the deck



Fig. 7. Maintenance work without traffic regulation



Bridge Engineering Institute Conference 2023 (BEI-2023)
Rome, Italy, July 17-20, 2023



4. Conclusion

All three of the new technologies introduced in this paper have a proven track record in Japan. However, there are issues such as demonstrating effectiveness and improving work efficiency. We intend to improve the level of performance of these technologies by continuing to conduct experimental studies and on-site demonstrations.

5. Acknowledgments

We would like to take this opportunity to thank Dr. Yasushi Kamihigashi of the Central Nippon Expressway Company Limited who provided us with information about Japan's expressways.



Bridge Engineering Institute Conference 2023 (BEI-2023)
Rome, Italy, July 17-20, 2023



Materials and Performance



Quality of Lamination Structure Made by 3D Printing under Different Lamination Conditions

Yuji Yamada^{1*}, Tomoko Fukuyama², Yunmi Kim³,
Hiroharu Kamada⁴, and Dhruva N. Katpady⁵

¹: Yamaguchi University, Yamaguchi, Japan; email: y-yamada@yamaguchi-u.ac.jp

²: Ritsumeikan University, Shiga, Japan; email: tmkfkym@fc.ritsumei.ac.jp

³: Hanbat National University, Daejeon, South Korea; email: kymmiss123@naver.com

⁴: Polyuse, Kanagawa, Japan; email: hiroharu.kamada@polyuse.xyz

⁵: Fukuoka University, Fukuoka, Japan; email: dhruva@fukuoka-u.ac.jp

Keywords: 3D printing technology; Quality of interlayer; Lamination conditions

Abstract: In this study, specimens of lamination structure were made by 3D printing using rapid hardening mortar. In addition, lamination time and season were changed when made the specimens. In order to evaluate the quality of joining part, these specimens were investigated about the mechanical properties, the shrinkage properties and the air permeability.

1. Introduction

Recently, the 3D printing technology is attracting attention as a construction method which can achieve an automated construction. In the 3D printing technology, mortar is used to make filaments, and structures are made by laminating the filaments. However, there is concern about durability of interlayer in the lamination structure. Also, in Japan, there are extreme climatic changes throughout the year. Therefore, in the actual construction, the environmental effects such as temperature and moisture may affect the quality of interlayer in a lamination structure. In addition, mortar which is used to lamination by 3D printing has a characteristic of rapid hardening. Therefore, an usable time of mortar for good lamination is short compared with normal concrete, and it makes difficult to obtain the high durability. In this study, the specimens of lamination structure using rapid hardening mortar were made. In addition, lamination time and season were changed when made specimens. Also, these specimens were evaluated about mechanical properties, shrinkage properties and mass transfer resistance.

2. Experimental Outline

2.1 Mix proportion of mortar

Prepacked mortar which is generally used as a material of patchwork repair was used in purpose of making filaments. Conditions of mix proportion were W/C=36%, S/C=1.3. In addition, polyamide fiber (length: 10mm) was mixed at 0.2 % (vs. total volume of mortar), and also expansive materials (type of CSA) was included. In order to get the rapid hardening, polymer was mixed.

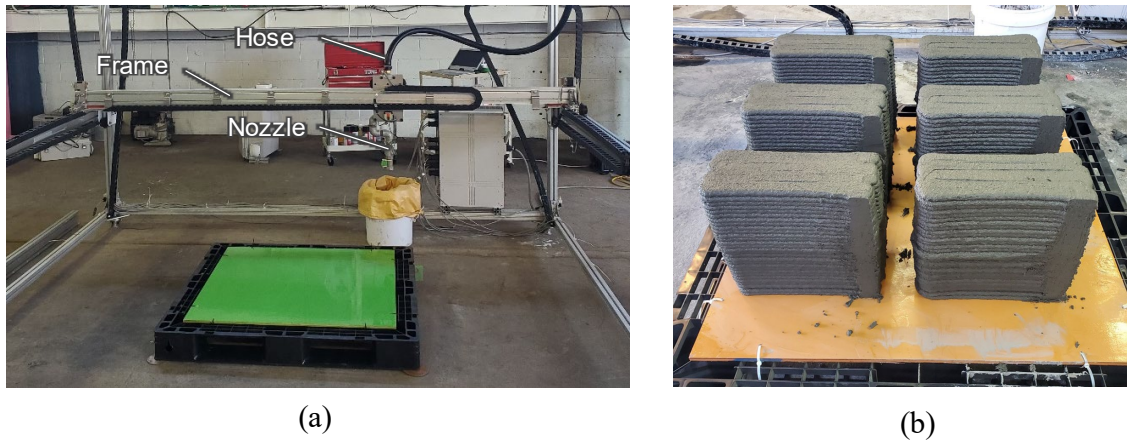


Photo. 1 Outline of 3DP specimen: (a) 3D printing equipment; (b) Overview of specimens

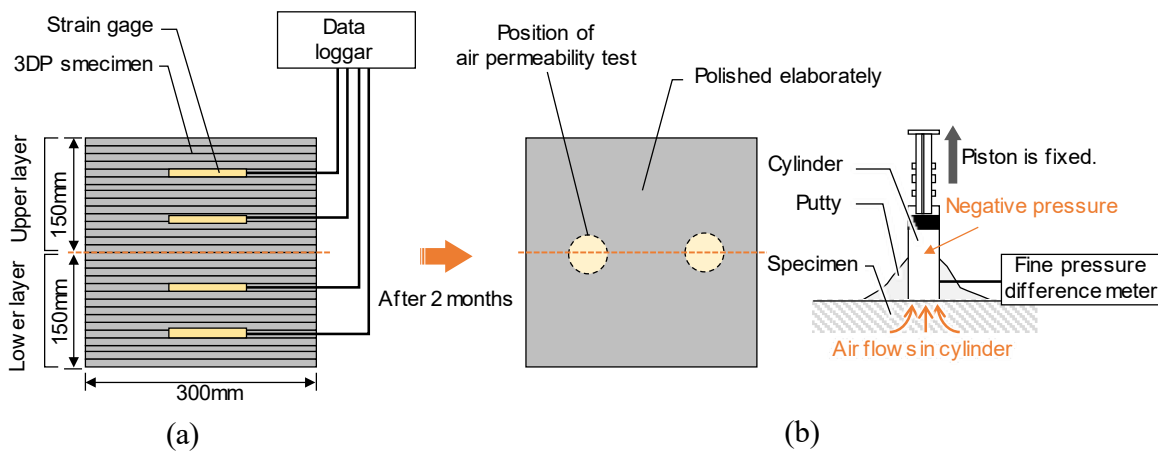


Fig. 1 Outlines of experiment: (a) Drying shrinkage test; (b) Air permeability test

2.2 Outline of Specimens

Outline of specimen is shown in Fig. 1. The specimens (3DP specimens) were made by 3D printing, as shown in Photo. 1. The lamination time between upper layer and lower layer was changed (0min. or 30min.). The specimens were made in summer (June) and autumn (October). After that, these specimens were exposed outside (environmental condition was general at mosphere) for 2 months (summer season specimen: June-August, autumn season specimen: October-December).

2.3 Test Methods

(1) Setting test of mortar

Setting test of mortar was conducted conforms to Japanese Industrial Standard (JIS A 1147).

(2) Mechanical Properties test

Compressive strength test was conducted. The specimens were cylinder (ϕ : 50mm, height: 100mm). The curing conditions were same with the above exposure conditions.

(3) Drying shrinkage test

The exposure specimens had been polished surface, and then those specimens were attached strain gages and measured the strain, as shown in Fig. 1 (a).

(4) Air permeability test

After the drying shrinkage test, exposure specimens were conducted the air permeability test by cylinder method (Watanabe et al. 2018). Outline of test method is shown in Fig. 1 (b). The joining part between a specimen and a syringe were sealed by a putty. The piston was pulled up and then fixed during 300second. variation pressure internal syringe was measured by a fine pressure difference meter.

3. Experimental Result and Discussion

3.1 Setting test results

The setting test results are shown in Fig. 2. Where, the air temperatures were the case of summer season: 30.1°C and the case of Autumn season: 23.5°C, mortar temperature were the case of summer season: 28.9°C and the case of autumn season: 22.3°C. The penetration resistance value of summer season was larger than that of autumn season. However, regardless of season, the time when penetration resistance value achieves 0.1N/mm² were less than 30 minutes. According to the research of the past (Okazawa and Sugamata, 2001; Matsushita and Sue, 2001), in order to prevent the cold-joint in construction of a concrete structure, the placing joint time interval must be shorter than the time which achieves the penetration resistance value = 0.1N/mm². It might be also similar in case of constructions by 3D printing technology too.

3.2 Results of drying shrinkage test

An example of the results in drying shrinkage test are shown in Fig. 3. The lamination time interval is 30minutes. The margins of the strain between the upper layer and the lower layer were large in case of autumn. The compressive strength of mortar were autumn season: 40.2N/mm² and summer season: 55.2N/mm². Therefore, the bonding strength between the upper layer and the lower layer of specimen which had been made in autumn season might be lower than that of summer. In addition, the autumn environment might be occurred the drying shrinkage easily compared with the summer environment due to the low moisture. From

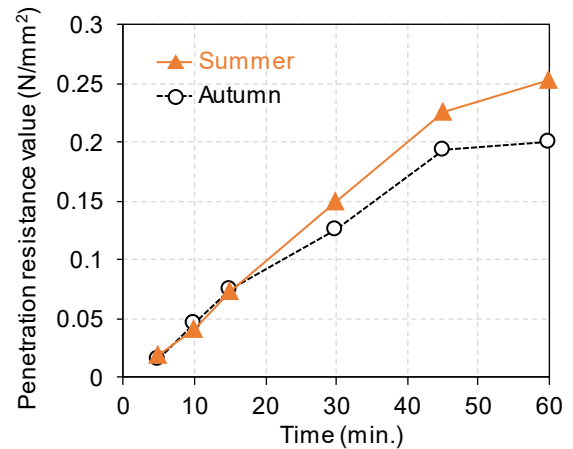
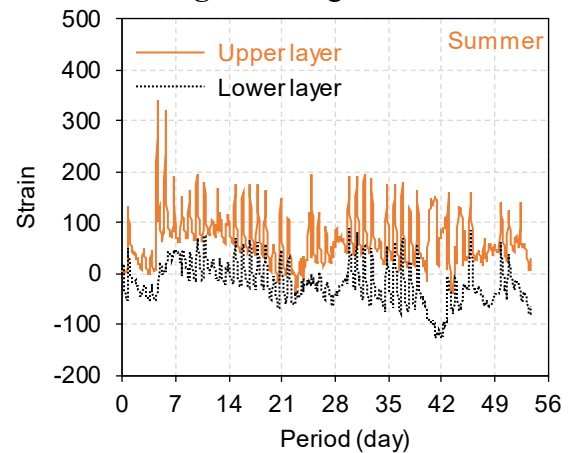
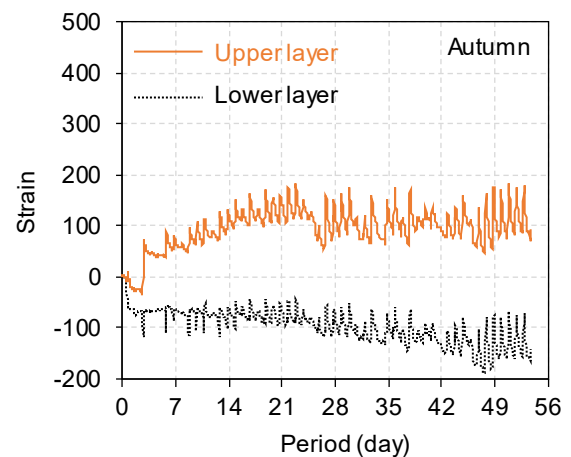


Fig. 2 Setting test results



(a)



(b)

Fig. 3 Results of drying shrinkage test:

(a) results of summer; (b) results of autumn

From

the above, these results assume to be effected by multiple cause including the physical properties of material and the environmental conditions.

3.3 Results of air permeability test

The results of the air permeability test are shown in Fig. 4. Where, the legends which are shown in Fig. 4 are “Season (Summer: S, Autumn: A)” - “lamination time interval (min.)”. A-0 and S-0 had the high airtightness, because the pressure fluctuations had been low. On the other hands, the pressure fluctuations of A-30 and S-30 had been striking. Therefore, A-30 and S-30 had the low airtightness compared with A-0 or S-0. In particular, the airtightness of A-30 was most inferior, because the pressure of A-30 rose faster than that of S-30. These results have a correlation with the results of the drying shrinkage test.

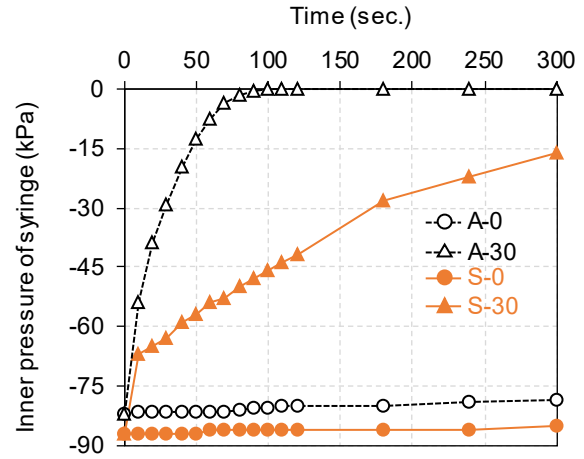


Fig. 4 Results of air permeability test

4. Summary

From the results of the drying shrinkage test and the air permeability test, the quality of the lamination gap was degraded, due to the time interval of lamination became the time which achieved at the penetration resistance value = 0.1N/mm². Also, a degree of deterioration was different, it was effected by multiple cause including the physical properties of material and the environmental conditions.

5. References

Satoshi Okazawa and Takumi Sugamata. 2001. Evaluation for part of placing on consolidated fresh concrete, Japan Concrete Institute, Concrete Journal, 39 (5), 83-88.

Hiromichi Matsushita and Yoshihiro Sue. 2001. A Study on Relationship between Condition of Placing on Consolidated Fresh Concrete and Occurrence of Cold Joint, Journal of Society of Materials Science, Japan, 50(8), 851-856.

Takeshi Watanabe, Kenjiroh Omoya, Kenta Kotani, Chikanori Hashimoto and Masayuki Sekigawa. 2018. Evaluation of Air Permeability of Cover Concrete by Simple Test Method Using Syringe, The 6th Japan-US NDT Symposium Emerging NDE Capabilities for a Safer World (Japan-US 2018).



Bond Strength Evaluation of Grout Materials for Closure Pour of Precast Concrete Bridge Deck Panels

Zhifu Yang¹

¹: School of Concrete and Construction Management, Middle Tennessee State University, Murfreesboro, Tennessee, USA; Zhifu.Yang@mtsu.edu

Keywords: Bond Strength; Grout Materials; Substrate Moisture; Curing temperature

Abstract: The use of full-depth precast concrete panels for rehabilitation of bridge decks allows fast installation and all-weather construction. The panel joints that are connected later with grout materials may de-bond under load, leading to a less desirable composite action. As a result, testing the bond capacity of various grout materials is essential to establish the quality and the serviceability of the closure pour. In this study, various prepackaged grout products (cementitious and epoxy) across US were requested and their bond strength was evaluated using flexural and slant shear bond tests. Different substrate moisture conditions (wet, SSD, and dry) as well as different curing temperature (23°C, 30°C, and 35°C) were used to prepare the composite specimens. Additionally, steel fibers were added to the grout materials and their effects on the bond capacity were investigated. It was found that most grout products showed acceptable to good bond capacity. Specifically, some products exhibited excellent bond strength. The surface moisture of substrate noticeably affected the bond capacity of grout products. However, different products showed different effects. Similarly, the curing temperature had great impacts on the bond strength. An increase in curing temperature mostly reduced the bond strength. Only a few products showed an increased bond strength at a higher curing temperature. Interestingly, for grout products with high bond strength, adding 3% steel fibers normally caused a reduced bond strength, while it significantly improved the bond strength for grout products with low bond strength.

1. Introduction

Conventionally, cementitious grouts, epoxy mortars or polymer concretes are used for the closure pour. While cementitious grouts are easier to mix and more compatible with the substrate; they are more prone to shrinkage. Oppositely, epoxy mortars or polymer concretes have extremely low permeability and dry shrinkage, as well as good adhesion with the substrate; but they are very sensitive to moisture variations and thermally incompatible with the substrate. As a result, testing of various types of grout materials under different service conditions is essential to establish the quality and serviceability of materials.

2. Materials, Proportions, and Experimental Programs

Twenty-five grout materials were collected from 16 different manufacturers. All products were prepackaged in 23-27kg bags or buckets. Twenty-three products were cementitious mortars/concretes and two products (#8 and #18) were epoxy-based mortars. The materials were mixed in a 0.06 m³ rotating drum mixer or in a bucket using a paddle mixer with a typical batch size of 25-32kg. Water was first added to the mixer or bucket and then the grout material was

introduced. An average water content recommended by the manufacturer was used, which typically resulted in a flowable mixture. The mixture proportion for the substrate concrete was: type I cement: water: 9.5mm crushed limestone: natural river sand = 1: 0.4: 2.43: 1.35. A water-reducing admixture and an air-entraining admixture were used to achieve a slump of 102 to 127mm, and a fresh air content of approximately 6.5%. The 28-day compressive strength of this concrete using 102x203mm cylindrical specimens was approximately 38.6 MPa. The substrate concrete was cured for 28 days, the fresh grout was poured into the mold to achieve the composite specimen. The flexural bond test was conducted on the composite specimens following ASTM C78 and the test setup is shown in Figure 1. The slant shear bond test was performed following the procedure similar to the one described in ASTM C882. The test setup is shown in Figure 1.

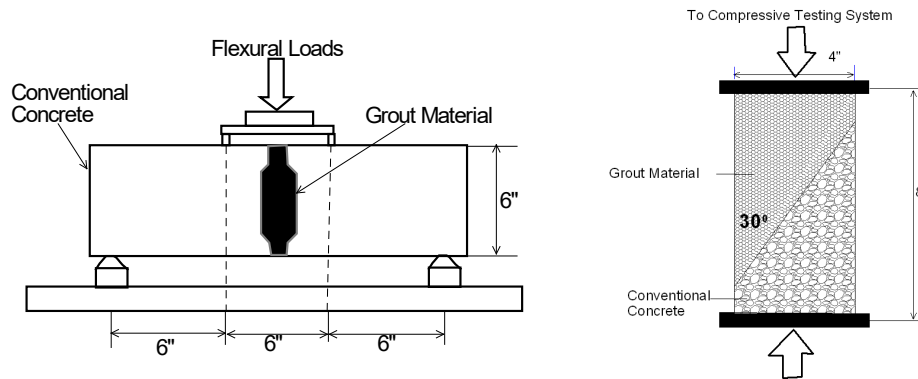


Fig. 1. Bond test setup

3. Results and Analysis

3.1 Effects of Substrate Surface Moisture on Bond Strength

The effects of substrate surface moisture on the bond strength and the failure plane are summarized in Table 1. The flexural bond strength varied widely with the substrate surface moisture conditions. Some grouts exhibited high flexural bond strength under all substrate surface moisture conditions; while some grouts including epoxy grouts, preferred dry substrate surface and some grouts favored wet or SSD substrate surface. When the moisture changed from SSD to wet, six products displayed a noticeable decrease in the flexural bond strength, thirteen products showed essentially insignificant changes in the flexural bond strength, and five products demonstrated a substantial increase in the flexural bond strength. Also, the failure plane did not change for most products. These results indicated that a wet substrate surface did not necessarily reduce the flexural bond strength. When the substrate surface moisture changed from SSD to dry, twelve products exhibited a reduced flexural bond strength, six products showed roughly equal flexural bond strength, and seven products even demonstrated a significant increase in the flexural bond strength. In addition, a slight increase in the interfacial failure was observed. A comparison of all these results suggested that a dry substrate would be more likely to reduce the flexural bond strength and cause a higher risk of debonding than a wet substrate. The effect of substrate surface moisture on the flexural bond strength also depended on the nature of the product. For examples, some products normally failed at the substrate at all moisture conditions. These grouts typically had high compressive strength and flowability. For low-strength grouts, failure normally occurred at the grout regardless of the moisture condition. For some grouts, the specimens normally failed along the interface despite of the moisture condition, indicating that these materials may be less penetrative. For the two epoxy grouts, dry

substrate typically showed better bonding and failure normally occurred at the substrate, whereas, wet or SSD substrates generally led to reduced bond capacity and resulted in the interfacial failure.

For the slant shear bond test, some products displayed almost equal slant shear bond strength at all three moisture conditions. Some products showed the highest slant shear bond strength with SSD, wet, or dry moisture condition. In general, ten products showed a noticeable reduction in the slant shear bond strength as the substrate surface moisture changed from SSD to wet. Six products demonstrated approximately the equal slant shear bond strength and eight products even displayed a significant increase in the slant shear bond strength. This again indicated that a wet substrate did not always reduce the slant shear bond strength. Similarly, when the substrate surface moisture changed from SSD to dry, ten products demonstrated a substantial increase, four products showed insignificant variation in the slant shear bond strength, and only ten products exhibited a reduced slant shear bond strength. This also indicated that a dry substrate surface did not always reduce the slant shear bond strength.

Table 1. Bond strength and failure plane (FP) of specimens with different substrate moisture.

Product ID	Dry		SSD		Wet		Dry		SSD		Wet	
	MPa	FP	MPa	FP	MPa	FP	MPa	FP	MPa	FP	MPa	FP
#1	2.8	I	4.1	IS	4.1	I	16.5	I	19.1	S	20.7	S
#2	5.6	S	5.7	S	4.8	S	19.6	S	22.3	S	23.3	S
#3	4.0	GSI	5.2	IGS	**	**	16.7	IGS	20.2	IGS	20.1	ISG
#4	2.6	I	4.5	I	4.4	G	11.5	I	10.4	I	17.8	I
#5	3.3	GS	4.6	S	5.2	S	21.1	GI	26.0	IGS	17.9	SI
#6	4.9	G	3.9	G	4.9	G	19.2	G	22.2	GS	18.4	G
#7	0.2	I	1.8	GI	1.0	GI	15.1	GIS	10.0	GI	7.0	IGS
#8	3.7	S	2.6	I	2.8	I	20.9	S	6.9	IG	17.0	IS
#9	1.2	I	3.6	G	3.8	G	18.6	SI	18.6	S	20.9	S
#10	4.1	G	4.1	G	4.1	G	16.7	IS	19.8	IG	20.0	SI
#11	3.1	GS	2.7	S	2.8	G	18.0	GIS	20.8	S	25.8	SG
#12	1.3	I	2.1	S	2.1	G	19.5	IS	20.1	S	20.1	SGI
#13	1.7	I	0.6	I	0.9	G	9.3	I	9.8	IG	9.9	IG
#14	2.4	GI	2.3	I	1.6	**	18.8	IG	16.1	IS	16.7	**
#15	4.6	G	2.9	G	3.8	G	14.4	SIG	17.6	GS	17.3	S
#16	4.4	IS	4.9	SI	3.6	GI	18.9	IS	19.8	IS	15.7	GI
#17	3.1	GI	4.4	IG	4.1	S	19.0	S	16.1	IS	16.9	SI
#18	3.5	S	2.5	IS	2.2	I	17.4	S	11.6	IS	7.3	I
#19	0.8	I	1.8	GS	1.8	G	6.8	I	19.9	ISG	19.0	GIS
#20	0.0*	I	2.2	I	0.0*	I	*	I	19.3	IG	*	I
#21	3.8	I	2.9	I	2.0	I	20.8	ISG	17.6	I	16.0	I
#22	1.3	I	1.5	I	2.8	I	22.6	S	20.8	IGS	18.9	ISG
#23	0.6	I	1.0	I	1.8	I	21.5	I	23.3	IGS	19.5	ISG
#24	0.6	I	0.8	I	0.5	I	9.4	I	4.0	I	1.5	I
#25	0.0*	I	0.0*	I	0.0*	I	2.8	I	2.4	I	5.3	I

Note: *specimens were broken along the interface during demolding. **the data was not recorded. I-failure occurred along interface; G-failure occurred at the grout; and S-failure occurred at the substrate concrete.

3.2 Effects of Curing Temperature on Bond Strength

Fifteen grout products were selected for this test at three curing temperature levels (23°C, 30°C, and 35°C). Table 2 summarizes all test results. The temperature change was found to have substantial impacts on the flexural bond strength. The 28-day flexural bond strength was reduced with the increasing curing temperature possibly due to reduced flowability of fresh grouts and poor quality of hydration products at higher curing temperature. Only a few products showed the highest flexural bond strength at 30°C. Similarly, a high curing temperature generally resulted in a reduced slant shear bond strength. This can be again attributed to the combined effect of the lowered flowability and a reduced quality of hydration products as the curing temperature became higher. This also explain why the composite specimens were more likely to fail at the interface at a high temperature level.

Table 2. Effects of temperature on the 28-day bond strength and failure plane of grout products

Product ID	Flexural bond test						Slant shear bond test					
	23°C		30°C		35°C		23°C		30°C		35°C	
	MPa	FP	MPa	FP	MPa	FP	MPa	FP	MPa	FP	MPa	FP
#1	4.1	IS	1.5	I	2.0	I	19.1	S	14.8	—	10.6	IG
#2	5.7	S	2.6	I	0.9	I	22.3	S	11.5	IS	7.7	I
#3	5.2	IGS	3.3	G	1.9	G	20.2	IGS	11.8	I	14.3	IG
#4	4.5	I	0.7	I	0.6	I	10.4	I	19.8	IS	16.5	IG
#5	4.6	S	3.8	**	2.6	I	26.0	IGS	21.0	—	17.4	IG
#6	3.9	G	4.5	S	0.6	I	22.2	GS	17.2	IGS	9.8	I
#7	1.8	GI	1.4	I	NA	NA	10.0	GI	8.9	GIS	NA	NA
#9	3.6	G	3.4	**	1.6	I	18.6	S	15.3	—	15.9	IG
#10	4.1	G	3.2	G	2.8	G	19.8	IG	18.5	IG	11.6	I
#14	2.3	I	1.3	I	0.2	I	16.1	IS	15.2	IS	15.3	IG
#19	1.8	GS	4.5	S	NA	NA	19.9	IGS	18.9	ISG	NA	NA
#20	2.2	I	0.6	I	1.3	G	19.3	IG	17.4	IG	19.7	IG
#21	2.9	I	1.8	I	2.2	I	17.6	I	9.4	I	16.7	IG
#22	1.5	I	4.1	S	3.5	I	20.8	IGS	15.9	IGS	18.4	IG
#23	1.0	I	2.3	I	1.3	I	23.3	IGS	15.5	IG	17.9	IG

Note: *specimens were broken along the interface during demolding. **the data was not recorded. I-failure occurred along interface; G-failure occurred at the grout; and S-failure occurred at the substrate concrete.

Steel fibers had distinct influences on the bond behaviors of composite specimens. Eight products showed a reduced flexural bond strength because of 3% steel fiber additions. These products mostly had high flexural bond strength (above 600 psi). This suggested that for grout products already having high flexural bond strength, steel fiber addition would have negative impacts on the bond strength. Conversely, six products showed an improved flexural bond strength as 3% steel fibers were added. These products typically had relatively low flexural bond strength (less than 600 psi), implying that adding steel fibers was beneficial in improving the flexural bond strength of these products. The benefit of steel fiber addition was also reflected by the failure plane. Without steel fibers, brittle failure typically occurred. When steel fibers were added, they typically bridged the cracks, leading to tougher and more ductile failure. Similar effects of adding steel fibers were observed for the slant shear bond test.

4. Acknowledgements

The author acknowledges the financial support from the Tennessee State Research and Planning (SPR) Program by the Tennessee Department of Transportation and the US Federal Highway Administration. The author is also grateful for the assistance from the TDOT Study Advisory Committee and from the lab manager and the students in SCCM of MTSU.



Bridge Engineering Institute Conference 2023 (BEI-2023)
Rome, Italy, July 17-20, 2023



5. References

ASTM C78-09, Standard Test Method for Flexural Strength of Concrete (Using Simple Beam with Third-Point Loading), 4pp.

ASTM C882-13, Standard Test Method for Bond Strength of Epoxy-Resin Systems Used with Concrete by Slant Shear, 4pp.



Experimental Investigation of the Effect of Debonding on PSC Girders

Shambhavi Dube^{1*} and Durgesh C. Rai²

¹: Doctoral Student, Dept. of Civil Engineering, Indian Institute of Technology Kanpur, Kanpur 208016, India; email: shamdube@iitk.ac.in

²: Professor, Dept. of Civil Engineering, Indian Institute of Technology Kanpur, Kanpur 208016, India; email: dcrai@iitk.ac.in

*: corresponding author

Keywords: Pretensioned girder; partial debonding; shear strength; excessive debonding

Abstract: In pretensioned girders, the straight strands are debonded (sheathed) to follow the external moment profile, which also reduces unwanted stresses and cracks in the end region of the girders. However, excessive debonding has detrimental effects on the shear strength of the girder. In the past, some major bridge projects in India suffered significant web shear cracking because of excessive debonding that was provided mainly based on loading requirements. To experimentally investigate the influence of partial debonding on the shear strength of pretensioned concrete bridge girders, I-shaped half-scale fully bonded and partially debonded girders have been designed, detailed, and fabricated in the laboratory at IIT Kanpur, India. Both ends of the girders are tested to compare the shear strength, stiffness, failure modes, and crack patterns. The test results indicated that the ultimate strength of the girder reduces significantly in debonded girders compared to fully bonded girders. The ultimate failure in the fully bonded girder was dominated by flexure shear crack in the bottom flange, whereas diagonal shear failure in the web was the primary failure mode for debonded girder.

1. Introduction

Debonding is performed in pretensioned bridge girders to follow the external bending moment profile thereby reducing end forces. This is achieved by breaking the bond between concrete and strands either through hard debonding with a rigid tube or soft debonding with a split sheath. Debonding is widely preferred over harping for its ease of manufacturing, making pretensioned girders a cost-effective solution for the industry. However, excessive debonding can result in reduced shear capacity and the appearance of diagonal cracks in the end region of girders which has been a persistent challenge. The AASHTO LRFD currently limits the amount of partial debonding to twenty-five percent of the total strand area within a pretensioned girder due to the detrimental effects that excessive debonding can have on the shear performance of girders. Nevertheless, other countries and some US states allow a higher percentage of debonding, up to seventy-five percent. The recent NCHRP Research Report 849 recommends going as high as sixty percent debonding of the total strand area. The recent version of the Indian Road Congress in its code (IRC 112-2020, Code of practice for concrete road bridges) permits debonding and limits it to thirty-three percent through its special publication IRC: SP:71-2018. As the earlier version of Indian code IRC 112-2011 had permitted debonding but was silent on the amount of debonding, some past bridge projects in India constructed before 2018 provided excessive debonding (up to seventy percent) following the flexural requirement and experienced visible

distress in the form of inclined web cracking. Currently, there is no unanimity on the degree of debonding among the various state of practice in the world. This experimental study is an attempt to improve current practices regarding the percentage of debonding followed worldwide.

2. Design and Fabrication of Specimen

Two pretensioned girders, fully bonded and 25% debonded, each 6 m in length and 800 mm in depth, were designed, detailed, fabricated, and tested for shear in the laboratory at IIT Kanpur, India. Both identical ends (A and B) of each girder were tested, resulting in four sets of data as shown in Fig. 1(a). Fig. 1(b) illustrates the cross-sectional details of the test specimen. In the 25% debonded girder, strands were debonded using a flexible tube to reduce prestress transfer shown in Fig. 1(c). Both girders were cast and prestressed together in a 13 m long casting bed as shown in Figs. 1(d)-(f). To prevent cracking, a 28-day curing period was selected for transferring the prestress into the concrete and a 28-day concrete strength of 60 MPa was achieved. The 7-wire pretensioned strands made of 1860 MPa low relaxation steel having a diameter of 9.5 mm were used. The experimental data indicated a Young's Modulus of around 230 GPa for all cases. The 2-legged 6 mm dia. @ 150 mm c/c transverse stirrups of 6 mm dia. mild steel having a yield strength of 550 MPa, as obtained from the tensile test of the bar were used.

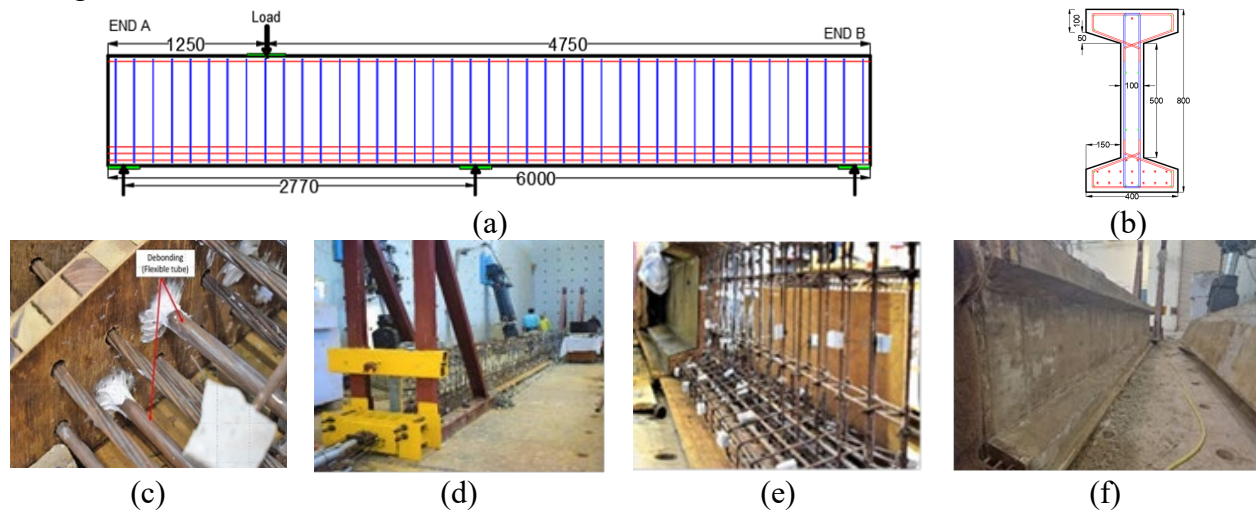


Fig. 1. Details of the fabrication (a) plan view; (b) cross-sectional view; (c) debonding of strands; (d) casting bed; (e) close-up view of stirrups and formwork; (f) removal of formwork

3. Test Setup and Instrumentation

At each end of the girder, 20 strain gauges were placed in pretensioned strands and 12 were placed in transverse stirrups at various cross-sections, as illustrated in Figs. 2 (a)-(d). Four additional strain gauges were installed at both ends of the debonded girder, at two sections: the point of debonding termination and a transfer length distance away from that point. A pretensioned force of 60 kN (i.e., prestress of 1095 MPa) was applied to each of the 17 strands symmetrically as shown in Figs. 2 (e) and (f) and measured using load cells at the dead end (see Fig. 2 (g)). Pretensioned strands were cut symmetrically in the cross-section using a gas cutter from the center gap between the two girders such that pretension force transfers to both girders simultaneously. Camber was measured for both girders using five LVDTs at $L/6$, $L/3$, $L/2$, $4L/6$, and $5L/6$ from the girder end (where L is the length of girder) and strains were recorded. The simply supported girder was mounted for testing on a Universal Testing Machine with a capacity of 2500 kN as shown in Fig. 3(a). The shear test was conducted on the girder with a span length

of 2770 mm, with the actuator load applied 1125 mm from the right end. Five LVDTs were placed at various points along the girder to measure the vertical deflection, and the horizontal movement was also recorded using another LVDT as shown in Fig. 3(b). Extensometer and LVDT were placed diagonally within the shear span to record compression and extension, which were later used to calculate the shear strains.

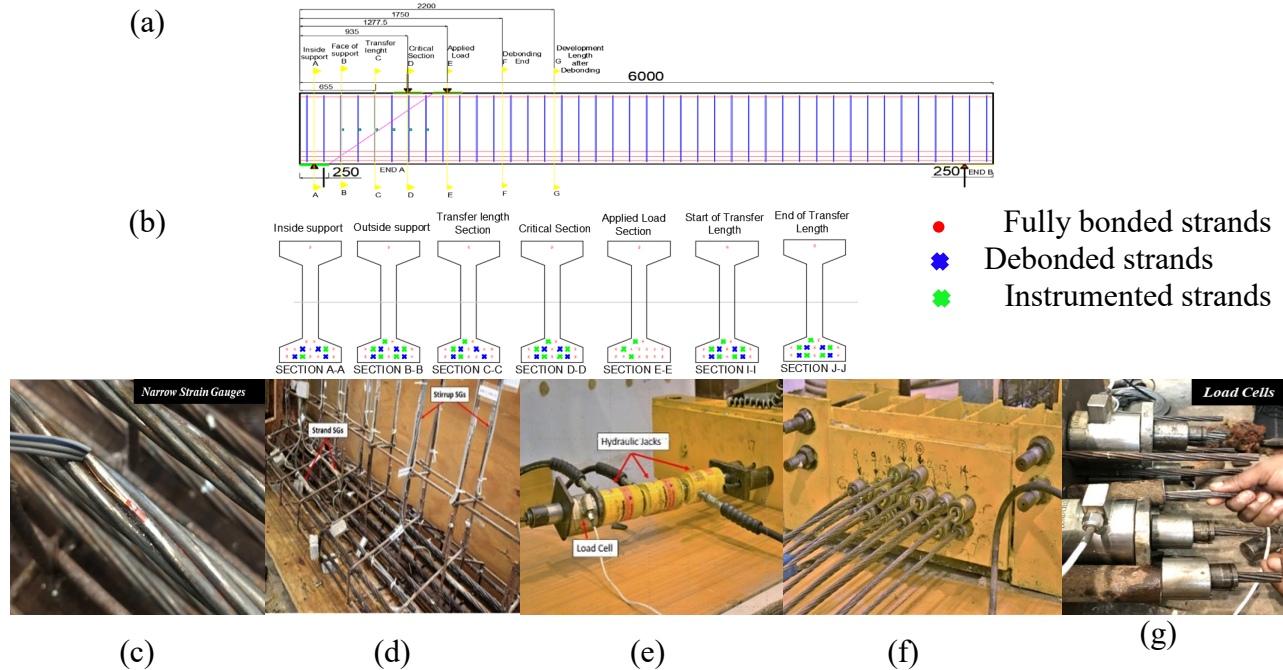


Fig. 2. Details of the test specimen (a) sections in plan view; (b) detailed strand profile in each cross-section; (c) application of narrow strain gauge; (d) strand and transverse strain gauges; (e) hydraulic jack for prestressing; (f) locked strands; (g) load cell to monitor applied prestress

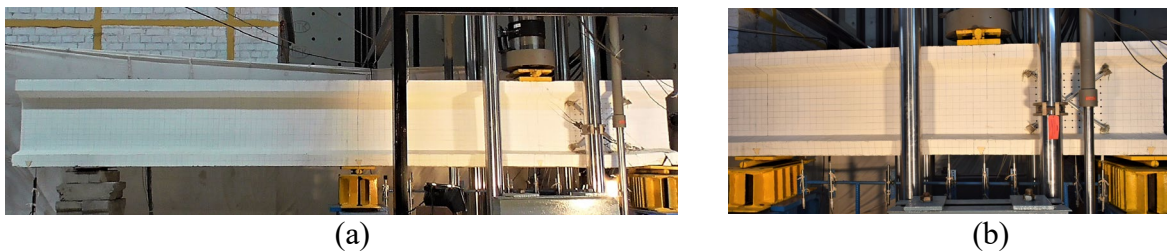


Fig. 3. (a) Test girder; (b) test span and instrumentation (LVDTs and extensometer)

4. Results and Discussion

The applied load has been plotted with measured deflection under the applied load for both ends of fully bonded and 25% debonded girders as shown in Fig. 4 (a). The experimental results have also been compared with theoretical deflections up to the elastic limit and deflections from ABAQUS analysis for fully bonded case. The girders achieved their predicted capacity and exceeded the capacities calculated using AASHTO LRFD standards. The first crack appeared at a load of 11% and 16% more than the predicted capacities obtained from AASHTO LRFD for fully bonded and 25% debonded girders, respectively. The maximum applied loads were approximately twice the load at which the first crack appeared (1211 kN and 1192 kN for fully

bonded and 988 kN and 1068 kN for 25% debonded case; ends A and B respectively). The results of the debonded girder tests indicated a reduction in shear strength. Prior to the occurrence of the first crack, the stiffness of the debonded girder was comparable to that of a fully bonded girder. However, once the crack appeared, the stiffness of the debonded girder degraded more rapidly. Although the difference in stiffness was not significant at 25% debonding, it is predicted to increase with higher debonding levels. The results clearly demonstrate that debonding led to an increase in shear strain and a decrease in shear strength in comparison to the fully bonded case. An extensometer and LVDT were placed diagonally to measure compression and extension in the region between the support and load (shear span), and the shear strain was calculated from this diagonal deformation. Figs. 4 (b) and (c) show the relationship between applied shear and calculated shear strains for both ends of fully bonded and 25% debonded girders and compared them with theoretical elastic shear strain. In general, for a particular value of applied shear, the shear strain was larger in debonded girder. As the girders were tested up to failure, crack angles are discernible in both fully bonded and 25% debonded girders as shown in Fig. 5. It is evident that the 25% debonded girder experienced more severe cracking and breakdown in the lower flange compared to the fully bonded girder, which had a higher level of prestress in the lower flange. Flexure shear cracks dominated the ultimate behavior of the fully bonded girder, whereas, in debonded girder, extensive web shear cracking governed the failure mode.

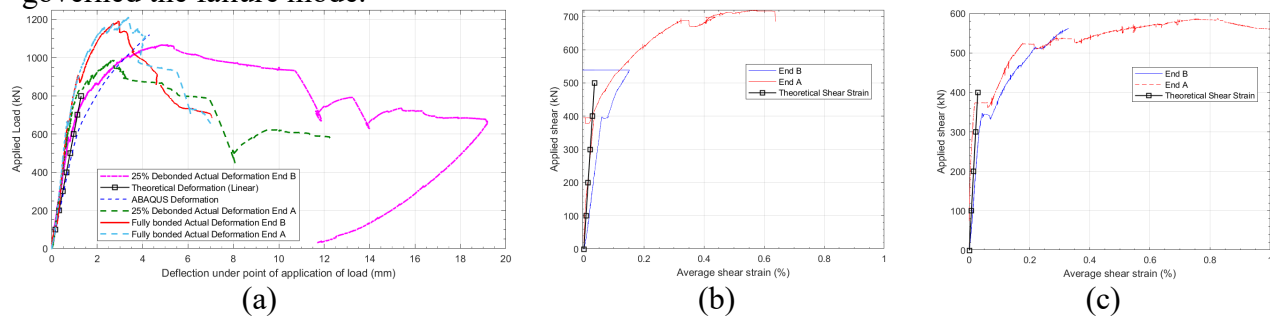


Fig. 4. (a) Applied load vs deflection plot; shear force vs deformation for: (b) fully bonded girder; (c) 25% debonded girder

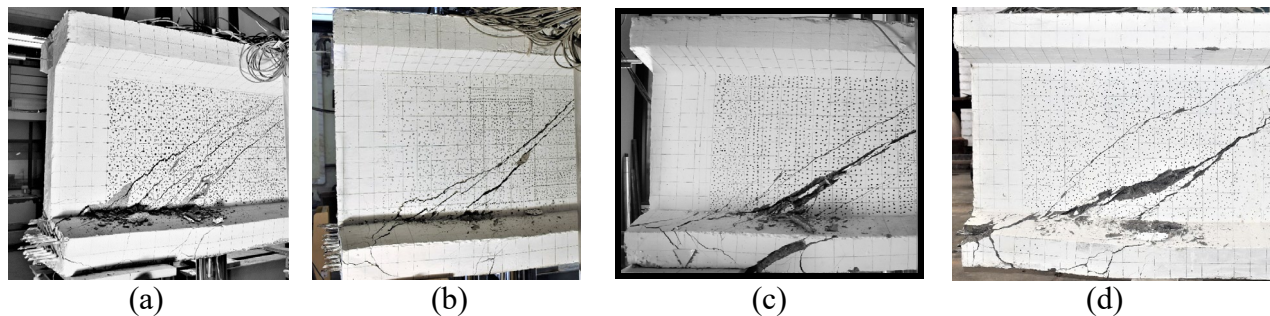


Fig. 5. Cracks and failure patterns: fully bonded girder (a) end A; (b) end B; 25% debonded girder (c) end A; (d) end B

5. Conclusion

There was a notable reduction in the shear strength of 25% debonded girder and a rapid drop in stiffness of debonded girder as compared to the fully bonded girder after the first crack. Although the difference in stiffness was not significant at 25% debonding, it is predicted to



increase with higher debonding levels. The 25% debonded girder exhibited a wider and increased number of diagonal cracks in the web compared to the fully bonded girder. To compensate for the reduction in shear strength and stiffness, either more stirrups or an increased web width is required. An extensive experimental study is needed to address this issue.

6. References

AASHTO. 2017. LRFD Bridge Design Specifications, Eighth Edition, American Association of State Highway and Transportation Officials, Washington D.C.

IRC 112, Indian Road Congress. 2020. Code of Practice for Concrete Road Bridges, IRC: 112-2020, New Delhi, India.

IRC 112, Indian Road Congress. 2011. Code of Practice for Concrete Road Bridges, IRC: 112-2011, New Delhi, India.

IRC, SP:71. 2018. Guidelines for design and construction of precast pre-tensioned girders for bridges, IRC: SP:71. 2018, New Delhi, India.

NCHRP 849 Research Report. 2017. Strand Debonding for Pretensioned Girders, National Cooperative Highway Research Program, Washington, D.C.



Investigation of Nitrogen Oxide Removal of Cementitious Materials Containing TiO₂

Byoungsun Park^{1*}, Suji Woo², Young Cheol Choi^{3*}, and Sung-Won Yoo^{4*}

¹: Department of Environmental Systems Engineering, Sejong Campus, Korea University, Sejong-si 30019, South Korea; email: bspark0927@korea.ac.kr

²: Department of Civil and Environmental Engineering, Gachon University, Seongnam 13120, South Korea

³: Department of Civil and Environmental Engineering, Gachon University, Seongnam 13120, South Korea; email: zerofo@gachon.ac.kr

⁴: Department of Civil and Environmental Engineering, Gachon University, Seongnam 13120, South Korea; email: imysw@gachon.ac.kr

*: corresponding author

Keywords: Nitrogen oxide removal; Titanium oxide; Cementitious materials; ISO-22197-1; photocatalytic reaction.

Abstract: Nitrogen oxide (NO_x) is one of the primary contaminated matters in the air environments. NO_x is harmful to the human body and causes respiratory diseases. Therefore, various technologies to remove NO_x are studied. It is known that NO_x can be removed using a photocatalytic reaction. Since the concrete structure has a large surface area and is exposed to the atmosphere, if a photocatalyst is mixed with the concrete so that the photocatalytic reaction can occur on the concrete surface, NO_x removal from the atmosphere can be efficiently performed. This paper investigates NO_x removal characteristics of cementitious materials containing titanium oxide (TiO₂). TiO₂ is the most widely used photocatalyst because it is inexpensive and convenient to use. TiO₂ powder was added during the mixing process of cementitious materials and was used in a ratio that partially replaces cement. Two types of cement composites (cement pastes and foam composites) were used. NO_x removal characteristics were investigated using the method presented in ISO-22197-1. It was investigated that the NO_x removal efficiency improved as the TiO₂ substitution rate increased. It was investigated that the NO_x removal performance of foam composites was superior to that of cement pastes. In addition, the NO_x removal efficiency was found to be affected by the thickness of the specimen.

1. Introduction

Nitrogen oxide (NO_x) is one of the main causes of air pollution and has harmful effects on the human body (Seo and Yun, 2017). In addition, NO_x is one of the precursors of particulate matter. Therefore, various studies are being conducted to remove NO_x in the air (Chen et al., 2021). One of them is to use a photocatalytic reaction (Yu and Brouwers, 2009). In the photocatalytic reaction, NO_x is oxidized to NO₃⁻ using ultraviolet (UV) light, and NO₃⁻ is removed by water (Yu and Brouwers, 2009). TiO₂ is the most widely used photocatalyst due to its economic feasibility and ease of use (Yu et al. 2006). Since the photocatalytic reaction requires UV light, it is

important to expose the photocatalyst to the outside. The concrete structure has a high surface area and is suitable as a site for photocatalytic reaction because it is built on the outside. Since the photocatalytic reaction appears only at the location where UV light is supplied, it is necessary to increase the amount of photocatalyst exposed on the concrete surface.

In this study, the NO_x removal performance of TiO₂-added cementitious composites was investigated. An experiment was conducted using foam composite and cement paste to investigate the effect of concrete surface area on NO_x removal performance.

2. Experiments

In this study, ordinary Portland cement (OPC) was used as binder. The density and Blain fineness of OPC were 3.1 g/cm³ and 3,260 cm²/g, respectively. The average particle size of OPC was 5.9 μm. TiO₂ in powder form was added to cementitious materials to impart photocatalytic reactivity. The ratio of anatase and rutile constituting TiO₂ was 8:2. Table 1 shows the mixture proportions of specimens. Cement pastes and foam composites were used to investigate the effect of porosity of cementitious materials on NO_x removal performance. Water to cement ratio is fixed as 0.3. The foaming ratio of foam composites was a fix at 63.6%. OPC was substituted as TiO₂ powder in the ratio of 3% by volume. The specimens were fabricated in the size of 200×50×20mm. The specimens were cured in the chamber at 23 ± 2 °C in temperature and 60 ± 10 % in relative humidity.

Table 1. Mixture proportions of specimens

	W/C	OPC [kg/m ³]	TiO ₂ [kg/m ³]	Foaming ratio (%)
Plain	0.3	500	-	-
PlainT3		485	21.9	
Foam		500	-	63.6
FoamT3		475	21.9	

To evaluate the NO_x removal performance of cementitious materials, a test equipment with reference to ISO-22197-1 was prepared. The test equipment consists of NO_x concentration analyzer, photocatalytic reaction chamber, UV lamp, NO gas and air supply equipment. Test specimens fabricated according to Table 1 were pretreated to remove contaminants on the surface using a UV lamp and a drying chamber. The pre-treated specimens were installed in the chamber. 1 ppm of NO gas was supplied at a rate of 3 L/min. UV light was irradiated for 3 hours from 2 hours after the specimen was placed. The experiment was continued for 1 hour after turning off the UV light.

3. Results & Discussion

Fig. 1 shows NO_x concentration obtained from experiments using cement paste and foam composite. In the experiment using Plain, the NO_x concentration reached about 0.95 ppm after supplying NO gas. On the other hand, in the experiment using foam, the NO_x concentration reached 0.95ppm, then decreased, and then recovered after 2 hours. Since the foam has a relatively high surface area compared to the plain, it is judged that NO_x is adsorbed. Due to the high surface area of the foam, the incorporation of TiO₂ seems to increase the efficiency of the photocatalytic reaction. In both specimens, NO_x concentration was constant regardless of UV light. This result means that NO_x removal reaction does not appear without TiO₂.

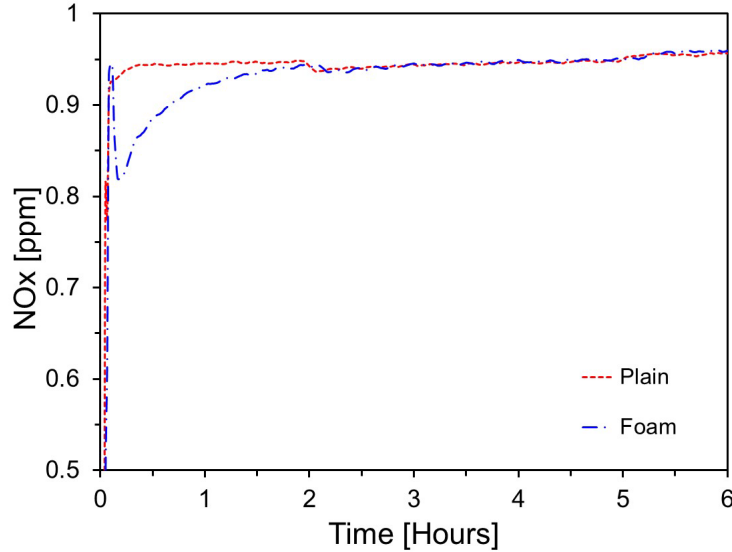


Fig. 1. NO_x concentration obtained from experiments using cement paste and foam composite

Fig. 2 shows NO_x concentration obtained from experiments using specimens incorporating TiO₂ powder. Unlike 1, NO_x decreased after irradiation with UV light. This is due to the photocatalytic reaction of TiO₂. Looking at the graph, the NO_x concentration of the two specimens was the same immediately after irradiation with UV light. As the UV light irradiation time increased, the NO_x concentration of PlainT3 increased compared to that of FoamT3. Due to the high surface area of Foam, more TiO₂ powder was exposed to the surface, which seemed to increase the efficiency of the photocatalytic reaction.

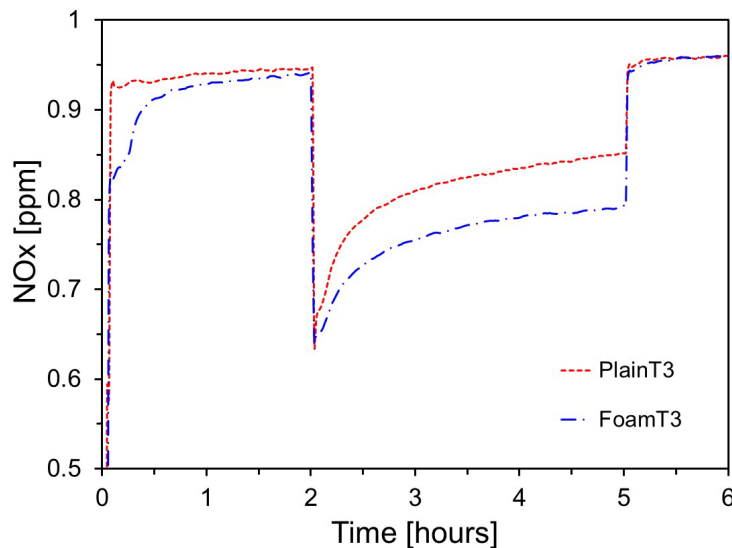


Fig. 2. NO_x concentration obtained from experiments using specimens incorporating TiO₂ powder

4. Conclusion

In this study, the NO_x removal performance of TiO₂-added foam composites and cement pastes was investigated. Foam composites showed increased adsorption of NO_x compared to cement



pastes due to their high surface area. When TiO_2 was added, the NO_x removal performance of foam composites increased compared to that of cement pastes. It can be seen that the NO_x removal performance can be improved by exposing more TiO_2 powder to the surface.

5. References

Seo, D. and Yun, T.S. 2017. NO_x removal rate of photocatalytic cementitious materials with TiO_2 in wet condition, *Building and environment*, 112, 233-240.

Chen, R., Zhang, T., Guo, Y., Wang, J., Wei, J., and Yu, Q. 2021. Recent advances in simultaneous removal of SO_2 and NO_x from exhaust gases: Removal process, mechanism and kinetics, *Chemical Engineering Journal*, 420, 127588.

Yu, Q. and Brouwers, H.J.H. 2009, Indoor air purification using heterogeneous photocatalytic oxidation. Part I: Experimental study, *Applied Catalysis B Environmental*, 92, 454–461.

Yu, K.-P., Lee, G.W.M., Huang, W.-M., Wu, C., and Yang, S. 2006. The correlation between photocatalytic oxidation performance and chemical/physical properties of indoor volatile organic compounds, *Atmospheric Environment*, 40(2) 375-385.

6. Acknowledgement

This work was supported by the National Research Foundation of Korea (NRF) grant funded by the Korea government (MSIT) (NRF-2020R1A2C2008926). This work was also supported by the Korea Conformity Laboratories (PUR04202302280031).



The Diagnosis Method for Neutralization of Concrete Using Microorganisms

China Kuratomi^{1*}, Atsushi Teramoto², So Fujiyoshi³, and Fumito Maruyama⁴

^{1*}: Hiroshima University, Higashi-Hiroshima, Japan; email: d231038@hiroshima-u.ac.jp

²: Hiroshima University, Higashi-Hiroshima, Japan; email: a-teramoto@hiroshima-u.ac.jp

³: Hiroshima University, Higashi-Hiroshima, Japan; email: sofu62@hiroshima-u.ac.jp

⁴: Hiroshima University, Higashi-Hiroshima, Japan; email: fumito@hiroshima-u.ac.jp

*: corresponding author

Keywords: neutralization; microbiome; DNA extraction; water repellency

Abstract: The risk of rebar corrosion in concrete piers is increased by pH neutralization due to carbonation. The progress of neutralization inside concrete is difficult to estimate through wholly nondestructive methods. In this study, we examine a new possible diagnostic method for neutralization by clarifying how the biological community in concrete are affected by (1) environmental factors causing neutralization and (2) the concrete after neutralization has occurred. First, specimens with different surface pore structures were prepared by changing the age of the demolding. Some of the specimens were coated with water-repellent or hydrophilic paint. Thereafter, the specimens were periodically moistened via two different supply methods: running water and spraying in accelerated carbonation period. After the accelerated carbonation test, microbial samples were obtained from the surface and interior of the specimens to investigate the differences in microbial community characteristics. The results indicated that the pore structure of the surface layer was the most significant factor affecting the rate of concrete neutralization. Although the coating had the effect of delaying the age at which neutralization began, it did not significantly affect the rate of subsequent neutralization progression, regardless of whether they were hydrophilic or hydrophobic materials. To quantitatively evaluate the number of microorganisms present at each location, DNA concentrations were compared. More microorganisms were found to be present in the surface layer than in the interior, and the DNA concentration in the surface layer was greater for concrete with a shorter demolded age and when water was supplied by running water, the DNA concentration in the surface layer decreased in this experiment. This indicates the effect of washing off microorganisms in the surface layer was greater than the effect of increasing the moisture content of the specimens. In addition, for samples taken from surface swabs, the results suggest that the Shannon diversity index is not dependent on the pore structure of the concrete, but rather on the type of surface coating.

1. Introduction

Microorganisms are found worldwide, and certain microorganisms are thought to inhabit concrete. Previous studies have shown that microorganism growth is characterized by the carbon dioxide concentration (Balzani *et al*, 2022), temperature and humidity (Hoeksma *et al*, 2015), and pH (Preiss *et al*, 2015) of the surrounding environment. Therefore, microorganisms inhabiting concrete might be characterized by the properties of the concrete and environment. External factors

influencing the progress of concrete neutralization include carbon dioxide, ambient humidity and temperature, and rainwater on the structure. In addition, the pH of the solution in the pores and pore size of the neutralized concrete changes. Therefore, if the properties of neutralized concrete can be related to the microbial habitat, a new diagnostic method could possibly be developed. In this study, the effects of external factors causing neutralization and concrete properties after neutralization on the microorganisms in concrete were clarified. Moreover, the applicability of a new diagnostic method developed for neutralization is discussed. Furthermore, the effects of concrete water supply, pore structure, and water repellency of the surface layer are described.

2. Experiment

2.1. Test Specimen

Concrete specimens with a water cement ratio of 53% and internal dimensions of 200×130×75 mm were cast using square styrol cases. Various concrete specimens were fabricated to assess the progression and velocity of neutralization using the following parameters: coarse and dense pore structure, water repellency of the specimen surface, and moisture supply method.

The specimens cured for 28 days were fabricated with and without hydrophilic and hydrophobic coatings (hereafter referred to as hydrophilic, hydrophobic, and 3w, respectively). In addition, the water repellency of the surface layer was differentiated.

2.2. Accelerated Neutralization Tests

Accelerated neutralization tests were conducted on the specimens described in Section 2.1. To limit the carbon dioxide infiltration path, the casting surface and four sides of the specimen were sealed with aluminum tape. Accelerated neutralization tests were conducted for up to 26 weeks at 20 °C with a relative humidity of 60% and carbon dioxide concentration of 5%, in accordance with JIS A 1153. Neutralization depth measurements and water supply were conducted at accelerated ages of 1, 4, 8, 13, and 26 weeks. The specimens for each parameter were watered with either a constant amount of running water applied to the test surface (hereafter referred to as "running water") or sprayed with a sprayer to form a mist (hereafter referred to as "spraying"). For the running water, a water reservoir was installed above the specimen with a partition raised to a fixed position to allow a fixed amount of water to flow at an approximately constant rate. For the spraying, the amount of water supplied was controlled by the amount of water emitted from the sprayer and number of times sprayed. Specimens not subject to a water supply were also established to investigate the degree of neutralization enhancement with and without a water supply.

2.3. Sampling

Samples for microbiological analysis were collected from the surface of the neutralized concrete specimens by swabbing and from 10 mm inside by breaking the specimens with a hammer. The 26-week measurements of all samples were used for the accelerated neutralization tests. Swabbing was applied twice to the same surface area of approximately 100×50 mm. The swab sticks and crushed samples were stored at -80°C to inactivate the microorganisms and maintain the microflora at the time of the DNA extraction procedure (Section 2.4).

2.4. DNA Concentration Measurement

DNA extraction was performed using the DNeasy® PowerBiofilm® Kit (QIAGEN) according to a developed protocol by the authors. The DNA concentration was measured by determining the

fluorescence using a trace spectrophotometer (DS-11FX, Denovix). The resulting DNA solution was subjected to a 2-step tailed PCR method to create a library. Subsequently, the sequencing was performed using the MiSeq system and MiSeq Reagent Kit v3 (Illumina) at 2×300 bp.

3. Results and Discussion

3.1. Accelerated Neutralization Depth

The neutralization depth, least-squares approximation, neutralization rate coefficient, and neutralization resistance of each specimen were calculated, as shown in Figs.1-4. The neutralization progression of the 1-day specimens at 26 weeks was approximately three times greater than that of the 28-day specimens. Demolding at a young age were deemed to result in a coarse pore structure thus facilitating carbon dioxide infiltration. Conversely, no difference in the neutralization rate coefficient owing to differences in the water supply method or water repellency of the surface were observed.

3.2. DNA Concentration

The average swab area for all specimens was 5256 mm^2 , and the average internal sample mass was 0.0649 g . The preliminary experiment revealed that the mass of the adhered material collected from a $150 \times 150 \text{ mm}$ concrete wall was 0.0239 g . The swab area in this experiment acquired approximately 0.0004 to 0.0040 g of adhered material. Based on this acquired amount, the DNA concentration, extracted from 1 g of the sample collected by the swab method, was approximately 15 to 1300 times greater than that of the internal sample. In comparison with previous studies (Kuratomi *et al*, 2022), this order of magnitude is reasonable and reconfirms that microorganisms are concentrated in the surface layer of concrete rather than the interior.

The DNA concentrations per swab area and per gram of internal sample were calculated by dividing the DNA concentration extracted in this experiment by mass of the swabbing sample and the internal sample used for extraction, respectively. These DNA concentrations are illustrated in Figs. 5 and 6. The DNA concentration detected via the swabbing method tended to be affected by the water supply method, with higher DNA concentrations extract in order: no water supply, spraying, running water extracting. This trend was particularly noticeable for

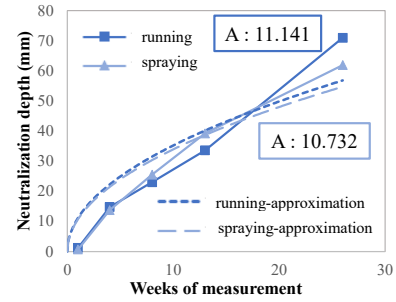


Fig. 1. The 1d specimen neutralization depth and neutralization rate coefficient A

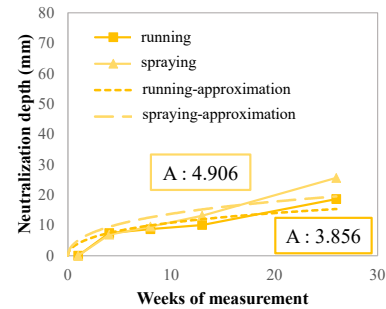


Fig. 2. The 3w specimen neutralization depth and neutralization rate coefficient A

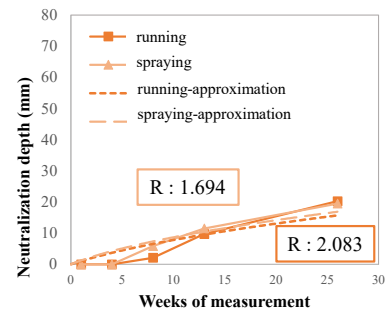


Fig. 3. Hydrophilic specimen neutralization depth and neutralization resistance R

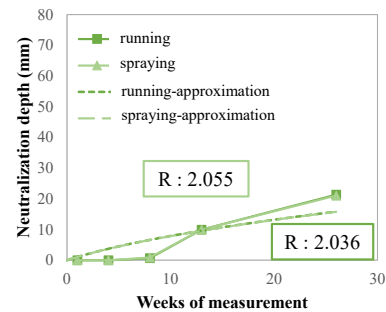


Fig. 4. Hydrophobic specimen neutralization depth and neutralization resistance R

specimens without water repellency. For the interior samples, the lowest DNA concentration was extracted from the sprayed specimens in the test system without a water-repellent coating, whereas the DNA concentration of the specimens without water supply tended to be lower in the test system with a water-repellent coating. These results indicate that microorganisms in concrete can be affected by water supply conditions and surface water repellency.

Fig. 7 shows the Shannon diversity index calculated from the obtained sequences data. The figure shows that the diversity of the microbial community in the surface layer of the hydrophilic paint film is higher than others, suggesting that the type of paint film may also affect the microbial community.

4. Conclusion

In this study, accelerated neutralization tests were conducted with different pore structures and surface layer water repellency. And microorganisms were detected on the surface and from the interior of the concrete. As a result, DNA was extracted from surface layer at concentrations several hundred times higher than the samples taken from the interior concrete. Microorganisms in concrete were found to be susceptible to the influences of external environmental factors and the materials property of surface layer. The above results may contribute to a significant simplification of bridge maintenance, which is currently carried out at great cost.

5. References

- Balzani et al. 2022. CO₂ biogeochemical investigation and microbial characterization of res wood ant mounds in a Southern Europe montane forest, *Soil Biology and Biochem.*, 166, 1-10
- Hoeksma et al. 2015. Effect of temperature and relative humidity on the survival of airborne bacteria, *Livestock Research Report*, 864, 1-27
- Kuratomi et al. 2022. The basic study of microbial detection method for concrete, *Proceedings of the Japan Concrete Institute*, 44, 1300-1305
- Preiss et al. 2015. Alkaliphilic bacteria with impact on industrial applications, concepts of early life forms, and bioenergetics of ATP synthesis, *Frontiers in Bioeng. and Biotech.*, 75(3), 1-16

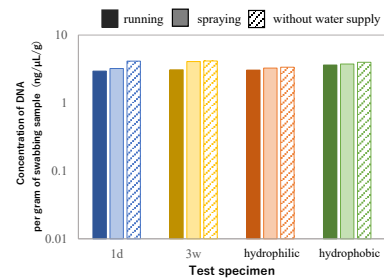


Fig. 5. DNA concentration per gram of swabbing sample

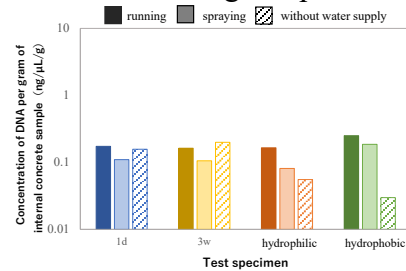


Fig. 6. DNA concentration per gram of internal concrete sample

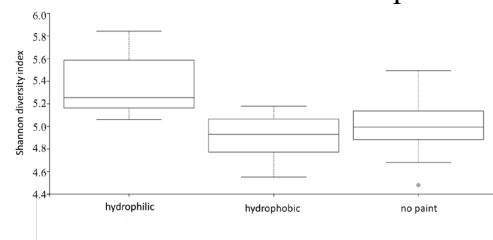


Fig. 7 Shannon diversity of microbiome on surface of specimens



Bridge Engineering Institute Conference 2023 (BEI-2023)
Rome, Italy, July 17-20, 2023



6. Acknowledgments

This work was supported by JST FOREST Program, Grant Number JPMJFR215N and the Fund for the Promotion of Joint International Research (Fostering Joint International Research (B)) of KAKENHI 22KK0064. The hydrophobic materials were provided by Dr. Tsujino (Shimizu Corp.) and Mr. Azuma (Toyo Aluminium K. K.)



Research on Fatigue Properties of Basalt Fiber Cement Stabilized Macadam

Wei Li¹, Peifeng Cheng¹, Wenmei Zhao¹, and Zhanming Zhang^{1*}

¹: College of Civil Engineering and Transportation, Northeast Forestry University, Harbin 150040, China; email: alicel2383@126.com

*: corresponding author

Keywords: Cement stabilized aggregates; Basalt fiber; Fiber dosing; Stress level; Fatigue performance

Abstract: In order to study the fatigue performance of basalt fiber-doped cement-stabilized macadam, three-point small beam bending fatigue tests were conducted for cement-stabilized macadam with different stress levels and basalt fiber doping. Based on the two-parameter Weibull distribution theory, the fatigue test results were analyzed and the fatigue equation was established. The mechanism of fatigue performance of basalt fiber reinforced cement stabilized macadam is explained by combining with micro-morphological observation method. The results show that basalt fibers are uniformly distributed in cement-stabilized macadam to form a network structure, so that the material is uniformly stressed and load concentration is avoided, and the reinforcing effect delays the expansion of fatigue micro-cracks. The fatigue life of cement-stabilized macadam can be increased by 2-5 times by adding basalt fibers at different stress levels. At a stress ratio of 0.6, the fatigue life of cement-stabilized macadam was increased by more than 5 times. In addition, the constructed fatigue prediction equation can be used to predict the fatigue life of cement-stabilized macadam at different load levels, which can be used as a reference for engineering applications.

1. Introduction

Cement-stabilized crushed stone materials are widely utilized in transportation engineering construction due to their notable characteristics, including high overall integrity and resistance to deformation. However, the combined effects of factors such as load, temperature, and humidity can compromise the tensile strength and deformability of cement-stabilized crushed stone, leading to the formation of cracks under fatigue conditions and consequent reduction in load-bearing capacity. Therefore, the prevention and mitigation of crack formation play a crucial role in enhancing the fatigue life and durability of cement-stabilized crushed stone [1]. The incorporation of fibers in cement-stabilized crushed stone materials has been found to improve their mechanical properties and resistance to fatigue cracking [2]. Basalt has been successfully employed in engineering applications to enhance the performance of asphalt mixtures [3], mitigate deterioration under aging conditions, and improve the mechanical properties of cement concrete and mortar[4]. In this research, the focus is on studying and applying the fatigue performance of cement-stabilized crushed stone materials reinforced with basalt fibers. The fatigue life is evaluated by conducting tests at different stress ratios and fiber contents. The analysis of fatigue test results and the development of fatigue equations are performed based on

the two-parameter Weibull theory. This study aims to provide valuable insights and guidance for investigating and utilizing the fatigue resistance of basalt fiber-reinforced cement-stabilized crushed stone materials.

2. Test Materials and Methods

2.1 Material

The experimental materials primarily consist of three main components: cement, basalt fibers, and aggregates. The cement material selected is ordinary Portland cement with a strength grade of 42.5, produced by a chemical plant in Heilongjiang Province, China. The cement content is 4.5%, meeting all the specifications required by the "Test Code for Cement and Cement Concrete in Highway Engineering" (JTG 3420-2020). The basalt fibers used are specially provided by a composite materials company in Zhejiang Province. These fibers are in the form of bundled cement composite short-cut strands, specifically designed for this study. The main performance indicators of the basalt fibers can be found in Table 1. The aggregates used in the experiment were sourced from a limestone quarry at a highway construction site in Heilongjiang Province, China. The primary component of the aggregates is limestone ore.

Table 1. Main technical indicators of cement

Standard consistency (%)	Initial setting time (min)	Final setting time (min)	Stability (mm)	3d Flexural strength (MPa)	3d Compressive strength (MPa)
27.5	325	412	qualified	5.6	22.4

2.2 Fatigue test method

The fatigue tests were performed using a UTM-30 universal testing machine. The loading method selected was a stress-controlled mode, which closely mimics the actual working conditions and ensures good reproducibility. The tests were conducted at a temperature of 15°C with a loading frequency of 10Hz. A half-sine waveform was employed as the load waveform, representing the ratio between the minimum and maximum cyclic stresses. The fiber dosages chosen were 0‰, 0.4‰, 0.6‰, and 0.8‰, while the stress levels for the fatigue tests were set at 0.6, 0.7, 0.75, and 0.8. For the fatigue tests on cement-stabilized crushed stone incorporating basalt fiber, standard small beam specimens with dimensions of 100mm × 100mm × 400mm were prepared. These specimens were subjected to a curing period of 90 days before testing. To minimize experimental errors, each group of samples underwent five parallel tests.

3. Results and Discussion

3.1 Fatigue Test Results

The results of the fatigue tests on cement-stabilized crushed stone specimens with different basalt fiber dosages are presented in Table 2, with the flexural strength based on various basalt fiber dosages as the reference. Within the stress range of 0.6 to 0.8, under the same gradation and cement content, the addition of basalt fibers effectively enhances the fatigue life of the cement-stabilized crushed stone specimens. The fatigue life of basalt fiber-reinforced cement-stabilized crushed stone is significantly improved, with an enhancement ratio ranging from 2 to 5 times. Under a stress ratio of 0.6, it can achieve a maximum increase of 5.61 times compared to ordinary cement-stabilized crushed stone.

Table. 2. Fatigue test results of basalt fiber cement stabilized gravel

Stress level	Average fatigue life (times)			
	Fiber content 0%	Fiber content 0.4%	Fiber content 0.6%	Fiber content 0.8%
0.80	7810	17921	25220	34217
0.75	25163	58746	84422	93531
0.70	174382	423387	719185	914915
0.60	891258	2756124	4325547	5000000*

Note: * indicates specimens that reached 5,000,000 cycles without failure.

To examine the relationship between the fatigue life of cement-stabilized crushed stone with basalt fiber and the dosage of basalt fiber, a curve fitting analysis was conducted. The basalt fiber dosage was selected as the independent variable (x-axis), while the logarithm of the average fatigue life was plotted as the dependent variable (y-axis). This analysis yielded the relationship between basalt fiber dosage and fatigue life at different stress levels, as depicted in Fig.1.

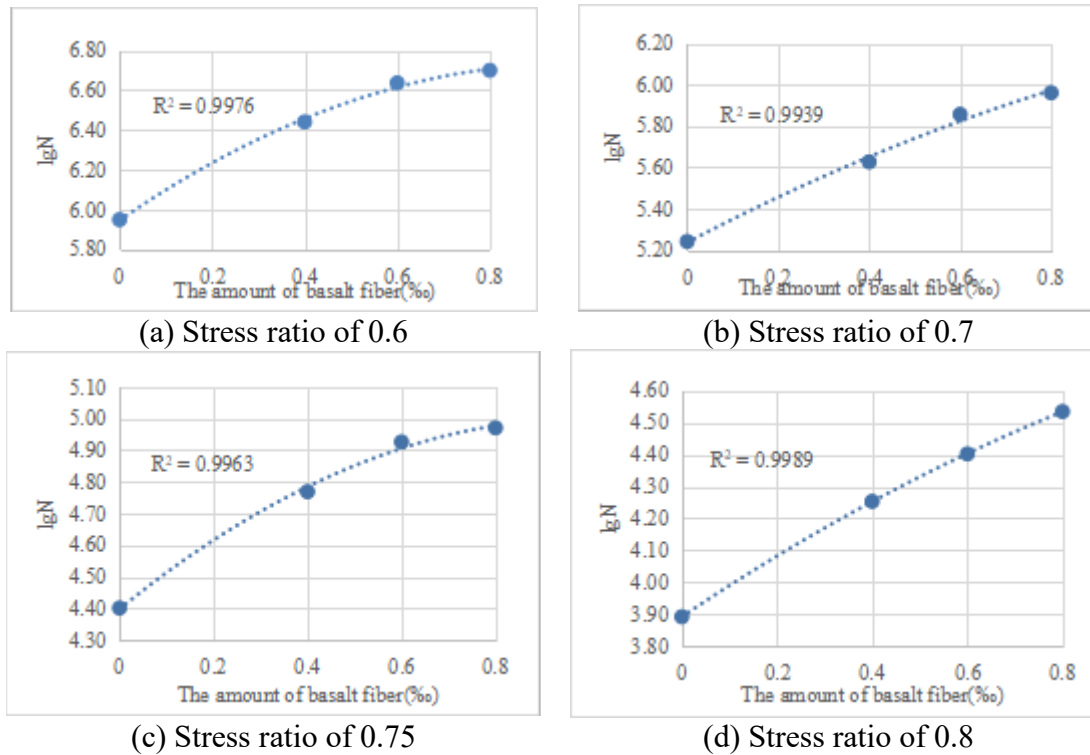


Fig.1. Relationship between basalt fiber doping and lgN for different stress ratio levels

$$\lg N = -0.8089x^2 + 1.5970x + 5.9473 \quad (1)$$

$$\lg N = -0.2864x^2 + 1.1495x + 5.2374 \quad (2)$$

$$\lg N = -0.6007x^2 + 1.2062x + 4.3982 \quad (3)$$

$$\lg N = -0.2448x^2 + 0.9971x + 3.8928 \quad (4)$$

From Fig.1, it is evident that the logarithm of the average fatigue life is well-fitted by a quadratic parabolic relationship with the dosage of basalt fibers. For stress levels of 0.6, 0.7, 0.75, and 0.8, the fitted quadratic parabolic equations describing the relationship between basalt fiber dosage and fatigue life are represented by Equations 1 to 4, respectively. In these equations, x denotes the dosage of basalt fibers, and N represents the number of fatigue cycles. It can be observed that the fatigue life values at different stress levels exhibit a monotonically increasing trend with an increase in basalt fiber dosage. However, as the stress level gradually increases, the fatigue life of basalt fiber-reinforced cement-stabilized crushed stone decreases.

3.2 Build the fatigue equation

In fatigue testing, it is common practice to utilize the S-N (Stress level-Fatigue life) curve to depict the experimental results, which aids in predicting the fatigue life of basalt fiber-reinforced cement-stabilized crushed stone under various stress levels. This approach holds significant engineering significance as it provides valuable guidance. An exponential function-type single-logarithm fatigue equation is chosen, as represented by Equation 5.

$$e^{QS}N = C \quad (5)$$

After taking the logarithm of both sides, Equation 5 can be transformed into Equation 6:

$$S = A - B \ln N \quad (6)$$

Where: $A = \lg C / Q$, $B = 1 / Q$, where Q and C are arbitrary constants.

3.3 Mechanism of anti-fatigue performance of basalt fiber reinforced cement stabilized macadam

In order to investigate the mechanism behind the enhanced fatigue resistance of basalt fiber-reinforced cement-stabilized crushed stone, the bonding between basalt fibers and the cementitious matrix, as well as the microstructural changes of basalt fibers under fatigue failure conditions, were examined. Microscopic images of the basalt fiber-reinforced cement-stabilized crushed stone in its normal state and at the fractured interface were captured using a JSM-7500F scanning electron microscope, as shown in Fig.2. From Fig.2(a), it can be observed that the basalt fibers are embedded within the cement-stabilized crushed stone, providing a structure that disperses stress and promotes a more even stress distribution, thereby preventing stress concentration. When the cement-stabilized crushed stone is subjected to repeated loading or temperature fluctuations leading to fatigue cracks, the basalt fibers prevent further crack propagation and act as reinforcement by bridging the fractured sections. Fig.3(b) reveals a dense and well-bonded interface between the fibers and the cement-stabilized crushed stone, without any signs of loose fibers being pulled out. Additionally, evidence of fibers being pulled and fractured within the mixture can be observed, indicating the fibers' effective crack-arresting ability and their role in enhancing the fatigue crack resistance of the cement-stabilized crushed stone material. During the micro-damage stage, the expansion of cracks encounters a dense network of randomly distributed fibers within the matrix, which effectively impedes fatigue damage, delays unstable crack propagation, and mitigates failure occurrence.

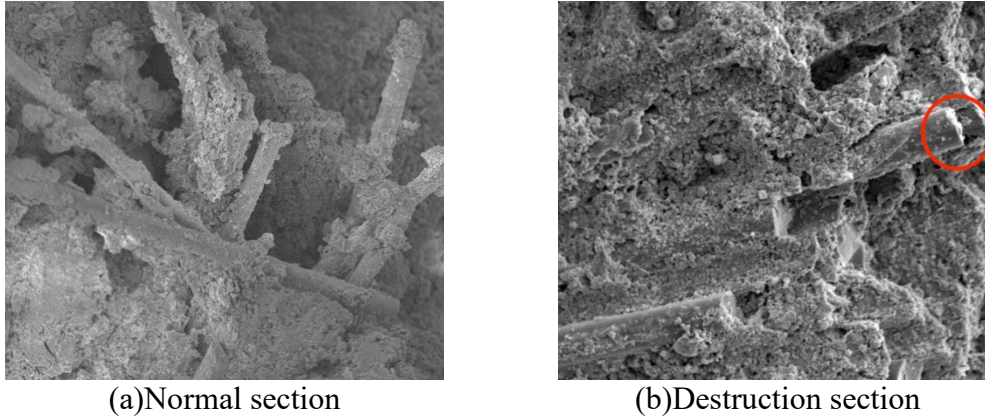


Fig.2. Microstructure of basalt fiber cement stabilized gravel

4. Conclusions

1. The addition of basalt fibers significantly enhances the fatigue life of cement-stabilized crushed stone. The inclusion of basalt fibers can increase the fatigue life of cement-stabilized crushed stone material by a substantial margin, ranging from 2 to 5 times. Under a stress ratio of 0.6, the incorporation of basalt fibers can even boost the fatigue life by up to 5.61 times.
2. Through regression analysis based on the Weibull distribution theory, a well-correlated fatigue equation has been developed to predict the fatigue life of cement-stabilized crushed stone material. This equation provides a reliable tool for estimating the fatigue performance of such materials.
3. Microscopic testing has revealed the beneficial effects of incorporating basalt fibers in the cement matrix. These fibers help disperse stress, prevent stress concentration, and effectively inhibit crack propagation within the mixture. As a result, the resistance of cement-stabilized crushed stone material to fatigue-induced cracking is significantly enhanced.

5. References

- [1] Baghini M S, Ismail A, Karim M R, et al. Effect of styrene-butadiene copolymer latex on properties and durability of road base stabilized with Portland cement additive [J]. *Construction And Building Materials*, 2014, 68: 740-9.
- [2] Ma Y H, Gu J Y, Li Y, Et Al. The Bending Fatigue Performance of Cement-Stabilized Aggregate Reinforced with Polypropylene Filament Fiber [J]. *Construction And Building Materials*, 2015, 83: 230-6.
- [3] Pirmohammad S, Amani B, Shokorlou Y M. The Effect of Basalt Fibres on Fracture Toughness of Asphalt Mixture [J]. *Fatigue & Fracture of Engineering Materials & Structures*, 2020, 43(7): 1446-60.
- [4] Sarkar A, Hajihosseini M. The effect of basalt fibre on the mechanical performance of concrete pavement [J]. *Road Materials And Pavement Design*, 2020, 21(6): 1726-37.



Bridge Engineering Institute Conference 2023 (BEI-2023)
Rome, Italy, July 17-20, 2023



Wind, Vibration, and Aerodynamics



Analysis of Dynamic Characteristics of Semi-Submersible Deep-Water Floating Foundation under Wind-Wave Coupling Actions

Honggang, Xu¹, Haiquan, Jing^{2*}, and Xuhui, He³

¹: School of Civil Engineering, Central South University, Changsha, China; email: xuhonggang1992@126.com

²: School of Civil Engineering, Central South University, Changsha, China; email: hq.jing@csu.edu.cn

³: School of Civil Engineering, Central South University, Changsha, China; email: xuhuihe@csu.edu.cn

*: corresponding author

Keywords: Deep-water floating foundation; Wind-wave coupling actions; Taut mooring cables; Dynamic response analysis

Abstract: The deep-water floating bridge is a novel concept aimed at solving the challenge of constructing traditional bridges in wide and deep fjords. Compared to conventional bridges, the deep-water floating bridge has significant advantages, including lower construction costs and better environmental protection. This paper proposes a semi-submersible deep-water floating foundation and conducted an analysis of the coupled dynamic characteristics of the semi-submersible deep-water floating foundation under the coupling actions of wind and waves by using ANSYS-AQWA. The research results indicate that wind loads have a controlling effect on the displacement response of the structure, while wave loads have a controlling effect on the acceleration response of the structure.

1. Introduction

As a novel form of bridge, the deep-water floating bridge can effectively solve the technical challenges of building traditional bridges in wide sea areas with high water depths. However, compared with traditional bridges, deep-water floating bridges are more susceptible to environmental loads. Therefore, accurately assessing their structural dynamic response is of great importance.

Many scholars have conducted extensive research on the structural form and dynamic response of deep-water floating bridges. Tang M et al. studied the hydrodynamic characteristics of a certain pontoon-type floating bridge in deep water under the influence of different foundation shapes and structural parameters based on the hydrodynamic calculation software AQWA. The results showed that a reasonable size of the windward face and interface shape can significantly reduce the wave force on the structure. Moreover, it was found that the hydrodynamic characteristics and economy of a semi-submersible foundation are significantly better than those of a fully submerged one (Tang et al. 2021). Wei K et al. used a tension leg foundation deep-water floating bridge as an example and analyzed the influence of tension leg parameters on the foundation stiffness and dynamic response of the floating bridge by

calculating the pulsating wind load and wave load using the finite element analysis method. The research results showed that increasing the immersion depth of the foundation and the inclination angle of the tension leg can effectively reduce the structural dynamic response (Wei et al. 2022).

Currently, research on deep-water floating bridges is still in the theoretical stage, and there are no engineering examples of such bridges worldwide. This article proposes a semi-submersible deep-water floating foundation. Different marine environments and load combinations are studied to investigate their effects on the structural dynamic characteristics.

2. Dynamic response analysis

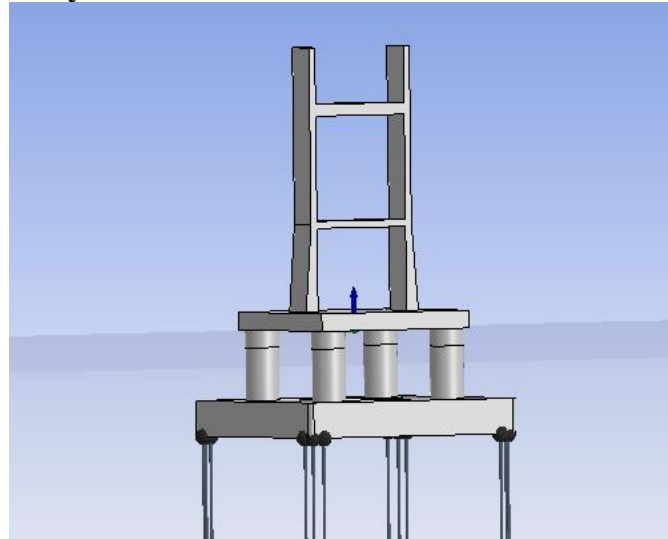


Fig. 1. Illustrated diagram of deep-water floating foundation

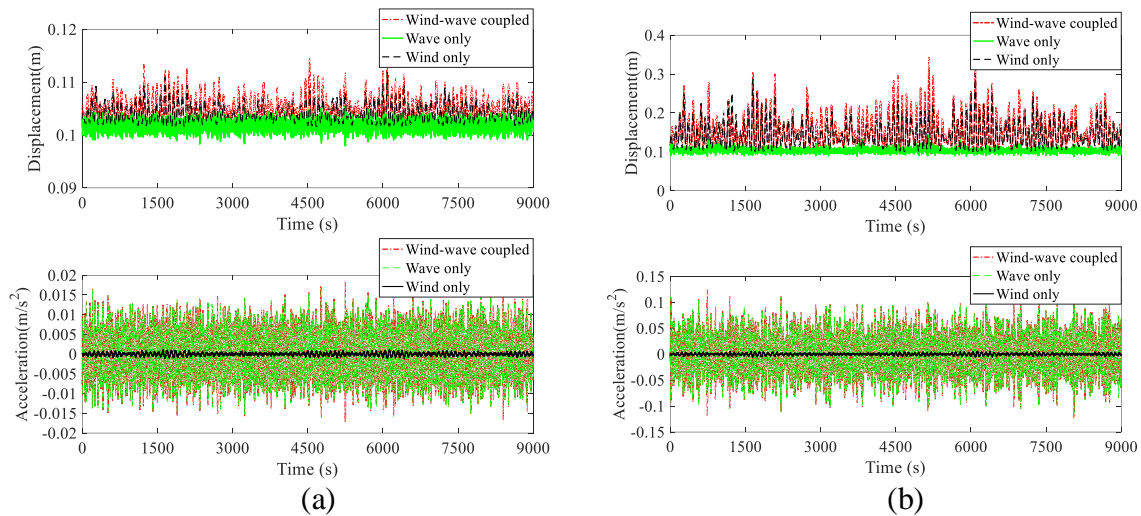
The proposed semi-submerged deep-water floating foundation in this paper consists of several key components, including the upper support platform, columns, lower floating box, and mooring system. The upper support platform supports the upper bridge structure and transfers the gravity load to the lower foundation. Its dimensions are determined by the bridge tower and lower floating box and it adopts a hollow box design. The columns connect the upper support platform and lower floating box and can also provide some buoyancy. The lower floating box mainly provides the required buoyancy for the floating foundation, and also has a ballast tank that provides restoring torque to maintain the structure vertically under external loads. It can also be used to adjust the overall center of gravity of the structure to maintain stability. The mooring system connects the floating foundation to the seabed and limits the overall displacement of the structure.

In order to investigate the role played by wind and wave loads in the coupling effect of wind and waves under different marine environments, this study examines the dynamic responses of structures under different load combinations. Specifically, this study investigates three load combinations: wind load only, wave load only, and wind-wave coupling. The wave parameters are determined based on the wind-wave deterministic relationship proposed by China (JTS 145-2015), under the given conditions of wind speed at 10 meters above sea level. The wind and wave parameters of each case are shown in Table.1.

Table 1. Characteristic parameters of wind and waves

	U10 (m/s)	Hs (m)	Ts (s)
Case 1	10	0.80	3.28
Case 2	20	1.96	4.75
Case 3	30	3.26	5.83
Case 4	40	4.58	6.64
Case 5	50	5.82	7.23

Figure 2 illustrates the displacement and acceleration responses of the structure under different loading combinations as the wind speed U10 increases from 10 m/s to 50 m/s. It is observed that both the displacement and acceleration responses of the structure increase with the increase of wind speed. The displacement and acceleration responses of the structure under wind-wave coupling are greater than those under wind load or wave load alone, and the structural response under coupling effects is not simply the superposition of the responses under individual loading conditions. When U10=10 m/s, the displacement response of the structure under wind load alone is greater than that under wave load alone, but the two loading conditions cause similar displacement responses. As wind speed increases, the displacement response of the structure under wind load alone becomes significantly greater than that under wave load alone, indicating that wind load plays a dominant role in controlling the displacement response of the structure. On the contrary, the acceleration response of the structure under wave load alone is much greater than that under wind load alone, indicating that wave load plays a dominant role in controlling the acceleration response of the structure.



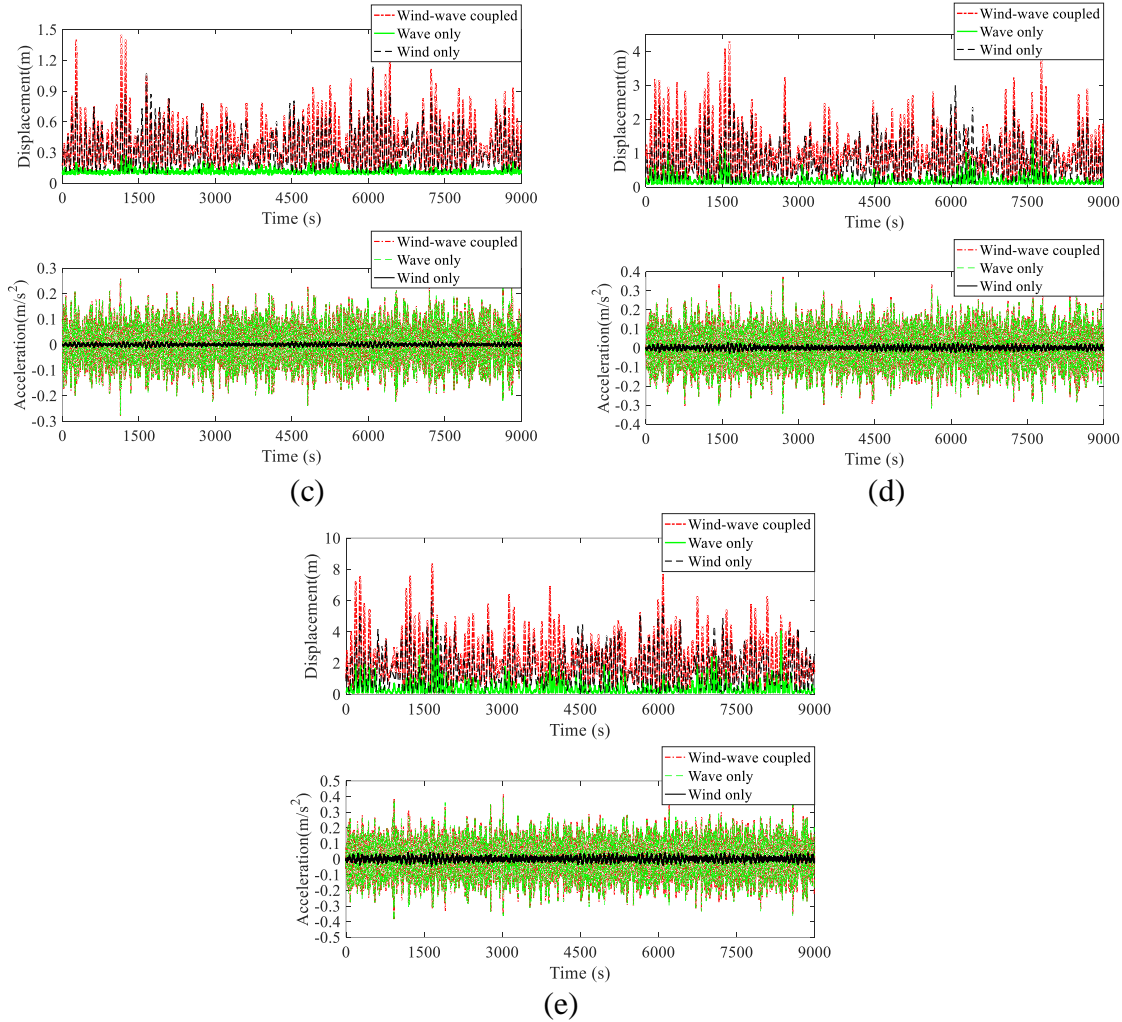


Fig. 2. Comparisons of structural dynamic response under various loading combinations: (a) $U_{10}=10\text{m/s}$; (b) $U_{10}=20\text{m/s}$; (c) $U_{10}=30\text{m/s}$; (d) $U_{10}=40\text{m/s}$; (e) $U_{10}=50\text{m/s}$

3. Conclusion

This article proposes a semi-submersible deep-water floating foundation and analyzes the coupled dynamic characteristics of the semi-submersible deep-water floating foundation under the coupling effect of wind and waves. The role of wind and wave loads in the coupling effect of wind and waves under different marine environments is studied. The research results indicate that the coupling effect of wind and waves is not simply the superposition of wind load and wave load. Wind load plays a controlling role in the displacement response of the structure, while wave load plays a controlling role in the acceleration response of the structure.

4. References

Wei, K. Zhang, F. Liao, X. and Qin, S.Q. 2023. Effect of tension leg foundation stiffness on dynamic responses of a long-span floating suspension bridge under wind and wave loads, 55(6), 47-62.



Bridge Engineering Institute Conference 2023 (BEI-2023)
Rome, Italy, July 17-20, 2023



Tang, M. Xiang, S and Cheng, B. 2021. Hydrodynamic property analysis of pontoon pile cap of deep-water floating bridge, 49(6), 78-84.

JTS 145-2015. Code of Hydrology for Harbour and Waterway.



Field Measurement Study on Wind Characteristics at the Bridge Site of Plateau Deep-Cut Canyon

Xinghui Kang¹, Yunfeng Zou^{2*}, Xuhui He³, and Longan Li⁴

¹: School of Civil Engineering, Central South University, Changsha, China; email: xinghuikang@csu.edu.cn

²: School of Civil Engineering, Central South University, Changsha, China; email: yunfengzou@csu.edu.cn

³: School of Civil Engineering, Central South University, Changsha, China; email: xuhuihe@csu.edu.cn

⁴: China Railway Major Bridge Reconnaissance & Design Institute Co. Ltd., Wuhan, China; email: lila@brdi.com.cn

*: corresponding author

Keywords: deep-cut canyon; wind characteristics; field measurement; non-stationary; turbulence

Abstract: The stiffness of long-span bridges across mountainous canyons is small, and wind has a significant impact on the structure. Affected by complex terrain, wind characteristics are significantly different between canyons and flat areas. Although there have been some studies on wind in canyons, the altitude and depth of canyons are relatively limited. There are large temperature gradients, both horizontal and vertical, in plateau deep-cut canyons, and local thermal drive greatly affects air flow. Existing studies are underrepresented, it is necessary to research the wind characteristics in plateau deep-cut canyons, under the comprehensive influence of complex terrain and thermal drive. In this study, a meteorological mast was built at the bottom of the canyon, and a long-term observation of wind was made using an ultrasonic anemometer. The drastic variation of instantaneous wind speed causes non-stationarity to be prominent, and the stability of fluctuating wind speed is studied by the run test. The applicability of the traditional stationary model is insufficient. Based on the discrete wavelet transform, the time-varying mean wind speed is extracted, and the turbulence characteristics are analyzed by the non-stationary model. The research results provide a reference for the wind resistance design of bridges in similar landforms.

1. Introduction

Accurately obtaining the wind characteristics at the bridge site is critical for the wind resistance design of long-span bridges. Generally, to study the wind characteristics of complex terrain by wind tunnel tests, computational fluid dynamics (CFD) and field measurements. Relatively, there are assumptions and simplifications in tests and CFD, and measurements are more direct and efficient. Measurement of wind fields is usually done to establish the meteorological mast or automatic weather station at the bridge site (Li et al., 2022), and there are also researchers who place sensors on construction catwalks, main girders or bridge towers (Yu et al., 2019). Affected by complex terrain, the wind speed in deep-cut canyons has strong non-stationarity, and the traditional stationary model overestimates the turbulence characteristics of the wind (Yu et al., 2019). The top of the plateau canyon is covered with perennial snow, and the bottom is relatively warm and dry. There are larger temperature gradients in the canyon, and local thermal drive has a

significant impact on wind flow (Li et al., 2022). In the study, a V-shaped plateau deep-cut canyon is selected as the research object. A meteorological mast was set at the bottom of the canyon and anemometers were installed, to obtain the mean wind characteristics, such as wind speed and wind direction. The stationarity of fluctuating wind speed was discussed by the run test, and the turbulence wind characteristics were analyzed based on the non-stationary model.

2. Canyon Topography and Measurement System

The wind field measurement is based on the construction of a long-span bridge on the Qinghai-Tibet Plateau. The landform of the bridge site is a typical V-shaped plateau deep-cut canyon, with an altitude of the mountaintop above 5000 m and a vertical height difference of over 2000 m. A meteorological mast was set up at the bottom of canyon, and an ultrasonic anemometer was placed at the top of mast, with a height of 40 m and a sampling frequency of 10 Hz, as shown in Fig. 1.

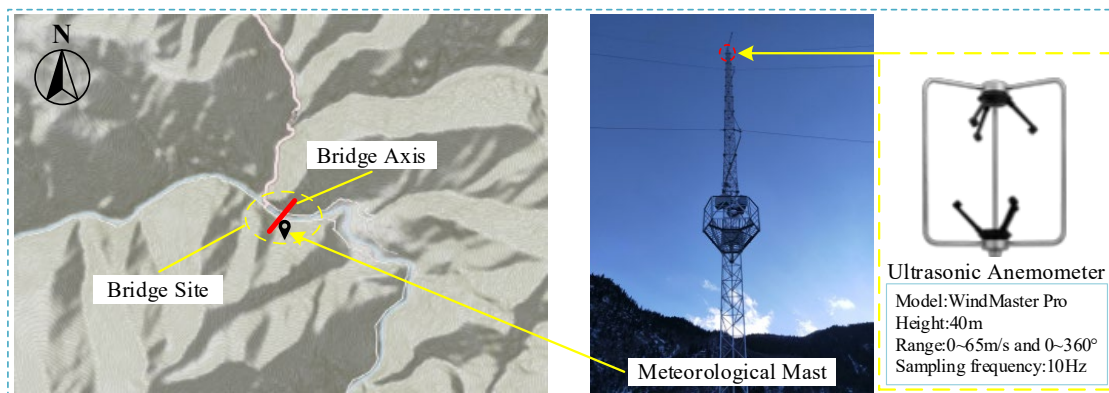


Fig. 1. Feature of canyon topography and layout of measurement system

3. Wind Characteristics

3.1. Mean wind speed and wind attack angle

The length of the basic time interval significantly affects the results of wind characteristics, and is uniformly taken as 10 min. Furthermore, the impact of low winds on the structure is relatively limited, and only 1225 samples with a mean wind speed higher than 6 m/s were studied, accounting for 2.3% of the total. The distribution of wind speed and wind attack angle is shown in Fig. 2. The wind speed from 90° to 180° of wind direction is lower, and with the increase in wind speed, the wind direction is concentrated in the range of 315° to 0°. The wind attack angle is basically negative from 90° to 270° of wind direction, and positive from 270° to 90°. The attack angle is significantly related to wind direction, and its value is more concentrated at high wind speeds.

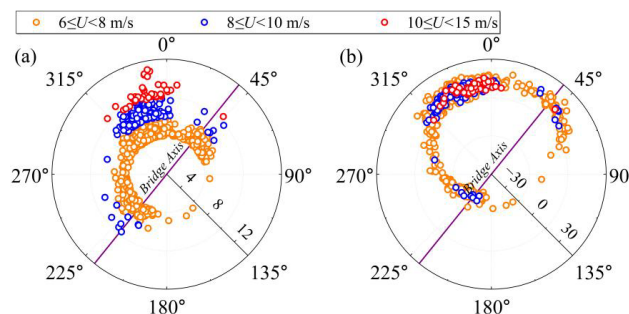


Fig. 2. Distribution of wind speed and wind attack angle: (a) wind speed; (b) wind attack angle

3.2. Wind speed model and stationary test

The fluctuating wind speed is obtained by subtracting its own mean value from the instantaneous wind speed. Stationary model assumes that mean wind speed remains constant, as shown in Eq. 1.

$$U(t) = \bar{U} + u(t) \quad (1-a)$$

$$V(t) = v(t) \quad (1-b)$$

$$W(t) = w(t) \quad (1-c)$$

where $u(t)$, $v(t)$ and $w(t)$ denote the zero-mean fluctuating wind speeds in downwind, acrosswind and vertical; and \bar{U} is the constant mean wind speed. Non-stationary model assumes that mean wind speed changes gradually over the basic time interval, as shown in Eq. 2.

$$U(t) = \bar{U}(t) + u(t) \quad (2-a)$$

$$V(t) = \bar{V}(t) + v(t) \quad (2-b)$$

$$W(t) = \bar{W}(t) + w(t) \quad (2-c)$$

where $\bar{U}(t)$, $\bar{V}(t)$ and $\bar{W}(t)$ denote the time-varying mean wind speed in downwind, acrosswind and vertical. Here, the discrete wavelet transform is used to extract the time-varying mean wind speed, db10 wavelet is selected, and the decomposition level is 9. The run test was used to analyze the stationarity of the fluctuating wind speed, the results as shown in Table 1. The non-stationarity of wind is stronger, decreased with the increase in wind speed. The non-stationary model can significantly reduce the non-stationarity of wind for the analysis of turbulence characteristics.

Table 1. Proportion of stationary fluctuating wind based on run test

Wind speed model	0~6 m/s (Mean wind speed)			6~15 m/s (Mean wind speed)		
	u	v	w	u	v	w
Stationary	13.4%	13.0%	13.0%	30.6%	34.3%	32.6%
Non-stationary	58.6%	58.6%	58.6%	68.1	68.2%	68.8%

3.3. Turbulence intensity and gust factor

Fig. 3 shows turbulence intensity, and Fig. 4 shows gust factor. The mean values in downwind, crosswind, vertical are 0.182, 0.149, 0.164 of turbulence intensity, and 1.482, 0.411, 0.439 of gust factor. The ratios between components are $I_u:I_v:I_w=1:0.82:0.90$, and $G_u-1:G_v:G_w=1:0.85:0.91$. Turbulence intensity and gust factor decrease with the increase in wind speed, and become more concentrated. The ratios of two groups are very close, and the distribution with wind direction is basically the same, which symbolizes the correlation between turbulence intensity and gust factor.

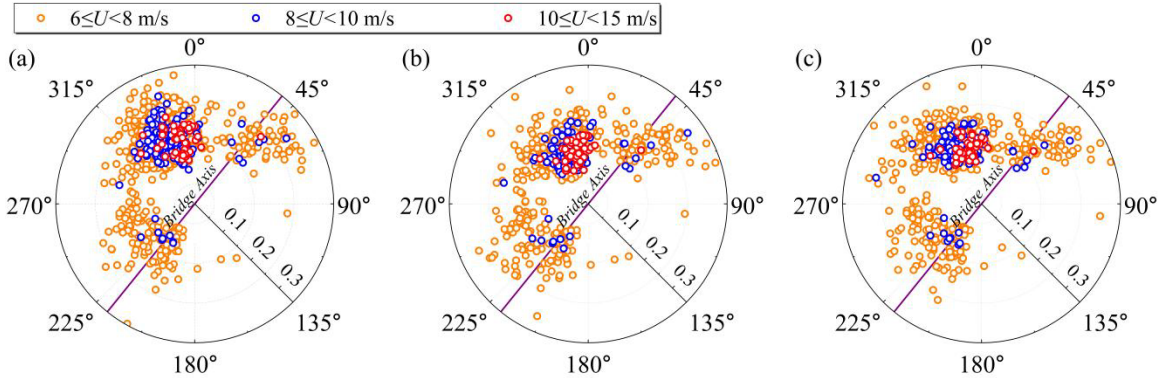


Fig. 3. Distribution of turbulence intensity: (a) I_u ; (b) I_v ; (c) I_w

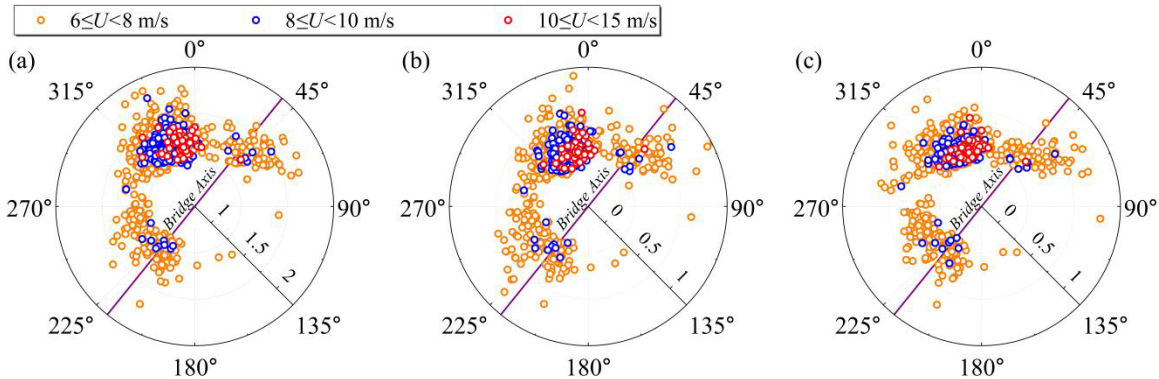


Fig. 4. Distribution of gust factor: (a) G_u ; (b) G_v ; (c) G_w

3.4. Turbulence integral scale

Fig. 5 shows the distribution of the turbulence integral scale, and the mean values of downwind, crosswind, and vertical are 28.8 m, 22.7 m, and 20.1 m, respectively. The ratio between the components is $L_u:L_v:L_w=1:0.79:0.70$. Turbulent eddies have larger scales at high wind speeds.

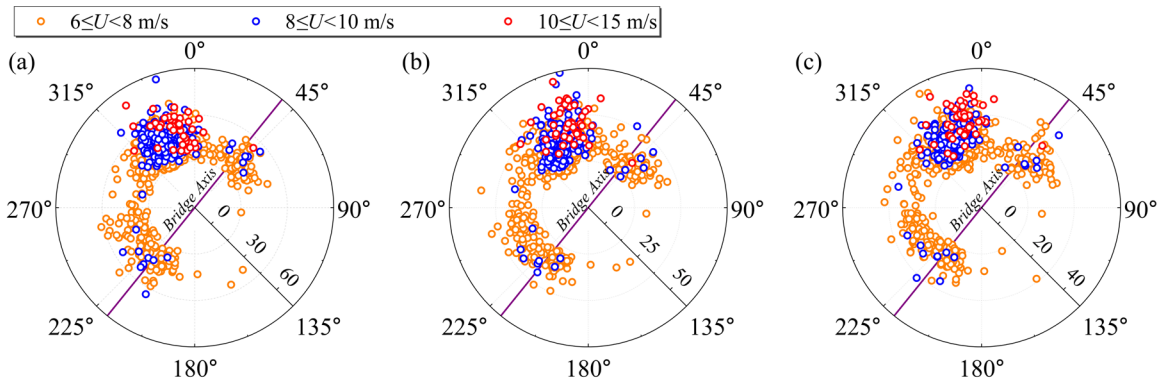


Fig. 5. Distribution of turbulence integral scale: (a) L_u ; (b) L_v ; (c) L_w

4. Conclusions

In this study, measurement of wind filed was carried out in a plateau deep-cut canyon. Restricted and obstructed by terrain, wind speed is low, with only 2.3% exceeding 6m/s. The non-stationarity of wind is prominent, and the turbulence characteristics are analyzed based on the non-stationary model. The correlations between turbulence characteristics and wind speed or wind direction are



discussed, and the values and ratios between components are given. Turbulence intensity and gust factor decrease, and the turbulence integral scale increases, with the increase in wind speed.

5. References

Li Y, Jiang F, Zhang M, Dai Y, Qin J and Zhang J. (2022) ‘Observations of periodic thermally-developed winds beside a bridge region in mountain terrain based on field measurement’, *Journal of Wind Engineering and Industrial Aerodynamics*, 225: 104996.

Yu C, Li Y, Zhang M, Zhang Y and Zhai G. (2019) ‘Observations of periodic thermally-developed winds beside a bridge region in mountain terrain based on field measurement’, *Journal of Wind Engineering and Industrial Aerodynamics*, 186, 94-104.



Dynamical Analysis of Vehicle-Bridge Interaction System under Ice and Wind Loads

Tianyu Wu^{1,2,*}, Wenliang Qiu¹, Guowen Yao², and Zengwei Guo²

¹: Faculty of Infrastructure Engineering, Dalian University of Technology, Dalian City 116024, China

²: State Key Laboratory of Mountain Bridge and Tunnel Engineering, Chongqing Jiaotong University, Chongqing City 400074, China

Abstract: This study constructs a complete analysis framework of ice-wind-vehicle-bridge interaction to investigate dynamic responses of the coupled system. Ice load, wind load, nonlinear soil spring and additional water mass are all integrated into a full bridge model based on a sea-crossing bridge with running vehicles. The results indicate that the combined action of ice and wind has no superimposed effect on the movement of the bridge, but has a restraining effect. The coupled dynamic responses of the vehicle cannot be combined by the superposition under separate ice and wind.

Keywords: Sea-crossing bridges; ice-wind-vehicle-bridge interaction; vibration analysis

1. Introduction

There is a harsh working environment for sea-crossing bridges in cold sea region. As well as being able to withstand the impact of ice load, it must also take into account the combined effect of strong wind, water-structure interaction, soft foundation on the seabed, and other complex factors. This poses a great threat to the safe operation of bridges. Therefore, the coupled vibration analysis of ice-wind-vehicle-bridge interaction system is an unavoidable research topic for the construction of bridges in cold sea region.

Many research scholars have carried out targeted studies on the analysis of vehicle-bridge coupled vibration. For the ice load action, Xia^[1] establishes a numerical analysis model of the vehicle-bridge coupled system under ice load and proposes an iterative method applicable to the time-integrated full process of the vehicle-bridge dynamic coupled system. Xia et al.^[2] systematically investigates the influence law of impact load type, impact intensity, train velocity on the safety index. Specifically, it describes the method for determining the impact intensity-train velocity threshold curve. Wu et al.^[3] defines the contact relationship between the wheels and the bridge deck by using the penalty function method, and analyzes the driving safety under the random vibration caused by ice load.

However, there is a lack of research on the vibration between vehicles and bridges under the combined action of ice and wind. As such, this study presents a framework for the dynamic analysis of coupled ice-wind-vehicle-bridge systems. It systematically studies the dynamic response of bridges and vehicles under the combined action of ice and wind loads, and analyzes the effects of different ice and wind velocities on the safety of traffic on bridges. The results of this study can be used as a reference to evaluate the driving safety of sea-crossing bridges in cold sea region.

2. Analysis Framework of Ice-Wind-Vehicle-Bridge Interaction System

2.1. Modeling of the high-sided road truck

This study focuses on the vehicle-bridge interaction of the high-sided road truck under lateral load. A two axle four-wheel light high-sided road truck is adopted in this study, as shown in Fig. 1. The light truck is composed of rigid body, spring and damper, with 13 degrees of freedom. The following generalized displacement vector can represent the dynamical system of the light truck used in this study.

$$V = \{Z_v, Y_v, \theta_v, \phi_v, \psi_v, Z_{s11}, Y_{s11}, Z_{s12}, Y_{s12}, Z_{s21}, Y_{s21}, Z_{s22}, Y_{s22}\} \quad (1)$$

where Z_v is the vertical displacement of the vehicle; Y_v is the lateral displacement of the vehicle; θ_v denotes the pitch angle of the vehicle; ϕ_v denotes the rotation angle of the vehicle; ψ_v represents swing angle of the vehicle. Z_{s11} , Z_{s12} , Y_{s11} and Y_{s12} respectively represent the vertical displacement and lateral displacement of the two rigid bodies on the front axle of the vehicle. Z_{s21} , Z_{s22} , Y_{s21} and Y_{s22} respectively represent the vertical displacement and lateral displacement of the two rigid bodies on the rear axle of the vehicle body.

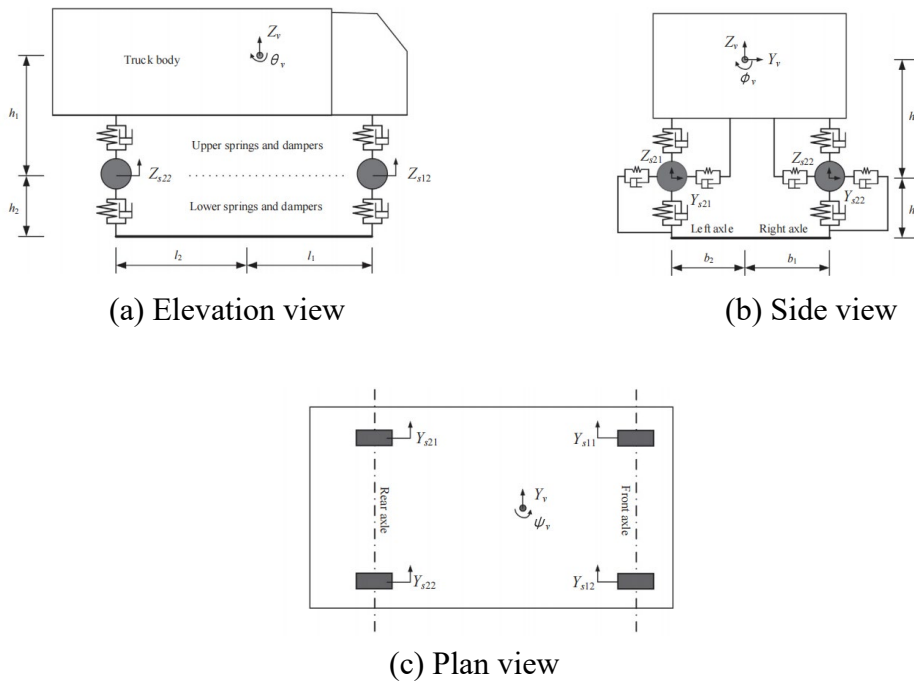


Fig. 1. The high-sided road truck

2.2. Modeling of the sea-crossing bridge

The overall configuration of (5×120) m non-navigable bridge is investigated in this study. The cross section form of the bridge girder is steel box girder section, and two-way 6 lanes are set, as shown in Fig. 2. In bridge design, the pile-cap is located at the design water level elevation, so drift ice can affect the large volume of the pile-cap, rather than acting on the pier or pile foundation. The overall bridge model is established based on ABAQUS finite element platform. The girder of the bridge is built by the spatial plate element (S8R). The piers, pile-caps, steel pipe piles are modeled by the three dimensional beam element (B31). The dynamic action of water is simulated by the additional water mass. The soil-structure interaction (SSI) is considered by using the classical p-y nonlinear soil spring. The full bridge model of vehicle-bridge

coupling system based on ABAQUS in this work, as shown in Fig. 3. In this study, the penalty function built into ABAQUS is used to define contact conditions between the vehicle and the bridge, allowing the separation and sliding between the wheel of the vehicle and the deck of the bridge.

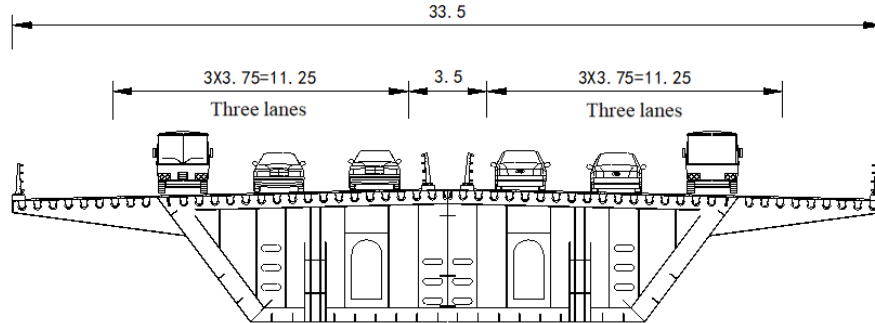


Fig. 2. Cross section configuration of the non-navigable bridge in this study (unit: cm)

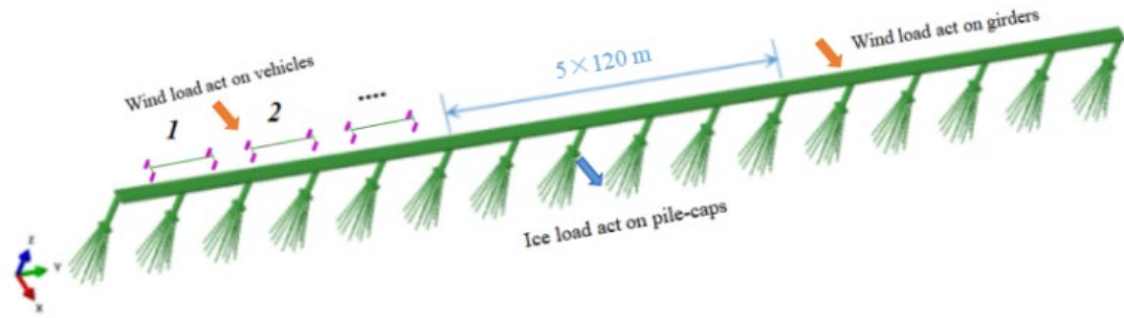


Fig. 3. Full bridge model of vehicle-bridge coupling system in ABAQUS

2.3. Coupled dynamic equation of ice-wind-vehicle-bridge interaction system

The coupled dynamic equation is established with full consideration of vehicles, bridges, additional water mass and soil-structure interaction. Ice load and wind load are applied to overall dynamic system as external loads. Therefore, the coupled dynamic equation of ice-wind-vehicle-bridge interaction system can be expressed as:

$$\begin{bmatrix} M_{bb} + M_w & 0 \\ Sym & M_v \end{bmatrix} \begin{Bmatrix} \ddot{w}_b \\ \ddot{w}_v \end{Bmatrix} + \begin{bmatrix} C_{bb} + C_i & C_{bv} \\ Sym & \bar{C}_v \end{bmatrix} \begin{Bmatrix} \dot{w}_b \\ \dot{w}_v \end{Bmatrix} + \begin{bmatrix} K_{bb} + K_s & K_{bv} \\ Sym & \bar{K}_v \end{bmatrix} \begin{Bmatrix} w_b \\ w_v \end{Bmatrix} = \begin{Bmatrix} F_{bb} + F_{ice} + F_{bw} \\ F_{vv} + F_{vw} \end{Bmatrix} \quad (2)$$

here subscripts bb , vv , and bv denote the bridge, vehicle, and vehicle-bridge interaction terms, respectively.

It should be noted that due to there is an additional damping term C_i , the new damping term in the motion equation includes the damping of the bridge structure and the damping caused by ice load.

3. External Excitation Loads

3.1. Ice-induced vibration model

After linearization, the multilinear relationship between ice compression strength and stress rate can be approximately expressed as:

$$\sigma_i = b_i + a_i \dot{\sigma}_i \quad (3)$$

where a_i and b_i are slope and intercept of segment i . σ_i is the crushing strength of ice.

Määttänen^[4] gives the expression of stress rate and relative velocity during the compressive failure of ice.

$$\dot{\sigma}_i = 8\sigma_1 v_r / \pi D \quad (4)$$

where D is the structure diameter.

Therefore, the total ice force on the structure can be written as:

$$F(v_r) = F(v_{ice} - \dot{u}) = A \times \sigma(v_{ice} - \dot{u}) = A \left(a_i \times (v_{ice} - \dot{u}) \frac{8\sigma_1}{\pi D} + b_i \right) = \left(A \times b_i + v_{ice} \times A \times a_i \frac{8\sigma_1}{\pi D} \right) - \dot{u} \times A \times a_i \frac{8\sigma_1}{\pi D} \quad (5)$$

where h is the ice thickness, A is the contact area under ice-induced vibration.

For the linearized ice load model, the ice load simulation can be divided into three piecewise functions according to the ice stress rate, which can be written as:

$$F(v_{ice}) = \begin{cases} \left(b_1 + v_{ice} \times a_1 \frac{8\sigma_1}{\pi D} \right) A \\ \left(b_2 + v_{ice} \times a_2 \frac{8\sigma_1}{\pi D} \right) A \\ b_3 A \end{cases} \quad (6)$$

The damping coefficient changes with the stress rate of ice, and its subsection expression can be written as:

$$C' = \begin{cases} a_1 \frac{8\sigma_1}{\pi D} A \\ a_2 \frac{8\sigma_1}{\pi D} A \\ 0 \end{cases} \quad (7)$$

3.2. Wind load

3.2.1. Wind load on bridges

The steady wind load on the girder of the bridge includes the lift force (L_{st}) in the vertical direction, the drag force (D_{st}) in the lateral direction and the bending moment (M_{st}) in the torsion direction, which can be expressed as:

$$L = \frac{1}{2} \rho U^2 B C_L \quad (8a)$$

$$D = \frac{1}{2} \rho U^2 B C_D \quad (8b)$$

$$M = \frac{1}{2} \rho U^2 B^2 C_M \quad (8c)$$

here U denotes the average wind velocity; B stands for the width of the girder; C_D , C_L and C_M represent the drag, lift and moment coefficients.

The buffeting force including aerodynamic admittance function of the bridge girder suggested by Scanlan^[5] can be expressed as:

$$L_b(t) = \frac{1}{2} \rho U^2 B \left[C_L I_{Lu} \frac{2u(t)}{U} + [C'_L + C_D] I_{Lw} \frac{w(t)}{U} \right] \quad (9a)$$

$$D_b(t) = \frac{1}{2} \rho U^2 B \left[C_D I_{Du} \frac{2u(t)}{U} + C'_D I_{Dw} \frac{w(t)}{U} \right] \quad (9b)$$

$$M_b(t) = \frac{1}{2} \rho U^2 B^2 \left[C_M I_{Mu} \frac{2u(t)}{U} + C'_M I_{Mw} \frac{w(t)}{U} \right] \quad (9c)$$

in which $L_b(t)$, $D_b(t)$ and $M_b(t)$ are the buffeting lift, drag and moment; C'_L , C'_D and C'_M are the slope of the C_L , C_D and C_M ; $u(t)$ and $w(t)$ denote the velocity components of fluctuating wind in horizontal and vertical direction; $I_{()}$ stands for the aerodynamic admittance function.

3.2.2. Wind load on vehicles

The aerodynamic wind loads on the vehicle can be calculated based on the quasi-steady approach whose formulae is determined by a function of the yaw angle ψ ^[6]. The aerodynamic load and moment on the vehicle can be calculated according to the following equations:

$$F_x = \frac{1}{2} \rho U_R^2 C_D(\Psi) A_f \quad (10a)$$

$$F_y = \frac{1}{2} \rho U_R^2 C_S(\Psi) A_f \quad (10b)$$

$$F_z = \frac{1}{2} \rho U_R^2 C_L(\Psi) A_f \quad (10c)$$

$$M_x = \frac{1}{2} \rho U_R^2 C_R(\Psi) A_f h_v \quad (10d)$$

$$M_y = \frac{1}{2} \rho U_R^2 C_P(\Psi) A_f h_v \quad (10e)$$

$$M_z = \frac{1}{2} \rho U_R^2 C_Y(\Psi) A_f h_v \quad (10f)$$

here F_x stands for drag force, F_y stands for side force, F_z stands for lift force, M_x stands for rolling moment, M_y stands for pitching moment and M_z stands for yawing moment; $C_D(\psi)$ denotes the drag force coefficient, $C_S(\psi)$ denotes the side force coefficient, $C_L(\psi)$ denotes the lift force coefficient, $C_R(\psi)$ denotes the rolling moment coefficient, $C_P(\psi)$ denotes the pitching moment coefficient, $C_Y(\psi)$ denotes the yawing moment coefficient; A_f denotes the reference area; h_v denotes the reference height.

4. Dynamic Responses Analysis

4.2. Influence of combined ice and wind loads

It can be seen from Fig. 4 that the maximum lateral displacement of the bridge girder under ice load is greater than that under combined ice and wind loads. Although the ice and wind loads are imposed along the same direction of the transverse bridge, the lateral dynamic response of the bridge is not a simple linear superposition of the displacement caused by ice and wind loads. It can be interpreted as when the ice load is applied to the pile-cap of the bridge substructure, the movement direction of the girder of the bridge superstructure is opposite to the application direction of the ice load. The wind load is directly applied to the

bridge girder, and the motion direction of the bridge girder under wind load is the same as the application direction of the wind load. Therefore, the combined action of ice and wind loads have no superposition effect on the movement of the bridge girder, but has a restraining effect in the opposite direction. In addition, it can be found that the maximum displacement of the bridge girder decreases with the increase of wind velocity. For example, when the wind velocities are 0 m/s, 10 m/s, 15 m/s and 20 m/s, the maximum lateral displacement are 62.75 mm, 59.46 mm, 57.51 mm and 55.05 mm, respectively. This again shows that the wind load and ice load have opposite contributions to the motion of the bridge girder. However, from the results, ice load has a greater impact on the dynamic response of the bridge girder than wind load.

It can be seen from Fig. 5 that the vertical displacement of the bridge girder under ice load is greater than that of under combined ice and wind loads. It can be interpreted as the ice load is only applied to the transverse bridge, which has little contribution to the vertical vibration of the bridge. However, wind load on the bridge includes the lifting force applied on the bridge girder, which can reduce the vertical displacement of the bridge girder. It can also be found that due to the increase of wind velocity, the lifting force on the bridge girder also increases, which makes the vertical displacement of the bridge girder show a decreasing trend.

It can be clearly seen from Fig. 6 that when only ice load acts on the bridge, the lateral contact force of the vehicle fluctuates at a lower average level. This is because when there is no transverse wind load acting on the bridge, the vehicle movement only occurs with the transverse vibration of the ice-induced bridge. However, when considering the combined effect of ice and wind loads on the bridge, it can be found that the lateral contact force of the vehicle increases significantly and fluctuates at a higher average level. For example, when the wind velocities are 0 m/s, 10 m/s, 15 m/s and 20 m/s, the average value of lateral contact force are 1.75 kN, 9.09 kN, 12.91 kN and 17.77 kN, respectively. This also shows that with the increase of wind velocity, the lateral contact force of the vehicle will also increase, which is very unfavorable to the driving safety.

It can be seen from Fig. 7 that the vertical contact force of the vehicle under the combined ice and wind loads is slightly larger than that under ice load. The vertical contact force of the vehicle is mainly affected by the pavement roughness, but the wind load also has a certain impact on the vertical contact force of the vehicle. With the increase of wind velocity, the vertical contact force of the vehicle increases slightly.

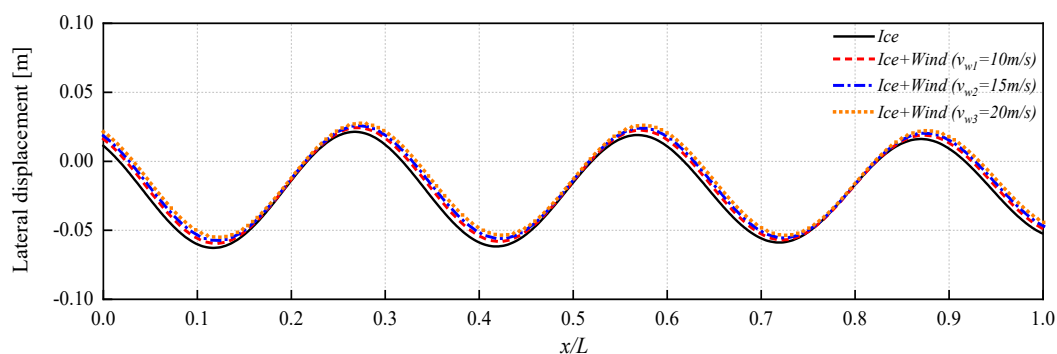


Fig. 4. Lateral displacement of bridge girder under combined ice and wind loads

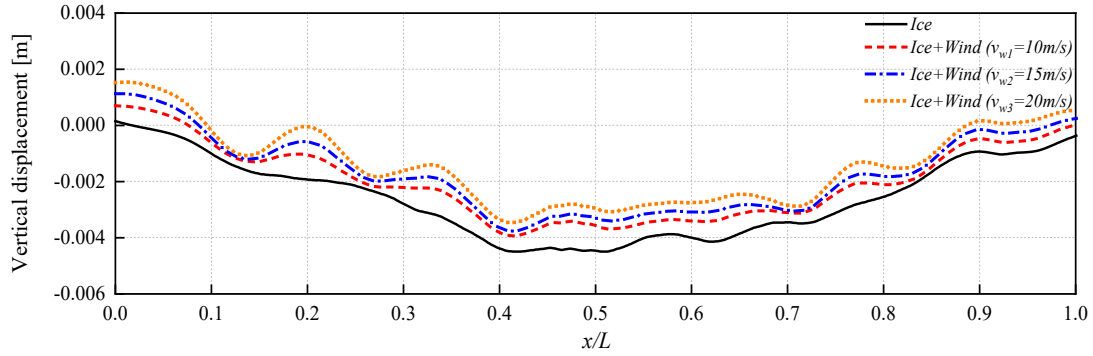


Fig. 5. Vertical displacement of bridge girder under combined ice and wind loads

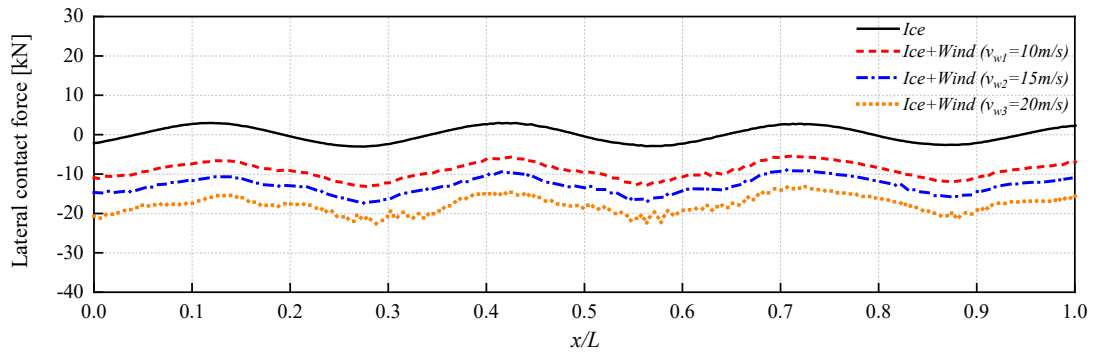


Fig. 6. Lateral contact force between tires and bridge deck under combined ice and wind loads

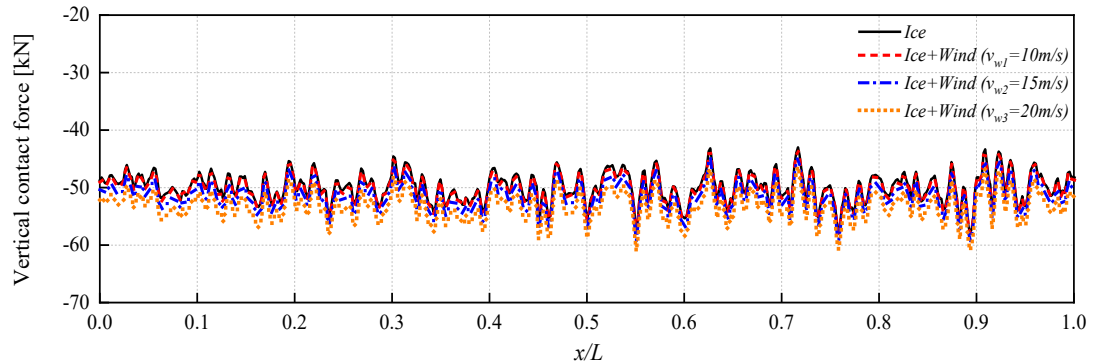


Fig. 7. Vertical contact force between tires and bridge deck under combined ice and wind loads

5. Conclusions

The ice load has a greater influence on the lateral dynamic response of the bridge, while the wind load has a more significant influence on the lateral dynamic response of the vehicle. Due to the different action characteristics of ice load and wind load on the vehicle-bridge interaction system, the lateral dynamic responses of the bridge and vehicle under separate ice and wind loads cannot be combined by superposition. The combined action of ice and wind should be reasonably considered in the driving safety analysis of sea-crossing bridges in ice covered waters.

6. Acknowledgments

This work was financially supported by the National Natural Science Foundation of China (52201313), the Fundamental Research Funds for the Central Universities (DUT22RC(3)091), State Key Laboratory Science Foundation of Mountain Bridge and Tunnel Engineering (SKLBT-2101).



7. References

- [1] Xia C Y. Dynamic responses of train-bridge system subjected to collision loads and running safety evaluation of high-velocity trains. Doctoral Dissertation, Beijing Jiaotong University, 2012.
- [2] Xia C Y, Lei J Q, Zhang N, et al. Dynamic analysis of a coupled high-velocity train and bridge system subjected to collision load. *Journal of Sound and Vibration*, 2011, 331(10): 2334-2347.
- [3] Wu T Y, Qiu W L, Kim C W, Chang K C, Lu X Z. Dynamic responses of a vehicle-bridge-soil interaction system subjected to stochastic-type ice loads. *Structure and Infrastructure Engineering*, 2021, 2023586: 1-20.
- [4] Määttänen M. On conditions for the rise of self-excited ice-induced autonomous oscillations in slender marine pile structures. Winter Navigation Research Board, 1978.
- [5] Scanlan R H, Jones N P. Aeroelastic analysis of cable-stayed bridges. *Journal of Structural Engineering*, 1990, 116(2): 279-297.
- [6] Zhou Y and Chen S. Fully coupled driving safety analysis of moving traffic on long-span bridges subjected to crosswind. *Journal of Wind Engineering and Industrial Aerodynamics*, 2015, 143:1-18.



Safety Analysis of Wind Barriers on the Bridge under the 400 km/h High-Speed Trains Loading of Slipstreams

Diany Guo¹, Yunfeng Zou^{2*}, Xuhui He³, and Haobo Liang⁴

¹: School of Civil Engineering, Central South University, Changsha and China; email: guodiany@csu.edu.cn

²: School of Civil Engineering, Central South University, Changsha and China; email: yunfengzou@csu.edu.cn

³: School of Civil Engineering, Central South University, Changsha and China; email: xuhuihe@csu.edu.cn

⁴: School of Civil Engineering, Central South University, Changsha and China; email: haoboliang0816@163.com

*: corresponding author

Keywords: high-speed railway; loading of slipstreams; wind barrier; dynamic response; concrete damage

Abstract: The loading of slipstreams induced by a high-speed train (HST) passing through the bridge at 400 km/h may generate repeated impacts on the wind barrier, which can cause significant dynamic responses and structural damage, such as concrete cracking at the foundation. This poses a threat to the long-term durability of the barrier itself. To accurately evaluate the effect of slipstreams on the wind barrier, this paper conducts a three-step study on the dynamic response of the wind barrier column structure and the structural damage of the anchor-end concrete under the loading of slipstreams. Firstly, numerical simulation is used to analyze the variation of slipstream loading on the wind barrier when a 400 km/h HST passes over the bridge, and the distribution and laws of wind pressure inside the barrier for trains are analyzed, determine the loading of slipstreams curve at the most disadvantageous position. Next, finite element analysis (FEA) is used to study the structural static and dynamic response of the wind barrier column under the slipstream loading, considering the influence of different wind barrier heights, column spacing, and distance between the center-line of the track and the wind barrier. Finally, nonlinear finite element analysis (NFEA) is used to calculate the degree of damage to the anchor-end concrete, the safety and durability of the wind barrier on the bridge when a 400 km/h HST passes over it are evaluated.

1. Introduction

With the further increase in the speed of high-speed railways, the 400 km/h high-speed railway will be put into use in the future. Compared with ground-level travel, bridge-level travel has the characteristics of high wind speed and prominent aerodynamic interference of the vehicle-bridge, and the operation of trains in high wind conditions will be limited or suspended. Previous studies have shown that the wind speed threshold for a train passing over a 32m simply supported beam bridge at a speed of 400 km/h is 12.5m/s (Li et al. 2021). Wind barriers installed on both sides of

the bridge are currently the most common protection measure, which can create a lower local wind environment to protect the operation of trains. However, high-speed trains will cause fluctuating pressure loads on the surrounding structures, resulting in structural deformation, bolt loosening, and other disasters (Carassale and Brunenghi, 2013). Currently, many scholars have focused on the vibration response of wind barriers. Belloli et al. (2012) conducted on-site experiments and wind tunnel tests to obtain the pressure load curve of train wind loads on sound barriers. They established a finite element model of sound barriers and calculated their vibration response. Tokunaga et al. (2013; 2016) conducted on-site measurements and numerical calculations on half-covered snow-type sound barriers. The results showed that the dynamic response of the sound barrier may resonate with the vibration frequency of the train, which is the superposition of resonance and dynamic effects of the train wind. Carassale and Brunenghi (2013) conducted on-site measurements of steel frame structures beside the track, measured the acceleration response of the structure, and established a mathematical model to predict the dynamic behavior of the structures. Rocchi et al. (2018) conducted on-site measurements to study the dynamic loads of different trains on sound barriers and measured the strain of the sound barrier base. Friedl et al. (2011) established a finite element model of sound barriers and analyzed the response of the structure under dynamic cyclic loads, obtaining the maximum deformation and stress on a single column, and finally calculated the fatigue performance of the sound barrier. Vittozzi et al. (2017) modeled upright barriers and conducted dynamic analysis with tuned mass dampers (TMD) installed at the top of the column. The results showed that the TMD system can effectively reduce vibration amplitude and cycle times, and reduce the stress and fatigue of the sound barrier base. Many scholars mainly focus on the dynamic response of wind barriers themselves, and rarely pay attention to other safety issues of wind barriers, such as concrete damage. This will greatly affect the estimated service life of wind barriers and pose a threat to the safety of train operation. Therefore, research on the safety of wind barriers for 400 km/h high-speed railway bridges is urgently needed.

2. Methodology

2.1 Computational fluid dynamics

This study adopts the “head car + middle car + tail car” formation mode and uses a combination of structured and unstructured grids to accurately simulate the detailed structures of the train and the barrier. The accuracy of the simulation is verified by comparing the results with the field measurements provided by (Xiong et al. 2018). The ultimate goal is to calculate the fluctuating wind pressure on the wind barrier under the slipstreams generated by a 400 km/h high-speed train.

2.2 FEA dynamic response loading

The dynamic response analysis of the wind barrier to the slipstream loading is carried out using the full method, which takes into account the train’s travelling wave effect. The loading of slipstreams induced by HST are applied to the wind barrier, as shown in Fig. 1, which illustrates the lateral force distribution pattern on the wind barrier when train reaches same locations.

2.3 NFEA concrete damage calculation

We established a finite element model of the wind barrier anchor and concrete using ABAQUS, and calculated the stress and deformation of each component using 8-node reduced integration solid elements (C3D8R). The concrete used the Mohr-Coulomb elastic-plastic constitutive model,

while other materials used linear elastic models. The structure of the finite element model is shown in Fig. 2. We applied dynamic response analysis to calculate the maximum displacement value of the wind barrier column and then determined the concrete damage.

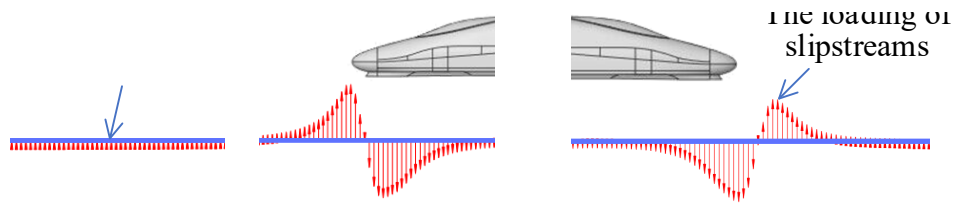


Fig. 1. Lateral force distribution pattern on the wind barrier when train reaches same locations (train moving left): (a)the train didn't arrive; (b)headstock arrive; (c)tailstock arrive

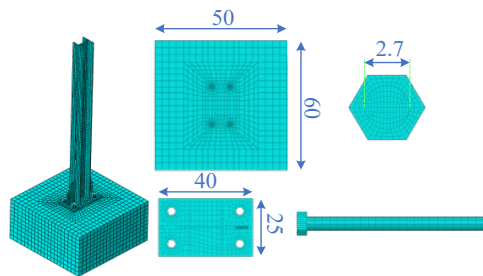


Fig. 2. Model grid (Unit: cm)

3. Results and Discussion

3.1 Slipstream effects of the wind barrier

From Fig. 3, it can be observed that as the train passes through the wind barrier area, the wind pressure on the barrier gradually decreases from bottom to top along the height direction, showing a trend of gradually decreasing. Along the length direction, it shows a pattern of larger pressure in the middle and smaller pressure at the entrance and exit.

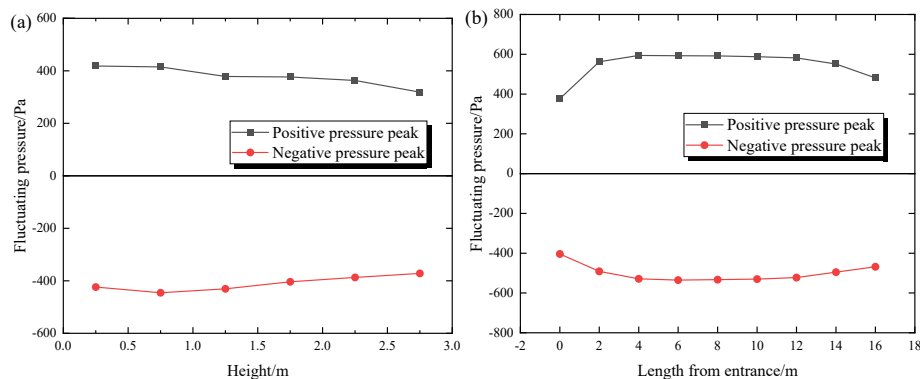


Fig. 3. Wind barrier pressure peak variation curve: (a) along the height direction; (b) along the length direction

3.2 Dynamic response of the wind barrier

Fig. 4 shows the dynamic response of the wind barrier, and Fig. 4 (a) shows the displacement response of the wind barrier. It can be seen that the peak displacement response of the wind barrier is basically consistent with the “head wave” and “tail wave” of the train pulsating wind load. The displacement response generated by the head wave is larger, with a maximum response of 1.7mm. Fig. 4 (b) shows the stress response of the wind barrier, which is also basically consistent with the slipstream loading. The maximum equivalent stress occurs at the bottom of the column, resulting in stress concentration.

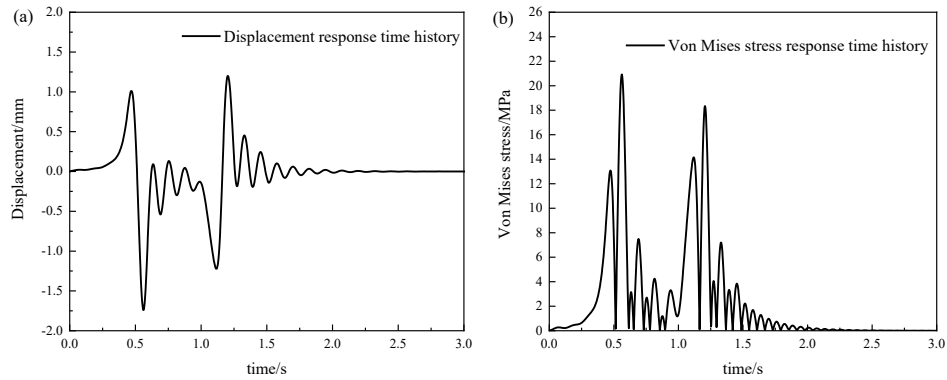


Fig. 4. Wind barrier response time history: (a) displacement; (b) Von Mises stress

3.3 Concrete damage of the anchor-end

Fig. 5 shows the stress state of the concrete at the anchor-end. Fig. 5 (a) shows the maximum principal tensile stress, with a maximum value of 1.97. and Fig. 5 (b) shows the tensile damage factor of the concrete, with a maximum damage factor of 0.969.

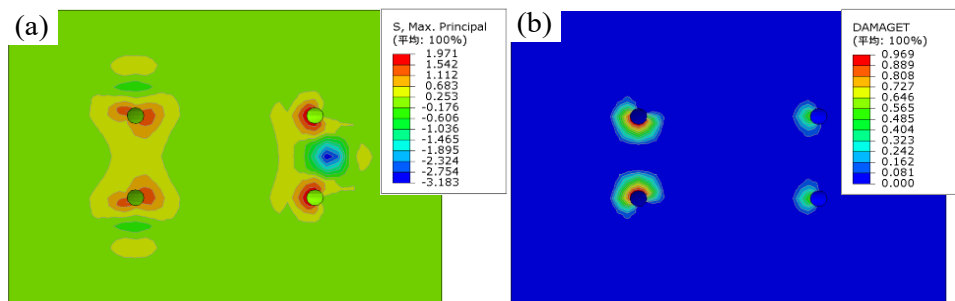


Fig. 5. Concrete stress state: (a) maximum principal stress; (b) tensile damage

4. Conclusions

According to the slipstreams loading that the wind barrier is subjected to when the high-speed train passes through the bridge, as well as the dynamic response of the wind barrier and the damage to the concrete at the anchor-end, it can be concluded that the slipstream loading from the passing train has a significant impact on the wind barrier, and the maximum displacement response of the wind barrier occurs at the top of the second pillar at the entrance. Additionally, there is a risk of damage and cracking to the concrete at the anchorage end of the wind barrier, so it is necessary to pay attention to the safety of the concrete at the anchor-end.



Bridge Engineering Institute Conference 2023 (BEI-2023)
Rome, Italy, July 17-20, 2023



5. References

Xiong X.H., Li A.H., Liang X.F., and Zhang J., 2018. Field study on high-speed train induced fluctuating pressure on a bridge noise barrier. *Journal of Wind Engineering and Industrial Aerodynamics*. 177, 157-166.

Soper D., Gillmeier S., Baker C., Morgan T., Vojnovic L., 2019. Aerodynamic forces on railway acoustic barriers. *Journal of Wind Engineering and Industrial Aerodynamics*. 191, 266-278.



Fatigue Analysis of Anchored Concrete Structures of Catenary Induced by Train Wind Load Considering Different Bolt Pre-tightening

Zhuole Shu^{1*}, Pengru Deng^{1,2}, Hanfeng Wang^{1,2}, and Xuhui He^{1,2}

¹: Department of Civil Engineering, Central South University, Changsha, Hunan, China; email: shuzhoule@csu.edu.cn

²: National Engineering Research Center of High Speed Railway Construction Technology, Central South University, Changsha, Hunan, China; email: pengrudeng@csu.edu.cn

*: corresponding author

Keywords: tunnel; catenary; anchored concrete structures; finite element analysis; fatigue

Abstract: The ancillary facilities in the railway tunnel are mainly affected by the wind load of the high-speed train which may be the cause of the cracks and deteriorations commonly observed in the concrete structure at the anchorage end. In this paper, nonlinear finite element analysis (FEA) is conducted on the concrete anchorage end of the catenary with different levels of bolt pre-tightening forces to calculate the structural stress fluctuation ranges when a train passing through a tunnel with high-speed beforehand, where the wind load is obtained from computational fluid dynamics (CFD) and the corresponding dynamic effect is included. Hereafter, based on the quasi-static explicit analysis method which has a small computational cost in the case of short time increments, the concrete cumulative damage caused by cyclic high-speed train wind loads and the fatigue life is calculated using the stress ranges of anchored concrete with different pre-tightening forces. The analysis results show that the tensile damage of concrete at the bolt hole interface mainly propagates in the depth direction with the increase of the number of cycles, and the minimum fatigue life of concrete under cyclic wind load is 127,500 under three bolt pre-tightening levels.

1. Introduction

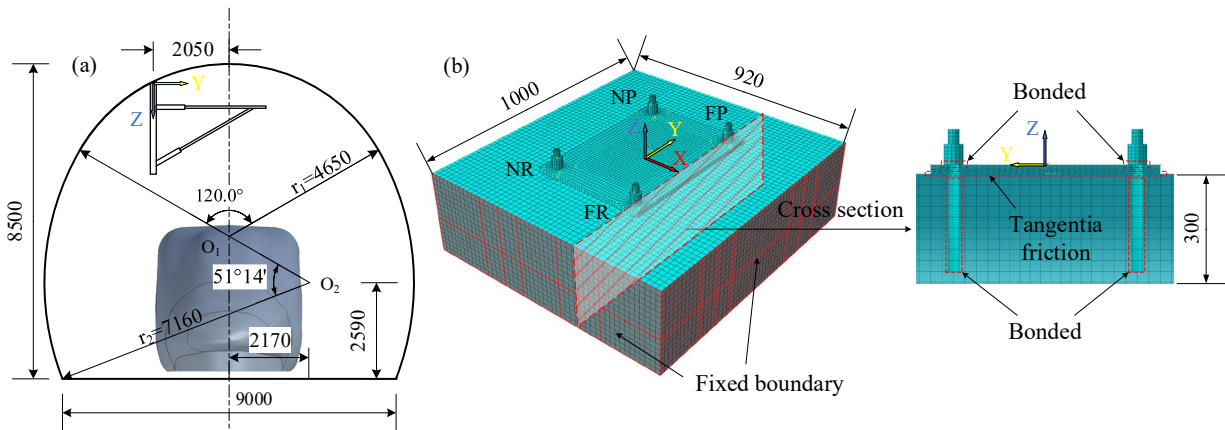
Owing to the limitation of test cost and time, the mechanical research on the anchored ancillary facilities in tunnels usually focuses on the strength of steel members under static loads (Li et al, 2017). However, the structural damage is normally initiated from the anchorage end system which is mainly composed of lining concrete and anchor rods in the form of local adhesion failure between rods and concrete or the development of concrete micro-cracks. As a result, the existing analysis tends to be relatively conservative. Moreover, the catenary is a cantilever structural with a relatively large windward area in the anchored accessory structures of a tunnel, the anchorage structure should be more prone to the cracking and damage under the action of cyclic wind load.

Therefore, fatigue analysis of the catenary in the tunnel under the high-speed train wind load was carried out focusing on the cracking and damage in the anchorage structures in this study. Firstly, CFD and structural dynamic calculation are conducted to calculate the train wind load imposed on the catenary and the amplification factor related to the dynamic effect. On this

basis, the nonlinear FEA method is used to calculate the damage of the anchorage concrete under the bolt pre-tightening, self-weight and working load, and train wind load. Furthermore, a new way of calculating the fatigue life of concrete by using the quasi-static explicit analysis is proposed.

2. Method

At first, a CFD model include train, tunnel and catenary with a ratio of 1:1 was established in *FLUENT*, it is shown in Fig. 1(a) and used to calculate the critical train wind load on the catenary when the train passed through a tunnel with a length of 800m at a speed of 350km/h. Secondly, the finite element static and dynamic analysis of the catenary structure containing the cantilever bracket (Qi et al, 2018) was carried out to calculate the dynamic amplification factor under the wind load. In the FEA calculation, the static implicit analysis based on *ABAQUS* was used to calculate the structural stress and damage of the model shown in Fig. 1(b) under bolt pre-tightening force, self-weight load and the single wind load. The nonlinear behavior of concrete in tension and compression was represented by the concrete damage plasticity (CDP) model. In order to simplify the boundary conditions in engineering, the contact between the steel plate of the catenary davit and the concrete was defined as “friction”, and the contact between the anchor bolts, and concrete, base plate was defined as “bonded”. The yield strength and elastic modulus of the steel plate and bolts are defined as “ $f_y=235$ MPa, $E_s=210$ GPa”, and those of concrete were defined as “ $f_c=20.1$ MPa, $f_t=2.01$ MPa, $E_s=30$ GPa”. In addition, the fatigue analysis of concrete was based on the quasi-static explicit calculation method, using the static calculation results as initial conditions to calculate the cumulative damage of the same model under cyclic wind loads, and the maximum number of given wind load cycles is 2 million.



Note: NP means the bolt that *near* the train passing side(X-), and *positive* side of cantilever bracket(Y+)
NR means the bolt that *near* the train passing side(X-), and *reverse* side of cantilever bracket(Y-)
FP means the bolt that *far* the train passing side(X+), and *positive* side of cantilever bracket(Y+)
FR means the bolt that *far* the train passing side(X+), and *reverse* side of cantilever bracket(Y-)
Bolt diameter: 20mm, Anchoring depth: 170mm

Fig. 1. Numerical models (mm): (a) dimensions of train-tunnel-catenary cross section; (b) boundary conditions of the anchorage structure

3. Results and Discussions

3.1 Structural behaviors of the concrete anchorage structure under once train wind load

Using the time history of the wind load calculated by CFD the structural dynamic amplification factor is calculated to be about 1.358. Correspondingly, the equivalent force and bending moment applied on the FE model of anchorage end structure at the defined origin of coordinates is calculated as shown in Table 1

Table 1. Loads applied to the FE model

Load step	Type	Direction and Value
1	Bolt pre-tightening	$F_z = 27272N$
2	The critical train wind load	$F_x = 664.28N, M_y = 855.58 \cdot m, M_z = -392.33N \cdot m$

The bolt pre-tightening force in this model is calculated as follows:

$$F_T = \frac{T}{KD} \quad (1)$$

where T is the tightening torque, defined as 120, 140 and 160N·m. K is the dimensionless coefficient of the tightening torque, defined as 0.22. D is the diameter of the bolt, defined as 0.02m (Kong et al, 2022).

From FEA, the largest equivalent stress of steel structure appears at the NP bolt, which is 137.68MPa, and it is less than the fatigue limit (181.1MPa) of this type of steel, steel structures are considered to have a fatigue life greater than 10 million under this cyclic wind loads. In addition, the distribution of concrete damage factors along the depth near each bolt hole is calculated using the tensile and compressive stress distributions as shown in Fig. 2.

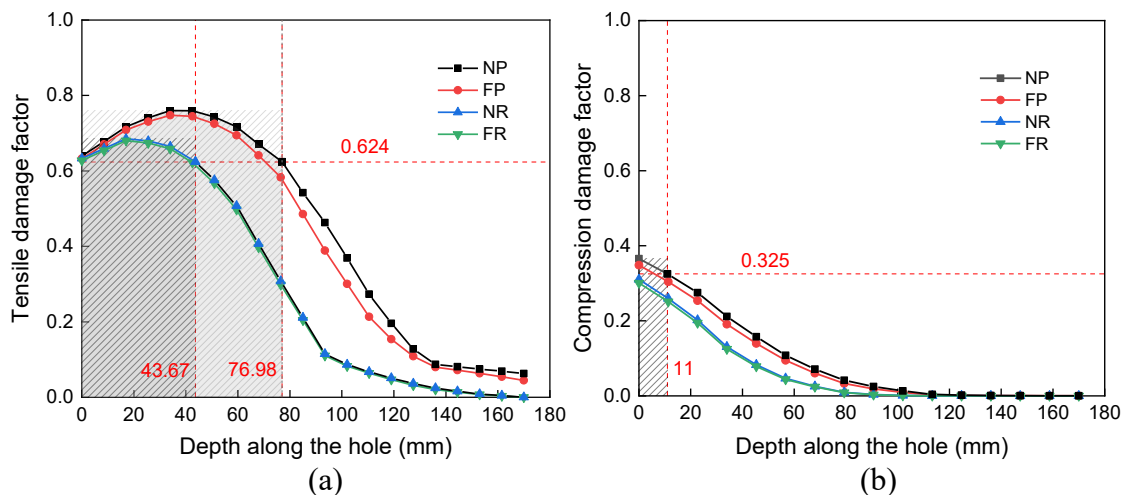


Fig. 2. Damage factor distributed along depth: (a) tensile damage; (b) compression damage

It can be found that the interface concrete at the bolt hole NP has a peak value of tensile damage factor of approximate 0.8. Referring the critical damage factors for judging the tensile and

compressive failure of concrete, i.e., 0.624 and 0.325, as proposed by (Zhou 2019), the depth of concrete failure is calculated to be about 77mm.

3.2 Fatigue behaviors of the concrete anchorage structure under cyclic train wind loads

The tensile damage distribution of the concrete near the NP hole under pre-tightening torque of 120 N·m and the cyclic train wind load is shown in Fig. 3(a). It was found that the fatigue failure of the concrete at the bolt interface is mainly caused by the propagation of the tensile damage factor in the depth direction, and the damage peak value is 0.83. For this reason, the fatigue lives of concrete with NP holes under three tightening torque were 312,500, 205,000, and 127,500. As shown in Fig. 3(b), the tensile damage of concrete rapidly deepens in the middle of the bolt as the bolt torque increases, and the damage distribution under the three torques is approximately the same when the anchorage concrete fatigue fails.

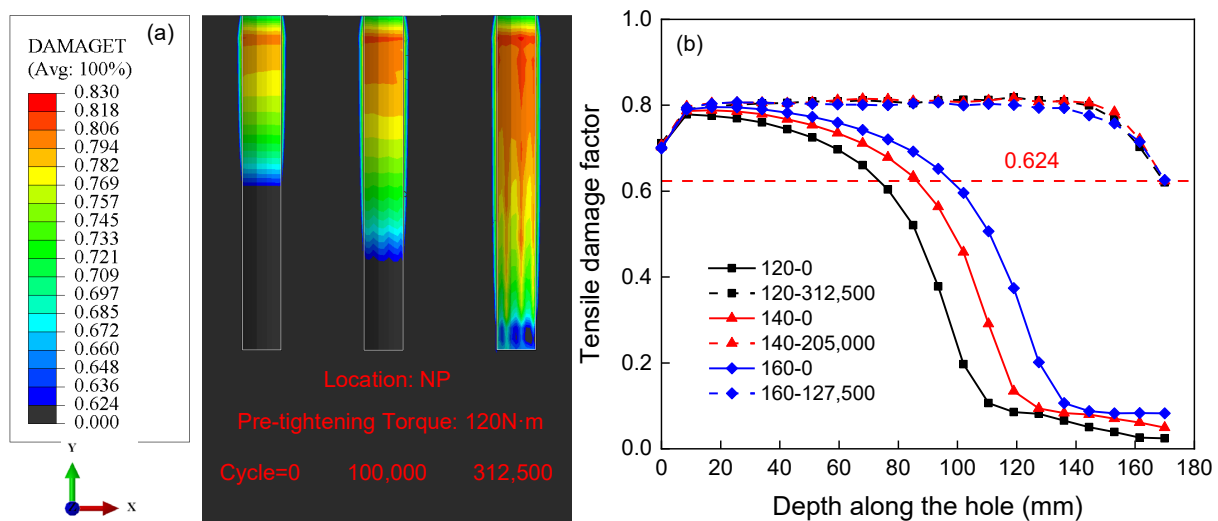


Fig. 3. Distribution of tensile damage factors: (a) different cycles; (b) different depths

4. Conclusions

In this paper, a quasi-static explicit analysis method is proposed to calculate the damage accumulation of anchored concrete, and it is found that the results of the concrete fatigue failure at the bolt hole interface is due to the rapid deepening of the tensile damage. Affected by different bolt pre-tightening levels, the fatigue life of concrete under the wind load is calculated with a minimum value of 127,500 cycles and a maximum value of 312,500 cycles.

5. References

Li, R., Zhang, W., Ning, Z., Liu, B., Zou, D., & Liu, W. (2017). Influence of a high-speed train passing through a tunnel on pantograph aerodynamics and pantograph–catenary interaction. *Proceedings of the Institution of Mechanical Engineers, Part F: Journal of Rail and Rapid Transit*, 231(2), 198-210.

Qi, G. F., Xiao, X. H., Zhao, H., & Chen, J. F. (2018). Fatigue life evaluation on key components of high-speed railway catenary system. *Journal of Central South University*, 25(8), 1958-1965.



Bridge Engineering Institute Conference 2023 (BEI-2023)
Rome, Italy, July 17-20, 2023



Xiao, Y., Chen, Z., Zhou, J., Leng, Y., & Xia, R. (2017). Concrete plastic-damage factor for finite element analysis: Concept, simulation, and experiment. *Advances in Mechanical engineering*, 9(9), 1687814017719642.

Zhou, Y., Shi, S., Cai, Q., Zhang, Y., Liang, J., & Chen, Y., (2019). Damage model of anti-slide pile based on energy loss and its application. *Journal of Geomechanics*, 25(6), 1107-1115. (in Chinese)

Kong, Q., Li, Y., Wang, S., Yuan, C., & Sang, X. (2022). The influence of high-strength bolt preload loss on structural mechanical properties. *Engineering Structures*, 271, 114955.



Influence of Spacing on Aerodynamic Interference of Parallel Rail-Cum-Road Bridges with Twin Separated Parallel Girders

Jing He¹, Yunfeng Zou^{2*}, Xuhui He³, and Lulu Liu⁴

¹: School of Civil Engineering, Central South University, Changsha and China; email: 214811083@csu.edu.cn

²: School of Civil Engineering, Central South University, Changsha and China; email: yunfengzou@csu.edu.cn

³: School of Civil Engineering, Central South University, Changsha and China; email: xuhuihe@csu.edu.cn

⁴: School of Civil Engineering, Central South University, Changsha and China; email: 18737198956@163.com

*: corresponding author

Keywords: parallel rail-cum-road bridges with twin separated parallel girders; numerical simulation; wind tunnel test; aerodynamic disturbance; flow field mechanism

Abstract: Main girder spacing is one of the main factors affecting the aerodynamic interference effect of double parallel bridges. In order to study the effect of main girder spacing on the aerodynamic disturbance effect of the parallel asymmetric double bridges, based on 2D unsteady Reynolds averaged Navier-Stokes (URANS) simulations, and the wind pressure distribution and flow field of asymmetric double-width girders in the gap-width ratios D/B (0.25 to 10) are verified by wind tunnel tests based on the numerical calculation results. The comparative analysis of wind pressure distribution and flow field characteristics of asymmetric double-width girders in the range of gap-width ratios D/B was carried out. The results show that when the spacing $D/B < 2.0$, the influence of aerodynamic disturbance on both upstream and downstream girders is more obvious, and the downstream girder becomes a single flow state because it is completely wrapped in the shear layer formed by the upstream highway main girder, which leads to a more significant effect of the aerodynamic disturbance. When the spacing is $D/B = 5.0$, the upstream wake is gradually dissipated in the gap, and the flow pattern of both gradually converges to that of a standalone girder, thus the aerodynamic interference gradually decreases.

1. Introduction

Large-span bridges arranged in a parallel configuration are favored by the engineering community because of their good capacity. The aerodynamic characteristics of double-width bridges are more complicated due to aerodynamic interference. The interference of various influencing factors is difficult to be accurately measured and described, so it is necessary to study the aerodynamic interference effect of double-width bridges in various ways. Many scholars have studied the influence of spacing on the aerodynamic characteristics of double-width bridges through wind tunnel tests or numerical simulations, and found that the downstream main girder is more significantly affected, and summarized the law of the change of the force

coefficient with spacing and wind angle of attack (Kwok, 2012; Laima, 2015). Chen et al (2014) used a high-resolution particle imaging velocimetry (PIV) system to measure and quantify the evolution of the non-constant vortex structure around double box decks and showed that the size of the vortex is affected by the spacing ratio. He et al (2021) used three-dimensional LES simulations to investigate the aerodynamic interference of parallel box girders with different spacing, and the results showed that the critical spacing for the interference is $G/B=0.25$ (where the flow has a large variation) and $G/B=5.0$ (greater than this spacing, the interference tends to 0). In summary, most of the relevant research objects are symmetrical double-width bridges with the same cross-sectional form, but less research has been done for parallel double-width bridges with different main girder cross-sections. Therefore, research on the s parallel rail-cum-road bridges with twin separated parallel girders is worthwhile.

2. Methodology

2.1. Numerical simulation settings

The cross-sectional form is appropriately simplified, and the influence of the bridge appurtenances such as railings and maintenance vehicle tracks are not considered. The model scales as 1:100, and the calculation domain is set as a rectangle of $10H \times 25B$ ($H=0.45\text{m}$, $B=0.38\text{m}$), and D is the net spacing between the two bridges, as shown in Fig. 1.

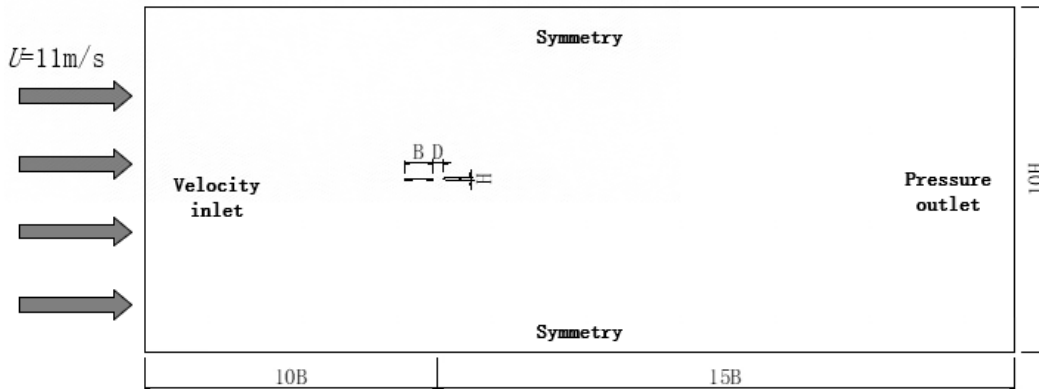


Fig. 1. Schematic representation of the computational domain

2.2. Numerical calculation validation

Three sets of grids (40W, 60W, 80W) were selected for grid irrelevance and checked for accuracy against the experimental results. 60W grid result fits well with the mean wind pressure coefficients of the wind tunnel tests, and the numerical simulation method is feasible.

3. Results and Discussion

3.1. Average wind pressure coefficient

As shown in Fig. 2, where the superscript “*P*” represents the position of the girders, the superscript “*S*” represents the standalone girder, and the superscript “*D*” represents the double-width girders. When $D/B < 2$, the average wind pressure coefficient decreases with increasing spacing, but is always larger than that of the standalone girder; while $D/B > 2$, the impact of aerodynamic interference upstream highway girder is smaller, and the wind pressure of the upstream highway girder is very close to that of the standalone girder.

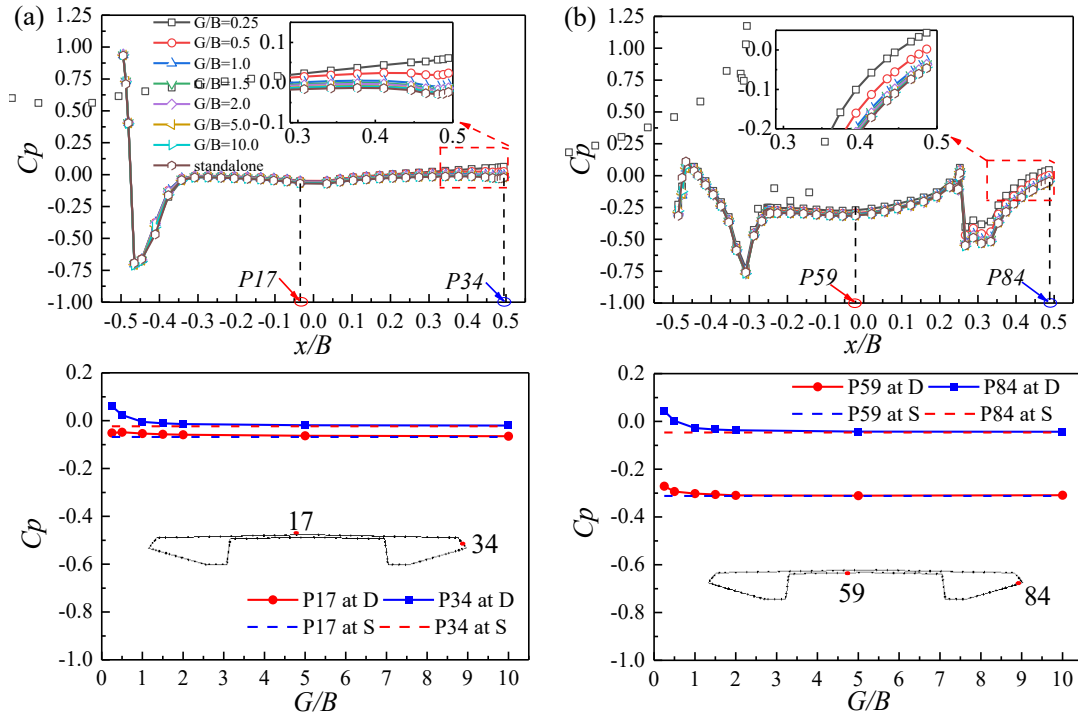


Fig. 2. Average air pressure coefficient on highway girder: (a) upper surface; (b) lower surface

In Fig. 3, the absolute value of wind pressure at the measurement points increases with increasing spacing. The wind pressure of the downstream railway girder is still different from that of the standalone girder when the spacing become larger, which shows that the aerodynamic interference of the spacing is more significant for the downstream girder.

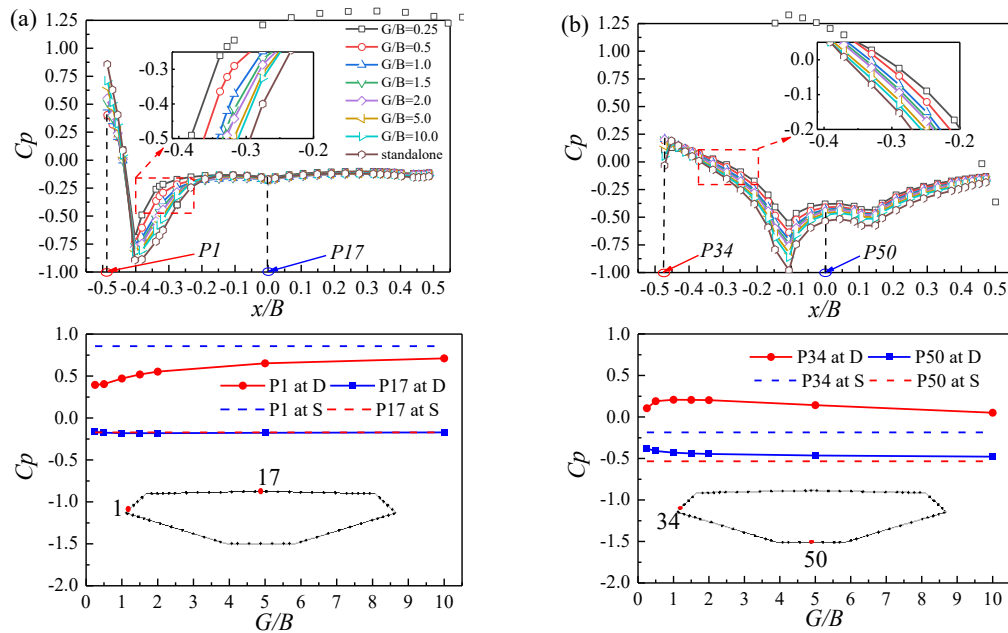


Fig. 3. Average air pressure coefficient on railway girder: (a) upper surface; (b) upper surface

3.2. Flow field diagram

Fig. 4 shows the vorticity diagrams of a standalone girder when facing the wind and the vorticity diagram when the highway girder is against the wind at different spacing. The wind pressure peaks all appear at the corner position of the girders, and the separation and reattachment of the flow at the corner of the girders and the impact at the gap are the reasons for the wind pressure peaks. When $D/B < 2.0$, the downstream girder is completely wrapped in the shear layer formed by the upstream highway girder, becoming a single-flow state, with regular vortex shedding at the end, leading to more significant aerodynamic interference. The wind pressure of the upper surface wind fairing increases with the increase of spacing, and the wind pressure of the lower surface wind fairing increases and then decreases; when $D/B = 5.0$, the upstream wake gradually dissipates in the gap, and the flow pattern of both gradually converges to that of the independent girder, thus the aerodynamic disturbance gradually decreases.

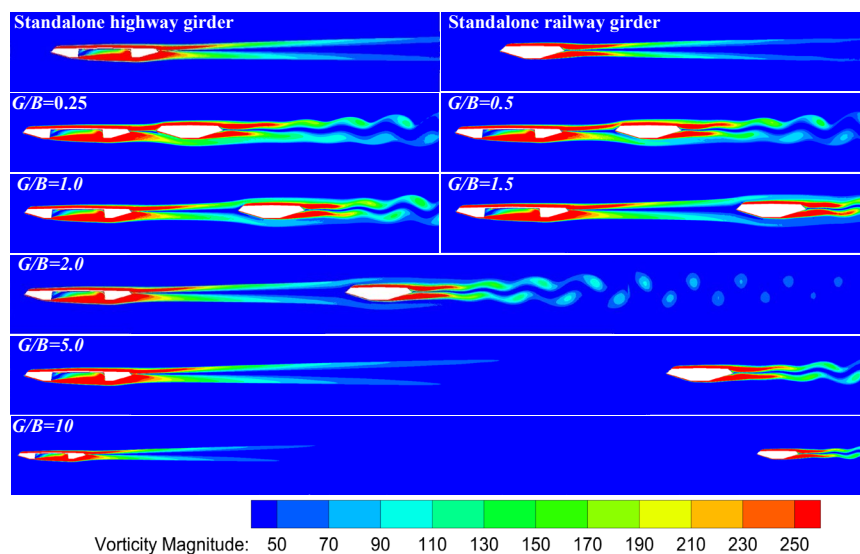


Fig. 4. Vorticity magnitude

4. Conclusions

In this study, when the spacing $D/B < 2.0$, the effect of aerodynamic disturbance on the average wind pressure coefficient of both upstream and downstream is more significant, and the interference on the downstream girder is more obvious than that of the upstream. When $D/B = 5$, the effect of aerodynamic interference is weakened, and the wind pressure of the double-width girder tends to be similar to that of the standalone girder.

5. References

- Laima S.J., Li H., 2015. Effects of gap width on flow motions around twin-box girders and vortex-induced vibrations. *Journal of Wind Engineering and Industrial Aerodynamics*, 139, 37-49.
- He X.H., Kang X.M., et al, 2021. Numerical investigation of flow structures and aerodynamic interference around stationary parallel box girders. *Journal of Wind Engineering and Industrial Aerodynamics*, 215, 104610.



Bridge Engineering Institute Conference 2023 (BEI-2023)
Rome, Italy, July 17-20, 2023



Monitoring



A Trust-Based Approach for Resilient UAV Networks Monitoring Bridges

Francesco Buccafurri^{1*} and Francesca Scoleri²

¹: University of Reggio Calabria, Italy; email: bucca@unirc.it

²: Master Graduate at University of Reggio Calabria, Italy; email: scolerifrancesca1@gmail.com

*: corresponding author

Abstract: Deterioration of bridges is a very serious issue for transportation agencies and governments, not only for the reduction of functionality and reliability of the infrastructure but also because it can put public safety at risk. The use of multiple *Unmanned Aerial Vehicles (UAVs)*, organized into a multi-hop wireless delay-tolerant self-organizing network, allows us to adopt comprehensive, inexpensive, and fast nondestructive inspections of bridges, thus enabling effective monitoring of the infrastructure. Unfortunately, the open architecture and the dynamic topology of the UAV network, makes it vulnerable to a variety of cyber attacks. Among other possible attacks, we focus on two types of attacks in this paper. The first regards the case in which the compromised UAV tries to send false observations to the base station. The second happens when the attacker takes control of the UAV and moves it to unexpected trajectories. Both cases can result in very negative effects. Taking advantage of the specific topology of bridges and, thus, the way in which the coverage path planning can be organized, we propose, in this paper, a trust-based mechanism that aims to degrade the reputation of an UAV that attempts to misbehave. The trust-based mechanism is distributed among UAVs, in such a way that each UAV can play the role of observer or referee. In the latter case, one UAV is in charge of *judging* the behavior of another UAV that is nearby. Coverage path planning is designed so that UAVs meet frequently during the flight. Using this approach, two global reputation rates for each UAV are calculated by the base station, based on past interactions. The first is called *Content Reputation Rate (CRR)* and refers to the reliability of the content of the observations sent by the UAVs to the base station. The second is called *Position Reputation Rate (PRR)* and refers to the reliability of the trajectory traveled by the UAVs. Some cryptographic mechanisms are also adopted to make the reputation system robust. In addition, slandering and self-promotion attacks are countered. The outcomes of this work seem promising, because the approach followed may increase the resilience of UAV networks without requiring additional resources, instead exploiting the normal task of UAVs, with a small addition of redundancy, which is still desirable in a critical application setting such as bridge monitoring.

1. Introduction

Unmanned Aerial Vehicles (UAVs) are widely used in the field of civil engineering and infrastructure monitoring. This is due to the fact that they represent a very flexible tool to accomplish tasks that, otherwise, would be much more expensive and complex to perform. Consider that the economic costs of modern UAVs is progressively decreasing, and, moreover, their mobility allows us to implement effective monitoring tasks without infrastructural investments. Finally, they allow visual inspections also in the case of areas hardly accessible for humans, with no safety risks for the operators, and with the possibility of reuse for multiple



missions (this is not the case of sensor-based monitoring). Anyway, UAVs and sensors can be also profitably combined, for example to make easier data collections and sensor control and to save the energy consumption of wireless sensors. The above considerations are particularly true in the case of road infrastructures such as bridges (especially in the case of big bridges), due to their conformation and location that makes difficult traditional monitoring.

To reduce the overall mission time and to increase resilience, UAVs often operate as a collaborative group. Usually, the collaboration does not regard the subject of the mission, but the way in which UAVs can communicate with the base station (which is the ground segment of the multi-UAV system). Indeed, a multi-hop wireless delay-tolerant self-organizing network is established between the UAVs to route data, according to the paradigm of *ad-hoc* networks. In words, routing is collaborative in the sense that the route depends on when UAVs meet each other during the flight, in such a way that a one-hop machine-to-machine communication can be performed. This way, data are forwarded from an UAV to another UAV, until they reach the base station (and vice versa). Therefore, delays can be generated (thus the network is said *delay-tolerant*). But for the particular application, we do not need real-time routing.

It is rather intuitive that a similar system, being based on the mutual collaboration of UAVs, strongly relies on the assumption that UAVs do not behave maliciously. However, this assumption is too strong in the real life, by considering that UAVs perform machine-to-machine communication protocols, thus they expose open communication ports, and then are prone to cyber-attacks. Therefore, attackers can corrupt nodes in the UAV network, to make different attacks, such as the *black/gray hole attack*, *sewage attack*, *witch attack*, etc. This way, not only data can be eavesdropped, but also message can be tampered or deleted and the whole behavior of the UAV can be completely compromised.

In this paper, among other possible attacks, we focus on two types of attacks. The first attack regards the case in which the compromised UAV tries to send false observations to the base station. The second attack happens when the attacker takes control of the UAV and moves it to unexpected trajectories. Observe that, both cases can result in very negative effects for the whole system and, directly or indirectly, can also put public safety at risk.

Taking advantage of the specific topology of bridges and, thus, the way in which the coverage path planning can be organized, we propose, in this paper, a trust-based mechanism that aims to degrade the reputation of an UAV that attempts to misbehave.

The contribution of this paper is then to increase the resilience of UAV networks without requiring additional resources. Indeed, our solution basically exploits the normal task of UAVs, with a small addition of redundancy, which is still desirable in a critical application setting such as bridge monitoring.

The structure of the paper is the following. In Section 2, we briefly illustrate the related literature. In Section 3, we present our trust-based method, while in Section 4 we draw our conclusions.

2. Related Work

In the scientific literature, there is an increasing interest in the application of UAVs to the field of civil engineering (Greenwood et. al, 2019). Non-destructive analysis conducted with UAVs is taking a prominent role in bridge monitoring in the recent years (Feroz and Abu Dabous, 2021; Duque et. al, 2018). UAVs are organized into fleets in which the UAVs themselves are nodes of a communication network (Khawaja et. al., 2017). As communication ports of UAVs must be enabled, cyber-attacks are possible, seriously threaten the reliability of UAV-based monitoring (Krishna and Murphy, 2017; Khan et. al., 2020). Many different approaches are adopted to

protect UAV networks. A first important objective is to prevent impersonation attacks. This is typically obtained by using classical cryptographic-based mechanism (Asokan et. al., 2007). Additional techniques can be used to counter other possible attacks. Our paper is framed in the context of trust-based approaches. The work that appears most related to our paper is (Ge et. al, 2020). In this work, the authors propose a provenance-aware distributed trust model for UAVNs that aims to achieve accurate peer-to-peer trust assessment and maximize the delivery of correct messages received by destination nodes. Our paper also adopts a trust-based approach, but focuses on different security issues, as illustrated in the introduction.

3. The Proposed Method

In this section, we describe the trust-based mechanism we propose to protect an UAV network used for bridge monitoring.

The trust-based mechanism is distributed among UAVs, such that each UAV can play the role of *observer* or *referee*. In the latter case, one UAV is in charge of *judging* the behavior of another UAV that is nearby. It is worth noting that the solution is specifically designed for the case of bridges, among all possible other applications. Indeed, as mentioned earlier, coverage path planning exploits the specific shape of bridges to ensure that UAVs meet frequently during the flight. Using this approach, two global reputation rates for each UAV are calculated by the base station, based on past interactions of UAVs. The first is called *Content Reputation Rate (CRR)* and refers to the reliability of the content of the observations sent by the UAVs to the base station. The second is called *Position Reputation Rate (PRR)* and refers to the reliability of the trajectory traveled by the UAVs. Some cryptographic mechanisms are also adopted to make the reputation system robust against impersonation.

Let us see more in detail the approach. The first step of our approach is the definition of a bridge-specific coverage path planning, which, based on the particular topology of the region to be monitored (a region that extends longitudinally), allows us to define a coverage plan that ensures that UAVs meet in flight so that they can communicate with high frequency. For space reason we cannot expand here the definition of the method, but it can be simply based on the application of any already known technique to a virtual definition of bridge regions, defined by overlapping squares that cover the entire monitoring surface with some addition shifting square used for shuffling UAVs.

Once this step is performed, we can define how to set the trust-based mechanism.

Recall that, according to the communication protocol of the UAV network, when one UAV encounters another UAV it sends the observation (photo, thermoscan, or other evidence) to the neighbor, so that it will then be conveyed to the base station. Thus, the fact that UAVs periodically must meet each other is native in the communication protocol. However, the bridge-specific coverage path planning, is used to make this feature more robust.

We can deal with two types of attacks: *(i)* the case in which the compromised UAV sends false observations, and *(ii)* the case in which the compromised UAV takes a physical path different from the predetermined one, which may mean that the attacker has taken control of the piloting.

When the UAV A sends the observation Ob to UAV B , it also sends its GPS location P , so it sends the tuple (ID, Ob, P) , where ID is its identity – we adopt cryptographic mechanisms to give assurance to the identity. The UAV B , which receives the observation, being nearby, can perform the same kind of observation, whose type, position etc., are all included in Ob , or otherwise can perform some checks (possibly relying on an artificial intelligence engine). Thanks to this verification, when forwarding the message, it adds a score to that message, called



content reputation rate - CRR. Similar thing it does about the position, because it can assess whether or not the GPS coordinates that UAV *A* is communicating to it are plausible, since it can compare them with its own. This way, the referee can compute another reputation rate, called *position reputation rate (PRR)*. Thus, *B* will forward the message: (*ID, Ob, P, CRR, PRR*), which will eventually reach the base station.

Based on this reputation model, the base station receiving the messages will detect compromised UAVs, because if an UAV is misbehaving, then it will receive negative rates from several neighboring UAVs, which play the role of *referee*. It is easy to see that self-promoting attacks are not possible by design (since the provided level of assurance of the UAV identity prevent impersonation attacks and thus an UAV cannot simulate to be a referee). Moreover, slandering attacks are contrasted by the fact that the computed reputation is global, in the sense that it derives from interactions with different UAVs. Therefore, the effect of a possible fake referee, is neutralized.

4. Conclusions

In this paper, a trust-based distributed model is proposed to counter two types of cyber-attacks that can threaten UAV networks used for bridge monitoring. The proposed approach is based on the concept of reputation, implemented via two global reputation rates, one related to the reliability of observation contents, the other related to the reliability of the UAV position. The outcomes of the paper appear promising, because the solution aims to increase the resilience of UAV networks, which is a very relevant aspect in the considered application scenario.

5. References

- Asokan, N., Kostianen, K., Ginzboorg, P., Ott, J., and Luo, C. 2007. Applicability of identity-based cryptography for disruption-tolerant networking. In *Proceedings of the 1st international MobiSys workshop on Mobile opportunistic networking* (pp. 52-56).
- Duque, L., Seo, J., and Wacker, J. 2018. Bridge deterioration quantification protocol using UAV. *Journal of Bridge Engineering*, 23(10), 04018080.
- Ge, C., Zhou, L., Hancke, G. P., and Su, C. 2020. A provenance-aware distributed trust model for resilient unmanned aerial vehicle networks. *IEEE Internet of Things Journal*, 8(16), 12481-12489.
- Feroz, S., and Abu Dabous, S. 2021. Uav-based remote sensing applications for bridge condition assessment. *Remote Sensing*, 13(9), 1809.
- Greenwood, W. W., Lynch, J. P., and Zekkos, D. 2019. Applications of UAVs in civil infrastructure. *Journal of infrastructure systems*, 25(2), 04019002.
- Khan, N. A., Brohi, S. N., and Jhanjhi, N. Z. 2020. UAV's applications, architecture, security issues and attack scenarios: A survey. In *Intelligent Computing and Innovation on Data Science: Proceedings of ICTIDS 2019* (pp. 753-760). Springer Singapore.
- Khawaja, W., Ozdemir, O., and Guvenc, I. 2017. UAV air-to-ground channel characterization for mmWave systems. In *2017 IEEE 86th Vehicular Technology Conference (VTC-Fall)* (pp. 1-5). IEEE.
- Krishna, C. L., and Murphy, R. R. 2017. A review on cybersecurity vulnerabilities for unmanned aerial vehicles. In *2017 IEEE International Symposium on Safety, Security and Rescue Robotics (SSRR)* (pp. 194-199). IEEE.



Evaluation Method for Grouting Condition in Post-tensioned PC Bridges Considering Directive Propagation Properties of Elastic Waves in the Wide-Range Ultrasonic Testing (WUT)

Takanori Kinoshita¹, Yoshino Sako², Kuniharu Fukushima³, and Isamu Yoshitake^{4*}

¹: H and B System Co, Ltd., Tokyo, Japan; email: kinoshita@hbsys.co.jp

²: Nippon PS Co. Ltd., Fukui, Japan; email: yoshino.sako@nipponps.co.jp

³: Nippon PS Co. Ltd., Fukuoka, Japan; email: k.fukushima@nipponps.co.jp

⁴: Yamaguchi University, Yamaguchi, Japan; email: yositake@yamaguchi-u.ac.jp

*: corresponding author

Keywords: Ultrasonic testing (UT) ; Prestressed concrete ; Elastic wave ; Laser Doppler vibrometer (LDV) ; Non-destructive inspection (NDI)

Abstract: Wide-range ultrasonic testing (WUT) is occasionally used to examine the grout filling-condition of post-tensioned PC bridges. The study focuses on improvement of inspection method of grouting condition. For this purpose, laboratory and field tests were conducted in the study. In the fundamental test, semicylinder specimens made with concrete and mortar were prepared to investigate the directivity of elastic waves. A laser Doppler vibrometer was used as the alternative receiver of WUT. The test results revealed that the elastic-waves propagation in mortar was highly linear. In addition, it was observed that the coarse aggregate influenced on the directivity of propagation waves. The elastic waves in concrete were in the range of -30° to 30° approximately. Based on the fundamental test, grouting conditions in the duct of actual PC bridges were examined to investigate the applicability of the improved system. It was confirmed that the developed inspection method can improve the accuracy for grouting conditions.

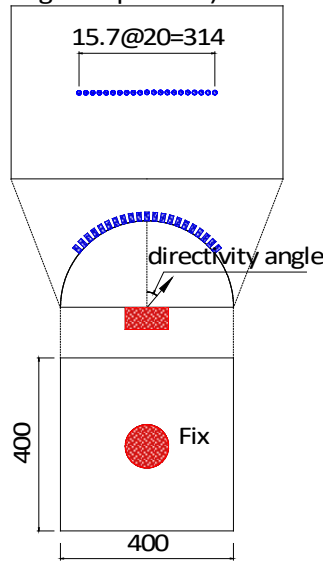
1. Introduction

Wide-range ultrasonic testing (WUT) is a non-destructive inspection method to evaluate grout filling-condition of post-tensioned PC bridges. The WUT evaluates the complete or incomplete grouting by comparing the peak frequency of elastic waves reflected from the duct [Fukushima *et al.* 2018]. The thresholding method cannot determine the grout-filling condition when multiple peaks are observed in the WUT [Hamaoka *et al.* 2014]. An additional evaluation method is required for improving the reliability of the WUT inspection. To examine the propagation of the transmitted waves in the WUT, fundamental test was conducted by using semi-cylindrical concrete specimens. The study focused on the time-variation of elastic waves to evaluate the grout filling condition. The purpose of the study was to propose an additional evaluation method based on the propagation characteristics of elastic waves in concrete. The applicability of the proposed method was confirmed at a post-tensioned PC bridge that embedded void and grout-filled ducts. This paper reports the fundamental experiment and verification of the proposed evaluation for the WUT.

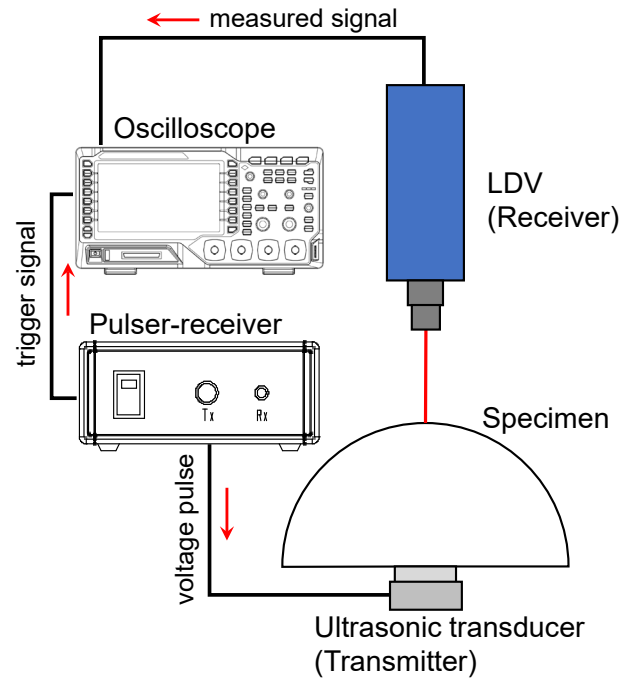
2. Fundamental Test

In the fundamental test, semi-cylindrical specimens made with concrete and no-shrink mortar were used. Dimensions of the specimen were 400 mm diameter and 400 mm high. Figure 1(a) shows an overview of the specimen. The transmitting transducer was fixed on the center of the plane. To observe the elastic waves, a laser Doppler vibrometer (LDV) was used in the test. Figure 1(b) shows the measurement system.

21 points measurement at intervals of 15.7mm
 (5degree equivalent)



(a)



(b)

Fig. 1. Fundamental test set-up: (a) overview of test specimen; (b) measurement system

The relationship between directivity angle and the maximum amplitude (absolute value) of the observed elastic waves is shown in Figure 2.

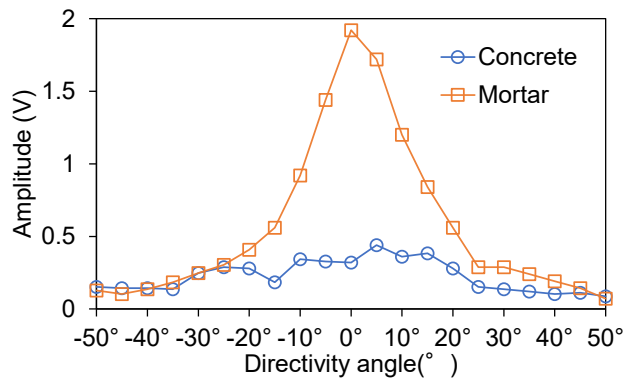


Fig. 2. Maximum amplitude of received wave

The amplitude of the mortar specimen reached the maximum value of 1.9 V at a directivity angle of 0° in the range of the directivity angle of $\pm 25^\circ$. The result shows that the directivity (straightness) of the transmitted wave is remarkable in mortar. On the other hand, for the concrete specimens, the amplitude was approximately 0.4 V in the range of -10° to 15° directivity angle. The maximum amplitude in concrete was lower than 25% of that in mortar. The observation was caused from the coarse aggregate effect, the scattering and attenuation of transmitted waves. The amplitude out of the range of -30° to 25° in concrete was almost constant, the elastic waves in concrete were in the range of -30° to 30° approximately. The experimental results imply that the closer arrangement of transducers may be effective because of the high directivity of the transmitted wave by the WUT transducer.

3. Field Test

In the field test, WUT inspection was conducted on post-tensioned PC bridges under construction. Based on the fundamental experiment, the transducers were placed along the ducts with a minimum distance of 97 mm between them. For comparison, the experimental parameters, the transducers distance of 150 / 200 / 500 mm, were also added. Note is that the transducers spacing of 200, 500 mm is often employed in actual surveys of the WUT. Figure 3 illustrates time-variation of the waveform in the WUT measurement with the transducer distance of 97 mm.

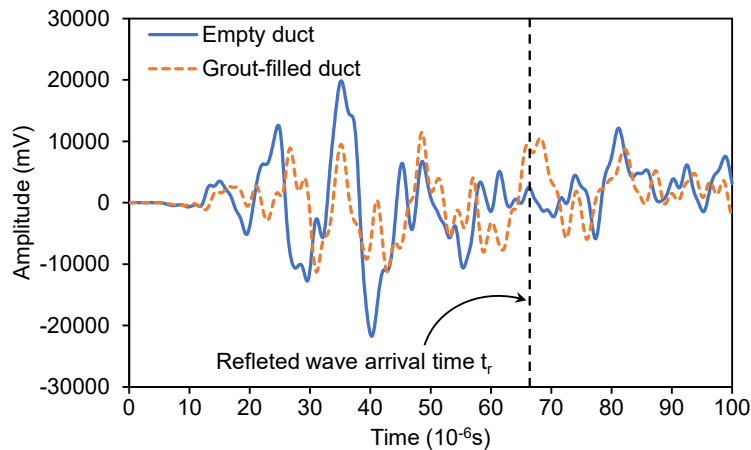


Fig. 3. Example of waveforms (distance between transducers is 97mm)

The amplitude of the waveform measured in concrete embedding the empty duct was greater than the grout-filled duct. Based on the characteristics, the study focused on the amplitude of the waveform that measured during the time t_r defined in Equation (1).

$$t_r = 2\sqrt{(a/2)^2 + (c_d + \phi)^2} / v \quad (1)$$

where, a is distance between transducers (center to center), c_d is covering depth of duct, ϕ is duct diameter, and v is elastic wave velocity in concrete.

To evaluate the grout filling condition, the averaged amplitude $|V_{av}|$ was used in the study. The definition of $|V_{av}|$ is described in Equation (2). The averaged amplitude $|V_{av}|$ in this study is shown in Equation (2). Figure 4 shows the averaged amplitude $|V_{av}|$ in the field test.

$$|V_{av}| = \frac{1}{t_r} \cdot \int_0^{t_r} |V(t)| dt \quad (2)$$

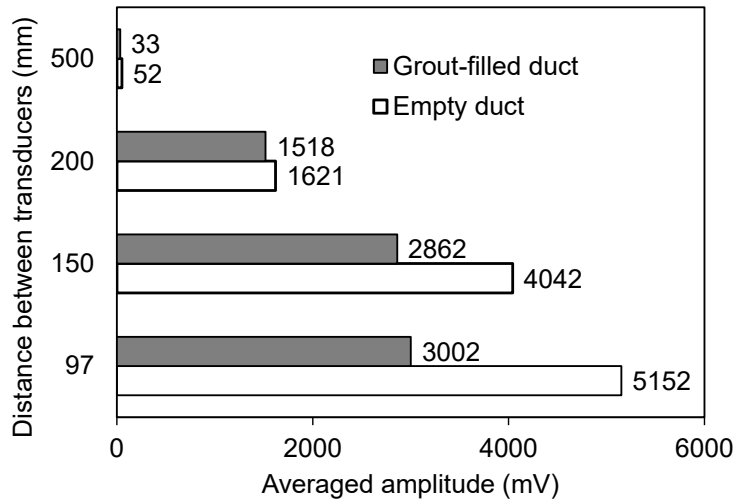


Fig. 4. Averaged amplitude before and after grouting ($a=97\sim500$)

Figure 4 confirms that the amplitude of the empty duct was greater than the grout-filled duct. In the transducers distance a of 97 mm, the averaged amplitude $|V_{av}|$ indicated a significant difference in empty and grout-filled ducts. The observed $|V_{av}|$ at the empty duct was 5152 mV, which was around 1.7 times greater than the $|V_{av}|$ of 2418 mV in the grout-filled duct. It was confirmed that the grout filling condition can be determined from the differences of averaged amplitude $|V_{av}|$.

4. Conclusions

A fundamental experiment was conducted to examine the directivity of the WUT transducer using half-cylinder specimens. Afterward, an evaluation of the grout filling conditions was attempted on the PC bridge under construction by WUT measurements based on the propagation characteristic. The main findings in this study are as follows:

- The significant directivity of elastic waves from the WUT transducer was confirmed.
- The averaged amplitude from the unfilled duct was approximately 1.7 times higher than the amplitude from the filled duct.
- The averaged amplitude of reflected waves is useful for evaluating the grout filling condition in PC duct.

5. References

1. Fukushima, K., Amaya, K., Kinoshita, T., Hara, M., Yamada, K., and Yoshitake, I., Field test of Wide-Range-ultrasonic Testing (WUT) to detect incomplete grout in posttensioned prestressed concrete bridges, 2018, The International Federation for Structural Concrete 5th International fib Congress, Melbourne, Australia.
2. Hamaoka, K.; Aoki, K., Hara, M., and Kinoshita, T., The filling survey of PC grout using the wide range ultrasonic testing, *Journal of Prestressed Concrete*, Japan, 2014, Vol.56, No.6, pp.35-40. (in Japanese)



Detection of Defects in Prestressed Concrete Bridge Box Girders Using GPR Image Reconstruction

Wael Zatar¹, Hien Nghiem², and Hai Nguyen³

- ¹ Professor and Director, Encova Center for Engineering and Safety, College of Engineering and Computer Sciences, Marshall University, Huntington, West Virginia, United States of America; email: zatar@marshall.edu
- ² Post-Doctoral researcher, Marshall University Research Corporation, Huntington, West Virginia, United States of America; email: nghiem@marshall.edu
- ³ Scientist, Engineer Research and Development Center, Urbana-Champaign, Illinois, United States of America; email: nguyenhai@marshall.edu

*: corresponding author

Keywords: nondestructive evaluation; ground-penetrating radar; synthetic aperture focusing technique; image reconstruction; 3D and 3D visualization; reinforced-concrete structures.

Abstract: Forty two percent of all bridges in the United States are at least 50 years old, and 46,154, or 7.5 percent of, bridges are considered structurally deficient. Corrosion of reinforcing steel and prestressing strands is a major cause of deterioration, reduced durability, or failure of bridge structures. Visual inspection typically examines surface discontinuities and relies heavily on inspectors' subjective assessments. Ground penetrating radar (GPR) provides a robust non-destructive testing method that has gained acceptance for evaluating subsurface condition of infrastructure components. This research effort aims at detecting defects in reinforced-concrete bridge decks using GPR systems. An enhanced synthetic aperture focusing technique was employed to reconstruct two- and three-dimensional GPR images. A method to determine time-zero is developed to improve the quality of the reconstructed images. The method was validated by evaluating reinforced-concrete slab specimens with internal defects. The validated technology is used to non-destructively evaluate full-scale prestressed concrete bridge box girders that have recently been decommissioned from the CR 30 Bridge over Tom Creek in West Virginia. These box girders were reported to be in fair condition during the latest routine inspection, completed in accordance with the National Bridge Inspection Standards. The proposed GPR visualization protocol was found to provide a great promise in detecting internal reinforcements and defects of the prestressed concrete bridge box girders. This research will benefit West Virginia Department of Transportation as the agency continues to safely maintain and preserve its 7,291 bridges.

1. Introduction

More than 40 percent of all bridges in the United States are at least 50 years old and 7.5 percent, or 46,154, of the nation's bridges are considered structurally deficient. Corrosion of reinforcing steel and prestressing strands is a major cause of deterioration, reduced durability, or failure of bridge structures. Roughly, twenty six percent of reinforced and prestressed concrete highway bridges in the United States need repair or replacement. A recent estimate for the nation's backlog

of bridge repair needs is \$125 billion. The United States needs to increase spending on bridge rehabilitation from \$14.4 billion annually to \$22.7 billion annually, or by 58%, to improve the condition. At the rate of investment provided in the past ten years, it will take until 2071 to make the repairs that are currently necessary, and the additional deterioration over the next 50 years will become overwhelming (Report Card for America’s Infrastructure, 2021). The nation needs a systematic program for bridge preservation whereby existing deterioration is recognized while developing preventive maintenance protocols. West Virginia Department of Highways (WVDOH) maintains 7,291 bridges. Twenty one percent, or 1,531, of these WVDOH bridges are structurally deficient. WVDOH reported an increase of structurally deficient bridges by 522 in the last 5 years. Moreover, WVDOH maintains 40.7 million square feet of bridge decks, of which approximately 6.6 million square feet is structurally deficient (Report Card for America’s Infrastructure, 2021). Heavily relying on subjective assessment, bridge visual inspection typically examines surface discontinuities of its components. Geophysicists have used GPR in soil explorations for the past few decades. The GPR technology has recently gained acceptance in evaluating subsurface condition of infrastructure components (ACI Committee 228, 2013). The technique showed potential in both detecting rebars and defects, and in estimating concrete cover and thickness of bridge decks (Alani et al., 2013, Benedetto et al., 2012, and Garg, S. and Misra, 2020). The primary objective of this research is to fill a knowledge gap in GPR imaging of reinforced and prestressed concrete transportation structures. The study aims at detecting defects in reinforced-concrete bridge decks and prestressed concrete box girders using GPR systems. Two- and three-dimensional visualization of concrete structures will assist determining which areas need further attention, or if components or the entire bridge should be replaced.

2. GPR System and Synthetic Aperture Focusing Technique

non-destructive testing electromagnetic energy GPR waves are subjected to attenuation and loss of energy as the waves propagate in a material. In materials with low conductivity such as dry sand, ice, and dry concrete, signals stay immaculate longer and are, thus, able to penetrate a considerable depth into the material. In contrast, GPR energy will be absorbed before getting far in conductive materials such as saltwater and wet concrete. GPR testing, therefore, is suitable for inspecting construction materials such as concrete, sand, wood, and asphalt. A typical GPR antenna consists of a transmitter (T) and receiver (R), one transmits the signal, and the other receives the reflected signal (Figure 1). GPR with 1.6 GHz antenna and 2.3” (58 mm) T-R offset was used in this study. Signal amplitudes vary from minimum negative to maximum positive corresponding to the color spectrum ranging from black to white in gray-color scale and from dark-blue to dark-red in jet-

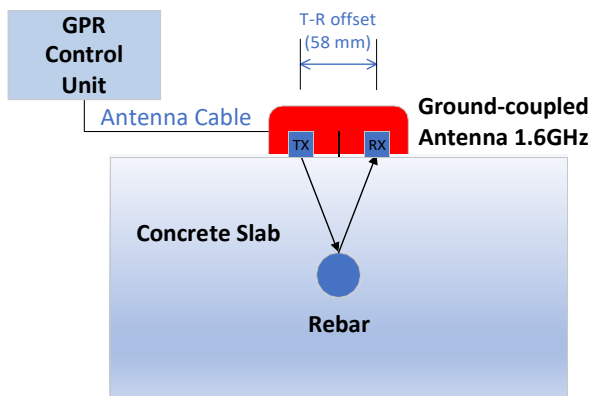


Fig. 1. Principle of GPR testing method

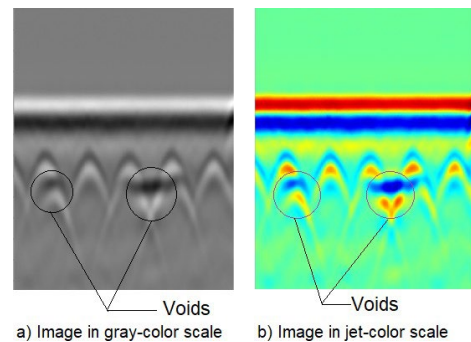


Fig. 2. Raw images of a B-scans

color scale (Figure 2). Long defects are displayed in localized black stripes (Figure 2a) or dark-blue stripes (Figure 2b) for negative signal and V-shaped white stripes (Figure 2a) or yellow-red stripes (Figure 2b) for positive signal. Images obtained from GPR device’s proprietary software might not result in accurate identification of rebars and defects.

3. Enhanced GPR Imaging and Visualization

Since the Synthetic Aperture Focusing Technique (SAFT) focuses signal amplitudes at points in the sampling area of large scans by coherent superposition, its utilization may result in improving image quality of internal rebars and voids (Zatar et al., 2020 and 2021). An enhanced synthetic aperture focusing technique (SAFT) was employed to reconstruct two- and three-dimensional GPR images. A correction function was developed to adjust reflection locations of the defects. A method to determine time-zero was developed to improve the quality of the reconstructed images. Computer code with a fully graphical interface, written in Delphi, was developed to overcome the GPR device commercial post-processing software’s shortcoming in reconstructing images.

4. GPR Imaging and Visualization of Prestressed Concrete Bridge Box Girders

The validated GPR technology is employed to non-destructively evaluate full-scale prestressed concrete bridge box girders that have recently been decommissioned from the CR 30 Bridge over Tom Creek in West Virginia. The box girders were reported to be in fair condition during the latest routine inspection that is completed in accordance with the National Bridge Inspection Standards. Figure 3 shows a longitudinal section of the box girders. Each girder is 32.5’ long. The girders are 36” in width and 17” in height. Each girder has two 10” diameter circular voids (Figure 4). Eleven tendons were placed near the bottom of each girder, two groups of five tendons with 2” spacing on the sides and one tendon at the center. Four #4 rebars were placed at the top of the girders. Stirrups with 12” spacing were used.

GPR data was collected, 97 scan lines in the lateral direction and 9 scan lines in the longitudinal direction, with scan spacings of 4”. All the bottom 11 prestressing tendons were clearly detected in the constructed image from B-scan in Figure 5. Reflection images showed two red strips because the 5 tendons on each side are closely arranged. Figure 6 shows 2D reconstructed images obtained from GPR top scans of one girder. They were constructed at 20”, representing the solid part of the cross section, and at 80”, representing the part of the cross section with two voids, from end of one box girder of CR 30 Bridge over Tom Creek in West Virginia. It can be observed that rebars and voids were detected at 20” and 80” distances from the girder’s end. Figure 7 shows B-scan in the longitudinal direction where the spacing of stirrups can be obtained accurately. This reconstructed image also shows that the concrete cover for rebars is uneven.

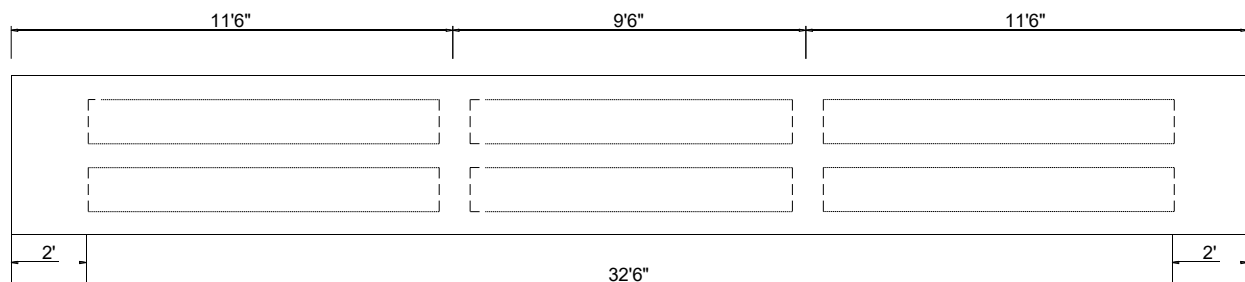


Fig. 3. Longitudinal section of prestressed concrete box girders of CR 30 Bridge over Tom Creek

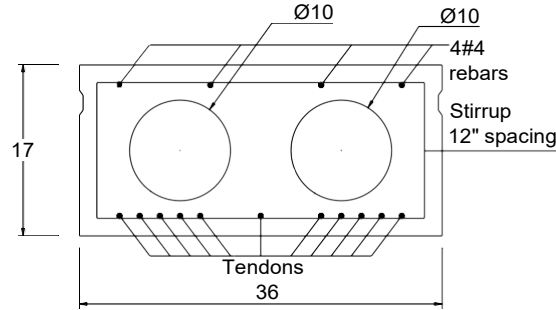


Fig. 4. Cross section of prestressed concrete box girders of CR 30 Bridge over Tom Creek, WV

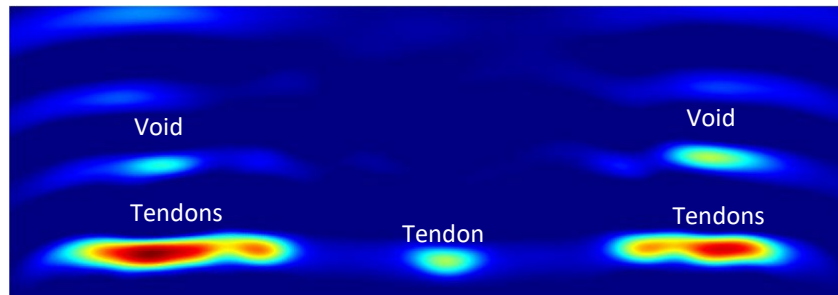


Fig. 5. 2D reconstructed image obtained from GPR bottom scans

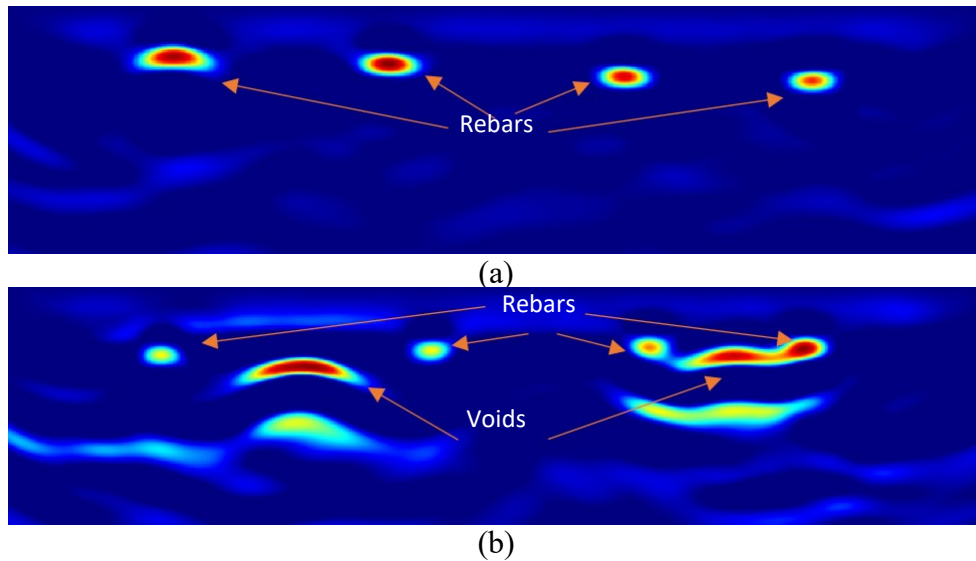


Fig. 6. 2D reconstructed images obtained from GPR top scans: (a) at 20” from end of box girder; (b) at 80” from end of box girder of CR 30 Bridge over Tom Creek in West Virginia

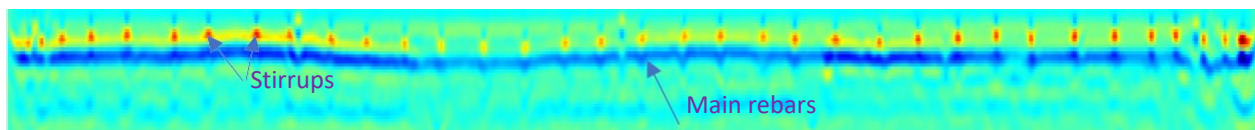


Fig. 7. 2D reconstructed images along CR 30 Bridge box girders (obtained from GPR top scan)



5. Conclusions

Enhanced synthetic aperture focusing technique and ground-penetrating radars were employed to image and assess current condition of reinforced and prestressed concrete bridges. The developed method and software were validated by non-destructively testing prestressed concrete box girders decommissioned from CR 30 Bridge over Tom Creek in West Virginia. The GPR reconstructed images clearly visualize rebars, tendons, and voids of the box girders. Moreover, the images showed stirrup spacings and rebar locations along the prestressed concrete bridge box girders. This research will benefit West Virginia Department of Transportation as the agency continues to safely maintain and preserve the 7,291 bridges included in its bridge inventory.

6. Acknowledgment

Special acknowledgement is due to Mr. Jimmy Wriston, West Virginia Secretary of Transportation and Commissioner of Highways, for the superior technical guidance and thoughtful monitoring of this project over the past several years. The authors would also like to acknowledge the financial contribution provided by the West Virginia Division of Highways to carry out this study. The authors would like to thank Dr. Cumhur Cosgun, Dr. Tu Nguyen, and Dr. Kien Dinh for the earlier developmental NDT research at Encova Center for Engineering and Safety at Marshall University.

7. References

- Report Card for America's Infrastructure. 2021. American Society of Civil Engineers, www.infrastructureportcard.org
- ACI Committee 228. 2013. Report on Nondestructive Test Methods for Evaluation of Concrete in Structures, Report ACI 228.2R-13, American Concrete Institute.
- Alani, A.M., Aboutalebi, M. and Kilic, G. 2013. Applications of ground penetrating radar (GPR) in bridge deck monitoring and assessment, *Journal of Applied Geophysics*, 97, pp.45-54.
- Benedetto, A., Manacorda, G., Simi, A. and Tosti, F. 2012. Novel perspectives in bridges inspection using GPR, *Nondestructive Testing and Evaluation*, 27(3), pp.239-251.
- Garg, S. and Misra, S. 2020. Efficiency of NDT techniques to detect voids in grouted post-tensioned concrete ducts, *Nondestructive Testing and Evaluation*, pp.1-22.
- Zatar, W.A., Nguyen, H.D. and Nghiem, H.M. 2020. Ultrasonic pitch and catch technique for non-destructive testing of reinforced concrete slabs, *Journal of Infrastructure Preservation and Resilience*, 1(1), pp.1-13.
- Zatar, W.A., Nguyen, H.D., Nghiem, H.M. and Cosgun, C. 2021. Non-Destructive Testing of GFRP-Wrapped Reinforced-Concrete Slabs, *Transportation Research Board 100th Annual Meeting*, paper No. TRBAM-21-03354.



Prestressing Force Distribution in Post-Tensioned I-Girder Bridges Measured Using Smart Strands

Se-Jin Jeon^{1*}, Sang-Hyun Kim², Sung Yong Park³, and Sung Tae Kim⁴

¹: Department of Civil Systems Engineering, Ajou University, Suwon-si, Korea; email: conc@ajou.ac.kr

²: Convergence Technology Research Team, Daewoo Institute of Construction Technology, Suwon-si, Korea; email: sanghyun.kim@daewooenc.com

³: Department of Structural Engineering Research, Korea Institute of Civil Engineering and Building Technology, Goyang-si, Korea; email: sypark@kict.re.kr

⁴: Department of Structural Engineering Research, Korea Institute of Civil Engineering and Building Technology, Goyang-si, Korea; email: esper009@kict.re.kr

*: corresponding author

Keywords: prestressed concrete; prestressing tendon; strand; prestressing force; prestress loss; fiber optic sensor; fiber Bragg grating

Abstract: The proper distribution of prestressing force(PF) is the basis for the design of prestressed concrete(PSC) structures. However, the PF distribution obtained by predictive equations of prestress losses has not been sufficiently validated by comparison with measured data due to the poor reliability and durability of conventional sensing technologies. Therefore, the Smart Strand with embedded fiber optic sensors was developed and applied to PSC structures to investigate the short- and long-term characteristics of PF distribution as affected by friction, anchorage seating, elastic shortening, concrete creep and shrinkage. The data measured in a 20 m-long full-scale specimen and a 60 m-long PSC girder bridge were analyzed by comparing them with the theoretical estimation obtained from several design equations. The study results also confirmed the need to compensate for the temperature variation in the long-term monitoring to derive the actual mechanical strain related to the PF. We expect our developed Smart Strand to be applied practically in PF measurement for the reasonable safety assessment and maintenance of PSC structures by improving several of the existing drawbacks of conventional sensors.

1. Introduction

Determining the proper distribution of the prestressing force(PF) in the tendons is crucial in the design of prestressed concrete(PSC) structures because it largely affects safety and serviceability. The PF varies along the length of a tendon and over time due to the short- and long-term losses of prestress. Although the PF distribution is usually estimated using several predictive equations for the prestress losses during the design of a PSC structure, these equations can only approximate the PF distribution. Although many attempts have been made to validate the theoretical distribution of the PF by using conventional sensing technologies, their outcomes were not very successful due to several drawbacks that led to unreliable data.

In order to overcome the abovementioned drawbacks and limitations of existing sensing technologies in the estimation of the PF distribution, Smart Strands with embedded fiber optic sensors have been developed recently (Kim et al., 2020; Kim et al., 2022).

The dimensions of the Smart Strand are almost identical to those of a regular seven-wire strand widely used in PSC structures, as shown in Fig. 1. The steel core wire of the regular strand is replaced with carbon fiber reinforced polymer (CFRP) and a fiber optic sensor with several embedded FBGs, while the CFRP core wire is manufactured.

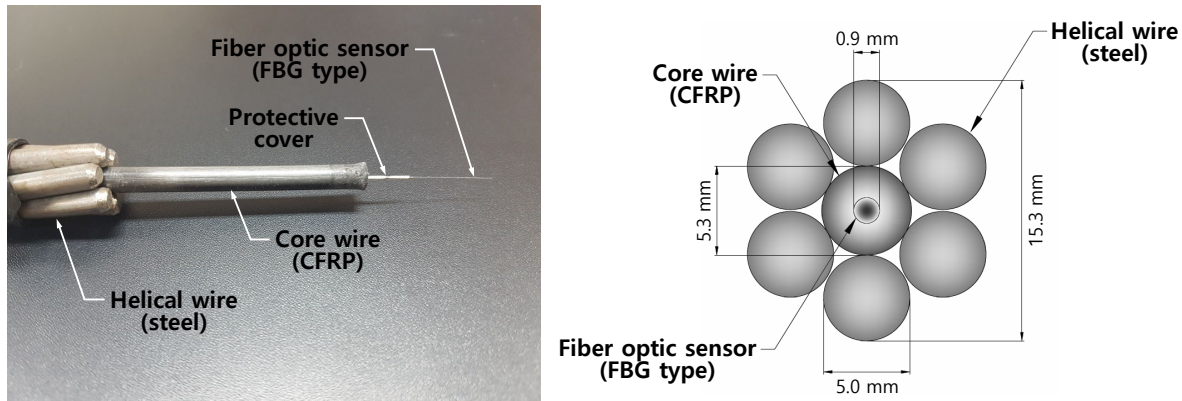


Fig. 1. Configuration of a Smart Strand

The wavelength of a reflected light wave measured at each FBG can be converted to the strain of Smart Strand by Eq. 1 when the effect of temperature is compensated (Jeon et al., 2022).

$$\varepsilon = \frac{1}{1 - p_e} \left\{ \frac{\Delta\lambda}{\lambda_B} - \left[\alpha_f + \xi + (1 - p_e)(\alpha_{smart} - \alpha_f) \right] \Delta T \right\} \quad (1)$$

where ε : mechanical strain of Smart Strand, p_e : photo-elastic coefficient (=0.22), $\Delta\lambda = \lambda - \lambda_B$: wavelength shift, λ : measured wavelength, λ_B : base wavelength, α_f : thermal expansion coefficient of an FBG (= $0.5 \times 10^{-6} / ^\circ\text{C}$), ξ : thermo-optic coefficient (= $6.2 \times 10^{-6} / ^\circ\text{C}$), α_{smart} : thermal expansion coefficient of Smart Strand (= $8.68 \times 10^{-6} / ^\circ\text{C}$), $\Delta T = T - T_B$: temperature change, T : measured temperature, and T_B : base temperature. The strain obtained in Eq. 1 can further be converted to the PF using the force-strain relationship of $P = (E_p A_p)_{smart} \varepsilon$, where $(E_p A_p)_{smart}$: equivalent $E_p A_p$ of Smart Strand, and E_p and A_p : modulus of elasticity and cross-sectional area of a strand, respectively.

2. Application of Smart Strands to Post-Tensioned Structures

Fig. 2 shows the post-tensioned 20 m-long full-scale specimen, where three types of Smart Strand with three, five, and seven equally spaced FBGs, respectively, were fabricated and selectively inserted into each duct, together with regular strands. Fig. 3 shows the PSC girder bridge with a 60 m span, where one Smart Strand was applied to one of the six ducts arranged in one of the 10 girders. The Smart Strand had seven FBGs and was inserted into the duct, together with 11 regular strands.

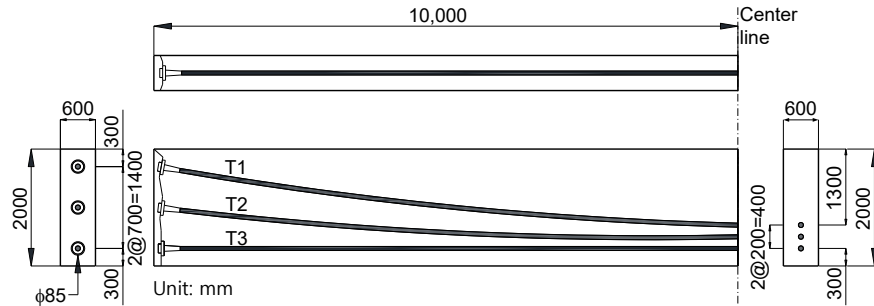


Fig. 2. Post-tensioned full-scale specimen

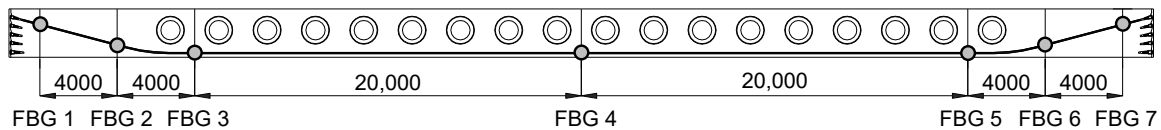


Fig. 3. PSC girder bridge

3. Short-Term Losses of Prestress

The PF distributions of the full-scale specimen and the PSC girder as affected by short-term prestress losses were represented in Fig. 4, where it apparently shows how the PF distributions are affected by each short-term prestress loss. The PF gradually decreases from the live end due to the friction loss during tensioning. Then, the PF distribution near the anchorage zone decreases due to the anchorage seating loss. The PF distribution further decreases according to subsequent tensioning of the remaining strands included in the other ducts. The measured PF distributions were also compared with those theoretically estimated. The overall trend of PF distributions in each stage of short-term prestress losses was similar for the measured and theoretical values, although they showed some differences in absolute values. These results in Fig. 4 confirmed the usefulness of the existing predictive equations for the short-term prestress losses in estimating the PF distribution for design purposes. However, the theoretical PF distribution was sensitive to the assumed values for the friction coefficients and slip displacement, which highlights the importance of reasonable design parameters.

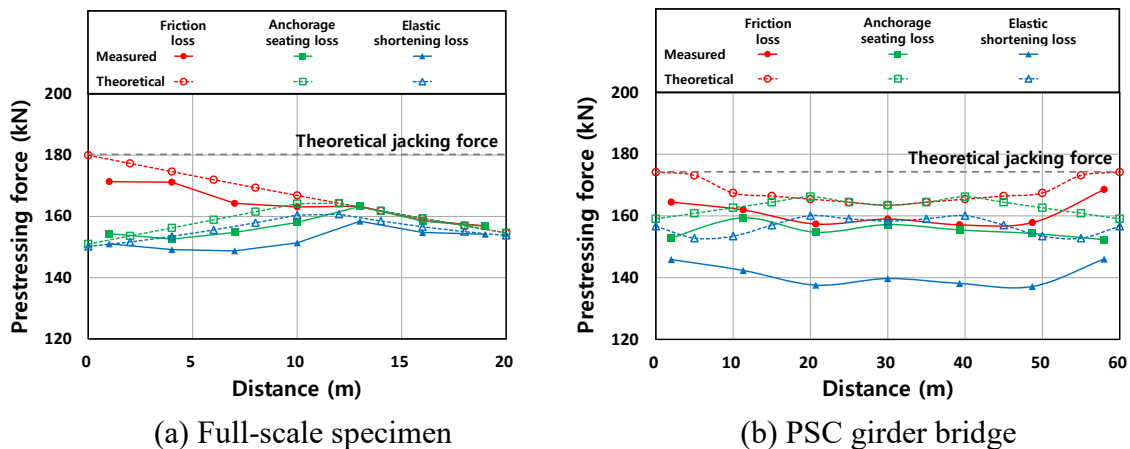


Fig. 4. Short-term PF distribution in measurement and theory

4. Long-Term Losses of Prestress

Fig. 5(a) presents the PF variation at mid-span of the full-scale specimen over time in both measurement and theory. Three Smart Strands(H1, H7, and H12) of T1 in Fig. 2 were representatively analyzed herein. Zero-day corresponds to the time after tensioning when the short-term losses had just occurred. The predictive equations for the long-term prestress losses induced by creep and shrinkage were compared with the measurements: ACI 209R, ACI 423.10R, and Eurocode 2. Among the three equations considered, Eurocode 2 showed relatively good agreement with the averaged measurement values.

Fig. 5(b) compares PFs at mid-span of the PSC girder between the predictive equations and the measurement. The figure suggests that several major construction stages caused significant PF fluctuations, in addition to the decreasing trend induced by long-term prestress losses. Overall, Eurocode 2 was in good agreement with the measured values, similar to the full-scale specimen.

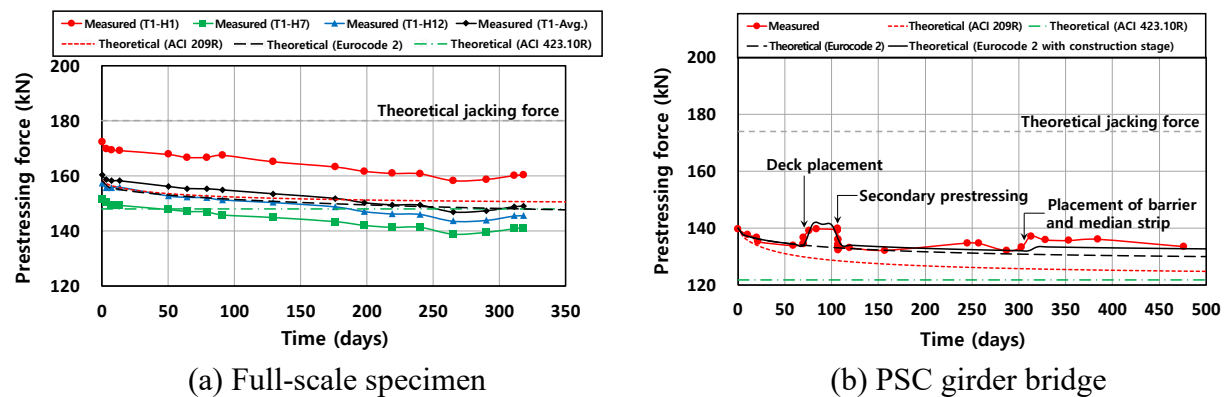


Fig. 5. Long-term PF distribution in measurement and theory

5. Conclusions

The Smart Strand with fiber optic sensors of FBG type was developed to investigate the effect of prestress losses on the prestressing force(PF) distribution.

The PF distributions were affected by the short-term prestress losses in the order of friction loss, anchorage seating loss, and elastic shortening loss. Overall trend of the measured and theoretical PF distributions was similar in each stage of the short-term prestress losses.

Regarding the long-term prestress losses, although the two approaches of measurement and theory produced a similar long-term trend of the PF distribution, the difference between them varied depending on the design equations. The equation of Eurocode 2 to estimate the long-term prestress losses showed relatively good agreement with the measurement, when compared to that of ACI 209R and ACI 423.10R. This can be attributed to the more refined form of the predictive equation of Eurocode 2 that addresses the time-dependency of the PF.

6. References

- Jeon, S.J., Park, S.Y., and Kim, S.T. 2022. Temperature compensation of fiber Bragg grating sensors in Smart Strand, *Sensors*, 22(9), 3282.
- Kim, S.H., Park, S.Y., and Jeon, S.J. 2020. Long-term characteristics of prestressing force in post-tensioned structures measured using Smart Strands, *Applied Sciences*, 10(12), 4084.



Bridge Engineering Institute Conference 2023 (BEI-2023)
Rome, Italy, July 17-20, 2023



Kim, S.H., Park, S.Y., Kim, S.T., and Jeon, S.J. 2022. Analysis of short-term prestress losses in post-tensioned structures using Smart Strands, *International Journal of Concrete Structures and Materials*, 16(1), 81-95.



Detection of Cable Section Loss in Cable-Stayed Bridge with Electromagnetic Sensor

Imjong Kwahk¹, Changbin Joh², Ji-Young Choi³, Kwang-Yeun Park⁴, and Joo-Hyung Lee^{5*}

¹: Korea Institute of Civil Engineering and Building Technology (KICT), Goyang-si and South Korea; email: kwakim@kict.re.kr

²: KICT, Goyang-si and South Korea; email: cjoh@kict.re.kr

³: KICT, Goyang-si and South Korea; email: legion@kict.re.kr

⁴: KICT, Goyang-si and South Korea; email: kypark@kict.re.kr

⁵: KICT, Goyang-si and South Korea; email: leejoohyung@kict.re.kr

*: corresponding author

Keywords: Cable section loss; Non-destructive testing; Electromagnetic sensor; bridge inspection; Total magnetic flux

Abstract: There are many islands in Korea, and several sea bridges, including cable-stayed bridges, have been constructed and serviced. Since cables of the cable-stayed bridges are a critical member for the structural safety of bridges, they are included in the subject of regular bridge inspection. However, inspecting its condition is practically impossible since the cable is inside the duct. Although various non-destructive evaluation methods, including Magnetic Flux Leakage, have been proposed and applied, there are still limitations to being applied in an actual bridge environment. Therefore, the Korea Institute of Civil Engineering and Building Technology developed a detachable cylindrical electromagnetic sensor using Faraday's law of induction, which states that changes in magnetic flux generate force, to detect section loss of the cable located in the duct. The section damage detection principle of the sensor is as follows. First, wrap the sensor around the cable and install it. When alternating current is applied to the primary coil of the solenoid-type sensor, a magnetic field is formed in the longitudinal direction of the sensor. At this time, when the sensor is moved, an induced electromotive force is generated according to Faraday's law. The magnitude of the force is proportional to the number of turns of the coil and the change rate of the magnetic flux passing through the cross-sectional area perpendicular to the magnetic field inside the sensor. So, the induced electromotive force is also decreased when the cable cross-section is reduced. By measuring the force with the secondary coil located in the sensor's center, it is possible to detect the section loss. Non-destructive tests with the developed sensor were performed on specimens fabricated to replicate the cable-stayed bridge's cable, and the damage detection capacity was evaluated. In addition, NDT was conducted on cables of an actual cable-stayed bridge to evaluate on-site applicability. When the EM sensor is improved through further research, it is expected that it could be applied as a means of cable inspection of the in-serviced bridges in Korea.

1. Introduction

The sea surrounds Korea on three sides, with many islands, especially in the West and South Seas. So, dozens of cross-sea bridges connect the island to the mainland or the island to the island. Because it has several advantages: low cost, ease of construction, and aesthetics (Zhao and Tonia, 2013), the cable-stayed bridge is commonly constructed as a cross-sea bridge in Korea.

The cable is the primary structural member supporting the superstructure loads for the cable-stayed bridges. Therefore, if severe defects or deterioration occurred in the cable, the bridge's structural safety could be severely compromised. Especially in the case of cross-sea bridges, cable corrosion due to salt damage could be very harmful to safety. However, despite its structural importance, there is no method to inspect the inside cable duct. Only it is possible to estimate the condition inside the cable by visual inspection and hammering.

Various non-destructive testing (NDT) methods, such as Magnetic flux leakage and Impact echo, have been suggested and applied to find defects inside the bridge duct. However, it was confirmed that the workability and accuracy were poor at the actual bridge site (Seoul Metropolitan Government, 2017). Therefore, it needs to improve the detection performance of cable section loss for effective bridge maintenance. The Korea Institute of Civil Engineering and Building Technology (KICT) developed an electromagnetic (EM) sensor that could detect the section loss of bridge cable.

2. The Electromagnetic Sensor to Detect Cable Section Loss

The developed EM sensor's basic detection principle is from the EM induction, commonly known as Faraday's law. According to the law, the electromotive force around a closed path equals to the negative of the time rate of change of the magnetic flux enclosed by the path (Jordan and Balmain, 1968).

When alternating current is applied to the solenoid-type sensor surrounding the cable, a magnetic field is formed inside the sensor. Then, the magnetic flux density changes with time, an induced electromotive force (emf), V_{ind} , is generated according to Faraday's law. It could be expressed in Eq. 1 (Kwahk et al., 2020). In here, N is the number of coil turns, Φ is the total magnetic flux, B is magnetic flux density, and A is cross-sectional area inside the sensor.

$$V_{ind} = -N \frac{d\Phi}{dt} = -N \frac{d}{dt} \int_A \vec{B} \cdot d\vec{A} \quad (1)$$

It is assumed that non-magnetic materials and air inside the sensor do not affect the induced electromotive force. Then, if the cable cross-section reduction has occurred due to corrosion, the induced emf will also decrease according to Eq. 1. The secondary coil located in the center of the sensor measures this induced emf, so that it is possible to determine whether or not section loss has occurred. The appearance of the developed sensor is shown in Fig. 1.

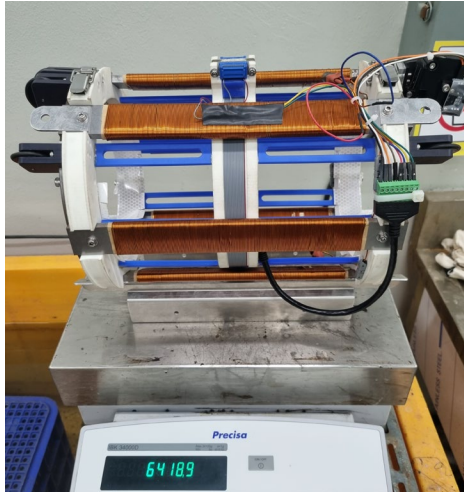


Fig. 1. Appearance of EM sensor



Fig. 2. Test set up

3. Non-Destructive Test with the EM Sensor

3.1. Details of the test cable specimens and test program

In order to evaluate the detection performance of the sensor, cable specimens with artificially damaged cross-sections were fabricated. The damage area ratio and damage length were used as test variables. The damage area ratio was set to 1.6, 3.2, 4.8, 6.5, and 8.1 %, and the damage length was determined to be 20, 50, 80, 120, and 150 mm. A total of 18 cable specimens (4.5 m length) were produced, including non-damaged specimens. In order to increase the effectiveness of the test, the specimens were fabricated with the identical material as the cable of a cable-stayed bridge completed in 2012.

To simulate the environment similar to the actual bridge condition, the NDT was conducted with the cable specimen installed at an angle in Fig. 2. The sensor was controlled via a laptop connected wirelessly via Wi-Fi. It was confirmed that it works even at a distance of several tens of meters. The alternating current value is applied to the sensor to generate the magnetic field and the emf is measured by the sensor at a sampling rate of 4,000 Hz.

3.2 Test results

Fig. 3 shows the peak value of the induced voltage along the length direction of the cable specimen. In the case of the undamaged specimen, the induced emf with a smooth curvature was measured along the longitudinal direction of the specimen. On the other hand, when there is damage, it could be seen that a rapid decrease in induced emf is measured at the corresponding location. The tendency of the induced emf according to the degree of cross-sectional loss and the length of the damage is currently under analysis.

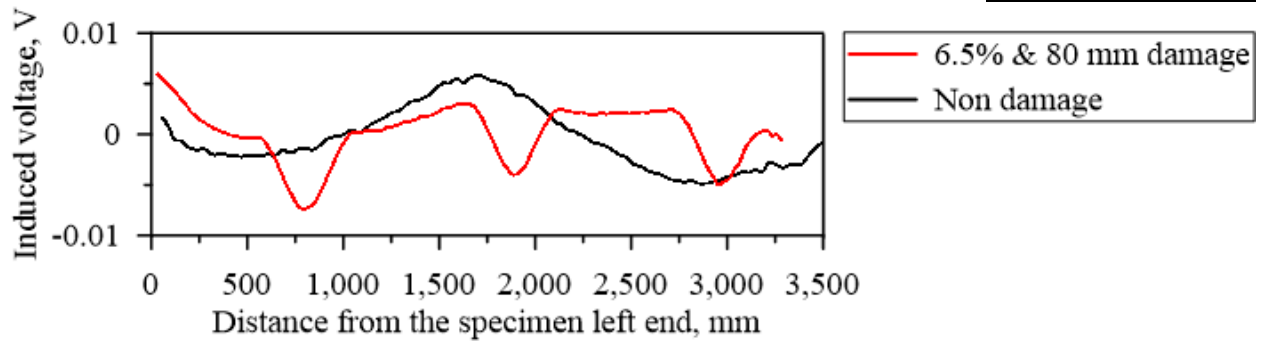


Fig. 3. Test results of non-damage and three 6.5 % section loss specimen

4. Conclusions

Despite its structural importance, there is no effective non-destructive test method to evaluate the cable's internal condition. Therefore, an EM sensor capable of detecting damage to a cable section was developed using the law of electromagnetic induction, and its performance was evaluated through an indoor NDT. As a result of the test, it was found that when the loss occurs to the cable cross-section, the induced electromotive force generated at the corresponding location is decreased compared to the undamaged cross-section. If the advanced sensor under development is achieved, such as applicability verification at the actual sea-bridge site, it is expected to be of great help in the maintenance of cable-stayed bridges in Korea.

5. References

- Jordan, E. and Balmain, K.G. 1968. *Electromagnetic Waves and Radiating Systems* (2nd edition). Prentice-Hall
- Kwahk, I., Park, K.Y., Choi, J.Y., Kwon, H., and Joh, C. 2020, Non-destructive for sectional loss of external tendon of prestressed concrete structures using total flux leakage, *Applied Sciences*, MDPI, 10, 7398.
- Seoul Metropolitan Government. 2017. *Report on PSC Box Girder Bridges' Tension Member Maintenance Plan in Seoul*.
- Ulaby, F.T. and Ravaioli U. 2016. *Fundamentals of Applied Electromagnetics* (7th edition). Pearson Education Korea.
- Zhao, J.J. and Tonnias, D.E. 2013. *Bridge Engineering* (3rd edition). McGrawHill Education (Asia).

Evaluation of Salt Resistance of Three-Component Cement Concrete by Unsteady Electrophoresis Test

Kohei Kanaoka¹ and Tatsuya Nukushina^{2*}

¹: Tokuyama college of technology, Yamaguchi and Japan; email: c17kanaoka@tokuyama-kosen.ac.jp

²: Tokuyama college of technology, Yamaguchi and Japan; email: nukushina@tokuyama-kosen.ac.jp

*: corresponding author

Keywords: chloride attack; Blast furnace cement; Three-Component Cement Concrete; Unsteady Electrophoresis Test; Effective diffusion coefficient

Abstract: In Japan, marine concrete structures use blastfurnace slag cement type B, which usually uses better chloride attack than ordinary portland cement. Although, in the long-term chloride ingress, control of maintenance costs are increasing due to repair and re -deterioration after repair. Three-Component Cement Concrete, which replaces the fly ash in the blastfurnace slag cement type B is considered to have higher salt -shielding property than blast furnace cement B concrete and ordinary concrete, but the durability of Three-Component Cement Concrete and the replacement rate of fly ash, which most salt -shielding property are not clear. Therefore, the replacement rate of fly ash which the most durable of the Three-Component Cement Concrete was investigated using an unsteady electrophoresis test with a short test period and a compression strength test.

1. Introduction

In order to improve the durability of concrete structures, the use of mixed cements that replace the industrial by-product and waste in cement is increasing. Above all, ground granulated blastfurnace slags (hereinafter, GGBS) are generated as by -products when producing pig iron in the shaft furnace, long-term strength and salt damage resistance can be expected to be improved.

However, the durability has been lowered due to chloride attack even with the blastfurnace slag cement type B, which replaces 40% to 60% GGBS from the ordinary portland cement (hereinafter, OPC). As such control of maintenance costs are increasing due to repair and re -deterioration after repair. Therefore, the practical application of the Three-Component Cement Concrete which replaces the fly ash (hereinafter, FA) in the blastfurnace slag cement type B (hereinafter, BB) has been replaced, has been attracting attention. FA is an industrial by -product that occurs when coal is burned at a coal power plant, and can be expected to improve long -term strength and chloride attack resistance as well as GGBS. The Three-Component Cement Concrete has not cleared the durability and the replacement rate of FA, which the most salt-shielding property. Therefore, in this study, the purpose was to evaluate durability due to changes in FA replacement

Table 1. Formulation of Mortar and experimental conditions

Type	W/B (%)	Unit Amount(kg/m ³)				Applied Voltage (V)	Energization time (h)	Number of specimens
		W	BB	FA	S			
BB	50	365	730	0	1000	30	24·48·72	1
BB-FA8		361	664	58				
BB-FA10		360	648	72				
BB-FA15		358	609	107				
BB-FA20		355	568	142				
BB-FA30		350	490	210				
BB-FA50		340	340	340				

BB: Blast furnace cement B type (Density:3.04g/m³, Specific surface:3960cm²/g), FA: Fly ash (Density:2.23g/m³, Specific surface:3170cm²/g), S: Crushed sand (Density 2.67g/m³)

rates, using the unsteady electrophoresis test that can obtain a concrete chloride penetration characteristics in a short time indoors and compression strength test.

2. Unsteady Electrophoresis Test

2.1. Materials and Formulation

Table-1 shows the materials and mix proportion of specimens, and the experimental conditions. Mortar, which is easy to produce a sample under test, is used because the replacement rate of FA, the most salt-shielding property is not clear. In order to evaluate the salt -shielding properties by the replacement rate of the FA, the unit amount of the fine aggregate was fixed to 1000 and the water cement ratio was unified to 50 %. FA was replaced by 8 %, 10 %, 15 %, 20 %, 30 %, and 50 % from the mass of cement. In addition, the name of the subsequent experimental case shall be abbreviated as a combination of the replacement rate of BB and FA, and for example, the FA10%replacement shall be "BB-FA10".

2.2. Test method

Three test specimens of $\Phi 100 \times 50$ mm dimensions were cut from the center of a $\Phi 100 \times 200$ mm test specimen cast by the formulation of Table-1 and used as test specimens. The applied voltage was constant at 30V. For measurement after the end of the energization, referring to the preceding research¹⁾, after fracturing the test specimen, spray a silver aqueous solution (0.1N) on the fracture surface, and 7points that area colored white were measured in depth, except 10 mm of both ends of test specimens. The average value was chloride ion penetration depth. Fig.1 shows the experimental setup of the unsteady electrophoresis test.

The Public Works Research Institute method was used for calculation methods for the execution diffusion coefficient²⁾. The formula of the Public Works Research Institute method is shown in (1).

$$D_{nssm} = k \cdot \frac{R(273+t)}{zF} \cdot \frac{L}{\Delta\phi} \quad (1)$$

D_{nssm} : effective diffusion coefficient($\times 10^{-12} \text{m}^2/\text{s}$), t :temperature ($^{\circ}\text{C}$), L : thickness of specimen (mm), X_d : chloride penetration depth(mm), R : Gas constant ($=8,134\text{J}/\text{K}\cdot\text{mol}$), z : Absolute value of chloride ions ($=1$), F : Faraday constant ($=9.648 \times 10^4 \text{J}/\text{V}\cdot\text{mol}$), $\Delta\phi$: applied

voltage (V), The penetration speed K was calculated based on the inclination of the approximation curve that passed through the origin in the relationship between the applied time and the chloride penetration depth.

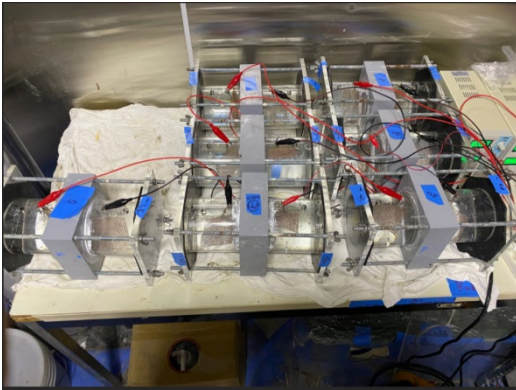


Fig. 1. Unsteady electrophoresis test

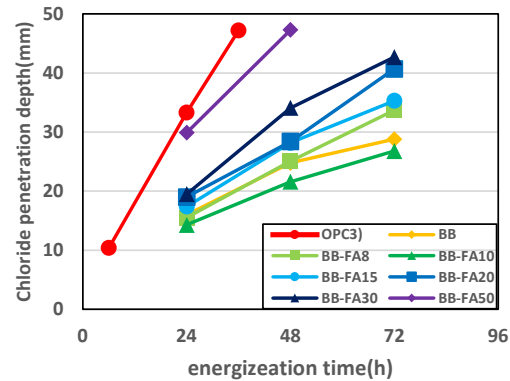


Fig. 2. Chloride penetration depth

2.3. Test results and consideration

Fig. 1 shows the relationship between the applied time and the chloride penetration depth. The case of OPC is referred to the previous study³⁾. In any mixture, the longer the applied time, the more chloride permeation depth. Also, the larger the replacement rate of the FA, the more the chloride penetration depth. The penetration depth at the same applied time is BB-FA10, BB-FA8, BB, BB-FA15, BB-FA20, BB-FA30, BB-FA50, OPC were increased in the order. chloride permeation depth of the BB-FA50 was measured a test body that the was energized 24,48 hours, because the entire fracture surface was colored white when the silver nitrate solution was sprayed on the fracture surface at the end of the power to 72 hours.

Fig 2 shows the calculation result of the effective diffusion coefficient. Fig 3 shows the

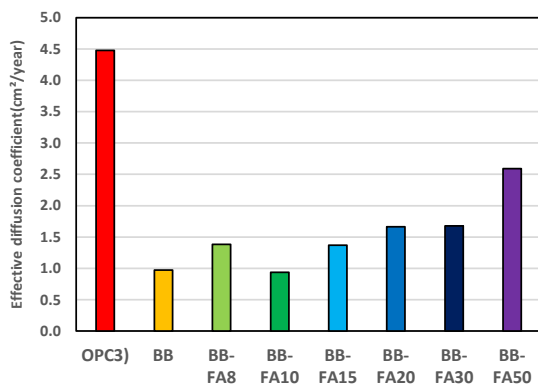


Fig. 3. Effective diffusion coefficient

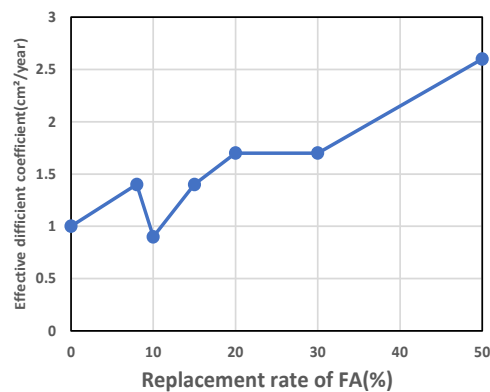


Fig. 4. Effective diffusion coefficient and the replacement rate of FA

relationship between the effective diffusion coefficient and the replacement rate of FA.

These figures indicate that BB-FA10 has the lowest effective diffusion coefficient. Also, the larger the FA replacement rate, the larger the effective diffusion coefficient.

From these results, it can be seen that replacement rate of 10% by FA has most salt-shielding property. And, the larger the replacement rate of the FA, the lower the amount of calcium hydroxide required for the reaction. Decreasing calcium hydroxide means the amount of unreacted BFS and FA are increasing and that the densification of void may have stagnated.

3. Compression Strength Test

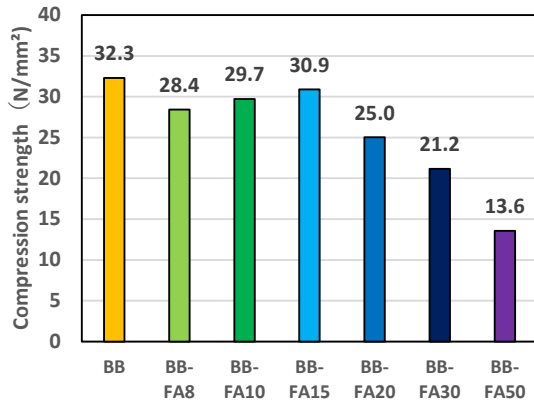


Fig. 5. Compression strength test

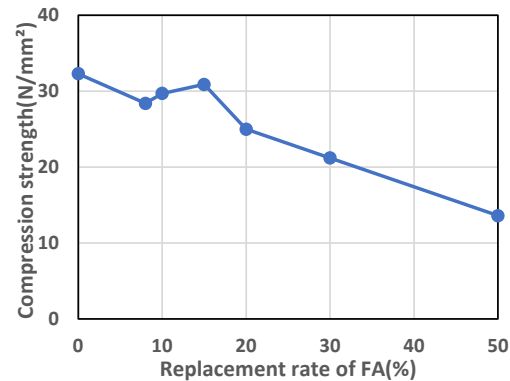


Fig. 6. Replacement rate of FA and compression strength

3.1. Formulation and test method

The test specimen used the formulation of Table-1. Three specimens were produced with dimensions of $\phi 50 \times 100\text{mm}$ for each formulation. The test specimen was demolded at 7 days of dimensions of $\phi 50 \times 100\text{mm}$ for each formulation. The test specimen was demolded at 7 days of the material age, and performed underwater curing until 28 days of the material age, and then performed a compression strength test. It was performed in accordance with JIS A 1108 (Japanese Industrial Standards).

3.2. Test Results and Consideration

Fig.5 shows the compression strength test result. Fig. 6 shows the relationship between FA replacement rate and compression strength. These figures indicate that the compression strength tended to decrease as the replacement rate of FA increased. On the other hand, the decrease in strength was minor up to about 15 % FA replacement. From this, it is considered that the higher the FA replacement rate, the lower the cement amount, and the strength did not appear.

4. Conclusions

In this study, the following findings were obtained by quantitatively evaluating concrete durability through the unsteady electrophoresis test and compression strength test.

- (1) The most highly salt-shielding property is that 40% of the blast furnace slag powder is replaced with the OPC and the FA is replaced by 10%.
- (2) The larger the replacement rate of FA, the greater the chloride penetration depth and the effective diffusion coefficient.
- (3) The larger the replacement rate of the FA, the lower the compression strength.



5. Reference

- [1] Takeshi IYODA et al, “Evaluation for curing effect on blast furnace slag concrete by unsteady-state electrophoresis test”, Cement Science and Concrete Technology, Vol.68, pp.275-282,2014
- [2] Yutaka WATANABE et al, “Chloride ion diffusion coefficient of concrete by rapid chloride penetration test calculation of the coefficient of chloride diffusion”, Concrete Engineering Annual Proceedings in Japan, Vol.24, No.1, pp.663-668,2002
- [3] Ryota KUMAMOTO et al, “Evaluation of Salt Resistance of Highly Durable Concrete by Unsteady Electrophoresis Test”, Japan Society of Civil Engineers,2022



Bridge Engineering Institute Conference 2023 (BEI-2023)
Rome, Italy, July 17-20, 2023



Field Testing



Grating on Bridge deck for Improving Flutter Performance: A Case Study of Cable-Suspended Bridge

Zhen Wang^{1*}, Xuhui He², Haiquan Jing³, and Lulu Liu⁴

¹: Department of Civil Engineering, Central South University, Changsha and China; email: wangzhen@csu.edu.cn

²: Department of Civil Engineering, Central South University, Changsha and China; email: xuhuihe@csu.edu.cn

³: Department of Civil Engineering, Central South University, Changsha and China; email: hq.jing@csu.edu.cn

⁴: Department of Civil Engineering, Central South University, Changsha and China; email: liululu2020@csu.edu.cn

*: corresponding author

Keywords: cable-suspended bridge; flutter; aerodynamic countermeasure; wind tunnel test; grating

Abstract: Wind tunnel tests were conducted to investigate the flutter performance and characteristics of a cable-suspended bridge girder at various angles of attack (AOAs). The results showed that the prototype bridge deck had poor flutter performance and was highly sensitive to variations in AOAs. For improving the flutter performance of the girder, the aerodynamic countermeasure of grating-installed on bridge decks with various grating-opening ratios (grating-ORs) was also conducted in wind tunnel tests. It was found that the grating-installed bridge deck was an effective way to increase the flutter critical wind speed (FCWS) of a cable-suspended bridge. The energy participation ratio (EPR) was considerably changed by the grating installed on the bridge deck. The EPR of both vertical and torsional motions shows high correlations with FCWSs, which may explain the improvement of FCWS.

1. Introduction

The cable-suspended bridge is a flexible system with cables as the main load-bearing structure and the deck laid directly on main cables, and the deck alignment is basically the same as the main cable alignment, as shown in Fig. 1. Its strong spanning capacity, fast erection speed, low engineering investment and construction difficulty, especially suitable for geological conditions in mountainous areas. Therefore, cable-suspended bridges play an increasingly important role in addressing the transport problems of mountain residents. Despite having many benefits, cable-suspended bridges perform poorly in wind resistance. Moreover, the wind environment that bridges must face with in mountainous regions is complex, with characteristics like large AOAs, non-uniform, and non-stationary. As a result, the poor wind resistance performance of cable-suspended bridges is becoming more and more evident and is a significant technical barrier to their promotion and application. Several cable-suspended bridges in China have reportedly been subjected to wind-induced vibration in recent years.

In the present study, a cable-suspended bridge, which has been subjected to flutter on 2021, was served as the research object. Since aerodynamic countermeasure is an economical and effective way to improve the aerodynamic stability of bridges (Ge and Xiang, 2009; Sato et al, 2002), an aerodynamic countermeasure of grating-installed on the bridge deck was selected. Experimental approaches were primarily considered when determining the flutter performance of the cable-suspended bridge. Flutter characteristics, including FCWSs and EPRs were also investigated.



Fig. 1. Cable-suspended bridge.

2. Wind Tunnel Test

Wind tunnel tests were carried in the wind tunnel of Central south university, and the information of the wind tunnel was reported by (He et al, 2018). The geometric scaling ratio of the section model is 1:10, the length is 1 m and the wind speed ratio is 2.08. The specific design parameters of the section model are shown in Table 1, and bridge decks with grating-OR of 0-40% at the AOA of $\pm 5^\circ$ were tested. In wind tunnel tests, the wind speed was measured using a Cobra probe. The displacement of the section model was measured by displacement signals using four Keyence laser transducers with a measuring range of 30 cm and a sampling frequency of 1000 Hz.

Table 1. Physical properties of section model

NO.	Items	Unit	Prototype	Scale ratio	Target value	Actual value
1	Mass	kg/m	1404.290	1/10	14.043	14.165
2	Inertia	kg·m ² /m	10922.850	1/10000	1.092	1.107
3	Vertical frequency	Hz	0.360	5	1.798	1.734
4	Torsional frequency	Hz	0.429	5	2.145	2.166
5	Frequency ratio	/	1.193	1	1.193	1.249
6	Vertical damping ratio	%	/	1	0.350	0.380
7	Torsional damping ratio	%	/	1	0.350	0.380
8	Wind speed ratio	/	/	1/2	/	/

3. Response Characteristics

3.1. FCWS

Fig. 2 illustrates the FCWSs of wind tunnel tests for the grating-installed bridge deck. The FCWS considerably increased when the grating-OR increased. Particularly when the grating-OR increased to 30%, the FCWSs at various AOAs meet the requirements of flutter checking wind speeds. As the grating-OR reached 30%, not flutter occurred at the highest test wind speed (70 m/s) for negative AOAs. The range of AOA without flutter at the maximum test wind speed was extended to 0° as the grating-OR reached 40%. For positive AOAs, the FCWS increases with

increasing grating-OR up to 20%, but then remains almost constant for higher grating-ORs. It is conceivable that there is an optimum grating-OR and that once achieved, the FCWS essentially remains unchanged.

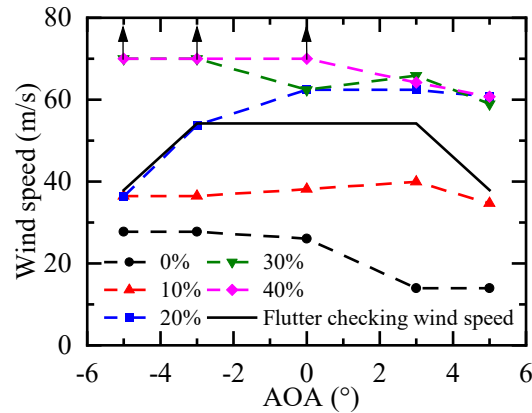


Fig. 2. Test results of FCWSs

3.2. Energy participation ratios

To further analyze the participation level of vertical and torsional degrees of freedom during the occurrence of flutter, the EPR was introduced to evaluate the flutter pattern. The EPR essentially represents the distribution of vibration energy in the vertical and torsional degrees of freedom and reflects the ratio of mechanical energy in the vertical and torsional motion of the total system mechanical energy, which can be calculated by the following equation:

$$P_h = \Psi^2 / (\Psi^2 + \eta^2); P_\alpha = \eta^2 / (\Psi^2 + \eta^2) \quad (1)$$

where, Ψ is the average amplitude ratio of vertical motion to torsional motion; η is the ratio of the radius of gyration r to the half-width b of the bridge deck.

Fig. 3 shows the variation of the EPR with the grating-OR at various AOAs. It can be seen that the EPR was influenced by both AOAs and grating-ORs. For the prototype bridge deck, P_h is greater than P_α at negative AOAs, the reverse is true at the AOA of 0° , and the latter is dominant at positive AOAs. The FCWS increases as P_h increases, and gets the lowest value at positive AOAs where P_h is at the lowest levels. For the grating-installed bridge decks, P_h increases with the increase of grating-ORs in most cases, and the same with the FCWS. Similar results were obtained by (Yang et al, 2015) in their study of the aerodynamic stability a twin box girder with various slot widths, i.e., the participation level of the vertical motion was highly correlated with the FCWS. It indicates that the EPR is one of important factors determining the FCWS. On the other hand, P_h increases rapidly with grating-ORs at negative AOAs and 0° AOA, while that increases slowly at positive AOAs. P_h attains a high level for a grating-OR of 10% at negative and 0° AOAs, whereas it attains an equivalent level for a grating-OR of 30% or 40% at positive AOAs. This may explain the reason why the FCWSs of negative AOAs and 0° AOA exceed the highest wind test speed with increasing of grating-OR, while the FCWSs of positive AOAs remain lower than that.

4. Conclusion

In the present study, for improving the aerodynamic stability of a cable-suspended bridge, a series of wind tunnel tests of the bridge deck with various grating-ORs and AOAs was conducted. The main conclusions can be drawn as follows:

- 1 The aerodynamic countermeasure of grating installed on the bridge deck significantly improved the flutter performance of the cable-suspended bridge. The FCWS increased as the grating-OR increased, but there was an optimal grating-OR. After reaching the optimal grating-OR, the FCWS increased very gently, especially for positive AOAs.
- 2 The EPR was effectively influenced by the grating-installed bridge deck at the same AOA. As the grating-OR increased, P_h significantly increased while P_α dramatically decreased, which was one of the key factors in enhancing flutter performance.

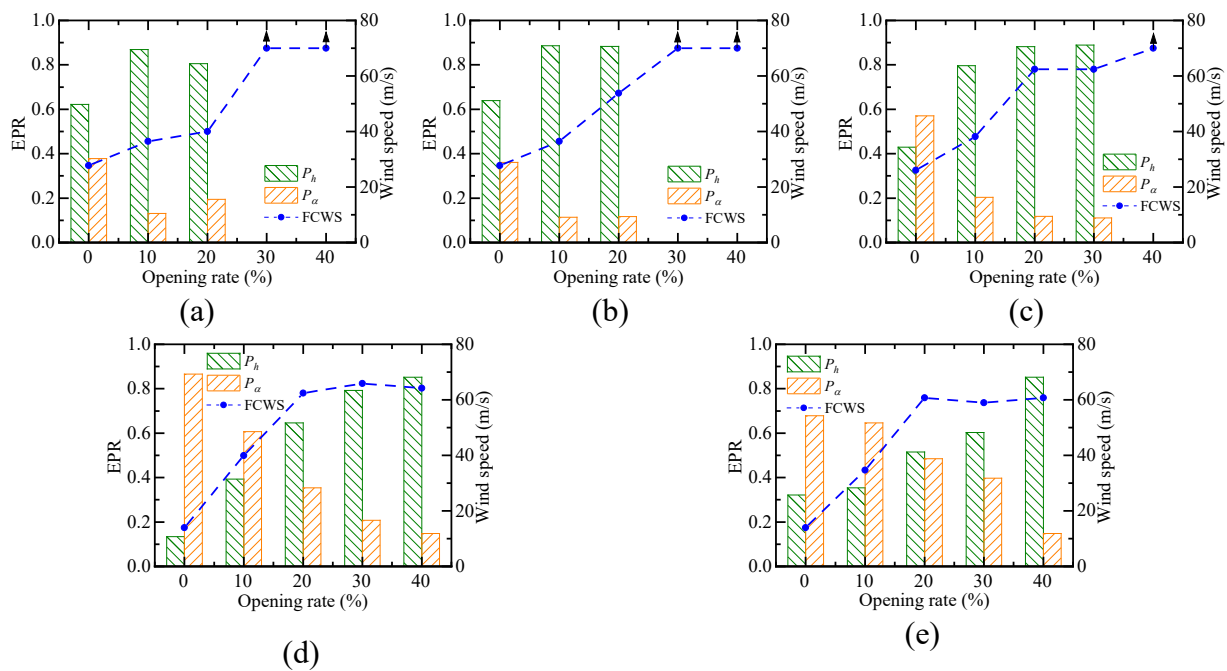


Fig. 3. EPRs at various AOAs: (a)-5°; (b)-3°; (c)0°; (d)3°; (e)5°

5. References

Ge, Y.J., Xiang, H.F., 2009. Aerodynamic stabilization for box-girder suspension bridges with super-long span, in: Proceedings of the In Proceedings of the 5th European and African Conference on Wind Engineering. Firenze University Press.

Sato, H., Hirahara, N., Fumoto, K., et al., 2002. Full aeroelastic model test of a super long-span bridge with slotted box girder. *Journal of Wind Engineering and Industrial Aerodynamics* 90, 2023-2032.

Yang, Y., Wu, T., Ge, Y., et al., 2015. Aerodynamic Stabilization Mechanism of a Twin Box Girder with Various Slot Widths. *Journal of Bridge Engineering* 20, 04014067.



Development of Elevated Road and Rail Projects in Singapore

Hooi Leng Phua^{1*}

¹: Land Transport Authority, Singapore; email: phua_hooi_leng@lta.gov.sg

*: corresponding author

Keywords: Jurong Region Line; Integrated Hub; Noise Barriers; Viaduct Segments

Abstract: Since the opening of Singapore's first Mass Rapid Transit (MRT) Line in 1992, the system has grown from the initial 67 kilometers and 42 stations to 240 kilometers and 175 stations presently, and will expand by 50% to 360 kilometers by 2040. Like many urban cities, Singapore is a built-up city state with very limited land space to meet its varied needs. Majority of the MRT lines and road expressways that were implemented in the past were constructed underground to free up the above-ground spaces for other developments. Whilst this intensifies the development potential and land value capture, the construction and operating costs for building underground is very prohibitive, and not necessarily always justifiable. To ameliorate the footprint and environmental impact of above-ground transport infrastructure on the landscape, deliberate effort is made at the planning and design stage to integrate them into developments to intensify the utilisation of the land.

1. Introduction

With a land area of only 730 square kilometers, Singapore is one of the densest cities in the world with a population density of over 8,000 people per square kilometer. A fine balance has to be struck amongst all the different competing demands for limited land, which is atypical of many developed cities. 12% of Singapore's land is already used for roads, almost the same used for housing. It is not sustainable for Singapore to continue to expand its road network to support the growth and development of its urban spaces. Singapore's land transport policy is centered on providing an efficient, safe, affordable public transport system that meets the needs of Singaporeans. With a robust and comprehensive rail network as the backbone, Singapore envisages to grow the existing rail network to 360km by 2030, such that 80% of all households can be within 10-minutes walking distance from a MRT station.

However, the construction of a transport system is a high cost investment that can take 7 to 10 years to construct. The cost and duration required to implement it is further compounded if it is underground. Hence, utilising underground space for transport infrastructure is very common in highly urbanised cities to minimise land sterilisation and maximise the development potential and value of the land above, is a careful balance planners must achieve.

2. The Jurong Region Line

Singapore is currently constructing the seventh line - Jurong Region Line (JRL) to provide direct connectivity between the North-Western and Western part of the island upon phase completion from 2027 (see Fig. 1). Comprising of 24 stations, an integrated depot and 24 kilometers route length, it is a fully above-ground medium rail system that serve existing and upcoming

developments under the overall longer-term plans to transform Singapore’s western business district.

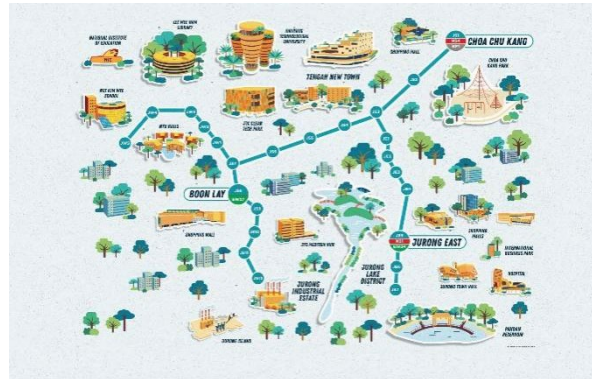


Fig. 1. Jurong Region Line Railway Map

Being elevated allows the stations to be closer-spaced and improve the accessibility of key activities nodes in the western region, serving commuters better. Without the need for extensive deep excavations next to adjacent buildings, sensitive structures and under utilities, it allows the construction period and cost to be greatly reduced.

However, there are numerous engineering challenges that have to overcome. Some of the structures of existing operational Boon Lay, Choa Chu Kang and Jurong East stations, with high daily ridership, have to be demolished and strengthened. Sections of the JRL viaducts will be constructed over busy roads, existing rail lines, and close to existing buildings. In addition, global supply chain disruptions, shortage of skilled manpower and material shortages have added other challenges to the construction works.

To help overcome these, digital twins are created to allow the architects and engineers to visualise and optimise the layout of the stations and commuter flow. Critical construction activities are modelled virtually, with each step of the works simulated to allow for a better understanding of the work sequence, risk identification and mitigation. Pre-fabrication and pre-casting are also used to form the station and viaduct elements. The viaducts comprise of about 12,000 precast segments, each weighing 20 to 40 tonnes, which are fabricated off-site, before transporting them to the required location to be lifted and placed by lifting girders (see Fig. 2(a)) or launching frames (see Fig. 2(b)). These methods allow the viaducts to be constructed faster, with lesser manpower and also reduces the disruptions and inconveniences to the communities where the works are being carried out in.



Fig. 2(a). Segmental Launching using Lifting Girder



Fig. 2(b). Balanced Cantilever using Lifting Frames

Conscious effort was made at the onset of its planning to integrate with existing and new developments to maximise the development potential of the corridor. The existing Jurong East Station, which already serves as an interchange of two existing lines will be expanded with the addition of a pair of stacked platforms to allow seamless transfer with the JRL. Instead of having two separate stations with more land take, the single expanded station with a common transfer level will connect all the six platforms without requiring commuters to exit and re-enter the faregates as they interchange between the three lines.

One environmental downside of an elevated railway line is the constant and permanent noise emitted from the running rails, which can be very debilitating to residents living next to the tracks. To overcome this, permanent noise barriers (see Figs. 3(a) and (b)) will be installed along the viaducts that are near residential areas.

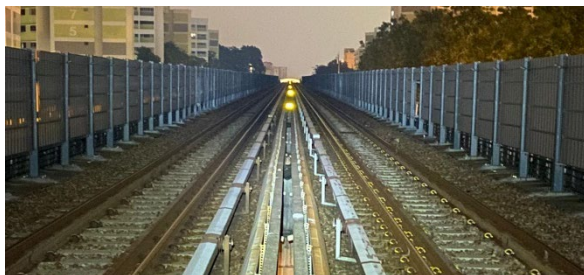


Fig. 3(a). Typical 2m height Noise Barriers



Fig. 3(b). Typical 5m Height Portal Type Noise Barriers at Track Turnout

3. Integrated Hub at Jurong East

The land parcel on the Northern end of Jurong East station, where the viaducts leading to the existing station crisscross, is being concurrently developed with a new 27-storey, 2-level basement, mixed use development comprising Grade-A office space, retail and civic facilities and a bus interchange that will be integrated with the expanded station. When completed by 2028, it will form a single Integrated Hub (see Fig. 4) in the center of the new Jurong Lake District. By constructing this new development together with the expansion and alteration works to the station, it minimises the overall duration and disruption to the operations of the station, and also obviates the added constraints that will be poised by the operations of a new completed line if constructed independently. Underpinning every aspect of the design and construction of this new development

is needed to maintain the operations and safety of the station and the five railway viaducts that are cutting through the plot.

When completed, a new four-storey Hub Plaza (see Fig. 5) will be the centroid of the existing station, new buildings and existing adjacent developments. This Hub serves to connect all the developments and station platforms both multi-directional, and also at different levels. Positioning the Hub Plaza away from the existing platforms was a key design consideration as the new transfer platform that is within it would not need to be constructed above the existing operational platforms, which would cause disruptions to the daily commuters and result in high risks to the operations of the station.



Fig. 4. The new Integrated Hub

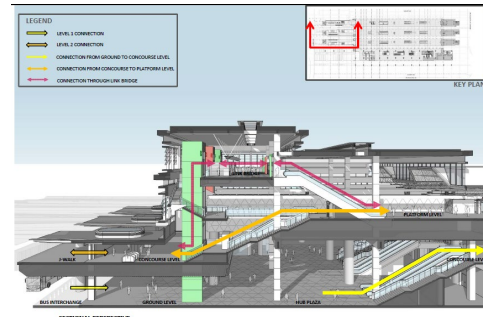


Fig.5. Sectional Layout of the Hub Plaza

4. North-South Corridor

The North-South Corridor (NSC) was originally conceptualized as a vehicular expressway to connect Northern Singapore and the city centre directly. The 21.5 kilometers expressway will improve the transport connectivity of the towns along this corridor. NSC is also Singapore's longest Transit Priority Corridor, featuring dedicated bus lanes, cycling trunk routes and pedestrian paths to serve public bus commuters, active mobility users and pedestrians. This is a shift away from typical expressways in Singapore, which are dedicated to moving large volumes of private motor vehicles around the island, to embracing multi-modes of transport within a shared corridor. Whilst majority of the NSC is underground as it meanders through the highly-densified corridor in the South, there is 8.8 kilometers of elevated road viaducts in the North where it is less developed.

5. Conclusion

Transport has always been one of the most important pillars of any modern economies, albeit also one of the most challenging. Planners must grapple with increasing demands for efficiency, security, reliability, cost-effectiveness and lately also care for the environment. These demands are made more challenging with the marked increase in projected ridership arising from population growth and rising affluence. The Land Transport Authority of Singapore has to continuously orchestrate long term integrated planning and optimise the infrastructure to sustain the continued development of Singapore's Road and Rail system.

6. References

Land Transport Authority 2013. Land Transport Masterplan 2013, 20-21



Structural Behavior of a 40+ Year Old PSC-I Concrete Bridge According to its Internal Tendon Loss in the Central Part

Yeonghun Seong¹ and Hyunjoong Kim^{2*}

¹: Hybrid Structural Testing Center, MyongJi University, Yongin, Republic of Korea; email: syh0896@mju.ac.kr

²: Hybrid Structural Testing Center, MyongJi University, Yongin, Republic of Korea; email: khjmju@mju.ac.kr

*: corresponding author

Keywords: PSC-I, Tendon, Rupture, Full-scale Experimental, Maintenance

Abstract : Prestressed concrete bridges with a type I girder (PSC-I), hastily built in the 1960s, have been increasingly deteriorating, making their internal tendon prone to rupture, leading to social and economic problems due to bridge collapse and emergency repairs. In this study, a post-tension PSC-I bridge, to be demolished after more than 40 years of service, was evaluated for its structural behavior due to internal tendon loss. The internal tendon of its central part, a weak flexural behavior part, was artificially cut to model an actual damaged structure; its structural behavior was then compared to that of an intact girder. The results showed that stiffness increased from 2.2% to 37.9% depending on the amount of internal tendon loss (loss ratio from 8.3–25%) in the central part of the bridge, with a load reduction of up to 78% when compared to an intact girder. The position of the neutral axis and maximum progress of the crack also increased rapidly due to the change in stiffness and decrease in internal force.

1. Introduction

In the 1960s, as Korea experienced rapid social development, new bridges were being constructed as fast as possible. However, these bridges now face maintenance problems. Prestressed concrete (PSC) bridges with internal tendons account for 28% of all domestic bridges. Due to their structure, internal tendons are causing particularly pressing issues in the social and economic areas, including rupture or section reduction from corrosion and deterioration. Tests on the structural behavior of PSC bridges before and after the rupture of their internal tendon have been conducted at home and abroad. However, upon examining previous research, it was found that it was limited to evaluating the design values and simple beam behaviors of aging bridges that have been in existence for over 40 years. In addition, when verifying the effect of internal tendon fracture, a new girder was created and performance evaluation was conducted based on the internal tendon fracture effect and loss amount by location. Therefore, research on structural performance evaluation is needed for aging bridges that have been in existence for over 40 years, specifically focusing on the loss amount of internal tendon by location in the central part of the bridge.

2. Experimental Method and Contents

In this study, a structural test of a over 40 years old PSC-I girder was conducted to understand the bridge’s structural behavior based on the loss of the internal tendon of the girder during actual use, the central internal tendon of a bridge to be tested was artificially ruptured to allow monitoring of the structural behavior changes according to the internal tendon loss rate (from 0 to 25%) and comparing them with an intact structure. Test model specifications and details of the experimental load cases and loading process are in Fig 1. Fig 2. and Table 1.

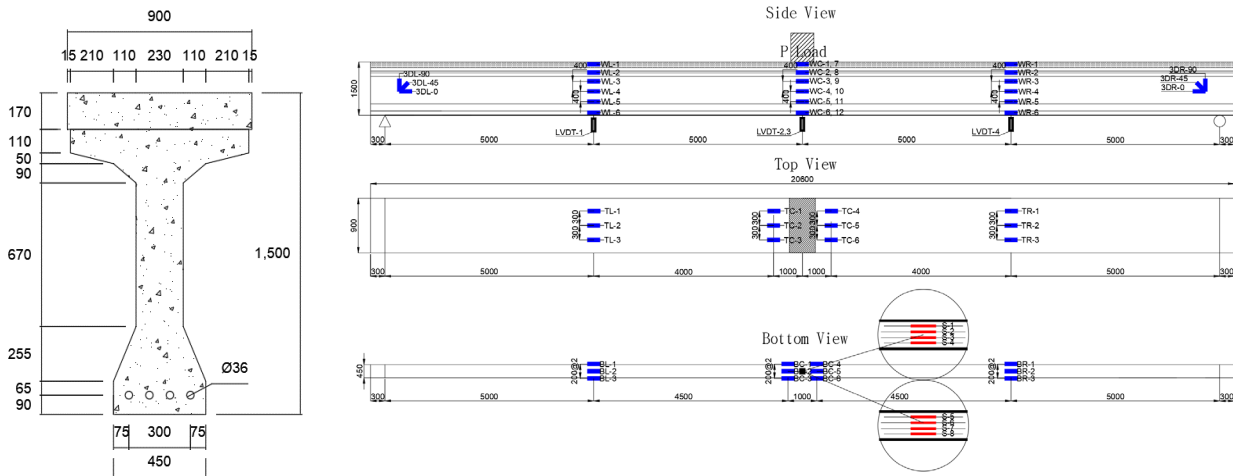


Fig. 1. Cross section of a PSC-I girder bridge and Sensor set-up layout



*Loss Ratio = Ruptured Steel Wire / 48 (=4 Tendons x 12 Wires)

Fig. 2. Schematic of the artificial rupture of the internal tendon

Table 1. Details of the experimental load cases and loading process

Load Case and parameters tested		P (kN)	Loading Process	Remarks
Reference Girder (Ref. Girder)	Elastic behavior	150	3 times	60% of computation crack load
	Crack load	300	1 time	120% of computation crack load
	Pmax behavior	869	1 time	-
Cutting Girder (8.3% Loss and 25% Loss)	Elastic behavior	150	3 times	60% of computation crack load
	Crack load	300	1 time	120% of computation crack load
	Nonlinear behavior	600	1 time	-
	Cutting strand	600	1 time	*Strand loss ratio: 8.3 %
	Cutting strand	600	1 time	*Strand loss ratio: 25 %
	Pmax behavior	679	1 time	-

3. Evaluation of the Flexural Behavior of A PSC-I Girder

Girders prepared for this study were tested for their maximum load, maximum displacement, concrete strain, and steel wire strain, as shown in Table 3, for three different loss conditions to evaluate the flexural behavior of a girder in use for more than 40 years and identify the behavioral characteristics in case of internal tendon rupture. The flexural behavior of the girder varied according to its internal tendon loss rate, as observed by the differences in stiffness after the crack load, which varied between 2.2–38%. However, because the experiment of the girder with an 8.3% loss ratio ended at the target load of 600 kN, the deviation of stiffness was compared and evaluated in the same load range.

Table 2. Test results

Experimental condition	P (kN)	Disp. (mm)	ϵ_c	ϵ_t	EI (Stiffness)
Ref. Girder	848.95	181.6	1,496	10,403	1
Girder with 8.3% Loss	600.0	66.0	735	2,853	0.97
Girder with 25% Loss	680.0	200.3	2,835	8,146	0.62

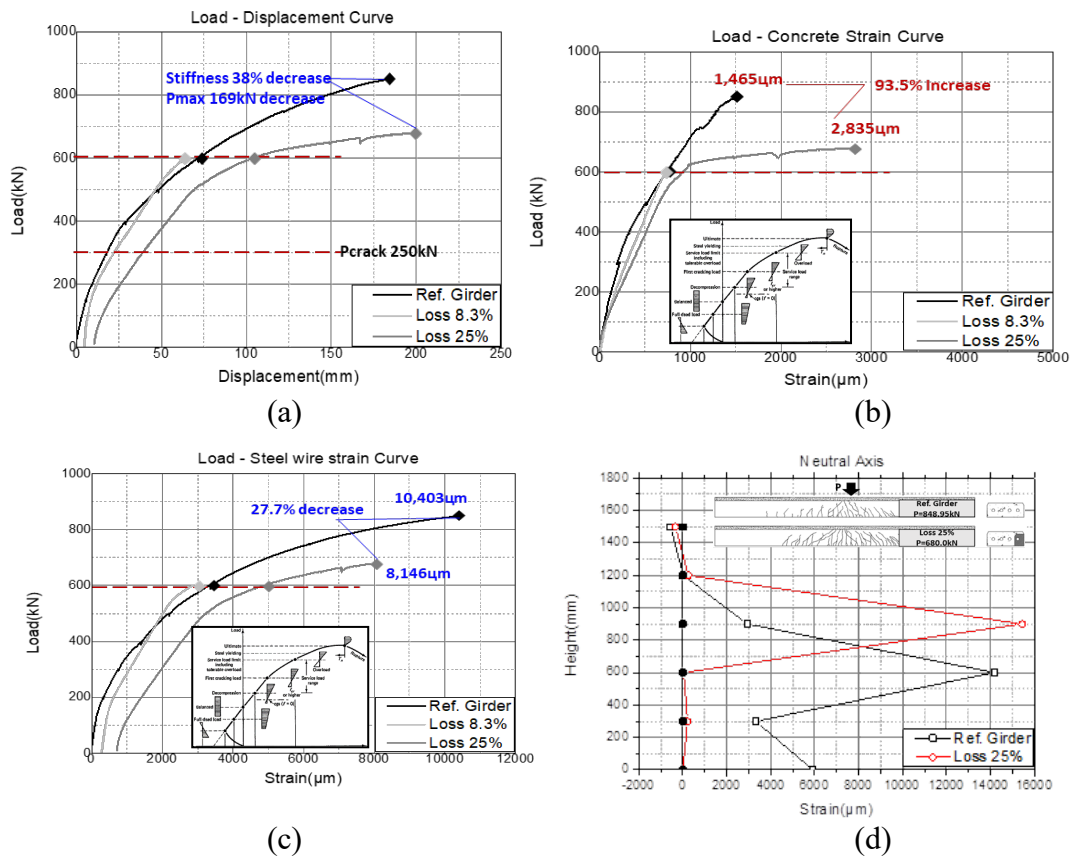


Fig. 3. Behavior of 45 years PSC-I girder : (a) Load–Displacement Relationship; (b) Load-to-Concrete Stress Relationship (Compression Part); (c) Load-to-PS Steel Wire Stress Relationship (Tension Part); (d) Neutral axis position and crack height change



4. Conclusion

In this study, the load-carrying capacity for the service load and ultimate load of an old PSC-I bridge in operation for over 40 years was examined. The flexural behavior characteristics, according to the loss rate of the internal tendon of the bridge, were identified by artificially rupturing its internal tendon. The following conclusions could be drawn by analyzing the change in stiffness through maximum load displacement, the change in material properties for each load stage through the change in strain in the compression and tension parts, and the crack progress pattern according to the change in the position of the neutral axis.

- 1) Old PSC-I bridges, as all bridges in general, show rapid displacement changes while experiencing crack loading. In this study, after the steel wire yielded, depending on the loss rate of the steel wire in the tension section (0 to 25%), a nonlinear displacement of up to 37.9% was observed.
- 2) The concrete in the compression part and steel wire in the tension part both generated a strain difference from 27.7% to 93.5%, depending on the loss rate of the steel wire. The plastic state that occurred after the steel wire yielded caused a rapid increase in the strain experienced by the concrete.
- 3) The flexural crack advanced up to the vicinity of the upper flange when the crack load was exceeded, and the position of the neutral axis and the height of the crack developed as the loss rate of the internal tendon was increased.
- 4) When the internal tendon is ruptured by corrosion—a frequent occurrence in many old PSC bridges—and a load greater than the service load is applied, a rapid change in structural behavior occurs depending on the internal tendon loss rate.

This study examined the flexural behavior characteristics of PSC-I bridges according to the amount of loss of the internal tendon in the central part. Further work is necessary to evaluate the flexural behavior according to internal tendon rupture for each PSC-I girder position. This information must be used to perform maintenance work on mid- to long-term bridges by predicting their behavior by FEM analysis, a reliable method to acquire information on the mechanics and durability characteristics of its constituent materials along the service life of bridges.

5. Acknowledgements

This work was supported by the Korea Agency for Infrastructure Technology Advancement (KAIA) through Grant 21CFRP-C163381-01, funded by the Ministry of Land, Infrastructure and Transport of Korea.

6. References

- [1] AASHTO. 2014. Bridge design specifications. Washington, DC: AASHTO.
- [2] ACI Committee 228 (2004), Nondestructive test methods for evaluation of concrete in structures, Report ACI 228.2R-98, American Concrete Institute, Farmington Hills, MI.



Bridge Engineering Institute Conference 2023 (BEI-2023)
Rome, Italy, July 17-20, 2023



- [3] Pessiki S., Kaczinski M., Wescott H. Evaluation of Effective Pre-stressed Force in 28-Year-Old Prestressed Concrete Bridge Beams. PCI Journal. 1996; 41(6): 78-79.

- [4] Shenoy C., and Frantz C. Structural Tests of 27-Year-Old Prestressed Bridge Beam. PCI Journal. 1991; 36(5): 80-90.



The Use of Engineered Cementitious Composite (ECC) Deck Overlay at Curry Street Bridge, Windsor, Ontario, Canada: Lessons Learned and Challenges

Don Gardonio¹, Steve Volpatti¹, Emad Booya², and Philip Loh^{3,4}

¹ Facca Incorporated, Ruscom, Ontario, Canada

² University of Windsor, Windsor, Ontario, Canada

³ Dura Concrete Canada Incorporated, Ruscom, Ontario, Canada

⁴ philip@facca.com

*: corresponding author

Abstract: Traditional High Performance Concrete Overlays for bridge decks deteriorate due to many factors. These factors can be due to excessive loading, shrinkage, weathering effect, etc. The replacement cost of existing deficient concrete pavement is expensive. Moreover, the design of maintenance materials requires the use of energy-efficient materials with a low environmental impact. Facca Incorporated, in collaboration with Dura Concrete Canada Inc., a change proposal was approved by the City of Windsor to replace the high performance concrete overlay by a high performance fibre reinforced composite (HPFRC) known as Engineered Cementitious Composite (ECC) material for use as an overlay, as part of the deck rehabilitation for Curry Avenue Bridge over the Grand Marais Drain in Windsor, Ontario. Using the Dura[®] ECC overlay developed by Dura Concrete Canada Inc. and Facca Inc., this innovative, bendable, and durable ECC product was installed successfully. The visual observations and inspections after more than 8 months in service revealed that there were no signs or indications of deterioration to the repaired Bridge overlay. This paper will provide details of the innovative design, field testing, batching process, the challenges encountered during the placement and the in-service field conditions after 8 months.

1. Project Background

The City of Windsor tendered a project to rehabilitate the Curry Avenue Structure over the Grand Marais Drain as per the Engineer's determination. The bridge is a simple span (16m) consisting of prestressed box beam girders with a concrete topping and a ductile high-performance concrete. The deck cross fall is 2% across the length of the structure. Since the topping is to be an exposed deck, the new overlay was to be high performance concrete. The deck was to be scarified 40 +/- 5 mm and then the topping removed locally at spalled and delaminated areas. The new high-performance overlay material in sections where the topping was removed was calculated to be up to 100mm in depth. This topping was to be reinforced with 10M dowels at 2.0m intervals and staggered every 1.0m and one layer of welded wire mesh was to be placed over the entire surface. Facca Incorporated was retained as the general contractor for the City of Windsor.

2. Innovation Change Proposal

During the pre-construction meeting, Facca Incorporated requested from the City of Windsor to replace the traditional High Performance Concrete mix for the deck overlay with by a high performance fibre reinforced composite (HPFRC) known as Engineered Cementitious Composite (ECC) material for using as an overlay due to its superior qualities in strength, durability and performance. Specifically, the mix proposed would have a longer life span, reach early strengths at a faster rate than a traditional mix and would far surpass the 50 MPa strength requirements at 28 days set for this contract. The City accepted the proposal with conditions.

3. Dura[®] ECC Mix Design

3.1. Mixture Design and Proportioning

High-Performance Fibre Reinforced Concrete Dura[®] ECC with a minimum 28-day strength of 60 MPa, was designed and implemented as repair materials. The mixture proportions with respect to cement mass are listed in Table 1. The fibres content was 2 percent by volume. As per the road conditions and specific requirements, the mixtures were designed to have thixotropic consistency. Thixotropic cementitious mixtures are known to be thick and viscous in normal condition but flow when subjected to external vibration or agitation.

Table 1. Mixture Proportioning with respect to cement mass

Material ID	Cement	SCM	Sand	Water	HRWR	WM
Dura [®] ECC	1	1.15	0.89	0.52	0.015	0.008

4. Dura[®] ECC Trial Batch

As part of the requirements of the change proposal, Facca Incorporated was to provide a trial batch of 2 m³ and cast the mix into a mold of 2.0 m x 4.0 m x 0.2 m depth to evaluate the workability and finishing properties. This test panel also required a 2% slope to simulate the bridge deck crossfall. Figure 1 shows the trial batch form.



Fig. 1. Form for the Dura[®] ECC Trial Batch

The trial batch was completed on April 30, 2021 in the presence of the Consultant Engineer and the City of Windsor Representative. The specified slump flow specified for this mixture was 200 mm to 250mm. Strength cylinders as per CSA A23.1/23.2 were fabricated as required from the placed trial batch to evaluate the strength. Figures 2 and 3 show the steps for fabricating a specimen from the trial batch ECC mix. The material thixotropic properties were confirmed and the material was able to stand up with the 2% slope without slipping or sagging. Curing measures of wet burlap, opaque poly and insulated tarps were installed.



Fig. 2. Filling the Trial Batch Form



Fig. 3. Levelling of the Dura[®] ECC mix on 2% slope (Left Side is low end)

The compression test results confirmed to the City the rapid and early strength gain and the higher than required 28-day required strengths. Generally, this trial batch met all performance requirements as well as the fresh properties (i.e., levelling) requirements, but the finishing requirements were yet to be confirmed.

5. Dura[®] ECC Overlay Placement

Placement of the new concrete overlay and patches to the box beam girders took place on May 29, 2021. Ambient temperature at the start of placement was 11°C, the day was sunny and relative humidity for the day hovered around 40%. After correction of screed elevations with the Consulting Engineer, the total depth ranged from 60mm to 130mm, and a total quantity of 17m³ of ECC were placed. Photos of the surface preparation and placement are shown respectively in Figures 4 and 5. The concrete was placed by concrete bucket and screeded using an air driven Allen Screed to level the overlay. Spiked rollers and tool placers were used to maneuver the concrete ahead of the screed. No concrete vibrators were used due to the plasticity of the mix. After the screed had passed, the modified tine rake was to be used to groove the surface perpendicular to the direction of traffic. However, due to the low relative humidity, once the screed passed the Dura[®] ECC, the surface was drying out too quickly. Therefore, the decision was made with the Consulting Engineer and the City to immediate apply the wet burlap and poly and to grind and groove the surface in the hardened state.



Fig. 4. Curry Avenue Surface Preparation



Fig. 5. Curry Avenue ECC Placement

Compressive cylinders were taken to track the strength gain throughout the curing and post curing period. All results for early breaks and 28-day strength (87 MPa average) far surpassed expectations, reaching design strength at 4 days (56 MPa average). As part of the completion of the deck overlay, the surface was diamond grinded, and grooves were cut in.

6. In-service Performance Dura® ECC

The visual observations and inspections after more than 8 months in service revealed that there were no signs or indications of deterioration to the repaired Bridge overlay. The bridge is subjected to heavy traffic volume since placement and exhibited several freeze-thaw cycles and dry-wet cycles. It is also worth noting that the bridge and Dura® ECC material was subjected to snow removal activities which include salting and/or plowing. Only hairline cracking has been identified on the surface that are below 0.3 mm in width. These types of cracks are not of a concern as per CSA A23.1.

7. Conclusions and Lessons Learned

For this project, Dura® ECC has proven to be a viable alternative to traditional High-Performance Concrete. Factors to consider would include:

- Placement of this mix can be achieved using traditional methods, equipment, and machinery.
- Both early strength and target strengths can be achieved, faster and higher than regular high-performance concrete.
- The materials is impacted of not only ambient temperature but also relative humidity during and after placement.
- Finishing requirements and alternative methods to achieve specified surface finish, were confirmed.
- Dura® ECC materials can sustain heavy traffic loading and extreme weathering exposure despite the age of the patch repair.

8. References

ASTM 2010. ASTM C 618, Standard Specification for Coal Fly Ash and Raw or Calcined Natural Pozzolan for Use, *Annual Book of ASTM Standards*.



ASTM 2013. ASTM C989, Standard Specification for Slag Cement for Use in Concrete and Mortars, *Annual Book of ASTM Standards*.

ASTM 2016. ASTM C1116, Standard Specification for Fiber-Reinforced Concrete, *Annual Book of ASTM Standards*.

ASTM 2015. ASTM C494. Standard specification for chemical admixtures for concrete, *Annual Book of ASTM Standards*.

Booya E., Adesina A., Gardonio D., Loh P., Das S., Mechanical and Durability Performance of an Innovative In-Situ Concrete Pavement Repair Patch, Transportation Association Canada, 2020.

CSA 2013. CSA A3001. Cementitious materials used in concrete, *Canadian Standards Association, Mississauga, Ontario*

CSA 2019. CSA A23.1/A23.2. Concrete materials and methods of concrete construction/Test methods and standard practices for concrete, *Canadian Standards Association, Mississauga, Ontario*



Transporting Heavy Weight Cargo, Diagnosis Philosophy, and a Case Study

Daniel Elmaleh* and Yehonatan Pestes²

¹: Via Bridges design and engineering, Tel Aviv Israel; email: Daniel@via-bridges.com

²: Via Bridges design and engineering, Tel Aviv Israel; email: Yoni@via-bridges.com

*: corresponding author

Keywords: Heavy weight cargo; Bridge loads; Bridge level gauges; Live load test

Abstract: Bridges are designed and built to meet specific load criteria. Despite safety margins in design, an overloaded transport cargo or vehicle may affect the sustainability of the structure and its life expectancy. However, the need to transport special cargo exceeding the design criteria could arise often. Such heavy-load transportation refers to the movement of vehicles that exceed the weight limits set by state or federal regulations. This type of transportation is often necessary to deliver oversized or overweight goods, such as heavy machinery, industrial or construction equipment. This article will discuss the measures taken for analyzing heavy cargo exceeding the standard weight limits. Also, a case study of a super heavyweight cargo weighing 548 tons transporting an electric transformer over a 3-span bridge, designed in the early 70s, was carried out. The bridge analysis included a documented deflection of a live load test before the actual transportation. The results were conveyed into a FEM model of the bridge. Further precautions were considered by monitoring the deflections of the bridge at the real-time transition of the cargo and measuring the natural frequencies of the bridge before and after the transition.

1. Introduction

As the 21st century progresses, industries continually evolve and demand heavy cargo transportation. Consequently, trailer trucks are becoming more advanced, which places an immense strain on the infrastructure of roadways and bridges. Superload trucks are designed to transport heavy components such as bridge girders and massive power transformers. These trailers have a particular configuration to evenly distribute the heavy load to multiple axles, ensuring load distribution comparable to the statistical live load defined in the code. Concerning the above, this article will discuss the following:

- a) Raise awareness about heavy loads' immediate and long-term effects on bridges.
- b) Discuss bridge loading according to the design philosophy outlined in the codes.
- c) Briefly discuss the dynamic amplification factor of heavy loads.
- d) Present a case study, a 548-ton cargo transfer crossing over a 3-span girder bridge

2. Loading Definition

Loading is a crucial factor in the design of bridges. The selection of the primary design load is based on identifying a single heavy vehicle, considering the probability of occurrence of multiple

vehicle loads. National design codes commonly use three types of statistical loads to simulate various loads, which are as follows:

- a) A system of concentrated loads with defined loads and distances.
- b) An evenly distributed load across the traffic lanes, combining concentrated loads along the lanes.
- c) An evenly distributed load across the traffic lanes, with less loading on some lanes.

The limit state design method is currently used in bridge design, with two essential characteristics. Firstly, it considers all possible limit states, and secondly, it is based on probabilistic methods.

The design depends on two parameters: the magnitude of the loads as it impinges the structure – meaning the load effect, and the resistance or strength of the component. Both the magnitude of the load effect and the resistance may be subjected to statistical variation, but also according to the structure's life expectancy. Therefore, safety factors for each of them are specified differently per country.

Extra attention should be paid when older bridges with outdated codes are subjected to heavy loads. Firstly, the bridge's condition may be unknown as it has been used for a substantial amount of its expected lifespan. Secondly, the evolution of design codes tends to increase load effects as industries develop and vehicles, such as trucks, become heavier, leading to larger statistical loads being incorporated into the codes. Fig. 1 presents a schematic graph of probability distribution to illustrate the aging of a structure effect as discussed above. Over time chances of failure increase, this can be seen as the area trapped in the middle of the graph.

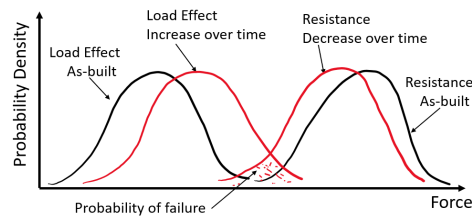


Fig. 1. Probability density distribution for load effect and resistance graph – presents the effect of structure age on its vulnerability.

3. Examining Bridges for Heavy-Weight Cargo

As previously mentioned, a bridge design is based on a probabilistic approach. Therefore, when examining a specific load on a bridge, it should always be compared to the statistical load in the design codes, considering the dynamic effects of the load. The ability of a bridge to withstand heavy loads depends not only on the weight of the cargo but also on the axle distribution and span length ratio of the bridge. Specifically, the influence line of the bridge should be considered concerning the specific load. Overall, it is crucial to thoroughly examine a bridge before subjecting it to heavy-weight cargo to ensure its safety and structural integrity. The following section will discuss an examination of a specific cargo load.

As discussed in section 2, the probability of a bridge failing increases as it ages. Given the fact that the bridge was constructed in the early 1970s - there is an ongoing debate about the best course of action, which involves several options:

- a) Diverting the cargo to an alternate route,
- b) Temporarily reinforcing the bridge using steel beams and hydraulic jacks for the duration of the transition period, or
- c) Conducting a live load test on the bridge to measure its actual deflections and increasing the accuracy of the calculation and modeling. The above would help calibrate the model and consider the actual stiffness distribution between the longitudinal girders.

These options were carefully evaluated in collaboration with the authorities and the owner of the bridge - the national transport infrastructure company, Netivei Israel. Rerouting the cargo's course was impossible, so the decision came down to either option (b) or (c). It's important to note that temporary bridge strengthening in Israel for a one-time transition is rarely done and must be considered meticulously, as it can affect the static schema.

Considering that the stress values were close to the specified code values, a recalibration of the analytical model through a live load test was deemed sufficient. This option was chosen as it increased the certainty level of the calculations and modeling without requiring significant structural changes to the bridge.

4.1 Conducting a Live Load Test on the bridge

The live load test aimed to determine the bridge's actual stiffness in both longitudinal and transverse directions. The test would enable us to calibrate the FEM model of the bridge accordingly. The above could also assist in tackling any "red flags" before the transition of the heavy cargo, for instance, radical deflections or cracks. An experimental load plan was devised, specifying the exact location of the loaded truck and providing instructions on the measurements to be taken, as well as the expected theoretical deflection. The test truck weighed 104 tons and had a trailer, corresponding to the bridge span in length. The location of the test truck path is identical to the future path of the heavy cargo.

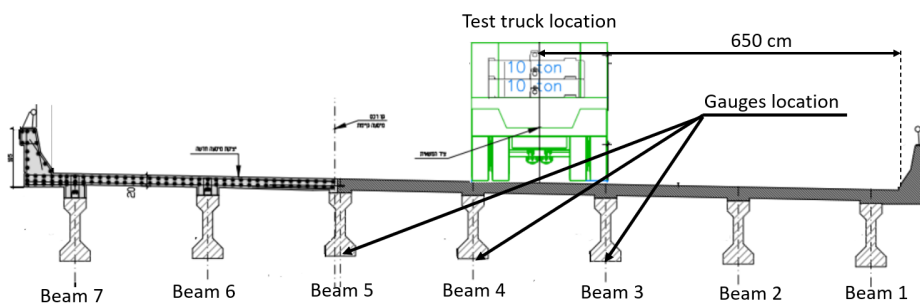


Fig. 3. Location of live load test and the gauges used to measure the deflection of the beams shown on a transverse section of the bridge.

For measurement purposes, gauges with an error tolerance of 0.01 mm were used. As shown in Fig. 3, measurement gauges were installed in three beams, each with one gauge at its midspan and two at its edges, for a total of nine gauges. The bridge's actual deflection was lower than

predicted by the analytical model, indicating that the longitudinal girders are stiffer than initially anticipated. The founding of the measurements can be seen in table 1 below. Consequently, a revised recalibrated model was established, taking into account the stiffer beams. This resulted in a slightly higher bending moment per girder, meaning the transverse distribution between the girders was reduced from the previous model. Even with the slightly higher values, re-examining the calculation gave a satisfying result within the design codes limits, only with a higher amount of certainty.

Table 1. Theoretical and actual deflection table (mm)

Tested beam	Test point	Theoretical deflection (mm)	Actual deflection (mm)	Deviation (%)	Average Deviation (%)
Beam 3	MP-1	2.538	2.42	4.9	9.1
	MP-2	3.017	2.62	15.2	
	MP-3	2.155	2.01	7.2	
Beam 4	MP-4	2.446	2.07	18.2	18.5
	MP-5	2.922	2.38	22.8	
	MP-6	2.096	1.83	14.5	
Beam 5	MP-7	1.469	1.1	33.5	38.0
	MP-8	1.766	1.35	30.8	
	MP-9	1.211	0.81	49.5	

4.2 Additional measurements during and after the crossing of the cargo

Verifying that the bridge would stay intact after the crossing of the cargo, additional measures were taken. With the help of experts specialized in dynamic measuring equipment, the following was carried out:

- Data of the natural frequencies before the crossing of the cargo.
- Deflection during the cargo crossing as a function of the time.
- Data of the natural frequencies after the crossing of the cargo.

The deflection of the beams as a function of the cargo time traveling can be shown in Fig 4. Consistently, beam 3 gets a higher deflection than beam 4; this difference can also be seen in the live load test. Comparing to deflections to theoretical calibrated model, the actual deflections are in fact lower, assuring the bridge state is on the safe side. Overall, changes in the natural frequency were documented to be minor.

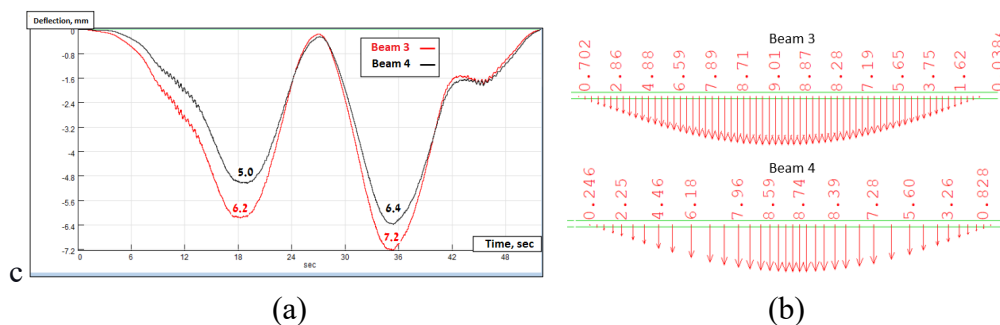


Fig. 4. (a) Beam 3 and 4 deflections (mm) as a function of time (sec) of the southern span of the bridge. (b) Maximum deflection from the FEM model (mm)



5. Conclusions

Running a probability-based analysis, the parameters involved in defining a limit state have an uncertainty factor taken into account; these factors vary depending on the age and current state of each particular bridge. Accordingly, transporting heavy-load cargo on bridges should be cautiously approached, mainly when dealing with older bridges. Conducting a live load test on the bridge can provide a more precise estimate of its stiffness, enabling a more accurate distribution of bending moments among its components. Adjusting the FEM model based on the stiffness distribution between the longitudinal girders allows a more precise prediction of the bridge's behavior under various loads. Ultimately, this will aid in guaranteeing the bridge's safety and longevity.

6. References

BS 5400 part 2 – specification for loads, 1978.

Dr. M. Mogilevski – Sorek bridge dynamic report, 2022.

System labs LTD – Sorek bridge live load test results report, 2022.

O'Connor, C., 2000. Bridge loads: An international perspective. CRC Press.

Israeli standard 1227 part 1 – loads on bridges: highway bridges, 1988.

Scholten, C., Enevoldsen, I., Arnbjerg-Nielsen, T., Randrup-Thompsen, S., Sloth, M., Englund, S. and Faber, M., 2004. Reliability-Based Classification of the Load Carrying Capacity of Existing Bridges-Guideline Document (Report 291).

BSI, U., 2008. National annex to eurocode 1: Actions on structures–part 2: Traffic loads on bridges, NA to BS EN 1991-2: 2003. British Standards Institution.



Development of Pre-Tension Method for On-Site Production of Prestressed Concrete Girders with Span Length between 20 m to 50 m

Dong-Woo Seo^{1*}, Sangki Park², Ki-Tae Park³, Hyun-Ock Jang⁴, and Yeon-Woo Shin⁵

¹: Korea Institute of Civil Engineering and Building Technology, Goyang, South Korea; email: dwseo@kict.re.kr

²: Korea Institute of Civil Engineering and Building Technology, Goyang, South Korea; email: skpark@kict.kre.kr

³: Korea Institute of Civil Engineering and Building Technology, Goyang, South Korea; email: ktpark@kict.kre.kr

⁴: JEnC, Suwon, South Korea; email: hojang@jenc.kr

⁵: Taesung ENC, Sejong, South Korea; email: yw817@taesungenc.kr

*: corresponding author

Keywords: Prestressed concrete girder; pre-tension; U-shaped; on-site production

Abstract: In Korea, the development of U-shaped prestressed girders is being attempted to increase the length of I-type girders. However, since the dead weight due to the post-tension method is large, a length of 30 m or less is common. In this study, the pre-tension method was applied without limiting the post-tension method to induce a decrease in self-weight and materials used due to a decrease in cross-sectional area. In addition, the author proposed the application of the in-situ pretension method using the internal reaction arm of the U-shaped girder. The prestressed concrete U-shaped girder bridge is composed of a concrete deck slab and a composite section. Compared to prestressed concrete I-type girders, structural performance characteristics such as resistance and stiffness are improved. Construction safety is also improved during the fabrication and installation phases, and elongation is reduced due to girder weight reduction. Therefore, it is possible to secure the aesthetics and economic feasibility of the bridge. Accordingly, it is expected that efficient construction will be possible with high-quality factory-manufactured and cast-in-place members. In this study, the pretension method was introduced to the field and the analytical performance of the anchoring block used for tension was verified.

1. Introduction

Among the superstructure types, prestressed concrete I-type girders have gradually increased their share due to improvements in design and construction methods over the past decade. As such, the rigid frame superstructure type and the prestressed I-type girder used in road bridges form a very large market and a lot of related technologies are being developed.

The advantage of rigid frame bridges is that they do not require repairs, such as no separate movement or bridge support. However, its application in long-span bridges is limited. In addition, prestressed concrete I-type girders have been introduced in Korea not long ago, so they have complex structures, ambiguous design standards, difficulty in construction (overturning due to

cross-sectional shape), and low economic feasibility. Feasibility due to increased material costs (Koo et al. 2005; Kim and Yang, 2008; Bae et al. 2017; Park et al. 2022).

Guo et al. A fully composite beam composed of U-shaped steel girders and angle connectors was introduced. They experimentally evaluated the beam and showed that it improved the bending behavior (Guo and Liu, 2018). Svoboda et al. reinforcing and repairing a U-shaped reinforced concrete bridge using post-tensioning with cable ducts. They concluded that post-tensioning with cable ducts is a very efficient way to reinforce existing bridges to increase their load-bearing capacity (Svoboda et al. 2019). Jang et al. It is mentioned that the adaptability of U-shaped girders is widely recognized due to the difference between U-shaped girders and conventional section girders (Zhang et al. 2019).

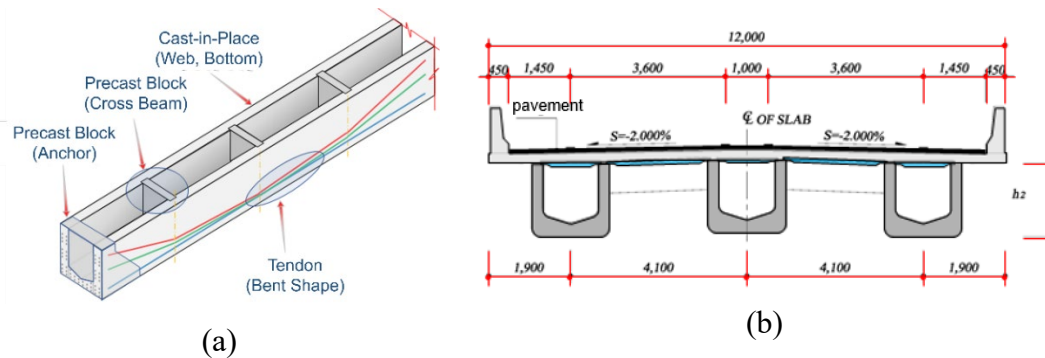


Fig. 1. Configuration and conceptual diagram of the pre-tensioned U-type girder for the (a) unit girder (precast and cast-in-place) manufacturing method and (b) closed bridge section

The PSC U-shaped cross-section girder bridge is composed of a concrete slab and a composite section. It is a very efficient and economical bridge that increases safety at the construction stage, lowers the height ratio by reducing dead weight, and secures the aesthetics of the bridge. It can also improve the construction quality and efficiency of high-quality factory-made members and in-situ integral castings. Fig. 2 shows (a) the process of applying tension using an anchoring block for tension and an internal reaction bar, and (b) the process of manufacturing a U-girder by pouring and curing concrete under tension.

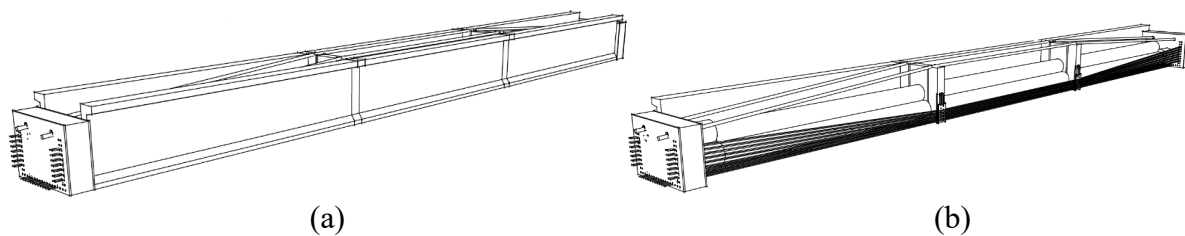


Fig. 2. Pre-tension method using an internal reaction arm and anchor block for (a) Anchor block-hydraulic cylinder-internal reaction arm (b) Concrete pouring and curing

2. Pre-Tensioning Method

As shown in Fig. 3, in order to fix the tension between the lower slab of the U-shaped girder and the outer wire, a tension fixing block is placed on both ends of the girder, and the outer wire

coming down from the inner deviator block pressurizes the hydraulic cylinder. It serves to tighten the strands without deformation by external force.

Figure 3 shows a schematic diagram of the force-reaction concept of an anchor block using a hydraulic cylinder and multiple stranded wires. Although this anchor block was analyzed and designed as a compression member, it can show bending behavior if the thickness is thin, and therefore it can be said that it is highly dependent on the strength of concrete and the thickness of steel plate.

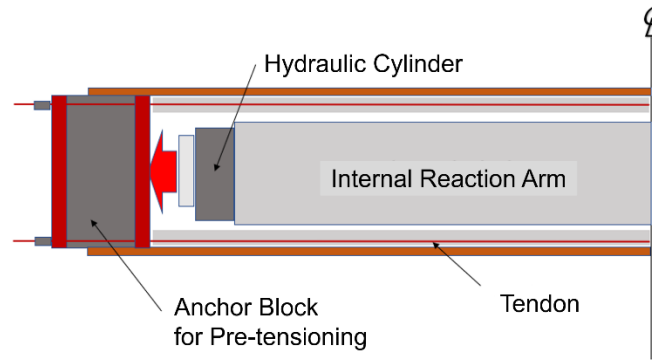


Fig. 3. Force transmission mechanism between internal reaction arm-hydraulic cylinder and strand anchorage

Figure 4 is an internal reaction arm (middle part of Fig. 4) using three PHC (Pre-stressed High-strength Concrete) piles in which hydraulic cylinders are arranged, a cross section of a pre-tension U-shaped girder, and introducing an external twisted wire and pre-tension. Anchoring blocks for tension are placed in rectangular positions. As long as the width of the girder does not change, this anchor block is designed to be applied to all heights and may be slightly changed depending on the cutting method of the strand in the future.

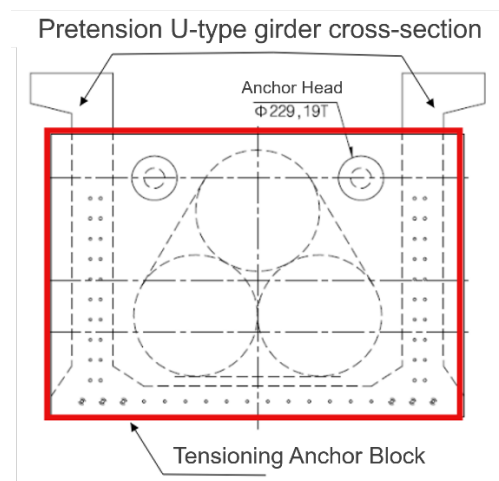


Fig. 4. Cross section of pre-tension U-type girder and anchorage block for tension

3. Consideration for Anchor Block for Pre-Tensioning

It must resist the tension of the outer strands for equilibrium of the inner reaction arm along with the rigid composite anchor block for tension. Therefore, it is necessary to review the following items before applying tensile force. Anchor blocks that can be moved and transported: A pair

must be able to move together as a set, the width and weight are limited for road movement, and the crane capacity is easy to install on site.

It is expected that the application of UHPC as a fixing device for compression members will greatly depend on the compressive strength of concrete by appropriately using it in consideration of usability such as weight and volume of ultra high strength concrete (UHPC). In the case of UHPC using steel fiber, it is judged that the tensile strength of about 10 MPa is a spherical shape and will be of great help to the tensile and shear resistance of the anchor block.



Fig. 5. Arrangement of internal reaction arm (PHC piles) and an anchoring block

A pretension method using a hydraulic cylinder that can be manufactured on site and is easy to move for repeated production and a concrete pile used as an internal reaction force is proposed as shown in Fig. 5. A performance verification experiment of a full-size girder ($L=40\text{m}$, $h=800\text{mm}$) is scheduled to be conducted in the near future.

4. Acknowledgments

This study was supported by the Ministry of Science and ICT (MSIT) grant by the Korea Institute of Civil Engineering and Building Technology (KICT). (Project Number: KICT-20230107).

5. References

Koo, M.-S., Kim, H.-H., Jung, Y.-D. 2005. A study of continuous PSC bridge with a reinforcement steel plate, In Proceedings of the Computational Structural Engineering Institute of Korea Annual Conference (Spring), 422–429.

Kim, K.-S., Yang, I.-H. 2008. PSC development of new type PSC beam girder bridges in Korea. Magazine of the Korea Concrete Institute, 20, 26–33.

Bae, K.-M., Min, K.-H., Lee, C.-O., Lim, N.-H. 2017. Analysis and improvement of long-term deflection of PSC I girder for railway bridges. Journal of Korean Society of Hazard Mitigation, 17, 9–15.

Park, S., Kim, J., Jung, K.-S., Seo, D.-W., Park, K.-T., Jang, H.-O. 2022. On-site construction method for U-girder with pre-tension and verification of analytical performance of anchoring block. Journal of Korea Society of Disaster & Security, 15(3), 67-77.



Guo, L., Liu, Y., Qu, B. 2018. Fully composite beams with U-shaped steel girders: Full-scale tests, computer simulations, and simplified analysis models. *Engineering Structures*, 177, 724–738.

Svoboda, A., Klusáček, L., Olšák, M. 2019. Strengthening and rehabilitation of U-shaped RC bridges using substitute cable ducts. *Advances in Materials Science and Engineer*, 1-21

Zhang, J., Jing, Y., Li, P., Han, W., Zhang, N., Zhou, Y. 2019. Experimental and numerical investigation on the ultimate vertical bearing capacity of U-shaped girder with damaged web. *Sensors*, 19, 3735.



Bridge Engineering Institute Conference 2023 (BEI-2023)
Rome, Italy, July 17-20, 2023



Environmental Effects



Temperature-Induced Variation in Geometric Characteristics of Existing Cracks in Double-Box Girders of Concrete Cable-Stayed Bridge

Xujia Liu^{1,2}, Youliang Ding^{1,2*}, Hanwei Zhao^{1,2}, Chunfeng Wan^{1,2}, and Fangfang Geng³

¹: Key Laboratory of Concrete and Pre-stressed Concrete Structures of the Ministry of Education, Southeast University, Nanjing 210096, China

²: College of Civil Engineering, Southeast University, Nanjing 210096, China

³: School of Architecture Engineering, Nanjing Institute of Technology, Nanjing 211167, China

*: Corresponding author

Keywords: crack propagation, service life, concrete cable-stayed bridge, temperature field

Abstract: The crack propagation of concrete cable-stayed bridge' main girder directly affects the service life of the bridge. To explore the influence of the temperature field on the existing crack width of the double-box main girder, a long-span concrete cable-stayed bridge is taken as an example. The temperature field and crack width of the main girder of concrete cable-stayed bridge are monitored. The analysis of the measured data shows that the variation of the inner surface temperature of the box in winter, spring and summer is approximately a cosine curve trend, and the maximum and minimum temperature in the main beam box are 35 °C and 0 °C in summer and winter respectively. The cracks in the inner wall of the box section of the main beam have obvious closing and opening phenomena with the change of temperature, and difference between maximum and minimum width approximately 0.9 mm, and the crack opening and closing trend shows a sinusoidal curve with the season, which is opposite to the temperature change trend, and the temperature-crack width shows a monotone decreasing linear correlation. It is difficult to repair cracks in the main girder due to the phenomenon of crack closure and opening, and the effect of conventional repair methods is not ideal, which is very consistent with the phenomenon of cracking again after crack repair.

1. Introduction

Due to the material characteristics of concrete, initial cracks will inevitably occur in concrete cable-stayed bridges during construction. After the concrete cable-stayed bridge enters the operation period, the crack width further increases due to the adverse factors such as vehicle and temperature. After the crack reaches a certain width, the harmful substances will go deep into the concrete, which will further lead to steel bar corrosion, concrete carbonization and other phenomena, at the same time, the crack may further expand. The sunshine temperature effect is an important factor in the process of crack formation and expansion. Therefore, in view of the existing cracks in concrete cable-stayed bridges, it is very necessary to study their temperature



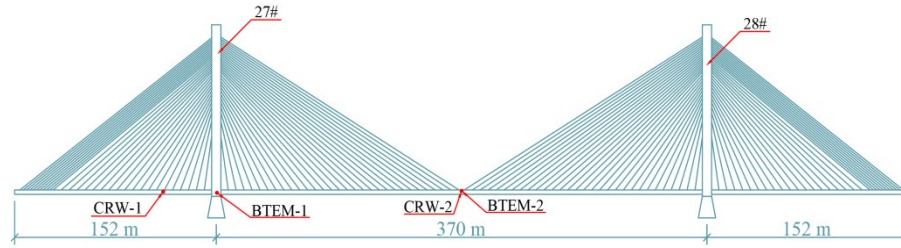
variation characteristics.

In order to study the temperature variation characteristics of existing cracks in concrete cable-stayed bridges, we should focus on the analysis of the temperature field characteristics of the bridge. On-site monitoring is an effective way to study the thermal field characteristics of the bridge. Many researchers have studied the temperature field of the bridge. For example, in early 1983, the temperature distribution of the composite box girder bridge was studied according to the monitoring data of the Maskova River Bridge (Dilger et al., 1983). It is concluded that the temperature difference is affected by geometric characteristics, material types and environmental factors. In order to study the temperature field distribution characteristics of long-span flat steel box girder suspension bridge, the statistical characteristics of temperature field and predicted the extreme temperature difference by using the long-term field measurement data of Runyang suspension Bridge in China was analyzed (Ding et al., 2012). Taking Incheon Bridge in South Korea as an example, the distribution law of temperature field of steel box girder of cable-stayed bridge by numerical method was analyzed (KIM et al., 2015).

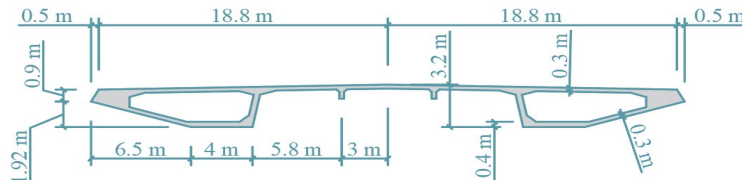
In order to further analyze the temperature variation and distribution characteristics of the bridge, as well as the temperature variation characteristics of the existing cracks. This paper takes a concrete cable-stayed bridge in China as the research background, based on the monitoring system of concrete cable-stayed bridge. The long-term temperature monitoring data and crack width time-varying data are obtained, the correlation characteristics between bridge temperature and crack width are analyzed, and the temperature-crack width fitting curve of concrete cable-stayed bridge is established. so as to provide a basis for bridge health and safety design, management and maintenance.

2. Example

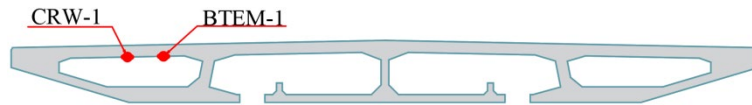
The bridge has a total length of 2062 m, a span of 152 m + 370 m + 152 m, a total width of 38.6 m and six lanes in both directions, as shown in Fig. 1 (a). Construction of the bridge began in March 2003, closed in August 2005, and was completed and opened to traffic at the end of 2005. The main girder is prestressed concrete box girder. The standard section of the main beam adopts a double-side box section, with a height of 3.2 m, a roof thickness of 0.3 m, a bottom plate thickness of 0.4 m, an edge oblique web thickness of 0.3 m and a middle web thickness of 0.4 m, as shown in Fig. 1 (b). The non-standard cross section of the main beam (cable tower position main beam section, side span cable dense area main beam section, side span closure section main beam section) adopts single box and four chamber section. Longitudinal and horizontal limiting devices are arranged at the junction of the tower and beam. The bridge cloth is equipped with temperature sensor and crack sensor, and the data acquisition frequency is 1/300 Hz. The specific location of the sensor is shown in Fig. 1 (a), (b), (c) and (d). (BTEM/ temperature sensor, CRW/ crack sensor)



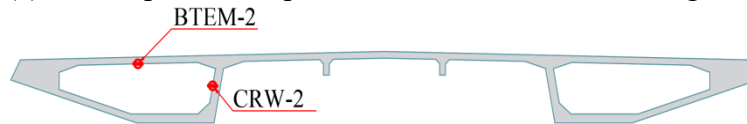
(a) Bridge elevation



(b) Cross section



(c) Sensor placement point at the location of the 27# girder



(d) Sensor placement point in the middle of the span

Fig. 1. Bridge structure and layout of measuring points

3. Analysis

As can be seen from Fig. 2 (a), from November 25, 2021 to July 22, 2022, the lowest and maximum temperature inside the main beam of the 27# bridge tower is 3.3 °C and 34 °C, the temperature difference between winter and summer is 30.7 °C, the minimum and maximum temperature in the middle of the span is 0.4 °C and 39.3 °C, and the temperature difference between winter and summer is 38.9 °C. As can be seen from Fig. 2 (b), from November 25, 2021 to July 22, 2022, the minimum and maximum values of roof crack width inside the main girder of No. 27 bridge tower are -0.735 mm and 0.278 mm, and the difference is 1.013 mm. The minimum and maximum values of web crack width in the middle of span are -0.428 mm and 0.278 mm, and the difference is 0.706 mm. Compared with Fig. 2 (a) and (b), the temperature and crack width show reverse change, that is, from November 25, 2021 to February 17, 2022, the temperature is lower and the crack opening is more obvious, while from June 9, 2022 to July 22, 2022, the temperature is higher and the crack shows a closing trend.

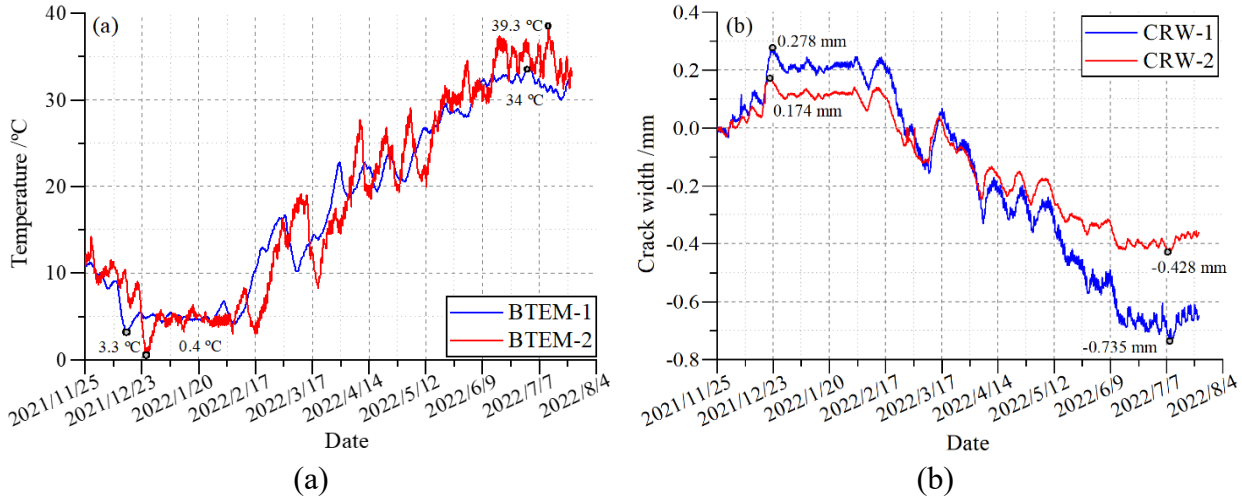


Fig. 2. Long-term monitoring data of temperature and crack width: (a) BTEM, (b) CRW

Fig. 3 shows the correlation between temperature and crack width (the monitoring data of temperature and crack width are averaged with 2 hours as the section). From Fig. 3 (a) and (b), it can be seen that the crack width decreases linearly with the increase of temperature. Through the means of data fitting, it can be seen that the crack opening is especially obvious when the internal temperature of the 27# main beam is close to 0 °C, and shows the same characteristics in the middle of the span. According to the fitting curve of Fig. 3 (a) and (b), the temperature change of the main beam in winter and summer is obvious, but the opening and closing of the roof crack in the 27# main beam is obvious, and the opening and closing of the roof crack is more sensitive than that in the web.

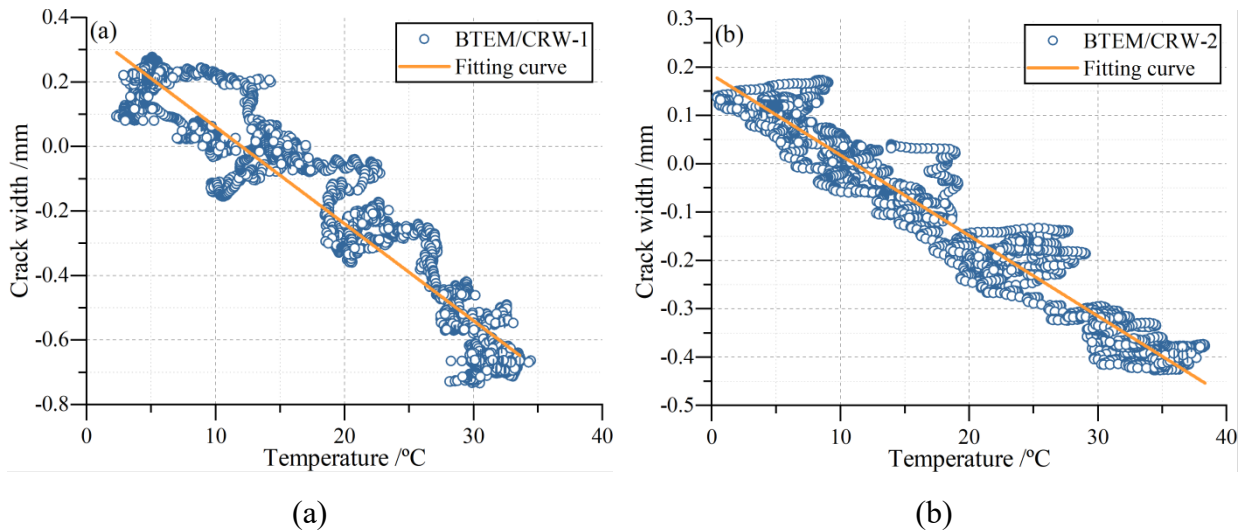


Fig. 3. Temperature-crack width correlation: (a) BTEM/CRW-1, (b) BTEM/CRW-2



4. Conclusion

The temperature field of concrete cable-stayed bridge is obviously related to the opening and closing degree of cracks, showing a linear decreasing trend as a whole, that is, the higher the temperature is, the smaller the crack width is. When the internal temperature of the bridge is low, the internal cracks of the bridge are in the trend of opening and expanding. At the same time, the variation trend of roof cracks in the box section of the bridge with temperature is more obvious than that of the web.

5. References

Dilger, W., Ghali, A., Chan, M., Cheung, M., and Maes, M.. 1983. Temperature stresses in composite box girder bridges, *Journal of Structural Engineering*, ASCE, 109(6), 1460-1478.

Ding, Y. L., Zhou, G. D., Li, A. Q., and Wang, G. X.. 2012. Thermal field characteristic analysis of steel box girder based on long-term measurement data, *International Journal of Steel Structures*, 12(2), 219-232.

Kim S. H., Park S. J., Wu J. X.. 2015. Temperature variation in steel box girders of cable-stayed bridge during construction, *Journal of Constructional Steel Research*, 122, 80-92.

Utilizing Pressurized Injection of Lithium Nitrite in Treating Alkali-Silica Reaction and Salt Damage in Concrete Structures

Shohei Notsu^{1*}, Tatsuya Kitada², Son Van Nguyen³, and Kazunori Era⁴

¹: Kyokuto Kowa Corporation, Hiroshima, Japan; email: notsu@kkn.co.jp

²: Kyokuto Kowa Corporation, Hiroshima, Japan; email: t-kitada@kkn.co.jp

³: Kyokuto Kowa Corporation, Hiroshima, Japan; email: n-son@kkn.co.jp

⁴: Kyokuto Kowa Corporation, Hiroshima, Japan; email: era@kkn.co.jp

*: corresponding author

Keywords: Alkali-silica reaction (ASR); Chloride contamination; Pressurized injection; Repair

Abstract: In recent years, a technique using nitrite ions has attracted attention as a means of repairing concrete that has been deteriorated due to salt damage. This paper verifies the applicability of the pressurized lithium nitrite injection method to salt damage, which was introduced as an Alkali-Silica Reaction (ASR) repair technology by (Kitada & Era 2019). Additionally, an example of application of this method to a bridge pier that has been deteriorated due to both ASR and salt damage is presented and the results are discussed.

1. Introduction

Concrete is a porous material that absorbs the salt used for de-icing the snow during winter season and airborne sea salt, which causes damage and deteriorates concrete. To repair the concrete that has been deteriorated due to salt damage, crack injection or surface protection is often used to block the chloride ions intrusion from the outside. However, even if the chloride ions intrusion from the outside is prevented, the corrosion will still continue to progress if the passive film of the rebar has already been damaged. Since the corrosion environment cannot be improved internally, re-deterioration continues to occur. Therefore, recently, attention is given to a repair technique that focuses on the regeneration of passive film on reinforcing bars by using nitrite ions (Era et al. 2010).

To apply the pressurized lithium nitrite injection method, a small hole is drilled in the affected concrete member, and lithium nitrite is injected into the concrete with a high pressure. (Kitada & Era, 2019) have explained this method in details.

A schematic diagram of this method is illustrated in Fig. 1.

Lithium nitrite used in the pressurized lithium nitrite injection method is a repair material consisting of nitrite and lithium ions. (Kitada & Era, 2019) focused on the effect of nitrite ions on suppressing the expansion of reactive aggregates, and introduced the pressurized lithium nitrite injection method as a repair technology for concrete deteriorated by Alkali-Silica Reactions (ASR).

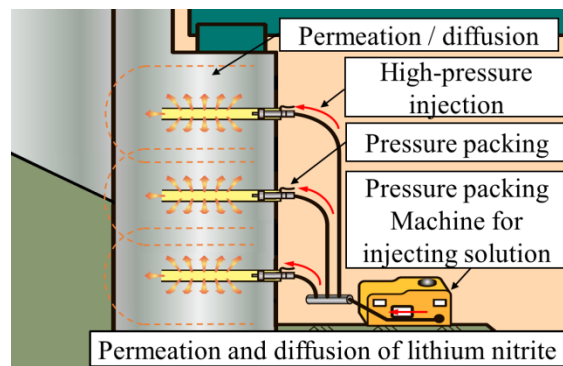


Fig. 1. Schematic diagram of the method

Additionally, nitrite ions have the effect of regenerating the passive film and improving the corrosion environment of the rebars. Thus, they can be suitable repair material to be used in repairing salt damage. This paper verifies the effect of applying pressurized lithium nitrite injection method to salt damage, as well as presenting example of applying this method to a bridge pier that has been deteriorated due to both ASR and salt damage.

2. Verification of Pressurized Lithium Nitrite Injection Method on Salt Damage

2.1 Experiment outline

In order to verify the anticorrosive property of pressurized lithium nitrite injection method on rebars, (Kojima et al 2020) created a specimen simulating reinforced concrete deteriorated by salt damage and conducted a laboratory experiment.

Two specimens (150 x 150 x 150 mm, lithium nitrite injected and 100 x 100 x 150 mm, with no lithium nitrite) were constructed using ordinary Portland cement, with a water cement ratio of 55%. Three round rebars with a dimension of $\phi 10 \times 130 \text{ mm}$ were placed with a 40 mm concrete cover in each specimen. In addition, in order to simulate deterioration due to salt damage, $\text{Cl}^-: 5.0 \text{ kg/m}^3$ was mixed in the concrete in advance. The embedded rebars were non-corroded rebars G0 and corroded rebars with different degrees of corrosion (G1 and G2) as shown in Fig. 2.

The specimens were air cured for 28 days, and on 67th day, an 80 mm hole was drilled in the center of the specimen as shown in Fig. 3. Lithium nitrite was injected with pressure ranging from 0.3 to 0.5 MPa. The injection was continued until the $\text{NO}_2^-/\text{Cl}^-$ molar ratio in the concrete reached 1.0 for the premixed Cl^- amount of 5.0 kg/m^3 . The injection was done for a maximum of 7 days. Hereinafter, the injected specimen will be referred to as M1 and the specimen which was not injected with lithium nitrite will be referred to as M0.

After injection was completed, the specimens were placed in a wet environment with a temperature of 20°C and a humidity rate of 90% for 190 days, during which the self-potential was measured. After that, the surface concrete of the specimen was cut with a concrete cutter to reduce the concrete cover of the specimen to 20 mm and the specimens were continuously exposed to an environment which simulated a salt-damaged environment while self-potential and Polarization resistance was being measured periodically. 340 days from the start of salt water penetration, a dismantling test was conducted to confirm the corrosion status of rebars, and to measure the corrosion weight, corrosion area ratio, and nitrite and chloride ion amounts. Next, the results of self-potential and polarization resistance are presented.

2.2 Results and discussion

Fig. 4. shows the time period of spontaneous potential for M0 and M1 specimens. The self-potential of the M0 specimen without pressurized lithium nitrite reduced immediately after it was left in a wet environment, and corrosion progressed early. On the other hand, the self-potential of the M1 specimen which was injected with lithium nitrite was maintained during the wet



Fig. 2. Rebar inside specimen

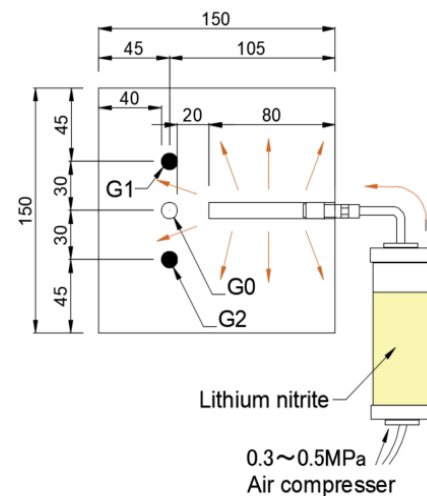


Fig. 3. Experiment summary

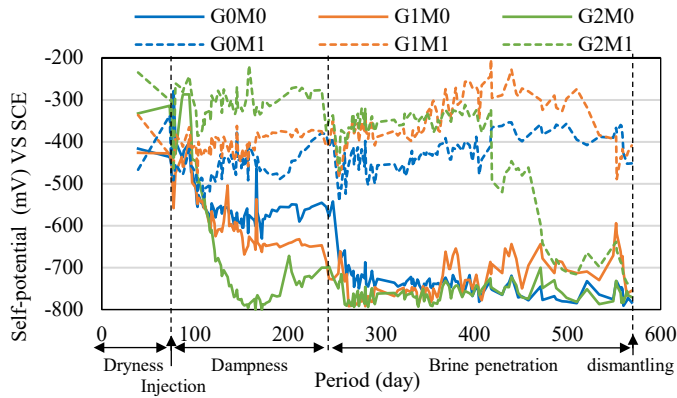


Fig. 4. Change overtime of self-potential

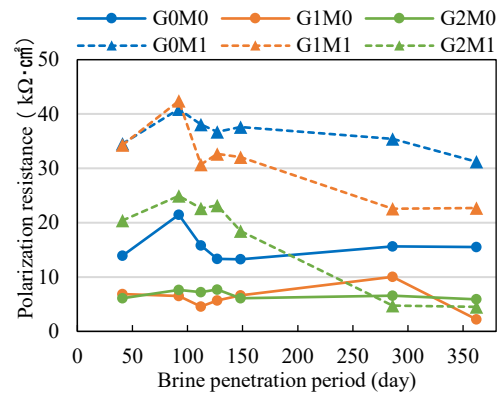


Fig. 5. Change in polarization resistance

environment period. However, the potential of the specimen with G2 rebar showed a reduction during the period of salt water infiltration. The self-potential at the time of dismantling was about the same as the specimen without injection, suggesting that corrosion had progressed. This is probably because the $\text{NO}_2^-/\text{Cl}^-$ molar ratio decreased with the penetration of Cl^- . Therefore, in an environment where there is a chance of new Cl^- penetration, a better practice is assumed to be using the pressurized lithium nitrite injection together with a surface protector material.

Fig. 5 shows the change in polarization resistance of G0, G1 and G2 rebars over a period of 350 days. G0 and G1 rebars always showed higher values in M1 than in M0. However, there was a tendency for a gradual decrease during the measurement period.

On the other hand, the strength of G2 reinforcing bars was higher than that of M0 until about 150 days in M1, but decreased with the number of days immersed in salt water, until it had the same value as M0 after about 280 days of measurement.

As mentioned above, the long-term rust prevention effect of this method was confirmed from the self-potential and polarization resistance results. However, it has been suggested that the $\text{NO}_2^-/\text{Cl}^-$ molar ratio in the concrete may decrease due to the penetration of Cl^- after the injection, especially when the corrosion of the rebar has progressed to the level of G2 rebar before the injection, and the corrosion prevention effect may be impaired. Therefore, if the reinforcement corrosion is severe, it is considered necessary to suppress the intrusion of Cl^- by combining surface protection work together with pressurized lithium nitrite injection method.

3. Example of Practical Application to Actual Structures

3.1 Outline of T-bridge

To utilize the developed technology, we have applied the pressurized lithium nitrite injection method to a T-bridge pier which has been deteriorated due to both ASR and salt damage, in 2017.



Fig. 6. Appearance of T-bridge



Fig. 7. Deterioration of T-bridge

The T-Bridge is a road bridge that was constructed in 1965 and is located on the Seto Inland Sea side of the Hyogo Prefecture, Japan as shown in Fig. 6. As it can be seen in Fig. 7, the P6 pier has been deteriorated as the rebars are exposed and there are visible map cracks in the surface.

In addition, a high chloride ion concentration of 3.8 kg/m^3 was detected, and according to the results of residual expansion test as per ASTM C1260, it exceeded 0.4% after 28 days of measurement, which is quite beyond the hazardous standard of 0.10%.

Based on the above investigation results, it was determined that the damage to the P6 pier of T-Bridge was due to combination of salt damage caused by salt blown from the sea, and ASR reaction due to alkali expansive aggregate. The pressurized lithium nitrite injection method was adopted as a counter measure.

3.2 Confirmation of effects of the method

To confirm the effects of applying this method, samples were collected from three different locations of the concrete member after the injection, and a residual expansion test was conducted using the JCI-DD2 method (current JCI-S-011 method). The amount of residual expansion in all samples was below the reference value of 0.05%. Therefore, it was determined that the pressurized lithium nitrite normally permeated and diffused into the concrete, and that the supply of lithium nitrite made the alkali silica gel non-swelling. In addition, visual follow-up surveys are being conducted every few years after injection, and it has been confirmed that no re-deterioration has occurred as of 2022, five years after applying the pressurized lithium nitrite injection.

4. Conclusion

- 1) It was confirmed that the pressurized lithium nitrite injection method has a long-term rust prevention effect on reinforced concrete deteriorated by salt damage. However, if Cl^- penetrates the concrete after applying the pressurized lithium nitrite injection method, the $\text{NO}_2^-/\text{Cl}^-$ molar ratio will decrease and the rust prevention effect will be vanished. If rebar corrosion is severe, it is necessary to combine this method with surface protection work to achieve desirable outcome.
- 2) As a result of applying the pressurized lithium nitrite injection method to a bridge pier that have been deteriorated due to both ASR and salt damage, the amount of residual expansion due to ASR was reduced. In addition, even as of 2022, five years after the repair, there were no signs of deformation or further deterioration.

5. References

Era, K, Tokuno, T, Minematsu, S, & Miyagawa, T (2010) "Study on the Long-term Durability of Lithium Ion Pressurized Injection, Proceedings of the concrete structure scenarios", JSMS, Vol10, pp. 167- 172,

Kitada, T, & Era K (2019) "Treatment of Alkali-Silica Reaction in Concrete Structures Using Pressurized Injection of Lithium Nitrite", Bridge Engineering Institute Conference 2019 (BEI-2019), Honolulu, Hawaii, USA, July 22-25, 2019, pp. 36-40,

Kojima, A, Hazehara, H, Okabe, Y, & Era, K (2020) "Evaluation of long-term corrosion protection performance of concrete with different amounts of Li nitrite pressurized into the concrete under saline degradation environment.", Proceedings of the Japan concrete institute, Vol.142, No.1, pp. 1468-1473 (in Japanese),

Fatigue of Steel Anchor Box on Cable-Stayed Bridges Considering Thermal and Vortex-Induced Vibration under Random Traffic Flows

Zhiwen Zhu^{1*}, Shuang Yan², Federico Accornero³, and Yichun Deng⁴

- 1: Shantou University, Shantou China; email: zhuzw@stu.edu.cn
 - 2: Shantou University, Shantou China; email: syan@stu.edu.cn
 - 3: Shantou University, Shantou China; email: federico@stu.edu.cn
 - 4: Hunan University, Changsha China; email: 913241281@qq.com
- *: corresponding author

Keywords: fatigue; steel anchor box; VIV of stayed cable; random traffic; thermal effects

Abstract: In order to evaluate fatigue performance of the steel anchor box with its stay cable presented with large amplitude vibration under in-service condition, continuous monitoring was carried out on a long-span cable-stay bridge to measure the acceleration of the stay cable and stress at details of its steel anchor box (SAB). The characteristics of stay cable vibration, as well as the stress at the SAB details contributed by loadings from vortex-induced vibration (VIV) of stay cable, passing vehicles and thermal action were investigated in time- and frequency domains. Hence the loading mechanism of VIV of stay cable and thermal action on the SAB was investigated. Based on the nominal stress method, the fatigue performance of the SAB under joint action of VIV of the stay cable, truck passage and thermal action were evaluated. It is found that the significant vibration of stay cable, characterized by the high-order multi-mode VIV and dominated by in-plane vibration with peak frequency mode appeared among the fifth to the seventeenth, occurred at the stay cable JB01 under mean wind speed range of 2m/s~9m/s, with observed maximum in-plane peak acceleration of 25m/s². The thermal action contributes significantly to the maximum stress range at the details of the SAB, but it only creates one stress cycle each day. Compared to the thermal action, the stress range generated by the passage of vehicles is low, but trucks produce significant large number of loading cycles; The inertial force produced by the VIV of the stay cable is applied to the SAB, but only produces extremely low stress at those details. Consequently, its effects on stress and fatigue of SAB are completely negligible. It is concluded that the fatigue evaluation of the steel anchor box needs to consider the thermal action. However, even considering the joint action of the VIV loading, thermal effect and truck passages, the fatigue life at the critical details of the SAB, i.e., the deck-side weld end of the upper and lower plate to the outer web, as well as both weld end of the bearing plate to the outer web of steel box girder, is remarkable higher than 100 years. Hence fatigue performance of the SAB under in-service condition satisfies the bridge design requirement.

1. Introduction

The complicated details of the steel anchor box (SAB), and the large and concentrated force acting by the stayed cable, may result in severe stress concentration and high local stress at some details. So far, only few studies on the fatigue performance of the SAB of cable-stayed bridge have been reported (Lin et al, 2012; Wu, 2020; Zhu et al, 2021). For cable-stayed bridges under in-service condition, the repeated passing trucks on the bridge deck will produce fluctuated axial

forces in the stayed cables, which will act on the SAB and will produce repeated fluctuating stress at the details of the SAB. In case of vortex-induced vibration (VIV) of the stayed cable (Liu, 2021), the inertia force of the stayed cable (VIV force) apply to the SAB at the cable end may be large, and the SAB will subject joint action resulting from the VIV force of the cable, truck loading on deck and thermal action on the whole bridge. The joint of the three actions may produce a high stress range in the welding details of the SAB, which may present fatigue issue at main girder connection with the stayed cables.

2. Test Setup

The propeller anemometer is installed at the centre of the main span at height of 5m above bridge deck, and a bidirectional accelerometer is fixed on the cable JB01 at the height of 6.22m. The strain gauges were mainly applied at those locations with severe stress concentration on the outer web. All sensors are connected to the data-acquisition system and then data are sent into the monitoring system. Figure 2 shows the arrangement of strain gauges applied at the fatigue-prone detail of the SAB.

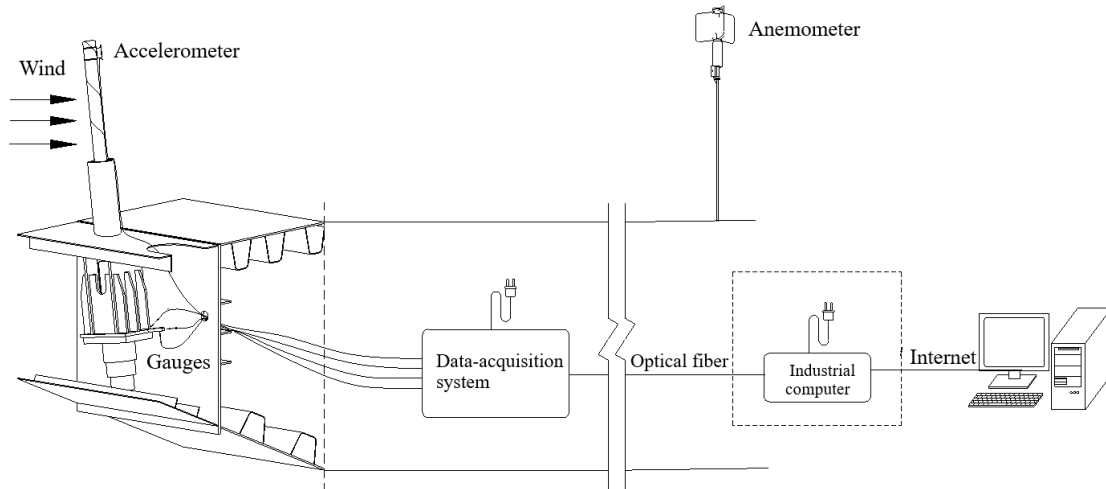


Fig. 1. Monitoring system

3. Vibration Monitoring and Analysis

Figure shows the vibration response of JB01 cable. It is clear that the observed cable vibration is dominated by its in-plane component, and the peak acceleration first rises and then drops with the increase of wind speed. In addition, the participating modes distribute among the 5th to the 17th. It is concluded that the observed cable vibration is the high-order multi-mode VIV.

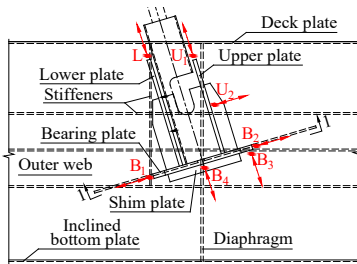


Fig. 2. strain gauge arrangement

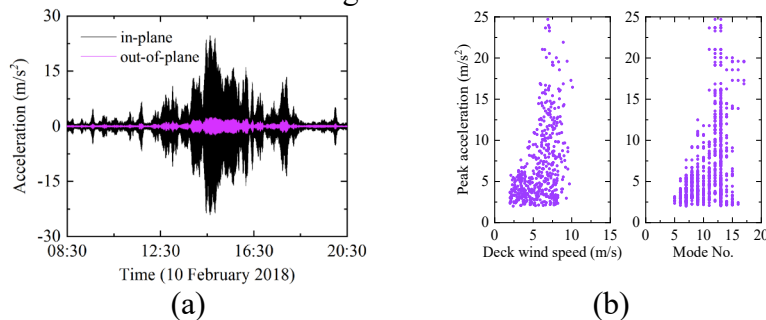


Fig. 3. Vibration response of JB01 cable, (a) time history; (b) peak acceleration

4. Stress Monitoring on SAB

Figure provides typical stress curves at details of the SAB under passage of a same truck. There is only one stress cycle created at those locations. It suggests that the SAB behaviors as the main loading-bearing component in the bridge, which only produce one stress cycle at its fatigue detail under one truck passage.

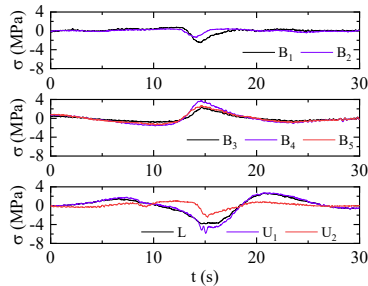


Fig. 4. Typical stress records at details of the SAB under truck passage

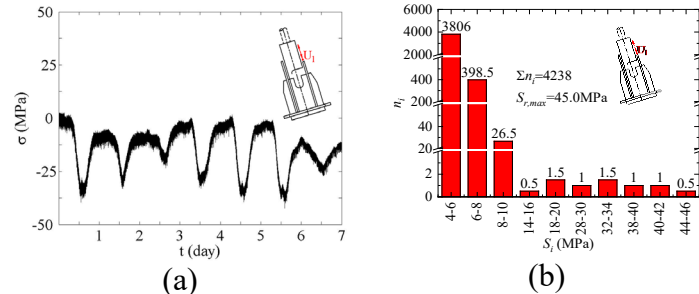


Fig. 5. 7-day measured stress records and stress spectrum at U_1 , (a) stress records; (b) stress spectrum

Figure plots the continuously measured stress and stress spectrum at locations U_1 in seven days. The seven-day stress curves show seven long-period waves, which is characterized by one cycle a day, significantly high stress than truck loading and variable-amplitude stress ranges that highly depends on the weather condition, such as the solar radiation, etc. If the thermal effect is excluded, the maximum stress ranges from the measured stress is only 10.7MPa. In addition, for the stress ranges higher than that in the seven-day measured stress spectrum shown in Figure 5, there is only seven cycles. Hence every day the thermal effect created one stress cycle. Check on monitored stress time histories at U_2 , L, B1, B1, B3 and B4 show similar features. This significantly high stress range is resulted from thermal effect on the whole bridge, which results in fluctuating forces in the stayed cable. Compared the maximum stress with and without thermal effect, thermal effect made major contribution to high stress ranges, hence it should be considered in fatigue evaluation of the SAB.

5. Loading Mechanism of VIV Force on SAB

When the bridge was in normal service condition without VIV of the stayed cable, the in-plane acceleration time history of the stayed cable and its counterpart of stress time history at L on the SAB are shown in Figure 6. Two periods of cable acceleration and stress at L are selected, i.e., one from 30s to 60s without truck loading, and another from 75s to 105s with a truck passing the bridge. The normalized spectrums of the two periods show no difference in frequency domain. Hence the truck passage provides little contribution to the cable vibration, and provides minor effect to the normalized spectrum of the stress time history.

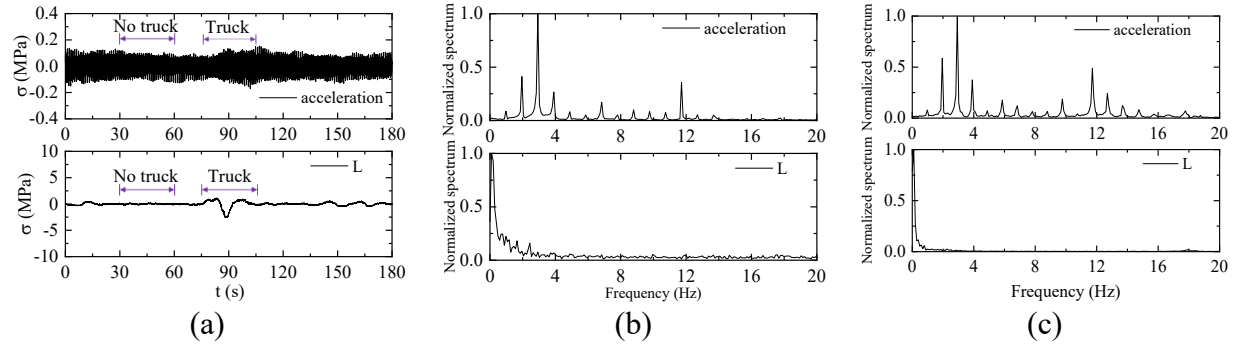


Fig. 6. Time- and frequency-domain plot of acceleration and stress when stayed cable without VIV, (a) time history; (b) frequency-domain plot in 30s to 60s; (c) frequency-domain plot in 75s to 105s

When the bridge was in normal service condition, but the VIV of the stayed cable occurred, the in-plane acceleration of the stayed cable and its counterpart of stress time history at L are shown in Figure 7. The VIV force is applied on the SAB, but its loading effect is quite smaller than that of the truck loading. However, even under the truck loading, the normalized spectrum of stress time history at L clearly indicates the peak frequency, which agrees well with the normalized spectrum of cable acceleration. It confirms that the SAB undergoes joint action of truck loading and VIV force, although the loading effect of the VIV force is significantly lower than the truck.

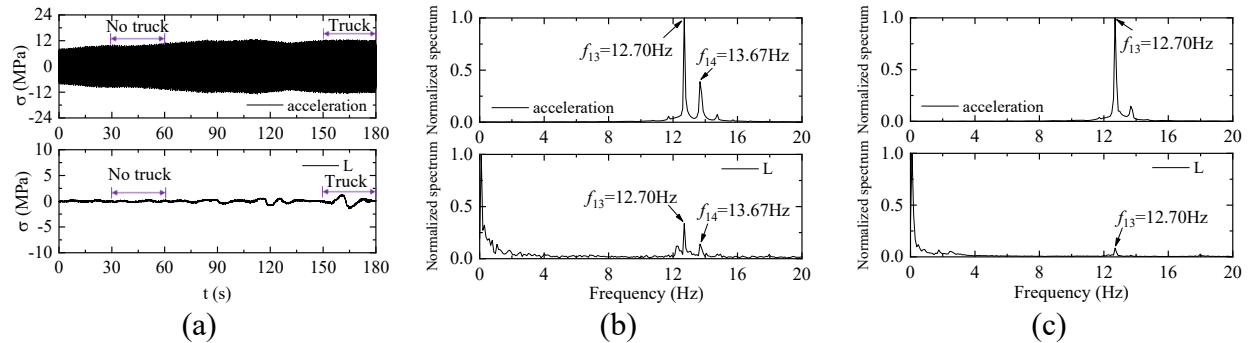


Fig. 7. Time- and frequency-domain plot of acceleration and stress when stayed cable with VIV, (a) time history; (b) frequency-domain plot in 30s to 60s; (c) frequency-domain plot in 150s to 180s

Compared to the thermal action and truck loading applied to the SAB, the VIV force produces extremely low stress at the SAB, and the effect on stress and fatigue is completely negligible.

6. Fatigue Life Estimation of SAB

The SAB is subjected to the variable-amplitude loading by trucks, thermal effect, or joint action of both, so the stress spectrum of the details should be obtained based on the statistical counting of the measured stress using the rain-flow counting method. Then calculated the fatigue life of the details according to Miner's law of linear cumulative damage and the S-N curve in AASHTO LRFD (AASHTO, 2017).

Table 1 shows the fatigue evaluation results at various locations of SAB. The maximum stress ranges at U_1 , L, B_1 and B_2 , are all higher than the CAFL of category E, as a result, finite life is expected at the four locations. The estimated fatigue life is significantly higher than the bridge design life of 100 years. However, the measured maximum stress ranges at U_2 , B_3 , B_4 and B_5 are low. Since their fatigue category is higher than category E, their fatigue life is infinite even considering the thermal effect, hence fatigue will not be a concern at those locations.

Table 1. Fatigue evaluation results at various locations of SAB

NO.	Maximum stress range (MPa)		Fatigue life (year)		CAFL (MPa)
	measured	without thermal effect	measured	without thermal effect	
U_1	45.0	10.7	2740.3	infinite	17.9
U_2	24.5	6.4	infinite	infinite	69.0
L	33.0	7.1	19020.7	infinite	17.9
B_1	47.7	5.3	8190.8	infinite	17.9
B_2	31.5	3.6	50369.2	infinite	17.9
B_3	28.1	7.0	infinite	infinite	69.0
B_4	21.0	6.8	infinite	infinite	69.0
B_5	33.5	5.4	infinite	infinite	69.0

7. Conclusions

Measurement of the cable acceleration and stress at details of the SAB was carried out for the stayed cable JB01 on a long-span cable-stay bridge. The feature of cable vibration was investigated, and the fatigue performance of the SAB under joint action of the VIV force of the stayed cable, truck passage and thermal action was evaluated, which will provide good suggestions for the fatigue research and anti-fatigue design of SAB.

8. Acknowledgements

Financial support for this study was provided by National Natural Science Foundation of China (51878269, 52278509), to which the writers gratefully appreciate.

9. References

- AASHTO (2017). AASHTO LRFD Bridge Design Specifications. 8th Ed., American Association of State Highway and Transportation Officials, Washington D.C.
- Liu, Z.W., Shen, J.S., Chen, Z.Q., et al (2021). Experimental study on aerodynamic control measures for vortex-induced vibration of stay-cable. *Journal of Vibration Engineering*, 34(03) 441-451. (In Chinese)
- Lin, C. H., Lin, K.C., Tsai, K.C., et al. (2012). Full-scale fatigue tests of a cable-to-orthotropic bridge deck connection, *Journal of Constructional Steel Research*, 70(3), 264-272.
- Wu, Q., Zhu, Z.W., Li, J.P. (2020). Fatigue evaluation of connection details on cable anchorage based on field measured stress spectrum. *Journal of Railway Science and Engineering*, 17(11) 2823-2831. (In Chinese)
- Zhu, Z.W., Li, J.P., Cai, J.Y., et al. (2021). Field investigation on fatigue of steel anchor box in



Bridge Engineering Institute Conference 2023 (BEI-2023)
Rome, Italy, July 17-20, 2023



cable-stayed bridge under in-service condition considering vortex-induced cable vibration,
Journal of Vibration Engineering, 34(1), 9-19. (In Chinese)



Mechanism of Control Method for the Alkali-Silica Reaction and Delayed Ettringite Formation Expansion Using Artificial Lightweight Aggregate

Atsushi Teramoto^{1*} and Moka Tanabe²

¹: Hiroshima University, Higashi-Hiroshima, Japan; email: a-teramoto@hiroshima-u.ac.jp

²: Hiroshima University, Higashi-Hiroshima, Japan; email: m221023@hiroshima-u.ac.jp

*: corresponding author

Keywords: ASR; DEF; artificial lightweight aggregate; X-ray CT

Abstract: The alkali–silica reaction (ASR) and delayed ettringite formation (DEF), which are typical expansive deteriorations of concrete structures, can be reduced by mixing artificial lightweight aggregate (ALA) with concrete. In this study, to clarify the mechanism by which ALA reduces ASR and DEF expansion, artificial lightweight fine aggregate (ALFA) and artificial lightweight coarse aggregate (ALCA) were mixed into specimens with accelerated deterioration. Thereafter, length change measurements and X-ray computed tomography (CT) imaging were performed. As a result, the degree of ASR expansion decreased as the proportion of ALA increased, and this effect was particularly significant for ALFA. With respect to the ASR, ALFA replaced 50%, and for DEF, a 100% replacement of the normal fine aggregate almost completely suppressed the expansion. The internal cracking of each specimen was observed by X-ray CT imaging, and the degree of cracking decreased in the specimens with reduced expansion, thus suggesting that the driving force of the expansion was reduced. Furthermore, with respect to the ASR, the amount of dissolved silica and decrease in alkali concentration were measured over time for ALFA and ALCA. It was confirmed that the fine powder content of ALA contributed particularly to alkali adsorption. These results confirm that ALA reacts with the alkali in the concrete and reduces its concentration. Finally, we conducted a numerical simulation to estimate the degree of expansion by uniaxial reactive model using various coefficients determined based on the results of aggregate reactivity tests. The results revealed that the degree of ASR expansion could be estimated by considering the alkali reactivity of ALA. Moreover, the mechanism of DEF reduction could not be numerically explained. As a hypothesis, the reaction of ALA powder with calcium hydroxide in the concrete via the pozzolanic reaction may reduce the potential of pH in the concrete system, thus resulting in the suppression of DEF.

1. Introduction

The expansion degradation of concrete in this paper refers to the alkali–silica reaction (ASR) and delayed ettringite formation (DEF). In particular, the ASR is the most common type of concrete deterioration, with numerous reports at piers worldwide. Both types of degradation are difficult to control upon occurrence. Artificial lightweight aggregate (ALA) has recently attracted attention as an ASR countermeasure. However, the mechanism of ASR reduction by ALA is



qualitatively and quantitatively unclear, and there are no verified cases of the inhibitory effect of ALA on DEF. Therefore, the aim of this study was to clarify the mechanism of ASR reduction by ALA, and to examine the applicability of ALA to DEF, which is a similar type of degradation.

2. Methods and Materials

There are two possible mechanisms by which ALA suppresses ASR: physical and chemical effects. For the physical effects, alkali silica gel (ASG) may be stored in the coarse voids inside the ALA to mitigate and detoxify the water absorption and expansion of ASG, and the ALA crushing may mitigate the expansion pressure of ASR due to its low strength. With respect to chemical effects, it was highlighted that the water contained in the ALA may be released into the pores of the concrete, thereby diluting the alkaline concentration of the pore water, and the ALA may react with the alkali in the concrete, thereby reducing the alkaline concentration. Moreover, there is no information on whether or not ALA reduces the expansion caused by DEF.

Furthermore, there is a lack of information on the aggregate sizes and amounts for which ALA is effective in controlling the respective expansions. Therefore, in this experiment, fine and coarse aggregates of ALA were mixed with the specimens that produced ASR and DEF, respectively.

2.1 Expansion and Mass Measurement

To evaluate the difference in the ASR and DEF reduction effects with respect to different particle sizes and amounts of ALA, a portion of the aggregate in the concrete of the formulation that promotes ASR and DEF was replaced with ALA, and the expansion was measured. The mixture proportions of the specimens are shown in Tables 1 and 2.

For the ASR specimens, the reactive aggregate percentage was fixed (30% in the coarse aggregate), and a portion of the non-reactive aggregate was replaced with ALA. Given that DEF

Table 1. Mixture proportions of ASR specimen

	Unit weight (kg/m ³)						Chemical Additives		
	Water	Cement	Fine Aggregate		Course Aggregate		Plasticizer C × %	AE Agent C × %	
			Non-reactive	ALA	Reactive	Non-reactive			ALA
AS-5	160	320	771	24.2	309	706	1.8	0.1	
AS-10			736	48.4					
AS-20			667	96.8					
AS-50			460	242					
AG-5			805	0		671			22.3
AG-10			635	44.6					
AG-20			565	89.3					
AG-50			353	223					

Table 2. Mixture proportions of ASR specimen

	Unit weight (kg/m ³)					Chemical Additives				
	Water	Cement	Fine Aggregate		Course Aggregate		Plasticizer C × %	AE Agent C × %		
			Non-reactive	ALA	Non-reactive	ALA				
DS-50	160	320	485	254	1059	0	1.8	0.1		
DS-100			123	508						
DG-5			847	0					1022	23.4
DG-10			985	46.9						
DG-20			911	93.8						
DG-50			688	235						
DG-100			318	469						
Control			1059	0						

requires a high temperature in the early stage of aging, the specimens were prepared in a thermostatic chamber at 20 °C for 4 h, and then cured at a high temperature of 90 °C for 12 h.

2.2 Chemical Method and Aggregate Reactivity Test

A chemical method (JIS A 1145) was used to confirm the reactivity of the reactive aggregate and ALA. In particular, 100 g of aggregate was immersed in 400 mL of 1 mol/L NaOH solution, and 10 mL of the solution was periodically drained off to confirm the effect of the aggregate particle size on the reactivity. The alkali concentration reduction (Rc) was measured by neutralization titration, and the silica elution (Sc) was measured by atomic absorption spectrophotometry.

3. Results and Discussion

Figs. 1 and 2 present the results of the expansion ratio. In the ASR shown in Fig. 1, both the coarse and fine ALA exhibited a greater decrease in expansion with an increase in the ALA ratio. Similarly, the DEF results shown in Fig. 2 indicate that ALFA was effective in suppressing expansion due to DEF, and that the replacement of all fine aggregate with ALA suppressed DEF expansion almost completely. Moreover, unlike ASR, ALCA was not effective in suppressing DEF expansion.

In this study, X-ray CT imaging was performed on the ASR and DEF specimens after 52 weeks of acceleration to confirm the internal properties of the concrete. Examples of the results are shown in Fig. 3. The X-ray CT images of the AG series reveal that the entrapped void increased with an increase in the amount of ALA (white box in left Fig.), whereas the porosity of the AS series decreased with an increase in the amount of ALA. Moreover, X-ray CT imaging revealed multiple cracks propagating through the reactive aggregate (red box in right Fig.). However, no cracks penetrated the ALA. Under the conditions employed in this study, the probability of the premature release of expansion pressure due to the crushing of the ALA was considered as low.

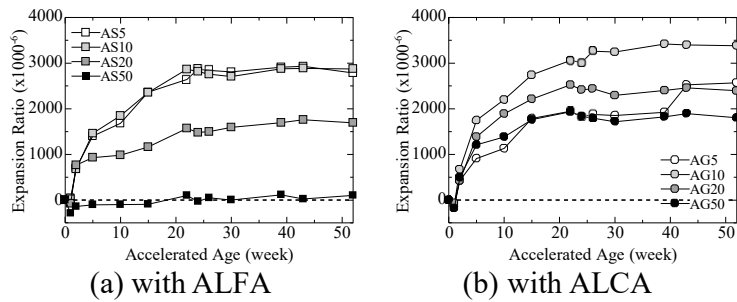


Fig. 1. ASR-induced expansion with ALA

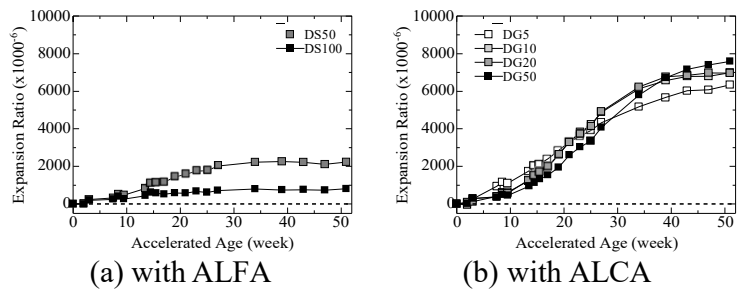


Fig. 2. DEF-induced expansion with ALA

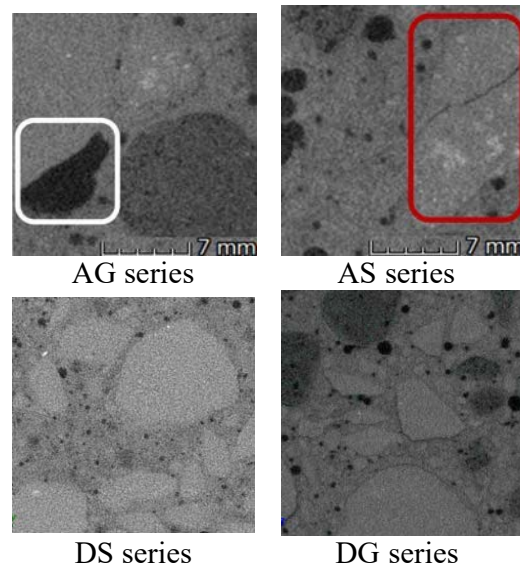


Fig. 3. Results of X-ray CT

As for the DEF specimens, the specimens mixed with ALFA showed almost no cracking at all, whereas the specimens mixed with ALCA showed gaps specific to DEF, not only around the regular aggregate but also around the ALCA.

4. Discussion from Aggregate Reactivity Tests and ASR Expansion Prediction Model

From the results of the aggregate reactivity test, the reactive aggregate and ALA used in this experiment resulted in a very large S_c in comparison with the R_c . Moreover, the alkali consumption of ALA increased with a decrease in the grain size.

In this study, based on the results obtained from the aggregate reactivity test, the ASR expansion was predicted using numerical model proposed by Uomoto et al. A comparison of predicted and experimental ASR expansion at week 52 of the accelerated case is shown in Fig. 4. As can be seen from the figure, the numerical predictions did not reproduce the differences between ALFA and ALCA, although they show a tendency to control the amount of expansion as the ALA replacement rate increases. In particular, it was difficult to reproduce the effect of ALFA on the suppression of ASR expansion. Possible reasons why the analysis fails to reproduce the ALFA trend are as follows. Previous studies confirmed that ALA milled powder undergoes a pozzolanic reaction. On the other hand, aggregate reactivity tests were performed by immersion in NaOH solution, and the calcium required for the pozzolanic reaction was not present. Therefore, the concrete with ALFA underwent a pozzolanic reaction with calcium supplied by the cement, and the increased alkali consumption prevented ASG due to the reactive aggregate, thus resulting in the prevention of ASR expansion. Assuming that a similar reaction is occurring in the DEF specimen, the DEF expansion might be decreased due to a decrease in pH, consumption of Ca(OH)_2 , and an increase in mass transfer resistance in the early stages of material aging via the pozzolanic reaction.

4. Conclusions

In this study, the mechanism by which ALA minimizes ASR and DEF expansion was investigated, and the findings can be summarized as follows:

- 1) When ALA was used to replace a portion of the concrete in the mixture proportion that produced ASR and DEF, both ALCA and ALFA reduced ASR expansion. Moreover, only the specimens with ALFA replacement exhibited decreased DEF.
- 2) The results of the ASR expansion prediction model indicated that the mechanism of ASR reduction by ALA is significantly influenced by the consumption of alkali, and that ALFA underwent a pozzolanic reaction, which resulted in a greater reduction in ASR expansion.
- 3) The DEF reduction effect was observed only for ALFA, thus suggesting that the pH decrease at the early stage of the material aging due to the pozzolanic reaction and the consumption of Ca(OH)_2 had a significant effect on the DEF reduction.

5. Acknowledgments

This work was supported by JST FOREST Program, Grant Number JPMJFR215N

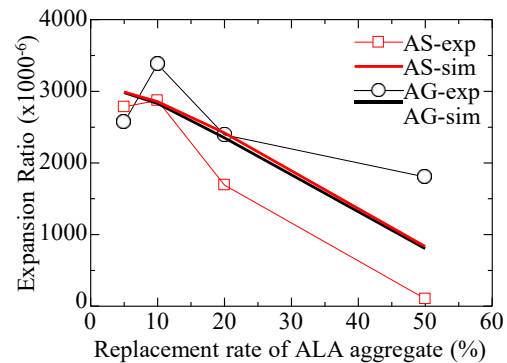


Fig. 4. Comparison of ASR predictions with experimental results.



Bridge Engineering Institute Conference 2023 (BEI-2023)
Rome, Italy, July 17-20, 2023



Repair and FRP Composites



Electromechanical Response of Smart Repair Material with Carbon Black Based on Rapid Setting Cement

Tae Uk Kim¹, Min Kyoung Kim², Lai Thanh Tu³, and Dong Joo Kim^{4,5*}

¹: Department of Civil and Environmental Engineering, Sejong University, 209, Neungdong-ro, Gwangjin-gu, Seoul 05006, Republic of Korea; email: rlaxodnr1117@gmail.com

²: Department of Civil and Environmental Engineering, Sejong University, 209, Neungdong-ro, Gwangjin-gu, Seoul 05006, Republic of Korea; email: mkkim9112@naver.com

³: Department of Civil and Environmental Engineering, Sejong University, 209, Neungdong-ro, Gwangjin-gu, Seoul 05006, Republic of Korea; email: thanhtuxdgt@gmail.com

⁴: Department of Civil and Environmental Engineering, Sejong University, 209, Neungdong-ro, Gwangjin-gu, Seoul 05006, Republic of Korea; email: djkim75@sejong.ac.kr

⁵: Railway Infrastructure Research Center, Sejong University, 209, Neungdong-ro, Gwangjin-gu, Seoul 05006, Republic of Korea.

*: corresponding author

Keywords: Self-sensing concrete, repair material, rapid setting cement, carbon black

Abstract: This research aimed to develop smart repair materials (SRMs) with self-sensing capacity at early age (24 hours) by using rapid setting cement and carbon black (CB). CB was reinforced by 0.5, 1.0, 2.0, and 3.0 wt.% of cement. The electrical resistance of SRMs was measured using the 2-probe method based on alternative current. The self-sensing capacity of SRMs was highest at 0.5 wt.% CB (CB05). The stress sensitivity coefficient (SSC) of CB05 at 24 hours was measured as 0.373 %/MPa; SSC decreased under more than 0.5 wt.% CB owing to the stabilization of conductive network. The electromechanical response of CB05 was further investigated at the age of 3 and 7 hours to investigate the effect of age on the self-sensing capacity of SRMs. The self-sensing capacity of SRMs was also affected by age owing to continued hydration. The SSC of CB05 increased from 0.229 to 0.672 %/MPa (193%) as the age increased from 3 to 7 hours, while it decreased from 0.672 to 0.373 %/MPa (44.5%) as the age further increased to 24 hours.

1. Introduction

Many concrete structures around the world have suddenly collapsed owing to early deterioration of concrete such as the bridge in Genova, Italy in 2018 and the building in Karachi, Pakistan in 2020. One of main reasons for catastrophic failure of concrete structures is concrete crack. Concrete cracks have to be timely repaired and maintained with suitable methods. Currently, epoxy resins (Kan et al. 2021) and cement-based materials (Assaad, 2018) have been used to repair concrete cracks. However, epoxy resin has shown low fire resistance, been poorly cured at low temperature, and generated cracks at the interface owing to different coefficient of thermal expansion with concrete structures. Besides, additional sensors or equipment are required to evaluate the quality of repair by using epoxy resin. Although visual inspection, image processing (Choi et al. 2019), and ultra-sonic wave (Kim et al. 2020) have been developed and applied to

inspect the condition of repaired cracks, the reliability of aforementioned method is still quite low.

This study proposed to develop and apply smart repair materials (SRMs) with self-sensing and rapid setting capacity. The self-sensing capacity of SRMs is expected to evaluate the quality of repaired cracks based on the measured electrical resistance of it in early age (in 24 hours) while the rapid setting property of SRMs is expected to quickly recover the mechanical performance of the deteriorated structures in short time. The SRMs containing carbon black (CB) with small particle size can be applied to concrete cracks with 0.3 mm crack width. This research aims to develop a smart repair material with high self-sensing capacity. Specific objectives are (1) to investigate the effect of CB content on the electromechanical response of SRMs, and (2) to discover the effect of age on the electromechanical response.

2. Materials and Test Setup

Rapid setting cement and CB were used in the composition of SRMs. The average particle size of CB was 120 nm. To investigate the effect of CB content on the strength and self-sensing capacity of SRMs, the content of CB as 0.0, 0.5, 1.0, 2.0, and 3.0 wt.% by cement was added to the test series of P, CB05, CB10, CB20, and CB30, respectively. Water to cement ratio was 0.6. Polycarboxylate based superplasticizer containing 25% solids and 75% water was used to enhance the workability of SRMs.

Figure 1 shows the test setup for the electromechanical response of SRMs. The loading speed and data frequency were 1 mm/min and 60 Hz, respectively. The electrical resistance of SRMs was measured by using alternative current (AC) based SI1260 impedance/gain-phase analyzer machine (Solatron, 1260 A). The electromechanical response of SRMs was investigated at the age of 24 hours and that of CB05 was further investigated at the age of 3 and 7 hours.

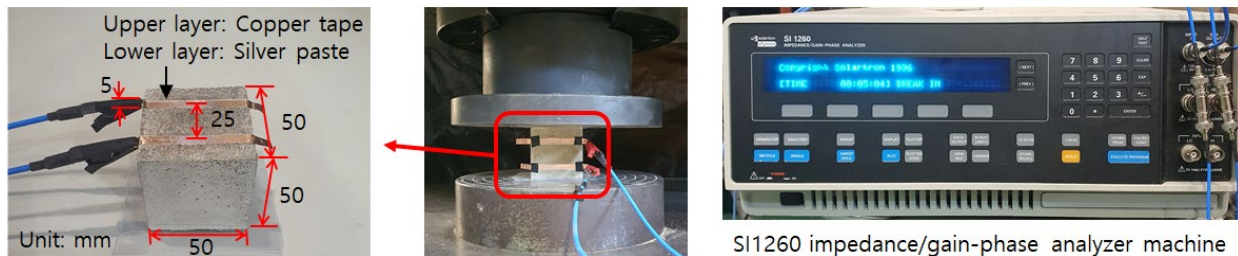


Fig. 1. Test setup for investigation of the electromechanical response of SRMs

3. Test Results

Figure 2 shows the compressive stress versus fractional change in resistivity (FCR) curves of SRMs corresponding to different ages, while Table 1 lists the electromechanical parameters of SRMs. As shown in Fig. 2, the fractional change in electrical resistivity (FCR) of SRMs generally increased as the compressive stress increased. The electrical resistivity (ρ), FCR and stress sensitivity coefficient (SSC) can be calculated using measured electrical resistance (R) of SRMs as provided in Eqs. (1), (2), and (3). In addition, the value of SSC was different corresponding to the different age of SRM.

$$\rho = R \times A / L \quad (1)$$

$$FCR = (\rho_i - \rho_t) / \rho_i \times 100 (\%) \quad (2)$$

$$SSC (\% / \text{MPa}) = FCR / \sigma \quad (3)$$

where A is the cross-sectional area ($= 2,500 \text{ mm}^2$), L is the distance between the two electrodes (gauge length = 25 mm), ρ_i is the initial electrical resistivity, ρ_t is the electrical resistivity at time t , and σ is the compressive stress.

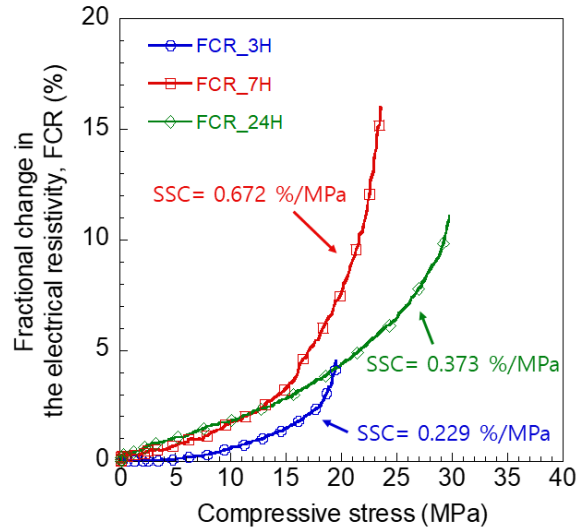


Fig. 2. Electromechanical response of CB05 corresponding to different age

Table 1. Electromechanical parameters of SRMs corresponding to different CB contents and age

Notation		σ (MPa)	ρ_i (k Ω -cm)	ρ_c (k Ω -cm)	$\Delta\rho$ (k Ω -cm)	FCR (%)	SSC (%/MPa)
P	24 h	28.69	22.79	20.46	2.34	10.25	0.354
CB05	3 h	19.55	6.44	6.15	0.29	4.48	0.229
	7 h	23.65	15.16	12.75	2.41	15.89	0.672
	24 h	29.79	23.25	20.67	2.58	11.08	0.373
CB10	24 h	27.55	15.50	14.23	1.27	8.21	0.298
CB20	24 h	25.34	17.20	15.82	1.38	8.02	0.316
CB30	24 h	24.22	7.85	7.59	0.27	3.40	0.140

σ : Compressive strength, ρ_i : Initial electrical resistivity, ρ_c : Electrical resistivity at peak stress, $\Delta\rho$: Change in the electrical resistivity

4. Discussion

4.1 The effect of functional filler on the self-sensing capacity of SRMs

CB05 among the investigated matrices in Table 1 produced the highest SSC (0.373 %/MPa) at the age of 24 hours. The SSC of SRMs at the age of 24 hours increased from 0.354 to 0.373 %/MPa (5.4%) as the content of CB increased from 0 to 0.5 wt.%, and then it decreased from 0.373 to 0.140 %/MPa (62.5%) as the content from CB further increased to 3.0 wt.%. With small content of CB, the SSC increased owing to more number of partially conductive path in the SRM matrix containing CB. Based on the increased number of partially conductive path within SRMs, the electrically conductive network within SRMs could be easily changed under external load. However, partially conductive paths were transformed to continuously conductive paths with more than 0.5 wt.% CB. The conductive network containing the increased number of continuously conductive paths became hard to be changed under external load, consequently the SSC decreased.

4.2 The effect of age on the self-sensing capacity of SRMs

The SSC of CB05 increased from 0.229 to 0.672 %/MPa (193%) as the age increased from 3 to 7 hours, while decreased from 0.672 to 0.373 %/MPa (44.5%) as the age further increased to 24 hours. At the age of 3 hours, SSC was low because the electrically conductive network of SRMs was stable owing to a lot of water not bound in hydrates. However, the SSC increased because the electrically conductive network became more easily changed under external load at the age of 7 hours owing to reduction of water with hydration and transformation of the continuously conductive paths into the partially conductive paths. At the age of 24 hours, and the compressive strength increased and the number of partially conductive path decreased owing to improvement of density and reduction of water in pores with continued hydration, thus SSC decreased.

5. Conclusions

This study investigated the self-sensing characteristics of the proposed smart repair materials (SRMs) corresponding to different CB contents (0, 0.5, 1.0, 2.0, and 3.0 wt.% by cement) at the early age (3, 7 and 24 hours). The reinforcement ratio of CB and the age of SRMs clearly affected the electromechanical response of SRMs. The following conclusions can be drawn:

- The SRM (CB05) containing CB (0.5 wt.% by cement) produced the highest stress sensitivity coefficient (SSC), 0.373 %/MPa, at the age of 24 hours.
- The amount of CB clearly affected on the SSC of SRM by changing the number of partially and continuously conductive electrical paths in the matrix.
- As the age increased from 3 to 7 hours, the SSC of CB05 increased from 0.229 to 0.672 %/MPa (193%) because of reduction in the water of matrix and the transformation of the continuously conductive paths to the partially conductive paths. However, it decreased from 0.672 to 0.373 %/MPa (44.5%) as the age further increased to 24 hours owing to the continued hydration.

Further research about the quality of crack repair and the self-sensing capacity of SRMs is required under different environments.

6. Acknowledgments

This work is supported by the Korea Agency for Infrastructure Technology Advancement (KAIA) grant funded by the Ministry of Land, Infrastructure and Transport (Grant RS-2022-00142566).

7. References

- Assaad J.J. 2018. Development and use of polymer-modified cement for adhesive and repair applications, *Construction and Building Materials*, 163, 139–148.
- Choi, Y.S., Kim, J.H., Cho, H.C., Lee, C.J. 2019. Asphalt concrete pavement surface crack detection using convolutional neural network, *Journal of the Korea Institute for Structural Maintenance and Inspection*, 23(6), 38-44.
- Kan, Y., Lee, M., and Lee, H. 2021. Experimental investigation of mode-I fracture toughness of real-cracked concrete repaired by epoxy, *Construction and Building Materials*, 293, 123490.
- Kim, J.H., Hong, J.Y., Kim, R.R., Woo, U.W., Choi, H.J. (2020) Development and application of IoT-based contactless ultrasonic system. *Journal of the Korea Institute for Structural Maintenance and Inspection*, 24(3), 70-79.



Bending Tests of GFRP Sandwich Panel Using a Rigid Polyethylene Core

Hiroki Iwata¹, Sumitaka Inoue², and Masahide Matsumura^{3*}

¹: Kumamoto University, Kumamoto, Japan; email: 223d8301@st.kumamoto-u.ac.jp

²: COMTEC Inc., Kumamoto, Japan; email: inoue@compotec.jp

³: Kumamoto University, Kumamoto, Japan; email: matsumura-m@kumamoto-u.ac.jp

*: corresponding author

Keywords: GFRP; polyethylene; sandwich panel; water absorption; three-point bending tests

Abstract: Sandwich plate panels, consisting of high-strength skin and lightweight core, are widely used in various fields such as airplanes, automobiles, and ships. Even for deck slabs of foot bridges, a sandwich panel made of high durable GFRP plates for the skins and of balsawood for the core is generally used for practical use the panel of lighter weight and of higher durability. However, previous studies pointed out that load-bearing capacity of the sandwich plate using the balsawood for the core might decrease when exposed to rain and snow for a long period, as strength and bending stiffness of water absorbed balsawood take smaller values compared with dried one. Then focused on in this study is a GFRP sandwich panel using a rigid polyethylene, having an independent foamed structure and showing low water absorption, for the core material to develop a higher durable deck slab for the foot bridges. The GFRP plates and the polyethylene core are integrated by using the VI molding technique in which resin is impregnated by vacuum pressure. Water immersion test, and three-point bending tests were conducted to check water absorption resistance and to understand the load-bearing capacity and the failure mode of the sandwich panels. The test results revealed that the GFRP sandwich panels show a good water absorption resistance and the shear failure in the core polyethylene were observed in all the specimens in the loading test, but a good applicability for structural use as the deck slab of the foot bridges within 1.2m in the span length.

1. Introduction

The Japanese climate is hot and humid, and wood decay fungi tends to grow in this environment. So, deterioration due to corrosion of wooden pedestrian slabs have been reported, then needs for slab replacement are increasing, but when pedestrian bridges are located in narrow areas such as mountainous regions, it is difficult to use heavy machines for construction. Therefore, a new slab having excellent durability and a lightweight structure transported by hand can be developed. Then, the authors focused on sandwich structures, of lightweight and high rigidity. Sandwich structures are widely used in various fields such as aircraft, automobiles, and ships. Even for deck slabs of pedestrian bridges, a sandwich panel made of high durable GFRP plates for the skins and balsawood for the core is generally used to realize the panel of lighter weight and of higher durability (Ishii et al. 2019). However, since the strength and modulus of elasticity of balsa materials decreases due to water absorption, the load-bearing capacity of balsa plated member may

decrease when exposed directly to rain or snow for a long period (R.L. Sadler et al. 2009). Then the load bearing capacity of the sandwich plate using the balsawood core also may decrease exposed under hot and humid environments. Then focused on in this study to develop a GFRP sandwich deck for the foot bridges using a rigid polyethylene for the core material, having an independent foamed structure, and showing a lower water absorption. Fig. 1 shows the GFRP sandwich panel with rigid polyethylene core. The thickness of the surface material GFRP plate as is 6 mm, and the thickness of the core material rigid polyethylene as is 25 mm. The GFRP plates and the polyethylene core are integrated by using the VI molding technique in which resin is impregnated by vacuum pressure. When the sandwich panel is used as deck slabs, then the panel is set between longitudinal members or between transverse ones bending moment is subjected. Failure modes of shown in Fig. 2. (a) and (b) are skin panel failures, (c) and (d) are core failures and (e) is delamination of bonding surface. In particular, failure mode (e) requires sufficient bond strength is expected due to water immersion because and arises a sudden loss of bearing capacity the skin and core materials can. Then, water immersion test and three-point bending tests were conducted to check resistance against water absorption resistance and to understand the failure mode of the sandwich panels.

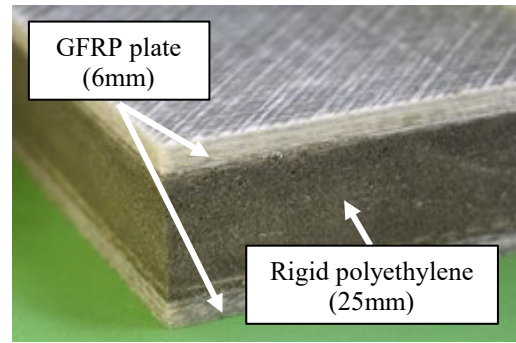


Fig. 1. Laminated configuration of GFRP sandwich panel with rigid polyethylene core

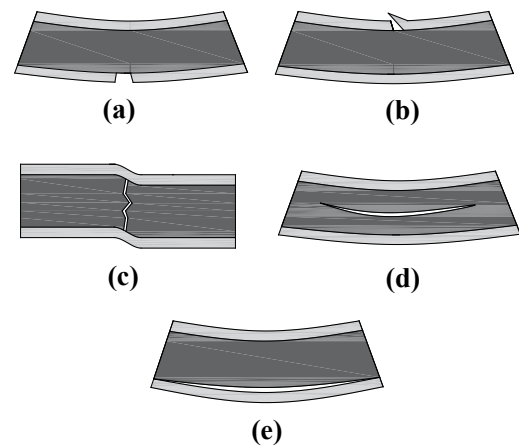


Fig. 2. Failure modes of sandwich panels subjected to bending moments (Miyairi 2019)

2. Water Immersion Test

Two test pieces (100 × 100 × t36 mm) were submerged into water at 20 °C in a thermostatic chamber during for 60 days. The dry mass is determined after the samples are dried in a hot-air dryer at 65 °C for three days. A water absorption rate was calculated from the Eq. (1) by measuring the mass using an electronic scale.

$$Q = \frac{M_2 - M_1}{M_1} \times 100 \quad (1)$$

where Q = water absorption rate; M_1 = dry mass; M_2 = wet mass.

Fig. 3 plots changes of averaged value of the water absorption rate shows. A rapid increase of the water absorption rate was observed in the first few days, and the maximum value was obtained 1.03 % after 60 days

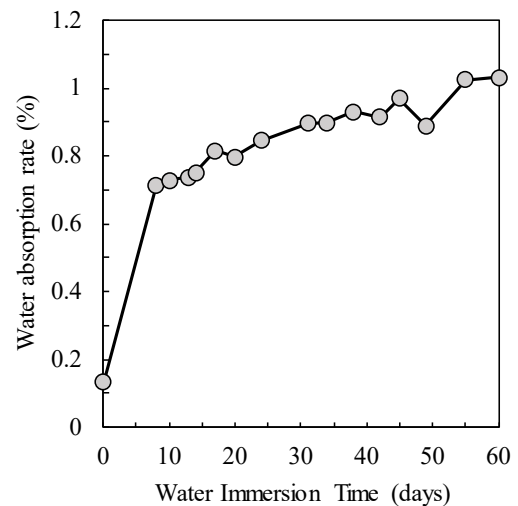


Fig. 3. Averaged value of water absorption rate

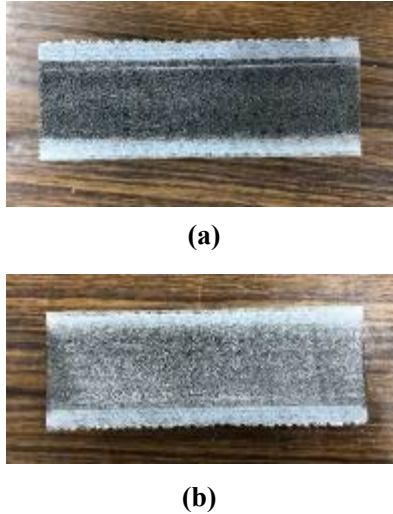


Fig. 4. Water immersion test GFRP sandwich panel after: (a) outer surface, (b) cut surface

of the water immersion. Previous studies revealed that the mass of the balsa wood increased to about six times after 60 days of water immersion, and that the rigid polyethylene, consisting of independent bubble structure had excellent water-absorption resistance. Fig. 4 shows the surface observation outer surface and cut surface of the test piece after the water immersion test. These demonstrate that water penetrating was not observed the inside into but slightly at the interface.

3. Three-Point Bending Tests

Figure 5 illustrates the loading method of three-point bending tests. The concentrated load is applied at the center of the specimen. A displacement transducer is set under the load point. Fig. 6 shows the damage at the interface after the test of the sandwich panels, No.3 and No.4 as examples. No failure of the GFRP plate and the adhesive between the GFRP plate and the rigid polyethylene was observed. The brittle shear failure and delamination in the rigid polyethylene were observed among most of the specimens, including No.3 at the maximum load. Only the delamination occurred of No.4. Fig. 7 pictures the loading point before and after the test, of No.2, where delamination occurred at the position of the interwoven glass fiber layer in the rigid polyethylene near the upper interface. Figure. 8

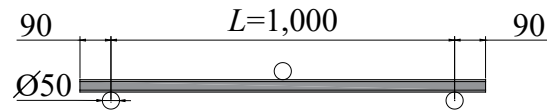


Fig. 5. Loading method of 3-point bending test (unit in mm)

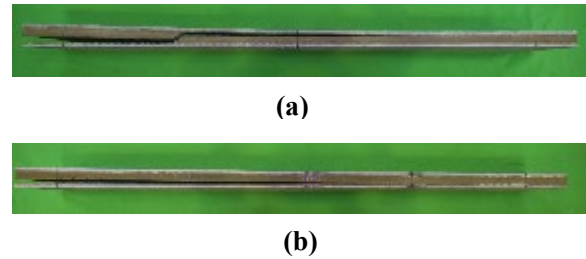


Fig. 6. Failure mode of sandwich panels after 3-point bending tests: (a) No.3, (b) No.4

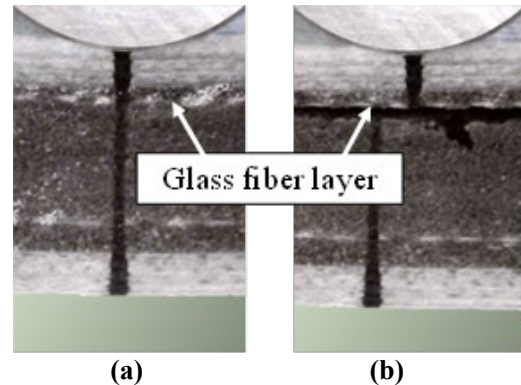


Fig. 7. Failure at the loading point before / after the test

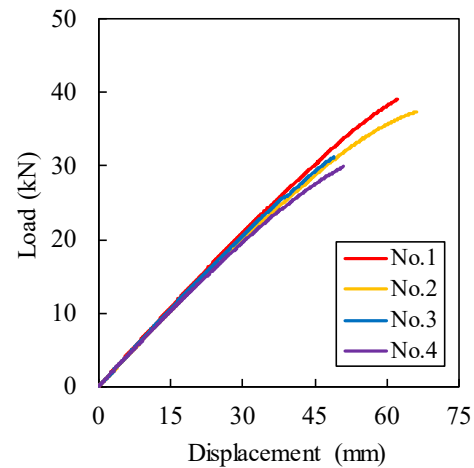


Fig. 8. Load-displacement relationship

plots the load–displacement relationship obtained from the experiment. The results are summarized in Table 1. Small differences in the initial bending stiffness. The classification of fracture modes is shown in Fig.2. No difference in experimental values due to differences in fracture mode was observed.

Then, Figure 9 illustrates the positions of the strain gages attached to the side and top and bottom surfaces. Figure 10 plots the strain distribution in the direction of the cross-sectional thickness at 5~25 kN. GFRP is more distorted than rigid polyethylene, and the assumption of plane retention is apparently not valid. The larger the load, the stronger the tendency.

4. Conclusions

In this study, water immersion tests and three-point bending tests were conducted check water absorption resistance and to understand the load-bearing capacity and the failure mode of GFRP sandwich panel. The following conclusions were drawn from the results of this study:

From the immersion test, it was confirmed that GFRP sandwich panels using rigid polyethylene as the core material have excellent water resistance.

From the strain distribution in the cross-sectional thickness direction, it was confirmed that the bending stress was sheared by the GFRP plate and reached its final stage through delamination of the glass fibers in the rigid urethane and the shear failure of the rigid polyethylene.

No peeling of the adhesive surface between GFRP and rigid polyethylene occurred, and it was confirmed that there was sufficient adhesive strength.

5. References

Ishii et al. 2019. An experimental study of GFRP-Balsa decks for footbridge slab, *Journal of Structural Engineering*, 65A, 786-798. (in Japanese).
R.L. Sadler et al. 2009. Water immersion effect on swelling and compression properties of Eco-Core, PVC foam and balsa wood, *Composite Structures* 90, 330-336.
Miyairi. 2009. Sandwich structure. (in Japanese)

Table 1. Summary of the test results

No.	Max.Load (kN)	Coefficient of variation	Displacemnet at Max.load (mm)	Fracture mode
1	39.11	0.11	62.21	(c) + (d)
2	37.45		66.11	(c) + (d)
3	31.28		49.00	(c) + (d)
4	29.91		50.85	(d)
Avg.	34.44	-	57.04	-

(c): shear failure, (d): delamination

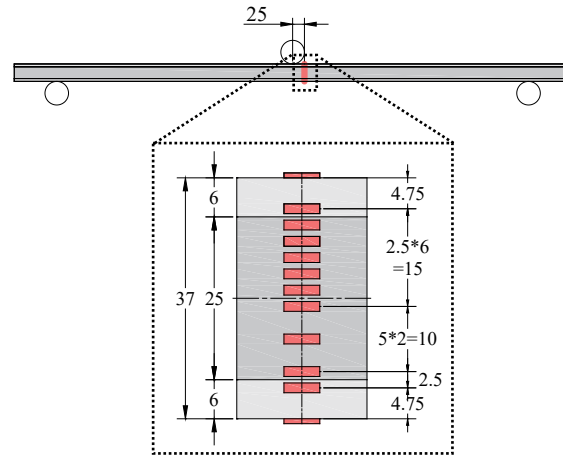


Fig. 9. Positions of strain gages attached to the side and top and bottom surfaces (unit in mm)

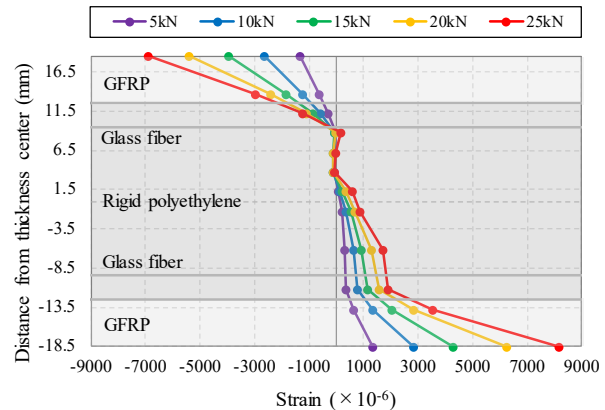


Fig. 10. Strain distribution in cross- sectional thickness direction



Analysis of Flexural-Bond Behavior of Beams Reinforced with CFRP

Dongkyu Lim¹ and Myoungsung Choi^{2*}

¹: Dankook University, Yongin, South Korea; email: ldk6482@gmail.com

²: Dankook University, Yongin, South Korea; email: choims@dankook.ac.kr

*: corresponding author

Keywords: CFRP bar; Bond strength; Flexural-bond; BS EN 12269

Abstract: Research and application of carbon fiber reinforced polymer (CFRP) as a substitute for reinforcement is increasing in the field of reinforced concrete, which has been uniformly established in the design of existing structures. CFRP reinforcement has superior material properties such as high tensile strength, lightness, and non-corrosiveness compared to steel, but excessive deflection and brittle failure due to low elastic modulus and elastic behavior are suggested as problems. This study conducted the 'Flexural-bond test' proposed by BS EN 1229 to evaluate the bonding characteristics of beams subjected to bending loads as a basic study for evaluating the structural performance of members using CFRP as reinforcement. As a result of conducting an experiment with steel and CFRP as reinforcement variables, the CFRP reinforcement member showed higher load resistance to bending load than steel, while the bond strength tended to be lower. Based on this, we tried to closely analyze factors that affect bond characteristics by using concrete strength, embedded length, and diameter of reinforcement as variables.

1. Introduction

Fiber Reinforced Polymers (FRP) are a composite of fibers with excellent mechanical properties and a matrix that constrains, molds, and transmits stress. Research and application of carbon reinforced polymers (CFRP) as reinforced substitute materials is on the rise in the field of reinforced concrete, which has been uniformly established in the design of existing structures. As shown in Figure 1, CFRP reinforcement have superior material properties such as high tensile strength, light weight, and non-corrosiveness compared to rebars, but excessive deflection and brittle destruction due to low elastic modulus and elastic behavior are suggested as problems. For this reason, an accurate understanding of material properties is required to be applied to an actual structure. In order for CFRP to be used as a reinforcement substitute, structural performance by sufficient bond must be secured during the synthesis behavior with concrete. In other words, it is judged that quantitative evaluation of bond characteristics is necessary for the integrated behavior of reinforcement-concrete. Therefore, this study conducted an experiment and FEM analysis to evaluate the bond characteristics of structures under flexural load to verify the structural performance of CFRP reinforcement, and compared and analyzed the flexural-bond behavior of rebars and CFRP reinforcement.

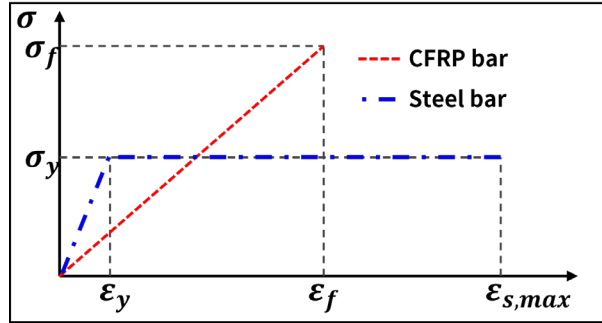
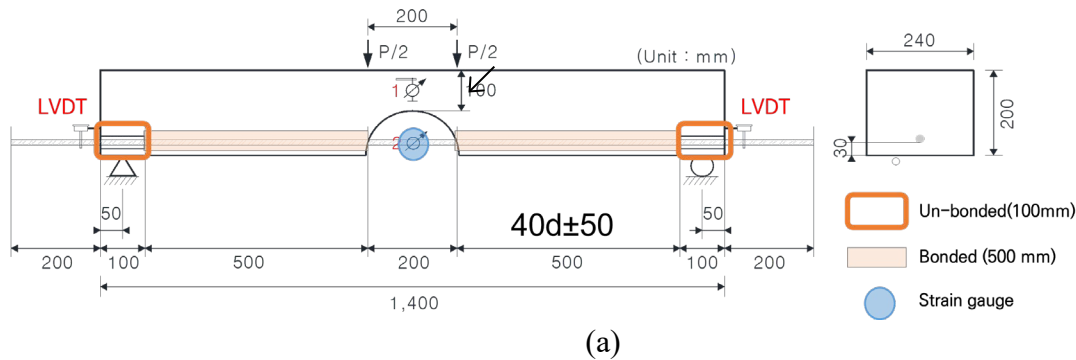


Fig. 1. Stress-strain curve by reinforcement type

2. Experimental Method and Materials

In this study, a beam-shaped test specimen with an arch proposed by BS EN 12269 was fabricated, and an experiment was conducted by simulating a flexural-bond behavior similar to an actual beam structure. Concrete beams were made with a design compressive strength of 35 MPa, and rebars and CFRP reinforcement were set as experimental variables. The reinforcements used have the same diameter of D13 (12.7 mm), and the yield strength of the steel rebar and CFRP bars were confirmed to be 400 MPa and 1850 MPa, respectively. The details and material properties of the test specimens and measuring gauges used are shown in Figure 2 and Table 1.



(a)



(b)

Fig. 2. Test specimen and gauge setting detail: (a) Conceptual diagram of test specimen (BS EN12269); (b) Specimen setting view

Table 1. Girder details

Concrete	$f_{ck} : 30 \text{ MPa}, \varepsilon_{cu} : 0.0033, E_c : 29,100 \text{ MPa}$
CFRP bar	$f_f : 1,800 \text{ MPa}, E_f : 130 \text{ GPa}, \text{Diameter} : \text{D13}(13 \text{ mm})$
Steel bar	$f_y : 450 \text{ MPa}, E_s : 210 \text{ GPa}, \text{Diameter} : \text{D13}(12.7 \text{ mm})$

f_{ck} : Design strength of concrete

ε_{cu} : Ultimate strain of concrete

E_c : Elastic modulus of concrete

f_f : Tensile strength of CFRP bar

E_f : Elastic modulus of CFRP bar

f_y : Yield strength of steel bar

E_s : Elastic modulus of steel bar

3. Result and Analysis

The average experimental results of each test specimen are shown in Table 2, and Figure 3 is a graph showing the load-displacement and load-strain relationship according to the reinforcement variables. The CFRP reinforcement specimen showed a maximum load of about 145% compared to the steel specimen, and the deflection amount was about 30%, confirming that brittle failure occurred after elastic behavior. The ultimate bond strength was defined as the bond stress at the time of concrete failure, and the CFRP reinforcement specimen was 17.29 MPa and 10.91 MPa, respectively, which were slightly lower in the rebar and CFRP reinforcement specimens. This is considered to have resulted in the yield of rebars and concrete crushing due to the concentration of stress on the rebar due to the high transverse restraint pressure on the steel when sufficient development length is secured. In the case of CFRP, splitting occurred in the vertical concrete cover due to the Wedge and Prying action. However, in order to accurately evaluate the bond strength, the reinforcement should not yield and pull-out or splitting should occur. Therefore, it is judged that experiments and analysis that supplement this should be conducted in future studies.

Table 2. Experimental result for Flexural-bond test

No.	Specimen	Ultimate load (kN)	Failure mode	Ultimate bond strength (MPa)
1	CFRP(D13)	51.85	Splitting	10.91
2	Steel(D13)	35.36	Concrete crushing / Steel yielding	17.29

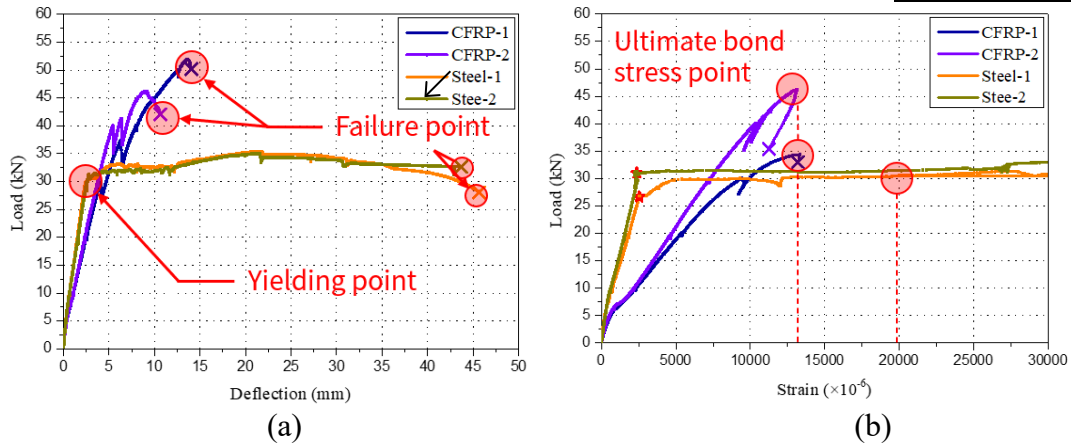


Fig. 3. Flexural-bond test results: (a) Relationship between load and deflection; (b) Relationship between load and strain

4. References

BS EN 12269. 2001. Determination of the bond behaviour between reinforcing steel and autoclaved aerated concrete by the "beam test" Short term test.

Biscaia, H. C., Chastre, C., Borba, I. S., Silva, C., & Cruz, D. 2016. Experimental evaluation of bonding between CFRP laminates and different structural materials. *Journal of Composites for Construction*, 20(3), 04015070.

Hassan, T., & Rizkalla, S. 2004. Bond mechanism of NSM FRP bars for flexural strengthening of concrete structures. *ACI Structural journal*, 101(6), 830-839.

Oh, H., Kang, T. S., & Oh, K. C. 2014. A flexural bonding characteristic of GFRP rebar embedded in concrete beam under cyclic loading. *Journal of the Korean Society of Hazard Mitigation*, 14(4), 51-58.

5. Acknowledgements

This work is supported by the Korea Agency for Infrastructure Technology Advancement(KAIA) grant funded by the Ministry of Land,Infrastructure and Transport (Grant RS-2021-KA163381).



Evaluation of Tensile Performance of CFRP Cable Anchorage System using Non-Corrosive Steel Material

Seung-Hyeon Hwang^{1*}, Ji-Young Kim², Jin-Young Yoon³,
Tae-Kyun Kim⁴, and Woo-Tai Jung⁵

¹: Korea Institute of Civil Engineering and Building Technology, Goyang, Gyonggi-do, Republic of Korea; email: shhwang@kict.re.kr

²: Korea Institute of Civil Engineering and Building Technology, Goyang, Gyonggi-do, Republic of Korea; email: jykim0421@kict.re.kr

³: Korea Institute of Civil Engineering and Building Technology, Goyang, Gyonggi-do, Republic of Korea; email: jyoon@kict.re.kr

⁴: Korea Institute of Civil Engineering and Building Technology, Goyang, Gyonggi-do, Republic of Korea; email: kimtaekyun@kict.re.kr

⁵: Korea Institute of Civil Engineering and Building Technology, Goyang, Gyonggi-do, Republic of Korea; email: woody@kict.re.kr

*: corresponding author

Keywords: carbon fiber-reinforced polymer; compression sleeve; non-corrosive steel material; anchorage system

Abstract: The anchorages used to fix and connect the cables to structures typically use steel, making it essential to minimize corrosion. The study proposes a fully corrosion-free cable system that includes anchorages, as carbon fiber-reinforced polymer (CFRP) cables, which have high tensile strength and are not affected by corrosion. The study modified the details of the sleeve anchorage proposed by Kim et al., which used SM45C steel material, to use duplex steel material, which has no effect on corrosion. The proposed CFRP cable sleeve anchorage using non-corrosive steel material was evaluated using tensile performance tests to determine its slip in the anchorage, failure mode, and stress-strain relationship. The results showed that the proposed CFRP cable sleeve anchorage using non-corrosive steel material performed almost as well as the sleeve anchorage of SM45C steel material, demonstrating that the new system can be used as a fully corrosion-free cable system that includes anchorages.

1. Introduction

The anchorage, which is generally a conventional cable and is crimped or swaged, is difficult to ensure complete corrosion resistance as it is usually used with plating or coating after machining. However, if the internal corrosion resistance of the anchorage can be ensured, a cable system that is not affected by corrosion can be achieved with carbon fiber-reinforced polymer (CFRP) cable, which is not affected by corrosion. Duplex, a type of stainless steel, contains a large amount of strengthening elements such as chromium, molybdenum, and nickel, and is a type of steel with excellent resistance to chloride corrosion, SSC, pitting, crevice corrosion, wear, and erosion (Rabi et al., 2022). Additionally, this type of steel has excellent mechanical properties because the size of the structure is smaller than that of other steel materials. In this study, an anti-corrosive steel

will be used to find the optimal specifications for a carbon fiber cable anchorage and to suggest a completely non-corrosive cable system accordingly.

2. Experimental Investigation

The non-corrosive anchorage for CFRP cables refers to the anchorage specifications of SM45C steel proposed by Kim and Jung (2022). The total length of the anchorage is 135.0 mm, with a central section at 95.0 mm and the points where fine angles are given on both sides being 20.0 mm each. The outer diameter of central section is 25.9 mm, the outer diameter at the end point is 24.0 mm, and the inner diameter is symmetrical at 11.0 mm on both sides. The experimental variables for the development of non-corrosive anchoring devices for CFRP cables were set at intervals of 0.1 mm for the outer diameter (d_o) of central section in the range of 25.5 - 25.9 mm. CFRP cables were manufactured in lengths of approximately 1,000 mm, with three samples for each variable, and the anchorages were installed at positions about 100 mm away from both ends of the CFRP cable. An aluminum insert was set between the CFRP cable and the anchorage. Tensile tests of the CFRP cable system were conducted using a 1,000 kN capacity UTM, with a displacement control rate of 5 mm/min.

3. Test Results and Discussion

The failure mode of the specimen, which had a d_o of 25.5 mm for the anchorage, resulted in slip between the anchorage and the CFRP cable, leading to the termination of the experiment (Fig. 2(a)). The failure mode of the specimens, which had an d_o of 25.6 mm and 25.7 mm for the anchorage, mostly showed a flower-shaped fracture (Fig. 2(b) and (c)). The failure mode of the test specimens, which had an d_o of 25.8 mm and 25.9 mm for the anchorage, showed a fracture at the inner end of the single anchorage system between the anchorage and the CFRP cable (Fig. 2(d) and (e)).

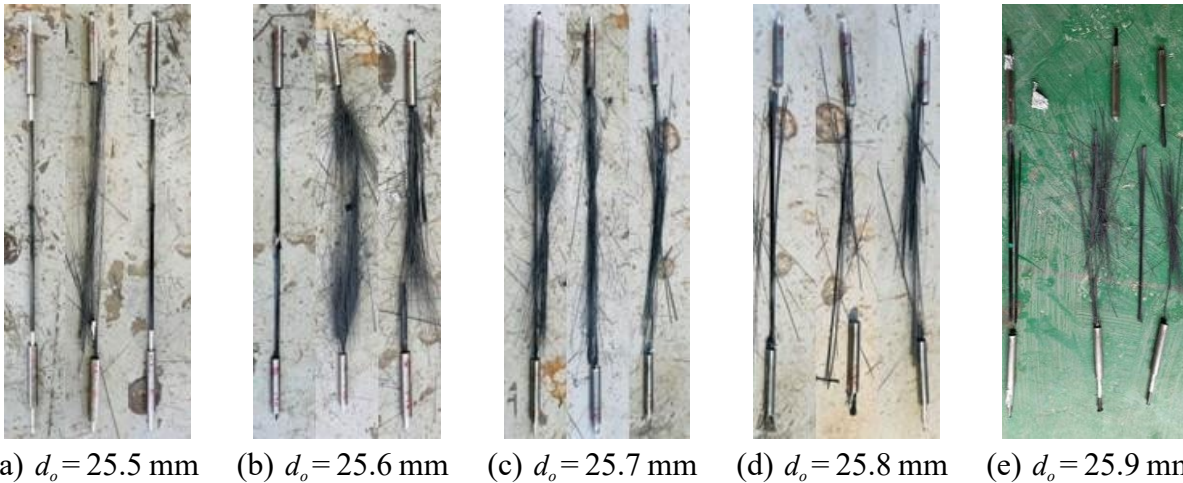


Fig. 1. Failure mode of CFRP cable anchorage systems

The tensile test results according to the variable outer diameter of the anchorage are shown in Table 1. The applied load-displacement relationship of the specimen, which had an d_o of 25.5 mm for the anchorage, showed linear behavior up to a displacement of approximately 15 mm, and thereafter, the displacement increased due to slip, but the load remained constant (Fig. 2).

The applied load-displacement relationship of the specimen, which had an d_o of 25.6 mm for the anchorage, was similar to that of the specimen with an anchorage d_o of 25.5 mm, but the amount of slip decreased. However, the applied load-displacement relationship of the specimens with anchorage d_o of 25.7 mm, 25.8 mm, and 25.9 mm increased linearly up to the maximum load. The axial stress-strain relationship of all specimens increased linearly up to the point of reaching the tensile strength(Fig. 3). The average tensile strength of the specimens with d_o of 25.6 mm and 25.7 mm was the highest at approximately 3,143 MPa and 3,140 MPa, respectively, within the d_o range of 25.5 - 25.9 mm(Fig. 4).

Table 1. Test results

Specimen		Applied load (kN)	Tensile strength (MPa)	Strain (μ)	Elastic modulus (MPa)
Outer diameter 25.5 mm	#1	206.5	2,629	14,375	182,892
	#2	211.1	2,688	14,782	181,810
	#3	215.9	2,749	15,022	183,021
	Average	211.2	2,689	14,726	182,574
Outer diameter 25.6 mm	#1	244.4	3,111	16,825	184,917
	#2	245.4	3,125	17,024	183,540
	#3	250.9	3,194	17,530	182,202
	Average	246.9	3,143	17,126	183,553
Outer diameter 25.7 mm	#1	249.3	3,174	17,141	185,191
	#2	258.1	3,286	18,082	181,723
	#3	232.5	2,961	16,168	183,111
	Average	246.6	3,140	17,130	183,342
Outer diameter 25.8 mm	#1	217.5	2,770	15,129	183,082
	#2	225.9	2,876	15,441	186,259
	#3	236.7	3,013	16,543	182,155
	Average	226.7	2,886	15,704	183,832
Outer diameter 25.9 mm	#1	205.8	2,621	15,058	174,037
	#2	215.0	2,737	16,037	170,681
	#3	204.3	2,601	15,101	172,250
	Average	208.4	2,653	15,399	172,323

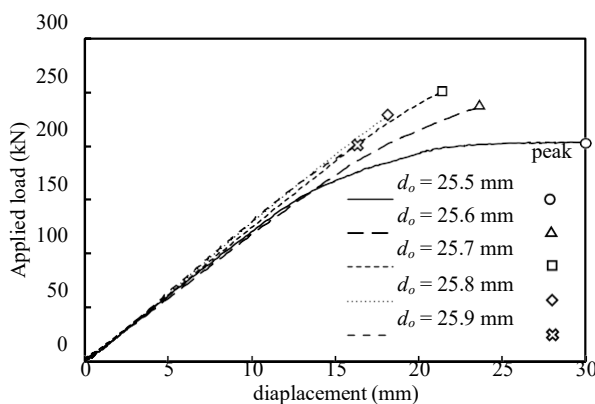


Fig. 2. Applied load-displacement relationship

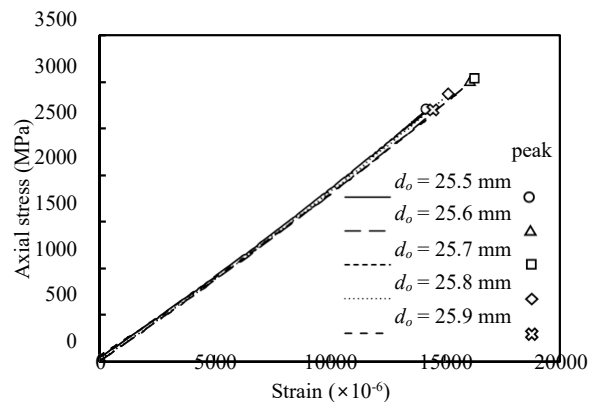


Fig. 3. Axial stress-strain relationship

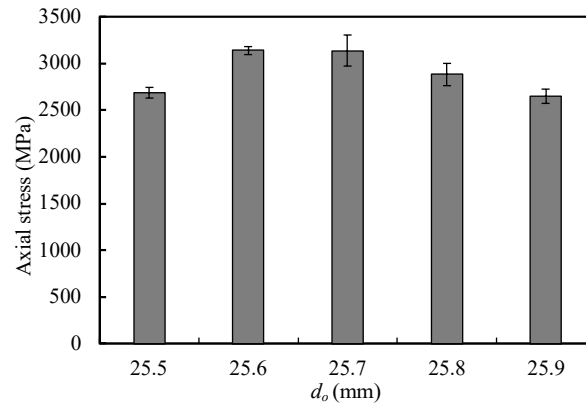


Fig. 4. Tensile strength results according to outer diameter

The average tensile strain of the specimens with d_o of 25.6 mm and 25.7 mm was also the highest at approximately $17,126 \mu$ and $17,130 \mu$, respectively, within the same range. The average tensile strain of the specimens with d_o of 25.5 mm, 25.8 mm, and 25.9 mm was approximately $14,726 \mu$, $15,704 \mu$, and $15,399 \mu$, respectively, and was proportional to the decrease in tensile strength of the specimens with d_o of 25.6 mm and 25.7 mm. The average elastic modulus of the specimens within the d_o range of 25.5 - 25.8 mm was approximately 183,000 MPa.

4. Conclusions

Based on tensile tests on the outer diameter of the CFRP cable non-corrosion anchorage system, the following conclusions were inferred:

1. The failure mode of the specimens with an outer diameter ranging from 25.6 - 25.7 mm for the anchorage system mostly showed a flower-shaped fracture.
2. The applied load-displacement relationship of the specimens with an outer diameter of 25.6 mm or less for the anchorage system showed slip between the CFRP cable and the anchorage, while the specimens with an outer diameter of 25.7 mm or greater showed a linear increase up to the maximum load.
3. The average tensile strength of the specimens with an outer diameter of 25.6 mm and 25.7 mm for the anchorage system was the highest, 3,143 MPa and 3,140 MPa, respectively.
4. The optimal outer diameter for the non-corrosion anchorage system for CFRP cables is 25.7 mm.

5. Acknowledgments

Research for this paper was conducted under the KICT Research Program (project no. 20230110-001, Development of high performance construction materials based on carbon (focus on insulation materials for building and corrosion free cable)) funded by the Ministry of Science and ICT.

6. References

Kim, T.K. and Jung, W.T. 2022. Improvement of Anchorage Performance of Carbon Fiber-Reinforced Polymer Cables, *Polymers*, 14(6), 1-18.

Ravi, M., Shamass, R., and Cashell, K.A. 2022. Structural Performance of Stainless Steel Reinforced Concrete Members: A Review, *Construction and Building Materials*, 325(28), 1-14.

Failure Mode and Adhesive Strength of Single Lap Joint of GFRP Laminated Plates with Different Fiber Volumes Bonded by a Low Elastic Adhesive

Masahide Matsumura^{1*}, Sumitaka Inoue², Hiroki Iwata³, and Yuto Anan³

¹: Kumamoto University; Kumamoto Japan, email: matsumura-m@kumamoto-u.ac.jp

²: COMTEC Inc., Kumamoto Japan; email: inoue@compotec.jp

³: Kumamoto University; Kumamoto Japan, email: 223d8301@st.kumamoto-u.ac.jp

⁴: Kumamoto University; Kumamoto Japan, email: 219d8302@st.kumamoto-u.ac.jp

*: corresponding author

Keywords: adhesive strength; single lap joint; GFRP; fiber volume; low elastic adhesive

Abstract: In this study, tensile tests of single lap joints, where two of GFRP laminated plates with different fiber volume are bonded by a low elastic adhesive, are carried out to discuss influences of fiber volume differences in the loading direction and of elastic modulus of the adhesives on failure mode and on adhesive strength of the joints. The GFRP plates used in the test consist of 13 and 22 layers having almost the same fiber volume in total; fiberglass mat of 1 direction and glass roving cloth are alternately laminated. Then test results indicated that failure mode changes depending on the fiber volume in the loading direction and the adhesive strength takes smaller value and fluctuates when the fiber volume takes smaller and the failure mode is delamination of the layers.

1. Introduction

Developments of a reliable joint connecting FRP members are keys to develop a longer span of FRP bridge structure. The adhesive strength is to be experimentally evaluated by tensile lap-shear test program using of the single lap specimen illustrated in Fig. 1. However, a lot of parameters influence on the test results such as failure modes, adhesive strength of single lap joint of GFRPs. This is because a bending moment due to an eccentric axial load, causing a rotation of the connected part, is subjected to the adhesive connection between the GFRP plates, and flexural and axial stiffness of the plates greatly influence on these tested values.

Then in this paper, GFRP plates molded by the Vacuum Infusion technique at room temperature having different fiber volumes, consisting of 13 and 22 layers of fiberglass mats and glass roving cloths, and a low elastic adhesive of 1 mm in the thickness are prepared for the test. The fiber volumes are varied by using 3 of different GF sheets commercially provided and 2 of the directions of 0 and 90 degrees.

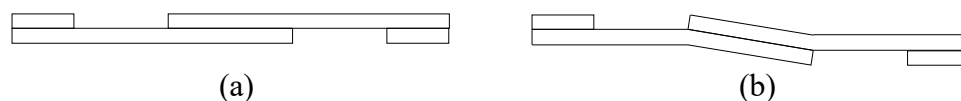


Fig. 1. Lap-shear test (a) test specimen, (b) expected deformation

2. Tensile Lap-Shear Test

The adhesive strength is obtained as the maximum load divided by the adhesive area, by the single lap-shear test. Here, the fiber volumes are varied by using 3 different fiber types; A to C of GF sheets commercially provided as listed in Table 1. As listed in Table 2, tensile modulus of the glass fibers take different values from 40 to 76, based on nominal values provided from suppliers. GFRP plates were alternate laminated structure of glass mats oriented in 1 direction and of roving cloth in 4 directions, and 13 layers for specimens A and B and 22 layers for specimen C because of the fiber volume per one sheet of Fiber type C is smaller. Tensile test results of the GFRP Plates of 3 fiber types are summarized in Table 4. Vinyl ester resin in Table 5 is used as adhesive and the GFRP plates were molded by the VI molding technique.

Test specimens illustrated in Fig. 2 are prepared. Both the bonding length and the width were 100 mm respectively, and a low modulus adhesive with an elastic modulus of 170 to 345 MPa, as listed in Table 7, mentioned later, was used for the test. The target adhesive thickness was 1 mm controlled by using glass beads of 1 mm diameter. Strain gauges were installed at the positions also shown in Fig. 2. 1,000 kN universal testing machine was used for the tests, and the loading speed was manually adjusted to 6 mm/min by reference to JIS K6850.

Table 1. Fiber types and test cases

Cases	Fiber type	Fiber angle	Numbers ^a
A-0-No.	A	0°	5
A-90-No.	A	90°	
B-0-No.	B	0°	
B-90-No.	B	90°	
C-0-No.	C	0°	
C-90-No.	C	90°	

^a: Numbers of specimen

Table 2. Fiber types and properties

Fiber Type		σ_t (GPa)	E_t (GPa)
A	SELCOM UNI	1.9-2.4	69-76
	SELCOM QI	1.9-2.6	73
B	JA EUL	0.9	40
	JA EQX	0.9	40
C	SHINDO W600G	-	70
	SHINDO F880G	-	70

σ_t = Tensile strength

E_t = Tensile modulus

Table 3. Fiber volumes and fiber directions

Dir. Fiber type	0°	+45°	-45°	90°	total (g/m ²)
	A	9300	2100	2100	2100
B	8928	2107	2100	2407	15542
C	9764	2180	2030	2708	16682

Table 4. Adhesive properties

	σ_t (GPa)	E_t (GPa)	τ (MPa)	φ (%)
MA560-1	17.2-20.7	172-345	11.7-15.2	>130

σ_t = Tensile strength

E_t = Tensile modulus

τ = Lap-shear strength

φ = Elongation ratio

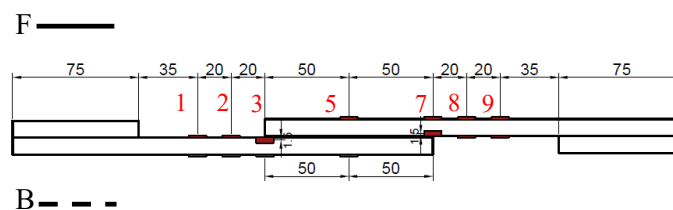


Fig. 2. Shape of test specimen (unit: mm)

3. Experimental Results

Table 5 shows the fracture modes of the specimens; an adhesive failure, AF, where the adhesive adhered to both surfaces of the GFRP plates like specimen A-0-No.5 and a GFRP delamination failure, DF, where the GFRP plate of one side delaminates like specimen A-90-No.2.

Table 6 summaries material test results of the GFRP plates and lap-shear test results by using the averaged values. Fig. 3 plots the relationship between the maximum loads and fiber volumes, with

Table 5. Failure modes

Failure Mode	0	90
	A-0-No.5	A-90-No.2
A		
	B-0-No.5	B-90-No.4
B		
	C-0-No.5	C-90-No.1
C		

Table 6. Test results

Cases	σ_t (GPa)	E_t (GPa)	Fiber ^a (g/m ²)	thickness ^b t (mm)	P_{max} (kN)	τ_{max} (MPa)	Failure Mode
A-0	558	30.2	9300	1.076	116.4	11.6	AF
				-	-	-	DF
A-90	230	17.6	2100	-	-	-	AF
				1.086	90.0	9.0	DF
B-0	570	32.5	8928	1.098	105.1	10.6	AF
				1.309	101.1	10.0	DF
B-90	191	14.7	2407	-	-	-	AF
				0.913	71.7	7.1	DF
C-0	513	30.8	9764	1.224	117.8	11.7	AF
				-	-	-	DF
C-90	220	17.9	2708	1.766	107.1	10.5	AF
				1.511	102.7	10.2	DF

a: Fiber volume of loading direction
b: thickness of adhesive layer

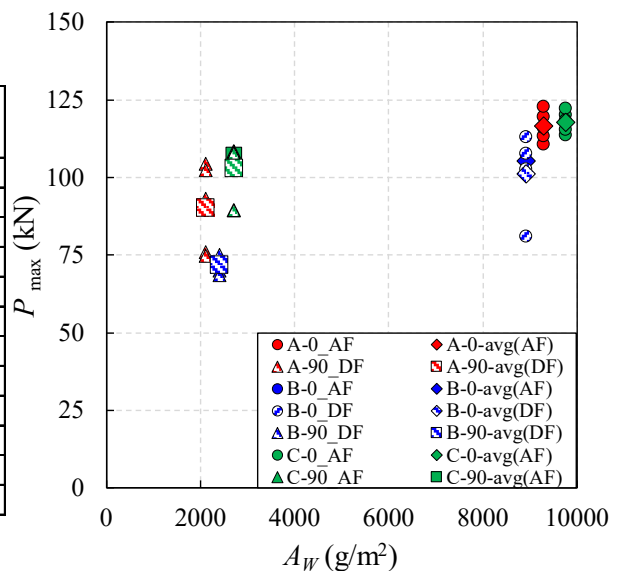


Fig. 3. $P_{max} - A_w$ relationship

the fracture modes of each specimen. The figure also plots the averaged value of the maximum load among which the same fracture modes was observed.

These test results explain that the maximum load becomes larger as the fiber volume increases, regardless of the differences of the fracture modes when the same GFRP fibers are used but the loading directions are different. When compared with the same GFRP fiber specimens, the maximum loads with AF take larger than those with DF. The specimen B-0, which takes the lowest elastic modulus and fiber volume in the 0° direction as indicated in Tables 2 and 3, 4 of specimens B-0 showed DF and the averaged strength of B-0 take the smallest among all the cases, while the fracture modes of the specimens A-0 and C-0 were AF. On the other hand, the maximum load of B-90, taking a larger fiber volume than A-90, was smaller than that of A-90.

Figure 4 shows bending moment diagrams at the maximum load, calculated from measured strains on the front and back surfaces. The figure indicates that the failure starts from the bonding edges where the bending moments become larger and the maximum bending moment was smaller among the specimen with DF of the failure mode.

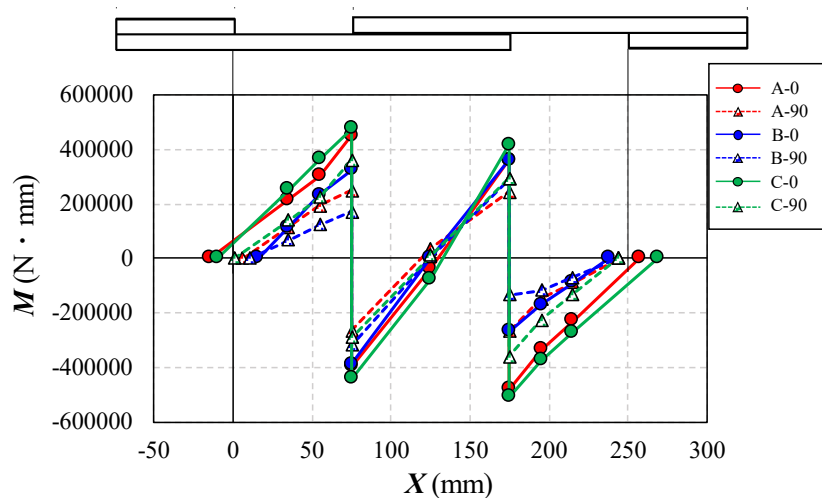


Fig. 4. Bending moment diagram at P_{max}

4. Summary

Tensile shear tests of GFRP single-lap adhesive bonded joints were conducted in this study by focusing on fiber volumes of glass fibers. The following is a summary of the results.

The test results indicate that the bonding strength and fracture modes vary depending on the mechanical properties of the glass fiber and the fiber volumes of the GFRP plates. Two types of fracture modes; Adhesive Failure, AF and Delamination Failure, DF, were observed in the tests. The maximum loads of AF tend to be higher as the fiber volumes of the GFRP plate take larger. On the other hand, DF was observed when bending moment subjected to the joints is smaller, for instance, when the elastic modulus of the GFRP plates take smaller. The bonding strength and fracture modes were different depending on the physical properties of the fibers and the fiber volume.



Bridge Engineering Institute Conference 2023 (BEI-2023)
Rome, Italy, July 17-20, 2023



Ultra-High Performance Concrete



Titanium Alloy Reinforced Ultra-High Performance Concrete (TARUHPC): A Next Generation of Advanced Materials for Civil Infrastructure

Mahesh Acharya¹, Jared Cantrell², Luis Bedriñana³, and Mustafa Mashal^{4*}

¹: Idaho State University, Pocatello, Idaho, USA; email: achamahe@isu.edu

²: Idaho State University, Pocatello, Idaho, USA; email: cantjare@isu.edu

³: Universidad de Ingeniería y Tecnología – UTEC, Lima, Peru; email: lbedrinana@utec.edu.pe

⁴: Idaho State University, Pocatello, Idaho, USA; email: mashmust@isu.edu

*: corresponding author

Keywords: TARUHPC; ensemble learning; machine learning; UHPC; pull-out test; bond strength prediction.

Abstract: The paper introduces a next generation of composite advanced materials titled “Titanium Alloy Reinforced Ultra-High Performance Concrete” (TARUHPC). In this solution, Titanium Alloy Bars (TiABs) and Ultra-High Performance Concrete (UHPC) are combined instead of conventional concrete and steel rebars which is widely known as “Reinforced Concrete.” TARUHPC is intended for construction of highly durable, resilient, and sustainable infrastructure. TiABs offer higher strength, superior fatigue performance, high strength-to-weight ratio, lighter weight, lower modulus of elasticity, reduce rebar congestion, smaller inelastic residual deformation, and excellent corrosion resistance compared to traditional reinforcing bars. At the same time, UHPC offers higher compressive strength, superior mechanical properties, and excellent durability compared to conventional or high-strength concrete. UHPC utilizes some of the byproducts such as fly ash and silica fume as supplementary cementitious materials to reduce the portion of hydraulic cement in the mix. This translate in reducing the carbon dioxide (CO₂) emissions of concrete while providing excellent durability and strength. In this research, experimental work is carried out to investigate various mechanical properties of TARUHPC, including bond strength of TiABs in UHPC through a series of pull-out tests.

By using these test results, and previous pull-out tests, an explainable data-driven model, based on ensemble learning, is proposed for the bond strength prediction of TiABs in UHPC. The proposed model showed great accuracy and provided important insights for planning future tests on TARUHPC elements. The results also showed that state-of-the-art techniques such as machine learning in combination with TARUHPC can help to better design highly durable infrastructure.

1. Introduction

Composite advanced novel materials have been continuously introduced in civil and critical infrastructures lately that would improve structural performance and durability. Some of these major advanced materials that has huge potential to benefit civil and critical infrastructure include Ultra-High Performance Concrete (UHPC) and Titanium Alloy Bars (TiABs). UHPC is one of the advanced cementitious composite materials with exceptionally high strength and high

durability compared to the conventional normal concrete. One of the unique features of UHPC is that it utilizes recycled products such as fly ash and silica fume as supplementary cementitious materials to reduce the portion of hydraulic cement (up to 70%) in the mix. Also, the addition of the steel fibers in the UHPC concrete can result in the added ductility in structures. UHPC offers higher compressive strength (9 times higher), superior mechanical properties, and excellent durability compared to conventional or high-strength concrete (Khadka et al. 2022). Similarly, the permeability for the UHPC concrete is about 100 times less than that of normal concrete, which is an important measure looking at the durability of the concrete.

Similarly, Titanium Alloy Bars (TiABs) is an advanced material that has been gaining popularity for applications in concrete structures. TiABs (Ti6Al4V) offer higher strength (2.5 times higher), superior fatigue performance, high strength-to-weight ratio, lighter weight (60% less), lower modulus of elasticity, reduce rebar congestion (50% less), smaller inelastic residual deformation (50% less), and excellent corrosion resistance compared to conventional rebars (Acharya et al. 2022 and Thapa et al. 2022). It has great potential mostly in construction and retrofitting of bridges and beams. Researchers at Idaho State University (ISU) are among the one's to carry out several experimental and analytical research to determine the mechanical properties of TiABs (Acharya et al. 2021 and Khadka et al. 2020). Research was carried out to identify mechanical properties for TiABs and compare them with a high strength alloy (e.g., grade 150 ksi). The grade of titanium used in the research is Grade-5 (Ti6Al4V) which is alloy of Titanium, Aluminum, and Vanadium. A series of tests such as tension test, hardness test, Charpy V-notch, galling tests and bond tests were carried out to compare TiABs against the 150 ksi high strength steel alloy and clearly, TiABs performed better.

2. Pullout-Test of TiABs in Concrete

A full-scale experimental investigation was carried out to evaluate the bond-slip relationship between rebar (TiABs) and concrete (UHPC and/or Normal Concrete). The size of the pullout specimen was 22 in x 10 in x 4 in. Embedment length of 5 in, and 9 in were used for the specimens. The specimens were tested in tension using the displacement-controlled servo-hydraulic actuator. The test-setup prepared for the specimen is presented in Fig. 1.

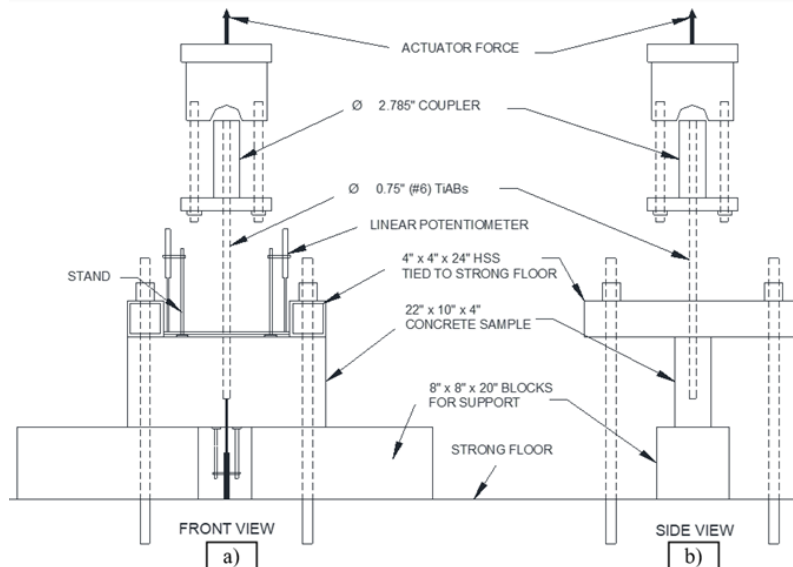


Fig. 1. Test setup: (a) Front view; (b) Side view

Testing was carried out on a total of four specimens (See Table 1). Specimen ID denotes the type of concrete, size of bar and the embedment length. E.g., U#6-5 denotes the specimen as UHPC beam embedded with #6 TiABs (ϕ 0.75 inch) and has an embedment length of 5 inch. Results showed better performance of the UHPC beam compared to the Normal Concrete beam as shown in Table 1. For the test-setup provided, the Normal Concrete beams had a premature failure with an average ultimate force of about 5.2 kips and a resulting shear stress of 0.35 ksi. However, UHPC beams performed exceedingly better with an average ultimate force of about 32 kips and a resulting shear stress of 2 ksi.

Table 1. Pullout test results

	Specimen ID			
	U#6-5	N#6-5	U#6-9	N#6-9
Ultimate Force (kip)	27.992	5.642	35.923	4.757
Slip at Ultimate Force(inch)	0.02510	0.00266	0.05025	0.00333
Embedment Length (inch)	5	5	9	9
*Shear Stress (ksi)	2.3760	0.4789	1.6940	0.2243
*Shear Stress ($\tau = P/\pi dl$); P = Ultimate force, d = Diameter of bar, l = Embedment length				

3. Bond Strength Prediction of TiABs on UHPC

The behavior of reinforcement, i.e., Titanium Alloy Bars (TiABs) in UHPC is generally determined by conducting pull-out tests. However, these tests need amounts of time and cost. So, the paper presents the application of artificial intelligence technique, i.e., machine learning, in predicting ultimate bond strength between UHPC and TiABs in-order-to identify appropriate technique that can save significant amount of time and cost of experimental testing. A total of 334 experimental data from the available literature are collected. The dataset description along with statistical feature is presented in Table 2.

Table 2. Statistical features of the dataset

	Description	Symbols	Minimum-Maximum	Mean	Standard Deviation
Inputs	Compressive Strength	f'_c (psi)	3481-29733	19190	8150
	Yield Strength	f_y (psi)	53896-140000	81033	18863
	Tensile Strength	f_u (psi)	84557-150000	103220	17074
	Bar Diameter	d (in)	0.31-0.98	0.62	0.15
	Embedment Length	l (in)	0.55-11.93	2.96	2.26
	Concrete Cover	c (in)	0.63-7.64	3.16	1.64
Output	Bond Strength	τ (psi)	259-12022	4683	3067

Various ML models were identified that could be built to train the pullout testing datasets. The major models that were considered for use in bond strength prediction were: a) Random Forest (RF), b) XGBoost (XGB), and c) AdaBoostR2 (ADB). Random Forest (Ho 1995) is the function that uses decision trees for regression analysis where each tree is built from a random subset of the training set. Similarly, XGBoost (Chen et al. 2016) is an implementation of gradient boosted decision trees designed for speed, performance, and an iterative decision tree algorithm with multiple decision trees. An AdaBoost regressor (Schapire 2013) is a meta-estimator that begins by fitting a regressor on the original dataset and then fits additional copies of the same

dataset but where the weights of instances are adjusted according to the error of the current prediction. As such, subsequent regressors focus more on difficult cases. This class implements the algorithm known as AdaBoostR2 which is a supervised instances-based domain adaptation method suited for regression tasks.

The dataset is split into 80% of training and 20% of testing data. The results from the ML models showed that RF has the testing accuracy, training accuracy, and R2 score of 22.3%, 67% and 0.89 respectively. Similarly, XGB was successful in obtaining testing accuracy, training accuracy and R2 score of 92.2%, 98.2% and 0.92 respectively. AdaBoost outperformed other models with testing accuracy (92.8%), training accuracy (98.2%) and R2 score (0.93). This is also verified with the Taylor diagram (Fig. 2). The results obtained with AdaBoost showed to perform better among the three models that were considered. From the result, it is evident that tools such as machine learning can be used to predict the bond strength of TiABs on UHPC. The testing accuracy is relatively lower compared to the training accuracy on all the models; but it is clear that these tools have potential to be used for prediction.

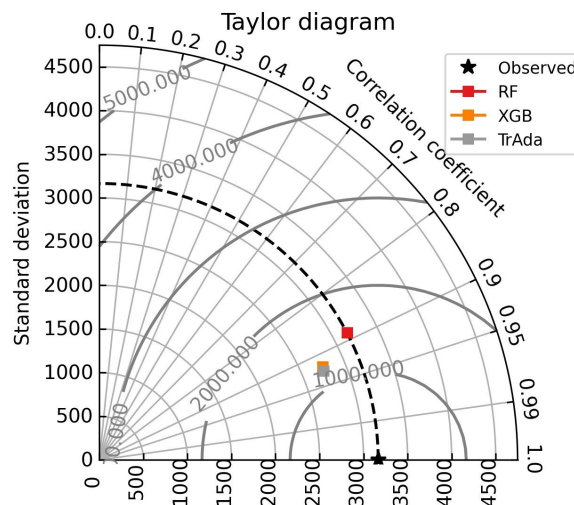


Fig. 2. Taylor diagram

4. Conclusions

Titanium Alloy Reinforced Ultra-High Performance Concrete (TARUHPC) has a huge potential for construction of highly durable (100+ years of service life), resilient, and sustainable infrastructure. Research was carried out to investigate the bond-slip relationship between TiABs reinforcing and UHPC. The results are compared against the Normal Concrete beam reinforced with TiABs. Results showed that TARUHPC beams performed exceedingly better with an average ultimate force of about 32 kips and a resulting shear stress of 2 ksi. Since, TARUHPC is an expensive material to carry out significant amount of tests; an explainable data-driven model, based on ensemble learning, is proposed for the bond strength prediction of TiABs in UHPC. Several machine learning models were considered and AdaBoost showed the best performance ($R^2 = 0.93$) for predicting the bond strength of TiABs on UHPC. Utilizing transfer learning, performance comparison of different transfer learning techniques, optimization, comparison with empirical models, and interpretability of the model is still on-going research to accurately define the bond-slip relationship between TiABs and UHPC.



5. References

Acharya, M. and Mashal, M. 2022. Titanium Alloy Bars for Construction of Resilient and Durable Concrete Structures. *12th National Conference on Earthquake Engineering*, Salt Lake City, UT, United States.

Acharya, M., Khadka, R. and Mashal, M. 2021. Preliminary Bond Testing and Splicing of Titanium Alloy Bars. *Transportation Research Record*, 2676(5), 410-427.
<https://doi.org/10.1177/03611981211067785>.

Chen, T. & Guestrin, C., 2016. XGBoost: A Scalable Tree Boosting System. *In Proceedings of the 22nd ACM SIGKDD International Conference on Knowledge Discovery and Data Mining*. New York, NY, USA: ACM, pp. 785–794. Available at:
<http://doi.acm.org/10.1145/2939672.2939785>.

Ho, T.K., 1995. Random decision forests. *In Proceedings of 3rd international conference on document analysis and recognition*. pp. 278–282.

Khadka, R., Acharya, M., Mashal, M. and LaBrier, D. 2022. Visualization of Macroscopic Structure of Concrete Based on X-ray Computed Tomography using Immersive Environments. *HCI 2022*, Springer, Cham. https://doi.org/10.1007/978-3-031-05939-1_2.

Khadka, R., Mashal, M., and Cantrell, J. 2020. Experimental Investigation on Mechanical Properties of Titanium Alloy Bars: Comparison with High-Strength Steel. *Special Publication of American Concrete Institute. ACI Symposium Publication Vol 341 (8)*. 160-187.

Schapire, R.E., 2013. Explaining adaboost. In *Empirical inference*. Springer, pp. 37–52.

Thapa, A., Mashal, M. and Acharya, M. 2022. Large-Scale Flexural Testing of Concrete Beams Reinforced with Conventional Steel and Titanium Alloy Bars. *International Association for Bridges and Structural Engineering (IABSE) Symposium*, Prague, Czech Republic.



Design of Ultra-High Performance Concrete Bridges

Benjamin Graybeal^{1*} and Rafic Helou²

¹: U.S. Federal Highway Administration, Washington, DC, USA; benjamin.graybeal@dot.gov

²: U.S. Federal Highway Administration, Washington, DC, USA; rafic.helou@dot.gov

*: corresponding author

Keywords: ultra-high performance concrete; UHPC; codes and specifications; structural design; engineering mechanics

1. Introduction

Advancements in concrete technology have led to a new structural material becoming available for use in bridge design, construction, and rehabilitation — ultra-high performance concrete (UHPC). As with any novel structural material, the new standards, specifications, and guidance covering the use of the material need to be developed so that engineering practice can safely and appropriately engage whatever advantages are associated with the new material. In the bridge sector in the United States, there is a groundswell of interest in potential structural applications of UHPC, particularly those which engage the enhanced mechanical and durability properties of UHPC to create longer span, lighter weight, resilient, and exceptionally durable structures. The U.S. Federal Highway Administration's UHPC research and development program has been at the forefront of developing needed structural design guidance and engineering property test methods, leading to a series of notable advancements that will facilitate the use of UHPC in the U.S. bridge sector. Central to this effort is the publication of report titled *Structural Design with Ultra-High Performance Concrete* that includes draft structural design guidance, draft material conformance guidance, and a pair of structural design and analysis examples (Graybeal and Helou 2023).

2. Material Performance and Conformance

The distinct material properties of UHPC both facilitate novel applications and necessitate the engagement of new test methods and conformance requirements. UHPC-class materials provide mechanical resistance that surpasses that expected from conventional and high performance concretes. The tensile mechanical behavior of UHPC is a defining characteristic of the material, with UHPCs exhibiting a cracking strength greater than 5 MPa and a sustained or increasing post-cracking strength through a localization strain of at least 0.0025. The localization strain is the elongation at which the material ceases to display a response with multiple, tightly-spaced cracks and begins to exhibit excessive widening of a single, dominant crack. Reliance on the tensile response of UHPC within the design of structural components necessitates the reliance on test methods that assess and verify the assumed behaviors. To this end, a test method akin to that used for structural metals has been developed, refined, and standardized in the United States (Graybeal and Baby 2013, AASHTO 2022). The AASHTO T 397 *Standard Method of Test for Uniaxial Tensile Response of Ultra-High Performance Concrete* provides the testing and



analysis methodologies required for the direct determination of key engineering properties necessary for structural design.

As with any structural material being used in an engineered system, the engineering properties that are relied upon for system performance must be verified as being available. This verification is commonly completed through material conformance specifications which delineate the fundamental properties that a material must exhibit, the methods for assessing the properties, and the processes for ensuring that the delivered product is acceptable. For UHPC, key performance metrics are the compressive mechanical response, the tensile mechanical response, and the durability. Additional prescriptive material conformance requirements related to required constituents, minimized contaminants, and casting and curing processes are also commonly stated. In support of AASHTO's efforts to promulgate UHPC structural design guidance for the US bridge sector (discussed below), the need for companion material conformance guidance is being addressed by the authors who have drafted a framework that is expected to be refined then balloted by AASHTO in 2024. A working draft of the material conformance guidance can be found in Graybeal and Helou (2023).

3. Structural Design Guidance for Ultra-High Performance Concrete

Efficient and appropriate use of structural materials requires that the fundamental behaviors of the material are understood and engaged safely within a structural system. A first principles-based approach, wherein engineering mechanics is heavily engaged as a predictive tool within the design process, is a common method for ensuring that new materials can be used in disparate applications without incurring undue risk. Although existing analysis and design methodologies for conventional concrete can be informative, any methodologies that rely on empiricism must be carefully considered before being engaged for a new class of concrete. To address the demand for US-based UHPC structural design guidance, the US Federal Highway Administration is executing a long-running program to conduct applied engineering research on UHPC structural components and to develop structural design guidance for use in the bridge sector.

During the 2018-2023 timeframe the research group completed a series of studies investigating UHPC material behaviors (El-Helou et al. 2022, Haber et al. 2018), flexural performance (El-Helou and Graybeal 2022a), beam shear performance (El-Helou and Graybeal 2022b, 2023), interface shear performance (Muzenski et al. 2022, 2023), and pretensioning loss behaviors (Mohebbi and Graybeal 2022, Mohebbi et al. 2022). The results of these studies, in conjunction with research and standardized guidance developed elsewhere, were combined to create a framework for the design of UHPC structures. Through work with AASHTO's Structural Concrete Design Committee, a *Guide Specification for Structural Design with UHPC* has been drafted and is being balloted in May 2023. Once passed and published, this document will allow for the design of UHPC structural components within an engineering mechanics-based framework that relies on fundamental properties of the material which have been determined through direct testing methods. The FHWA-developed draft of the *Guide Specification for Structural Design with UHPC* can be found in Graybeal and Helou (2023).

4. Compelling Applications

The interest in using UHPC for engineered structures is founded upon the recognition that some existing challenges are not being appropriately addressed by existing solutions. As evidenced by



the perspective offered in Graybeal et al. (2020), UHPC's novel properties can allow for the design and delivery of lighter, longer-spanning structures, far more durable structures, and elegant structures that facilitate combination of form and function. In the surface transportation infrastructure sector, one such compelling application is in bridge superstructures. UHPC elements, including pretensioned girders, post-tensioned segmental boxes, and spliced girders, can resist greater structural demands through enhanced mechanical properties and reduced dead load, leading to longer spans and shallower structures. For example, grade separation highway interchanges might go from including four spans to including two spans; also, highway viaducts and approaches to long-span bridges could be constructed with longer spans and fewer piers.

Another compelling application is precast, prestressed piles. The mechanical and durability properties of UHPC allow for the delivery and installation of piles that 1) are lighter and thus easier to transport and handle, 2) are able to be driven more rapidly using larger equipment, and 3) are far more durable than existing steel or conventional concrete solutions. This application is particularly relevant in coastal areas that commonly need to construct infrastructure in locations with environmentally aggressive subsurface conditions.

Further examples include local elements within portions of structures that are subjected to harsh environments. The use of UHPC overlays for bridge decks subjected to deicing salts is continuing to gain adherents as the value in lengthening the lifespan of existing infrastructure is recognized. The use of precast UHPC shells for mass concrete pours in aggressive environments is also gaining attention as it is recognized that this solution can offer both accelerated construction and enhanced long-term durability.

5. Concluding Remarks

As novel structural concepts centered on the advantageous mechanical and durability properties of UHPC continue to be developed, there is a greater need for formal UHPC material conformance and structural design guidance. The U.S. Federal Highway Administration's decades of work in this topic area is being leveraged by AASHTO to facilitate the drafting, balloting, and delivery of the needed guide specifications. It is anticipated that these publications will enable owners, designers, and constructors to broadly and consistently engage UHPC within their normal practice of delivering safe, reliable, and resilient infrastructure.

6. References

AASHTO. 2022. *Standard Method of Test for Uniaxial Tensile Response of Ultra-High Performance Concrete*. T 397-22. Washington, DC: American Association of State Highway and Transportation Officials.

El-Helou, R., and B. Graybeal. 2022a. "Flexural Behavior and Design of Ultrahigh-Performance Concrete Beams." *Journal of Structural Engineering*, 148(4), doi: 10.1061/(ASCE)ST.1943-541X.0003246.

El-Helou, R., and B. Graybeal. 2022b. "Shear Behavior of Ultrahigh-Performance Concrete Pretensioned Bridge Girders." *Journal of Structural Engineering*, 148(4), doi: 10.1061/(ASCE)ST.1943-541X.0003279.



El-Helou, R., and B. Graybeal. 2023. “Shear Design of Strain-Hardening Fiber-Reinforced Concrete Beams.” *Journal of Structural Engineering*, 149(2), doi: 10.1061/JSENDH.STENG-11065.

El-Helou, R., Z. Haber, and B. Graybeal. 2022. “Mechanical Behavior and Design Properties of Ultra-High Performance Concrete.” *ACI Materials Journal*, 119(1), 181-194, doi: 10.14359/51734194.

Graybeal, B., and F. Baby. 2013. “Development of Direct Tension Test Method for Ultra-High-Performance Fiber-Reinforced Concrete.” *ACI Materials Journal*, 110(2), 177–186.

Graybeal, B., E. Brühwiler, B.-S. Kim, F. Toutlemonde, Y. Voo, and A. Zaghi. 2020. “International Perspective on UHPC in Bridge Engineering.” *ASCE Journal of Bridge Engineering*, 25(11), doi: 10.1061/(ASCE)BE.1943-5592.0001630.

Graybeal, B., and R. Helou. 2023. *Structural Design with Ultra-High Performance Concrete*. Report No. FHWA-HRT-23-077. Washington DC: Federal Highway Administration.

Haber, Z., I. De la Varga, B. Graybeal, B. Nakashoji, and R. El-Helou. 2018. *Properties and Behavior of UHPC-Class Materials*. Report No. FHWA-HRT-18-036. Washington, DC: Federal Highway Administration.

Mohebbi, A., and B. Graybeal. 2022. “Prestress Loss Model for Ultra-High Performance Concrete.” *Engineering Structures*, 252: 113645, doi: 10.1016/j.engstruct.2021.113645.

Mohebbi, A., B. Graybeal, and Z. Haber. 2022. “Time-Dependent Properties of Ultrahigh-Performance Concrete: Compressive Creep and Shrinkage.” *Journal of Materials in Civil Engineering*, 34(6), doi: 10.1061/(ASCE)MT.1943-5533.0004219.

Muzenski, S., Z. Haber, and B. Graybeal. 2022. “Interface Shear of Ultra-High Performance Concrete.” *ACI Structural Journal*, 119(1), 267–280, doi: 10.14359/51733008.

Muzenski, S., Z. Haber, and B. Graybeal. 2023. “Monolithic and Non-Monolithic Interface Shear Performance of Ultra-High Performance Concrete.” *Engineering Structures*, 281: 115667, doi: 10.1016/j.engstruct.2023.115667.



Axial Compression Performance of UHPC Filled Square Duplex Stainless Steel Tube Short Columns

Hongyuan Tang^{1*}, Xiaowei Hu², Jinjun Liu³, and Duan Hong⁴

¹: Xihua University, Chengdu, China; email: tanghyseu@163.com

²: Xihua University, Chengdu, China; email: 549936159@qq.com

³: Xihua University, Chengdu, China; email: 1670495023@qq.com

⁴: Xihua University, Chengdu, China; email: 2443515688@qq.com

*: corresponding author

Keywords: concrete-filled steel tube; duplex stainless steel; UHPC; axial compression; calculation model

Abstract: In order to study the axial compressive behavior, nine UHPC filled duplex stainless steel tube (UFSST) short columns, three concrete filled conventional carbon steel short columns, and three hollow duplex stainless steel tube specimens are designed. The main parameters include the thickness of duplex stainless steel tube and the strength of core concrete. The results show that the confinement coefficient is the main factor influencing the failure mode and ultimate capacity of UFSST short column. With the increase of thickness of the tube from 4 mm to 8 mm, the failure mode of UFSST short columns changed from shear type to "waist drum" type. And the average increase rate of ultimate bearing capacity of UFSST short columns is 55.43%, the average increase rate of ductility is 17.45%. Based on the test results and confined concrete model of Mander, the prediction formula of ultimate bearing capacity of UFSST short column with good accuracy is established by superposition principle.

1. Introduction

Ultra-high performance concrete (UHPC) is a kind of hydraulic cementitious material with ultra-high strength and good crack resistance under dynamic load. A lot of researches Domestic have been carried out on the mechanical properties of UHPC filled steel tube (UFST) columns. However, at present, there are relatively few studies on the UHPC filled stainless steel tube (UFSST) columns. In order to understand the mechanical properties of the UFSST with cross section, such as the failure mode, axial load-displacement curve, and the interaction mechanism between square stainless steel tube and UHPC, the axial compression tests of 12 UFSST with square cross section short columns are carried out in this paper, Taking the thickness of the outer stainless steel tube and the strength of core concrete as the main parameters, the purpose is to provide theoretical basis and experimental reference for the structures.

2. Experimental Program

2.1. Specimens design

The test designed square short column specimens with three thicknesses (4 mm, 6 mm and 8 mm), three concrete strength grades (C40, UHPC120 and UHPC150), nominal height of 360 mm

and a group of hollow square stainless steel tube short column specimens. The main parameters of each test specimen are shown in Table 1.

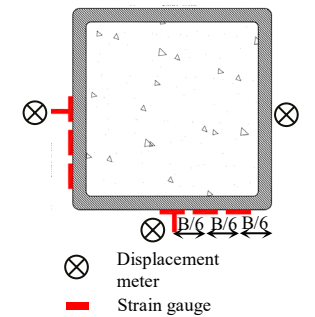
Table 1. Main parameters and test results of specimens

Specimen number	t_{test}/mm	B_{test}/mm	L_{test}/mm	$\rho_s/\%$	N/kN
S-0-4	4.63	119.27	360.5	-	1501.6
S-0-6	6.34	119.00	360.2	-	2742.6
S-0-8	8.32	118.04	360.5	-	3600.3
S-40-4	4.42	119.28	361.5	19.52	2140.4
S-40-6	6.28	118.57	360.2	29.37	3037.4
S-40-8	8.53	118.04	361.0	41.40	3952.7
S-120-4	4.54	119.00	360.9	19.98	2869.8
S-120-6	6.44	118.62	361.5	30.09	3429.5
S-120-8	8.02	117.91	360.5	39.06	4284.6
S-150-4	4.45	119.29	360.5	19.65	2720.8
S-150-6	6.48	118.75	361.2	30.30	3423.4
S-150-8	8.29	117.71	361.5	40.20	4395.7

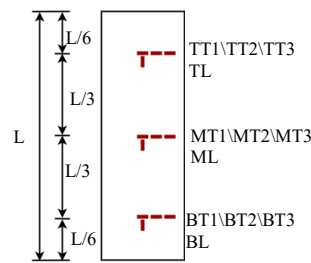
Note: t_{test} , B_{test} , and L_{test} are the thickness, width, and height of the outer stainless steel tube, respectively. Steel ratio $\rho_s = A_s/A_c$, where A_s and A_c are the cross-sectional area of the outer stainless steel tube and the core concrete, respectively. N is the tested ultimate bearing capacity.

2.2. Measurement scheme and loading system

The arrangement of strain gauge is shown in Fig. 1. The data of displacement gauge, pressure sensor and strain gauge are automatically collected by DM-YB1860 dynamic and static test and analysis system. The loading device is shown in Fig. 2.



(a) The vertical view of strain gauge



(b) Schematic diagram of strain gauge arrangement



(a) loading device

Fig. 1. Measurement arrangement

Fig. 2. Loading device

3. Experiment Results and Analyses

3.1. Failure modes of specimens

The failure modes of specimens are shown in Fig. 3. The specimen is always in the collaboration state of core concrete and stainless steel tube during the whole loading process. For the specimen with smaller thickness, the specimen shows shear failure, as shown in Figs. 3(c) and 3(m). For

the specimen with larger thickness, the failure of the specimen is "waist drum" type as shown in Figs. 3(g) and 3(n).

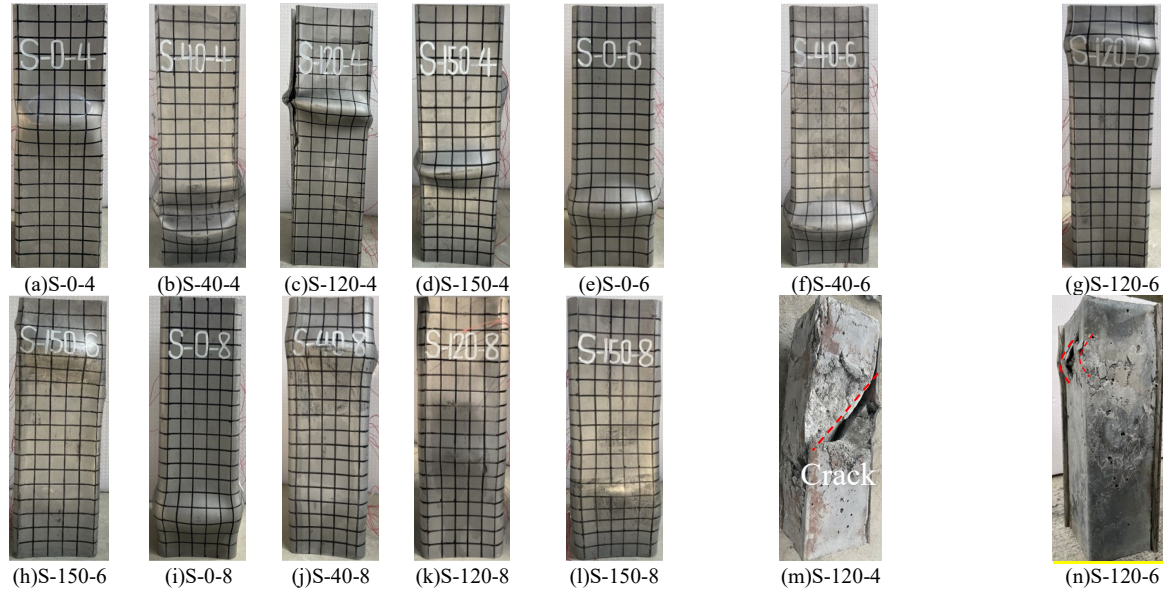


Fig. 3. Failure model of specimens

3.2. Axial load-displacement curve

The axial load-displacement curve of hollow stainless steel tube is shown in Fig. 4 (a). With the increase of the thickness of the stainless steel tube, the ultimate bearing capacity is significantly improved. Specimens S-0-6 and S-0-8 exhibit obvious strain hardening behavior, while specimen S-0-4 has almost no strain hardening behavior.

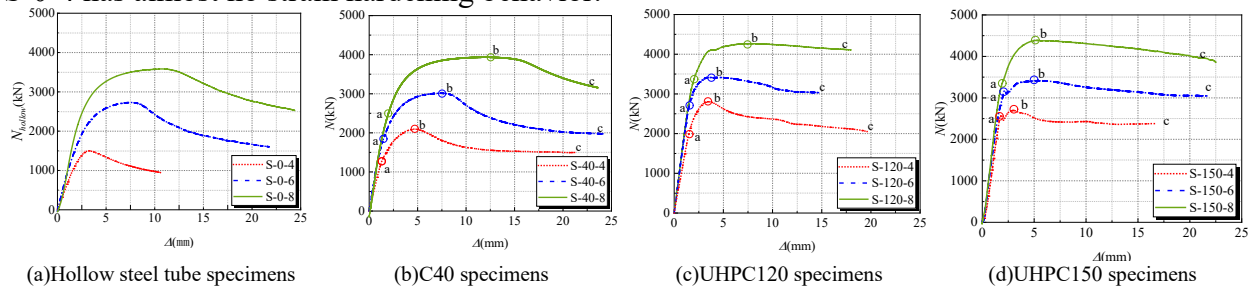


Fig. 4. Axial load-displacement curves of specimens

Figs.4(b)~(d) are the axial load-displacement curves of specimens with ordinary strength concrete and UHPC. The development trend of the curves can be divided into elastic stage (0-a section), elastic-plastic stage (a-b section) and plastic flow stage (b-c section).

4. Calculation of Axial Compression Bearing Capacity

4.1. Lateral effective restraint stress reduction factor

In this study, it is assumed that the effective constraint zone of the UHPC filled square duplex stainless steel tube short columns is within $(t+2At)$ from the outer edge of the specimen, the area within $(B-2t-2At)$ of the specimen edge is the weak constraint zone, B is the outer diameter of the

specimen, t is the wall thickness of the stainless steel tube, A is the multiple undetermined coefficient of the distance from the edge of the effective restraint zone to the inner wall of the stainless steel tube and the thickness of the stainless steel tube, and the boundary equation of the weak constraint zone is assumed to be a quarter arc, see Fig. 5.

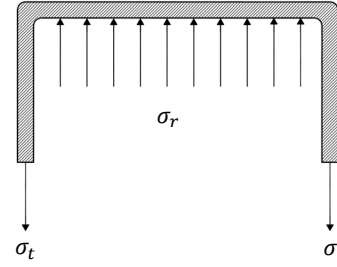
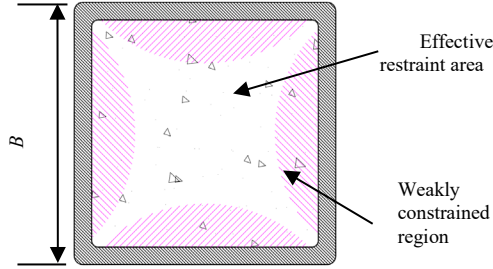


Fig. 5. Core concrete effective restraint area **Fig. 6.** Force diagram of the square stainless steel tube

4.2. Calculation method of axial compression bearing capacity

According to Sakino et al, under the ultimate bearing capacity state, the longitudinal stress σ_l and transverse stress σ_t of steel tube is given by:

$$\sigma_l = 0.89\sigma_{0.2} \quad (1)$$

$$\sigma_t = 0.19\sigma_{0.2} \quad (2)$$

According to the stress equilibrium condition shown in Fig. 6, the constraint stress of steel pipe on core concrete under ultimate load state is as following:

$$\sigma_r = \frac{2t\sigma_t}{B-2t} \quad (3)$$

Based on YAN et al, the lateral effective restraint stress is determined by:

$$\sigma'_r = K_{et}\sigma_r \quad (4)$$

According to the constrained concrete model proposed by Mander et al, the axial compressive strength of core confined concrete is determined through Eq. (3):

$$f_{cc} = f_{ck} \left(-1.254 + 2.254 \sqrt{1 + 7.94 \frac{\sigma'_r}{f_{ck}} - 2 \frac{\sigma'_r}{f_{ck}}} \right) \quad (5)$$

A_s is the cross section area of stainless steel tube, and is given by:

$$A_s = 4(c-t)t \quad (6)$$



where, c and t are the width and thickness of the outer square stainless steel tube.

The axial compression bearing capacity of square UFSST column is calculated by the superposition principle, as shown in Eq. (5):

$$N_{uc} = f_{cc}A_c + \sigma_l A_s \quad (7)$$

5. References

Mander, J. and Priestley, M. 1988. Theoretical Stress-Strain Model for Confined Concrete, *Journal of Structural Engineering*, 114(8),1804-1826.

Sakino, K., Nakahara, H., and Morino, S. 2004. Behavior of Centrally Loaded Concrete-Filled Steel-Tube Short Columns, *Journal of Structural Engineering*,130(2), 180-188.

YAN, Yanxiang., XU, Lihua., and CAI, Heng. 2019. Calculation methods of axial bearing capacity of short square UHPC filled high strength steel tubular columns, *Journal of Building Structures*, 40(12), 128-137.



Seismic Retrofit of Precast and Cast-in-Place Piers Using Ultra High-Performance Concrete (UHPC)

Kathryn Hogarth¹, Manish Acharya², Arya Ebrahimpour³, and Mustafa Mashal^{4*}

¹: Idaho State University, Pocatello, Idaho, United States; email: hogakat2@isu.edu

²: Idaho State University, Pocatello, Idaho, United States; email: manishacharya@isu.edu

³: Idaho State University, Pocatello, Idaho, United States; email: ebraarya@isu.edu

⁴: Idaho State University, Pocatello, Idaho, United States; email: mashmust@isu.edu

*: corresponding author

Keywords: Bridge Piers; Seismic Retrofit; UHPC; Concrete Jacket; Large-scale Testing

Abstract: Recently Idaho State University completed large-scale experimental and analytical investigation of a new precast pier system for applications in seismic zones. The precast pier system uses the concept for Concrete Filled Steel Tubes (CFSTs) in plastic hinge locations. Extensive testing on precast cantilever and bent piers was conducted to investigate seismic performance under quasi-static cyclic loads. Results were compared against benchmark cast-in-place specimens. Testing showed superior performance of the precast pier compared to cast-in-place. Based on the experimental results, the precast pier technology was implemented in an actual bridge located in seismic zone in Idaho. For wider applications of the precast pier technology, it is important to investigate appropriate retrofitting strategies for post-earthquake repair. Some of the proposed methods to retrofit CFSTs have only been investigated analytically and have not been experimentally tested. There is a critical need for experimental results to validate the analytical models before any retrofitting methodologies may be implemented onsite. In this research, concrete jacketing using Ultra High-Performance Concrete (UHPC) is proposed as an innovative retrofitting strategy for the precast pier. UHPC offers advantages such as high strength, excellent durability, smaller jacket thickness, accelerated construction, strong bond with hardened concrete and reinforcing bars, among other benefits. The UHPC jacket is intended to re-instate the pier's stiffness, strength, and ductility after the earthquake. In this research, four damaged columns will be tested; two precast columns incorporating CFSTs in plastic hinges and two cast-in-place columns as benchmark specimens. The research will show if the specimens retrofitted with UHPC jackets have comparable seismic performance to the original specimens.

1. Introduction

This project focuses on the retrofitting of concrete bridge piers. In the first phase of the project, two half-scale bridge bents were designed and experimentally tested in the Idaho State University (ISU) Structural Lab (SLAB) under earthquake style loading. One of the bents modeled a typical cast-in-place (CIP) bridge connection, while the other bent modeled a pier connection developed by ISU and Idaho Transportation Department (ITD). The design of the bridge connection incorporating CFSTs can be seen in Figure 1. Both bridge bents were tested to

failure and the results were processed and compared to one another. After testing of the bents, the piers have been dismantled and are to be retrofitted for testing.

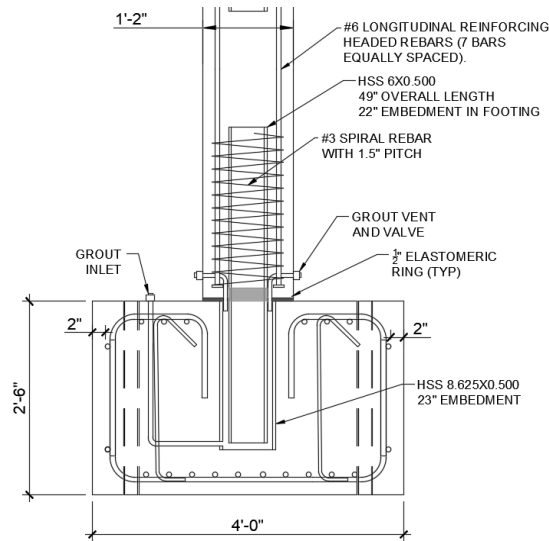


Fig. 1. Pipe-Socket Connection for Column-to-Footing Connection (1’=30.4cm, and 1”=2.54cm)

2. Literature Review

A literature review of retrofitting methods for bridge piers was conducted and investigated methods including steel jacketing, concrete jacketing, fiber reinforced polymers (FRP), and external yielding elements. The most ideal retrofit method found was the use of ultra-high-performance concrete (UHPC) jacketing. Normal Strength Concrete (NSC) has lower strength compared to UHPC in both compressive and tensile strength. UHPC's strength spans from 124.11 to 227.5 MPa, which is significantly higher than NSC's compressive strength, which is only between 20.7 and 41.3 MPa. Additionally, UHPC's tensile strength is higher than NSC's, with a range of 6.89-24.13 MPa compared to NSC's range of 2.75-3.45 MPa.

2.1 UHPC Jacketing Literature Review

A study by (Farzad et al., 2019) investigated the application of UHPC jacketing in bridge repair strategies. The results indicated that this approach significantly improved the lateral strength, deformation, energy dissipation capacity, and stiffness deterioration of the structure. Additionally, (Joe and Moustafa, 2016) demonstrated that utilizing UHPC instead of conventional concrete in bridge piers has several advantages. Not only does it require 75% less material, it is also better for the environment as it can lower the carbon footprint by up to 35% when used with a compressive strength of about 172.37 MPa. Due to these benefits, the number of UHPC bridges is growing each year. As of 2020, there were 341 in-service bridges in the United States that use UHPC, and the trend is increasing each year (Office of Research, Development, and Technology at the Turner-Fairbank Highway Research Center, 2021).

3. Concept for Retrofit

After literature review, the basis of retrofitting the precast pier is to utilize a UHPC jacket in the plastic hinge zone of the pier. The concept can be seen in Figure 2.

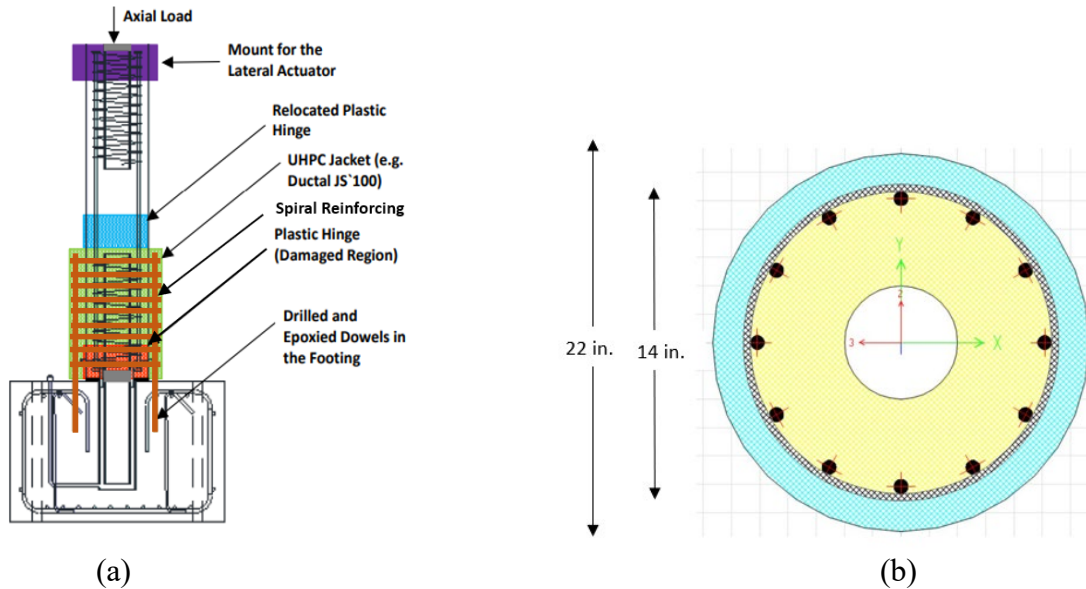


Fig. 2. Overall Concept for Retrofit: (a) Concept for UHPC Jacket (Green); (b) Cross-section of Precast 1 Retrofit (1 in. = 2.54 cm)

Note that since the pipe in this specimen is fractured, the moment capacity contribution from the pipe is taken to be negligible (i.e., a conservative assumption). Also note that for this specimen all of the cover concrete spalled, therefore the entire section, excluding the pipe, is taken to be UHPC. The jacket is designed to sit at a 4 in. (10.16 cm) thickness out from the original column diameter (14 in. or 35.56 cm), with an overall diameter of 22 in. (55.88 cm). After the success of Precast 1, Precast 2 is constructed without caging, but with the jacket thickness of 4 in. (10.16 cm). Following the success of Precast 1 and Precast 2 piers, CIP 1 and CIP 2 are retrofitted with smaller jackets of 3 in. (7.62 cm) and 2 in. (5.08 cm), respectively.

4. Construction and Test Set-up

The first step for construction is to roughen the surface for the pour, as well as drill the concrete to allow for the tension dowels to be epoxied in. The next step is to assemble the cage. (Note, only Precast 1 has epoxied dowels and caging). Lastly, the form is assembled and the UHPC is poured. Note that the jacket is poured while the pier is under a 30-kip (133kN) axial load to simulate the structure of a bridge. After the pier is poured and cured, the pier is instrumented and moved into the lab to get ready for testing. The test is accomplished by programming the hydraulic actuator to run a loading protocol similar to the bent loading protocol, which has been scaled down for one pier. The loading protocol is a quasi-static cyclic loading.

5. Results

A summary of the testing results can be seen in Table 1. Furthermore, Figure 3 gives the backbone curves for the piers.

Table 1. Summary of Results

	Precast 1	Precast 2	CIP 1	CIP 2
Maximum Force	30.76 kip (136.83 kN)	30.65 kip (136.34 kN)	25.08 kip (111.56 kN)	25.2 kip (112.1 kN)
Maximum Drift	7.38%	9.38%	9.81%	10.19%
Moment Capacity from Top of Jacket	133.3 kip-ft. (180.73 kN-m)	132.82 kip-ft. (180.08 kN-m)	108.68 kip-ft. (147.35 kN-m)	109.2 kip-ft. (48.06 kN-m)
Initial Yield Drift	0.76%	0.95%	1.22%	1.07%
Dissipated Energy	216.5 kJ	262.7 kJ (154.1 kJ)*	316.08 kJ (167.4 kJ)*	322.76 kJ (127.4 kJ)*

* corresponding energy dissipated at 7.38% drift (failure of Precast 1)

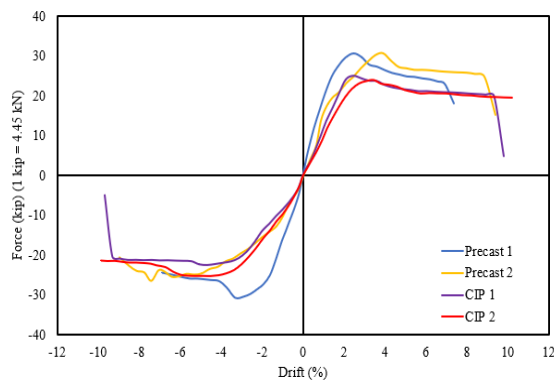


Fig. 3. Backbone Curves of Bridge Piers

6. Conclusion

This project covers seismic retrofit of pipe-socket connected piers. The project investigated the suitability of UHPC jacketing methods. For Precast 1, a 4 in. (10.16 cm) UHPC jacket is used with light caging. Precast 2 incorporated a 4 in. (10.16 cm) UHPC jacket with no caging. Both methods for retrofit were successful. Precast 1 pushed the plastic hinge up the column face with no separation from the footing. Precast 2 succeeded in pushing the plastic hinge up the face of the column with separation from the footing and partial failure due to rocking. CIP 1 incorporated a 3 in. (7.62 cm) UHPC jacket, and CIP incorporated a 2 in. (5.08 cm) UHPC jacket. CIP 1 and 2 were both successful in pushing the plastic hinge up the face of the column. CIP 1 had little to no gap opening, while CIP 2 had a larger gap opening, likely due to the smaller jacket size. Large-scale testing has recently been completed at ISU, further data will be presented and published as it is analyzed.

7. References

Farzad, M., Shafieifar, M., and Azizinamini, A. 2019. Retrofitting of bridge columns using UHPC, *Journal of Bridge Engineering*, 24(12).

Joe, C.D. and Moustafa, M. 2016. Cost and ecological feasibility of using UHPC in Bridge Piers. *First International Interactive Symposium on UHPC*.

Office of Research, Development, and Technology at the Turner-Fairbank Highway Research Center. 2021. *Deployments: Deployments of UHPC in Highway Bridge Construction*.



Bridge Engineering Institute Conference 2023 (BEI-2023)
Rome, Italy, July 17-20, 2023



Railway Bridges

Numerical Investigation of Aerodynamic Characteristics of High-Speed Railwaytrain-Bridge System under Tornado-Like Winds

Xuhui He¹ and Simin Zou^{2*}

¹: School of Civil Engineering, Central South University, Changsha, China;
National Engineering Research Center for High-Speed Railway Construction, Changsha, China
email: xuhuihe@csu.edu.cn

²: School of Civil Engineering, Central South University, Changsha, China;
National Engineering Research Center for High-Speed Railway Construction, Changsha, China;
email: simin_zou@csu.edu.cn

*: corresponding author

Keywords: Tornado; High-speed railway; Trains; Bridges; Aerodynamic characteristics

Abstract: As the high-speed railway emerges in Eurasia, a comprehensive understanding of the aerodynamic problems – particularly extreme wind events – is vital to the success of the safety, operational efficiency, and transportation industry. In addition to very high and transient wind speed in a relatively short time, some key distinguishing attributes of the winds associated with tornadoes are the swirling winds with multiple wind directions and the probable existence of a very different wind profile. Such knowledge of the effect of extreme wind on the train and bridge system has been hindered by a lack of available field test data. However, limited full-scale data along the height and radial position are available to identify and reliably establish a description of this wind velocity profile and field with their effect on the high-speed train. In light of limited full-scale data to arrive at a consensus on quantifying key parameters characterizing the tornado winds, the wind field associated with each component of tornado winds, such as the velocity field and pressure field and propagation to load effects on the high-speed railway train-bridge system are carried out using high-fidelity computational fluid dynamics (CFD) in this study.

1. Introduction

Compared with other transportation means, the high-speed railway has many advantages: high efficiency, energy-saving significantly and smooth operation, therefore, it has been widely developing globally (He & Zou, 2021). Considering the high-speed train need to run in a very coordinated, straight-line fashion sustaining locomotion for a considerable time, the bridges have been widely used as a vital component in the high-speed railway (HSR) network worldwide. For example, the Japanese HSR system has an average bridge ratio of 47% and Chinese Taiwan is reported as 73%. The average bridge occupation ratio is greater than 50% and the Beijing-Shanghai Express railway reaches 97% in China. In addition, the frequency of severe tornado disasters worldwide has been rising and higher and China has not been spared. According to statistics, there has been an annual average of more than 43 tornadoes in the past 50 years, frequently occurring in recent years with a far larger rate than previous estimates. The worst tornado of all time occurred in 2016, an EF4 tornado affecting the city of Yancheng in Jiangsu Province, which killed 99 people and injured more than 800 people. It should be noted that

almost all tornadoes occur each year in eastern China (especially in Jiangsu and Guangdong), but the location of a single tornado does not significantly affect laws. However, there is a high risk of railway exposure to tornadoes amid global warming.

Numerical simulations have a critical role in studying tornadoes' near-surface wind fields. Numerical simulation is more efficient and economical to analyze the three-dimensional velocities and pressure fields due to the strong turbulence motion near the surface and the center of the vortex. Especially numerical simulations can generate complete and detailed data in space and time, which allow for calculations of time-averaged wind speeds, short-term gusts, flow fields, and variations in space and time. Such information is particularly vital to the civil engineering community. With the rapid development in recent years, fast convergence rate, low computational complexity, and excellent numerical stability of the numerical algorithm are the goals we continuously strive to pursue.

In this study, the tornado-induced effect on a high-speed train running on a bridge was calculated numerically by IDDES simulations in a three-dimensional model. In Section 2, the numerical algorithms used in this study were introduced. The details of the tornado simulation and calculation accuracy were discussed in Section 3. The tornado-induced aerodynamic forces acting on a high-speed train were investigated in Section 4. In order to decrease the accident rate of the train and evaluate the aerodynamic performance, the current common height of the train in operation is created and analyzed in this article.

2. Numerical Algorithms

All the simulations presented were completed in the commercial software Ansys Fluent 19.2. The time-dependent IDDES (based on the SST k-w model) used in this paper is a hybrid RANS-LES model. The difficulties associated with using the standard LES models, particularly in near-wall regions, have led to the development of hybrid models that combine the best aspects of RANS and LES methodologies in a single solution strategy (Spalart et al., 1997).

In the DES approach, the unsteady RANS models are employed in the boundary layer, while the LES treatment is applied to the separated regions. The LES region is normally associated with the turbulent core region, where large unsteady turbulence scales dominate. In this region, the DES models recover LES-like subgrid models. In the near-wall region, the respective RANS models are recovered.

The Improved Delayed Detached Eddy Simulation (IDDES) model is a hybrid RANS-LES model (consisting of a combination of various new and existing techniques) that provides a more flexible and convenient scale-resolving simulation (SRS) model for high Reynolds number flows.

3. Tornado Generation

The regression equations of tangential velocity and radial velocity along the height are expressed as follows:

$$V_t = 20.61\left(\frac{z}{20}\right)^{0.1774} \quad (4)$$

$$V_r = \begin{cases} -31.14\left(\frac{z}{20}\right)^{0.169}, & z < 20m \\ 45.14\left(\frac{z}{20}\right)^{0.1826} - 76.48, & z \geq 20m \end{cases} \quad (5)$$

where z is the height above the ground, these wind velocity profiles are used as the input at the velocity-inlet within the inlet height range.

Fig. 1 shows the mesh system of the numerical tornado simulation. In order to accurately capture the flow fields of tornado-like vortices and quantitatively investigate the wind loading on the train in the central part of the convergent zone and the vicinity near the ground, a fine mesh is considered.

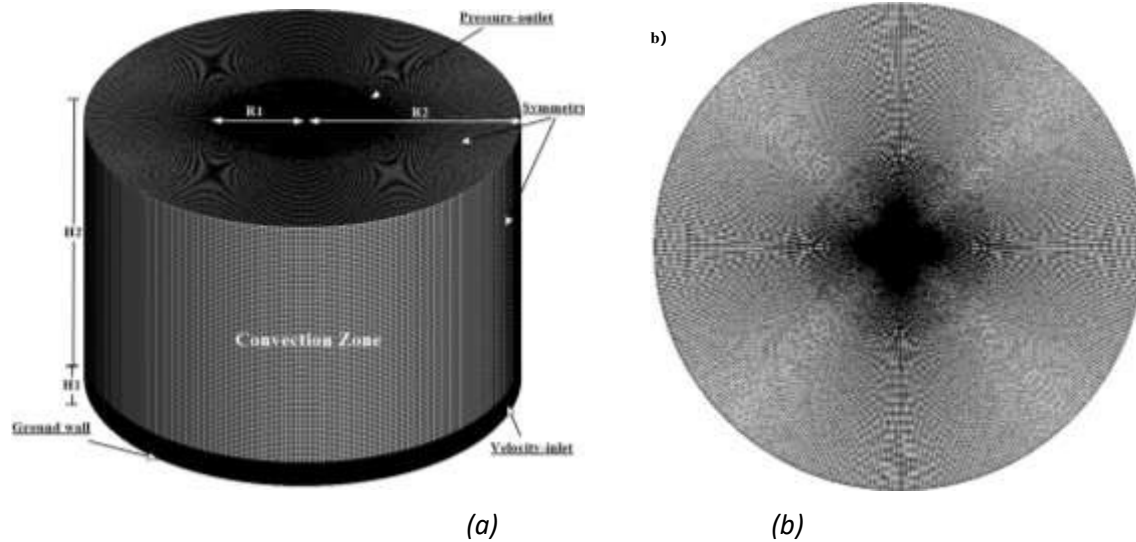


Fig.1 Computational domain and grid layout

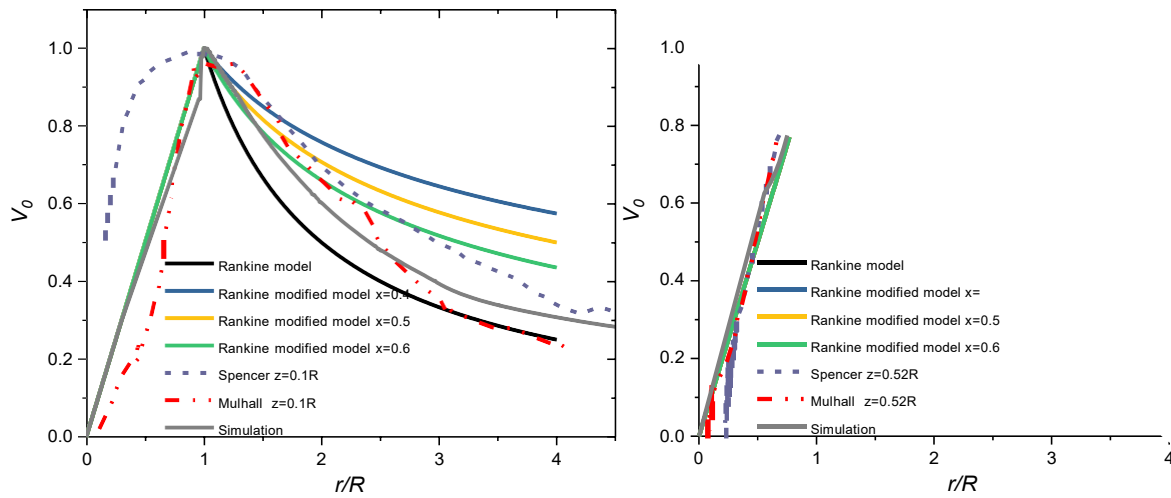


Fig.2 Comparison of the tangential velocity distribution with those of the tornado and model at different heights ($Z=0.1R$ & $Z=0.52R$)

Fig.2 presents the normalized tangential velocity profiles to compare with those of the tornado events and the analytical model. The distance from the vortex center, r , is normalized by the core radius r_m . The velocity of tornado events from full-scale tornados at Spencer, South Dakota, and Mulhall, Oklahoma, recorded by Haan et al.(2008), are plotted with the present result in the figure. For the Rankine model, the overall maximum tangential velocity V_R of each volume and the corresponding radius r_m were used to calculate the tangential velocity in these models. Overall, the simulation result better agrees with the radar data and analytical model.

Also, decay factors of 0.4-0.6 result in a better match with the simulation, consistent with previous studies findings.

4. Tornado Effects on a Running Train on the Bridge

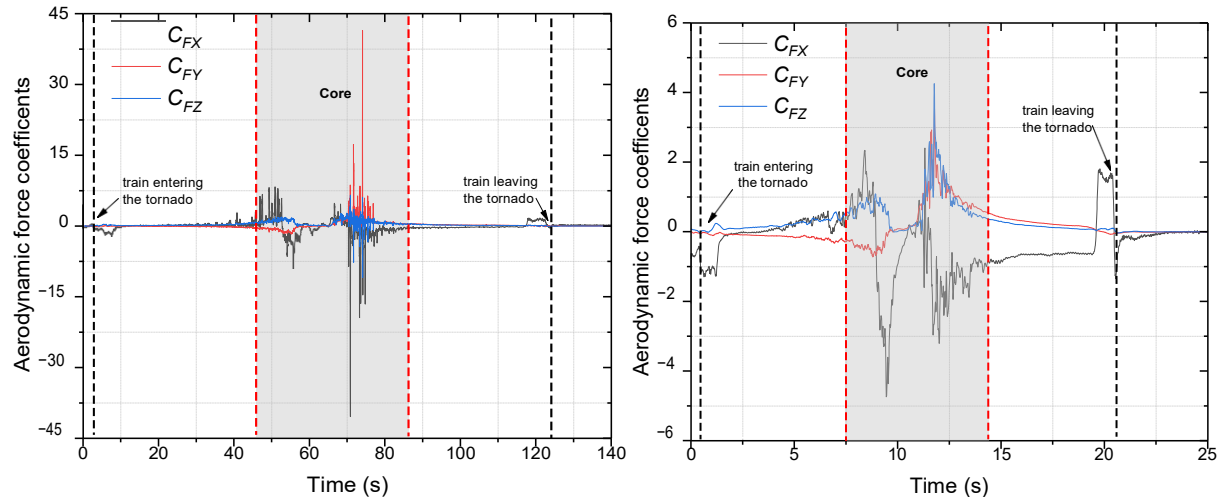


Fig. 3. Time history of aerodynamic forces coefficients

The model train and bridge were made based on a 1:1 scale of the CRH train with three cars and a simply-supported box girder. The bridge is selected to locate about 4.5 m above the ground and along the whole diameter of the tornado. In order to get the historical time forces on the train, the train was tested in a stationary tornado with a train operation speed of 50 km/h and 300km/h. At each location, the time-averaged aerodynamic forces were obtained by simulating the 400s, and the first 10s data were removed to eliminate the transient results. Because of the almost zero tangential velocity at the center of a tornado, the resulting aerodynamic force distribution here does not vary substantially. The absolute values of aerodynamic force coefficients go for a maximum at the core region due to the effect of the tornado's maximum tangential velocity, indicating that the tornado flow has a devastating effect. The large value of C_{Fz} at the $r/R=1$ and beyond should be due to the large vertical wind velocity near its core boundary. It means a ground effect exists when the train and bridge are near the surface and buoyancy on the bridge falls off with the distance from the tornado center. It should be noted that one of the main damage from tornadoes is caused by buoyancy.

5. Conclusion

Improved delayed detached eddy simulation (IDDES) for tornado flow around a train was applied and the results show Aerodynamic forces coefficient of sections varies with distance from the tornado center, the absolute values reach a maximum at $r/R=1$. Meanwhile, enormous buoyancy is generated here due to a ground effect exists. This was the first step toward a realistic simulation that reproduces the effect of a tornado on a running train on the bridge. It should be noted that the train at the different positions in the tornado is still being concerned, more details on the effects of the tornado will be explored further.

6. References

Haan, F.L., Sarkar, P.P., Gallus, W.A. Design, construction and performance of a large tornado simulator for wind engineering applications. *Eng.Struct.* 2008, 30(4),1146-1159.

He X.H, Zou S.M. Advances in wind tunnel experimental investigations of train-bridge systems. *Tunnelling and Underground Space Technology*, 2021,104157.



Effects of Splitter Plates on the VIV Performances of Twin Separated Parallel Decks for a Rail-Cum-Road Bridge

Lulu Liu¹, Xuhui He^{2*}, Yunfeng Zou³, and Zhen Wang⁴

¹: Central South University, Changsha, China; email: liululu2020@csu.edu.cn

²: Central South University, Changsha, China; email: xuhuihe@csu.edu.cn

³: Central South University, Changsha, China; email: yunfengzou@csu.edu.cn

⁴: Central South University, Changsha, China; email: wangzhen@csu.edu.cn

*: corresponding author

Keywords: Splitter plates; Vortex-induced vibration (VIV) ; Wind tunnel test; The rail-cum-road bridges; Computational Fluid Dynamics (CFD)

Abstract: Installing the splitter plates at decks is among the passive aerodynamic solutions for eliminating vortex-induced vibration (VIV). However, the influence of splitter plates on the VIV performances are more complicated due to aerodynamic interference between highway and railway decks. To study the effects of splitter plates, wind tunnel experiments were conducted for measuring VIV performance under two opposite flow directions, while the surrounding flow field of static twin decks with and without splitter plates is numerically simulated by Computational Fluid Dynamics (CFD). A wide range of width (L) varying from 0 to 80 mm for twin asymmetrical parallel models are selected to investigate the effect of splitter plates on VIV performance. The results showed that the incoming flow direction affects the VIV response. The highway deck has poor vertical and torsional VIV performance, and the VIV region and amplitude are different under different locations. While the railway deck only has vertical VIV when located upstream. In addition, the splitter plates can impede the process of vortex generation, shedding and impinging at the gap between the highway and railway deck, thus effectively suppressing the VIV of twin decks.

1. Introduction

The Long span twin parallel bridges are a unique type of rail-cum-road bridges that may greatly increase cross-straits' capacity and enhance transportation. However, wind-induced response problems such as static wind stability and interactive vortex-induced vibration (VIV) of bridges caused by complex inter-gap aerodynamic disturbance effects (Seo et al., 2013). The thin-walled splitter plate is one of the effective measures to control the VIV among passive controls (Akilli et al., 2005). There is little relevant research about the influence of the thin-walled splitter plate on the VIV performance, and the research on splitter plate is always for a single bridge but an integrated evaluation of the overall performance of twin parallel decks. Is this method of splitter plates on VIV-suppression applicable, or are the consequences of the VIV-suppression effect and aerodynamic characteristics on the adjacent bridge more complex? All these issues need to be considered in the study. Therefore, the effect of splitter plate on wind-resistance performance of twin separated parallel decks requires further detailed investigation.

2 Experimental Study of Vortex-Induced Vibration

2.1 Experimental setup

Fig. 1 graphically depicts the span deck cross section. As shown in Figs. 2 and 3, using an independently constructed twin decks model elastic suspension device, the VIV measurement test was carried out at the wind tunnel. Four laser displacement transducers with 500 Hz sampling rates and 30 s sampling times were used to measure the vibration response (see Fig. 2). Vertical and torsional vibration could occur freely in the highway and railway model. The dynamic features of the highway and railway bridges are shown in Table 1. Seven different widths of splitter plates were made from ABS plates and fixed to each side of the twin decks in turn in order to study the VIV-suppress effect of the splitter plates. Wind tunnel experiments were conducted to test the VIV amplitude of the decks under various wind directions. The exact test conditions are shown in Table 2.

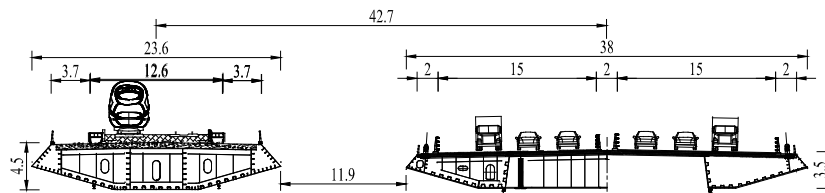


Fig. 1. Cross section at mid-span position (unit: m)

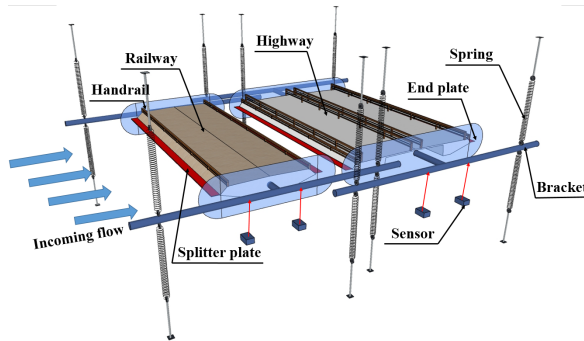


Fig. 2. System for section model testing support

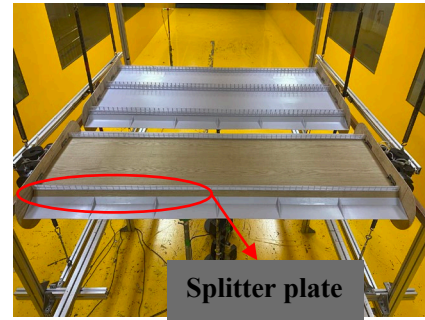


Fig. 3. VIV tests of wind tunnel

Table 1. Dynamic parameters

Parameter	Railway decks		Highway decks	
	bridge	model	bridge	model
Geometric scale λ_s	-	1:50	-	1:50
Mass m (kg/m)	49600	16.28	52500	21
Mass moment of inertia J (kg·m ² /m)	2870000	0.452	2350000	0.376
Vertical frequency f_v (Hz)	0.463	5.371	0.348	4.028
Torsional frequency f_t (Hz)	1.031	11.963	0.856	9.930

Table 2. Test conditions

Cases	Wind directions	Wind angle α	Damping ratio ζ_v/ζ_t	Width of splitter plates (scale model) L (mm)
Case1	Figure 5 (a)	3°	0.34%/0.32%	0, 20, 30, 40, 50, 60, 70, 80

2.2 VIV Performance with Various Splitter Plates

As shown in Fig. 4(a), when the wind blows from the UH to the DR, the vertical VIV displacement of the UH deck gradually decreases with the width of the splitter plate. When the splitter plate width is $L = 50$ mm, one of the VIV regions even disappears directly, the vertical VIV region becomes only one, and the maximum VIV amplitude is 82 mm. When the width increases to $L = 80$ mm, the vertical VIV of the UH deck does not occur at all. As shown in Fig. 4(b), for the torsional VIV, the VIV response gradually becomes weaker as the splitter plate's width increases. When the width is $L = 20$ mm, the torsional VIV region is changed from three to one, and the maximum torsional amplitude is reduced by 20%. As the width of the splitter plates keeping increasing, the amplitude of the torsional VIV continues to decrease, and the speed range continues to decrease. When the width is $L = 50$ mm, the torsional VIV for UH deck completely disappears. And if the width of the splitter plate continues to increase, there is also no torsional VIV. It demonstrates that the splitter plate can successfully reduce the torsional VIV.

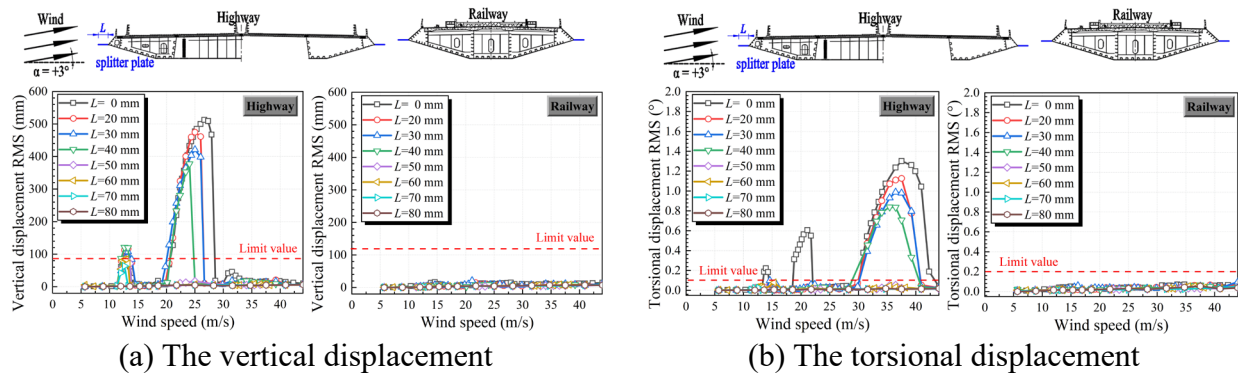


Fig. 4. VIV of the twin decks (Wind blows from UH to DR)

As shown in Fig. 5(a), when the wind blows from the UR to the DH, the vertical VIV displacements and VIV region of the UR and the DH deck also gradually decrease with the splitter plate's width. When the width is $L = 20$ mm, the DH deck's maximum vertical VIV displacement is decreased to 82 mm, which is reduced by 73%, which also meets the requirements of the specification. When the width increases to $L = 50$ mm, the VIV of the UR even disappears directly. The DH deck's vertical VIV amplitude is sensitive to the splitter plate's width. But for the DH decks, As the width of the splitter plate keeping increasing, although the amplitude of the vertical VIV continues to decrease, the amplitude is obviously smaller, but the vertical VIV does not completely disappear until the width is $L = 80$ mm. As shown in Fig. 5(b), for the torsional VIV, with the increase of the splitter plate's width, there is no new torsional VIV phenomenon in the DR deck.

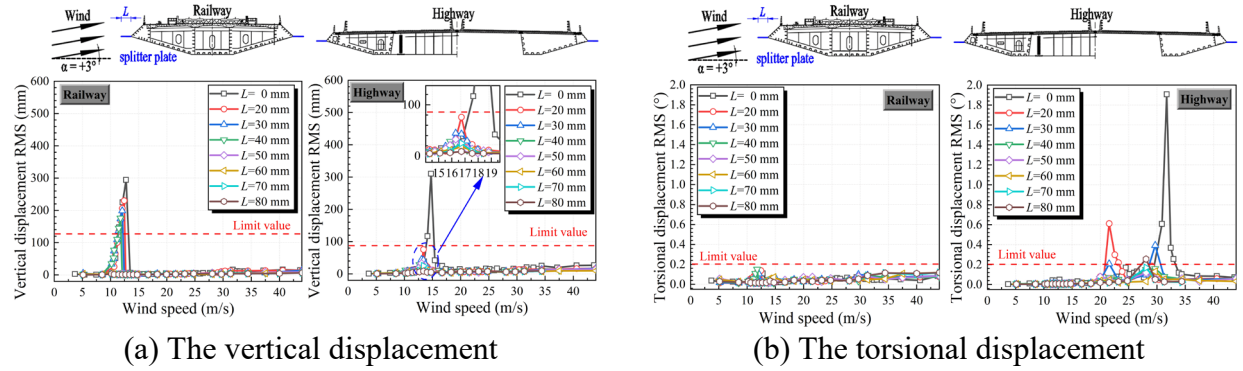


Fig. 5. VIV of the twin decks (Wind blows from UR to DH)

To sum up, the splitter plates on each sides of the twin decks affects the vertical and torsional VIV. It is more appropriate to comprehensively select the width for $L = 50$ mm.

3. Numerical Simulation of Flow Field around Static Decks

2D models of static highway and railway decks was chosen for CFD simulation to examine the influence of splitter plates on the flow visualization. On the basic of the wind tunnel tests parameters, the computational domain settings in the simulations made are shown in Fig. 14. taking the $L = 50$ cm splitter plates as an example, the numerical simulation results are compared with and without the splitter plates on twin decks to analyze the effect of the splitter plates.

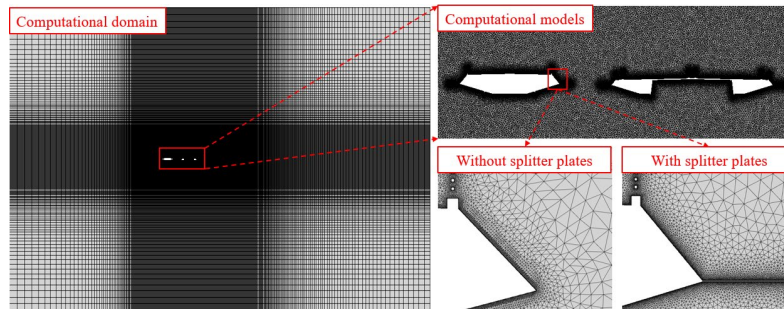


Fig. 6. Layout of computation domain discretization and mesh scheme

As shown in Fig. 7(a), distinct vortices periodically shed from the leeward side of the upper and lower surfaces of the UR deck and then impinged on the windward side of the DH deck. The vortex shed from the UR deck' upper surface flows directly over the upper surface of the DH deck, while the vortex shed from the UR deck' lower surface impinged the winding nozzle of the DH deck. And when the splitter plates were installed on each sides of the twin deck, the splitter plates make the flow field separate in advance and affects its wake shedding. Besides, as shown in Fig. 7(b), the flow around the railway and highway decks becomes smooth and no periodic vortices are generated. In other words, once the splitter plates are installed, the highway and railway bridges tends to be streamlined under the airflow.

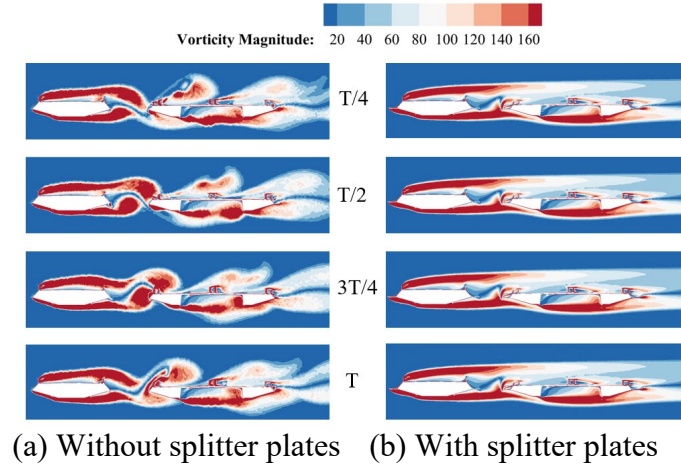


Fig. 7. Vortex contour around twin girders

4. Conclusion

The splitter plates can impede the process of vortex generation, shedding and impinging at the gap between the highway and railway decks, thus effectively suppressing the VIV. So that the incoming flow can flow steadily through the railway deck upstream and the highway deck downstream.

5. References

- Akilli, H., Sahin, B., Filiz Tumen, N., 2005. Suppression of vortex shedding of circular cylinder in shallow water by a splitter plate. *Flow Measurement and Instrumentation* 16, 211-219.
- Seo, J.-W., Kim, H.-K., Park, J., Kim, K.-T., Kim, G.-N., 2013. Interference effect on vortex-induced vibration in a parallel twin cable-stayed bridge. *Journal of Wind Engineering and Industrial Aerodynamics* 116, 7-20

Aerodynamics of a High-Speed Train Crossing the Wake of a Bridge Tower in Different Yaw Angles

Zuyu Xie^{1,2}, Huan Li^{1,2*}, Xuhui He^{1,2}, and Zhirui Huang^{1,2}

¹: School of Civil Engineering, Central South University, Changsha, China; LI Huan
lihuan2016@csu.edu.cn

²: National Engineering Research Center of High-speed Railway Construction Technology, Changsha, China

Abstract: Bridge tower shows different effects obviously in different yaw angles for its windward area varies, which may result in complex wake and cause transportation problems (Wu et al. 2022). This study concentrates on the aerodynamic characteristics of a CRH-3 high-speed train passing through the bridge tower at the yaw angle of 15° and 90° . Shielding Effect of the tower bridge between the yaw angle of $0^\circ \sim 90^\circ$ at the location of the peak value of CFi. is also studied The scaled ratio of the train, bridge and bridge tower are 1:25. In this test, the train is fixed on the bridge and the bridge tower is placed on guideways. Aerodynamic force of the train is tested with the change of location of the bridge tower. The experiment is tested in a close-loop low-speed wind tunnel. The test section is 12m in width, 3.5m in height, and 18m in length. The wind speed in the low-speed section can vary from 0 to 25 m/s, with the turbulence intensity lower than 0.5%.The test model is shown in Fig.1.

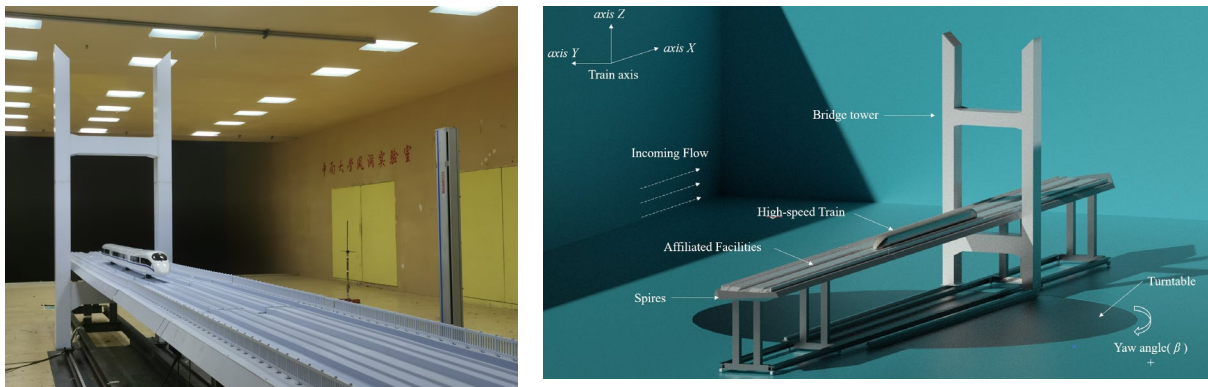


Fig. 1. Layout of test

For the abstract, the results of leeward condition are mainly described.

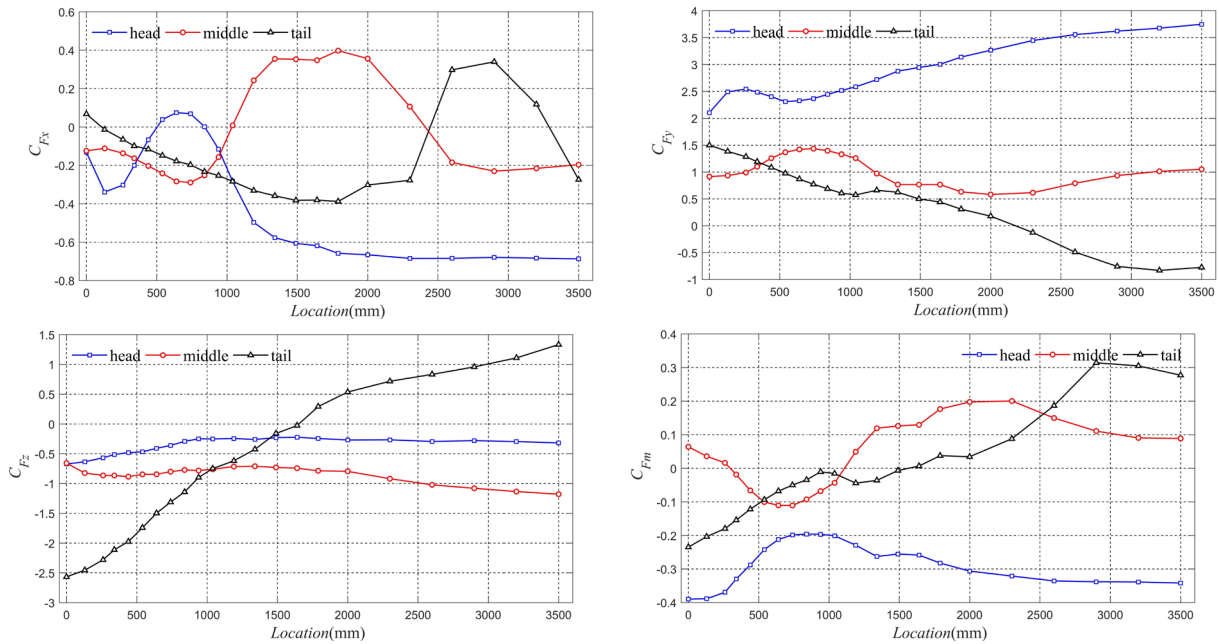


Fig. 2. Aerodynamic force of CRH-3 trains ($\beta = 15^\circ$)

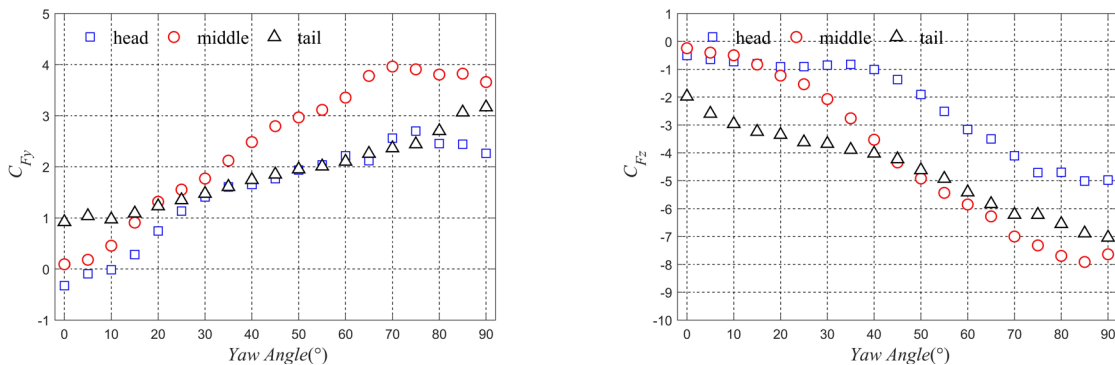


Fig. 3. Aerodynamic force of CRH-3 trains in different yaw angles ($\beta = 0 \sim 90^\circ$)

As the Fig.2 shows, in the leeward condition, the aerodynamic forces on the head train, middle train, and trailing train were significantly affected by the wind-shielding effect of the bridge towers, with significant changes observed in the C_{Fx} and C_{Fm} coefficients. When each of the three train was blocked by the bridge towers, there was a sudden increase in aerodynamic forces, with a noticeable sinusoidal variation pattern. In Fig.3, as the yaw angle changed, the bridge towers significantly affected the vertical aerodynamic force coefficient, C_{Fz} , of the leading car. Within a yaw angle range of 0° to 40° , the variation range of C_{Fz} for the leading car varies slightly, which indicates the head train is affected by the bridge tower, which is consistent with the actual situation.

1. References

Wu, J. F., et al. "Aerodynamic characteristics of a high-speed train crossing the wake of a bridge tower from moving model experiments." *Railway Engineering Science* 30(2): 221-241, (2022).

Concrete Structure Damage Analysis of the Anchoring End of Wind Barriers of High-Speed Railway Bridge under Wind Load of Train

Haobo Liang¹, Yunfeng Zou^{2*}, Xuhui He³, and Dianyi Guo⁴

¹: School of Civil Engineering, Central South University, Changsha, China; email: haoboliang0816@163.com

²: School of Civil Engineering, Central South University, Changsha, China; email: yunfengzou@csu.edu.cn

³: School of Civil Engineering, Central South University, Changsha, China; email: xuhuihe@csu.edu.cn

⁴: School of Civil Engineering, Central South University, Changsha, China; email: guodianyi@csu.edu.cn

*: corresponding author

Keywords: concrete damage; wind barriers; high-speed railway bridges; train wind load; concrete damaged plasticity model

Abstract: The installation of wind barriers can effectively reduce the impact of cross wind on the train and improve the safety and comfort of the train running on the bridge. However, a large transient aerodynamic pressure will be generated when the train passes through wind barriers at high speed. Repeated impact of such pressure wave on the wind barrier for a long time may cause damage and cracking of the concrete at the anchor end of the wind barrier, which will seriously threaten the operation safety of the high-speed train. In this study, based on computational fluid dynamics (CFD) analysis, the time history curve of train wind load acting on the wind barrier column is obtained. Then, *ANASY* is used to calculate the displacement time-history curve of the wind barrier column under the train wind load, and determine the most unfavorable position of the load on the wind barrier column. Finally, the finite element model of the wind barrier column-concrete pedestal was established by *ABAQUS* to explore the stress and damage distribution of concrete structure at the anchoring end of wind barrier under train wind load. The research results serve as a reference for the safety assessment of damage and its maintenance and reinforcement of concrete structures at the anchoring end of wind barriers.

1. Introduction

Wind barriers can effectively improve the safety of train running in windy environment, but its structure needs to withstand the pulsating wind pressure generated by the passage of high-speed trains, which will threaten the structural safety of the wind barrier. The expansion and compression effects of the train pulsating wind pressure have caused vibration, fatigue and loosening of bolts at the connection site of the wind barrier components (Xiong et al., 2020). As the speed of the train increases from 300km/h to 400km/h, the pulsating pressure caused by the train will increase rapidly with the square of the train speed (Tian et al., 2007), and the corresponding safety problem of wind barrier structure will become more prominent. Moreover, the concrete fatigue effect at the connection between the wind barrier column and the bridge structure is small. The concrete at the connection of the column foundation is prone to crack under the action of fatigue working load.

At the same time, according to the test results of scholar (SOPER D et al., 2019): the maximum lateral force under the pulsating wind pressure load of the train (running speed of about 228km/h) can reach 2166N, the load cycle of a single running direction can reach 234 times per day, and the number of load cycles in the 20-year maintenance-free period exceeds 1.5 million. With the continuous action of wind load on the wind barrier, the concrete cracks will increase and deepen, and the consequent cumulative damage, fatigue effects and changes in the mode of stress, etc., if not dealt with in time, it is highly likely lead to serious wind barrier overturning. Therefore, it is necessary to study the effect of the pulsating pressure generated when the train passes through on the damage of the concrete structure at the anchored end of the wind barrier.

2. Calculation Method

2.1. CFD numerical simulation

ANSYS Fluent was used to establish a numerical simulation model of wind barrier-train-bridge, which used a typical high-speed railway 32m double-line simply supported girder bridge and CRH2 Harmony high-speed train as the research objects, and used a wind barrier with a height of 3m and wind permeability of 0%. The high-speed train adopts a three-car formation model (front, middle and tail) with a total length of 76.4m (25.7+25+25.7m). The total length of the bridge model is 352m, and the wind barrier is set in the middle of the entire length of the bridge. The three-dimensional compressible SST k- ω turbulence model was selected for the calculation model, and the 3-marshalling CRH2 bullet train was simulated at the speed of 400km/h through a 352m long bridge by sliding grid method, and finally the wind load time of the train was obtained, as shown in Fig. 1.

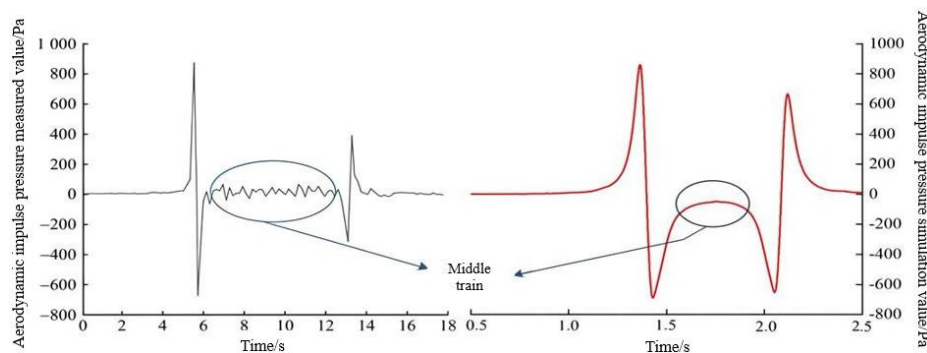


Fig. 1. Comparison between measured and simulated aerodynamic impulse pressure

2.2. Structural dynamic response analysis

Based on the actual material parameters of the wind barrier column, the design parameters were defined and the *ANSYS* finite element model was established. The train wind load obtained by CFD numerical simulation is applied to the wind barrier column. Meanwhile, considering the traveling wave effect of the train wind, the dynamic response of the wind barrier column under the train pulsating wind load is calculated by transient analysis method, and the maximum displacement time history curve of the wind barrier column is calculated, as shown in Fig. 2.

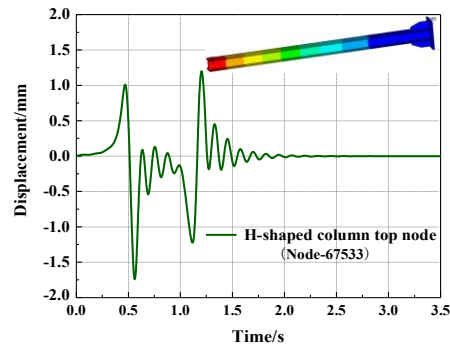


Fig. 2. Maximum displacement response time history of wind barrier column

2.3. Structural nonlinear finite element damage analysis

A finite element model consisting of wind barrier column, concrete pedestal, and U-shaped anchor bolts (M27) was established using *ABAQUS*, as shown in Fig. 3. Based on the code provisions, apply sufficient pretightening force (calculation formula of bolt pretightening force: $F_T = T/K \cdot D$, where T is the torsional torque; K is the dimensionless coefficient of torsional torque, 0.22; D is the nominal diameter of the bolt, 27mm.) to the U-bolt to compress the wind barrier column and concrete pedestal, where the interaction between the wind barrier column and concrete is set as surface-to-surface contact. The analysis step is set up in two steps, the first step considers only the bolt pretightening force, and the second step adds the train wind load. The nonlinear constitutive relationship of concrete is defined by the plastic damage model (CDP) derived based on the specification. On this basis, the internal force distribution of the wind barrier anchoring structure under the most unfavorable train wind load is calculated, and the stress and structural damage state of concrete near the U-bolt holes are evaluated.

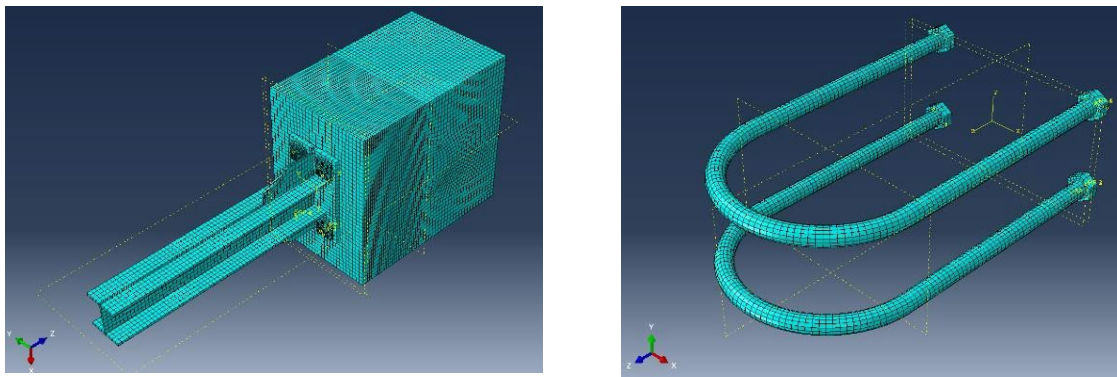


Fig. 3. Finite element model: (a) Column of wind barrier and concrete pedestal; (b) U-shaped anchor bolts.

3. Analysis of the Results

The judgment criterion of damage factor is introduced, as shown in Fig. 4. When the compressive stress of concrete exceeds the peak value of compressive stress, the concrete is judged to be compression damage. When the tensile stress of concrete exceeds the peak value of tensile stress, and the strength drops to 50% of the peak value, the concrete is judged to be tensile damage. According to the specification and the simulated calibration test, the critical damage factors of compression and tension of C30 concrete are calculated, which are 0.325 and 0.624, respectively.

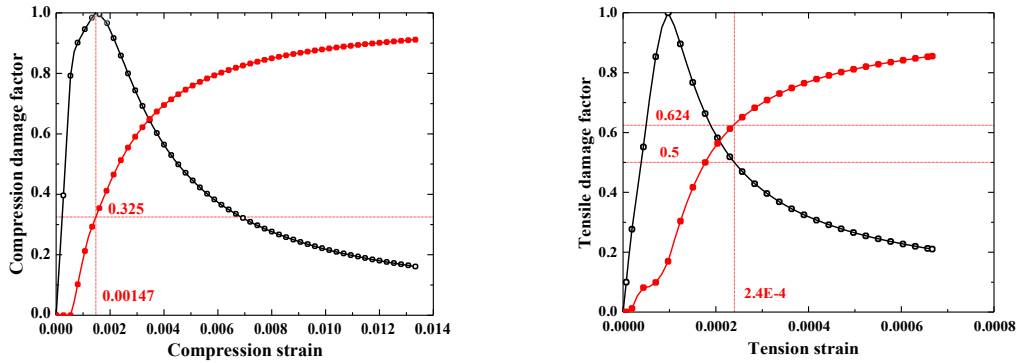


Fig. 4. Correspondence of damage factor and strain: (a) compression damage; (b) tensile damage.

Based on the structural dynamic response analysis, the displacement time-history curve of the wind barrier column is obtained, and it is found that the maximum displacement can reach 1.75mm and act on the top of the wind barrier column. The displacement time history was applied to the nonlinear finite element damage analysis of the structure, and the distribution nephogram of the concrete tensile and compression damage factors at the bolt holes was obtained, as shown in Fig. 5. According to Fig. 5, under the combined action of train wind load and bolt pretightening force, the maximum tensile damage factor of surface concrete near the bolt hole is 0.833, while the maximum compressive damage factor is 0.022. The tensile damage factor exceeds 0.624, indicating that the surface concrete is damaged by tension.

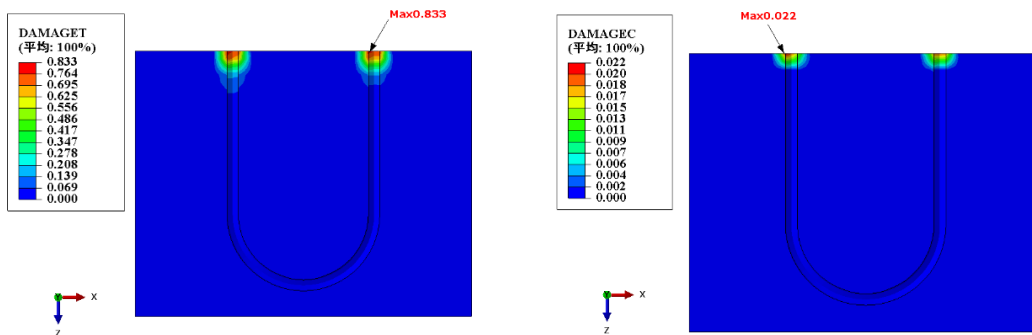


Fig. 5. Distribution nephogram of concrete tensile and compression damage factors at the location of U-bolt holes

4. Conclusions

Under the action of bolt pretightening force and train wind load, the anchor concrete near each bolt hole has a risk of damage within a certain depth. Specifically, the peak value of tensile damage factor of the surface concrete near the bolt hole on the windward direction was 0.833, and the peak value of compression damage factor was 0.022, and the surface concrete is damaged by tension at this position. The concrete near the bolt hole has the risk of low cycle fatigue damage and anchorage damage under the action of train wind cycle load.

5. References

Xiong, X. H., Yang, B., Wang, K. W., Liu, T. H., He, Z., and Zhu, L. (2020). Full-scale experiment of transient aerodynamic pressures acting on a bridge noise barrier induced by the passage of high-speed trains operating at 380–420 km/h. *Journal of Wind Engineering and Industrial Aerodynamics*, 204, 104298.



Parametric Study on the Aerodynamic Characteristics of Wind-Guide Barriers for Train-Bridge System

Shuo Jiang^{1*}, Yunfeng Zou², Xuhui He³, and Dianyi Guo^{4*}

¹: School of Civil Engineering, Central South University, Changsha and China; email: 992334207@qq.com

²: School of Civil Engineering, Central South University, Changsha and China; email: yunfengzou@csu.edu.cn

³: School of Civil Engineering, Central South University, Changsha and China; email: xuhuihe@csu.edu.cn

⁴: School of Civil Engineering, Central South University, Changsha and China; email: guodianyi@csu.edu.cn

*: corresponding author

Keywords: Wind-Guide Barriers; train-bridge system; aerodynamic characteristics; wind field; wind tunnel test

Abstract: This paper presents a new type of wind guide barrier(WGB). Through wind tunnel tests, the key parameters of three types of WGBs were studied, (including two flow guiding parameters - the main wind deflector angle θ_l the sub-guide wind angle size h_l , and one shielding parameter - the root width B_l of the WGB), and their effects on the aerodynamic characteristics of the high-speed train(HST) and blunt body box beam system and the bridge deck wind field were investigated. To verify the windproof performance of the WGB, tests were conducted with no barrier and a 30% ventilation rate rigid wind barrier. The aerodynamic forces and wind pressure distribution of the train and bridge were obtained using force and pressure measurement methods, and the wind field on the bridge was tested using a moving wind speed testing system. The results show that the shielding effect is the main factor affecting the windproof performance of the WGB. When the WGB is installed, the average wind pressure distribution on the train is comparable to that of using a traditional wind barrier. At the same time, the WGB can guide the oncoming flow, and the maximum ratio of the transverse wind speed and the vertical wind speed on the bridge deck can reach 0.25 and 0.17, respectively, reducing the resistance of the WGB and the bridge-wind barrier system by 32% and 12%, respectively. The change in the main wind deflector angle has a minor impact on the wind field on the bridge deck, and has no significant effect on the aerodynamic characteristics of the train-bridge system. The sub-guide wind angle size has a significant effect on the transverse and vertical wind guiding effects, reducing the sub-guide wind angle size increases the maximum transverse wind speed ratio by more than 0.1, and also increases the maximum aerodynamic force on the train. Increasing the root width of the WGB can enhance the shielding and guiding effects, and can suppress the jet flow intensity near the bridge deck, which is beneficial for windproof of the train.

1. Introduction

The shielding effect of wind barriers creates a relatively safe local wind environment for HST (Kozmar et al., 2014). Researchers believe that the reduction of average wind speed and the variation of turbulence are two important factors that affect the windproof performance (Takeda et al., 1985; Dong et al., 2007, 2010). (Xiang et al., 2014) evaluated the wind-sheltering performance of wind barriers using the DEA method, indicating that reasonable wind barrier height and porosity would make HST have better aerodynamic performance, and other studies have reached similar conclusions (He et al., 2014; Chu et al., 2013). However, we cannot only focus on the windproof performance of wind barriers, and the study of bridge-barrier system is also important. Wind barriers transmit wind loads to bridges, which significantly increase the bridge's drag coefficient, as well as the train's drag and lift coefficients on the bridge(Zhang et al. 2017). This paper studies a new type of WGB that deflects the airflow horizontally for aerodynamic design. Through wind tunnel tests, the study investigates the effects of three WGB parameters on the aerodynamic characteristics of HST and bridges. In addition, the wind field characteristics on the bridge deck were also tested, and the wind speed and turbulence field after the wind barrier were analyzed, including the three-direction wind speed components and turbulence intensity, to comprehensively evaluate the windproof performance.

2. Outline of the Experimental Procedure

As shown in Fig. 1(a), 30 measuring points were arranged for each train section, and 42 measuring points were arranged for each bridge section. The wind speed point layout scheme is shown in Fig. 1(b), and a gradually denser layout is adopted from the top to the bottom. The relevant parameters of the WGB have been listed in Table 1.

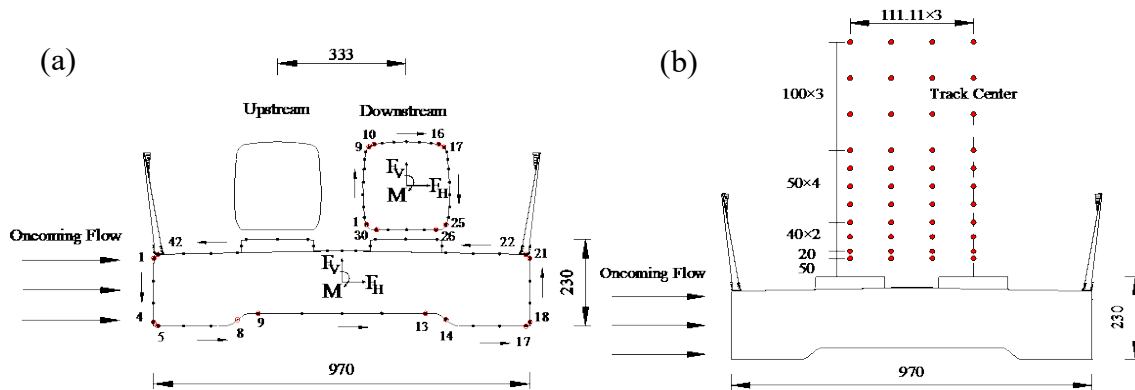


Fig. 1. Experimental details: (a) arrangements of pressure taps on the train and bridge cross section; (b) arrangement of wind speed measuring points (Unit: mm)

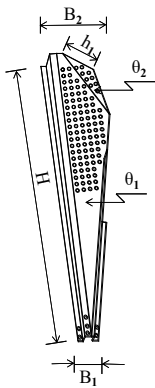
3. Results and Discussion

Fig. 2 show the average and extreme aerodynamic forces of the train when it is located on the windward sides of the bridge. The red and blue lines in Fig. 2 respectively represent the average aerodynamic force of the train without barriers and with a traditional wind barrier installed. When a type 4 WGB is installed, the average aerodynamic force of the train is close to that when a traditional wind barrier is installed, indicating that WGB can provide a similar windproof performance for trains as traditional wind barriers. As shown in Fig. 2(a), when θ_l is slightly adjusted, the average aerodynamic force of the train remains almost unchanged, but the extreme aerodynamic force of the train is greatly affected by the angle of the windward surface. When $\theta_l=20^\circ$, the C_H extreme value increases from 0.24 to 0.45, and at the same time, the C_V extreme

value increases from 0.52 to 0.71. As shown in Fig. 2(b), when B_I is increased from 0.25m to 0.3m, the average C_H and average C_V of the train will be reduced to varying degrees, but the extreme C_H of the train will increase. At the same time, it should be noted that when B_I is further

Table 1. Types of WGB experiment

Design parameters of WGB	Wind barrier types	Width of WGB root	Angle of main deflector plate	Size of the upper deflector angle
		B_I (mm)	θ_I ($^\circ$)	h_I (mm)
		No barrier		
		Rigid wind barrier (30% ventilation rate)		
	1			
	2			
	3	300	20	350
	4	300	10	350
	5	300	20	500
	6	350	10	350
	7	250	10	350



increased, the average aerodynamic force of the train does not change significantly, so the optimal value of B_I should be between 0.25m and 0.3m. As shown in Fig. 2(c), although increasing h_I can reduce the wind load on the WGB itself, both the average aerodynamic force and extreme aerodynamic force of the train will increase. The maximum C_V of the train increases by 60%, which will increase the train's derailment coefficient. Overall, B_I and h_I are WGB parameters that have a relatively large impact on the aerodynamic forces of the train, while θ_I has a relatively small impact. When optimizing the WGB parameters, the adjustment of the first two parameters should be emphasized.

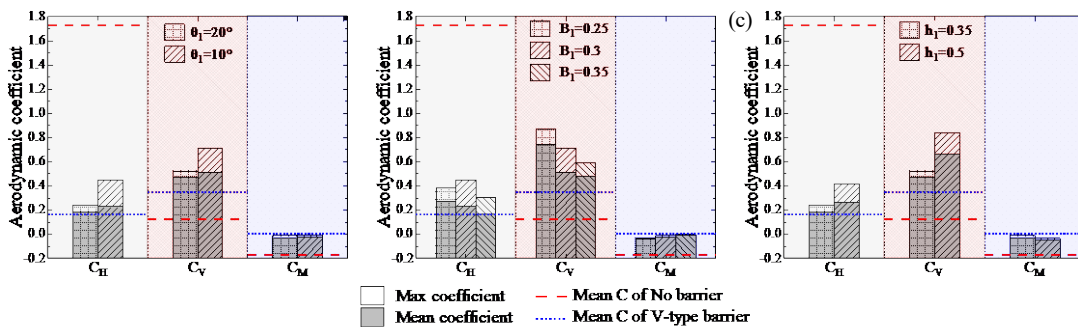


Fig. 2. Effect of WGB parameters on HST aerodynamic force (upstream): (a) Angle of main deflector plate θ_I ; (b) Width of WGB root B_I ; (c) Size of upper deflector angle h_I

Fig. 3 illustrates the C_V and C_H of the bridge-barrier system, as well as the C_H of the WGBs with different installations. Generally speaking, the C_H of the WGB roughly follows the law of increasing with B_I and decreasing with θ_I and h_I . Compared with the traditional vertical wind barrier, the installation of WGB (Type 4) with the same ventilation rate can reduce the maximum

resistance and barrier resistance of the bridge-barrier system under various train-bridge combinations by 12% and 32%, respectively.

The contour lines of the wind speed components in three directions under type 4 were given in Fig. 4. From Fig. 4(a), it can be observed that the incoming flow is obstructed by the barrier and flows around, forming a shear layer above the barrier. On the other hand, due to the formation of a jet through the gap at the bottom of the barrier, a high wind speed area with a wind speed ratio of more than 0.6 can be observed at the bottom of the barrier. From Fig. 4(b), it can be seen that the lateral wind speed basically shows a trend of decreasing as it moves further away from the barrier. Affected by the jet, there is a high lateral wind speed near the bridge deck on the windward side; At the top of the barrier and below the shear layer, there is a large range of lateral airflow deflection, with a maximum lateral wind speed ratio of -0.25. The distribution of vertical wind speed is similar to that of crosswind wind speed, with an extreme value of 0.17 for the vertical wind speed ratio.

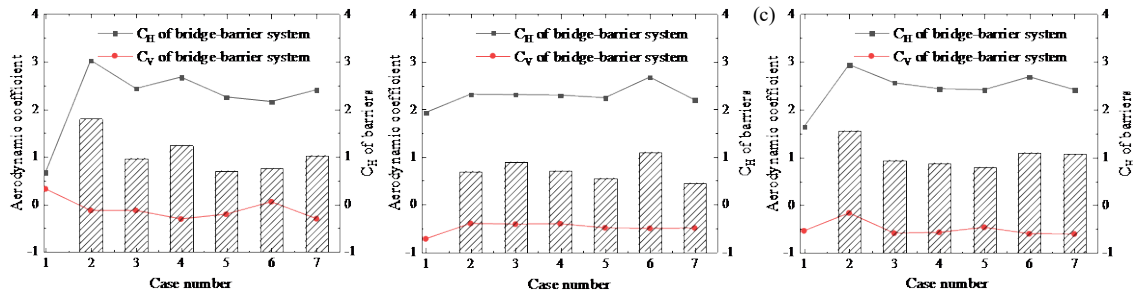


Fig. 3. Aerodynamic forces of bridge and barrier: (a) Without train; (b) The train is located upstream; (c) The train is located downstream

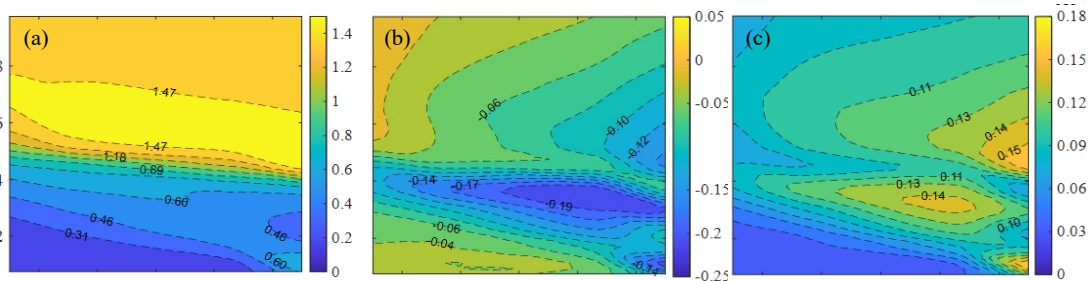


Fig.4. Mean wind speed contour lines of type 4: (a) streamwise wind speed; (b) transverse wind speed; (c) vertical wind speed. In all diagrams the wind blows from right to left-hand side.

4. Conclusion

- (1) The WGB provides comparable windproof performance for the train while reducing barrier resistance and the resistance of the bridge-barrier system by 32% and 12%, respectively.
- (2) The design parameters of B_l and h_l for the WGB have a significant impact on the average aerodynamic forces of the train.
- (3) The WGB can effectively reduce the wind speed on the bridge and has a strong guiding effect on the airflow. The maximum values of the transverse wind speed ratio and vertical wind speed



Bridge Engineering Institute Conference 2023 (BEI-2023)
Rome, Italy, July 17-20, 2023



ratio behind the WGB can reach 0.25 and 0.17, respectively.

5. References

He, X. H., Zou, Y. F., Wang, H. F., Han, Y., Shi, K. 2014. Aerodynamic characteristics of a trailing rail vehicles on viaduct based on still wind tunnel experiments. *Journal of Wind Engineering and Industrial Aerodynamics*, 135, 22–33.



Bridge Engineering Institute Conference 2023 (BEI-2023)
Rome, Italy, July 17-20, 2023



Earthquake and Dynamics

Experimental Evaluation on Seismic Behavior of Precast Concrete Walls with Developed Vertical Joints for Enhanced Shear Strength

Kyo Young Moon¹, Sung Jig Kim^{2*}, and Chunho Jang³

¹: Department of Architectural Engineering, Keimyung University, Daegu, South Korea;
email: mky9404@gmail.com

²: Department of Architectural Engineering, Keimyung University, Daegu, South Korea;
email: sjkim4@kmu.ac.kr

³: Department of Civil Engineering, Keimyung University, Daegu, South Korea;
email: chunho@kmu.ac.kr

*: corresponding author

Keywords: Precast concrete wall; Vertical joint; Cyclic loading test; Seismic performance

Abstract: This paper introduces the newly developed vertical joints between Precast Concrete (PC) wall panels to improve their in-plane shear capacity and ductility. The three types of vertical joints are developed based on the existing vertical joints. The developed vertical joint systems are responsible for increasing shear strength, stiffness, and shear transfer capacity between PC walls through the dovetail-shaped metal laths, shear keys and reinforcing bars. To evaluate the seismic performance of PC walls with developed vertical joints, four specimens including the conventional and developed vertical connections were designed and constructed. The experimental results showed that the PC walls with developed vertical joints not only had improved strength and ductility, but also exhibited better crack and damage control, when compared to the specimen with the conventional connection.

1. Introduction

The Precast Concrete (PC) structures has been widely used due to the advantages of high-quality fabrication, construction cost savings, reduced material consumption, and rapid construction (Zhangfeng and Zhengxing, 2019; PCI, 2010). Due to limitations in transportation and lifting equipment, there are generally many restrictions on the size of PC members. Therefore, in the case of a structural wall having a large size compared to other members, the PC wall is usually manufactured in a factory as a relatively smaller sized wall and thus, joints are inevitably created between the PC walls during installation on size. The behavior of these joints can cause severe damage to PC members under seismic loads and can have a significant impact on the overall performance of the structure.

The mechanical behavior of the PC walls depends on the shear transfer capacity of the joints between the precast components (Zhi et al. 2020). The connection details with inadequate force transfer capacity and poor structural performance such as strength, ductility, and stiffness, could cause severe damages and brittle failure of the entire structure when subjected to earthquake. Therefore, in this study vertical connections between PC wall panels are newly developed to prevent brittle failure and provide sufficient in-plane shear and ductility. A total of four specimens

were constructed and investigated through static cyclic loading tests. The seismic performance of developed connections is evaluated by comparing those of the wire loop connection.

2. Developed Vertical Connections of PC Wall

In this study, three types of vertical connection were developed to improve upon the existing joint by increasing the transverse reinforcement ratio and friction force at the joint interface, as illustrated in Fig. 1. Typically, these connections are constructed by casting the mortar after installing the reinforcing bars between the PC wall panels. The slit between the PC walls is designed to be 20mm according to Korea Design Standard (KDS 41 17 00).

The first connection is a dovetail-shaped metal lath with headed rebars as shown in Fig. 1(a). The second and third connections are similar to the traditional connection as shown in Fig. 1(b), but with a higher transverse rebar ratio of about 24.6%, as compared to the traditional connection (Lee et al. 2022). In the third connection, shear keys are added to the connection surface as shown Fig 1(b). The dovetail-shaped metal lath and shear keys are expected to enhance the stiffness and shear strength of the vertical connection by increasing the friction forces on the connection surface. All developed connections aim to improve the shear transfer capacity through the reinforcing bars.

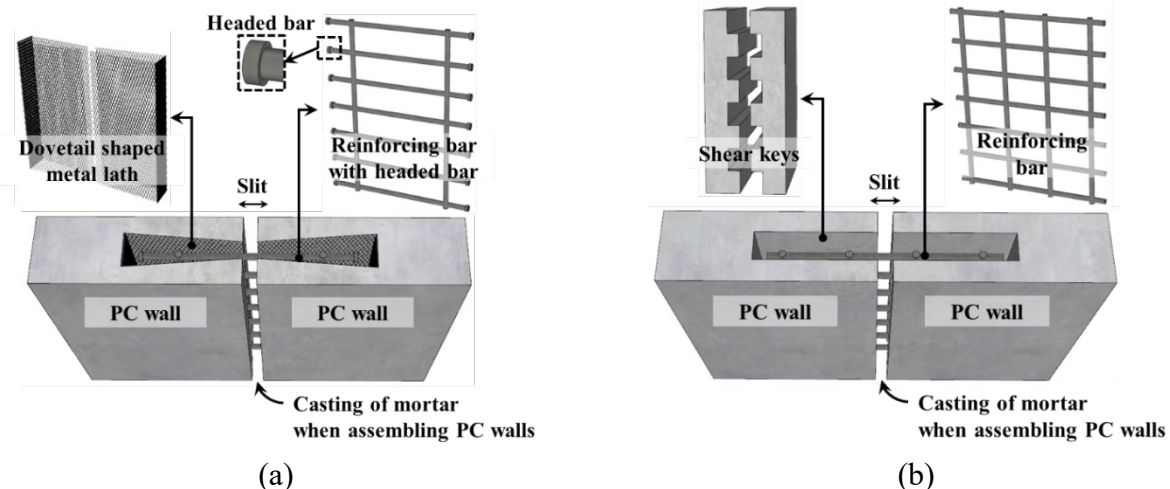


Fig. 1. Developed vertical connections; (a) Dovetail-shaped connection; (b) Connection with rebars and shear keys

3. Experimental Program

A static cycle loading test was conducted to evaluate the seismic performance of the PC walls with developed vertical joints. Details of test specimens are summarized in the Table 1. All specimens have the same geometric configuration except for the panel width, which varies depending on the type of vertical connection. This is because the slits between the PC walls differ according to the type of connection. The clear height and thickness of the PC walls are 2700 mm and 200 mm, respectively. The specimen PWL, which has wire loop connections, was selected as the reference structure for an existing vertical connection. The specimen PWD, PWR, and PWRs have the proposed connections in this study, and their descriptions are shown in Table 1. All specimens were subjected to lateral cyclic loads with a constant axial load of 1,092kN, which represents 10% of the ultimate axial capacity of the wall ($0.1f'_cA_g$). The lateral displacement history was imposed with multiple cycles at each displacement level to reflect the effect of strength degradation characteristics.

Table 1. Details of specimen

Specimen Name	Description of connection	Geometric configuration (mm)		Material and section details			
		Slit	Panel width	f_c' (MPa)	f_m (MPa)	ρ_v (%)	ρ_h (%)
PWL	Wire loop	100	860	32.13	52.16	0.33	0.34
PWD	Dovetail-shaped metal lath and reinforcing bars	20	900	33.33	57.81	0.32	0.34
PWR	Reinforcing bars	20	900	27.44	60.34	0.32	0.34
PWRS	Reinforcing bars and shear keys	20	900	30.04	63.43	0.32	0.34

f_c', f_m = concrete and mortar strength, respectively

ρ_v, ρ_h = vertical and horizontal reinforcement ratio, respectively

4. Experimental Results

Fig. 2 shows crack patterns of all specimens at the drift ratio of 1.0%. The average envelope curve and cumulative energy dissipation of all specimens are illustrated in Fig. 3. All specimens showed a similar crack pattern as shown in Fig. 2. The specimen PWL suffered the most severe damage with large cracks. Among the specimens with developed vertical connections, the specimen PWR had the most severe cracks and damage at the vertical connection. In contrast, in the case of the specimen PWD and PWRS, few cracks were observed at the vertical connection.

Compared to the specimen PWL, the maximum lateral force of the specimen PWR decreased by up to 2.42%, while those of specimens PWD and PWRS increased by 5.53% and 3.48%, respectively. Furthermore, the cumulative energy dissipation capacity of the specimens with developed vertical connection increased by up to 3.98%, when compared to the specimen PWL.

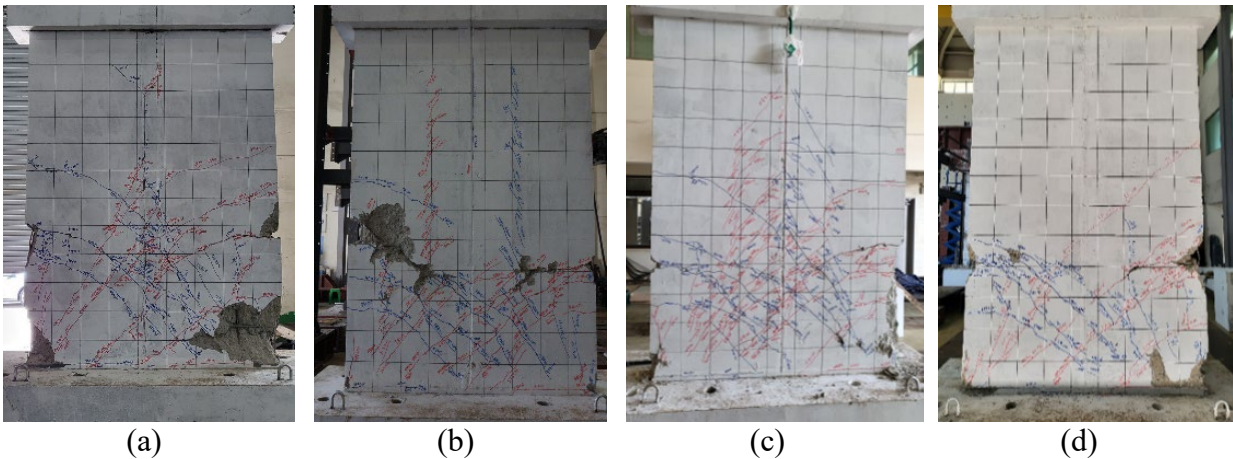


Fig. 2. Cracks patterns of specimens; (a) PWL; (b) PWD; (c) PWR; (d) PWRS

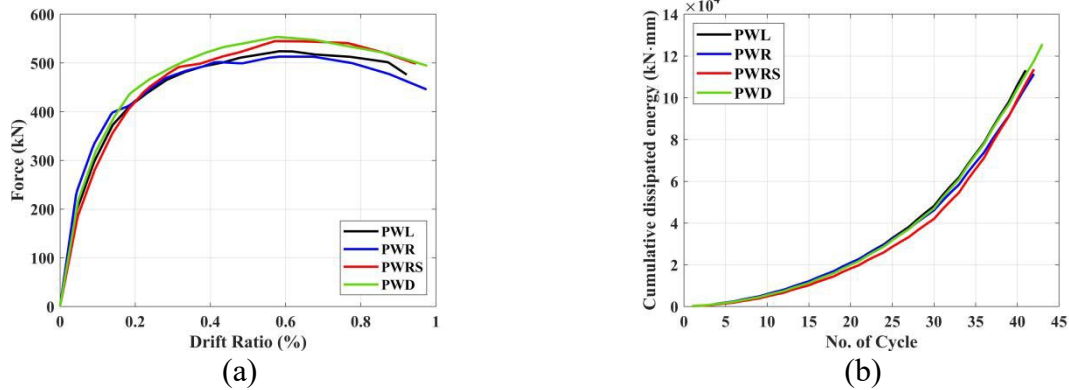


Fig. 3. Average envelope curve and cumulative energy dissipation

5. Conclusion

In this study, newly developed vertical connections were proposed to improve the shear strength of vertical connection and their seismic performance was evaluated through the static cyclic testing. Compared to the specimen with a conventional connection, maximum strength and energy dissipation capacity increased by up to 5.11% and 3.98%, respectively. In addition, the developed connections were effective in damage and crack control. Based on the experimental investigation, it could be concluded that the proposed vertical connections could improve the seismic performance of PC walls.

6. Acknowledgments

This research was supported by a grant (RS-2021-KA161540) from Technology Business Innovation Program funded by Ministry of Land, Infrastructure and Transport of Korean government.

7. References

- Architectural Institute of Korea. 2019. In Seismic Building Design Code (KDS 41 17 00), Ministry of Land: Seoul, Korea
- Dang, L., Liang, S., Zhu, X., Zhang, M., & Song, Y. 2021. Seismic performance of precast concrete wall with vertical energy-dissipating connection, *The Structural Design of Tall and Special Buildings*, 30(2), e1820.
- Lee, W. J., Kim, M., Lee, D., Ju, H., & Kim, K.H. 2022. Seismic Performance Evaluation of Intermediate Precast Structural Walls. *Journal of Next-generation Convergence Technology Association*, 6(3), 421-432
- PCI Industry Handbook Committee. 2010. PCI design handbook: precast and prestressed concrete. In: *Prestressed Concrete Inst*, 7th ed., Chicago, IL
- Zhangfeng, Z., & Zhengxing, G. 2019. Seismic performance of the spatial model of precast concrete shear wall structure using grouted lap splice connection and cast-in-situ concrete. *Structural Concrete*, 20(4), 1316-1327.
- Zhi, Q., Xiong, X., Yang, W., Liu, S., & Xiong, J. 2020. Experimental study on the shear behavior of precast wall concrete joints with/without dowel reinforcement. *Materials*, 13(7), 1726.

Hybrid Testing of CFST Columns in Rigid-Frame Bridges Subjected to Horizontal and Vertical Ground Motions

Riadh Al-Mahaidi^{1*}, Javad Hashemi², and Ali Al-Attraqchi³

¹: Professor, Swinburne University of Technology, Melbourne, Australia,

email: ralmahaidi@swin.edu.au

²: Associate Professor, Swinburne University of Technology, Melbourne, Australia,

email: jhashemi@swin.edu.au

³: former PhD student, Swinburne University of Technology, Melbourne, Australia,

email: ali.yasir.w@gmail.com

* corresponding author

Keywords: hybrid testing; CFST bridges; vertical ground motions

Abstract: In this paper, a hybrid simulation of a concrete-filled steel tube (CFST) rigid-frame bridge structure is presented. The bridge structure is constructed using CFST columns of circular and square cross-section shapes, and it is subjected to combined horizontal and vertical ground motions. The testing is performed using the multi-axis substructures testing (MAST) system at Swinburne University of Technology in Melbourne, Australia. The results demonstrate the remarkable seismic performance of CFST columns, emphasizing their advantages in enhancing the seismic resistance of critical and post-disaster bridges that are susceptible to strong vertical ground motions.

1. Introduction

Assessing the seismic performance of bridge structures has been a difficult task because of their size and geometry. The conventional experimental methods such as shake table testing have proven to be risky and impractical due to the possibility of structure collapse. A feasible alternative approach is hybrid simulation, which involves experimental testing of the critical section of the structure, while the remaining parts are simulated using numerical methods (Hashemi et al., 2016; M. J. Hashemi and Al-Mahaidi, 2017; Hashemi et al., 2017; Del Carpio et al., 2017). Many studies have used hybrid simulation for the seismic performance of bridge structures (Stathas et al., 2017; Chae et al., 2017; Bousias et al., 2017), but most have focused on horizontal ground motions only, with limited data available on combined horizontal and vertical ground accelerations. The vertical component can be significant at near-fault sites and could cause significant damage to reinforced concrete (RC) columns. CFST members, which are known for their high ductility and energy absorption capacity, have been proposed as a potential solution for piers susceptible to significant vertical acceleration in bridge construction. Although CFSTs have been widely studied experimentally, their behaviour under horizontal and vertical boundary forces is still not well understood, making it challenging to anticipate their response during post-disaster operations. This study aims to examine the seismic performance of circular and square CFST columns under combined horizontal and vertical ground accelerations using hybrid simulation.

2. Description of Rigid-Frame Bridge Structure

The bridge design was previously studied to investigate the effects of combined vertical and horizontal ground motions on RC bridge piers using hybrid simulation tests by Kim et al. (2011). The design was based on the western side of the United States in a seismic zone. The prototype bridge structure was designed according to the Federal Highway Administration (FHWA) of the U.S. Department of Transportation with two double-column bents and a total span of 97.6m divided into three smaller spans, as shown in Fig. 1. The RC columns were replaced by CFST columns with a clear height of 6m and the bridge deck consisted of a cast-in-place concrete box girder with integral bent caps and laterally-restrained abutments. The columns were modelled using beam-with-hinges elements in OpenSees and the plasticity model was calibrated using the results of a 3-dimensional mixed-mode quasi-static cyclic experiment. Full details about the bridge and modelling can be found in Al-Attraqchi et al. (2020).

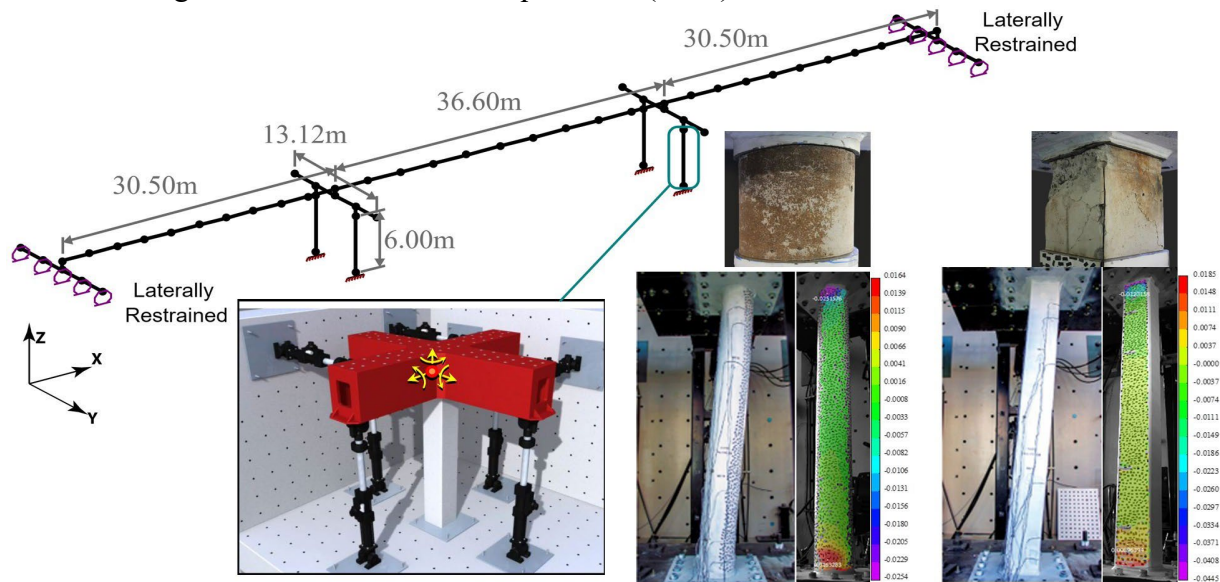


Fig. 1. Numerical model of rigid-frame bridge, MAST system, and the circular and square columns being tested

3. Hybrid Simulation

The Multi-Axis Substructure Testing (MAST) system in the Smart Structures Laboratory at Swinburne provides a powerful tool for investigating the effects of extreme loading events on large structural components using hybrid simulation testing (Hashemi et al., 2015). A sophisticated 6-DOF control system utilizes eight high-capacity hydraulic actuators to enable the application of complex multi-directional deformation or loading schemes to structural components.

During the hybrid simulation, the bridge structure was subjected to the Northridge 1994 Sylmar Converter station ground motion records, which have a high peak ground acceleration (PGA) of over 0.3g and a vertical-to-horizontal (V/H) ratio greater than 0.6. This ground motion was responsible for significant damage to half of the bridges in the area and led to the collapse or demolition of 9 bridges. The vertical component was scaled up to 0.748g to achieve a V/H ratio of 1.2, which has been seen in previous earthquake records. To cover the full response range, five intensity levels of combined horizontal and vertical ground motions were consecutively applied to push the structure to 0.25% (elastic), 2.0%, 4%, 6% and 8% maximum drift ratios, respectively.

The hysteresis responses of circular and square columns are illustrated in Fig. 2 by plotting the base shear versus the drift ratios; also, the axial forces of the columns are represented by the colour map to emphasize the effect of the axial force level on the hysteresis response. It is clear, especially from the bigger cycles, that the $P - \Delta$ effects are significant, and the lateral force resistance oscillates as a result of the axial force changing from compression to tension. Large hysteresis loops are another indicator that suggests adequate ductility and energy dissipation without approaching collapse. The collapse limit state is often defined as a percentage of loss from the ultimate lateral strength, which was not observed in these columns.

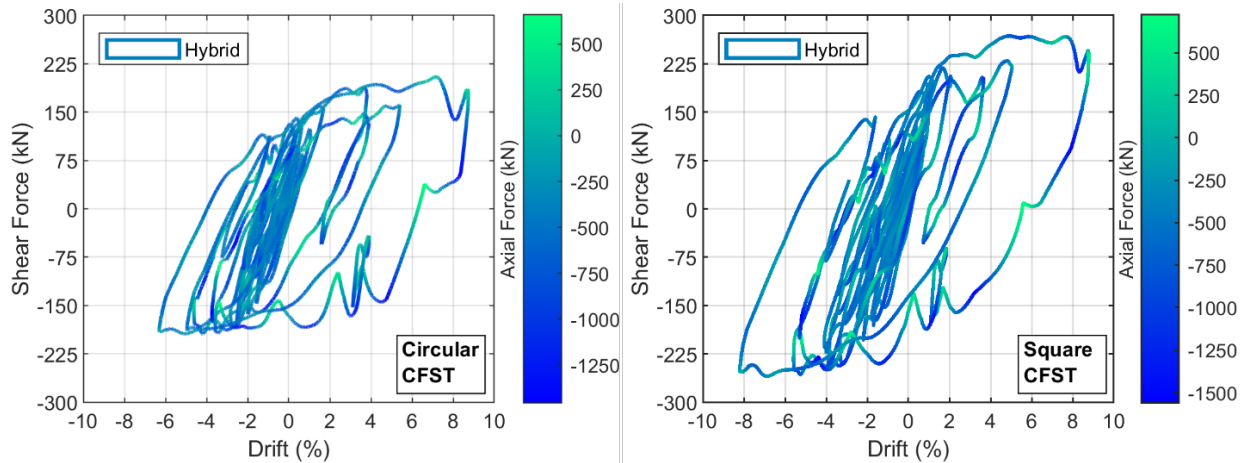


Fig. 2. Hysteresis-response showing the shear force and lateral drift and the color showing axial load

Other than a small residual displacement of about 50 mm, no major physical damage was found at the end of the tests. The physical damage that was seen manifested as outward bulging at the top and bottom of the columns in the region of the plastic hinge was brought on by the yielding/buckling of the steel and the crushing of the concrete. **Fig. 3** displays the observed damages at the top and bottom of both columns as well as the depth of the bulging. For the square and circular columns, respectively, the greatest bulging depth was 7.2 mm, and it happened at the top in the plastic-hinge zone for both columns. For the square column, the damage was outwardly distributed to one side, whereas for the circular column, it was distributed to both sides.

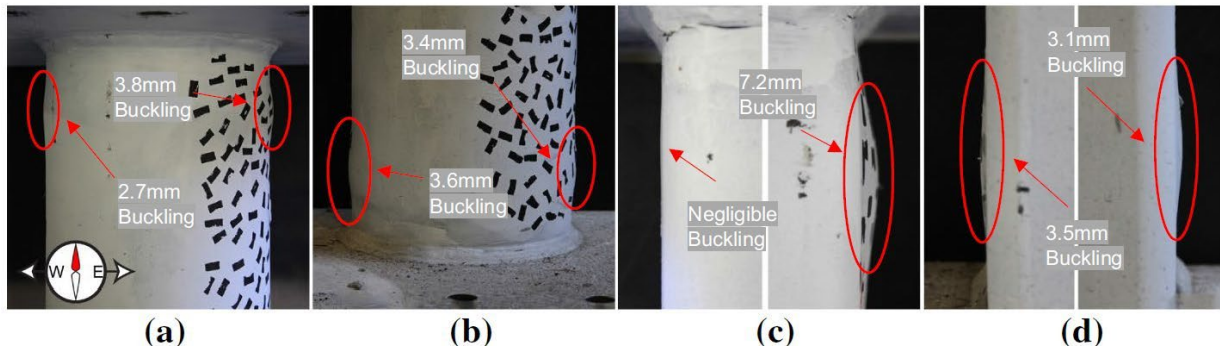


Fig. 3. Observed damages at the end of hybrid simulation; (a) circular column top; (b) circular column bottom; (c) square column top; (d) square column bottom



4. Conclusion

This research investigated the seismic response of a three-span, double-column bridge constructed using concrete-filled steel tube (CFST) columns, using a pioneering experimental technique called multi-axis hybrid simulation testing. Two types of CFST columns, circular and square, were examined and subjected to progressively increasing levels of Northridge ground motion. The findings demonstrated that both types of columns exhibited excellent seismic performance, with ductile behaviour, substantial hysteresis loops, and minimal physical damage. The circular column performed slightly better than the square column. These findings underscore the potential of CFST columns in constructing resilient bridges with minimal recovery costs and downtime, particularly in near-fault locations subjected to extreme multi-directional seismic loads.

5. References

- Al-Attraqchi AY, Hashemi MJ and Al-Mahaidi R (2020) Hybrid simulation of bridges constructed with concrete-filled steel tube columns subjected to horizontal and vertical ground motions. *Bulletin of earthquake engineering* 18(9): 4453-4480.
- Bousias S, Sextos A, Kwon O-S, et al. (2017) Intercontinental hybrid simulation for the assessment of a three-span R/C highway overpass. *Journal of Earthquake Engineering*. 1-22.
- Chae Y, Park M, Kim C-Y, et al. (2017) Experimental study on the rate-dependency of reinforced concrete structures using slow and real-time hybrid simulations. *Engineering Structures* 132: 648-658.
- Del Carpio RM, Hashemi MJ and Mosqueda G (2017) Evaluation of integration methods for hybrid simulation of complex structural systems through collapse. *Earthquake Engineering and Engineering Vibration* 16(4): 745-759.
- Hashemi MJ, Al-Mahaidi R, Kalfat R, et al. (2015) Development and validation of multi-axis substructure testing system for full-scale experiments. *Australian Journal of Structural Engineering* 16(4): 302-315.
- Hashemi MJ, Al-Ogaidi Y, Al-Mahaidi R, et al. (2017) Application of Hybrid Simulation for Collapse Assessment of Post-Earthquake CFRP-Repaired RC Columns. *Journal of Structural Engineering* 143(1).
- Hashemi MJ, Mosqueda G, Lignos DG, et al. (2016) Assessment of Numerical and Experimental Errors in Hybrid Simulation of Framed Structural Systems through Collapse. *Journal of Earthquake Engineering* 20(6): 885-909.
- Kim SJ, Holub CJ and Elnashai AS (2011) Experimental investigation of the behavior of RC bridge piers subjected to horizontal and vertical earthquake motion. *Engineering Structures* 33(7): 2221-2235.
- M. J. Hashemi HHTYA-OJLW and Al-Mahaidi R (2017) Collapse Assessment of Reinforced Concrete Building Columns through Multi-Axis Hybrid Simulation. *ACI Structural Journal* 114(2).
- Stathas N, Skafida S, Bousias S, et al. (2017) Hybrid simulation of bridge pier uplifting. *Bulletin of earthquake engineering* 15(8): 3385-3398.



Seismic Performance of Precast Segmental Bridge Columns with Resettable Sliding Joints: Joint Responses and Simulation

Feng Liang^{1*}, Yingqi Liu², and Francis T.K. Au³

¹: The University of Hong Kong, Hong Kong, China; email: liangf@connect.hku.hk

²: Wuhan University of Technology, Wuhan, China and The University of Hong Kong, Hong Kong, China; email: selbyliu@whut.edu.cn

³: The University of Hong Kong, Hong Kong, China; email: francis.au@hku.hk

*: corresponding author

Keywords: Concrete bridges; piers; precast segments; self-centering; simulation.

Abstract: Precast segmental bridge columns with planar sliding joints possess large displacement capability and energy dissipation under quasi-static cyclic tests. Though the planar sliding joints can increase the ability to survive in moderate to high seismicity regions, the adjacent column segments often result in excessive residual relative displacement after seismic action, leading to costly and sometimes difficult repairs. The other concern is the joint resistance against vehicle braking, collision and wind load on the bridge. To increase the self-centering capability and lateral resistance of the planar joints, a system with 2-dimensional resettable sliding keys has been proposed. The innovative system adopts V- or W-shaped resetting guide keys, a smooth segment interface with relatively low coefficient of friction, and partially debonded tendons that go through ducts installed inside the concrete component. This study extends the conceptual design to a gentle 3-dimensional (3D) pyramid-shaped resettable joint and conducts a numerical simulation of column joints subjected to lateral loading. The responses of a resettable sliding joint include three Phases: (i) small flexural deformation before sliding initiates; (ii) joint sliding; and (iii) activation of tendons locking upon reaching sliding capacity. In addition, the effects of bond failure, material damage, and plasticity are also discussed. The force-drift curves of the resettable sliding joint show: (a) the process of sliding initiation; and (b) the combined effects of bearing forces, friction resistance and concrete damage on the overall stiffness. Comparison of the results shows that the proposed system has large initial stiffness, good energy dissipation and recentering capacity.

1. Introduction

Precast segmental bridge column (PSBC) is one of the Accelerated Bridge Construction techniques aiming for fast and green construction and less traffic disruption. PSBC is classified into emulative and non-emulative types. The non-emulative design can be further categorized as pure rocking, hybrid rocking and hybrid sliding columns (Sideris et al. 2014) according to the joint setting and energy dissipation methods (Zhang and Alam, 2020). In an attempt to promote PSBC in moderate to high seismicity regions, resettable sliding joints (RSJ) with a partially debonded system have been proposed (Au et al. 2019, Liu et al. 2021). The system consists of V- or W-shaped resetting guide keys, which comprise interfaces with relatively low coefficient of

friction (CoF) to allow sliding, and ducts and duct adaptors that accommodate partially debonded prestressing tendons, as shown in Fig. 2(a). This study extends the conceptual design to a pyramidal-shaped joint with a convex component at the top interface and a concave part at the bottom interface in the 3D perspective (Fig. 1(a)). The duct adaptors have a larger diameter than the ducts, forming the unbonded region together with unrestrained tendons. With the 3D configuration, the joint allows some relative joint sliding and some resetting tendency.

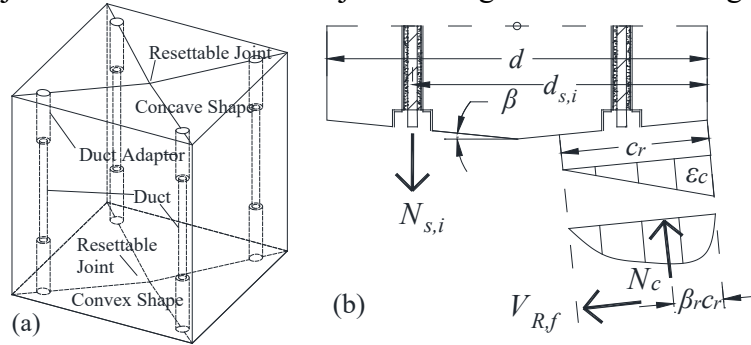


Fig. 1. Design of RSJ. (a) 3D pyramid-shaped configuration; (b) Normal stress and strain distribution at concrete surface and tendon forces.

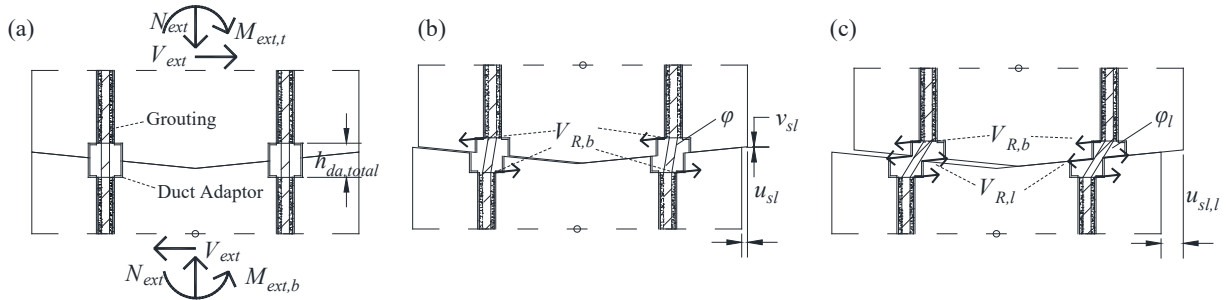


Fig. 2. Responses of RSJ subjected to external shear and moment. (a) Phase 1, before sliding initiates; (b) Phase 2, sliding with both horizontal and vertical displacements; and (c) Phase 3, sliding reaches the limit.

2. Joint Responses

Fig. 2 shows the forces acting on adjacent parts of RSJ in different phases. The axial force N_{ext} is assumed to be constant, while the shear force V_{ext} and moment M_{ext} are assumed to increase monotonically. Before the initiation of sliding, i.e., Phase 1 in Fig. 2(a), the component of resultant force along the slope is smaller than the static friction of the RSJ, leading to elastic flexural deformation as a cantilever column. Both the axial force and moment are resisted by the concrete section and the tendons. The corresponding resistant moment M_R with respect to the centerline of the joint as shown in Fig. 1(b) is:

$$M_R = M_c + M_{PT} = \left(\frac{d}{2} \times \frac{1}{\cos\beta} - \beta_r c_r \right) N_c + \sum_i (d_{s,i} - \frac{d}{2}) N_{s,i} \quad (1)$$

where M_c and M_{PT} are the resistant moment contribution from concrete and post-tensioned strands, respectively; β = inclination of RSJ; d = depth of concrete section; c_r = contact depth; β_r = stress distribution factor determining the location of concrete contact force N_c ; $d_{s,i}$ =

distance between tendon No. i and extreme compression fiber of segment and $N_{s,i}$ = the corresponding tendon force. The external axial force N_{ext} and the total prestressing force N_{PT} are resisted by the concrete, leading to:

$$N_c \cos\beta + V_{R,f} \sin\beta = N_{ext} + N_{PT} = N_{ext} + \sum_i N_{s,i} \quad (2)$$

where $V_{R,f}$ is the friction force, a portion of the total shear resistance force V_R of RSJ. In Phase 1, the external axial force N_{ext} is constant, while the prestressing force N_{PT} and the corresponding moment M_{PT} also remain the same as the initial values $N_{PT,initial}$ and $M_{PT,initial}$, respectively.

Once the static friction force is overcome, the RSJ starts relative motion with both horizontal and vertical displacement u_{sl} and v_{sl} , respectively, due to the slope. The process is shown as Phase 2 in Fig. 2(b), where $v_{sl} = |u_{sl}| \tan\beta$. Assuming negligible deformation of tendons in the bonded region, the sliding leads to a deviation angle φ between the unbonded region of tendon and the vertical as well as vertical elongation of tendon v_{sl} . The bearing forces between the unbonded tendons and the sides, $V_{R,b}$, along the slope also contribute to the shear resistance V_R . The deviation angle φ can be estimated from:

$$\tan\varphi = \frac{|u_{sl}|}{h_{da,total} + v_{sl}} \operatorname{sgn}(u_{sl}) \quad (3)$$

where $h_{da,total}$ = total height of two adjacent duct adaptors. Owing to the elongation upon initiation of sliding, the updated tendon force is $N_{PT,sl} = EA_{PT} \left(\frac{1}{\cos\varphi} - 1 \right) + N_{PT,initial}$, where E and A_{PT} are the Young's modulus and cross-sectional area of tendons, respectively.

As sliding reaches the limit, $u_{sl,l}$, in Phase 3 with the unbonded tendons getting into full contact with the duct adaptors, as shown in Fig. 2(c), the joint is subjected to the force induced by dowel action, $V_{R,l}$. The sliding limit $u_{sl,l}$ is determined by the radii of duct adaptor and tendon, i.e., $u_{sl,l} = \frac{D_{da} - D_{PT}}{2}$. The total shear resistance V_R along the slope is:

$$V_R = V_{R,f} + V_{R,b} + V_{R,l} = \mu N_c \operatorname{sgn}(u_{sl}) + N_{PT,sl} \sin(\varphi + \beta) + \frac{K_l}{\cos\varphi} \langle |u_{sl}| - u_{sl,l} \rangle \operatorname{sgn}(u_{sl}) \quad (4)$$

where K_l is the horizontal stiffness due to dowel action; $\langle u \rangle$ is the ramp function defined as $\langle u \rangle = u$ for $u \geq 0$, and $\langle u \rangle = 0$ for $u < 0$, giving the dowel force upon closure of the gap. The total resisting shear force in Phase 3 comprises three components, i.e., friction force $V_{R,f}$, bearing force $V_{R,b}$ and dowel action $V_{R,l}$. On the one hand, the inclination β contributes a certain amount to the shear resistance according to Eq. (4). On the other hand, the external forces along the slope is $V_{ext} \cos\varphi - N_{ext} \sin\varphi$. Therefore, part of the external axial force also acts as the restoring force and thus increases the stiffness of the system.

Eqs. (1)-(4) will degenerate to the case of flat interface by setting $\beta = 0$ as described by Sideris et al. 2014. The three phases are simulated ignoring any bond failure of the partially debonded system. The bond strength governs when bond slip takes place, considering that the grout is

subjected to bearing stresses, dowel action and the increasing tendon force. The stiffness of RSJ will decrease significantly after bond failure. A numerical study is conducted using ABAQUS CAE to evaluate the performance of resettable sliding joint in the three phases and the influence of bond failure. Two numerical models are examined here, i.e., the RSJ with a 6° inclination and the reference model with flat interface.

3. Simulation

The 3D RSJ model, as shown in Fig. 1(a), comprises two concrete segments of size $0.35 \text{ m} \times 0.35 \text{ m} \times 0.4 \text{ m}$ with four prestressing tendons each having a cross-sectional area of 140 mm^2 , where the bonded regions are modelled as cohesive contact. Embedded constraints are adopted at the two ends of tendon, which simulate the anchorages and ensure that the tendon keeps working even after bond failure. The bottom face of the bottom segment of RSJ is in dry contact with an elastic concrete base having a high CoF of 0.9, which effectively allows minor rocking but no sliding. The RSJ interface has a low CoF of 0.1 to facilitate sliding. The unbonded parts of tendons may be under bearing stresses and dowel action. A concrete damaged plasticity model and a plastic strand model are adopted to evaluate the performance. The top face of the joint is subjected to cyclic lateral loading under displacement-control to five levels ranging from 0.44% to 3.5% drift ratio based on the total height of 0.8 m, while the external axial force is 100 kN.

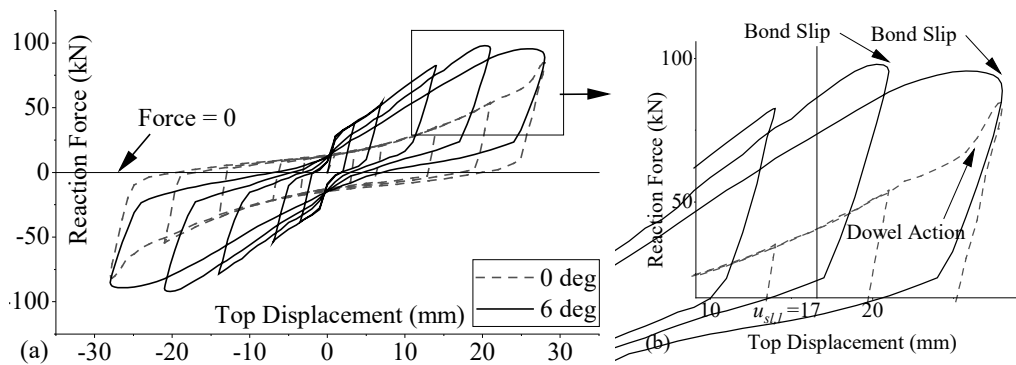


Fig. 3. Hysteretic response of 0° sliding joint and 6° resettable sliding joint. (a) Lateral reaction force versus top displacement; (b) Enlarged part of Fig. 3(a) showing bond slip and dowel action.

Fig. 3(a) shows the responses of a 6° RSJ and a 0° flat sliding joint (SJ). In Phase 1, there is no relative sliding for the two joints and thus they have the same stiffness. However, as described in Eq. (4), the RSJ has higher shear resistance than that of the flat SJ. The figure shows that the lateral force to initiate sliding of the RSJ is nearly twice that of the flat SJ. For the top drift between 3.5 to 15 mm in Phase 2, the stiffness of the RSJ is also larger than that of the flat SJ. At the initial stage of Phase 2 for the flat SJ, only friction resists the external force and the stiffness rises with the increasing deviation of tendons due to sliding as shown in Eq. (3). However, no hardening phenomenon is observed for the RSJ in Phase 2, because with the tendon elongation and hence the rising tendon force, the resulting concrete damage at the two embedded ends somewhat balances the hardening effects of tendons. The flat SJ enters Phase 3 when sliding reaches 24 mm as shown in Fig. 3(b), when the dowel force significantly increases the shear resistance. Phase 3 for the flat SJ appears to be delayed when the top displacement exceeds the sliding limit as rocking at the bottom joint also contributes to the top drift. However, before the RSJ enters Phase 3 as shown in Fig. 3(b), bond failure occurs due to the rising tendon force,



causing severe concrete damage. Therefore, the stiffness of the RSJ decreases without any hardening phenomenon due to dowel action. Fig. 3(a) shows that the RSJ has much better recentering capability upon unloading despite the concrete damage and plastic tendon deformation in the final loading cycle, while the flat SJ has much bigger residual displacement. The drift-force curves for the RSJ in Fig. 3(a) also enclose relatively large areas, suggesting good energy dissipation of the system.

In summary, this numerical study has obtained the three phases of responses of resettable and flat sliding joints to imposed cyclic lateral displacement. With the V-shaped resetting guide keys, the RSJ performs better in respect of initial stiffness, energy dissipation and resetting capability. The first aspect is essential for serviceability when relative joint displacement is undesirable under vehicle braking, collision and wind load on bridges. The excellent energy dissipation and self-centering capability of the RSJ during an earthquake will help not only to ensure structural safety but also to reduce repair costs.

4. References

Au, F.T.K., Liu Y.Q., Yuan, Y., Su, R.K.L., and Lam, N.T.K. 2019. Seismic performance of precast segmental bridge columns with resettable sliding joints: feasibility study, Proceedings of the Bridge Engineering Institute Conference, 594-598.

Liu, Y.Q., Yuan Y., Liang, F. and Au, F.T.K. 2021. Resetting response of precast segments with gently keyed interface under seismic action, *Earthquake Engineering & Structural Dynamics*, 50 (2), 601-618

Sideris, P., Aref, A.J. and Filiatrault, A. 2014. Quasi-static cyclic testing of a large-scale hybrid sliding-rocking segmental column with slip-dominant joints. *Journal of Bridge Engineering* 19 (10), 04014036

Zhang, Q. and Alam, M.S. 2020. State-of-the-Art Review of Seismic Resistant Precast Bridge Columns. *Journal of Bridge Engineering*, 25(10), 03120001



Effects of Vertical Ground Motions on the Response of Long-Span Prestressed Bridges

Hsiao-Hui Hung^{1*}, Chang-Wei Huang², and Yi-Hui Lu²

¹: National Center for Research on Earthquake Engineering, Taipei, Taiwan; email:
hhung@narlabs.org.tw

²: Department of Civil Engineering, Chung Yuan Christian University, Taoyuan, Taiwan

*: corresponding author

Keywords: near-fault earthquakes; time history analysis; balanced cantilever bridge

Abstract: The purpose of this study is to investigate the vertical seismic effects on the long-span prestressed bridge, and further to explore the conservatism of domestic seismic design codes for bridge in Taiwan for vertical earthquakes. The influence of vertical seismic effect on the seismic performance of a representative bridge is discussed by numerical analysis method. From the analysis, the differences between the results obtained by different analysis methods suggested in domestic code are compared, and the results are also compared with those obtained by adopting actual near-fault earthquakes as input through time history analysis. The analysis results show that the bridge internal force due to vertical ground excitations obtained by the static analysis method in the domestic bridge seismic design code is more conservative than that obtained by the dynamic method. In addition, the vertical seismic effects of near-fault earthquakes are strongly dependent on the frequency content of the earthquake in the vertical directions.

1. Introduction

In the early seismic design of bridges, vertical ground motions were mostly not taken into account. However, in recent years, as countries around the world have successively suffered from severe structural damage due to near-fault earthquakes, people noted that in addition to a larger velocity pulse, another notable difference between near-fault earthquakes and far-field ones is that the near-fault earthquakes are often accompanied by larger vertical excitations. Therefore, the vertical seismic effect has gradually attracted people's attention (Button et al. 2002) and has also been included in the seismic design of the structures recently. However, there is still no consistent standard for the consideration of vertical seismic effects in the seismic design codes of bridges in various countries. Until a more complete study is available, the Taiwan seismic design code for bridges revised the vertical design seismic forces with conservative considerations in 2019.

According to the Taiwan's seismic design provisions for highway bridges (MOTC 2019), for bridges located in near-fault zone, the effect of vertical seismic force should be considered. In this design code, vertical earthquake adopts the same design response spectrum as horizontal earthquake, but with a smaller magnitude. The magnitude of vertical earthquake is assumed to be 2/3 times the horizontal one. The seismic analysis methods can be categorized into static analysis

method and dynamic analysis method. For static analysis method, the lateral design force for design earthquake is the value of the design response spectrum at the fundamental period of the considered bridge multiplied by its gravitational load. The vertical design seismic force can be divided into contribution from superstructure and substructure. For the superstructure, the seismic force is the weight of superstructure multiplied by the plateau segment values of the vertical seismic design response spectrum. For the substructure, the seismic force is the weight of the substructure multiplied by the vertical spectral acceleration at period of zero. The dynamic analysis method includes elastic response spectrum method, elastic time history analysis method and nonlinear time history analysis method. For response spectrum method, the input response spectra for both horizontal directions and vertical direction are the same as that for the static analysis. For time history analysis method, all input ground motions shall be matched to the design spectrum as mentioned above using the time domain method.

In summary, it can be found that Taiwan's seismic design code adopts the same response spectrum for vertical ground motions and horizontal ground motions, but the magnitude of vertical one is taken as 2/3 of that of the horizontal one. In addition, for the static analysis, regardless of the fundamental vertical period of the bridge, the value of the design spectral acceleration conservatively adopts the value of the plateau segment of the design response spectrum, which is also the maximum value of the spectrum. In order to explore the conservatism of domestic bridge seismic design codes for vertical earthquake, and further to understand the actual impact of vertical ground excitations on the seismic performance of bridges, this study takes a long-span RC prestressed bridge as an example to numerically study this issue.

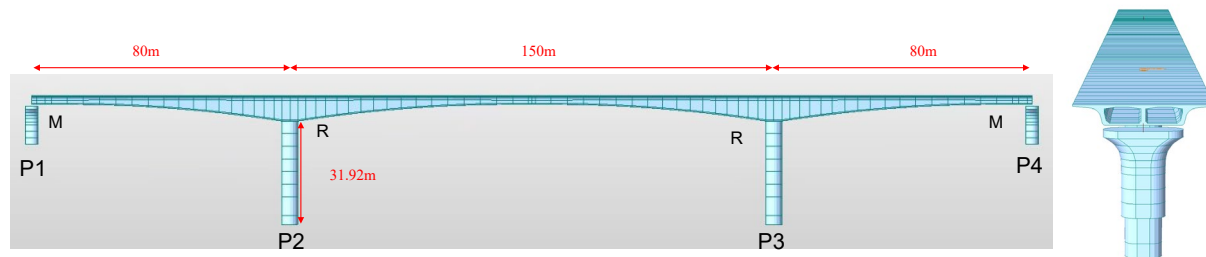


Fig. 1. Layout of the considered bridge

2. Description of the Considered Bridge

The representative bridge considered in this study is a three-span segmental, cast-in-place concrete cantilever bridges with a span configuration of 80m+150m+80m, as shown Fig. 1. The substructures are all hollow elliptical RC columns. Among them, Piers P2 and P3 are integral with the superstructure, and Piers P1 and P4 are connected to the superstructure by movable constraint in the longitudinal direction and hinge constraint in the transverse direction. To conduct the seismic analysis, a structural model of the bridge was established by commercial software Midas/Civil. This model includes 69 construction segments and 258 continuous prestress tendons. In addition, time-dependent behavior of concrete and tendon was considered using construction stage analysis. Using this analysis model, the modal analysis was conducted at first and the fundamental structural periods for the bridge were obtained. The obtained fundamental periods in the longitudinal (x), transverse (y) and vertical (z) direction are 1.46sec, 1.55sec and 1.1sec, respectively.

3. Seismic Analysis

The scope of the study involves linear analyses of the representative bridge by static analysis method, response spectrum method and linear time history analysis method according to the local design code. The analysis results are then compared with time history analysis under the input of two actual near field ground motions to investigate the conservatism of domestic bridge seismic design codes for vertical earthquakes.

The considered bridge is assumed to be located in Hualien City, Hualien County, which is among the most seismically active areas in Taiwan. Fig. 2 shows the design response spectra of Hualien City, which will be used in the static analysis and response spectrum analysis in this study. Also given in Fig.2 is the matched spectrum of the compatible earthquake matched to the site's design spectrum code. In order to figure out the difference between the behavior of the bridge under the actual near-fault earthquake and the analysis results according to the code, this study selected two real earthquake records for dynamic time history analysis. One was the records recorded at station HWA009 during 2018 Hualien earthquake (Richter magnitude scale =6.3), and the other was recorded at station TCU068 during 921 earthquake (Richter magnitude scale =7.3). The response spectra for these two real earthquake records are also shown in Fig.2.

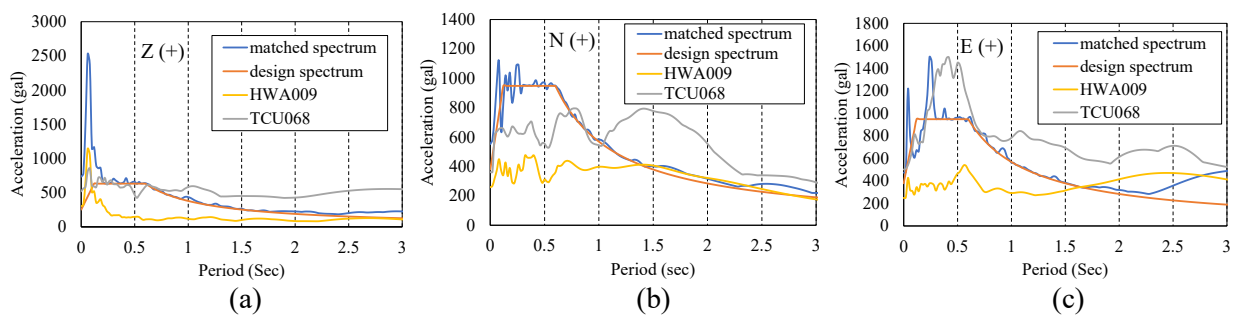


Fig. 2. Response spectrum in (a) vertical direction; (b) north-south direction; (c) east-west direction.

4. Analysis Results

Fig. 3 shows the member forces of bridge superstructure obtained by different analysis methods due to seismic forces. In these figures, H represents the analysis results considering only horizontal ground excitations, and H+V represents the analysis results considering both horizontal and vertical ground excitations. To account for the directional uncertainty of earthquake motions, a combination of seismic forces following 30% combination rule was adopted for the static analysis and response spectrum analysis. For the time history analysis, simultaneous occurrence of ground motions in different directions were considered, including simultaneous input of two horizontal ground accelerations (H case), or simultaneous input of two horizontal and one vertical ground accelerations (H+V case). By comparing the results of cases H and H+V, we can find that the influence of vertical earthquakes on the superstructure member forces of such a three-span concrete cantilever bridge is mainly in the bending moment M_y and shear force V_z at the location close to the middle supports, and the axial forces at the middle span. Vertical earthquake has no effect on the other internal forces of the superstructure, including the moment M_z , shear V_y along the transverse direction and torque, so they are not shown in this paper. In the comparison of results obtained by different analysis methods, the static analysis

method as expected is much more conservative than the response spectrum analysis method. In terms of the time history analysis results of real near-fault earthquakes, the vertical seismic effect of HWA009 is quite insignificant, but on the contrary, the vertical earthquake effect of TCU068 is relatively much larger. The observation mainly due to the fact that the response spectral value of HWA009 at the period of 1.1 sec, that is the vertical fundamental structural period of the considered bridges, is very small. On the other hand, the response spectral value of TCU068 at the period of 1.1sec is much larger. In the comparison with the real near-fault earthquake action, the results of the three analyses according to the code are greater than the results under the action of HWA009, but the results under the action of TCU068 are underestimated. This result indicates that the effect of near-fault earthquake on the seismic performance of the long span PC bridge is highly dependent on the site-specific characteristic of the records. Therefore, more research is needed before complete conclusions can be drawn.

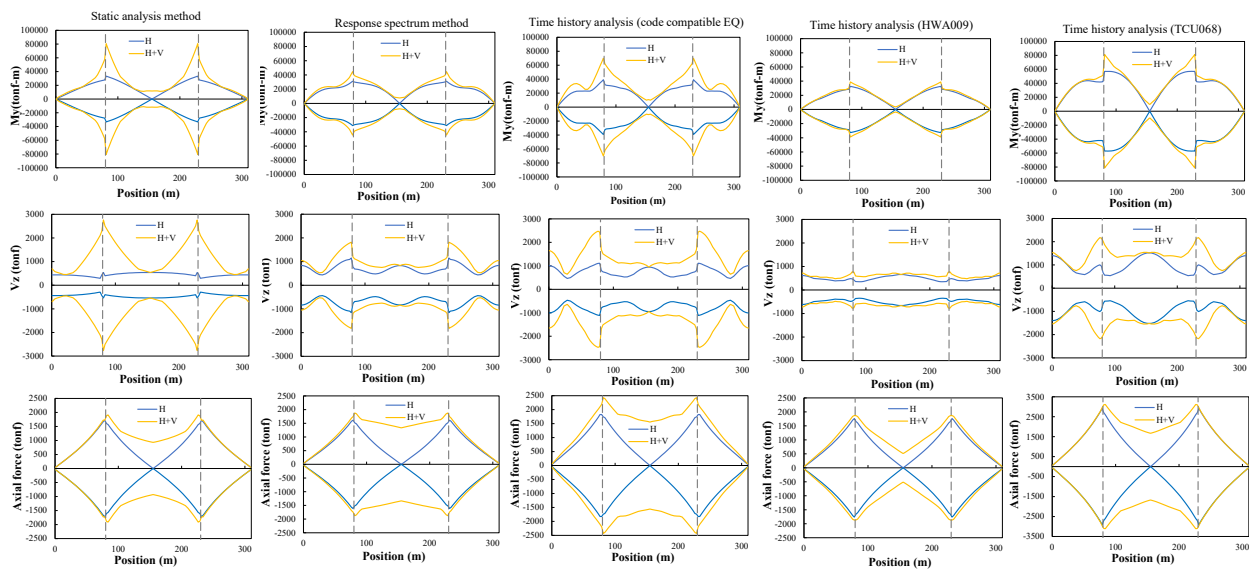


Fig. 3. Comparison diagram of the influence of vertical earthquake on member forces obtained by different analysis methods.

It should be noted that the above analysis results are based on linear analysis, that is, without considering the nonlinearity of the pier, if the nonlinearity of the pier is taken into account, the influence of the vertical seismic force will be more prominent due to the reduction of the internal forces of superstructure that are induced by lateral forces after the connected piers yielded.

5. Conclusions

This study investigates the vertical seismic effect on the seismic performance of a long span prestress concrete bridge using numerical analysis method. The analysis results show that the major influence of vertical seismic forces is on the bending moment of the main girder at the intermediate supports. In addition, the vertical seismic effects of near-fault earthquakes are strongly dependent on the site-specific characteristic of the earthquake.



Bridge Engineering Institute Conference 2023 (BEI-2023)
Rome, Italy, July 17-20, 2023



6. References

- Button, M.R., Cronin, C.J., and Mayes, R.L., 2002, Effect of vertical motions on seismic response of highway bridges, *Journal of Structural Engineering*, 128(12), 1551-1564.
- MOTC, 2019, *Seismic Design Code for Highway Bridges*. (in Chinese).



Seismic Performance Assessment of Wall Piers Supported by Pile Foundation

Shin-Tai Song^{1*} and Wen-Li Huang²

¹: Associate Professor, Department of Civil Engineering, National Chung-Hsing University, Taichung, Taiwan, R.O.C.; email: ssong@nchu.edu.tw

²: Graduate Research Assistant, Department of Civil Engineering, National Chung-Hsing University, Taichung, Taiwan, R.O.C.; email: wendy310322@gmail.com

*: corresponding author

Keywords: seismic performance; pile foundation; wall pier; capacity spectrum approach

Abstract: Piles in foundation are designated as the critical members of wall pier bents under transverse seismic loads. In this paper, the seismic performance of a wall pier bent is assessed using a nonlinear static procedure based on capacity spectrum approach. The approach uses nonlinear pushover analysis to assess the capacity of a wall pier and design spectrum to assess seismic demand. The ductility capacity of the wall pier at its performance limit state is compared with the ductility demand imposed by the design level seismic load. Satisfactory seismic performance can be guaranteed if the ductility demand does not exceed the ductility capacity. The effect of riverbed scouring on seismic performance of wall pier is also illustrated in this paper.

1. Introduction

Wall piers are widely used as the substructure for bridges with a relatively narrow deck and tall piers. Wall piers provide high lateral stiffness to ensure stability in the transverse direction of bridges. Given that this type of bridge pier behaves like a rigid wall under lateral loads, the primary damage mechanism is brittle shear failure, which must be avoided. A newly issued seismic performance evaluation specifications for highway bridges in Taiwan (MOTC 2020) designates the piles in the foundation as the critical members of wall pier bents under transverse seismic loads. A limited level of inelastic deformation is permitted at the pile/pile–cap interface. Brittle shear failure is prevented by ensuring that the shear strength of the wall pier is sufficiently larger than the lateral strength of the foundation. The seismic performance of a wall pier supported by a pile foundation can be assessed by comparing its ductility capacity with the ductility demand under the design level earthquake loads.

2. Method for Seismic Performance Assessment

In this study, the performance of wall piers under transverse seismic loads is assessed using an analytical procedure based on capacity spectrum approach, which was proposed in ATC-40 (ATC 1998) and later enhanced in FEMA-440 (NEHRP 2005). The capacity spectrum of the bridge bent is constructed based on the lateral pushover curve through an approach recommended in ATC-40 (ATC 1998). The points corresponding to the performance limits of the bridge are identified in the capacity spectrum to ensure satisfactory performance of the bridge bent. The ductility capacity of the bridge bent is equal to the ratio of the displacements at the specified performance limit and the effective yield limit state. The seismic demand on the structure is assessed using the acceleration–displacement design response spectrum, which is constructed based on the seismic demand in the

specification (MOTC 2020). The damping effect from structural yielding and the associated seismic demand reduction must be considered during the construction of the demand spectrum. The ductility demand imposed on the bridge bent is determined by the point where the demand spectrum intersects with the capacity spectrum. The detailed procedure for finding the displacement ductility demand of the structure is available in literature (ATC 1999; FEMA 2005). The seismic performance can be assessed by comparing the ductility demand with the ductility capacity at the performance limit.

3. Wall Pier Bent and Finite Element Model

A multi-span bridge in the West Coast Expressway in Taiwan is selected as the illustrative example. The geometry of the wall pier and the pile foundation is plotted in Fig. 1. The compressive strength of the concrete is $f'_{ce} = 45 \text{ MPa}$. The yield strength of reinforcements is $f_y = 475 \text{ MPa}$. The finite element model of the bridge bent is constructed in the earthquake engineering simulation platform *OpenSees* and shown in Fig. 1. The wall pier is modeled by elastic elements with extremely high stiffness. The piles are modeled by beam-column elements with fiber section. Because the piles are designated as the seismic critical members for wall pier bent, the performance limit is defined as the inelastic deformation at the pile/pile-cap interface reaching the *damage-control* limit state. The strains recommended for the *damage-control* limit state to avoid subsequent replacement of the structure are available in ACI318-19 (ACI 2022), with a confined concrete compressive strain limit of 0.015 and a longitudinal steel tensile strain limit of 0.050. The bridge is assumed to be located at a medium sand site, with an effective friction angle of $\bar{\phi} = 35^\circ$. In the finite element model, the soil resistance on piles is modeled by three types of spring, representing the friction and lateral forces applied on the pile and bearing resistance at the pile tip. The bridge is originally designed with the piles fully embedded in the soil, that is, $L_a = 0 \text{ m}$. However, the bridge suffers from the pile exposure of $L_a = 6 \text{ m}$ caused by riverbed scouring.

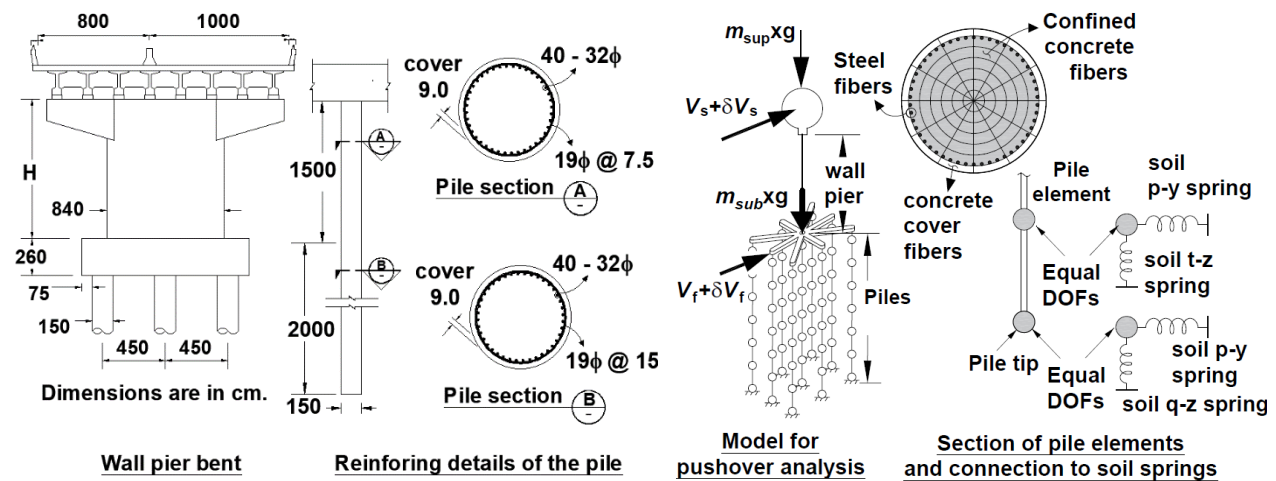


Fig. 1. Geometry and finite element model of a bridge bent

4. Capacity and Demand Spectra

The capacity spectrum of the wall pier bent is constructed based on the load-displacement curve from monotonic pushover analysis. Figure 2 shows the capacity spectra of the wall pier bent before riverbed scouring (i.e., $L_a = 0 \text{ m}$) at a scour depth of $L_a = 6 \text{ m}$. The equivalent yield limit state of

the wall pier is determined by the bilinear idealization of the capacity spectrum. The ductility capacity of the wall pier bent at the *damage-control* limit state is $\mu_{cap} = 1.89$ when the piles are fully embedded. The overturn of the wall pier under lateral loading imposes large axial force on the leading row of the piles. The figure shows that the piles in the first row of the foundation are only subjected to an axial force of $P_{1^{st} row} = 3185$ kN before the lateral push load is applied. The axial force increases about 6 times to $P_{1^{st} row} = 18895$ kN when the pile is at the *damage-control* limit state. At the scour depth of $L_a = 6$ m, the ductility capacity of the wall pier bent at the *damage-control* limit state reduces to $\mu_{cap} = 1.75$. The axial force on the leading row of the pile is $P_{1^{st} row} = 12537$ kN. In view of the effect of soil nonlinearity, the effective damping ratio at yield limit state can be determined by performing cyclic pushover analysis of the wall pier bent with a lateral displacement up to the equivalent yield displacement. The effective damping ratios at the yield limit state are estimated to be $\zeta_{el} = 10\%$ for $L_a = 0$ m and $\zeta_{el} = 8.5\%$ for $L_a = 6$ m. The 5% damping acceleration–displacement design response spectrum correlated to the maximum considered earthquake (MCE_R) at the bridge site is plotted in Fig. 2. The response spectra at damping ratios of $\zeta = 8.5\%$ and $\zeta = 10\%$ are also plotted in Fig. 2 and used to construct the demand spectrum for seismic performance assessment.

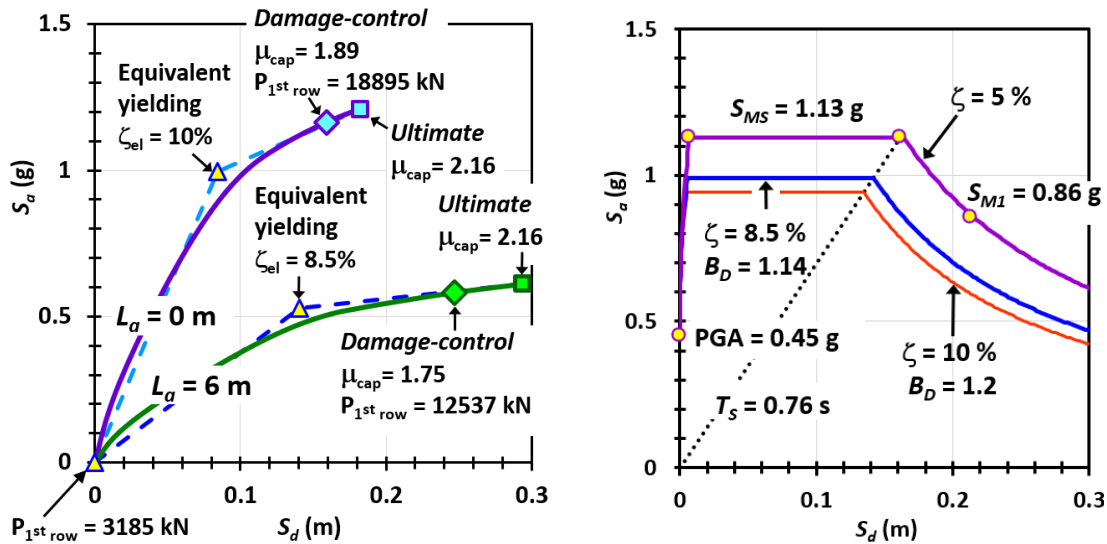


Fig. 2. Capacity spectra of the bridge bent and MCE_R acceleration–displacement spectrum of the site

5. Seismic Performance Assessment of the Wall Pier Bent

The seismic performance of the wall pier bent is assessed by capacity spectrum approach. An iterative process is recommended in ATC-40 (1999) for finding the point where the demand spectrum intersects with the capacity spectrum. The demand spectrum needs to be scaled down because of the damping effect caused by the inelastic deformation of the wall pier bent. Specifically, FEMA 440 (NEHRP 2005) suggests a correlation between the inelastic deformation, characterized by the displacement ductility factor μ , and hysteretic damping ζ_h . The equivalent damping ζ_{eq} of the yielded wall pier bent is the sum of effective damping ζ_{el} at the yield limit state and hysteretic damping ζ_h after the yield limit state. The damping coefficient B_D from ASCE7-16 (ASCE 2017)

is used for scaling the demand spectrum. The results of the seismic performance assessment are plotted in Fig. 3. For the scour depth of $L_a = 0$ m, the demand spectrum intersects the capacity spectrum at a displacement ductility demand of $\mu_{dem} = 1.10$, which provides a hysteretic damping of $\zeta_h = 0.05\%$. The equivalent damping of the wall pier bent is $\zeta_{eq} = 10.05\%$, and the damping coefficient is $B_D = 1.201$. For the scour depth of $L_a = 6$ m, the displacement ductility demand is assessed to be $\mu_{dem} = 1.58$, providing a hysteretic damping of $\zeta_h = 1.43\%$. The equivalent damping of the wall pier bent is $\zeta_{eq} = 9.93\%$, and the damping coefficient is $B_D = 1.197$. The similar damping coefficients make the demand spectra for $L_a = 0$ m and $L_a = 6$ m almost identical. The figure shows that prior to riverbed scouring, the ductility demand caused by MCE_R is $\mu_{dem} = 1.10$, which is 42% smaller than the ductility capacity of $\mu_{cap} = 1.89$. The wall pier is design with satisfactory seismic performance. When the scour depth reaches $L_a = 6$ m, the ductility demand increases to $\mu_{dem} = 1.58$, which is only 9.7% smaller than the ductility capacity of $\mu_{cap} = 1.75$. Riverbed scouring considerably deteriorates the seismic performance of the wall pier bent.

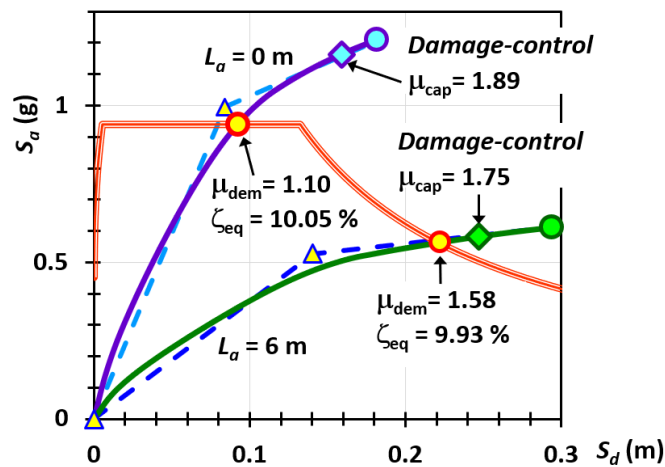


Fig. 3. Seismic performance assessment of the wall pier bent

5. Acknowledgements

This research was sponsored by the Ministry of Science and Technology of Taiwan, R.O.C., under Grant No. 110-2625-M-005-003. The financial support is gratefully acknowledged.

6. References

- American Concrete Institute (ACI) 2022. Building Code Requirements for Structural Concrete and Commentary, ACI318, Farmington Hills, Michigan, U.S.A.
- American Society of Civil Engineers (ASCE) 2017. Minimum Design Loads and Associated Criteria for Buildings and Other Structures, ASCE7-16, Reston, Virginia, U.S.A.
- Applied Technology Council (ATC) 1996. Seismic Evaluation and Retrofit of Concrete Buildings. ATC-40, Redwood City, California, U.S.A.
- Ministry of Transportation and Communications (MOTC) 2020. Seismic Performance Assessment and Retrofit Design Specifications for Highway Bridges, Taipei, Taiwan, R.O.C.
- National Earthquake Hazards Reduction Program (NEHRP) 2005. Improvement of Nonlinear Static Seismic Analysis Procedures, FEMA 440, Washington, D.C., U.S.A.



Bridge Engineering Institute Conference 2023 (BEI-2023)
Rome, Italy, July 17-20, 2023



Experimental Techniques



Flexural Behavior of 3D-Printed Beam Members

In-Hwan Yang ^{1*}, Quang-The Bui ², Jihun Park ², Jungwoo Lee ³, and Changbin Joh ³

¹: Kunsan National University, Kunsan, South Korea; email: ihyang@kunsan.ac.kr

²: Kunsan National University, Kunsan, South Korea

³: Korea Institute of Civil Engineering and Building Technology, Goyang, South Korea

*: corresponding author

Keyword: 3D printed mortar; flexural behavior; interlayer reinforcement; rebar

Abstract: 3D printing, which is a promising technology in the construction field, has been rapidly developing in recent years. Because of the layer-by-layer production process, most of 3D-printed structures are applied to the structure under compression or covers like columns and walls. Therefore, this study was conducted to investigate the flexural behavior of 3D-printed beam members. Additionally, some methods to improve the flexural behavior of the 3D-printed beams were performed. To reach these aims, four different beam members were printed and examined under 4-point loading test. The effects of interlayer reinforcement, penetrating into mortar layers with hole of beams, and longitudinal rebars on the bending behavior of 3D-beam members were examined. The failure pattern of the 3D-printed beams was observed, and the performance of interlayer reinforcement was evaluated. The 3D-printed beams without longitudinal rebar were abruptly collapsed at the interlayers of the beams. The flexural capacity and post-cracking behavior of the 3D-printed beams reinforced with rebar were significantly improved. In addition, the improvement of flexural behavior by adding interlayer reinforcement to the 3D-printed beam was presented. The addition of the interlayer reinforcement enhanced the flexural capacity by approximately 25% and improved the ductility of the beams.

1. Introduction

Nowadays, the application of 3D printing technology has been paid more attention to the construction field because of its reducing construction time, construction without formwork, design freedom, etc. Due to the layer-by-layer constructing process, bonding strength at interlayer of the 3D printed structure is considered as the strength of the structure. Additionally, the 3D-printed structure has the anisotropy properties (Joh et al., 2020; Wolfs et al., 2019) thereby most 3D-printed structures were applied as wall, column, or structure subjected to compression (Kreiger et al., 2019). To improve strength of 3D-printed structure in tension, reinforcement for 3D-printed structure is necessary. According to the previous studies, the flexural strength and post-cracking behavior of the 3D printed mortar were improved significantly by using the reinforcement for the 3D printed mortar. Although several studies were conducted to investigate the properties of 3D-printed mortar (Ma et al., 2019; Park et al., 2021), the evaluation of 3D-printed mortar in large scale is still limited. Therefore, this study was performed to examine the flexural behavior of the 3D-printed beam subjected to flexure as well as the feasibility of reinforcement for the 3D-printed structure.

2. Mixtures

The mixture used for the 3D-printing process is given in Table 1. In this study, Ordinary Portland cement (OPC) with a specificity of 3.14 g/cm^3 was used as a cementitious material. To improve the extrusion and bonding properties, silica fume (SF) with a SiO_2 content of 91.3% was used as a supplementary cementitious material. Class C Fly ash (FA) used in the mixture had a specific gravity of 2.26 g/cm^3 and a loss on ignition of 2.8%. Sand with a size range from 0.16-0.2 mm was selected to ensure good extrusion during the printing process. To increase the concrete filament extrusion under the low water-binder ratio of 0.29, a high-performance water-reducing agent (HWRA) was added to the mixture. Finally, the mixture included a viscosity agent to prevent segregation of the materials and enhance the viscosity of the mixture.

Table 1. Mixture of the 3D printing mortar

W/B	Unit weight (kg/m^3)						
(%)	Water	OPC	SF	FA	Sand	HWRA	Viscosity Agent
0.29	240	576	79	172	1154	8.27	1.65

Note. OPC: ordinary Portland cement, SF: silica fume, FA: fine aggregate, and HWRA: high-performance water-reducing agent.

3. Experimental Program

The beam dimensions are shown in Figure 1. Four beams were printed by layer with a thick of 10 mm. To prevent the buckling failure during the printing process, the breaking time of 30 minutes was set per each 30 printed layers. Table 2 lists the parameter of the beam member.

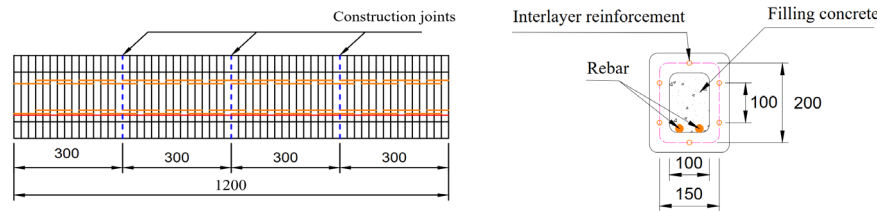


Fig. 1. Beam dimensions

Table 2. Parameter of beam members

Beam name	Interlayer reinforcement	Filling concrete	Rebar
L1-F0-R0	$\Phi 3\text{mm}(\text{SL}=40\text{mm})$	–	–
L1-F1-R0	$\Phi 3\text{mm}(\text{SL}=40\text{mm})$	–	–
L0-F1-R1	–	Yes	$2\Phi 13\text{mm}$
L1-F1-R1	$\Phi 3\text{mm}(\text{SL}=40\text{mm})$	Yes	$2\Phi 13\text{mm}$

To improve the tensile strength of the 3D-printed beams, steel interlayer reinforcements with a diameter of 3 mm and a spliced length of 40 mm were penetrated into the printed layers of the L1-F0-R0, L1-F1-R0, and L1-F1-R1 beams. In addition, the L0-F1-R1 and L1-F1-R1 beams were reinforced by 2 steel rebar with a diameter of 13 mm and the filling concrete. To investigate the flexural behavior of the printed beams, a four-point bending test was performed. The printed beam was put on a pair steel roller supports with a span length of 900 mm. A displacement control speed of 1.5 mm/min was applied in this bending test. The actual bending

beam test is exhibited in Figure 2. One LVDT was set under the beam to measure the displacement during the test.

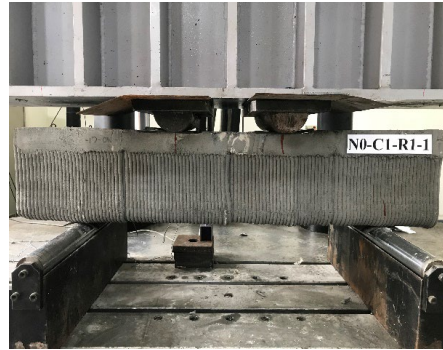


Fig. 2. 4–point bending test

4. Flexural Behavior

The failure pattern of the 3D–printed beam with and without rebar and filling concrete are presented in Figure 3 and 4. It shows that the 3D–printed beams without rebar and filling concrete were collapsed by the abrupt separation of middle section. Meanwhile, by reinforcing rebar and filling concrete, this failure was prevented definitely in the L0-F1-R1 and L1-F1-R1 beams. These beams were failed by a shear crack occurring from the support to the loading point.



Fig. 3. Failure pattern of 3D printed beam without rebar and filling concrete

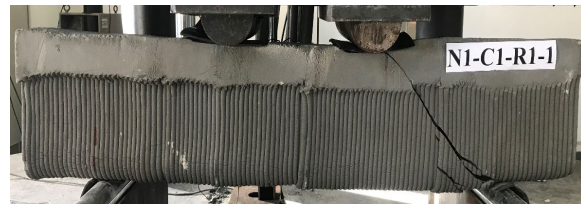


Fig. 4. Failure pattern of 3D printed beam with rebar and filling concrete

Figure 5 illustrates the load-deflection curves of four 3D–printed beams.

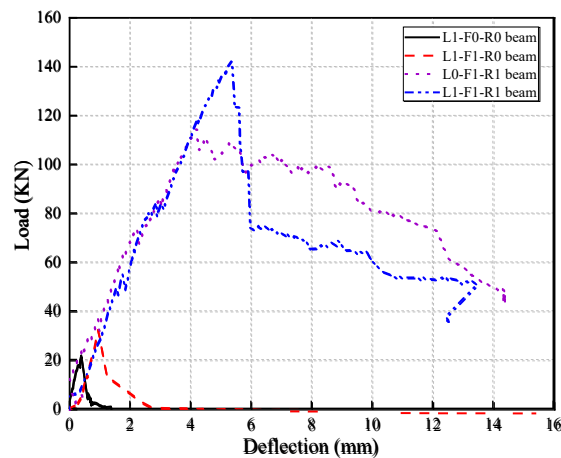


Fig. 5. Load-deflection curves



The test results show that the L1-F0-R0 beam, including only interlayer reinforcement presented the lowest load capacity of 21.66 kN. By including interlayer reinforcement and filling concrete, load capacity of the L1-F1-R0 was enhanced by 46.2% with a value of 31.67 kN. The superior improvement in flexural behavior were exhibited in the L0-F1-R1 and L1-F1-R1 beams including rebar and filling concrete. For the L0-F1-R1 beam, the maximum load was 114.37 kN and the ultimate deflection of this beam was 14.36 mm. It implied that the load capacity of the 3D–printed beam was improved by approximately 5 times by using rebar and filling concrete in the hole of the beam. The largest load capacity of 142.22 kN was obtained in the L1-F1-R1 beam, which was enhanced by interlayer reinforcements, rebar, and filling concrete. It indicates that with the addition of interlayer reinforcement, the load capacity of the 3D–printed beam was improved by approximately 25% when compared the L0-F1-R1 and L1-F1-R1 beams. In addition, the deflection of the beams including rebars and filling concrete were higher than that of the beams without rebar.

5. Conclusions

The flexural behavior of the 3D–printed beam was evaluated in this study, and some conclusions could be drawn as follows:

- The failure pattern of 3D–printed beam implies that the bonding strength between the interlayers played importance roles in flexure. Therefore, the reinforcement is required for the 3D–printed member.
- The addition of the interlayer reinforcements enhanced the load capacity of the 3D–printed beam by approximately 25%.
- The flexural behavior of the 3D–printed concrete was improved significantly by using rebar and filling concrete.
- By combining interlayer reinforcement, rebar and filling concrete, the L1-F1-R1 beam exhibited the superior performance of the flexure when compared to the others.

6. References

Joh, C., Lee, J., Bui, T. Q., Park, J., & Yang, I.-H. (2020). Buildability and Mechanical Properties of 3D Printed Concrete. In *Materials* (Vol. 13, Issue 21).
<https://doi.org/10.3390/ma13214919>.

Kreiger, E. L., Kreiger, M. A., & Case, M. P. (2019). Development of the construction processes for reinforced additively constructed concrete. *Additive Manufacturing*, 28, 39–49.
<https://doi.org/https://doi.org/10.1016/j.addma.2019.02.015>.

Ma, G., Li, Z., Wang, L., & Bai, G. (2019). Micro-cable reinforced geopolymer composite for extrusion-based 3D printing. *Materials Letters*, 235, 144–147.
<https://doi.org/10.1016/j.matlet.2018.09.159>.

Park, J., Bui, Q.-T., Lee, J., Joh, C., & Yang, I.-H. (2021). Interlayer Strength of 3D-Printed Mortar Reinforced by Postinstalled Reinforcement. *Materials*, 14(21), 6630.
<https://doi.org/10.3390/ma14216630>.



Bridge Engineering Institute Conference 2023 (BEI-2023)
Rome, Italy, July 17-20, 2023



Wolfs, R. J. M., Bos, F. P., & Salet, T. A. M. (2019). Hardened properties of 3D printed concrete: The influence of process parameters on interlayer adhesion. *Cement and Concrete Research*, 119, 132–140. <https://doi.org/10.1016/j.cemconres.2019.02.017>.



ELSS Joint: Development of Semi-Rigid Joint for Joining Precast Prestressed Concrete Slabs in Japan

Mohammad Emran Nasery^{1*}, Tatsuhiko Mimoto², and Nobuaki Sakurai³

¹ Kyokuto Kowa Corporation, Hiroshima, Japan; email: Nasery@kkn.co.jp

² Kyokuto Kowa Corporation, Hiroshima, Japan; email: Mimoto@kkn.co.jp

³ Nippon Steel Engineering, Tokyo, Japan; email sakurai.nobuaki.xd8@eng.nipponsteel.com

* Corresponding author

Keywords: Precast concrete slabs; Joint; Loop joint; ELSS joint; Productivity; Slab replacement

Abstract: Approximately 40% of the expressways in Japan have been used for 30 years or more. These expressways have deteriorated due to aging, excessive traffic load, and environmental factors. Large-scale renewal and repair projects, which include bridge slab replacement, have been launched all over Japan. Because the expressways are in operation, slab replacement work needs to be done as quickly as possible. However, the commonly used loop joints for joining precast prestressed concrete slabs do not allow the construction time to be shortened due to their structural complexity. This study evaluates the structural durability of a newly developed semi-rigid joint, called the Economy, Labor Saving, Speedy (ELSS) joint, and its advantages over the commonly used loop joints in terms of construction time and efficiency (labor man-hours). To confirm the structural durability of the ELSS joint, the results of a wheel load running test are reported. Furthermore, a loop joint and the ELSS joint are compared in terms of material usage and construction time using an example. The results show that for joining precast prestressed concrete slabs, the ELSS joint provides sufficient structural durability, shortens construction time, reduces labor man-hours and material usage, and simplifies future slab replacement work compared to loop joints.

1. Introduction

The majority of the roads and bridges in Japan were constructed during a period of high economic growth after World War II. Approximately 40% of Japanese expressways have been used for 30 years or more. These expressways have deteriorated due to aging, fatigue loading caused by heavy traffic, and environmental factors such as damage from salt (used as an anti-freezing agent) (Kita et al., 2020). To address this challenge, Nippon Expressway Company (NEXCO), which is the main operator of expressways in Japan, has launched large-scale renewal and repair projects. As part of these projects, the renewal, repair, and reinforcement of highway bridge slabs are being carried out. Slab replacement work has thus increased all over Japan. The replacement work, which is expected to cover approximately 230 km, is mostly for reinforced concrete (RC) slabs that have deteriorated due to fatigue.

The completion of these large-scale renewal projects faces some challenges. NEXCO aims to complete these projects with minimal traffic closure, efficient replacement work, improved durability of the slabs (slabs should have a life span of 100 years), and simplified future maintenance work. Thus, precast prestressed concrete slabs are the best option in terms of

construction time and durability. Precast slabs are commonly joined using RC joints called loop joints, as shown in Fig. 1. However, loop joints have several limitations, such as the required formwork, complex rebar arrangement, inability to be used for thin slabs, required concrete casting and curing, lengthy construction time, difficult future replacement (loop joint rebar must be cut), and need for several skilled workers.

To address these challenges, Nippon Steel Engineering and Kyokuto Kowa Corporation have collaboratively developed a new semi-rigid joint, called the Economy, Labor Saving, Speedy (ELSS) joint, that has sufficient durability while reducing the construction time and simplifying the construction method compared to those for loop joints. The ELSS joint is shown in Fig. 2.

The ELSS joint is the result of several experiments conducted to determine the best joint filler materials, required thickness and shape of the joint, and structural performance and durability under static and dynamic loading. From the results of several experiments and analyses, it was concluded that if (i) slabs are additionally reinforced with rebar in areas adjacent to the slab-joint interface, (ii) the joint filling material has a Young's modulus of 1/20 to 1/3 of that of the slab concrete, (iii) the joint has a width of at most 40 mm, (iv) a joint filler material with a bond tensile strength equivalent to or greater than that of polymer cement mortar or epoxy resin mortar is used, and (v) the bond tensile strength is equal to or greater than the tensile strength of the concrete in the slab, then the bond shear strength at the slab-joint interface will be sufficient to prevent slab-joint peeling or detachment and the vertical displacement will not cause any degradation of the water resistance and asphalt durability (Kita et al., 2017; Sakurai et al., 2018; Kita et al., 2020).

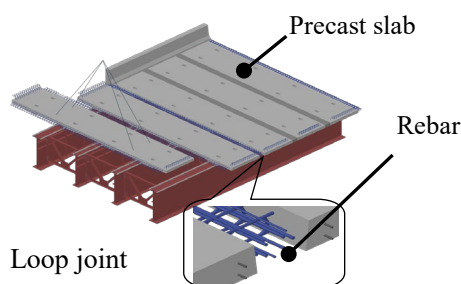


Fig. 1. Diagram of conventional loop joint

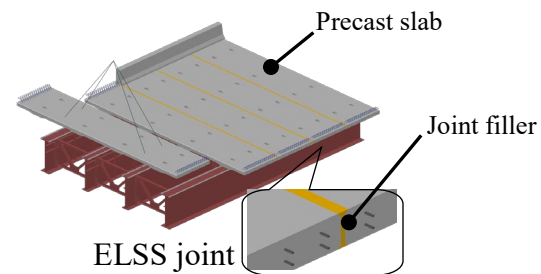


Fig. 2. Diagram of ELSS joint

2. ELSS Joint Characteristics and Advantages

The ELSS joint has a simpler construction method than that for loop joints as there is no rebar in the joint, which greatly reduces the joint casting time and future replacement work. Moreover, as starter bars coming out of the precast slabs are not necessary for the ELSS joint, the formwork and rebar arrangement for the precast slabs in the factory can be simplified, improving manufacturing productivity. The maximum transportable panel (slab) size in Japan is 2.5 m. The slabs designed for loop joints have a maximum transportable width of 2.1 m and those for the ELSS joint have a maximum transportable width of 2.4 m.

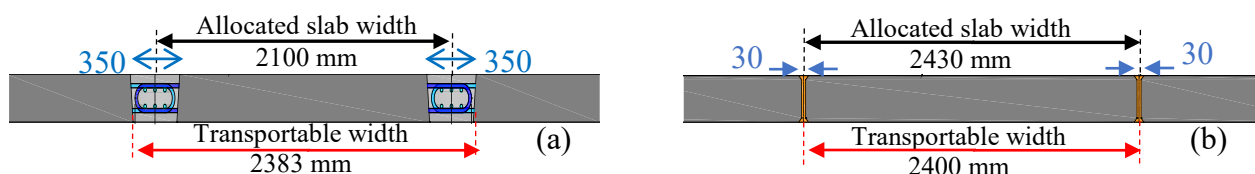


Fig. 3. Cross-sectional view of (a) loop joint and (b) ELSS joint

This longer maximum width can reduce the number of slabs that need to be designed and manufactured for the ELSS joint by about 15% on average, which will shorten the slab manufacturing time in the factory and replacement activity on site. Figure 3 shows cross-sectional views of a loop joint and the ELSS joint.

3. Wheel Load Running Test for Fatigue Durability of Slab-ELSS Joint Connection

According to the Specifications for Highway Bridges of the Japan Road Association, the RC slabs need to be examined and verified for fatigue durability through step loading. To achieve this, a running wheel load of 250 kN was run over the slab back and forth 100,000 times and the deflection and cracks at the bottom face of the slab were evaluated (Goto et al., 2020). The durability was then judged by checking whether there was any water leakage on the bottom face of the slab when water was pooled on the top of the test specimen. To verify the fatigue durability of the ELSS joint, we conducted a wheel load running test (NEXCO test method 442-2019) on two slabs connected by an ELSS joint (joint width: 25 mm). The two specimens were constructed as per NEXCO test method 442-2019. The ELSS joint materials used for these specimens were polymer cement mortar and epoxy resin mortar, respectively. The results show that there was no water leakage in the test specimens where negative bending was not present (the top face of the slab-joint connection was in compression). This means that the ELSS joint can be used in NEXCO projects for slab-joint connections for which the top face is in compression without any safety concerns.

4. Comparison of Loop Joints and ELSS Joint in Actual Bridge Construction Project

To compare the differences in using the two types of joints, a three-span continuous steel non-composite slab girder bridge with an overall length of 123.1 m (each span had a length of 40.7 m and a total width of 10.66 m) was selected. The RC slabs were to be supposedly replaced with prestressed concrete slabs. Table 1 presents the material usage for the loop joints and the ELSS joint for this project. As shown, there is a drastic difference in material usage; the ELSS will reduce the project cost and shorten the construction time. The number of precast slabs required for loop joints and the ELSS joint is 61 and 50, respectively. This means that a shorter production time is required for precast slabs when the ELSS joint is used. Additionally, the reduction in material, rebar, and formwork usage for the ELSS joint is substantial.

Table 1. Comparison of using loop joint and ELSS joint

		Loop joint	ELSS joint	Difference
Total number of precast slabs		61	50	↓11
Joint	Materials	49.4 m ³	4.6 m ³	↓44.8 m ³
	Rebar	8.851 tons	0.000 tons	↓8.851 tons
	Formwork	201 m ²	36 m ²	↓165 m ²

Furthermore, Table 2 and Fig. 4 demonstrate that using the ELSS joint can reduce the overall construction time by 11% and the labor man-hours by 14%, particularly in slab manufacturing and joint construction.

Table 2. Construction time comparison of loop joints (blue) and ELSS joint (orange)

Activity	1 st Month			2 nd Month			3 rd Month			4 th Month		
	10	20	30	10	20	30	10	20	30	10	20	30
Traffic operation switching	[Gantt chart bars]											
Removal of existing floor slab / temporary precast floor slab	[Gantt chart bars]											
Precast floor slab joint	[Gantt chart bars]											
Bridge construction work	[Gantt chart bars]											
Traffic operation switching	[Gantt chart bars]											



Fig. 4. Productivity (man-hours) comparison of loop joints and ELSS joint

5. Conclusion

This study evaluated the characteristics of the ELSS joint and its advantages over the conventionally used loop joints for joining prestressed concrete bridge slabs in Japan. The results show that using the ELSS joint reduces the construction time, material usage, and labor man-hours and simplifies future replacement work compared to using loop joints, while providing the required structural performance and durability. In future research, we will expand the usage of the ELSS joint that is subject to different types of loading. Particularly, we are trying to find ways to achieve a desirable result when using the ELSS joint in slab-joint connections subjected to a negative bending moment (the top face of the slab-joint connection is in tension).

6. References

Goto, S, Nagatani, T, Homma, A & Hirano, K (2020) ‘Proposal of fatigue durability evaluation method for PC slabs’ *Journal of Structural Engineering, Japan Society of Civil Engineers* Vol 66A, pp. 762-773,

Kita, S, Nakayama, H, Sakurai, N, Maekawa, K, Maruno, M, Satake, S, Oigawa, Y & Taniguchi, S. (2017) ‘A study of strength evaluation of a joint structure using a beam model in semi-continuous precast floor slabs’, *Journal of Structural Engineering, Japan Society of Civil Engineers*, Vol 63A, pp.49-56.

Kita, S, Sakurai, N, & Maekawa, K (2020) ‘Durability Evaluation with Wheel Running Tests and Computational Simulations on Precast PC Slab with Half Rigid Joint Under the Negative Bending Moment’. *Journal of Japan Society of Civil Engineers, Ser. E2 (Materials and Concrete Structures)*, 76(4), pp.403-420.

NEXCO Test method, Volume 4, (2019) *Structural test method*, 442-2019, P.91-94

Sakurai, N, Maekawa, K & Matsui, S (2018) ‘Semi-rigid Connections for Precast Concrete Slabs, Bridges and Foundations’, Vol.52, No.9, pp.29-36,



Horizontal–Vertical Ratio for Concrete Pumping Pipe

Ki-Yeol Kim¹, Young-Jin Kim², and Myoung-Sung Choi^{3*}

¹: Dankook University, Youngin, South Korea; email: kiyeol520@naver.com

²: Korea Concrete Institute, Seoul, South Korea; email: kimcrete@naver.com

³: Dankook University, Youngin, South Korea; email: choims@dankook.ac.kr

*: corresponding author

Keywords: Concrete pumping; Pipe; Rheology; Horizon-vertical ratio; Computational fluid dynamics

Abstract: For the construction of high-rise building, a horizontal pipe pumping test is usually conducted and using obtained test results, vertical actual constructing condition could be evaluated. In this study, horizontal and vertical pumping experiments are performed under various mixing and construction conditions using rheology-based quantitative performance prediction technology to derive a horizontal–vertical ratio of concrete pumping pipe for evaluating concrete pumping performance. Computational fluid dynamics is used to analyze the correlation between experimental results and additional vertical lengths. Analysis results confirm that compressive strength and plastic viscosity correlate with vertical and horizontal correlation coefficients; the pipe length, flow rate, and yield stress have no significant effect on the correlation coefficient. Based on analysis result considering various factors, multiple regression analysis is performed to propose horizontal–vertical ratio relationship for the concrete pumping pipe.

1. Introduction

Concrete pumping is used to transport concrete to a target location using a pump and piping. The concrete transport via pumping is highly efficient in terms of the amount of poured concrete, pouring time, and cost compared to methods that use buckets, conveyors, and chutes. Further, concrete pumping can ensure even pours at sites where entry of large equipment is restricted or difficult. Thus, high-rise buildings are constructed using concrete pumping at most construction sites.

To this end, a quantitative prediction method for pumping performance was developed recently based on rheology; this method has applied to actual construction sites. Other studies have investigated the concrete pumping mechanism and influencing factors, and various basic technologies required for pumping design have been developed based on such studies.

Thus, in this study, pumping tests for horizontal and vertical pipes were conducted under various mixing and construction conditions. We used the rheology-based quantitative pumping performance prediction technology to overcome the limitations of the existing horizontal–vertical ratios. The test results and computational fluid dynamics (CFD) analysis results were analyzed to propose a new horizontal–vertical ratio of the concrete pumping pipe.

2. Pumping Tests

2.1 Material properties

Concrete mixtures used in the vertical and horizontal pipe pumping tests include the general-strength concrete of 24, 27, and 30 MPa and high-strength concrete of 40, 60, and 80 MPa; these mixtures are commonly used in the field. Table 1 lists the materials and the mix proportions for each strength. Ordinary Portland cement with a specific gravity of 3.15 was used. For fine aggregates, natural river sand with a particle size of 0.08 ~ 5 mm was mixed with crushed stone at a 7:3 ratio. The fine aggregate had a specific gravity of 2.59, fineness modulus of 2.81, and a moisture content of 2.43%. A coarse aggregate made of limestone with a maximum size of 20 mm was used, and it had a specific gravity of 2.61, fineness modulus of 5.65, and moisture content of 0.8%. The mixing water was adjusted by considering the moisture content of the fine and coarse aggregates. A PC-based high-range water-reducing admixture (HRWRA) was used, and the amount used was shown as a percentage (%) compared to the weight of the binder listed in Table 1.

Table 1. Mix properties used for horizontal and vertical pipe pumping test

Material	Design strength					
	Normal strength (MPa)			High strength (MPa)		
	24	27	30	40	60	80
Ordinary portland cement (kg/m ³)	245	263	287	282	297	389
Water-binder ratio	0.48	0.45	0.40	0.35	0.32	0.25
Fly ash (kg/m ³)	35	38	41	47	54	33
Blast furnace slag (kg/m ³)	70	75	82	141	162	195
Slica fume (kg/m ³)	-	-	-	-	-	33
Gravel (kg/m ³)	921	900	910	961	958	891
Sand (kg/m ³)	905	884	828	751	696	696
High-range water-reducing admixture (%)	0.35	0.31	0.28	0.18	0.24	0.25

2.2 Experimental pipe

Pumping tests for horizontal and vertical pipes are conducted to obtain the vertical and horizontal correlation coefficients for concrete pumping, as shown in Figs. 1. The horizontal pipe pumping test was conducted using pipe lengths of 100, 200, 500, and 1000 m, as shown in Fig. 1(a). In this test, pressure gauges were installed 10 m from the pump outlet and at 3 m before the outlet for each target pumping length to measure the pressure. For the curved pipe, a 90° curved pipe with a radius of 1.0 m was used. The number of installed curved pipes was minimized to reduce their influence because there has been considerable controversy over the influence of curved pipes on the pressure drop. Fig. 1(a) shows the pressure measurement locations for the entire length of the horizontal pipe pumping test.

Fig. 1(b) shows the vertical test was conducted using vertical pipe lengths of 100 and 200 m. In this test, the first pressure gauge was installed 20 m from the pump inlet in the horizontal section, and the last pressure gauge was installed 3 m before each outlet in the vertical section, similar to that in the horizontal pipe pumping test. For the curved pipe, a 90° curved pipe with a radius of 1 m was used. One curved pipe was installed at the location of the first pressure sensor, and the other at the outlet. All pipes had a diameter of 127 mm and a thickness of 7.7 mm.

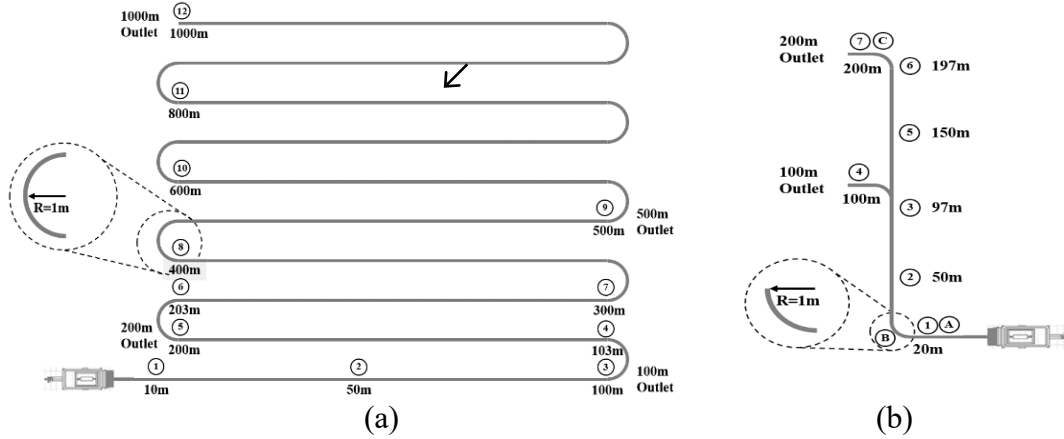


Fig. 1. Concrete pumping test: (a) Schematic ground plan of the horizontal pumping circuits and the location of the pressure gauges; (b) Schematic ground plan of the vertical pumping circuits and the location of the pressure gauges

In the tests, the flow rate was calculated considering the filling coefficient by adjusting the stroke time of the pump under various mixing conditions; the pressure was measured using the pressure gauges installed in the pipes.

3. Result of Analysis

3.1 Prediction of vertical pumping performance using the CFD technique

The experimental and analysis results for vertical heights of 100 and 200 m were compared to verify the analytical technique used; the results are shown in Fig. 3. The results show that the CFD technique is effective under the experimental conditions of this study. Therefore, it is worth to apply for the additional lengths of 500 m and 1000 m. The experimentally determined thickness of the lubrication layer and the rheological constants of the concrete and lubrication layer were used as input data, and the pressure required for the target flow rate at each vertical length was determined and utilized for analyzing the horizontal-vertical ratio.

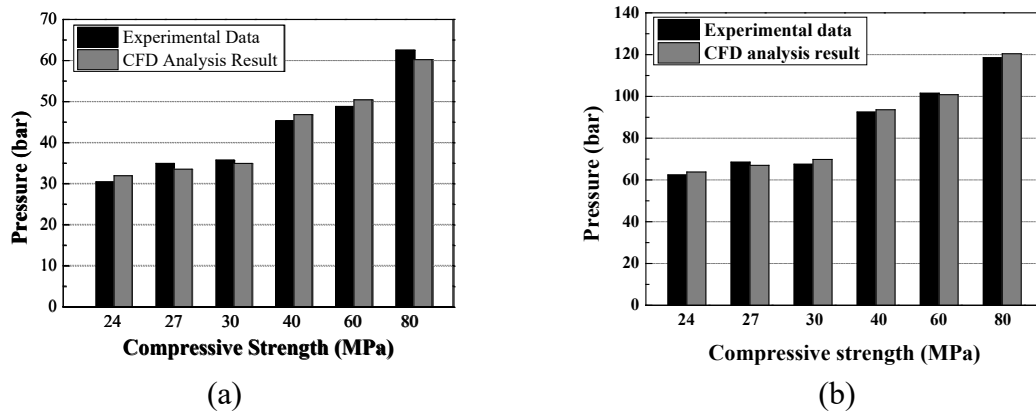


Fig. 2. Comparison between experimental data and CFD analysis: (a) 100 m case; (b) 200 m case

3.2 Horizontal–vertical ratio

The pumping tests for the horizontal and vertical pipes and CFD analyses were conducted under various compressive strengths, pipe lengths, and flow rate conditions; the horizontal–vertical ratios were derived. The analysis results indicated that the compressive strength and plastic viscosity are closely related to the horizontal–vertical ratio, and the pipe length, flow rate, and yield stress have no significant influence on the horizontal–vertical ratio. Based on the analysis of the experimental results derived in this study, multiple regression analysis was conducted for each variable set; a relationship for the horizontal–vertical ratio was proposed as

$$Y = 4.8 - 0.73\mu_L \tag{1}$$

where Y denotes the horizontal–vertical ratio, and μ_L denotes the plastic viscosity of the lubrication layer. That is, the horizontal–vertical ratio is directly affected by the plastic viscosity of the lubrication layer in the same manner as the concrete pumping performance.

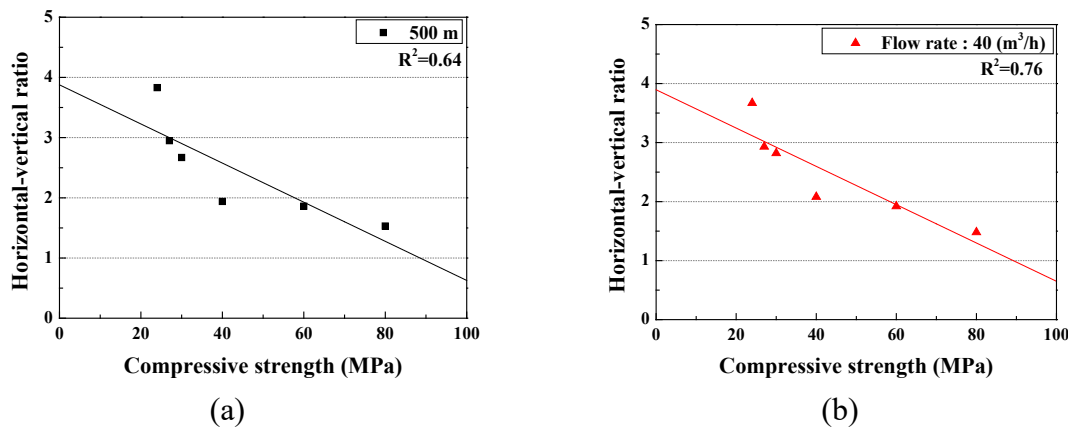


Fig. 3. Variation of horizontal-vertical ratio: (a) according to pipe length; (b) according to flow rate

4. Conclusion

In this study, horizontal and vertical pipe pumping tests and computational fluid dynamics (CFD) analysis were conducted under various mixing and construction conditions using rheology-based quantitative pumping performance prediction technology to derive the vertical-horizontal correlation used for concrete pumping performance evaluation.

5. Acknowledgements

This work is supported by the Korea Agency for Infrastructure Technology Advancement (KAIA) grant funded by the Ministry of Land, Infrastructure and Transport (Grant RS-2021-KA163381).

6. References

Choi, M.S. 2013. Prediction of concrete pumping performance base on the evaluation of lubrication layer properties, Korea Adv. Inst. Sci. Technol.



Bridge Engineering Institute Conference 2023 (BEI-2023)
Rome, Italy, July 17-20, 2023



Kwon, S.H., Park, C.K., Jeong, J.H., Jo, S.D., and Lee, S.H. 2013. Prediction of concrete pumping: part i-development of new tribometer for analysis of lubricating layer, Journal of ACI Materials, 110, 647–655



Over Torque Test Method to Assess the Concrete Strength

Kenji Tada*¹, Tatsuki Hatakeyama², and Tetsuya Ohmura³

¹: JUST Co. Ltd., Kanagawa, Japan; tada@just-ltd.co.jp

²: Tokyo City University, Tokyo, Japan; g2281646@tcu.ac.jp

³: Tokyo City University, Tokyo, Japan; tohmura@tcu.ac.jp

*: corresponding author

Keywords: torque; concrete strength; concrete screw; drilling; screw-in

Abstract: Recently, the demand for seismic assessment, structural survey, and quality control has further increased. The top priority is the concrete strength for assessment of the concrete structure. Generally, some concrete samples are taken to test the concrete strength, however, that needs much cost, labor, work period, and the heavy-duty equipment of concrete core drill. In addition, the concrete strength of the concrete samples must be tested in a laboratory after taking the concrete samples. On the other hand, the rebound hammer method, so-called the ‘non-destructive test,’ would sometimes be used, though the accuracy of the concrete strength was suspicious. And a public assessment with the non-destructive test is not accepted in Japan because of the accuracy of the test. In this study, we developed the over-torque time integration test method using a small drill. The method is independent of the worn condition of the drill bit and the drilling pressure. In the method, at first, a small guide hole is drilled. Second, a small concrete screw is slowly tightened to the head with a manual screwdriver. Then, the small concrete screw is driven while measuring the torque. The torque measured at this time is called over-torque. Finally, the concrete strength is assessed compared with the concrete strength and the over-torque-time property relationship. A lot of the over-torque test methods were performed while measuring the torque, and the test results were examined. The torque was steeply increased at the start screw-in. Next, the torque is kept while driving the drill to some extent. Finally, the torque steeply dropped down. Just a drilled small hole was left. The relationship between the concrete strength and over-torque-time property was shown and we confirmed that the over-torque test method could be highly valuable to assess the concrete strength.

1. Introduction

Large earthquakes, for example, the Kobe earthquake in 1995, Niigata Prefecture Chuetsu Earthquake in 2004, the Great East Japan Earthquake in 2011, and the Kumamoto earthquake in 2016, have occurred, and the subsequent colossal earthquake could hit Tokyo in the near future. Recently, the demand for seismic assessment, structural survey, and quality control has increased in that background. The well-known key thing is the concrete strength for an assessment of a concrete structure.

Generally, some concrete samples are taken to test the concrete strength, however, that needs much cost, labor, work period, and the heavy-duty equipment of concrete core drill. In

addition, the concrete strength of the concrete samples must be tested in a laboratory after taking the concrete samples.

On the other hand, the rebound hammer method, so-called the ‘non-destructive test,’ would sometimes be used, though the accuracy of the concrete strength was suspicious. And a public assessment with the non-destructive test is not accepted in Japan because of the accuracy of the test.

In a past study, a small drilling test for concrete strength was reported focusing on the average consumed power while drilling. However, the test result might depend on the worn condition of the drill edge and the drilling pressure.

In this study, we developed the over-torque time integration test method using a small drill. The method is independent of the worn condition of the drill bit and the drilling pressure. In the method, at first, a small guide hole is drilled. Second, a small concrete screw is slowly tightened to the head with a manual screwdriver. Then, the small concrete screw is tightened while measuring the torque. The torque measured at this time is called over-torque. Finally, the concrete strength is assessed compared with the concrete strength and the over-torque-time integral value.

2. Test

2.1. Test specimen

Figure 1 shows the test specimen. Specimens 100mm in diameter and 200mm in height were prepared at first and cut at the center of the height next. Specimens were tested on the mid-cut face of the lower specimen. Three same specimens were made for each of the 16 different concrete strengths., and a total of forty-eight specimens were tested.

Their concrete strength f'_c was in the range of 4.84 to 94.2 N/mm² for specimens. The maximum aggregate size was 20mm.

2.2. Test setup and measurement

Photo 1 shows the test setup. The telemeter to measure the torque was first jointed between the screwdriver bit and the driver chuck. Next, a computer was connected to the telemeter via the data logger.

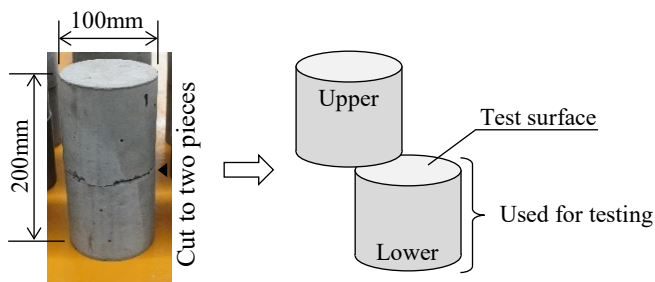


Fig. 1 Specimen

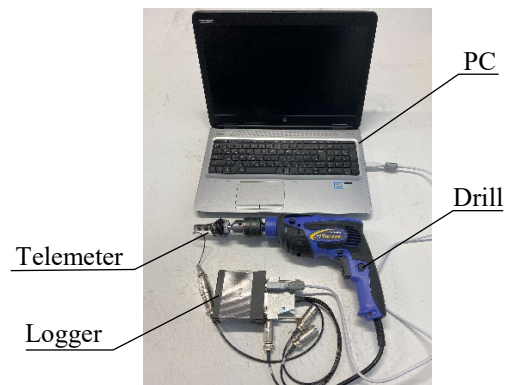


Photo 1 Test setup

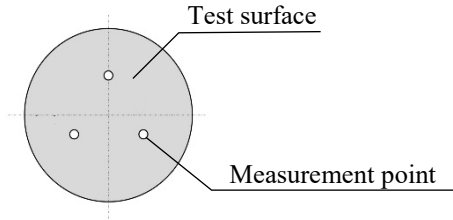


Fig. 2 Measurement position

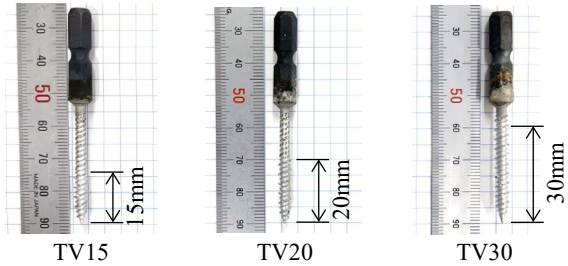


Photo 2 The test screw

Firstly, the guide hole was drilled without measurement. Second, the test screw is slowly tightened to the head with a manual screwdriver. Then, the test screw is tightened while measuring the torque. The test was stopped when the torque was reduced to zero. Photo 2 shows the test screw. For the test screw, a hexagonal bit was braze welded to the concrete screw head with a length of 35 mm under the neck and a shaft diameter of 7 mm. Forty-eight test screws were prepared for each of the three types of test screws, with the length of the screw blade part from the tip 15, 20, and 30mm. Figure 2 shows the measurement position. The vertex of an equilateral triangle with the center of gravity at the center of the test surface was used as the measurement point. A new test screw was used for each measurement point, and the measured value of one specimen was the average value of the measured values measured at three measurement points.

3. Test Results

3.1 Maximum torque and concrete strength

The torque was steeply increased for all specimens when the test screw started to be screwed in. Finally, the torque drastically dropped to zero after repeatedly increasing and decreasing for a while. Table 1 shows the test results. N/A was indicated to be impossible to measure the torque because of the test screw defect. TV 15, 20, and 30 indicate the length of the screw blade part. Figure 3(a) shows the maximum torque and concrete strength. Three regression lines by the least squares method indicated the lengths of the screw blades 15, 20, and 30 mm. Maximum torque tends to increase as concrete strength increases.

Table 1. Test results

No.	f'c(N/mm ²)	Maximum torque (N · m)			No.	f'c(N/mm ²)	Maximum torque (N · m)			No.	f'c(N/mm ²)	Maximum torque (N · m)					
		TV15	TV20	TV30			TV15	TV20	TV30			TV15	TV20	TV30			
6	4.84	①	0.232	0.146	1.468	11	24.1	①	0.860	1.588	2.100	16	72.4	①	2.378	2.771	2.820
		②	0.206	0.412	1.083			②	1.077	2.074	1.668			②	1.591	1.905	2.881
		③	0.371	0.187	1.404			③	1.544	1.397	1.600			③	1.875	2.577	2.823
7	10.2	①	0.220	0.588	1.321	12	26.7	①	2.104	2.114	1.775	17	81.1	①	2.295	2.637	—
		②	0.489	0.976	1.485			②	0.939	1.613	2.229			②	2.763	2.257	3.087
		③	0.577	0.605	1.365			③	0.883	1.309	1.560			③	2.661	2.728	2.285
8	15.2	①	0.766	1.405	2.069	13	29.2	①	1.237	1.324	2.370	18	82.7	①	2.791	2.823	2.934
		②	1.071	1.268	1.743			②	0.761	1.331	1.789			②	2.895	2.807	2.958
		③	1.166	0.280	1.547			③	0.642	1.005	1.748			③	—	2.831	—
9	19.8	①	1.217	0.983	2.168	14	39.2	①	1.930	2.351	—	19	89.9	①	1.852	2.200	—
		②	1.316	1.101	1.155			②	1.943	1.286	1.726			②	1.877	2.122	2.288
		③	0.681	1.845	2.126			③	—	1.328	1.520			③	2.339	1.687	—
10	22.5	①	1.243	1.464	2.263	15	61.2	①	1.869	2.360	2.867	20	90.8	①	1.597	1.765	—
		②	1.363	2.074	1.444			②	2.385	1.988	2.843			②	2.186	1.841	2.462
		③	0.611	1.247	1.612			③	2.552	2.751	2.854			③	2.078	1.943	—
													①	1.355	1.843	2.813	
													②	—	1.751	—	
													③	—	—	—	

TV15, 20, and 30 indicate the length of the screw blade part.

3.2 Torque time history

Figure 3(b) shows an example of the torque time history. It approximately tends to be increased following an increase in the concrete strength.

The torque was steeply increased at first, and the torque was kept for a couple of seconds next and finally dropped down to zero.

The torque time history property was influenced by the concrete strength and the coarse aggregate location.

3.3 Torque time integral value and concrete strength

Figure 3(c) shows the integral torque time value and concrete strength. The dot lines respectively indicated the regression lines.

The integral torque time value was increased following the increase in the concrete strength.

The variance is approximately smaller. And the dispersion for the specimen of the length of the screw blade 20mm was much less than others.

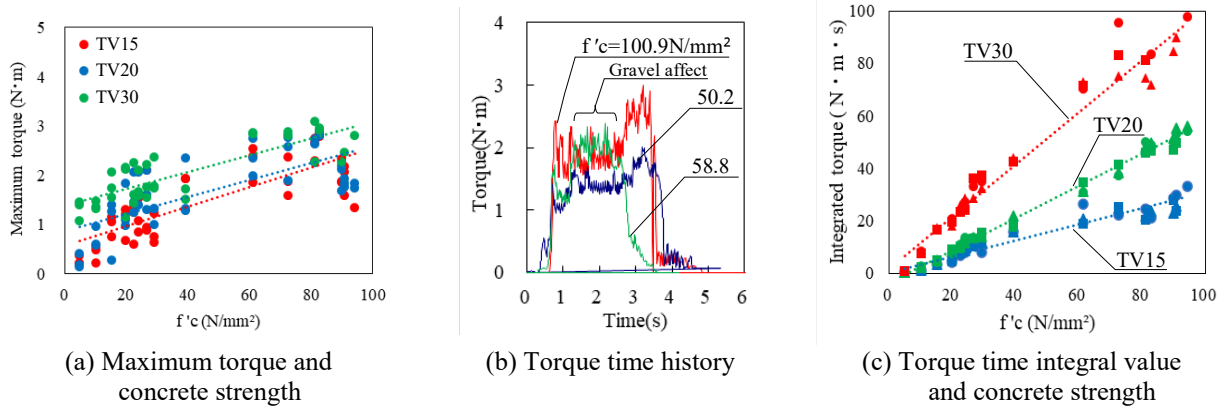


Fig. 3 Correlation between each test result and concrete strength

4. Conclusions

We developed the over-torque test method with a small drill. The method was to drill a guide hole first, slowly tighten the test screw to the head with a manual screwdriver, and slowly screw it in while measuring the torque until it reached zero.

The specimen was a concrete cylinder. Since the strength of concrete was considered to be affected by the settling of aggregates, the test was performed on the cut surface of the lower specimen obtained by cutting it to half the height.

After reviewing the test results, we came to the following conclusions.

- 1) The over-torque test method we developed was simple to perform and get the torque data.
- 2) Torque time history tends to increase as concrete strength increases.
- 3) The maximum torque was correlated with the concrete strength.
- 4) The torque time integral value was correlated with the concrete strength.
- 5) For the standard deviation, the test results for the length of the screw blade 20mm were much better than that of 15 and 30mm.
- 6) The dispersion was shown as the relationship between the torque and concrete strength. Therefore, to improve the accuracy, it is necessary to test with a wide variety of concrete and obtain more data.



Application of Automatic Welding Robot in Integrated Construction of Bridge Pile Foundation

Liangjun Hu ^{1*}, Xiaoli Sun ², and Jun Yang³

¹: Postdoctoral Mobile Station ,Tsinghua University ,Beijing, China; 2. Guangzhou Institute of Building Science Company Limited, Guangzhou, China; Guangzhou Municipal Engineering Testing Co., Ltd., Guangzhou, China; Liangjun_hu@outlook.com

²: Guangzhou Municipal Engineering Testing Co., Ltd., Guangzhou, China; 24620011@qq.com

³: Guangzhou Municipal Engineering Testing Co., Ltd., Guangzhou, China; yangjun851113@163.com

*: corresponding author

Keywords: pile foundation; welding robot; bridge construction

Abstract: Undertaking construction work in the summer can be challenging and draining, especially for welders who must wear protective gear and operate in high-temperature conditions. Technological innovations ought to offer workers a more respectable and comfortable work experience. In line with this, an automatic welding robot has been developed to enhance the efficiency and quality of bridge pile foundation construction. Prestressed high-strength concrete (PHC) pipe piles are a popular and cost-effective method used in bridge construction thanks to their high single-pile bearing capacity, strength, and reliability. However, the manual welding of large-diameter (over 600 mm) pipe piles is a low-efficiency and unstable construction process that can compromise the quality of the pile foundation, thereby affecting the overall quality of the bridge. To address this challenge, the reconstruction and expansion project of the Shenzhen-Shanxi Expressway has developed a pile-beam integrated (PBI) machine that utilizes factory prefabrication and mechanized assembly in-situ to enhance the quality and speed of bridge construction. In addition, to further improve construction progress, our research team has developed and employed automatic welding robots for the connection work of piles, which have been installed in the piling area of the PBI machine. Our study demonstrates that using automatic welding robots in large-diameter PHC pipe piles can significantly reduce physical labor and improve the efficiency and quality of bridge pile foundation construction. In addition, the welding robot has helped achieve an intelligent, rapid, and standardized construction process, thus contributing to the overall success of the expressway project.

1. Introduction

Prestressed High Strength Concrete Pile (PHC Pipe Pile) has the advantages of high single pile bearing capacity, high pile body strength, strong ability to penetrate the soil layer, fast construction speed, low cost per unit bearing capacity[1][2]. The annual usage of prestressed

concrete pipe piles exceeded 300 million linear meters in China, which are widely used in high-rise buildings, bridges, ports, wharves and other projects.

Connecting prestressed pipe piles using manual welding involves several technical steps, requires high expertise, and poses health risks due to arc light and radiation exposure. Additionally, labor-intensive manual welding is time-consuming, impacting the construction schedule, while the welding industry is facing a shortage of workers and an aging workforce. To address these challenges, the research team developed a welding robot designed for connecting prestressed concrete pipe piles by studying the working principles and applications of existing automatic welding equipment. The paper first presents the fundamental construction of the newly developed pipe pile welding robot. Subsequently, the welding quality was evaluated through an indoor steel pipe welding test using the robot. Lastly, the robot was applied to the reconstruction and expansion project of Shenshanxi Expressway in Guangdong, and its effectiveness in the field was evaluated through the welding test of bridge pipe piles.

2. Fundamental Construction of Welding Robot

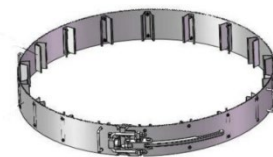
Fig. 1 illustrates the structure of the prestressed concrete pipe pile welding robot, which mainly consists of a welding trolley, a control box, welding equipment, steel belt guide rail, and a mobile storage cart. The welding trolley includes a clamping mechanism, swing device, driving wheel, motor, etc. The control box includes controller, control handle, servo controller, etc. The welding equipment comprises not only the automatic wire feeder and welding machine but also other essential welding auxiliary equipment such as the power box, shielding gas, among others. The walking track adopts a puller-type quick locking mechanism [3][4], which realizes quick locking and at the same time forces the steel belt to exert radial pressure on the pipe pile. With the help of this force, the track can hold the pipe pile tightly. The mobile storage cart is mainly used to store the welding trolley, welding machine, control box and its pipelines, etc., which can realize the transportation and movement of the whole machine.



(a) welding trolley



(b) welding equipment



(c) steel belt guide rail

Fig. 1. Fundamental construction of welding robot

3. Indoor Model Test Research

For this experiment, pre-aligned steel pipes and pipe pile end plates with a diameter of 1m were used as a scaled model of engineering pipe piles. The indoor welding experiment focused on the three-layer welding process of the welding robot. Before welding, install the steel belt guide rail and welding trolley to secure the guide rail onto the pipe pile and ensure smooth operation. The weld depth is 15 mm, with a width ranging from 14.5 mm to 15.5 mm,

and the maximum axial deviation of the upper and lower pipe piles is 3 mm. The scaled model tests primarily the three-pass welding process. The three-layer welding process achieves excellent welding effectiveness and high efficiency. Fig. 2 illustrates the welding process and outcomes of the three-pass layer welding on the machine. The first layer welding produces a uniform weld seam with minimal curling, meeting the requirements of back-sealing welding. High current and large swing parameters are applied during the second filling welding to ensure sufficient support surface for the third covering welding. The third layer welding produces a full, uniform, and continuous weld seam with smooth filling and no defects such as pores or slag inclusions, satisfying the requirements set forth in the "Technical Standards for Prestressed Concrete Pipe Pile" (JGJ/T 406-2017). The total welding time for three-layer welding with a single welding robot is 45 minutes, which can be further improved by controlling two welding robots simultaneously.

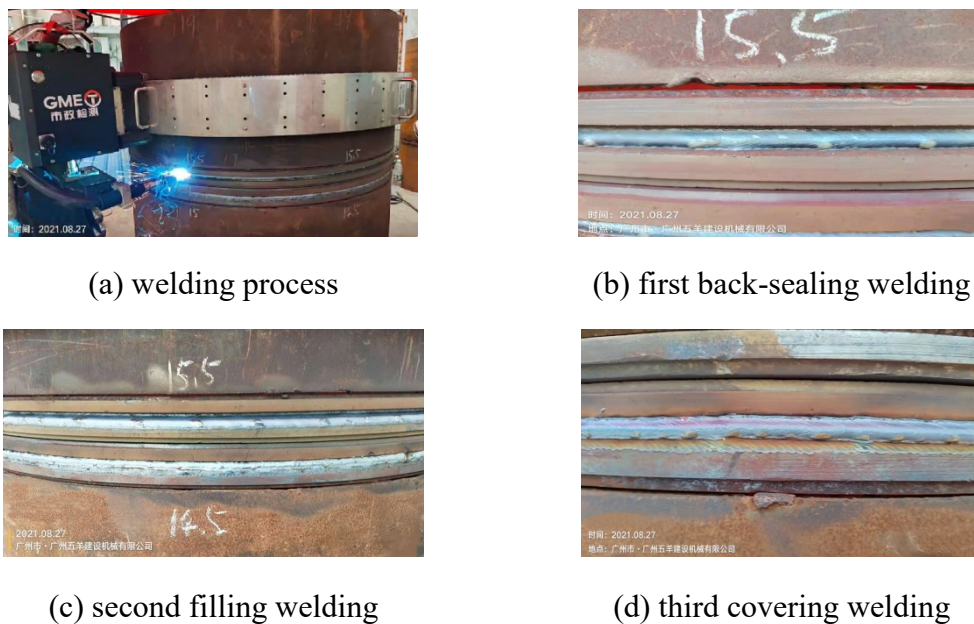


Fig. 2. Indoor model welding test

4. Application of Welding Robot on Bridge Pile

The TJ10 Meilong Super Bridge of Shenshan West Expressway is being reconstructed and expanded. The stressed concrete high-strength pipe piles have a pile length of 34 m and a diameter of 1000 mm with a wall thickness of 140 mm. The pile arrangement form is 12m+10m+12m, with the upper part being a PRC (prestressed reinforced concrete pile) pile and the lower part being a PHC pile. Fig. 3(a) shows the pile-beam integrated (PBI) machine used in the bridge construction, and the pipe pile foundation for the bridge utilizes the hammering method to sink the pile. The steel belt guide rail and welding trolley are installed before on-site welding, and the weld width of pipe piles on-site typically ranges from 12-14 mm. Figs. 3(b) and (c) display the on-site welding process of the welding robot and the appearance of the weld after welding. The figures illustrate that the automatic welding seam is even and has a flat appearance. When compared to the timeliness of on-site manual welding, the welding process using two workers to weld a single weld usually takes

60 minutes, while the welding robot takes at least 50 minutes (including 8-10 minutes of preparation time before welding). Additionally, only one welder is required to operate the equipment and monitor the welding process. Although the efficiency of automatic welding has significant room for improvement compared to manual welding, the welding quality and efficiency have been unanimously recognized by the application units. From the perspective of field application, The entire set of welding equipment is heavy, making it challenging to move on muddy or uneven construction sites. Equipment installation and commissioning require workers to have high welding operation and learning ability. The design integrates the control system, welding machine, wire feeder, and other components to increase portability and provide standardized welding theory and operation training for operators, enhancing welding efficiency.



(a) a pile-beam integrated (PBI) machine with a welding robot (b) welding process of bridge pipe pile (c) the appearance of the weld

Fig. 3. Application of welding robot in integrated construction of bridge pile foundation

5. Conclusion

The paper presents a welding robot designed for splicing prestressed pipe piles, whose reliability and technical advantages are demonstrated through indoor simulation welding tests and bridge pipe pile applications. The main conclusions are as follows:

- (1) The welding robot adopts a puller type quick locking mechanism, which can realize the quick locking of the steel belt guide rail.
- (2) The welding robot adopts the welding process of three layers of welding. The surface of the weld seam is full and uniform and there is no internal defect, which can meet the welding quality requirements.
- (3) For prestressed pipe piles with a diameter of 1 m, it takes about 40 minutes to complete the automatic welding of a single weld, which is 1/3 less than manual welding, and the labor intensity of workers is significantly reduced.

6. References

- [1] Yang Zhijian. Research on Seismic Performance of Prestressed High-strength Concrete Pipe Piles. Tianjin University, 2014.
- [2] Tang, Mengxiong, Zao Ling, and Yuliang Qi. 2023. Bending Strength of Connection Joints of Prestressed Reinforced Concrete Pipe Piles, Buildings 13, no. 1: 119. <https://doi.org/10.3390/buildings13010119>.



Bridge Engineering Institute Conference 2023 (BEI-2023)
Rome, Italy, July 17-20, 2023



[3] Sun Xiaoli, Zhou Zhiguo, Wang Wenjian, Yang Jun, Hu Liangjun, Zhao Jinming, Yuan Qibao, Zou Kai, Xie Huihua. Quick assembly and disassembly of pipe pile welding vehicle with locking track [P] Patent No.: ZL 202110638939.0. 2022.03.11

[4] Sun Xiaoli, Zhou Zhiguo, Wang Wenjian, Yang Jun, Zhao Jinming, Yuan Qibao, Xie Huihua, Chen Jinhai. A quick docking and automatic welding equipment for pipe piles [P] Patent No.: ZL. 2020 2 1876358.8. 2021.05.24.



Structural Behavior of Precast Concrete Beam-Column Joints

Jaehyung Heo¹, DongIk Shin¹, Yeon Je Choi¹, Dong-Hwan Kim², Hyeong-Gook Kim²,
Kil-Hee Kim², and Jung-Yoon Lee^{3*}

- ¹: Department of Civil, Architectural, and Environmental System Engineering, SungKyunKwan University, Suwon, Republic of Korea; email: gjwogud97@naver.com
²: Department of Green Smart Architectural Engineering & Urban Systems Engineering, Kongju National University, Kongju, Republic of Korea; email: kimkh@kongju.ac.kr
³: School of Civil, Architectural Engineering and Landscape Architecture, SungKyunKwan University, Suwon, Republic of Korea; email: jungyoon@skku.edu

*: corresponding author

Keywords: precast concrete; beam-column joints; seismic design; energy dissipation; stiffness

Abstract: Precast concrete (PC) technology has been known for a long time, and the advantages of PC structures have been widely known, but there are not many cases of constructing high-rise PC structures. In order to construct high-rise PC structures, it is necessary to secure technologies such as bonding, assembly, and lifting, and in particular, earthquake-resistant design is required. The basic design principle of seismic design of PC structures is that PC structures should secure the safety and serviceability required in monolithic structures. Different countries apply different methods to assess the emulation of PC structures. For example, ACI 374.1-05, ACI PRC-550.1-09, and ACI ITG 5.1-07 evaluate the strength, energy dissipation and stiffness of PC structures on an absolute criteria. On the other hand, Japanese PC guidelines relatively evaluate the structural performance of PC structures by comparing to the behavior of cast-in-place concrete structures. In this paper, the structural performance of 160 specimens was analyzed to evaluate the basic performance for the emulation of PC moment frame. The analytical results indicated that when the connection of PC members was properly designed, the structural performance of PC members was almost similar to that of cast-in-place concrete members.

1. Introduction

The basic design principle of seismic design of precast concrete (PC) structures is that PC structures should secure the safety and serviceability required in monolithic structures. It is difficult to make the structural performance of PC structures equal to that of cast-in-place (CIP) concrete. In the structural design codes, PC structures with performance above a certain limit value are considered to have the same performance as CIP concrete structures. The design codes certifies that the performance of a PC structure that exceeds a certain threshold is equal to that of a CIP structure. These PC structures can be designed by applying seismic coefficients applied to CIP structures. Performance evaluation of these PC structures is called emulation evaluation.

Different emulation evaluation methods are being applied for PC structures in each country. For example, in ACI 374.1-05 (2005), PC structures are considered to have equivalent performances to CIP concrete structures when they exhibit the following behaviors:

1. The test module shall have attained a lateral resistance (load or moment) equal to or greater than E_n before its drift ratio exceeds the value consistent with the allowable story drift limitation, where E_n is the nominal lateral resistance of test module determined using specified geometric properties of test members, specified yield strength of reinforcement, specified compressive strength of concrete, a strain compatibility analysis for flexural moment strength, and a strength reduction factor of 1.0
2. The maximum lateral resistance (E_{max}) shall have not exceeded exceed the lateral strength (λE_n), where λ is the specified overstrength factor for the test column.
3. The third complete hysteresis curve at the critical drift ratio shall have satisfied the following conditions:
 - Peak force for a given loading direction shall have been not less than 0.75 E_{max} E_{max} for the same loading direction
 - The relative energy dissipation ratio shall have not less than 1/8.
 - The secant stiffness from a drift ratio of -0.0035 to a drift ratio of $+0.0035$ shall have been not less than 0.05 times the stiffness for the initial drift ratio.

These guidelines are the absolute emulation evaluation criteria. The absolute method evaluates the performance of the precast structure based on its own characteristics, such as the strength, stiffness, and load-bearing capacity. It does not compare the performance of PC structures with those of CIP concrete structures.

On the other hand, “AIJ Guidelines for the Design of Structural PC Emulating Cast-In-place Reinforced Concrete”(AIJ, 2002) evaluates emulation differently from the ACI 374.1-05 guidelines. In this guideline, the structural performance of PC structures must be verified by comparing them with those of CIP concrete. That is, it is based on relative emulation evaluation criteria, as follows (Lee *et al.*, 2023):

1. The flexural yielding strength of PC members must be equal to or greater than that of the CIP concrete members.
2. The strength of PC members must be equal to or greater than that of the CIP concrete members.
3. The strength at the second complete hysteresis curve at the critical drift ratio must remain within 80 %.
4. The deformation at flexural yielding of PC members should not differ by more than 20 % from that of CIP concrete members.

The relative method compares the behavior of the precast structure with that of an equivalent cast-in-situ (CIS) structure. This method is based on the assumption that the behavior of the CIS structure is well understood and predictable. Both evaluation methods have their advantages and disadvantages. The choice of method depends on the specific requirements of the structure and the degree of accuracy desired. Evaluating emulation based on “absolute criteria”, such as in the

ACI 374.1-05 guideline, is simple, because the performance of CIP concrete members needs not be reviewed. However, the relative energy dissipation ratio and stiffness are significantly affected by the size and material properties of the member, leading to severe performance variations. In general, the absolute method requires more detailed information about the structure and the materials used. Conversely, emulation evaluation based on the relative criteria has the advantage of faithfully reflecting the basic requirements for emulation. However, the performance of CIP concrete members must be additionally evaluated. (Lee *et al.*, 2023)

In this paper, the structural performance of 160 specimens was analyzed to evaluate the basic performance for the emulation of PC moment frame.

2. Analysis of 160 Beam-Column Joints

To evaluate the emulation of PC structures, 160 beam-column joint specimens were collected in the existing literature. Among the collected specimens, non-structural failure specimens, such as damage to the connecting hardware or local failures, were excluded. Specimens from the literature were tested for various variables. The 160 beam-column joints consisted of 45 CIP and 115 PC specimens. There were 133 internal joints and 27 external joints. To evaluate the emulation of the PC frame, the ductility ratio ($\mu_\theta = \theta_u / \theta_y$) of the 160 beam-column joints was evaluated according to the variables. The drift ratio (θ_y) at flexural yielding was determined as the drift ratio when 66.67% of the maximum load and the origin where the load was 0 were connected based on the proposal of Pan and Moehle (1989). The ultimate drift ratio (θ_u) is the ratio when the load is reduced to 95 percent of the maximum load. Figure 1(a) shows the ductility ratio (μ_θ) vs. the strength ratio (V_{jn} / V_{jby}) of the specimen. The strength ratio (V_{jn} / V_{jby}) was calculated by dividing the joint strength by the beam flexural yield strength. The specimens were divided into CIP and PC. In Fig. 1 (a), the ductility ratio (μ_θ) increases slightly as the strength ratio (V_{jn} / V_{jby}) increases. When V_{jn} / V_{jby} is less than 1, μ_θ is approximately 2; however, when V_{jn} / V_{jby} is 2, μ_θ increases to approximately 5. Specifically, θ_u exhibited an almost constant trend regardless of the type of concrete (CIP or PC). Figure 1(b) compares the ductility ratios of the specimens classified by the ratio of the flexural strengths of the column and beam ($\sum M_c / \sum M_g$). The relationship between $\sum M_c / \sum M_g$ and ductility was similar to that between V_{jn} / V_{jby} and ductility. That is, the ductility ratio (μ_θ) increases slightly as $\sum M_c / \sum M_g$ increases. However, the effect was not as pronounced as that of V_{jn} / V_{jby} on μ_θ . In Fig. 1(b), μ_θ also exhibits a constant trend regardless of the type of concrete (CIP or PC). Consequently, because μ_θ shows an almost constant tendency regardless of the type of concrete, it seems to satisfy the relative emulation that compares the performance of the CIP structure with that of the PC structure. However, as μ_θ varies from approximately 0.7–9, showing a large range of change, the evaluation result will be different depending on the member characteristics if the emulation is evaluated based on absolute criteria. When comparing the strength of PC and CIP specimens, the strength reduction rate of the two types of specimens was almost similar. The strength of the specimen decreased as the drift ratio increased, so there were specimens that did not satisfy absolute emulation evaluation criteria depending on the size and conditions of the specimen.

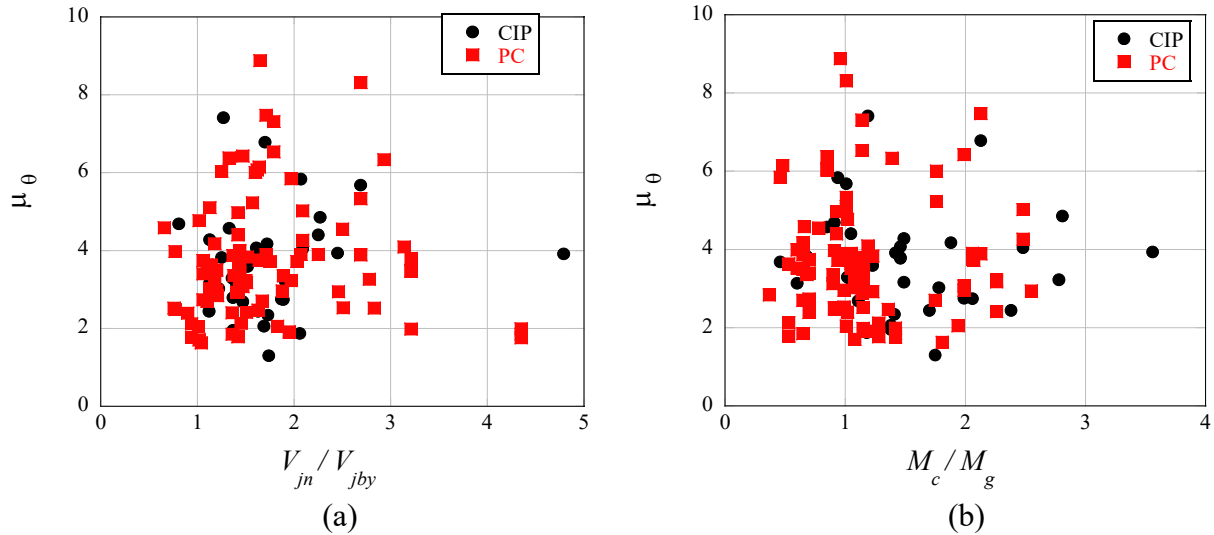


Fig. 1. Behavior of prestressing steel in strengthened girders subject to live load: (a) Ductility ratio vs. V_{jn} / V_{jby} ; (b) Ductility ratio vs. $\sum M_c / \sum M_g$

3. Conclusions

The analytical results indicated that emulations of PC intermediate and special moment resisting frames should be evaluated based on drift ratios of 2% and 3.5% respectively. The strength reduction rate of PC member was almost the same as that of the CIP concrete member when the drift ratio was 2 percent, but decreased as the drift ratio increased. The relative and absolute emulation evaluation results were consistent for energy dissipation ratio and stiffness. However, the absolute emulation evaluation method for special moment resistance frames was too strict for special moment resistance frames.

4. Acknowledgments

This research was supported by the National Research Foundation of Korea (NRF) grant funded by the Korea Government (MIST), under the project "Development of Seismic Design Method for Reinforced Concrete Beam-Column Assembles of Moment Resistance Frames" (2023R1A2C3002443)

5. References

- AIJ. 2002. Guidelines for the Design of Structural Precast Concrete Emulating Cast-in-place Reinforced Concrete, Architectural Institute of Japan.
- ACI T1.1-01. 2005, Acceptance criteria for moment frames based on structural testing and commentary, American Concrete Institute.
- Lee, J.-Y., Heo, J., Byun, H.-W., Kim, K.-H., and Shin, D. 2023. Comparison of Two Emulation Evaluation Methods of Precast Concrete Structures, Engineering structures, Submitted paper.
- Pan, A., and Moehle, J.P. 1989. Lateral displacement ductility of reinforced concrete flat plates, ACI Structural Journal, 86(3), 250-258.



Diaphragm Wall Mono-Shaft as an Economical Time Saving Bridge Deep Foundation

Yoni Pestes^{1*} and Daniel Elmaleh²

¹: Via Bridges design and engineering, Tel Aviv Israel; email: Yoni@via-bridges.com

²: Via Bridges design and engineering, Tel Aviv Israel; email: Daniel@via-bridges.com

*: corresponding author

Keywords: Bridge foundation; Seismic design; Mono-shafts; Diaphragm wall boring

Abstract: Deep foundation is a widely used type of bridge foundation across the world. Typically, round concrete piles are arranged in groups to support the bridge's columns and abutments. These columns can vary in type and shape, depending on the substructure's functionality and aesthetic design. To connect the columns and the pile groups, a pile cap is used. These underground structures must be of sufficient height to anchor the reinforcement from the bridge's columns and piles. However, reaching the piles' level often requires extensive excavation, which can pose a challenge when building the bridge pier near existing structures or a roadway. One common solution to this issue is to use large circular mono-shafts. However, this approach results in a specific column type that is limited by the diameter of the shaft and the available space for the foundation's location. To offer an alternative foundation type, this paper presents a case study of a diaphragm wall mono-shaft foundation. The study will outline the considerations that went into designing this foundation, taking into account relevant codes, manufacturing, and construction limitations.

1. Introduction

The placement of bridge piers is a critical factor in determining the span length of a bridge during the preliminary design phase. This decision can help identify the optimal bridge type and solution and determine the super-structure's static height. By minimizing the need for excavation and getting as close as possible to the obstacle to be bridged, a more efficient and economical solution can be achieved. This paper focuses on the detailed design of the Pinhas-Rosen Bridge, a light train bridge constructed in a dense urban area abundant with utilities and obstacles in the municipality of Tel-Aviv, Israel. In this design-built (DB) tender, the client's bridge design in the preliminary phase used conventional solution of column based on group of piles connected with a pile cap. This method required extensive excavation and construction of sheet pile wall when getting close to the active road. The contractor's design team proposed an alternative mono-shaft diaphragm wall solution that eliminated the need for expensive and time-consuming sheet pile wall and pile cap casting, resulting in a more economical and efficient solution. Additionally, this approach reduced the maximum span length and optimized the static height of the pre-cast prestressed U-shaped beams, helping the design team win the DB tender for the contractor, by substantially reducing the cost of the project.

2. Bridge Description

The Pinhas Rosen Bridge is located in the Tel-Aviv municipality of Israel and forms part of a new 40km green line light train aimed at reducing traffic congestion in the center of Israel. The bridge is designed to elevate the double-track green line over Pinhas Rosen Road, spanning a length of 321.8m and comprising 13 spans, with a maximum span length of 29.0m. The bridge is divided into four sections ranging from 48.6m to 125.1m in length, each section is separated by expansion joints (see Fig 1). The superstructure comprises of U-shaped precast prestressed girders measuring 1.45m in height with a 0.25m cast-in-situ deck. The girders in the middle piers of each section are fixed to the column, while elastomeric bearings are used for the expansion joint pier, allowing for an elastic connection. In the middle fix piers, the trapezoidal-shaped concrete columns are directly placed and connected to the bridge foundation; concrete rectangular diaphragm wall drilled mono-shaft foundation.

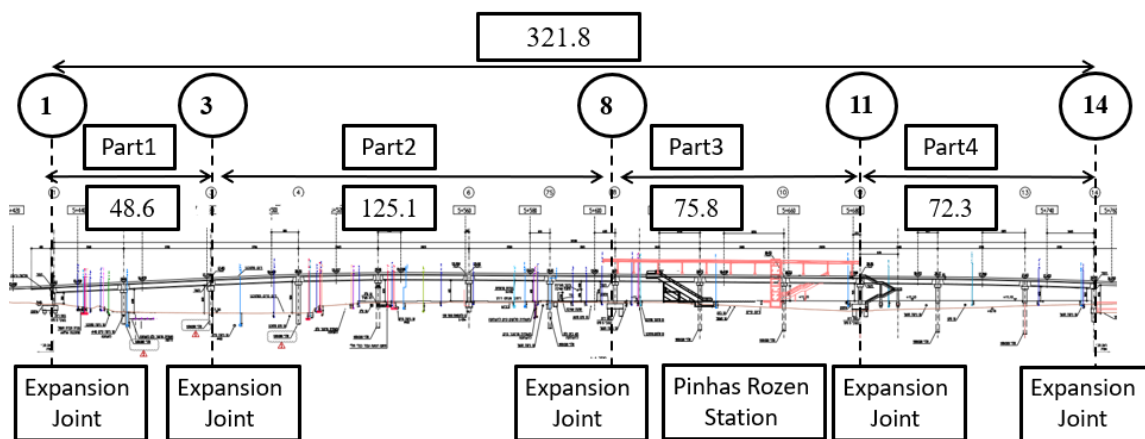


Fig. 1. Pinahs Rosen bridge longitudinal section

3. Rectangular Diaphragm Wall Drilled Mono-Shaft Foundation

The Pinhas Rosen Bridge incorporates several innovative design features that helped to reduce the overall project budget and secure the tender. One main feature is the use of rectangular diaphragm wall drilled mono-shaft foundations. This approach eliminated the need for an oversized pile cap that would have required massive excavation. It should be noted, however, that the absence of pile caps meant that the boring process required meticulous attention to detail. To minimize deviations during boring and construction, the contractor used concrete guides for each shaft. Given that the bridge supports two rail tracks, each pier is composed of two columns connected directly over the foundation at the ground level with a non-contact spliced rebar connection.

The bridge's piers can be classified into two types. Piers 2-4 are configured with four U precast beams and one deck, resulting in a pier in the form of a frame as can be seen in Fig 2. (a). This configuration allows for a park walking and bicycle route to pass between the frame's columns, resulting in a smaller column contour compared to the foundation shape (Type II shaft, Caltrans 2019). For this type of pier, a 1.2m x 2.8m diaphragm wall foundation was used. On the other hand, piers 5-13 support train tracks that are split, so each column is individually supported between 2-3 U precast beams as can be seen in Fig 2. (b). This results in a larger column contour compared to the foundation shape. For this type of pier, a 1.0m x 3.2m diaphragm wall

foundation was used. The foundation dimension was chosen to account for the pier's vertical load, element capacity, and contractor equipment

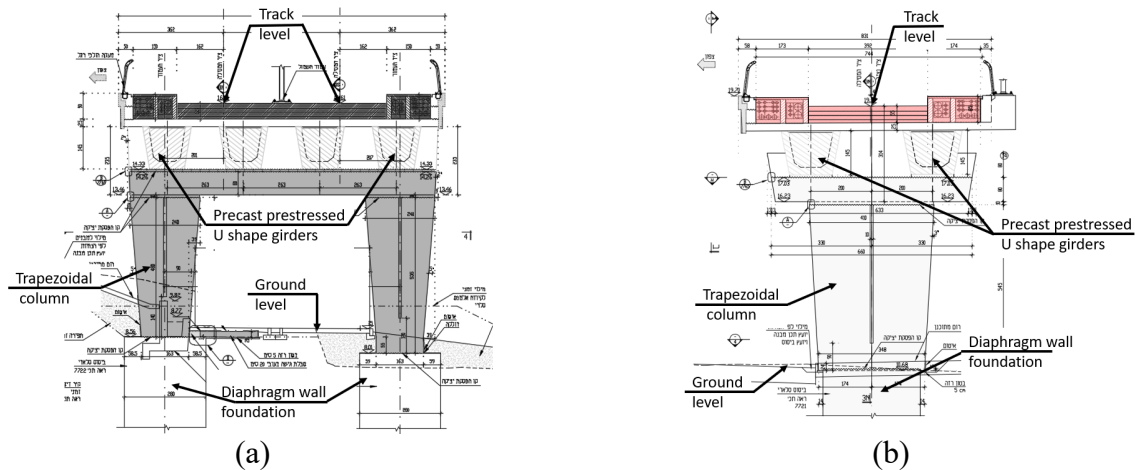


Fig. 2. Pinahs Rosen bridge cross sections - (a) Piers 2 and 4 frame; (b) Pier 5-13 fixed column

4. Column and Diaphragm Wall Design

The bridge design was developed using SOFiSTiK FEM software, with the aim of accurately modeling the bridge's geometry. The superstructure was modeled using the grillage method, and a rigid connection was established between the superstructure and the columns, taking into account the diaphragm transverse beam casting between the longitudinal beams and the columns. The columns were modeled using beam elements, which were directly connected to the diaphragm wall foundation that was also modeled as beam elements (refer to Fig. 3).

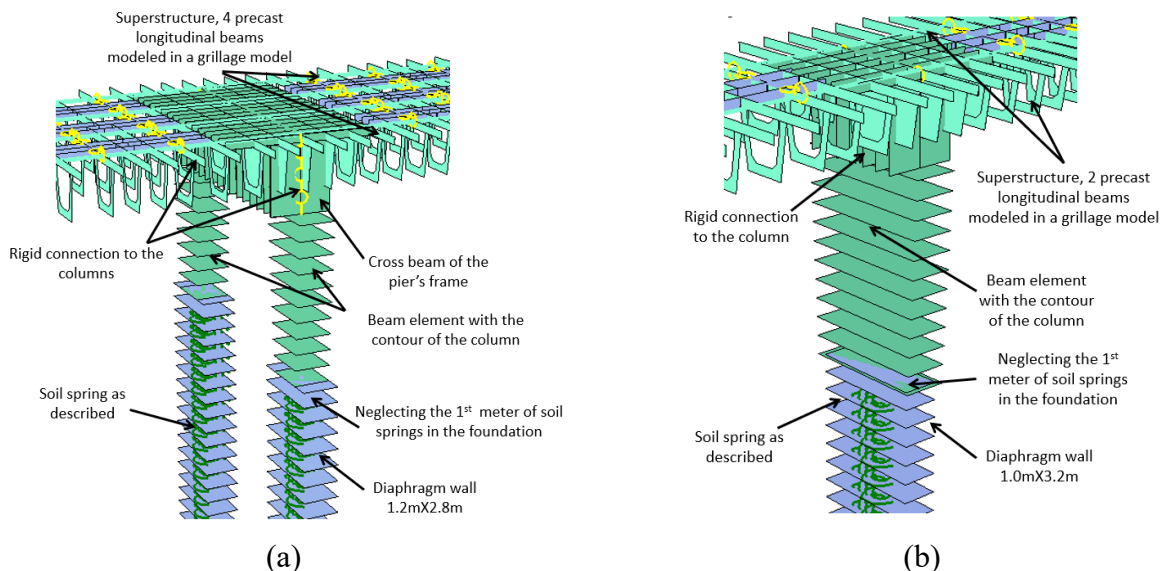


Fig. 3. Pinahs Rosen bridge FEM of the piers (a) Piers no. 2 frame; (b) Pier no. 12 column

To model the interaction between the structure and the soil, springs were used in the X and Y directions. The soil profile in the area of the bridge consisted of clayey sands and sand-clay mixtures (SC) up to a depth of 5.0m, and sand with fines and gravel (SP-K1) below that. The horizontal soil subgrade reaction was calculated to be 14,000kN/m³ between depths of (-1.0) - (-5.0m) and 30,000kN/m³ below. The design of the column was done taking into consideration vertical service loads due to dead load, temperature, creep and shrinkage, live loads such as train movement and pedestrians. Also, horizontal service live loads from braking, traction and centrifugal loads of the train. Additionally, the design considered extreme event loads such as earthquake and wind loads. For earthquake design, modal analysis was carried out, which considered the frequencies of the bridge and local ground acceleration to predict the horizontal forces due to a seismic event.

The earthquake modal analysis, together with the calculation of horizontal forces resulting from constant loads (e.g., concrete creep and shrinkage) generated a bending moment diagram (refer to Fig. 5). Fig. 5(a) illustrates the bending moment diagram of pier 2, displaying a frame-like behavior in both directions, with the bending moment tending to zero at ground level, making it an ideal location for splicing the rebar. Fig. 5(b) shows the bending moment diagram of pier 12, with a frame-like behavior in the longitudinal direction, where the bending moment also tends to zero at ground level, providing an optimal location for splicing the rebar. In the transverse (robust) direction of the column, the maximum bending moment occurs near the mid depth of the foundation, far from the spliced area. As the transverse direction is robust, the column's bending moment capacity is much larger than the calculated bending moment. This solution allows the bridge design to meet the Israeli standard (IS) and Caltrans requirements for seismic event.

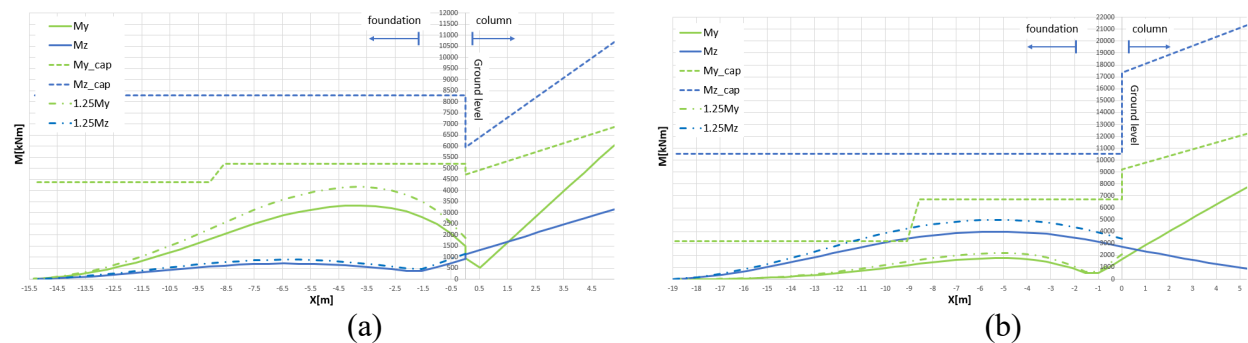


Fig. 5. Bending moment for seismic loading combination and bending moment capacity in longitudinal(y) and transverse(z) direction - (a) Pier 2; (b) Pier 12

5. Rebar Design

The calculations were performed considering bi-axial bending moments, as specified in EN-1992-1-1-2004 section 5.8.9 and accounted for the increase in bending moment resulting from construction imperfections and buckling. To determine the active length of the column for buckling, the point of fixity method, as described by Robinson et al. (2006), was used. The column's capacity was calculated using an interaction diagram, which takes into account the axial loading and the appropriate bending moment capacity. It is important to note that the design of the column and the foundation top half included a minimum of 1.0% reinforcement in accordance with IS 1227/1.

The produced forces for design, including axial, shear, and bending moments, were compared to the calculated column capacity. Based on this analysis, the column can be divided into four critical parts.

- a) The top of the column is connected rigidly to the superstructure and is anticipated to undergo the greatest bending moment in the longitudinal weak direction and transverse robust direction, making it the predicted location of the plastic hinge. In accordance with IS 1227/1, confinement reinforcement needs to be provided for a section of 80% of the maximum bending moment or l_c , which is the section height in the direction of seismic force, whichever is greater.
- b) The ground level, or splice zone, marks the connection between the diaphragm wall foundation and the column. As this type of connection is not covered by Israeli standards, AASHTO and Caltrans limitations were used. For piers 2-4, which have oversized foundations compared to the columns (Type II shafts), an inner longitudinal rebar, smaller than the diaphragm foundation contour, was embedded 3.0m ($D_{c,max} + 48l_{bl}$) according to Caltrans 2019 section 8.3.2. The inner longitudinal rebar protrudes and is connected with a non-contact splice to the column. This type of connection was studied by Masud et al., (2020) and can be seen in piers 2-4 and 5-13. The rebar splice was embedded 2.0m into the column to be as close as possible to the column longitudinal rebar. The distance between the foundation protruding rebar and the column rebar was limited to 4ϕ (longitudinal rebar) or 50mm, as per EN 1992-1-1:2004 section 8.7.2. If this distance was exceeded due to the column's trapezoidal shape or contour, the overlap was increased by the clear space between the longitudinal rebars. Additional transverse reinforcement was added to fully develop the capacity of the longitudinal non-contact lap splice and prevent brittle failure. It's important to note that the element's capacity in this section was determined based on the smaller cross-section of the column (pier 2-4) or diaphragm foundation (pier 5-13).
- c) The location of the bottom maximum bending moment was checked for bi-axial bending moment and met the requirement of $1.25M_{max} < M_{cap}$ (Caltrans 2019). This is in order to reduce the potential for plastic hinge to form in a location that is difficult to examine.
- d) The bottom half of the foundation was checked with the minimum required reinforcement in the section (0.6% of the overall cross section) also making sure that $1.25M_{max} < M_{cap}$ (Caltrans 2019). limitation was fulfilled.

Overall, the design of the bridge column was thoroughly analyzed and optimized to ensure its structural integrity under various loads and conditions.

6. Conclusion

This paper introduces a novel method for constructing a monolithic diaphragm wall bridge foundation. The rebar configuration in the foundation and the column was carefully designed. Examining the produced bending moment in both directions to predict the location of potential plastic hinges. This examination together with construction limitation led to be preferred location for the splice zone at the ground level. The method offers several advantages, such as faster construction without the need for a pile cap, the ability to place the columns and foundation closer to obstacles or roadways, and a greater variety of column shapes compared to circular



mono shafts. However, there are also some potential disadvantages to consider. Firstly, the high amount of reinforcement needed for the column and diaphragm wall foundation can make threading the diaphragm wall foundation into the column a challenging task. Secondly, it is essential to carefully investigate the location of potential plastic joints that may form during a seismic event and pay close attention to the location and details of the splice rebar. Lastly, it is crucial to be aware that using a column on top of a single foundation element can increase the influence of deviation of the pier and the magnitude of the bending moment that can result from eccentricity.

7. References

- AASHTO. AASHTO LRFD Bridge Design Specifications, 8th ed. Washington, D.C.: American Association of State Highway Transportation Officials; 2017.
- Caltrans, Seismic Design Criteria Version 2.0, State of California Department of Transportation, April 2019.
- EN 1992-1-1 (2004) (English): Eurocode 2: Design of concrete structures - Part 1-1: General rules and rules for buildings [Authority: The European Union Per Regulation 305/2011, Directive 98/34/EC, Directive 2004/18/EC]
- Israeli standard 1227 part 1 – loads on bridges: highway bridges, 1988.
- Masud, M., Chen, H., Sawab, J., Huang, H.W., Xu, B., Mo, Y.L. and Hsu, T.T., 2020. Performance of non-contact lap splices in geometrically dissimilar bridge column to drilled shaft connections. *Engineering Structures*, 209, p.110000.
- Robinson, B., Suarez, V., Robalino, P., Kowalsky, M. and Gabr, M., 2006. Pile bent design criteria. NCDOT Research Project 2005, 19.



Performance Comparison of Nonlinear Dampers for Suppressing Vortex-Induced Vibration of Flexible Bluff Structures

Jingwei Zhang¹, Xiaojun Wei^{1*}, and Xuhui He¹

School of Civil Engineering, Central South University, Changsha, China
Email: zhangjingwei2019@csu.edu.cn; xiaojun.wei@csu.edu.cn; xuhuihe@csu.edu.cn

*: corresponding author

Keywords: Nonlinear dampers; Vortex-induced vibration; Flexible bluff structures; Multiple modes

Abstract: Flexible bluff structures under wind excitations are prone to vortex-induced vibrations (VIVs). Linear dampers designed for a single mode may be ineffective in suppressing VIV when the excited mode is not the target mode. Nonlinear dampers, characterized by broadband vibration energy absorption, are more appropriate for suppressing VIV involving multiple modes and/or with the dominate mode varying with wind velocity. This paper aims to provide a performance estimation of nonlinear dampers, with cubic stiffness element or/and cubic damping element, in VIV mitigation of flexible structures. The governing equations of fluid-structure-damper systems are established, where the vortex-induced force is described using a wake oscillator model in consideration of fluid-structure interaction. A flexible circular cylinder is employed for the performance comparison of a linear tuned mass damper and three nonlinear dampers in mitigating VIV involving multiple modes. The optimal parameters of all the dampers are identified using a brute force approach. The research outcomes are helpful in developing a suitable nonlinear damper for VIV control of flexible bluff structures.

1. Introduction

Vortex-induced vibration (VIV) of flexible structures may result in serviceability and fatigue problems (Wu et al., 2012). Adding dampers is one of the main countermeasures to control undesired VIV (Fujino and Siringoringo, 2013). Among them, linear dampers are used widely due to its simplicity. However, a linear damper usually mitigates the structural vibration dominated by a single target mode only. Nonlinear dampers, featured by broadband vibration control capability, are promising for VIV mitigation involving multiple modes and/or with the dominant mode varying with wind velocity. (Gendelman et al., 2001). Nevertheless, it is unclear what type of nonlinear dampers is the most appropriate one. This paper aims to compare the control performance of dampers with cubic damping or/and cubic stiffness for suppressing VIV of flexible bluff structures. A flexible circular cylinder with a linear/nonlinear damper is employed for numerical demonstration purposes.

2. Governing Equations of Fluid-Structure-Damper Systems

This section describes the mathematical modelling of coupled fluid-structure-damper systems, where different types of dampers are considered. The schematic of a coupled system is shown in

Fig. 1. The primary structure is assumed to be an elastically supported circular cylinder subjected to uniform wind and vibrate only in the cross-flow direction. The vortex-induced force is described through a wake oscillator model (Facchinetti et al., 2004). A damper is attached inside the cylinder to mitigate VIV of the structure. Four types of dampers considered here, namely, a linear tuned mass damper (LD), a single degree of freedom (SDoF) nonlinear damper with linear viscous damping and cubic stiffness (ND1), a SDof nonlinear damper with cubic viscous damping and linear stiffness (ND2), and a SDof nonlinear damper with cubic viscous damping and cubic stiffness (ND3). The governing equations of a coupled system can be expressed in modal space as

$$m_k \ddot{\eta}_k(t) + 2m_k \omega_k \xi_k \dot{\eta}_k(t) + m_k \omega_k^2 \eta_k(t) = F_w(x, t) - F_d^{i,j}(t) \quad (1)$$

$$\ddot{q}_k(t) + \varepsilon \omega_k^0 \frac{\int_0^L \varphi_k(x) \left(\sum_{n=1}^N \varphi_n(x) q_n(t) \right)^2 \sum_{n=1}^N \varphi_n(x) \dot{q}_n(t) dx}{\int_0^L \varphi_k^2(x) dx} - \varepsilon \omega_k \dot{q}_k(t) + \omega_k^2 q_k(t) = \frac{A}{D} \ddot{\eta}_k(t) \quad (2)$$

$$m_d \ddot{y}_d(t) \varphi_k(x_d) = F_d^{i,j}(t) \quad (3)$$

in which

$$F_w(x, t) = \frac{1}{4} \rho U^2 D C_{L0} q_k(t) \int_0^L \varphi_k^2(x) dx - \gamma \omega \rho D^2 \dot{\eta}_k(t) \int_0^L \varphi_k^2(x) dx \quad (4)$$

$$F_d^{i,j}(t) = \left[c_{d,i} \left(\sum_{n=1}^N \varphi_n(x_d) \dot{\eta}_n(t) - \dot{y}_d(t) \right)^i + k_{d,j} \left(\sum_{n=1}^N \varphi_n(x_d) \eta_n(t) - y_d(t) \right)^j \right] \varphi_k(x_d) \quad (5)$$

where $y_s = \sum_{n=1}^N \varphi_n(x) \eta_n$, $q = \sum_{n=1}^N \varphi_n(x) q_n$ and y_d are structural displacement, wake variable, and displacement of the damper, respectively. N represents the total number of considered modes. The over dot denotes the derivative with respect to time t . η_k and q_k are the k th-order modal coordinates of y_s and q , respectively. m_k , ω_k , ξ_k and $\varphi_k(x)$ are the modal mass, natural frequency, damping ratio and mode shape of the k th-order mode of the primary structure, respectively. x , x_d and L denote the coordinate along the length direction of the structure, the location where the damper is installed and the total length of the structure, respectively. m_d , $c_{d,i}$, $k_{d,j}$ and $F_d^{i,j}$ are the mass, damping, stiffness and the force of the damper, respectively. i and j represent the power of the damping term and stiffness term, respectively. F_w is the VIV force exerted on the structure, which is assumed to be fully correlated along the structural length. D , U and ρ are the feature dimension of the structure, uniform wind velocity and air density ($\rho = 1.225 \text{ kg/m}^3$ in this paper), respectively. ω , γ , C_{L0} , ε and A are the vortex-shedding frequency, fluid-added damping coefficient, reference lift coefficient, van der Pol parameter and scaling parameter, respectively.

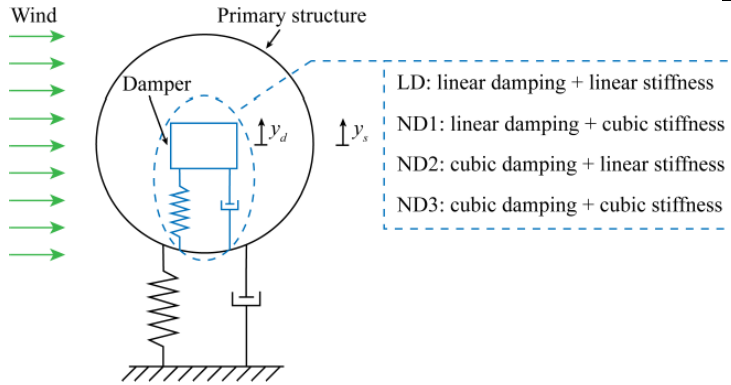


Fig. 1. Schematic diagram of a coupled fluid-structure-damper system.

3. Numerical Example

A flexible circular cylinder is considered as the primary structure in this section (Zhang et al., 2022). The cylinder is assumed to be a simply supported Euler-Bernoulli beam. The mode shape, natural frequency and modal mass can be determined from $\varphi_k(x) = \sin(k\pi x/L)$, $\omega_k = k^2\pi^2\sqrt{EI/(\bar{m}L^4)}$ and $m_k = \bar{m} \int_0^L \varphi_k^2(x)dx$, respectively. The first five modes are considered to estimate the performance of different dampers on VIV control involving multiple modes, and the damping ratio of each mode is set to be $\xi_k = 0.13\%$. The physical mass per unit length, total length, feature dimension and stiffness of the cylinder is taken to be $\bar{m} = 0.044 \text{ kg/m}$, $L = 3 \text{ m}$, $D = 0.02 \text{ m}$ and $EI = 1.7815 \text{ Nm}^2$, respectively. Parameters in the wake oscillator model are taken to be $S_i = 0.2$, $\gamma = 0.8$, $C_{L0} = 0.3$, $\varepsilon = 0.3$ and $A = 12$ (Facchinetti et al., 2004). The responses of the coupled systems are estimated using the Newmark-beta numerical integration method with initial conditions of $\eta_k(0) = 0.01D$. Parameters of the damper installed at the mid-span of the cylinder are optimized through parametric analyses that aims to minimize the structural steady-state displacement response. Both linear and nonlinear dampers are designed to minimize the 1st-mode VIV response at the wind velocity $U = \omega_1 D / 2\pi S_i$. The mass ratio is set to be $\mu_d = m_d / m_1 = 5\%$. The optimal stiffness and damping coefficients of dampers are listed in Table 1.

Table 1. Optimal parameters of different dampers.

	LD	ND1	ND2	ND3
Stiffness coefficient ^a	1.56×10^{-1}	6.50×10^5	1.56×10^{-1}	6.50×10^5
Damping coefficient ^b	1.44×10^{-4}	8.93×10^{-3}	6.37	6.28×10^2

^a: units of linear, quadratic and cubic stiffness are (N/m), (N/m²) and (N/m³), respectively.

^b: units of linear, quadratic and cubic damping are (Ns/m), (Ns²/m²) and (Ns³/m³), respectively.

Fig. 2 presents the performance of linear and nonlinear dampers on VIV control of the flexible circular cylinder. The linear damper LD designed for 1st-mode can mitigate only the VIV of this target mode. Moreover, when the vortex shedding frequency is not equal to the 1st-mode natural frequency, the control performance of the linear damper is inferior to that of the nonlinear dampers. The nonlinear dampers ND1, ND2 and ND3 are capable of controlling VIVs involving

multiple modes, e.g. 1st-mode, 3rd-mode and 5th-mode, due to its broadband vibration absorption capability. ND2 exhibits similar performance in suppressing the 1st-mode and 3rd-mode VIVs to that of ND1 but better performance in suppressing the 5th-mode VIV. This means that dampers with cubic viscous damping are more effective for suppressing higher-order mode VIV than those with cubic stiffness. Compared with ND2, ND3 is capable of slightly narrowing lock-in ranges of VIV due to the introduction of cubic stiffness, while ND3 has worse control performance in controlling the 5th-mode VIV. Noted that nonlinear dampers are ineffective in controlling 2nd-mode and 4th-mode VIVs. This is due to the fact that the damper is installed at the mid-span, the node of these modes.

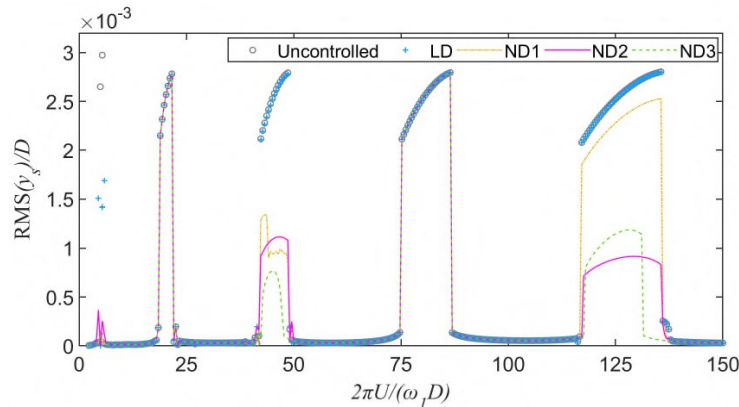


Fig. 2. Performance of different dampers on VIV control of the circular cylinder. ($RMS(y_s/D)$ denotes the root-mean-square value of the dimensionless steady-state displacement of the cylinder at the location with the largest response.)

4. Conclusions

Nonlinear dampers are superior in VIV control of flexible bluff structures to the linear damper due to their capability of mitigating VIV involving multiple modes and their insensitivity to the variation of vortex-shedding frequency. Among them, dampers with cubic viscous damping nonlinearity are more effective than those with cubic stiffness or with both cubic stiffness and cubic viscous damping.

5. References

- Facchinetti, M. L., De Langre, E. and Biolley, F. 2004. Coupling of structure and wake oscillators in vortex-induced vibrations. *Journal of Fluids and Structures*, 19, 123-140.
- Fujino, Y. and Siringoringo, D. 2013. Vibration mechanisms and controls of long-span bridges: a review. *Structural Engineering International*, 23, 248-268.
- Gendelman, O., Manevitch, L. I., Vakakis, A. F. and M'Closkey, R. 2001. Energy pumping in nonlinear mechanical oscillators: Part I - Dynamics of the underlying Hamiltonian systems. *Journal of Applied Mechanics-Transactions of the ASME*, 68, 34-41.
- Wu, X., Ge, F. and Hong, Y. 2012. A review of recent studies on vortex-induced vibrations of long slender cylinders. *Journal of Fluids and Structures*, 28, 292-308.
- Zhang, M. J., Wu, T. and Oiseth, O. 2022. Vortex-induced vibration control of a flexible circular cylinder using a nonlinear energy sink. *Journal of Wind Engineering and Industrial Aerodynamics*, 229.

Control the Torsional Flutter of a Rectangular Plate with Flexible Membrane at Its Leading Edge

Ziqiang Zhang¹, Hanfeng Wang^{1,2*}, Zhiwei Liu¹, and Chi Zhang¹

¹: School of Civil Engineering, Central South University, Changsha, China

²: National Engineering Research Center for High-speed Railway Construction, Changsha, China; email: wanghf@csu.edu.cn

*: corresponding author

Keywords: Torsional flutter; Leading edge vortex; Serrated flexible membrane; Flow control

Abstract: The wind resistance performance of large span bridges in mountain canyons is a key concern in current wind engineering. Due to the complex wind environment of canyon terrain, the average wind attack angle (α) of bridge deck can often reach $\pm 5^\circ$, obviously larger than the range of $\pm 3^\circ$ in the criterion. Traditional passive aerodynamic measures (such as wind nozzles, etc.) may be difficult to meet the complex wind resistance requirements of large span bridges in mountainous areas. Therefore, a novel adaptive deformation passive aerodynamic measure is proposed. In this paper, a simplified rectangular plate with a width to thickness (W/D) ratio of 20, which had one degree of freedom in torsional direction, was used as the tested model. Torsional circular frequency of the model = 40.9 rad/s, mass per unit length $m = 1.67$ kg/m and damping ratio $\zeta = 1\%$. Serrated flexible membrane, with a Young's modulus of 0.2 Gpa, a thickness of 0.06 mm, and a length of $2D$, were fixed at the leading edge of the plate to test their effects on its torsional flutter. All experiments were conducted in an open-circuit low-speed wind tunnel with a test section of 450 mm in width, 450 mm in height, and 1200 mm in length. The tested α was 5° , which was considered as the most unfavorable angle of attack. The torsional vibration amplitude of the plate was measured, with the reduced wind speed U_r ranged from 0 - 8.85, and the corresponding Reynolds number (Re) was 0 - 1.55×10^5 . The flow field around the plate was also measured using Particle image velocimetry (PIV) to reveal the control mechanism. For the uncontrolled case, the flutter starts at $U_r = 6.77$. For the controlled case with the membrane utilized, the membrane starts flapping at $U_r = 6.52$, prior to the flutter of the plate. Once the membrane flaps, it significantly suppresses the flow separation from the leading edge of plate, reducing the separation bubble on its upper surface. The leading-edge vortex (LEV), which directly associated with the torsional flutter, is also considerably weakened by the flapping membrane, together with thus reducing the torsional moment of the plate. The experimental results shows that the flutter critical wind speed increases by approximately 19 %, from 6.77 to 8.07, when the flexible membrane is utilized.

1. Introduction

With the construction of large span bridges across the sea and mountainous areas, the wind environment at the bridge site has become increasingly complex. According to observation analysis and wind tunnel simulation research on strong wind characteristics in coastal and mountainous areas (Pang, 2006), the maximum wind attack angle of bridge deck height is

generally greater than 5° , and the flutter performance of bridge section will be further weakened at high attack angle. However, previous study (Zhao et al., 2015) have shown that traditional aerodynamic measures do not have universal control for complex inflow and wind-induced vibration. Inspired by adaptive flow control measures in aerospace field (Tan et al., 2021; Gong et al., 2021; He et al 2022;), a new type of lightweight, flexible and deformable passive aerodynamic measure is designed.

2. Experiment Details

All experiments were conducted in an open-loop low-speed wind tunnel with a test section of 0.45m in width, 3m in height, and 1.2m in length, respectively. More details of the wind tunnel are introduced in Liu et al. (2023). The test model was made of abs material, with length $L = 420\text{mm}$, width $B = 200\text{mm}$ and thickness $D = 10\text{mm}$, as shown in Fig.1a. Serrated flexible membrane with $q = 10\text{mm}$, $s = 10\text{mm}$ and $h = 5\text{mm}$ was installed on the leading edge of the rectangular plate at 5° wind angle of attack, as shown in Fig.1b. The main parameters of the model and flexible membrane are shown in Table 1:

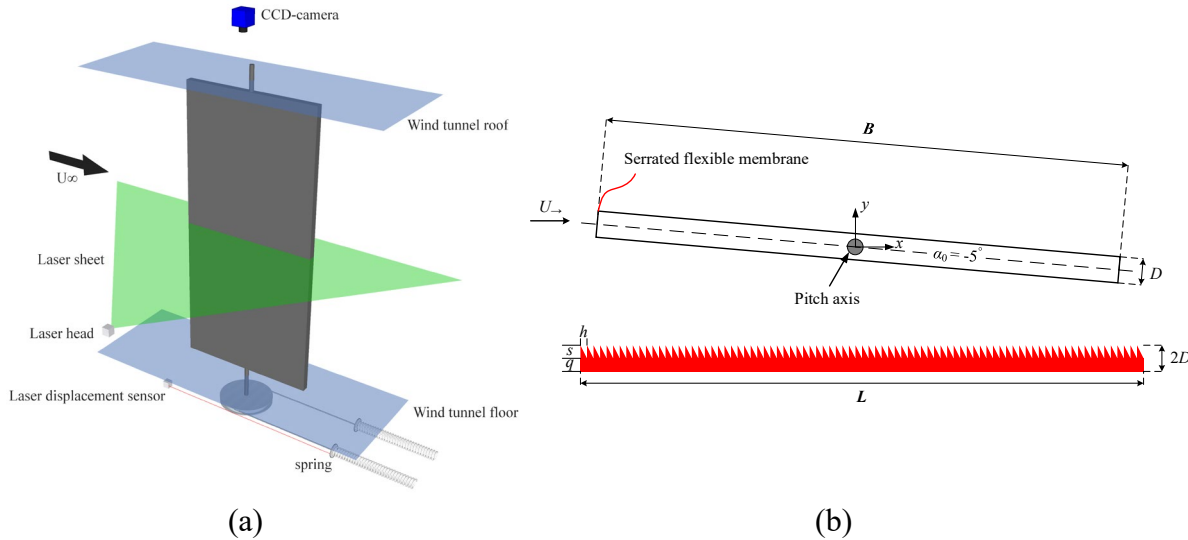


Fig. 1. Experimental Setup: (a) 3D Sketch; (b) Cross-section of the model and shape of serrated flexible membrane

Table 1. Main parameters of rectangular plate model of serrated flexible membrane

Main parameters	
Damping ratio /%	1.00
Natural circular frequency /(rad/s)	40.90
Natural frequency f_d /Hz	6.51
System stiffness /(Nm/rad)	9.37
Rotational inertia /(kg.m ²)	0.0056
Material of membrane	polyethylene
Membrane thickness /mm	0.06
Young's modulus of membrane /Gpa	0.20

3. Results and Discussion

3.1 Amplitude characteristic

In fig.2, it can be found that nonlinear soft flutter occurs on the rectangular plate of both cases, consistent with the phenomenon reported in Zhu et al 2015. The rectangular plate remains a stable limit cycle vibration after the critical wind speed for vibration starting, and the vibration amplitude increases approximately linearly with the increase of wind speed as shown in fig.3. In the uncontrolled case, the torsional flutter of rectangular plate occurs at $U_r = 6.77$. After installing flexible membrane on the plate, the critical flutter speed of rectangular plate increased to about 8.07, which is about 19% higher than the uncontrolled case.

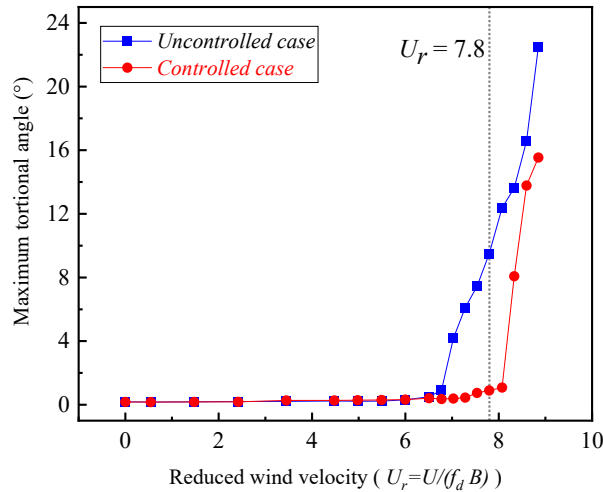


Fig. 2. Variation of with U_r

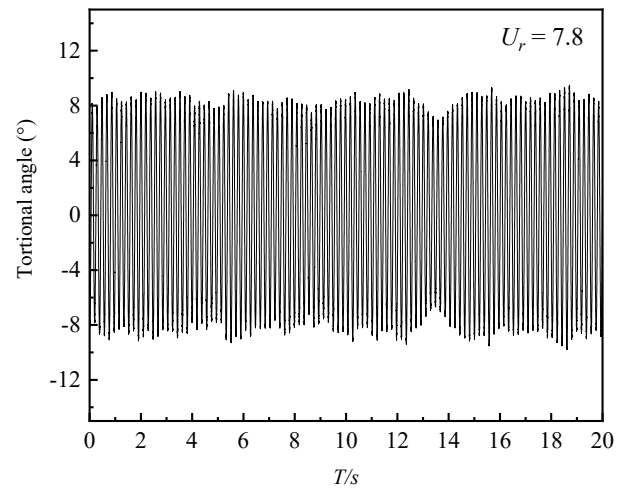


Fig. 3. Displacement time history with $U_r = 7.8$

3.2 Flow characteristics

Flow characteristics of flow field above the fixed rectangular plate at 5° and $U_r = 7.80$ was investigated by PIV. The maximum torsional amplitude of uncontrolled case is 8° , while the controlled case remains almost stationary at $U_r = 7.80$. Fig.4 shows the time averaged vorticity field and streamwise velocity which is calculated using the 2000 random sampled PIV snapshots. The flapping configurations of the flexible membrane was recorded using a high speed camera by Liu et al 2023 as shown in Fig.4b. In the uncontrolled case, there is a large-scale leading-edge vortex above the rectangular plate as shown in Fig.4a. It can also be observed that the flow separates from the leading edge of the rectangular plate and reattaches to the near trailing edge of the plate, coupling with the wake in Fig.4c. The initiation, separation and reattachment of leading-edge vortex creates a large separation bubble, however, a large amount of airflow on the upper surface of the rectangular plate separates, resulting in a sharpening change in the pitching moment of plate, which may lead to aerodynamic negative damping and torsional flutter.

In the controlled case, it can be discovered that the sizes of leading-edge vortices and separation bubble above the rectangular plate were both significantly reduced by the flapping serrate flexible membrane in Fig.4b,d. The reattachment point of flow moved forward from the trailing edge to the position of $0.6B$ of rectangular plate and the vortex core also moved forward from $0.55B$ to $0.22B$ of rectangular plate, compared to uncontrolled case. Consequently, the flapping serrated flexible membrane can weaken the rapidly changing in pitching moment caused by separation of airflow, thereby delaying the occurrence of torsional flutter.

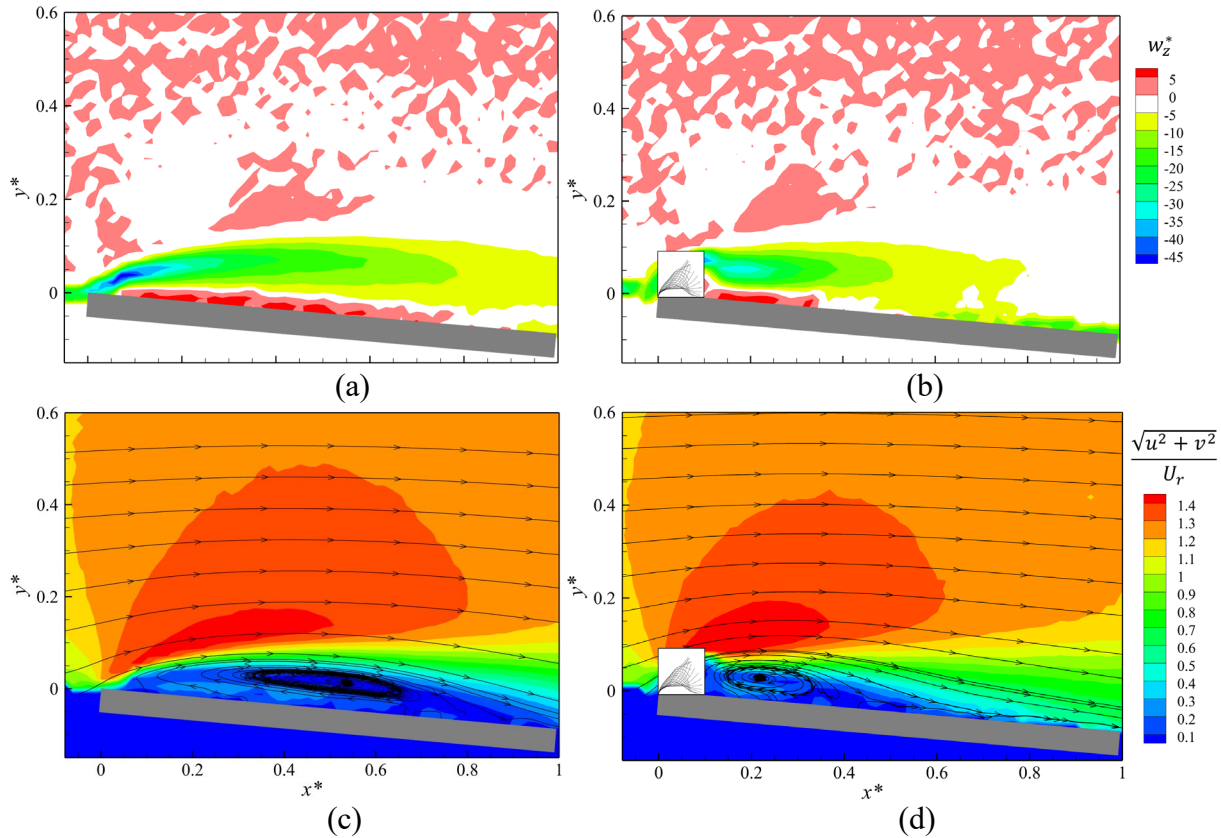


Fig. 4. Mean spanwise vorticity (top) and mean streamwise velocity (bottom): (a) (c) for uncontrolled case; (b) (d) for controlled case

4. Conclusion

- (1) The new type of lightweight, flexible and deformable passive aerodynamic measure is designed and investigated, which is expected to provide a better option for bridge aerodynamic measures in the future.
- (2) The flapping serrated flexible membrane can increase the flutter critical wind speed of rectangular plate by approximately 19%, from 6.77 to 8.07.

5. Reference

Zhao Lin, Ge Yaojun, Guo Zengwei and Li Ke, 2015 Review and Reflection on Wind Vibration Control of Long Span Cable Supported Bridges - Passive Control Effects and Active Control Strategies for Main Beams *Journal of Civil Engineering*, 48 (12), pp. 91-100

Gong Xu'an, Zhang Xin, Ma Xingyu, Fan Ziye and Jiang Nan, 2021 Bionics overlaid control airfoil flow separation experiment *Journal of Aerodynamics*, 39 (6), pp. 184-195

Tan, J., Wang, Z. and Gursul, I., 2021. Self-excited flag vibrations produce post-stall flow control. *Physical Review Fluids*, 6(10), p.L102701.



Bridge Engineering Institute Conference 2023 (BEI-2023)
Rome, Italy, July 17-20, 2023



Liu, Z., Wang, H. and Zhao, C., 2023. Flow over a forward-facing step with a flexible membrane at its leading edge. *Experimental Thermal and Fluid Science*, p.110922.



Bridge Engineering Institute Conference 2023 (BEI-2023)
Rome, Italy, July 17-20, 2023



Modeling and Advanced Analysis



Unseating of Bridge Decks-Codal Provisions and Fragility Analysis

Shambhavi Dube^{1*}, Nirav Thakkar², and Durgesh C. Rai³

¹: Doctoral Student, Dept. of Civil Engineering, Indian Institute of Technology Kanpur, Kanpur 208016, India; email: shamdube@iitk.ac.in

²: Frmr. Graduate Student, Dept. of Civil Engineering, Indian Institute of Technology Kanpur, Kanpur 208016, India; email: nirav.thakkar@gmail.com

³: Professor, Dept. of Civil Engineering, Indian Institute of Technology Kanpur, Kanpur 208016, India; email: dcrai@iitk.ac.in

*: corresponding author

Keywords: bridge bearing; elastomeric pad; fragility analysis; seismic forces; unseating; incremental dynamic analysis (IDA)

Abstract: Bridges are lifeline structures, and their continued operation during and after earthquakes is critical. In the last few decades, there has been a dramatic increase in bridge failures caused by earthquakes worldwide. The use of elastomeric pads helps in reducing seismic forces on the substructure. However, it generates higher displacement demand, causing problems like unseating and collapse of the deck slab. The performance of a bridge under an earthquake largely depends on the dynamic characteristics of the bridge which in turn depends on deck span and pier height. To understand the effect of the elastomeric pad on the seismic performance of a wide range of RC bridges, a group of nine bridges with various spans and pier heights was considered. Primary components of the bridge i.e., precast concrete girders, elastomeric pads, and piers were designed for these span lengths and pier heights as per Indian Codal provisions. The bridges were modeled using the finite element software, SAP2000. The vulnerability of the bridges was investigated for three damage states, namely unseating, collapse, and low pressure. The problem of instability and unseating is a function of the size of the bearing, the width of the supports, and the minimum normal pressure on the bearings. Incremental Dynamic Analysis (IDA) of the sample bridges was carried out with twenty far-field ground motions recorded on soft rocks or stiff soils, and displacement of bearing is recorded along all three directions, which are further used for vulnerability analysis. Codal provisions for the requirement of a minimum support length were reviewed and compared for various international codes. Fragility curves have been developed corresponding to 60%, 80%, 100%, 120%, and 140% of the capacity for RC bridges with elastomeric pad bearings for the instability, unseating, and low-pressure damage states. A significant effect of the size of the elastomeric pad and seating width was observed on fragility curves. Results for maximum acceptable PGA and fragility curves can be used to determine the potential damages from earthquakes and to assign prioritization for retrofitting the existing bridges.

1. Introduction

Elastomeric pads, also known as neoprene pads, have been found to impose less seismic force on piers compared to other types of bearings (Pan et al., 2010; DesRoches et al., 2004; Chiang, 2008). They are cost-effective, durable, simple to detail, fabricate, and install, while also allowing for thermal expansion and girder rotation. Due to these advantages, elastomeric pads are a popular choice for bridge bearings in developing countries like India. RC bridge decks supported by elastomeric pad bearings can move freely over the substructure during an earthquake, enabling large displacements. However, an additional anchorage system may be necessary to handle excessive displacement demand (Chiang, 2008). In India, some seismic codes in practice do not allow the use of elastomeric pads in high seismic zones, while others permit their use without anchorage, restraints, or shear keys, even in highly seismic areas. Often, bridge deck girders are not anchored to bearing pedestals or pier cap beams, making it likely that the deck will collapse due to excessive displacement during a design-level earthquake. Recent earthquakes have shown that bridges with elastomeric bearing pads are prone to unseating and collapse (Rai et al., 2006). These problems can be prevented by ensuring sufficient seat length, as specified by international codes based on factors such as span length, pier height, ground acceleration, and seismic displacement demand. To evaluate the impact of elastomeric pads on the seismic performance of RC bridges, a group of nine bridges with different spans (10 m, 20 m, and 30 m) and pier heights (5 m, 15 m, and 25 m) was examined. The study defined damage states based on deformations in the elastomeric bearings in both longitudinal and transverse directions and the minimum normal pressure on the bearings.

2. Design of Primary Components of Bridges

A three-span simply supported concrete bridge is used for the present study as shown in Fig. 1a. The seismic design is carried out in both longitudinal and transverse directions of the bridge. The design forces are obtained by combining i) 100% longitudinal + 30% transverse and ii) 30% longitudinal + 100% transverse direction loading. Foundations and abutments are considered rigid enough to consider that design ground accelerations are directly applied to the bottom of the pier and the bottom of the abutment bearing. Nine bridge samples are considered with span lengths of 10 m (short), 20 m (intermediate), and 30 m (long-span bridge); and pier heights taken as 5 m (short), 15 m (intermediate), and 25 m (long period bridges). Type I, Type IV, and Type VI AASHTO I-Beams are used for 10 m, 20 m, and 30 m spans.

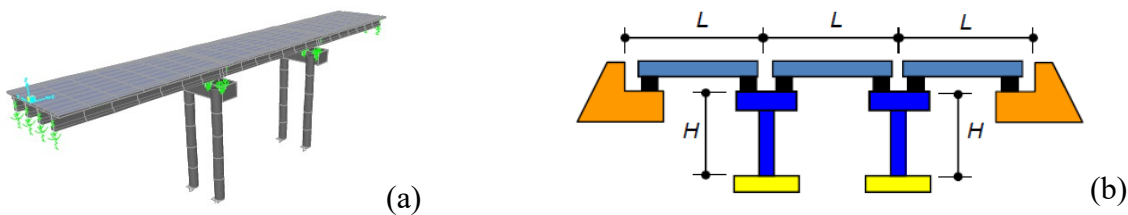


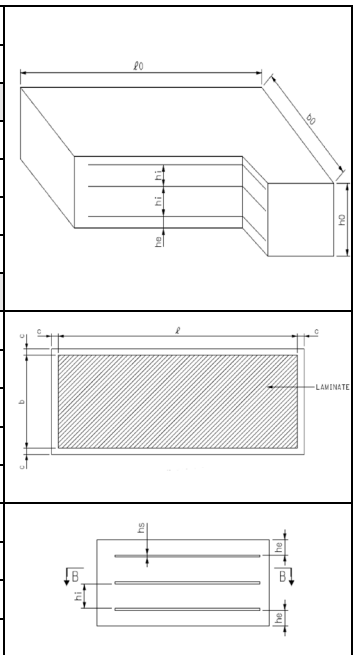
Fig. 1. (a) SAP 2000 model of a three-span bridge; (b) Schematic elevation of bridge

2.1. Design of Elastomeric Pads

Elastomeric pads shall be designed to resist the shear stress generated primarily by axial compression, lateral displacement, and girder rotation while also meeting the stability and serviceability criteria. The design load for bearings is calculated by combining dead loads and vehicle loads as per IRC 6 guidelines. The elastomeric pads were designed based on IRC 83 (Part II) and the key specifications are provided in Table 1.

Table 1. Design summary of elastomeric pads

Description	Span length		
	10 m	20 m	30 m
Design loads per bearing			
Dead load (kN)	90	265	470
Imposed load w/o impact (kN)	345	470	530
Horizontal load (kN)	25	25	25
Rotation of girder end (rad)	2.0E-4	4.4E-4	11.7E-4
Geometrical details			
Overall length of pad l_0 (mm)	320	400	500
Overall width of pad b_0 (mm)	200	250	250
Side cover c (mm)	6	6	6
Thickness of internal layers h_i (mm)	8	10	10
Thickness of external layers h_e (mm)	4	5	5
Thickness of laminates h_s (mm)	3	3	3
Numbers of internal layers n	2	3	3
Total thickness of pad h_0 (mm)	33	52	52
Total elastomer thickness h (mm)	24	40	40



3. Finite Element Modelling

The bridge is modeled using CSI SAP2000. The modulus of elasticity for M30 grade concrete is determined to be 27.4 GPa based on IS 456:2000. The piers are modeled as elastic beam-column elements, which are expected to be subjected to significant axial forces and bending moments and are likely to experience plastic hinges. To account for this, P-M2-M3 hinges are modeled at the top and bottom of the piers, following the guidelines in FEMA 356 to reflect the frame action along the transverse direction of the bridge. The pier cap beam is modeled as an elastic beam-column element, while the bridge deck is modeled as a single equivalent elastic beam-column element. The foundation is assumed to be rigid and provides support to the pier, restraining all six degrees of freedom at the bottom of the pier. The abutment is rigid and elastomeric pads are modeled as Friction Isolator link elements with a coefficient of friction of 0.2.

4. Provisions for Seating Width in Various National Codes

The recent version of the Indian Code for Seismic Design of Road Bridges IRC SP:114 prohibits the use of elastomeric bearings in high seismic zones IV and V. Instead, PoT, POT Cum PTFE, and spherical bearings must be used. Earlier codes lacked this restriction, leading to many bridges with elastomeric bearings in these high seismic zones. Deck unseating occurs when the maximum bearing displacement along the longitudinal direction of the bridge exceeds the minimum seating width requirement shown in Table 2 calculated using various national codes.

Table 2. Comparison of required minimum support length as per various codes

Span Length, m		10			20			30		
Pier Height, m		5	15	25	5	15	25	5	15	25
Period, second		0.77	1.26	1.56	1.20	1.76	1.98	1.33	1.85	2.28
Required minimum support length, mm	IS 1893/IRC: 6	380	480	580	405	505	605	430	530	630
	AASHTO	380	480	580	405	505	605	430	530	630
	CALTRANS	252	552	852	252	552	852	252	552	852
	Japanese code	750	750	750	800	800	800	850	850	850

As per IRC 6, the combined effects of dead and vehicle loads result in an elastomeric pad length of 320 mm, 400 mm, and 500 mm for spans of 10 m, 20 m, and 30 m respectively. Existing bridges with these pad lengths are prone to unseating failure during earthquakes, particularly those with greater pier heights. Consequently, a vulnerability analysis should be conducted to assess the potential for unseating failure and to propose appropriate retrofitting measures.

5. Assessment of Fragility

Nine bridge configurations were designed for a 0.36g PGA. Figs. 2a and 2b compare the IS 1893 design spectrum to the mean spectrum of 20 selected ground motions provided in Thakkar, 2011, normalized to the 1.0g hazard level. The Spectral Displacement Response Spectra (Fig. 2b) were obtained through Incremental Dynamic Analysis (IDA) for the selected ground motions. Newmark's method with $\gamma = 0.5$ and $\beta = 0.25$ is used for time integration and 5% proportional damping is assumed for periods of 0.35 s and 2.5 s. The maximum displacement at bearings and minimum pressure on the elastomeric pad is obtained by performing IDA and further utilized to create fragility curves for three damage states under various hazard levels. Bearing instability occurs when the maximum transverse displacement exceeds half the width of the bearing and deck unseating occurs when the maximum longitudinal displacement exceeds the minimum seating width (SE) requirements. A damage state of low pressure is defined as a minimum normal pressure on the elastomeric bearing below 1 MPa for all 9 bridges in the sample.

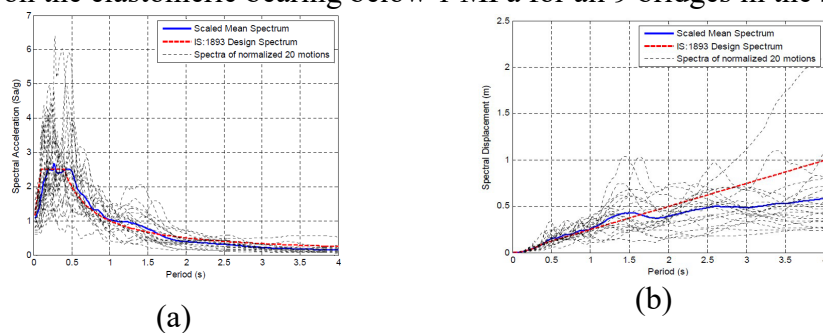


Fig. 2. (a) Acceleration response spectrum; (b) Displacement response spectra

A fragility curve describes the probability of exceeding a damage state as a function of chosen ground motion intensity parameter. The probability that the demand exceeds the structural capacity can be computed using Eq. 1. where S_d, S_c, Φ are structural demand, structural capacity, structural normal distribution functions, respectively; and β_d and β_c are the logarithmic standard deviation for demand and capacity, respectively. This study utilized the procedure described by Pan et al., 2007 to generate fragility curves for bridges.

$$P_f = P\left(\frac{S_d}{S_c} \geq 1\right) = 1 - \Phi\left(\frac{\ln(1) - \lambda}{\sigma}\right) = \Phi\left(\frac{\lambda}{\sigma}\right); \lambda = \ln\left(\frac{S_d}{S_c}\right); \sigma = \sqrt{\beta_d^2 + \beta_c^2} \quad (1)$$

6. Results and Discussion

The Figs. 3a-3c, concludes that with the same pier height, the probability of failure decreases with an increase in the span of the bridge mainly due to increased weight distribution and hence stabilizing pressure on the bearings. However, a noticeable increase in the probability of failure occurs when the pier height increases from 5 to 15 meters for a constant span length. The probability of failure remains relatively constant for further increase in pier height to 25 m likely due to the dynamic properties of the bridges. From Figs. 3d-3f, it is observed that the risk of failure is highest for the low pressure damage state and lowest for the unseating damage state for any span length or pier height. This indicates that during an earthquake, there is a higher probability of the normal pressure on elastomeric bearings dropping below the low pressure damage threshold of 1 MPa. Transverse ground motion components can cause uplift reactions on some bearings that are comparable with the reactions from gravity loads.

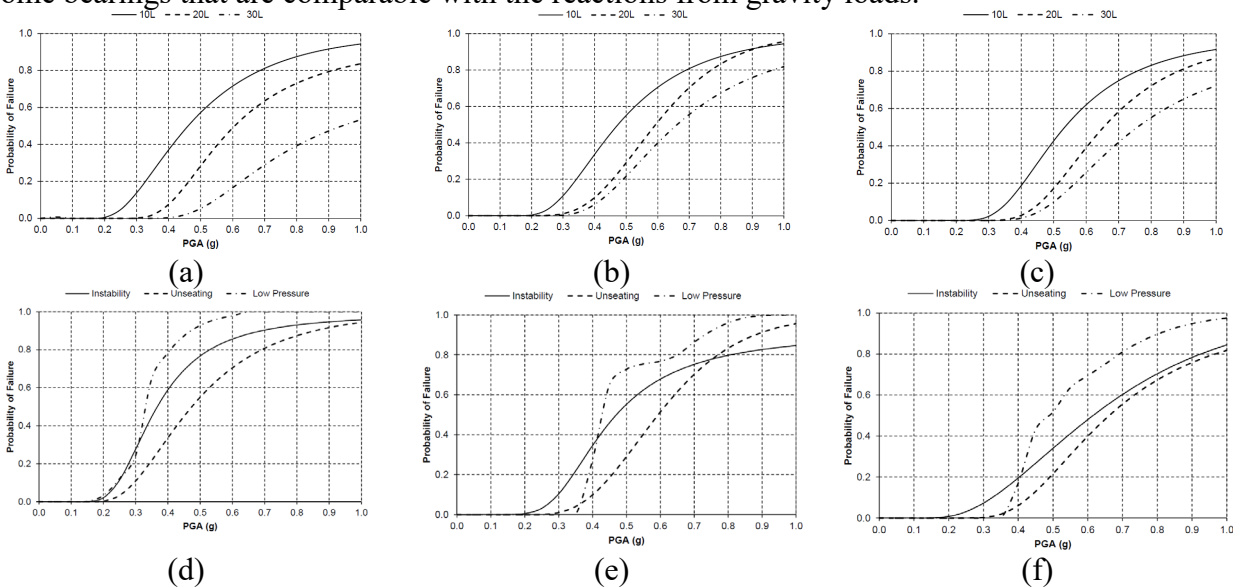


Fig. 3. Fragility curves for unseating of bridges with (a) 5 m; (b) 15 m; (c) 25 m pier height for unseating damage state; comparison of damage states of 15 m pier height and (d) 10 m; (e) 20 m; (f) 30 m span length

7. Conclusion

Past earthquakes have taught us the importance of providing adequate seat length to prevent bridge deck collapse. In general, the risk of failure is high for unseating damage state, even for low hazard levels. Results showed that the risk of failure increases with pier height and decreases with bridge span. Bridges with small piers have a low risk of unseating, indicating that elastomeric pads may be suitable. The acceptable maximum PGA that can be allowed for the sample bridges with elastomeric pad bearings was found in the range of 0.11g to 0.41g and the existing bridges with a design PGA greater than 0.41g are susceptible to unseating failure and need retrofiting. The fragility curves developed in this study can aid in assessing earthquake-related potential losses and prioritizing retrofiting efforts such as seismic links, STUs, vertical hold-down devices, and anti-dislodgement devices in the horizontal direction. However, these



curves are based on approximations and a limited sample of bridges, so their accuracy and applicability in practical situations need to be further investigated with a larger sample of bridges with different span lengths and pier heights.

8. References

AASHTO. 2017. AASHTO LRFD Bridge Design Specifications, American Association of State Highway and Transportation officials (AASHTO), Eighth edition, Washington DC.

BIS IS 1893-Part 3. 2014. Criteria for Earthquake Resistant Design of Structures - Bridges and Retaining Walls, Bureau of Indian Standards (BIS), New Delhi, India.

BIS / IS 456. 2000. Plain and Reinforced Concrete – Code of Practice, Fourth Revision, Bureau of Indian Standards (BIS), New Delhi, India.

CALTRANS. 2019. Seismic Design Criteria, California Department of Transportation (CALTRANS), V2.0.

Chiang J C. 2008. Application of Functional Bearing System to the Seismic Retrofit of Bridge, Fourth US-Taiwan Bridge Engineering Workshop, Paper 16, Princeton, New Jersey.

DesRoches, R., Choi, E., Leon, R.T., Pfeifer, T.A. 2004. Seismic Response of Multiple Span Steel Bridges in Central and Southeastern United States. II: Retrofitted, Journal of Bridge Engineering, ASCE, Vol. 9, No. 5, pp. 473-479.

FEMA 356. 2000. Pre-standard and Commentary for the Seismic Rehabilitation of Buildings, Federal Emergency Management Agency, Washington, D.C. 2000.

IRC 83-Part 2. 1987. Standard Specifications and Code of Practice for Road Bridges Section: IX Bearings - Elastomeric Bearings, Indian Road Congress (IRC), New Delhi, India.

IRC 6. 2017. Standard Specifications and Code of Practice for Road Bridges, Section: II Loads and Load Combinations, Indian Road Congress (IRC), Seventh Revision, New Delhi, India.

IRC SP:114. 2018. Guidelines for seismic design of road bridges, Indian Roads Congress (IRC), New Delhi, India.

Japanese JRA. 2012. Design Specifications for Highway Bridges: Part V - Seismic Design, Japan Road Association.

Pan, Y., Agrawal, A. K., and Ghosn, M. 2007. Seismic Fragility of Continuous Steel Highway Bridges in New York State, Journal of Bridge Engineering, ASCE, Vol. 12, No. 6, pp. 689-699.

Pan, Y., Agrawal, A.K., Ghosan, M., Alampalli, S. 2010. Seismic Fragility of Multispan Simply Supported Steel Highway Bridges in New York State. II: Fragility Analysis, Fragility Curves, and Fragility Surfaces, Journal of Bridge Engineering, ASCE, Vol. 15, No. 5, pp. 462-472.



Bridge Engineering Institute Conference 2023 (BEI-2023)
Rome, Italy, July 17-20, 2023



Rai, D.C., Murty, C.V.R., Jain, S.K., Kaushik, H.B., Mondal, G., Dash, S.R., Tang, A., Yashinsky, M., and Eskijian, M. 2006. The Effect of the December 2004 Great Sumatra Earthquake and Indian Ocean Tsunami on Transportation Systems in India's Andaman and Nicobar Islands, *Earthquake Spectra*, Vol. 22, No. S3, pp. S561-S579.

Thakkar, N. 2011. Performance evaluation of Elastomeric Pads as Bridge Bearings under Earthquake Loads, M. Tech. Thesis, Department of Civil Engineering, IIT Kanpur.



Finite Element Modeling of Compressive Membrane Action in Transversely Prestressed Deck Slabs

Amir Sana

University of Wollongong in Dubai, Dubai, United Arab Emirates; sanaamir@uowdubai.ac.ae, sanaamir.1919@gmail.com

Keywords: concrete; bridges; finite element; compressive membrane action

Abstract: It has been established in literature that compressive membrane action enhances the punching shear capacity of a laterally restrained slab. In this research an attempt has been made to compute the compressive membrane forces and to determine the level of the membrane action developed in a laterally restrained and transversely prestressed concrete deck slab. It is difficult, if not impossible, to theoretically predict the membrane action that can be developed in a slab. This issue can be resolved by adopting a finite element approach rather than using cumbersome analytical methods. A 3D solid model of an existing bridge was developed in TNO DIANA 9.4.4 software package and several nonlinear analyses were carried out. The pre-/post processor used for the finite element model in this research is midas FX+ (3.1.0) for DIANA. This paper describes the step-by-step procedure to model compressive membrane action in the deck slab. Such a numerical study will encourage engineers to use finite element as a tool to analyze existing and new structures.

1. Introduction

In the Netherlands, many old bridges with thin transversely post-tensioned concrete decks cast in-situ between the flanges of long, precast concrete girders, were found to be critical in punching shear when assessed by the Eurocode 2 “Concrete structures” (EN 1992-1-1:2005, 2005). However, no visible signs of distress are observed which may be due to the presence of residual bearing capacity (Amir, 2014). Bridges are usually designed on traditional flexural theories and it has been discovered that under concentrated wheel loads, the laterally restrained deck slabs mostly fail in punching shear rather than in flexure and at loads much higher than expected due to “Compressive Membrane Action” (CMA) that occurs in slabs whose edges are laterally restrained by stiff boundary elements. When a load is applied, the slab edges tend to move outwards and the restraint induces in-plane arching forces in the slabs enhancing the bearing capacity. This, in combination with transverse prestressing, can significantly enhance the bearing (punching shear) capacity (Amir et al. 2016). One of the aims of this research was to prove that sufficient CMA can develop in the bridge deck slab enhancing its bearing capacity. For this purpose, a 1:2 scaled model of a real approach bridge (Fig. 1) experimental, numerical and theoretical approaches were used to estimate the bearing capacity and CMA. This paper describes the numerical modeling procedure to simulate CMA in the deck slab. The details of the material properties, test setup, loading pattern etc. can be found in (Amir, 2014; Amir et al. 2016).

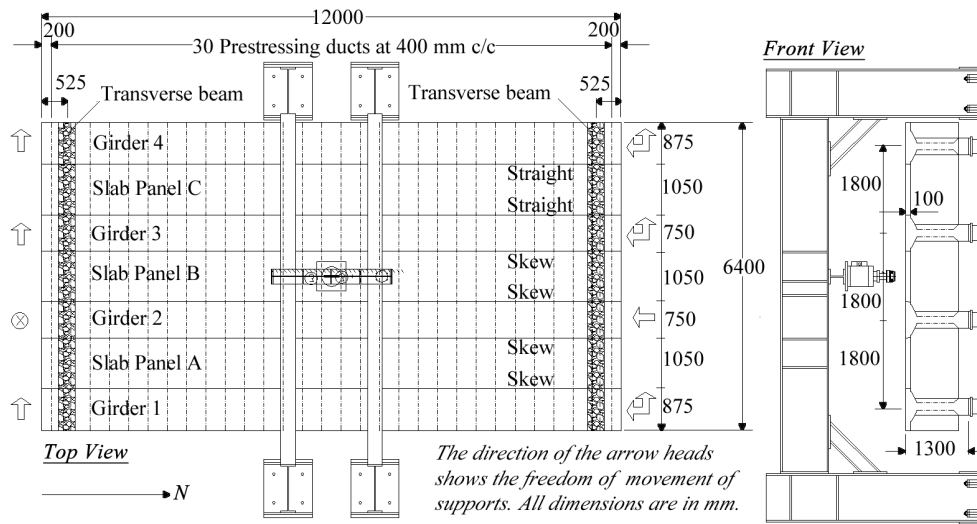


Fig. 1. Top view and front view of the experimental setup

2. Finite Element Modeling

For the nonlinear analysis of the deck slab, a 3D solid finite element model (Fig. 2) of the prototype bridge deck was developed in TNO DIANA 9.4.4 (Midas FX+ 3.1.0, 2012). A fine mesh of elements was provided around the loaded area and ducts were modeled only in that part of the slab. Away from the loaded area, coarse mesh of elements was provided to reduce the simulation time. For concrete, an elastic-perfectly plastic model (CONSTA) was used in compression, an exponential softening curve (HORDIJK) was used in tension, and a “Total strain crack rotating model” was used for smeared cracking. A fracture energy of 0.15 N/mm was assumed for the deck slab concrete and the poisson ratio for all the concrete components, was taken as 0.2. For the embedded grid reinforcement, the von Mises plasticity criterion was used with a poisson ratio of 0.3. An incremental-iterative procedure was used for the nonlinear analysis and the modified Newton Raphson method was used for the solution. The prestressing load was applied to the bridge deck as an external pressure. The applied load was displacement-controlled; therefore, a default force and energy based convergence criterion was employed. More detail can be found in Amir et al. 2019.

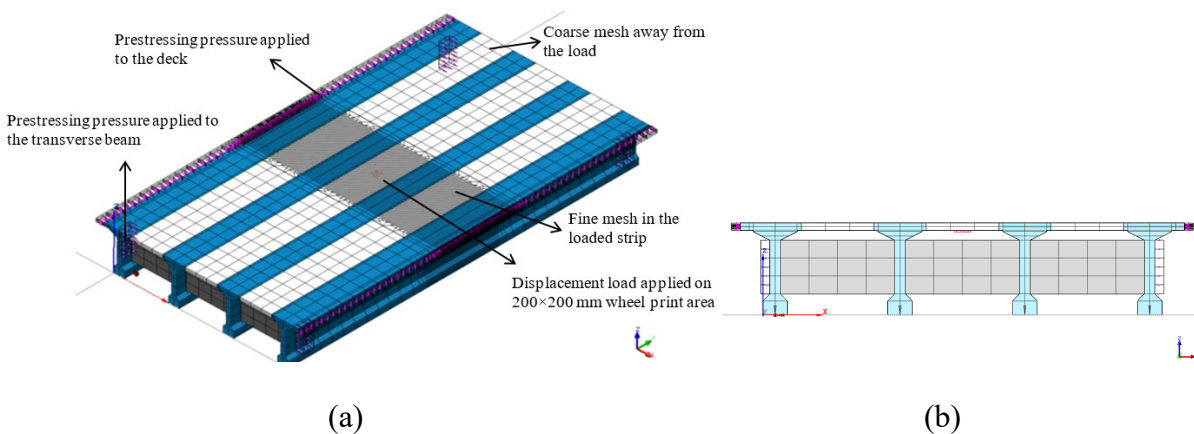


Fig. 2. The finite element solid bridge model: (a) 3D view; (b) Transverse cross-section.

3. Modeling of Compressive Membrane Action (CMA)

A new technique of providing a layer of composed elements was used in the model to calculate the in-plane forces arising from CMA. DIANA 9.4.4 specifies a composed element via a base element and a composition of regular solid elements (Fig. 3). The base element layer forms a reference plane for which the generalized moments and forces are calculated by integration in the local z direction over the elements in the composition of each base element. The selection of the type of base element depended on the type of the solid elements in the composition. The main application of composed elements is in the post processing of analysis results. They have no mechanical properties of their own.

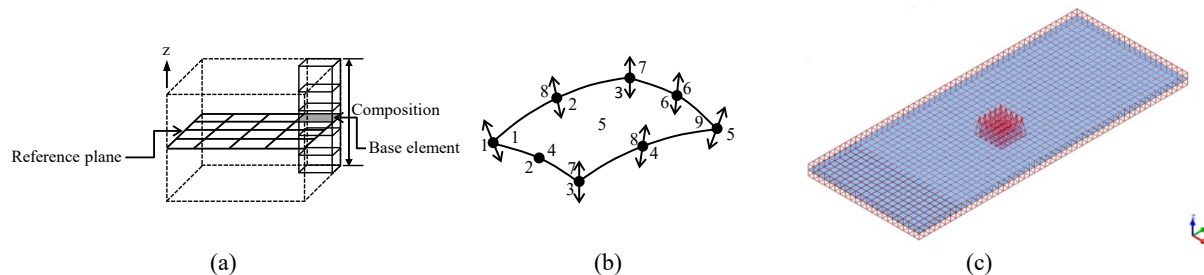


Fig. 3. Composed elements (Midas FX+ 3.1.0, 2012): (a) Base elements in a structural composition; (b) CQ8CM base element for CHX60 brick; (c) Base element layer provided within the solid element composition surrounding the loaded area in a typical slab.

The solid elements in the loaded area were CHX60 bricks, so for composed elements CQ8CM was used (Midas FX+ 3.1.0, 2012) as shown in Fig. 3(b). The CQ8CM element is an 8 node, quadrilateral curved base element and can only be provided where CHX60 elements are used in a composition. The default integration scheme is 3×3 which matches that of CHX60 element. The thickness of the base element CQ8CM was given equal to the thickness of the structural composition, i.e. the thickness of the deck slab (100 mm). Fig. 4 shows how the composed elements were provided in the finite element bridge model. Since these elements were used for the calculation of compressive membrane forces, they were only applied in the area of interest i.e. the loading area and its surroundings minus the area having ducts because composed elements can only be provided in structured meshes. It is worth noting that the in-plane forces obtained were expected to include both the transverse prestressing and membrane forces.

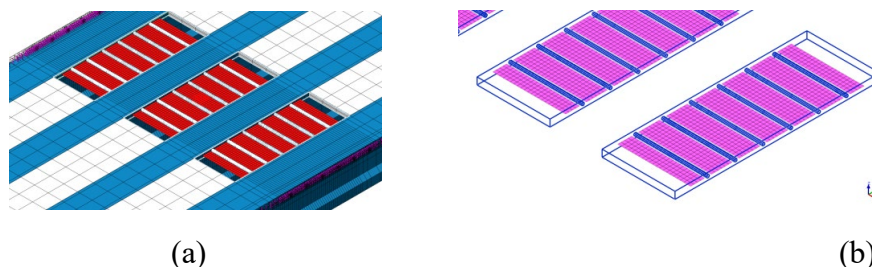


Fig. 4. Composed elements provided in the bridge model fine mesh strip: (a) 3D view of the composed element layer provided within the fine mesh area of the deck slab; (b) 3D wire framing view of the composed elements in the fine mesh slab strips extracted from the bridge deck model.

4. Results and Conclusions

Several nonlinear analyses were carried out varying the Transverse Prestressing Level (TPL). Fig. 5(a) shows the relationship between the distributed in-plane force (compressive in nature) and the failure load for various TPLs at the ultimate stage. It can be observed that the in-plane force increases with the increasing prestress and the relationship is almost linear. Subtracting the initial prestressing force from the total in-plane force corresponding to that particular TPL gives a constant value of the compressive membrane force (CMF ≈ 370 N/mm) for the deck slab showing that CMF alone is independent of the transverse prestressing level. This is also seen in in Fig. 5(b) that shows the relationship between TPL and the in-plane force (sum of the transverse prestressing force and the compressive membrane force) developed in the bridge deck. It can be concluded that regardless of the magnitude of the prestressing applied, a certain level of *default* compressive membrane force is developed in the plane of the deck slab due to the built-in restraint available in the form of edge supports (girders), diaphragms, surrounding slab area etc., if all other parameters remain the same (type of loading, concrete strength etc.).

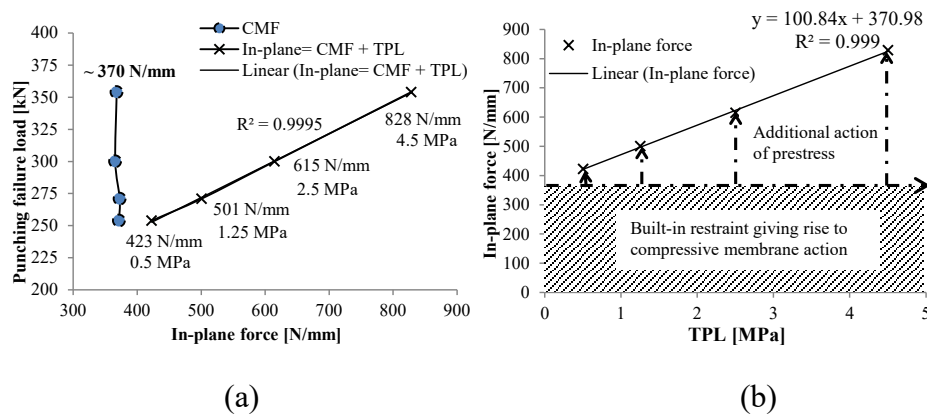


Fig. 5. CMA: (a) Relationship between the punching load and the in-plane force for various transverse prestressing levels; (b) In-plane forces due to the initial prestressing and due to the built-in restraint (compressive membrane force, CMF) in the model bridge deck slab.

5. References

- Amir. 2014. Compressive Membrane Action in Prestressed Concrete Deck Slabs. PhD thesis. Delft University of Technology, Delft, the Netherlands, 282 pp.
- Amir, S., van der Veen, C., de Boer, A., and Walraven, J.C. 2016. Experiments on Punching Shear Behavior of Prestressed Concrete Bridge Decks, *ACI Structural Journal*, 113 (03), 627-636.
- Amir, S., van der Veen, C., de Boer, A., and Walraven, J.C. 2019. Numerical investigation of the punching shear capacity of transversely prestressed concrete deck slabs, *fib Structural Concrete*, DOI: 10.1002/suco.201800285.
- DIANA. FX+. 2012. User's Manual 9.4.4. Delft: TNO Building and Construction Research.



Modelling of Bend Corners of FRP Reinforcement for Concrete Structures Considering Material Anisotropy

Yuanzhang Yang¹ and Weijian Zhao^{2*}

¹: Department of Architectural and Civil Engineering, Zhejiang University, Hangzhou, China; email: yy701@zju.edu.cn

²: Department of Architectural and Civil Engineering, Zhejiang University, Hangzhou, China; email: zhaoweijian@zju.edu.cn

*: corresponding author

Keywords: FRP reinforcement; FE modeling; bent corners; material anisotropy

Abstract: The bend corner of Fibre-reinforced polymer (FRP) reinforcement has been shown significantly lower tensile strength than the straight portion. However, the premature failing mechanism at bent corners has not been fully understood. This paper presents a numerical investigation into the bent-corner strength of FRP stirrups with rectangular cross-sections based on a refined Finite Element modelling approach using Hashin's failure criterion. The models are established and validated against existing experimental research. Analyses of the mechanism of strength reduction at the bent corners of FRP stirrups with rectangular cross sections are conducted. It shows that the tensile stress developed at the bent corners are extremely higher than the average tensile stress in the elastic range, which could be caused by the material anisotropy, concrete compression and bonding. Their contributions to the stress concentration at the bent corners vary along with the increasing average tensile stress.

1. Introduction

Fiber-Reinforced-Polymer (FRP) has been used in the construction industry for concrete structures (RC) for over four decades. Specifically, to resist shear force, FRP stirrups are used for concrete structures. However, the high strength of FRP materials cannot be fully utilized at the bent corners of the FRP stirrups. Numerous experimental investigations have been conducted to study the bent corner strength of FRP stirrups. It is found that the bent corner strength is only 24%-85% of the uniaxial tensile strength [1, 2]. Based on the experimental research, several empirical models of the bent-corner strength were proposed for the prediction of the reduced bent-corner strength [1-7]. However, to date, due to the empirical nature of the prediction models, the models' validities vary depending on the size of the database used for calibration. The failure mechanism of the bent corners of FRP reinforcement has not been fully understood. This paper established refined FE models simulating the bent corner of FRP reinforcement with rectangular cross-sections based on Hashin's failure criterion [8]. The models were verified against an experimental research in the literature and the mechanism of the reduced strength at bent corners was analyzed focusing on the stress concentration and damage accumulation.

2. Reference Experimental Research and Finite Element Modelling

The reference tests were adopted from the experimental work of Spadea, Orr [7], where six groups of 18 specimens were tested by pulling the concrete blocks by the testing machine with the steel bolts until failure, as shown in Fig. 1. Six refined FE models were established for the corresponding groups of test specimens based on the ABAQUS platform, as shown in Fig. 2. To reduce the calculation expenditure, quarter models were adopted for calculation, capitalizing on the symmetry of the specimens in the direction of the applied load (Z axis) and the width of FRP stirrups (Y axis).

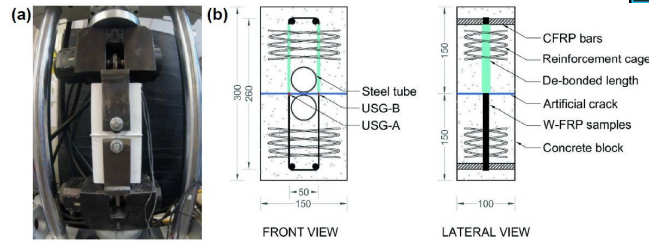


Fig. 1. Test setup of FRP reinforcement specimens (a) and design configurations (b) [7]

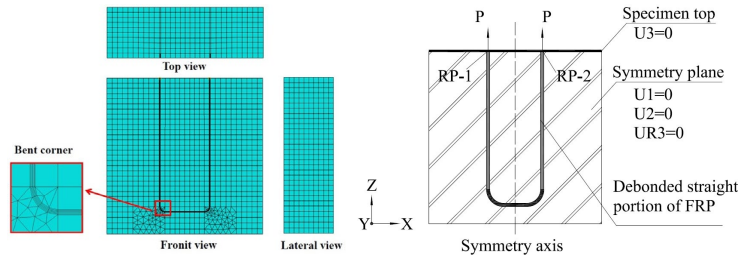


Fig. 2. Discretization and boundary condition of the simulation models

For concrete material modelling, the constitutive relations from the Chinese design code for concrete structures GB50010 [9] was adopted and the material properties of concrete are shown in Table 1. A bi-linear progressive damage model based on the Hashin [8] failure criterion was adopted to model the FRP stirrups. The material properties of the FRP stirrups are shown in Table 2.

Table 1. Concrete material properties

Concrete	f_{cr} (MPa)	f_{ctr} (MPa)	E_c (GPa)
Value	38	2.9	33

Table 2. Calculated material properties of FRP stirrups

Specimens	x^l (MPa)	x^r (MPa)	y^l (MPa)	y^r (MPa)	s^l (MPa)	s^r (MPa)	E_1 (GPa)	E_2 (GPa)	ν_{12}	G_{12} (GPa)	G_{13} (GPa)	G_{23} (GPa)
Reference	1378	950	40	125	97	45	129.0	5.6	0.32	1.33	1.33	1.86
1(t=0.7mm)	1537	1060	45	139	108	50	109.5	6.6	0.32	1.33	1.33	1.86
2(t=1.0mm)	1503	1036	44	136	106	49	108.7	6.6	0.32	1.33	1.33	1.86
3(t=1.3mm)	1484	1023	43	135	104	48	107.7	6.7	0.32	1.33	1.33	1.86
4(t=1.6mm)	1487	1025	43	135	105	49	107.1	6.7	0.32	1.33	1.33	1.86
5(t=1.9mm)	1426	983	41	129	100	47	106.6	6.8	0.32	1.33	1.33	1.86
6(t=2.2mm)	1384	954	40	126	97	45	105.8	6.8	0.32	1.33	1.33	1.86

3. Model Validation

3.1. Ultimate failure load

The validity of the FE modelling was verified by the comparisons of ultimate capacity. The simulated and tested failure loads are compared in Table 3. The comparisons show that FE models established in this work can effectively simulate the failure load of FRP reinforcement with rectangular cross-sections at bent corners. For all six sets of specimens, the discrepancy of P_{fb} between the simulations and tests varied from 1.10% to 7.40%.

Table 3. Failure load comparison

Specimens	1	2	3	4	5	6
Tested P_{fb} (kN)	4.1	6.38	9.19	11.91	14.06	16.01
Simulated P_{fb} (kN)	4.22	6.45	9.87	11.75	13.3	15.16
Error (%)	2.92	1.1	7.4	1.34	5.41	5.31
Mean error (%)	3.9					

4. Failure Mechanism of the FRP Bent Corners

4.1. Tensile stress distribution and damage accumulation

Along with the increasing applied load, Fiber Tension (FT) damage was observed on the first element at the inner perimeter of the bent corner, adjacent to the straight part. It was observed that the initially FT damaged elements carried higher tensile stress than the remaining outer elements along the thickness direction, as shown in Fig. 3 (left).

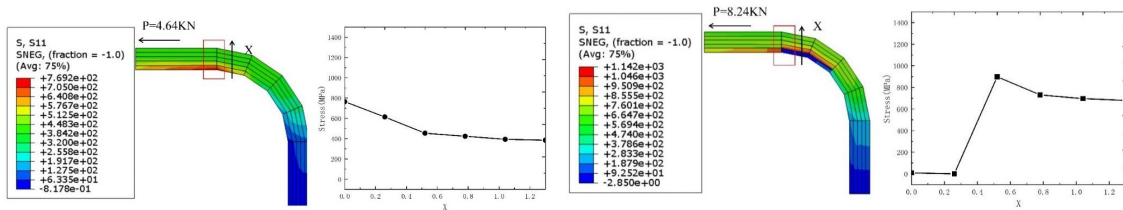


Fig. 3. Tensile stress distribution of the bent corners before (left) and after (right) FT damage appearance

With increasing load, the FT damage maintained at the same locations until FT damage factor reached 1.0, indicating the fibers were fully damaged under tension, as shown in Fig. 3 (right). The location of tensile stress concentration shifted from the initially FT damaged element to outer layers of elements. Consequently, the outer layer elements began to endure FT damage. The FT damage accumulated along with the increasing higher applied load. When the specimens reached their ultimate capacities, all five layers of FRP elements along the thickness direction endured FT damage, with approximately half of which were fully damaged. The location of the tensile stress concentration was close to the outer perimeter of the FRP bent corner.

4.1. Contributing factors to the tensile stress concentration

The tensile stress concentration of the FRP stirrup specimens was the critical reason for the FT damage accumulation and resulting failure of the bent corners. This stress concentration could be caused by two reasons: 1) bending moment at bent corner and 2) the anisotropy of the FRP material. To quantify the proportions of stress concentration contributed by FRP anisotropy and the applied bending moment at the bent corners in the elastic range, additional FE models were established. Model I had the same geometrical dimensions and friction coefficient ($\mu = 0.2$) as the model of Group 3 (Error! Reference source not found.) but the material properties of the reinforcement were set as isotropic- elastic, which had the same tensile strength and elastic modulus of FRP in the axial direction. Model II had the same setting as Model I, except for being set as zero to exclude the influence of bonding. The maximum tensile stresses for Group 3, Model I and Model II were compared at 100MPa, 200MPa and 300 MPa of average tensile stress, as shown in Figure 4. The difference between the maximum stress and average stress for Group 3 could be calculated as the summation of the contributions from material anisotropy and the applied bending moment (including compression from concrete and friction). For Model II, the difference between S_{max} and S_{ave} could be considered as the contribution of concrete compression. Whilst the difference of S_{max} between Model I and Model II and that between Group 3 and Model I could be considered as the contributions of friction and material anisotropy, respectively. In the elastic range, the material anisotropy accounted for 45% to 55% of the tensile stress concentration, followed by compression from concrete accounting for 34% to 48% and friction accounting for 7% to 13%.

Table 4. Contributions to tensile stress concentration in elastic range

S_{ave} (MPa)	S_{max} (MPa)			Difference of S_{max} and S_{ave} (MPa)	Contributions		
	Group 3 (MPa)	Model I (MPa)	Model II (MPa)		Material anisotropy (%)	Compression of concrete (%)	Bonding (%)
100	262	172	155	162	55%	34%	11%
200	465	338	303	265	48%	39%	13%
300	691	517	490	391	45%	48%	7%

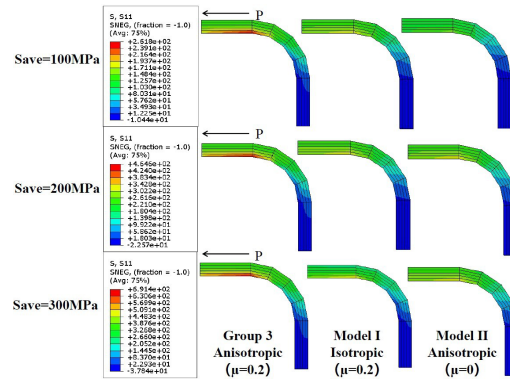


Fig. 4. Tensile stress distribution of model of Group 3, Model I and Model II

5. Conclusions

This paper presents a numerical investigation into the failure mechanism of the FRP bent corners with rectangular cross sections. The following conclusions are supported by this work:

1. The modelling approach developed in this work can effectively simulate the failure of FRP bent corners, verified against tested data.
2. The tensile stress concentration at the bent corners of FRP reinforcement was the major reason for the initial damage occurrence. The resulting damage developed from the inner perimeter of the bent corner to the outer perimeter with increasing applied load.
3. The tensile stress concentration was impacted by the compression from concrete, bonding and the material anisotropy of FRP, the proportions of which vary along with the average tensile stress

6. Acknowledgement

The authors acknowledge and are grateful for the support of the National Natural Science Foundation of China (52208216) and the Zhejiang Provincial Natural Science Foundation (LQ21E080021), who funded and resulted in this study.

7. Reference

1. Ahmed, E.A., et al., Bend Strength of FRP Stirrups: Comparison and Evaluation of Testing Methods. *Journal of Composites for Construction*, 2010. 14(1): p. 3-10.
3. El-Sayed, A.K., E. El-Salakawy, and B. Benmokrane, Mechanical and structural characterization of new carbon FRP stirrups for concrete members. *Journal of Composites for Construction*, 2007. 11(4): p. 352- 362.
4. Imjai, T., et al., Strength Degradation in Curved Fiber-reinforced Polymer (FRP) Bars Used as Concrete Reinforcements. *Polymers*, 2020. 12(8): p. 1653.
5. Lee, C., M. Ko, and Y. Lee, Bend strength of complete closed-type carbon fiber-reinforced polymer stirrups with rectangular section. *Journal of Composites for Construction*, 2014. 18(1): p. 04013022.
6. Nakamura, H. and T. Higai, Evaluation of Shear Strength on Concrete Beams Reinforced with FRP.
7. Concrete Library JSCE, 1995. 1995(26): p. 111-123.
8. Nagasaka, T., H. Fukuyama, and M. Tanigaki, Shear performance of concrete beams reinforced with FRP stirrups. *ACI Special Publication*, 1993.



Bridge Engineering Institute Conference 2023 (BEI-2023)
Rome, Italy, July 17-20, 2023



9. Spadea, S., J. Orr, and K. Ivanova, Bend-strength of novel filament wound shear reinforcement. *Composite Structures*, 2017. 176: p. 244-253.
10. Hashin, Z., Failure Criteria for Unidirectional Fiber Composites. *Journal of Applied Mechanics*, 1980, 47(2): p. 329-334.
12. CABB, Code for design of concrete structures, in GB50010-2010. 2016, Chinese Academy of Building Research: Beijing.



Water Pressure Variation on Porous Calcium-Silicate-Hydrates Using Molecular Dynamics

Shota Takinami^{1*}, Ryo Yoshida², and Ryo Kobayashi³

¹: Nagoya Institute of Technology, Aichi, Japan; email: clz16025@ict.nitech.ac.jp

²: Nagoya Institute of Technology, Aichi, Japan; email: yoshida.ryo@nitech.ac.jp

³: Nagoya Institute of Technology, Aichi, Japan; email: kobayashi.ryo@nitech.ac.jp

*: corresponding author

Keywords: Molecular dynamics; calcium silicate hydrate (C-S-H); simulation

Abstract:

Many experiments have shown that water in the pores of concrete plays an important role in the capabilities and deterioration process of cement paste, but there are many unclear issues about the calcium silicate hydrate (C-S-H) of its microstructure. One of these concerns is the change in volume of C-S-H with water content. Ca/Si ratio of the crystal structure has a significant effect on the volume change of C-S-H, which varies with the type of concrete. Ordinary Portland Cement (OPC) has a large Ca/Si ratio but a small volume change. There are many experiments and analysis that ignore the volume change due to drying and wetting. Recently, however, environmentally friendly Blast Furnace Slag (BFS) has increasingly been in use. It has a smaller Ca/Si ratio than OPC, and its volume change is larger. It is therefore necessary to reconsider the assumptions of many experiments. In this study, the molecular dynamics (MD) method was used to understand the physical properties of C-S-H. Water molecules were placed between two C-S-H layers to check water migration. The pressure in the C-S-H layer was investigated by varying the number density of water molecules, interlayer distance, and temperature, and it was confirmed that when the number of water molecules was constant, a water column was formed by the intermolecular forces of water molecules. This water column exerts pressure in the cohesive direction on the C-S-H layer. As the number of water molecules is further increased, the pressure in the direction of cohesion is transferred to the direction of expansion to the extent that the space between layers is filled. It is suggested that this pressure-induced volume change process is a factor that should be considered in many studies and experiments.

1. Introduction

Portland cement is the second most widely used industrial product on earth after water, and one of the most important industrial products supporting the society. Although microcrystalline C-S-H, the major hydrate of Portland cement, is the main hydrate that determines the strength and Young's modulus of concrete, pore structure, and mass transfer resistance that govern the durability of reinforced concrete, the composition, structure, and other details of C-S-H have not been clarified. The calcium/silica ratio (Ca/Si) in the crystalline structure of C-S-H has a significant influence on the volume change, which depends on the type of cement. Ordinary Portland cement (OPC) has a large Ca/Si ratio but a small volume change. As a result, there are many experiments and analysis

that ignore the volume change caused by drying and wetting. However, in recent years, the use of environmentally friendly blast furnace slag (BFS) has widely increased, which has a smaller Ca/Si than OPC, and thus the volume change due to water content is greatly affected.

2. Method

2.1 C-S-H model

In this study, the Tinf_14sc model is used for a multimeric structure model of Tobermorite minerals proposed by Richardson, and reproduce C-S-H by sandwiching water molecules between them from above and below. The Tinf_14sc model is a monoclinic system classified in the space group 'P21/c' and consists of angles $\alpha = 90.000^\circ$, $\beta = 95.500^\circ$, and $\gamma = 90.000^\circ$. The box is $11.300 \text{ \AA} \times 7.300 \text{ \AA} \times 28.800 \text{ \AA}$. However, in order to make the simulation easier to handle, the box $11.300 \text{ \AA} \times 7.300 \text{ \AA} \times 28.667 \text{ \AA}$, was made consisting of angles $\alpha = 90.000^\circ$, $\beta = 90.000^\circ$, and $\gamma = 90.000^\circ$. The SPC model, a simple point charge model, was used for the water molecules.

Table 1. Various parameters of the SPC model

O (g/mol)	H (g/mol)	q_o [C]	q_H [C]	r (\AA)	θ (°)
15.994	1.008	-0.82	0.41	1	109.5

Table 2. SPC Model Lennard Jones Potential Parameters

i	j	σ_{ij} (\AA)	ϵ_{ij} (Kcal/mole)
O _w	O _w	3.16412	0.161776
H _w	O _w	-	-
H _w	H _w	-	-

2.2 Molecular dynamics (MD) Method

Molecular dynamics (MD) is a method that reproduces molecular behavior derived from Newton's second law, in which the particles constituting the system are modeled as the simplest mass points, and the time evolution of the position and velocity of each atom is shown in Equation (1).

$$m_i \frac{\partial^2 r_i}{\partial t^2} = - \frac{\partial U}{\partial r_i} \quad (1)$$

where m_i and r_i are the mass and position vector of atom i , respectively, and U is a function of the potential energy of the system. In this study, equation (2) was used for U .

$$U = \sum_i \sum_{j>i} 4\epsilon_{ij} \left[\left(\frac{\sigma_{ij}}{r_{ij}} \right)^{12} - \left(\frac{\sigma_{ij}}{r_{ij}} \right)^6 \right] + \sum_i \sum_{j>i} k \frac{q_i q_j}{r_{ij}} \quad (2)$$

where r_{ij} is the distance between two atoms, k is the proportionality constant that defines Coulomb's potential, and q_i is the atomic charge. The first term is the Lennard-Jones potential describing the repulsion due to the overlap of atoms and the attraction due to the van der Waals interaction. The second term is the Coulomb potential, which describes the electrostatic interaction. The following Adams et al. equation is used to determine the charge

$$q_{Ai} = \frac{V_{id}(A_i)}{\sqrt{n_{Ai}}} \frac{\sum_j \frac{V_{id}(X_j)N_{Xj}}{\sqrt{n_{Xj}}}}{\sqrt{\sum_i \frac{V_{id}(A_i)N_{Ai}}{\sqrt{n_{Ai}}}}}, \quad q_{Xi} = \frac{V_{id}(X_j)}{\sqrt{n_{Xj}}} \frac{\sum_i \frac{V_{id}(A_i)N_{Ai}}{\sqrt{n_{Ai}}}}{\sqrt{\sum_j \frac{V_{id}(X_j)N_{Xj}}{\sqrt{n_{Xj}}}}} \quad (3)$$

where A_i is the i -th cation, X_j the j -th anion, V_{id} the ideal charge of the element, N the number of atoms in the system, and n the principal quantum number. Instead of the Lennard-Jones potential, P.A. Bonnaud et al. adopted the mathematical form used in the PN-TArZ model shown in equations (4) and (5).

$$U_{ij}(r_{ij}) = A_{ij} \exp(-b_{ij}r_{ij}) - \sum_{n=3}^5 f_{2n}(r_{ij}) \frac{C_{2n}^{ij}}{r_{ij}^{2n}} \quad (4)$$

$$f_{2n}(r_{ij}) = 1 - \sum_{m=0}^{2n} \frac{(b_{ij}r_{ij})^m}{m!} \exp(-b_{ij}r_{ij}) \quad (5)$$

This was used to represent the intermolecular forces in the repulsive and attractive portions of the interaction between the Tobermorite system C-S-H. Since the software used in this study, LAMMPS (<https://www.lammps.org/>), cannot use the PN-TArZ model as it is, the PN-TArZ model was approximated to the Lennard-Jones potential.

Table 3. Charge of each atom in the Tinf_14sc model

T _{∞_14sc}	Ca	Si	O
N	8	12	36
V_{id}	2	4	2
n	4	3	2
q	1.1939	2.7573	-1.18425

Table 4. Lennard Jones for Tobermorite system Potential Parameters

i	j	σ_{ij} (Å)	ϵ_{ij} (Kcal/mole)
Ca	O _w	3.211577733	0.0993886
Si	O _w	3.844182653	0.01794068
H	O _w	2.66	0.1272912
Ca	H _w	2.65	0.0675658
Si	H _w	3.3979572	0.00959296
O	H _w	3.27333	0.163726

3. Results

3.1 Column of water

The number of water molecules was increased, and when the density exceeded a certain number, a column of water was formed so that water molecules adsorbed on the upper and lower walls were bound together.

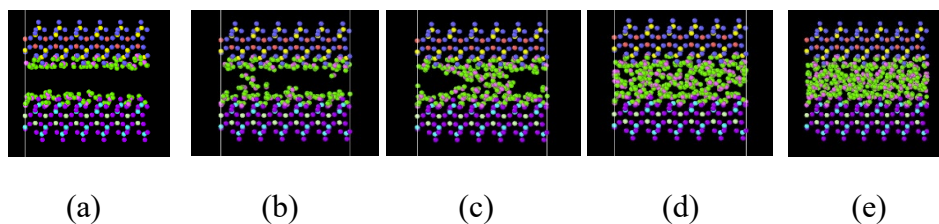


Fig. 1. Formation of water column: number density ($/m^3$) (a) 0.0121, (b) 0.0181, (c) 0.0217, (d) 0.0301, (e) 0.0362

Time averages of at least 100 times were performed. Standard errors were calculated to account for variations in the estimated quantities. Number density of water molecules and the pressure in the direction of expansion are shown when $H=10$ Å and $T=300$ K. Error bars indicate standard errors.

When a column of water is formed, pressure in the direction of cohesion tends to occur. When the number density of water molecules fills the interlayer, the pressure shifts from the direction of cohesion to the direction of expansion.

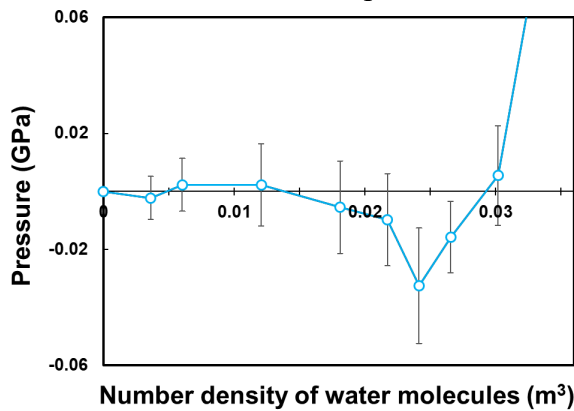


Fig. 2. Number density of water molecules and pressure on the C-S-H wall in the direction of expansion

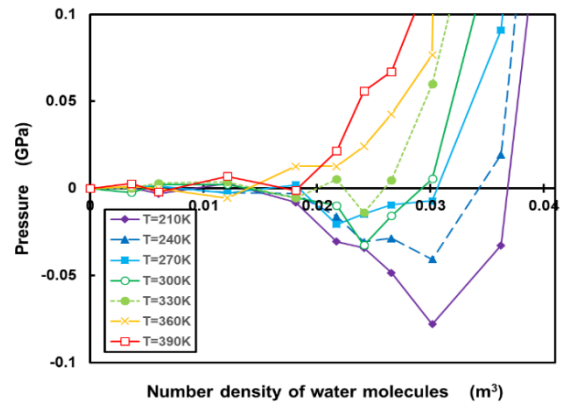


Fig. 3. Temperature change, number density and pressure

3.2 Relationship between temperature and pressure

Under the temperature $T=330\text{K}$, cohesive pressure due to the column of water was observed. The lower the temperature, the greater the force in the direction of cohesion. This is because the lower the temperature, the lower the thermal energy of water molecules, the less the water column is disrupted, and the greater the attraction between water molecules.

In the real external environment, water at temperatures of 270K is solid, but in this simulated environment, water molecules are fluid and not individuals even at temperatures of 270K . In the microscopic world, temperatures such as melting points are often different from the actual external environment

4. Conclusion

The following was clarified

- (1) As the number density of water molecules between C-S-H layers is increased, water columns are formed above a certain interlayer distance, which exert inward cohesive pressure on C-S-H walls.
- (2) The lower the temperature, the greater the pressure in the cohesive direction due to the water column.
- (3) If the number density of water molecules is made larger than the number density at which water columns are formed, the interlayer is eventually filled with water molecules. The pressure in the direction of cohesion is then transferred as the force in the direction of pressure.

5. References

P.A Bonnaud, Q.Ji, B Coasne ,R.J-M.Pellenq, and K.J.Van Vliet : Thermodynamics of Water Confined in Porous Calcium-Silicate-Hydrates, *Langmuir* 2012, volume 28, issue 31, pages 11422–11432, June.2012



Bridge Engineering Institute Conference 2023 (BEI-2023)
Rome, Italy, July 17-20, 2023



Stefan Adams, R.Prasada Rao:High power lithium ion battery materials by computational design, physica status solidi applications and materials science, volume 208 , issue 8,pages 1746-1753, August.2011

Ian G. Richardson: Model structures for C(A)-S-H(I), Acta Crystallographica Section B, B70 , pp903-923, Dec.2014



Real Imperfections of Longitudinally Stiffened Plates Compared to the Proposed Imperfections in EN 1993-1-5

N. Thomas^{1*}, A. Weinhuber^{1*}, M. Mensinger¹, C. Holst¹, and J. Ndogmo¹

¹: Technical University of Munich, Munich, Germany; email: nadine.thomas@tum.de, a.weinhuber@tum.de, mensinger@tum.de, christoph.holst@tum.de, ndogmo@mytum.de

*: corresponding author

Keywords: steel bridges; imperfections; laser Scanning; buckling behavior; stiffened plates

Abstract: For the buckling verification of longitudinally stiffened plates according to EN 1993-1-5 [1] using the Finite-Element Method, imperfections can be considered either as geometrically equivalent imperfections or with 80% of the geometric imperfections according to DIN EN 1090-2 [2] and additionally structural imperfections according to Annex C [1]. The resulting values are often contradictory. Therefore, to verify this regulation, imperfections of real bridge components were measured. The measurements were carried out at the Technical University of Munich during the replacement construction of the Thulba viaduct. The measured imperfections are compared with the different imperfection regulations for buckling verification according to EN 1993-1-5 and the regulations for manufacturing tolerances according to DIN EN 1090-2. The investigations aim to clarify whether the assumptions of the standards are sufficiently defined and whether the regulations are consistent with the execution of real bridge components.

1. Introduction

The replacement of the Thulba viaduct is a steel-composite bridge with a box section in northern Bavaria, which was built in 2021 using the incremental launching method. The bridge has a total of 7 spans of 45 m – 55 m – 70 m – 90 m – 75 m – 70 m – 55 m and a final length of 460 m. Large-scale buckling tests were carried out at the Technical University of Munich in 2017 in frame of this new bridge construction. Questions concerning the design of the longitudinal stiffened panels under biaxial loading during launching, such as the failure of the single panel under lateral load, the deflection of the longitudinal stiffeners, the load introduction and recommendations for maximum possible manufacturing deviations were clarified here. The results were published in [3] and [4]. In addition, the geometry of several panels of the new bridge were additionally measured using 3D laser scanning during construction. The measurement takes place at a fixed defined bridge section on both sides between four transverse bulkheads. Laser scans are performed in this bridge section at three different displacement times. In addition, the temperature influence on the component was investigated by further scans (day and night measurement). This paper presents the first measurement results and compares them with the imperfections from current regulations for the buckling verification and the manufacturing tolerances. Furthermore, only the panels between the longitudinal stiffeners are analyzed in this paper. This allows a basic global comparison and a comparison with the imperfection regulations for sub- or single panels.

2 Existing Regulations for Imperfections

Especially for buckling verification, the correct assumption of imperfections is essential for the design of the components. On one hand, the imperfection must be chosen sufficiently large to consider imperfections from the production process conservatively enough, on the other hand, it must not deviate too much from the real construction in order to guarantee an economic construction. In addition it has to cover structural imperfections from residual stresses. For buckling verification, the imperfection which has to be considered in a FE calculation is regulated in EN 1993-1-5 Annex C. Imperfections used in FE calculations should normally include both geometric and structural imperfections (residual stresses). In cases where more accurate separate approaches of geometric and structural imperfections are not possible, geometric equivalent imperfections can be used. Geometrical imperfections may be applied in the form of the modal buckling figure. A value corresponding to 80% of the geometric manufacturing tolerances is recommended. The manufacturing tolerances are specified in DIN EN 1090-2. Structural imperfections may be applied with a residual stress distribution whose course and amplitude can be expected on average from the manufacturing process. As a rule, the direction of the imperfections is to be set in such a way that the lowest bearing capacity is achieved. For geometrical equivalent imperfections, the approaches in Table C.2 and Fig. C.1 of EN1993-1-5 may be used. When considering the interaction of different imperfections, a leading imperfection is usually to be selected, this is applied at 100% to the modal buckling figure, the accompanying imperfections may be reduced to 70%. If the buckling verification is performed using the reduced stress method and the column-like behavior occurs, the imperfection is considered in form of an imperfection coefficient α when determining the reduction factor χ_c . The imperfection coefficient α shall normally correspond to the buckling curve a with $\alpha = 0.21$ for unstiffened plate sections. For stiffened plate sections, α is usually replaced by the increased value α_e to account for larger imperfections of welded plates. To compare the measurements with the manufacturing tolerances given in [2], No. 7 of Table B.1 from [2] is used as a substitute, since no separate regulations are given for deviations for the stiffened plate and the single panels. This regulates the deviation via the web height b and applies to the web curvature of welded sections.

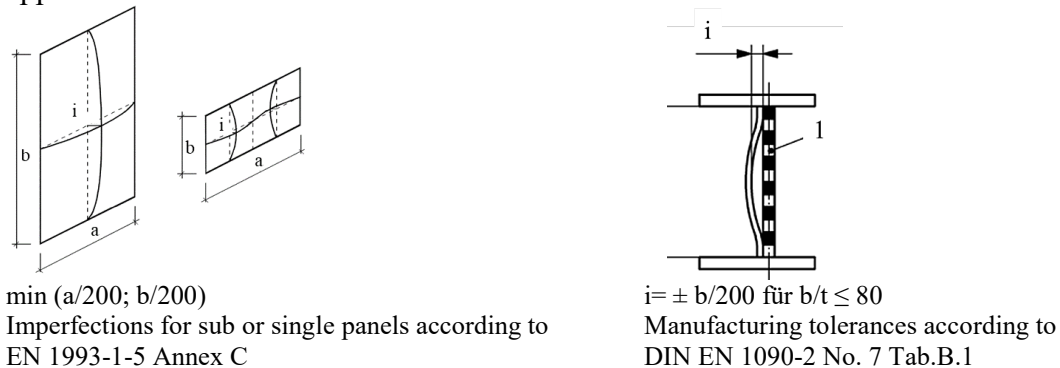


Fig. 1. regulations on imperfections

3. Metrological Support by 3D Laser Scanning

3D laser scanners capture the geometry of the environment in a high spatial resolution using a laser beam that is deflected in any direction by a rotating mirror. The result is a 3D point cloud which allows the panels to be analyzed for deformations. In order to be able to initially detect the manufacturing imperfections of the construction component, various factors must be taken into

account in the metrological support. On one hand, it is important to ensure absolute point accuracy, and on the other hand, the webs are measured with a high resolution of max. 5 mm point spacing. The conditions are realized by measuring with the HDS7000 laser scanner from Leica with a setting of the resolution of the scanner of 3.1 mm to 10 m. The single point accuracy of the scanner can be assumed to be <1 mm. For complete coverage of the webs, it is necessary to select multiple viewpoints for the scanner to a) minimize shadowing by the stiffeners, b) ensure point accuracy (avoid glancing intersections), and c) ensure sufficient resolution. The data acquired from different viewpoints are pre-registered via sprayed targets and transferred to uniform coordinate system as best as possible using the Iterative Closest Point Algorithm (ICP Algorithm). A registration uncertainty of the individual scans <1 mm can be determined. The first scans are made when the bridge is still in the assembly yard. The first imperfections of the component can already be derived here in the load-free state and allows a deformation analysis to manufacturing processes. These can be calculated from the registered point clouds. The imperfections are to be considered as the perpendicular distance of the individual points to an ideal plane. Since the material thickness can also vary within a web due to the constructional design, the ideal planes must be estimated locally from the point cloud. Otherwise, a change in material thickness at the joints would show up as apparent deformation. In addition, the calculated imperfections of all individual points are interpolated to a uniform 5 mm grid to minimize any measurement noise that may be occurring. In order to make the imperfections accessible to all project participants, a special Matlab tool is provided in which the determined imperfections can be visualized and retrieved for individual points (see fig. 2). Figure 2 shows an example of the determined imperfections of the field 40-39 (west side) in the load-free condition, which already show amounts of up to -6 mm.

4. Comparison of Measurement Results with Different Standards

When comparing the measured deviations perpendicular to the plate with data from [1] and [2], maxima at the edges of the plate are not taken into account, since welds and transitions to the next component are also located here, which may be included in the results. In addition, for global buckling, the maximum deviation of the inner area of the entire panel is decisive; for local buckling, the deviation of the inner areas of each sub panels are decisive. Figure 2 shows one 3D scan of a plate as an example with the respective names of the dimensions.

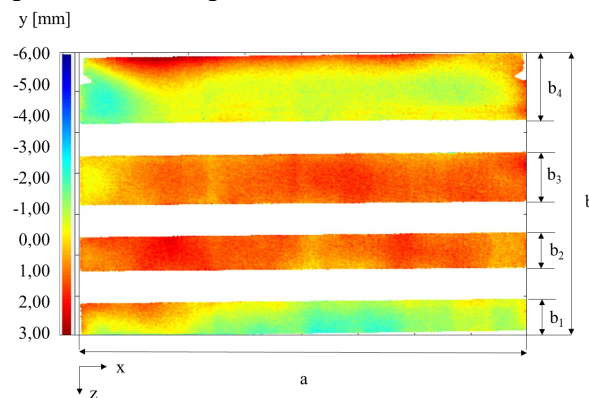


Fig. 2. Example of evaluation of one panel with designations

The maximum measured deviation of each panel is compared with the data of the global geometric equivalent imperfection according to EN 1993-1-5:2019 Annex C [1] and with reference to Table B.1 No. 7 of DIN EN 1090-2 [2] to the entire web height b . The measured

valued are significantly smaller for every panel (see table 1). The external dimensions of the web and the deviations from the 3D scan, as well as the values according to [1] and [2] are summarized in Table 1. Table 2 summarizes the height of each sub panel of each web. For each web, the sub panel with the maximum deviation from the 3D scan is given and then compared with the data of the local geometric equivalent imperfection according to EN 1993-1-5:2019 Annex C [1] and with Table B1 No. of DIN EN 1090-2 [2] with reference to b to the respective sub panel. In this comparison, the values for each sub panel are slightly exceeded.

Table 1. External web dimensions an global maximum deviation

Web	Length a [mm]	Height b [mm]	Max. deviation in the sub-panel [mm]	Min (a/400; b/400) [1]	± b/200 [2]
40-39 West	3977	3445	2,90	8,61	17,23
40-39 Ost	3968	3169	2,50	7,92	15,85
41-40 West	3977	3439	-4,00	8,60	17,20
41-40 Ost	3968	3163	2,70	7,91	15,82
42-41 West	3977	3394	-3,10	8,49	16,97
42-41 Ost	3968	3118	3,10	7,80	15,59

Table 2. Web dimensions and local maximum deviation

Web	b ₁ [mm]	b ₂ [mm]	b ₃ [mm]	b ₄ [mm]	Position of the maximum deviation in the sub-panel	Max. deviation in the sub-panel [mm]	Min (a/200; b/200) [1,2]
40-39 West	440	425	600	840	b ₁	2,90	2,20
40-39 Ost	440	425	600	564	b ₂	2,50	2,13
41-40 West	440	425	600	834	b ₃	-4,00	3,00
41-40 Ost	440	425	600	558	b ₂	2,70	2,13
42-41 West	440	425	600	789	b ₂	-3,10	2,13
42-41 Ost	440	425	600	513	b ₂	3,10	2,13

5. Summary

The 3D Laser scans of the Thulba viaduct, provide important results for the design and execution of steel and steel composite bridges. In this paper it could be shown with a global and local comparison that the measured values are in a good range. The local comparison with Table B.1 No.7 is not quite correct. In the real component, the stiffeners also deform. The assumption of table B.1 No. 7 [2] as well as the assumption of local imperfection according to [1] assume a "0 position" of these stiffeners. In the measurement, the deformations of the longitudinal stiffeners are also taken into account in the sub panels.

6. References

- [1] DIN EN 1993-1-5:2019-10: Eurocode 3: Design of steel structures –Part 1-5: Plated structural elements; German version EN 1993-1-5:2006 + AC:2009 + A1:2017 + A2:2019 (October 2019).
- [2] DIN EN 1090-2:2018-09: Ausführung von Stahltragwerken und Aluminiumtragwerken –Teil 2: Technische Regeln für die Ausführung von Stahltragwerken; Deutsche Fassung EN 1090-2:2018
- [3] M. Mensinger, J. Ndogmo N. Thomas (née Maier), U. Kuhlmann und V. Pourostad: Untersuchungsbericht Nr. 118001: BAB A7, Würzburg - Fulda, BW613a, Talbrücke Thulba, Beuluntersuchungen; Technische Universität München, MPA Bau Abteilung Metallbau. 2019.
- [4] Kuhlmann U., Mensinger M., Thomas N. (née Maier), Pourostad V., Ndogmo J., Schlussbericht AIF IGF Nr: 20455, Längsausgesteifte Beulfelder unter mehrachsiger Beanspruchung“, Universität Stuttgart und Technische Universität München, 2021



Structural Damage Prediction with Multi-Level Neural Networks Using Modal Group Response

Yunfeng Zou¹, Xuandong Lu^{2*}, Xuhui He³, and Chenzhi Cai⁴

¹: School of Civil Engineering, Central South University, Changsha, China; email: yunfengzou@csu.edu.cn

²: School of Civil Engineering, Central South University, Changsha, China; email: xuandonglu@csu.edu.cn

³: School of Civil Engineering, Central South University, Changsha, China; email: xuhuihe@csu.edu.cn

⁴: School of Civil Engineering, Central South University, Changsha, China; email: chenzhi.cai@csu.edu.cn

*: correspondence author

Keywords: large dimension; closely spaced modes; modal group; multi-level neural networks

Abstract: The system with large dimension and closely spaced modes in civil structures affects the development of damage prediction. In this paper, the empirical mode decomposition with intermittence criterion is used to extract the modal group including several closely spaced modes, and the multi-level neural networks are applied to reduce the damage searching dimension. Before practical application, the modal group strain energy is constructed as features from the modal group response to train the feedforward neural network to locate the damaged region, and the reconstructed modal group is used as features to train several neural networks for internal damage prediction of each substructure. Structural damage will be first located at the substructural level and then be quantified at the elemental level. The numerical study is performed to verify the feasibility of the proposed method.

1. Introduction

Damage prediction based on modal analysis is widely performed. However, the difficulties in its practical applications include two aspects. On one hand, when the response includes modal responses with closely spaced modes, the accuracy of extracting modal parameters will significantly decrease, thereby affecting the accuracy of damage prediction. On the other hand, this method is essentially an inverse problem that requires iterative solutions on structural matrices. However, large-scale structures are often with large dimensions, which leads to a high consumption of computational resources and time in matrix operations. As the number of searching elements increase, the computational efficiency and accuracy of the inverse problem significantly decrease. For the former, model reduction and multi-level model neural networks (NNs) could be introduced to reduce matrix computation and damage searching dimensions, respectively. For the latter, a potential improvement strategy is to construct modal group strain energy (MGSE) and reconstructed modal group (RMG) from modal group response (MGR) as

features of NNs, which is used for substructural level and elemental level damage prediction respectively, so as to avoid directly extracting singular modal information. In this paper, the feasibility of the proposed method is verified by the numerical case of a transmission tower. The results indicate its superiority over traditional methods.

2. Modal Group Reconstruction

Several modes that are hard to separate into the single-frequency response due to frequency proximity is set as a modal group. Assuming that N_g modal groups are sorted, and the g -th modal group contains the g_1 -th to g_g -th modes, the modal relation between m_1 -DOFs and m_2 -DOFs (m_1 and m_2 can be larger than 1) at the g -th mode group can be expressed as:

$$\boldsymbol{\varphi}_{m_1 g} \boldsymbol{\varphi}_{m_2 g}^{+l} = \mathbf{d}_{m_1 g} \mathbf{d}_{m_2 g}^{+r} \quad (1)$$

Where $\mathbf{d}_{m_1 g}$ and $\mathbf{d}_{m_2 g}$ denote MGR extracted from measurement by empirical mode decomposition (EMD) (He et al., 2023); $\boldsymbol{\varphi}_{m_1 g}$ and $\boldsymbol{\varphi}_{m_2 g}$ are matrix blocks corresponding to m_1 -DOFs and m_2 -DOFs under the g -th modal group; the superscript $+l$ and $+r$ represent left inverse and right inverse, respectively. Only if the number of measured a-DOFs is larger than the number of its modes contained in the modal group can $\boldsymbol{\varphi}_{ag}^{+l}$ be effective.

3. Substructure-Level Damage Locating

Based on finite element, assuming that the original structure is divided into N_s substructures, according to Craig-Bampton fixed interface modal synthesis method (He et al., 2023), the original structure model can be transformed into a super-element model (SEM) with much smaller dimension after modal transformation. To reduce the search dimension, the damage is first located at the substructural level. The signal “~” is added to the top of the character to indicate SEM terms. The equivalent damage factor $\tilde{\theta}$ as labels of the feedforward neural network (FNN) is preset to obtain a set of training data, and the global stiffness matrix is expressed as:

$$\tilde{\mathbf{K}}(\boldsymbol{\alpha}) = \tilde{\mathbf{K}}_u + \sum_{s=1}^{N_s} \tilde{\theta}_s \tilde{\mathbf{K}}_s, \quad (-1 \leq \tilde{\theta}_s \leq 0) \quad (2)$$

Where $\tilde{\mathbf{K}}_u$ is the undamaged global super-elemental stiffness matrix, and $\tilde{\mathbf{K}}_s$ represents the contribution of the s -th super-element to the global stiffness matrix.

As the training features of LNN at substructural level, MGSE is defined as:

$$\tilde{\mathbf{F}}_{sg}^f = [\tilde{\boldsymbol{\varphi}}_g \tilde{\boldsymbol{\varphi}}_{mg}^{+l}]^T \tilde{\mathbf{K}}_s [\tilde{\boldsymbol{\varphi}}_g \tilde{\boldsymbol{\varphi}}_{mg}^{+l}] \quad (3)$$

Where $\boldsymbol{\varphi}_g$ and $\boldsymbol{\varphi}_{mg}^{+l}$ are the global and measured modal group. Due to the difficulty of providing global measurement for input, non-measured components in $\tilde{\boldsymbol{\varphi}}_g$ is replaced by corresponding ones in the undamaged SEM. As for the pre-built LNN, the input is expressed as:

$$\tilde{\mathbf{F}}_{sg}^m = [\boldsymbol{\varphi}_g \boldsymbol{\varphi}_{mg}^{+l}]^T \tilde{\mathbf{K}}_s [\boldsymbol{\varphi}_g \boldsymbol{\varphi}_{mg}^{+l}] \quad (4)$$

Where the part in $\boldsymbol{\varphi}_g \boldsymbol{\varphi}_{mg}^{+l}$ corresponding to measured DOFs is calculated by Eq. 1, while others are extracted from the SEM. The LNN receiving the input will provide the probability of damage of each substructure. The closer the result is to 1, the more likely the substructure is damaged.

4. Element-Level Damage Prediction

Only damage within single substructure is considered (the most likely condition in the real-time monitoring). The FNN for the possibility of damage in each substructure will be constructed in advance. The s -th substructure is used as an example for illustration. Assume that the stiffness matrix of the s -th substructure is composed of Ne_s elements and is formed similar to Eq. 2:

$$\tilde{\mathbf{K}}(\boldsymbol{\alpha}) = \tilde{\mathbf{K}}_u + \sum_{i=1}^{Ne_s} \theta_i \tilde{\mathbf{K}}_i, \quad (-1 \leq \theta_i \leq 0) \quad (5)$$

Where $\tilde{\mathbf{K}}_s$ denotes the elemental contribution of the i -th element in the s -th super-element to the global stiffness matrix; θ_i denotes the i -th elemental damage factor as the label. To train the FNN, features expressed as $\tilde{\boldsymbol{\varphi}}_{m_1g} \tilde{\boldsymbol{\varphi}}_{m_2g}^{+l}$ are calculated by the SEM, where $\tilde{\boldsymbol{\varphi}}_{m_2g}^{+l}$ and $\tilde{\boldsymbol{\varphi}}_{m_1g}$ are corresponding to measured DOFs inside or near the s -th substructure. According to the substructure-level locating results, the corresponding FNN used for element-level prediction is enabled. The input from measurement in this level is expressed as $\boldsymbol{\varphi}_{m_1g} \boldsymbol{\varphi}_{m_2g}^{+l} = \mathbf{d}_{m_1g} \mathbf{d}_{m_2g}^{+r}$.

5. Numerical Case

A tower numerical case shown in Fig. 1(a) example was studied to demonstrate the feasibility of the proposed method. The finite element model of the tower is established in ANSYS, with a total of 808 nodes and 928 elements, including 4824 DOFs. The bottom support of the tower is prone to be damaged, thus only 36 elements at this location are considered for damage prediction. Base on that, the model is divided into 5 substructures (S1-S5), in which S1 is transformed into a super-element retaining 30 master DOFs in ANSYS. The transient excitation is applied to the structure. The Fourier spectrum of the acceleration and 6 modal groups (MGI~MGVI) are shown in Fig. 1(b). At the level of Substructure, 4 substructures in the monitoring region are considered with 8 equivalent damages (0, -0.02, -0.04, -0.06, -0.08, -0.10, -0.12, -0.14) respectively, and then 4096 sets including features and labels are calculated in the SEM. Although cases of single damage are only considered in the following text, a dataset with a wider distribution of damage may be used to establish an LNN that better fits the inherent mechanism of damage prediction. At the elemental level, 9 elements in each substructure are considered with 3 elemental damages (0, -0.15, -0.3), and 19683 training sets are obtained from each substructure. Bayesian adaptive learning framework is used to optimize the hyperparameter in each iteration of NNs. The iterative process of each NN is shown in Fig. 1(c), in which 4 NNs of element-level prediction are with the same iteration curve due to the symmetry of the tower, and the final elemental loss is much larger than the substructural loss because both the dataset and outputs of the former are larger than those of the latter.

As the validation of constructed NNs, 4 damage conditions were considered. Preset damaged elements are marked in Fig. 1(a). Table 1 lists the damage prediction results. In Table 1, substructure-level locating results is shown by the predicted value $\hat{\theta}$ of the preset damage, and

the absolute value of maximum errors e_{umax} in undamaged elements. Besides, $MSE = \sum_{i=1}^{Ne_s} (\theta_i - \hat{\theta}_i)^2$ is used to estimate the global accuracy of elemental results. It can be seen that the proposed method can accurately predict the local damage.

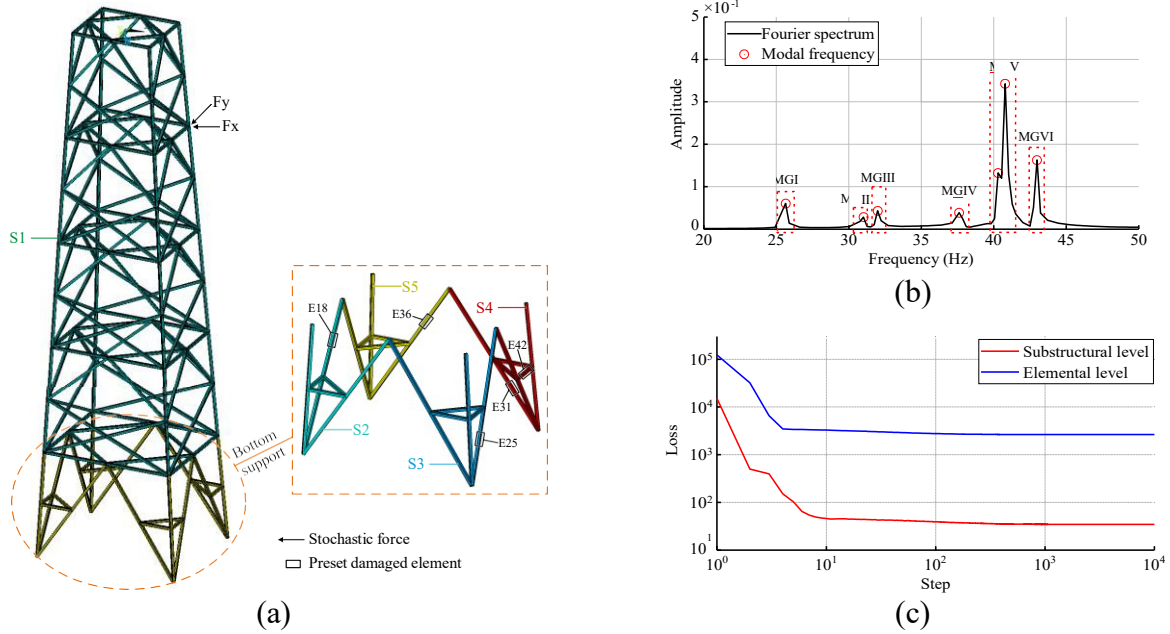


Fig. 1. Information of tower model and NN training: (a) tower model; (b) Fourier spectrum and defining modal groups; (c) iterative process of NNs

Table 1. Damage prediction results

Damage conditions	Damaged element	Preset damage θ_i	Substructural level		Elemental level	
			$\hat{\theta}$	e_{umax}	$\hat{\theta}$	e_u
1	E18	-0.1	-0.263	0.048	-0.113	0.005
2	E25	-0.15	-0.329	0.052	-0.148	0.012
3	E31, E42	-0.1, -0.2	-0.470	0.031	-0.104, -0.188	0.020
4	E36	-0.25	-0.466	0.054	-0.241	0.023

6. Conclusion

This paper introduced the theory of the proposed damage prediction method with multi-level neural networks using modal group response, and presented the results of a numerical case to investigate its feasibility. Compared to traditional model updating method, NNs performed in damage prediction can construct a direct relationship from features to labels in advance, thus more timely monitoring can be provided. RMG and MGSE as features of NNs from modal groups are used to improve the problem of difficulty in predicting damage in the premise of closely spaced modes. As for data training in the large-dimension structure, model reduction and multi-level NNs are applied to decrease the calculation consumption. The proposed method is applied to conditions about single damage, which accounts for the majority in real-time monitoring. Multiple damages will be studied in the future study.

7. References

- He, J., Guan, X. and Liu, Y. 2012. Structural response reconstruction based on empirical mode decomposition in time domain. *Mechanical Systems and Signal Processing*, 28, 348-366.
- Zhang, C. and Xu, Y. 2017. Multi-level damage identification with response reconstruction. *Mechanical Systems and Signal Processing*, 95, 42-57.



Use of Steel Orthotropic Box Girders for Light Weight Long Span Bridges - Analysis and Design of Pedestrian Bridge in Dubai

Tharun John Joseph^{1*}, Anirudh Desai², Koyya Satyanarayana³, Bogdan Barbulescu⁴ and Kannaw Shrivatsa⁵

^{1*}: Bridge Engineer, Jacobs Engineering Group, Dubai, UAE; email: Tharun.Joseph@jacobs.com

²: Lead Engineer, Jacobs Engineering Group, Hyderabad, India; email: Anirudh.Desai@jacobs.com

³: Section Manager, Jacobs Engineering Group, Hyderabad, India; email: Satyanarayana.KoyyaVV@jacobs.com

⁴: Senior Associate Director, Jacobs Engineering Group, Bristol, UK; email: Bogdan.Barbulescu@jacobs.com

⁵: Project Manager, Jacobs Engineering Group, Dubai, UAE; email: Kannaw.Shrivatsa@jacobs.com

*: corresponding author

Keywords: steel structure, structural dynamics, finite element modelling

Abstract: Orthotropic Steel Decks are efficient structural systems capable to increase the durability, redundancy and efficiency of steel structures and therefore reduce the associated self-weight of the structure. Generally, a typical orthotropic steel deck system (OSD) consists of a flat steel deck plate, stiffened by a series of closely spaced longitudinal ribs with support by orthogonal transverse floor beams. In orthotropic box girders, the OSD is an integral part of the steel box framing and therefore acts as its flange. The use of stiffened steel plate over one-dimensional beams as load carrying elements, results in a higher strength-to-weight ratio of structural members. This has led to an increase in the use of orthotropic steel decks, especially for long-span bridges. This paper summarises the analysis and detailed design of the recently completed pedestrian bridge on King Salman bin Abdul Aziz Road. The bridge connects all corners of a four-way junction with a tram crossing, with the longest span measuring 76m. The footbridge is located at one of the prime locations in the city and hence, aesthetics and functionality was of prime importance to the Employer. The complex geometry, long design spans and space constraints for the substructure were the major challenges in designing this footbridge structure. This infinity shaped four-way bridge is made up of orthotropic steel box girders with 4.8x2.0m trapezoidal cross-sections, with the main curved spans connected at the centre to provide torsional stability (Fig 1). The top and bottom flanges of the box are made up of thin plates stiffened with trapezoidal closed ribs longitudinally to increase the flexural buckling resistance of the compression flanges. Equally spaced internal transverse ring-stiffeners are provided along box girders to retain the fabricated configuration of the girder when subjected to torsion and avoid girder distortion that would have resulted in additional longitudinal warping stresses as well as out-of-plane bending stresses in the individual plates of the box sections. The

structure was modelled and analysed in Midas CIVIL finite element software. A detailed dynamic analysis was performed to study the complex dynamic forces induced by pedestrians and determine all critical vibrational modes in longitudinal, transverse and vertical directions. In-house design sheets based on AASHTO LRFD were developed exclusively for the project due to the complex shape and uncommon cross-sections. While the 3D line beam model was sufficient for section design and studying the global behaviour and vibrational modes, it did not fully capture the complex load path at the corners and box girder intersections. Hence, a more realistic 3D Finite Element Model using shell plates was created to substantiate the design assumptions and understand the complex interaction between the bending, distortion and twisting of the deck at the corners and intersections. The 3D model helped to validate the detailed design, obtain a realistic estimate of the deflections and understand the complex load path and therefore avoiding critical stress concentrations, optimise member sizes and providing the required camber diagrams along each web of curved box girders.

1. Introduction

Jacobs was appointed by the Contractor (Besix group) as a Design Consultant to design for construction a pedestrian bridge required to connect all 4 sides of one of the busiest junctions in Jumeirah Beach Residence, Dubai as part of the Design and Build Contract. A non-conventional pedestrian crossing was indispensable at this location due to the high concentration of pedestrian traffic and congestion due to tram and vehicular movement from all sides. The design and layout of the bridge were finalized after considering all the requirements and constraints at the junction.

1.1. Architecture

The bridge has a unique infinity shape, composed of 4 steel decks, linking all 4 corners of the junction for a smooth pedestrian movement in all directions. The 4 decks form a continuous infinity shape structure that is simply supported on 4 circular concrete piers with conventional pot bearings placed in each corner. The longitudinal spans are 76m and 72m and the transverse spans are 48m and 26m. Elevators and staircases are provided in all 4 corners for ease of pedestrian access.

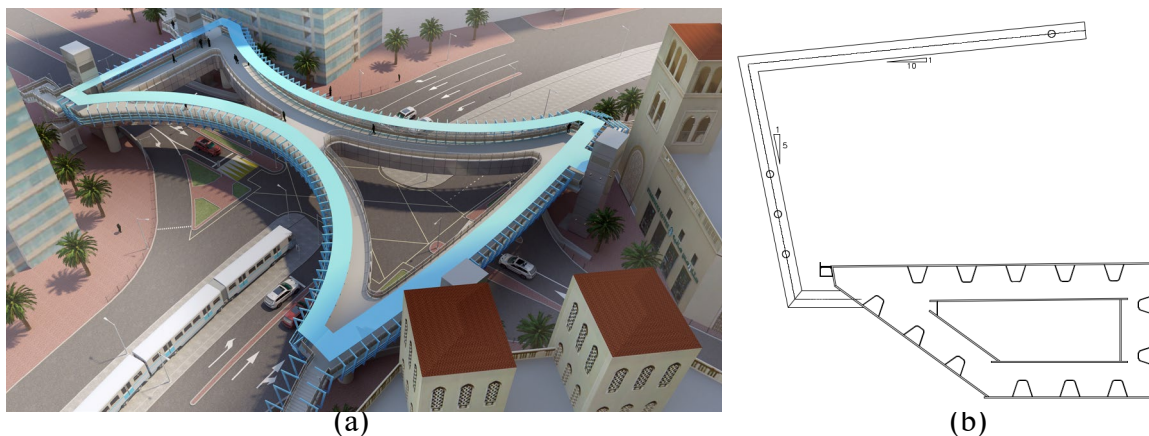


Fig. 1. (a) Birds eye view of the bridge and (b) Typical cross-section of the girders

1.2. Steel Orthotropic Box Girder

The curved shape and long design spans required an efficient section with high strength-to-weight ratio and hence, orthotropic steel deck system integral with the supporting bridge superstructure framing as a top flange common to both the transverse floorbeams and longitudinal box girders was chosen. A typical orthotropic box girder is made up of flat, thin steel plates stiffened by closely spaced longitudinal and transverse ribs. These ribs result in increased rigidity and considerable material saving compared to conventional steel structures.

2. Analysis & Design

The footbridge was modelled and analysed in Midas Civil and detail designed using design sheets developed in-house. The loads and structural steelwork design are based on AASHTO LRFD Bridge Design Specifications, 4th Edition (AASHTO, 2007). Basic section and substructure design was done based on the results obtained from the 3-D line beam model. 3-D line beam model was created to understand the overall behaviour of the structure and extract internal forces and bending moments for designing the steel cross-sections. However, a detailed 3-dimensional solid model was additionally created and analysed to validate the assumptions regarding stress flow and member design. The cross-section was designed based on the results extracted from the line beam model. Standard steelwork details (trapezoidal stiffeners, floor beams, their intersections and required cut-outs, etc.) were designed based on AASHTO LRFD Level 1 design but clearly supplemented with 3D line beam and full 3D finite element shell plate analysis models to capture both global and local behaviours.

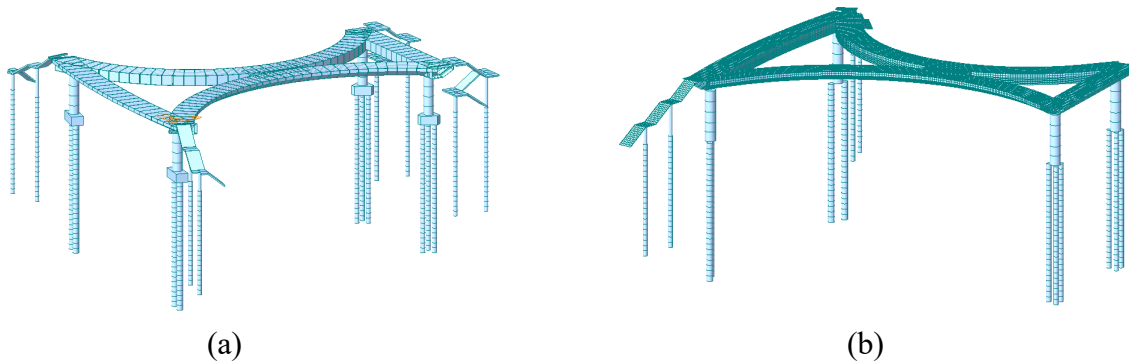


Fig. 2. (a) 2-D Line model and (b) 3-D Plate models created to analyse the bridge.

2.1. Major Challenges & Issues

Reduced plate thickness and complicated weld details possessed a major risk of fatigue cracking as observed in many orthotropic box girder bridges around the world, especially at the rib-to-deck plate joint and that between the transverse and longitudinal ribs (FHWA, 2012). This was mainly due to the stresses developed due to the in-plane flexure of the transverse ribs combined with the out-of-plane twisting of the longitudinal ribs. In addition, the complex shape of the bridge made the sharp corners prone to high concentrations of stresses. The interaction between the adjacent spans was complex and it was observed that the loads transferred from the long, curved spans caused significant twisting of the shorter side spans. The curved and side spans intersected at different angles in each of the four corners, which affected the symmetry of the structure. Hence, special design considerations had to be given to the load path and the internal flow of stresses in each of these corners to produce an optimum design.

All these issues were carefully studied to mitigate all possible construction/operational challenges. Complete Joint Penetration (CJP) welds were used between all structural members to improve the fatigue strength of welded joints between and the ribs and deck plate (Dung et. al., 2015). At critical welding locations, base metal materials with improved through-thickness properties and specific welding details were prescribed to mitigate risk of lamellar tearing. Staircases to the edges of the transverse spans were designed to be isolated from the steelwork bridge superstructure to avoid the deck torsion effects being transferred to the staircases. A detailed 3-dimensional plate model of the entire bridge was created to analyse the stress flow, the concentration of stresses, and effects of dynamic loading and to study the behaviour of all structural members in detail as well as determining the precamber diagrams for each box girder web.

2.2. 3-D Finite Element Model and Design Validation

A detailed 3-dimensional shell plate model helped to understand the overall as well as local flow of stresses along the longitudinal and transverse directions of the bridge deck, especially at the four corners. It was observed that the bending and torque transferred from the longitudinal curved spans of the bridge resulted in high concentration of stress at the junctions with the transverse spans. This model helped the design team to fix the plate and rib dimensions and the spacing at the corners. Furthermore, the 3-D model was able to accurately capture the magnitude of rotation of all the spans based on which, the required camber design information was produced.

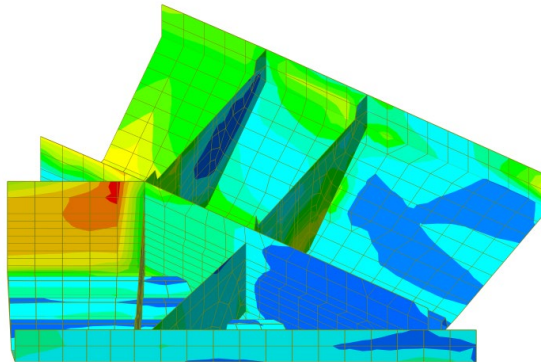


Fig. 3. High concentration of stresses at the corner

2.3. Dynamic Analysis

Pedestrian Dynamics Analysis was specifically complex and required detailed design using discrete finite element analysis (3D line model) where the steelwork superstructure, concrete substructure and piled foundations were modelled. This allowed the determination of all critical pedestrian induced vibration modes in longitudinal, transverse and vertical directions, based on the vibration analysis flowchart from SETRA (SETRA, 2006).

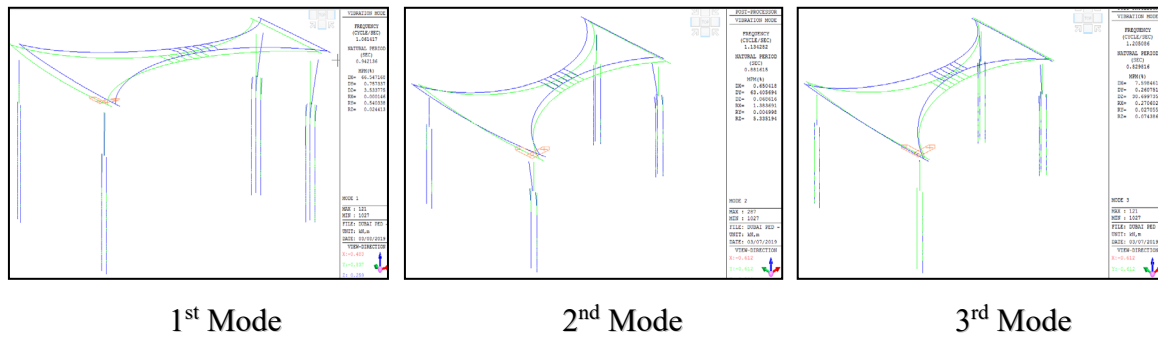


Fig. 4. Critical pedestrian induced vibration modes

3. Conclusions

- 1) Orthotropic box girders can be successfully used for light-weight long-span bridges with complex shapes. Decks and webs were typically made up of 16-20mm plates and ribs with 8-10mm plates.
- 2) 3-dimensional plate model helped to accurately capture the intricate details with respect to stress flow, concentration of stresses and displacement/rotation of each structural element. This helped to arrive at optimum member sizes and required camber.

4. References

- AASHTO. 2007. AASHTO LRFD Bridge Design Specifications, American Association of State Highway and Transportation Officials.
- AISC. 1963. Design Manual for Orthotropic Steel Plate Deck Bridges, American Institute of Steel Construction.
- Bethlehem Steel Corporation. 1981. Designer's Guide to Steel Box Girder Bridges.
- Dung, C. V., Sasaki, E., Tajima, K. and Suzuki, T. 2015. International Journal of Steel Structures, 15, 299-310.
- FHWA. 2012. Manual for Design, Construction and Maintenance of Orthotropic Steel Deck Bridges, US Department of Transportation Federal Highway Administration.
- NSBA. 2005. Practical Steel Tub Girder Design, National Steel Bridge Alliance.
- SETRA. 2006. Technical Guide - Footbridges Assessment of Vibrational Behaviour of Footbridges under Pedestrian Loading, Service D'études Techniques des Routes et Autoroutes.



Analytical Study of Fracture Behavior of Post-Tension Anchorage Zone Using FEM

Kyun-Tae Lee¹, Jun-Mo Yang², and Jin-Kook Kim^{3*}

¹: Department of Civil Engineering, Seoul National University of Science and Technology, Seoul, Republic of Korea; email: nome585@naver.com

²: Department of Civil Engineering, Keimyung University, Daegu, Republic of Korea; email: jm.yang@kmu.ac.kr

³: Department of Civil Engineering, Seoul National University of Science and Technology, Seoul, Republic of Korea; email: jinkook.kim@seoultech.ac.kr

*: corresponding author

Keywords: post-tension; anchorage zone; bearing plate; lateral confinement; construction quality

Abstract: In the post-tension anchorage zone, even if an anchorage design that has been verified by passing the performance test is used, the anchorage zone or bearing plate may be destroyed if the prestressing steel strands are tensioned during construction. In this study, load transfer tests and parametric analysis were performed for lateral confinement variables, possible construction errors and product defects to identify the causes of the failure of the anchorage zone and bearing plate during construction. Through comparison with the experimental results, it was verified that the finite element analysis model can effectively simulate construction errors and damage to the anchorage device. A parametric analysis was performed with anchorage device tensile strength, anchor head effective bearing area ratio, spiral reinforcement start position, spiral reinforcement spacing, spiral reinforcement outer diameter, anchorage device rib damage, and concrete voids under the ribs as variables. Based on the analysis results, the factors affecting the fracture of the anchorage device were analyzed, and the strength characteristics of the post-tension anchorage zone according to design and construction parameters were analyzed.

1. Introduction

With post-tension concrete, tension is transmitted to the concrete through the anchorage as it is tensioned, inducing high levels of compressive stress and local bursting stress under the bearing plate of the anchorage. Because anchorage devices are customized products that require a long development period and are expensive, most studies focus on the strength of the concrete, the size of the anchorage, and/or details about reinforcement techniques through experiments and numerical analyses (Kim et al. 2021; Kwon et al. 2018). However, even with the proper design of the anchorage device and anchorage zone, with the performance verified through load-transfer experiments and various studies, there have been cases of anchorage zone fractures when steel strands are placed under tension. In addition, considering that anchorage devices are made of cast iron, the product may not be uniform, and partial damage may occur during the construction process or when receiving a load. Hence, research on these types of possible damage is necessary.

In this study, to investigate the cause of the failure of the anchorage and bearing plate during construction, load-transfer experiments were conducted to check for possible construction errors and product defects, and parameter analysis was performed. The finite element analysis model was verified through a comparison with the experimental results, and a parametric analysis was conducted using possible construction errors and product defects as variables. Based on the analysis results, the factors influencing the failure of the anchorage device were analyzed, as were the strength characteristics of the post-tension anchorage zone according to the design and construction variables. Finally, by synthesizing the results of the study, design directions to prevent the failure of the anchorage zone were presented.

2. Load-transfer Experiment

The experiment was performed according to the procedure of EAD 16004-00-0301 (EOTA 2016). Based on the nominal strength of the steel strand, a load between $0.8 F_{pk}$ and $0.12 F_{pk}$ was repeatedly applied more than ten times, and when the stabilization criteria were met, an extreme load was measured by applying such a load. Based on the experimental specimen 15H-1 fabricated to meet the design criteria, the starting position of the spiral reinforcement, the strength of the spiral reinforcement, the pitch of the spiral reinforcement, and the outer diameter of the spiral reinforcement were tested as variables, as shown in Table 1.

Table 1. Test specimen details

	D_t (mm)	f_y (MPa)	s (mm)	D (mm)	$P_{u,EXP}$ (kN)	$P_{u,PTI}$ (kN)
15H-1	50	400	50	330	3,353	3,512
15H-2	100	400	50	330	3,254	3,512
15H-3	50	500	50	330	3,440	3,512
15H-4	50	400	70	330	3,129	3,037
15H-5	50	500	60	330	3,315	3,387
15H-6	50	500	60	300	3,288	3,040

D_t = distance from the top surface to the starting position of the spiral reinforcement

s = pitch of the spiral reinforcement

D = outer diameter of the spiral reinforcement

$P_{u,EXP}$ = ultimate strength from the experiment

$P_{u,PTI}$ = ultimate strength calculated using the PTI calculation formula

The modes of failure of the anchorage are generally defined in three types (Kim et al. 2019): local zone failures due to inadequate concrete strength or reinforcement levels, spreading failures due to longitudinal rupture cracks caused by inadequate reinforcement, and failures at boundaries between reinforced and unreinforced parts. Here, all specimens were fractured in the bearing plate of the anchorage device shown in Fig. 1 during the experiment. The reduction of the effective bearing area following the fracture of the anchorage device followed by the local failure of concrete on the lower surface of the anchorage device is defined as a fourth failure mode. When comparing the experimental results with the PTI bearing strength, the findings were similar on average, and it was determined that the method used to calculate the confinement force of PTI was effective.

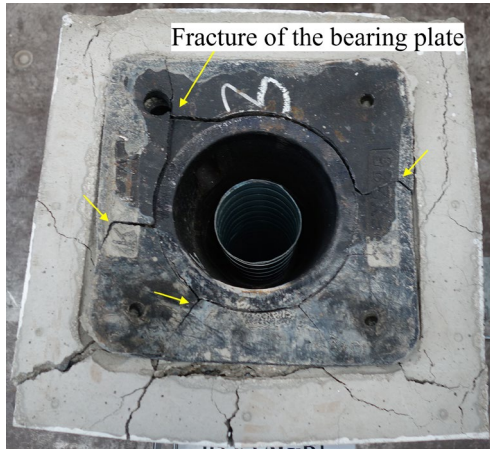


Fig. 1. Fracture of the bearing plate

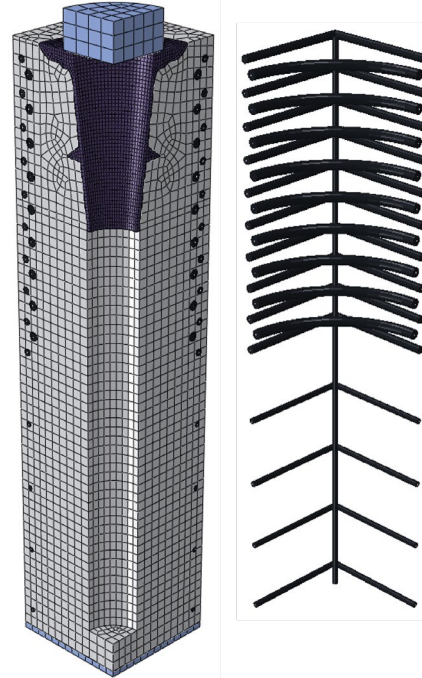


Fig. 2. Finite Element model

3. Parametric Analysis

Based on the experimental results, the modeling process here utilized conditions identical to those used with the specimen shown in Fig. 2, and only a quarter of the specimen was modeled for efficiency of the analysis. The material model for the nonlinear analysis of each member was defined to be similar to the experimental results, and the contact conditions and boundary conditions between each member were identical to those in the experiment. The validity was reviewed by comparing the load-displacement curves in the experimental results and the analysis results. A parametric analysis was also conducted to determine the effects of variables not reflected in the design formula as well as any construction errors and/or product defects on the behavior of the anchorage zone.

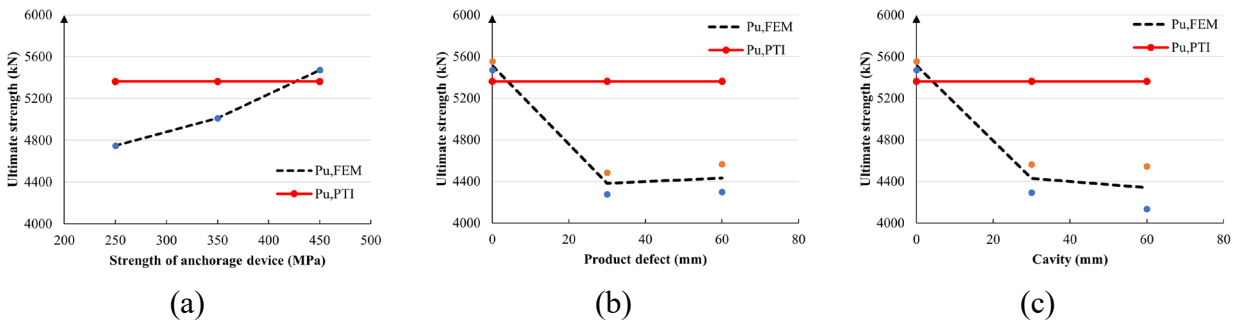


Fig. 3. Results of parametric studies: (a) effects of the strength of the anchorage device; (b) effects of the product defects; (c) effects of the cavities



4. Results and Conclusions

The strength of the anchorage device and effective bearing area ratio are the major factors influencing the failure of the bearing plate of the anchorage device, and when the bearing plate is fractured, this value appears to be lower than the bearing strength predicted by existing design formulae. The ultimate load was found to decrease as the starting position of the spiral reinforcement moved away from the upper surface. The ultimate load was found to decrease when the outer diameter of the spiral reinforcements was decreased. This result showed a tendency similar to that of the bearing strength calculation result of the PTI design equation. With regard to damage to ribs and concrete voids due to defective anchorage device products, the ultimate load was found to be 15% to 23% lower than in the design strength. A large difference was observed depending on the product defects or presence of voids, and the difference in the ultimate load depending on the size of defects or voids was small.

The Ultimate load of the model, which variables the voids of concrete, failure of the bearing plate, and defects of the anchorage device, was derived below the ultimate strength calculated through the bearing strength formula. Therefore, these variables are judged to be the main cause of failure in the anchorage zone during construction. To prevent the failure of the anchorage zone, it is important to design these components appropriately. In addition, during construction, it is necessary to check whether the production of the anchorage device is abnormal, and attention should be paid to the quality of the concrete construction materials to prevent voids from forming.

5. Acknowledgements

This work was supported by the National Research Foundation of Korea(NRF) grant funded by the Korea government(MSIT) (No. 2022R1F1A1074002).

6. References

- EOTA. 2016. Post-Tensioning Kits for Prestressing of Structures (EAD 160004-00-0301), Brussels, Belgium; European Organization for Technical Approvals (EOTA)
- Kim, J. K., and Yang, J. M. 2021. Analysis of Bearing Strength of Post-Tensioning Anchorage Zone with Respect to Relative Bearing Area and Lateral Confinement Design. *Applied Sciences* 11(18), 8386.
- Kim, J., Kwak, H. G., Kim, B. S., Kwon, Y., and Bouhjiti, E. M. 2019. Finite Element Analyses and Design of Post-Tensioned Anchorage Zone in Ultra-High-Performance Concrete Beams. *Advances in Structural Engineering* 22(2), 323-336.
- Kwon, Y., Kim, J. K., and Yang, J. M. 2018. Development of Efficient Anchorage Device and Estimation of Its Bearing Strength of Posttensioning Anchorage Zone. *Journal of Structural Engineering* 144(3), 1-10.



Development of Shrinkage and Creep Prediction Model for SCC (B4-TW-SCC) and Implementation in Bridge Design Software

Wen-Cheng Liao^{1*} and Jenn-Chuan Chern²

¹: National Taiwan University, Taipei, Taiwan; email: wcliao@ntu.edu.tw

²: National Taiwan University, Taipei, Taiwan; email: jcchern@ntu.edu.tw

*: corresponding author

Keywords: SCC; shrinkage; creep; prediction model

Abstract: At present, the design methodology and formula, particularly in shrinkage and creep, of Self-Compacting Concrete (SCC) projects in Taiwan are identical to those of Vibrated Concrete (VC), but there are differences in the composition and proportion of the materials in various regions, and obvious differences between the VC and SCC in engineering properties. In this study, the test data of shrinkage and creep in Taiwan and abroad were collected following the framework and parameters of the Northwestern University (NU) database to establish cloud-based analysis SCC database. Based on the Model B4-TW shrinkage and creep prediction model modified by Model B4, this study revised the characteristics of SCC and the localization to develop B4-TW-SCC. In B4-TW-SCC, the modification is mainly about the effect of high volume of cementing material weight and high sand ratio, as well as the effect of drying shrinkage changes on the drying creep. It is worth noting that efficiency in data mining and analysis of huge sets of data are significantly improved by analysis database in development of B4-TW-SCC. The creep curve and data point for specific SCC can be further generated on this cloud-based analysis database and directly implemented in common bridge design software for practical application.

1. Introduction

Creep and shrinkage of concrete, which are found under the influence of environmental effects and conditions of long-term stress, affect the strength, deformation, and durability of structural members, and in turn affect the life-cycle and serviceability of structures. In addition, long-span structures like bridges, high-rise buildings, and domes also require displacement control during the construction phase in order to achieve the design criteria. Creep and shrinkage are influenced by the materials and the mix design of the concrete, as well as surrounding stressors and environmental temperature and humidity. Experiments and prediction models should be used as a basis during the design phase of construction. Moreover, various types of high-performance concrete, such as high-strength concrete, light-weight concrete, self-compacting concrete, fiber reinforced concrete, fly ash or slag concrete, have been developed and taken into practical use due to advances in material technology and the recycling of resources. When using new types of concrete, such as those mentioned above, experiments and prediction models are also required to clarify the properties of creep and shrinkage. However, experiments for determining those



properties of concrete are time-consuming and costly. In order to shorten construction time, non-major structures which are not deformation-sensitive usually rely on prediction models or the combination of prediction models and short-term experiments.

Typical procedures for the development of prediction models are: (1) Collection of experimental creep and shrinkage data, (2) Analysis of existing prediction models, (3) Establishment of a database and analysis program, and (4) Establishment of a prediction model of the target (or local) material. As result, major research institutions, including the ACI (1982), CEB (1991), RILEM (2013), AASHTO (2014) and JSCE, academic institutions or scholars including the University of Ottawa, Zdeněk Bažant of Northwestern University (1995), and Jenn-Chuan Chern of National Taiwan University (2018), had established databases or developed prediction models respectively. However, the source, amount, and bases for comparison of data from each database are different, which often leads to discrepancies when comparing the performance of prediction models. As a result, Bažant and others established large-scale databases open for public use. Due to the continuous increase of research on concrete creep and shrinkage, the scale of databases has also continued to grow. Limited to traditional data file formats and analytical methods, previous studies encountered many difficulties.

This study presents a new processing program for the use of concrete deformation databases in Taiwan and extends to high performance concrete. This database is the first analysis system and fast-access cloud database for shrinkage and creep of concrete in the world, named “shrinkage and creep database in Taiwan”, SCDT (<http://scdt.ncree.org/>). SCDT uses MS-SQL as its database management system; it also uses Python programming language in the writing of programs for analysis and post-processing. It has been found that these new processing programs are far superior in terms of efficacy than previous types. In fact, when analyzing large amounts of data, they can be over several times as effective. In addition, per the needs of research, convenient SQL syntax may be used to quickly perform selection comparison on the multiple parameters which affect concrete deformation and their range, and thus easily perform cross analysis, a process which is extremely time consuming in older methods.

2. Database Analysis Method of SCDT

SDCT collects 1,412 sets of creep data and 1,995 sets of shrinkage data for vibrated concrete and 475 sets of creep data and 1,587 sets of shrinkage data for self-compacting concrete from around the world. Each set of data consists of data points taken at different times in a single creep or shrinkage test. The purpose is to analyze and compare data among the TW, NU, and JSCE from the past 40-plus years. Besides the considerable scope of data, this study also faces challenges, such as the variety of admixtures, range of concrete strength, type of cement, and data mining of complicated conditions. As a result, the two traditional methods mentioned above are unable to provide high levels of efficiency for this study. Instead, this study uses a new procedure for database management and analysis—using Python and MS-SQL to integrate data access, mining, and high-efficiency analysis on a single platform.

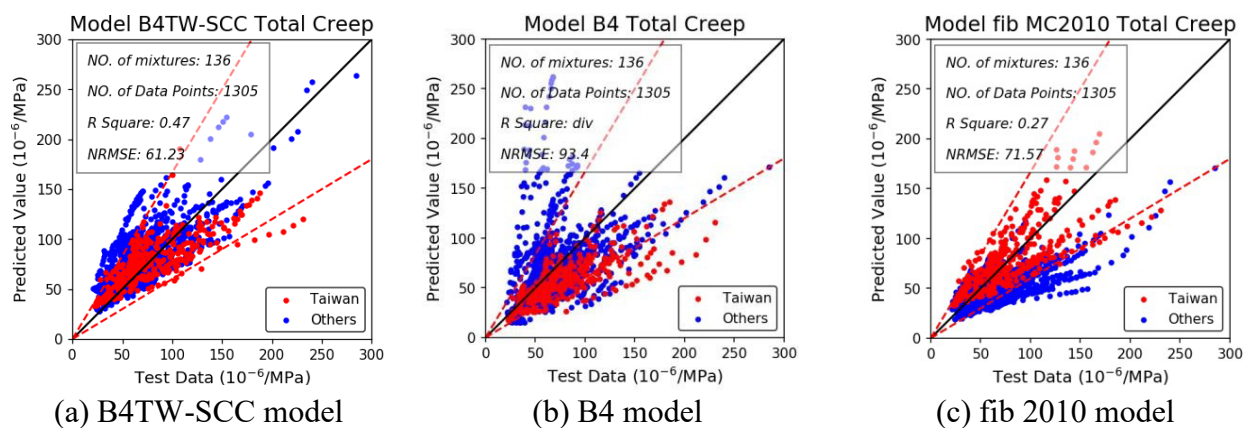
SCDT used MS-SQL for the establishment of databases and Python for the programming of prediction models. Taking advantage of the portability of SQL, this study successfully integrates into a single interface the automatic output of data filtering, data mining, formulaic analysis, graphical results, and statistical indicators. This new database management procedure, which uses MS-SQL and Python. It may be seen that the inconveniences resulting from outputting and inputting data over different interfaces (inconvenience experiences in traditional database management procedures) have been greatly reduced, accompanied by an increase in the

efficiency of research in concrete deformation. By the use of an intuitive and easy mining language, SCDT can accomplish analyses which would have been difficult or time-consuming using the traditional methods of analysis, such as searching for data sets whose mix design properties are similar to those in Taiwan’s national databases.

3. B4TW-SCC for Creep Prediction of SCC

B4TW-SCC was developed based on B4 model and optimized by data-mining with SCDT. The first is the static modulus of elasticity which has different formulae among the available prediction models for conventional concrete. To have highly accurate formulae of elastic modulus for SCC, the relationship between this modulus and compressive strength should be determined initially before other optimization steps for creep compliance are carried out. Second, the instantaneous compliance q_1 was verified for different loading ages because this parameter anchors the entire multi-decade prediction model (Wendner et al., 2015a). In the next step, the basic creep compliance parameters q_2 , q_3 , and q_4 were optimized. The final step is calibration for drying creep compliance parameter q_5 . In each step of optimization, the parameters depending on the concrete composition were considered in the process, the water-to-cementitious material ratio was found to be the most important for the magnitude of all the components of the compliance parameters, and second most important is the aggregate to cementitious material ratio (Wendner et al., 2015b). The individual influencing parameters were identified using various statistical coefficients R^2 and NRMSE, and screening assessments between predicted values and experimental data were used to have the highest efficiency.

The results B4TW-SCC model was optimized for the total creep function of SCC using cement type R as illustrated in Fig. 1. All the dots were scattered uniformly around the standard line ($x=y$), and most of them were distributed in two red dash lines with an allowable error range of $\pm 40\%$. In addition, the red and blue dots in the plots represent the test data collected from Taiwan and other countries around the world, respectively. For the purpose of estimating the accuracy of the B4TW-SCC model, the evaluation was carried out based on the comparison of this model and other prediction models for SCC as well as the models for conventional concrete, including B4, fib MC2010 and ACI 209R-92. As the results are shown in Fig. 2, the B4TW-SCC model had the lowest values of statistical coefficient NRMSE, which indicated the minimum error in both cases of creep prediction for the NTU-SCC database.



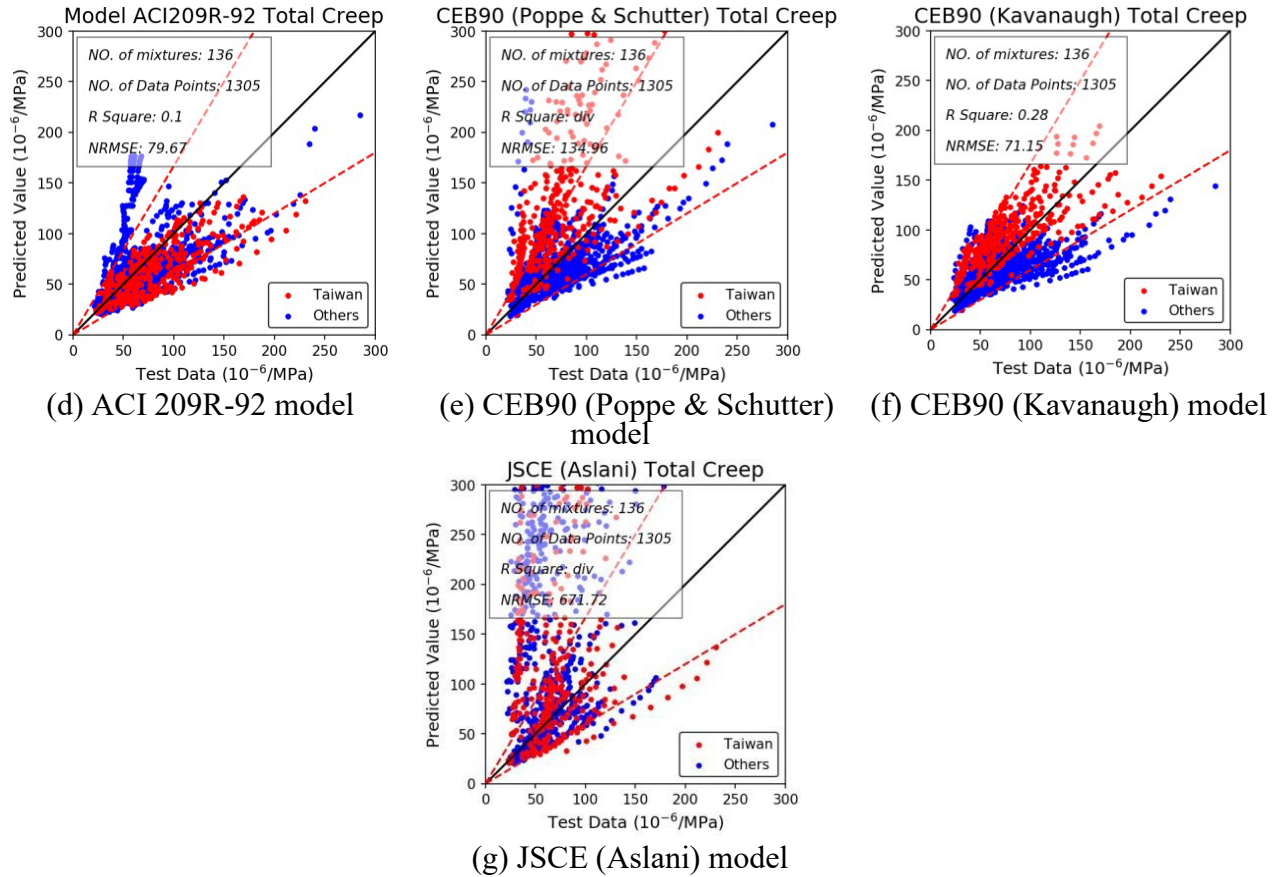


Fig. 1. The predicted comparison in total creep of SCC

4. Example: Long-Term Deflection Analysis of Prestressed Bridges

In practice, when designing and evaluating the long-term deflection and service life of bridges in Taiwan, international shrinkage and creep predictions models are often used. The more commonly used prediction models include ACI, AASHTO and CEB-FIP. Whether the above models are used to predict the shrinkage or creep of concrete in Taiwan, they are obviously underestimated. If they are directly applied, the long-term deflection and prestress loss of bridges are notably underestimated. This study selects an existing pre-stressed concrete bridge built by the cantilever construction method, uses MIDAS Civil to build a model, and applies a variety of shrinkage and creep prediction models, including ACI 209R-92, AASHTO LRFD 2014, CEB MC90, CEB MC10, GL2000, Model B3 and Model B4TW (2020), etc., to discuss the differences in the analysis of different prediction models for bridge long-term deflection and prestress loss.

The case selected in this study is the Anshuo to Caopu section of the Taiwan Provincial Highway No. 9. This case has 3 spans in total, with a total length of 310m (80+150+80). For 69 segments of construction, the mix design and environmental parameter are listed in Table 1. The loads considered in the analysis of this study include the self-weight, the weight of the partition beam, the wet weight of the concrete, the load of the working vehicle and the formwork, the load of the second phase and the pre-stressed steel tendons, etc.

Table 1. Mix proportions and environmental parameters used in simulation

w/cm	agg/cm	cement (kg/m ³)	ggbs (kg/m ³)	fly ash (kg/m ³)	f _{c28} (MPa)
0.40	3.55	356.25	74.25	47.5	42.8
coarse aggregate (kg/m ³)	fine aggregate (kg/m ³)	R.H. (%)	V/S (cm)	cement type	curing ages (day)
977.3	707.7	80	27.45~43.71	I	3

There are obvious differences in the prediction results of different shrinkage and creep prediction models in this case. Taking the segment with a V/S of 27.445cm and a loading age of 7 days as an example, the total shrinkage prediction and total creep results are shown in Figure 2 (a) and (b), respectively. It can be found that the prediction results of ACI 209R-92 and AASHTO LRFD 2014, regardless of shrinkage and creep, have the phenomenon of rapid development in the early stage and flattening at the earliest. This is an error caused by unreasonable consideration of the influences of V/S. For other models, even though the development trend is relatively close to that of Model B4TW (2020), the predicted values are very different. It can be seen that if it is applied to the analysis of prestressed bridges, the long-term deflection and prestress loss will be notably underestimated.

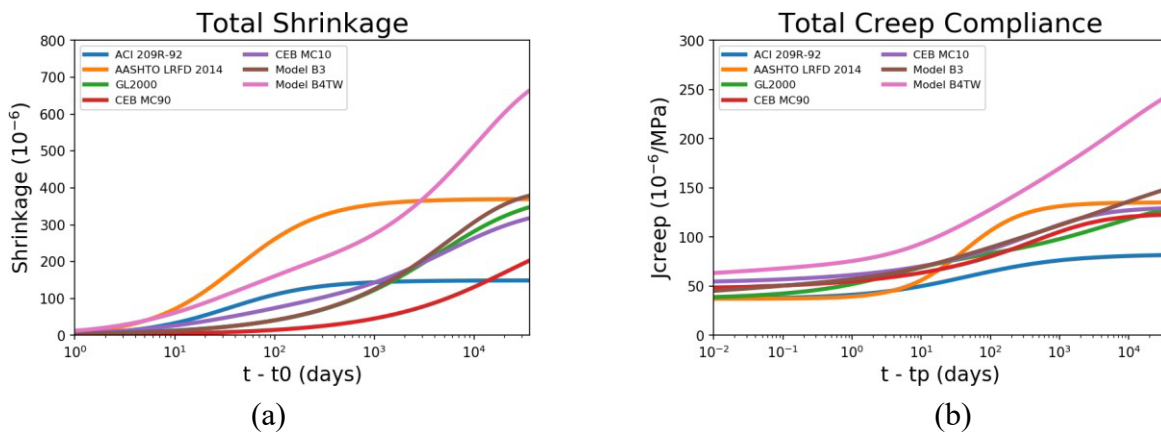


Fig. 2. The predicted comparison for different models for (a) total shrinkage and (b) total creep

The long-term deflection of prestressed concrete bridges can be composed of static load, prestressed tendon, shrinkage and creep. The total deflection and components of each deflection at the middle of the bridge are shown in Figure 3. The deflection caused by static load has nothing to do with shrinkage and creep, so the results obtained by all prediction models are the same. The deflection of tendon arching will be affected by shrinkage and creep. The greater the shrinkage and creep, the greater the loss of the tendon. The deformation development of obvious, shrinkage and creep is similar to the material shapes in Figure 2. From this case analysis, it can be found that the greatest contribution to the long-term deflection of the bridge is creep, which accounts for about 52% of the total deformation, and it develops rapidly in the early stage, and tends to be flat in about 2500 days; although the deformation caused by shrinkage only accounts for the total deformation 14% of that, but it still continues to occur when the bridge age reaches 100 years, which is one of the main reason for the continuous deformation of the bridge.

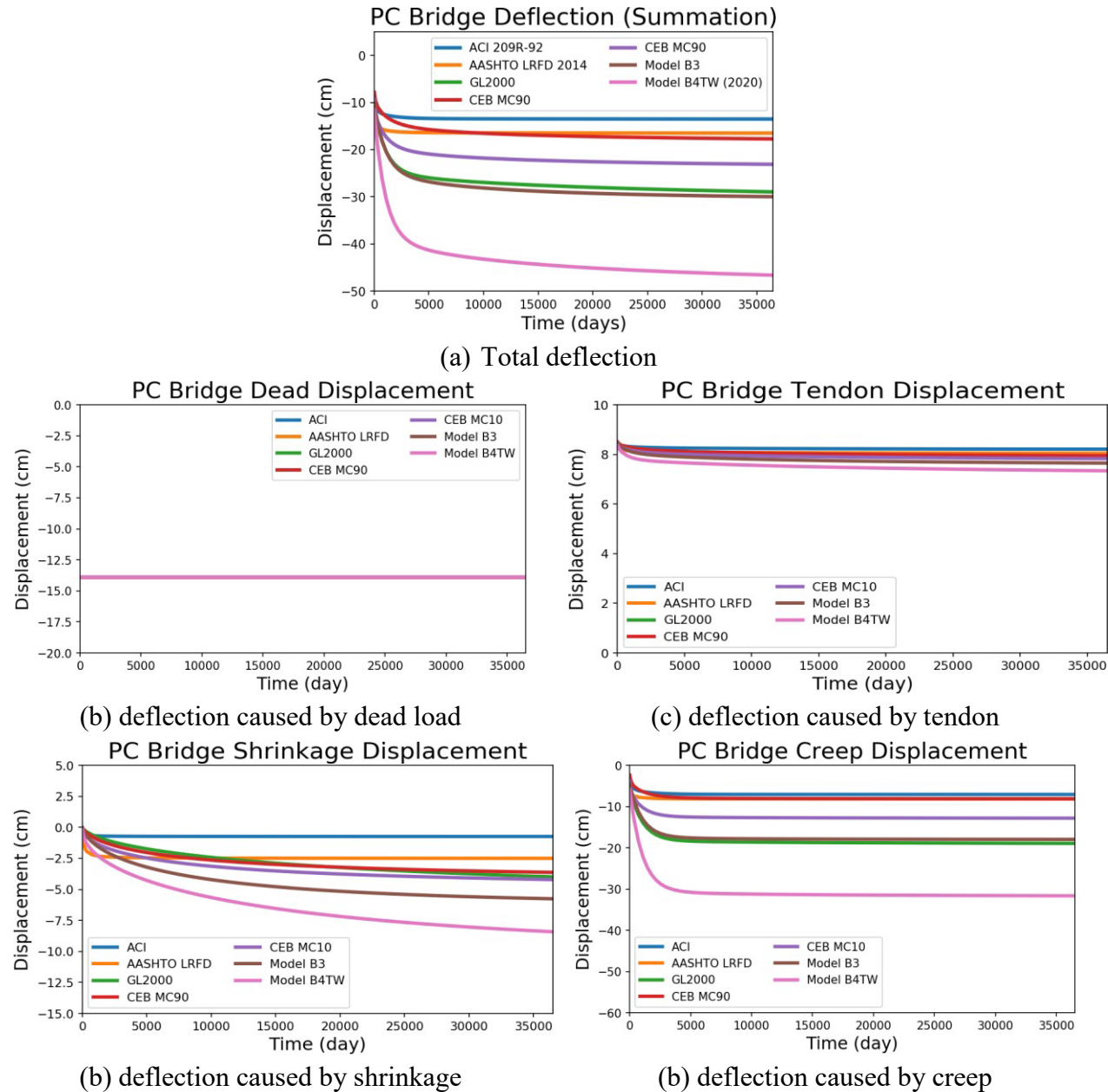


Fig. 3. Simulated deflection obtained by different prediction models

Since V/S is an independent variable for calculating shrinkage and creep, bridge segment with different V/S will have different shrinkage and creep prediction values. In the above analysis, each type of creep change needs to input 41 loading age curves, and each curve needs to input 108 points, and there are 19 V/S in this case, so a total of $41 \cdot 108 \cdot 19 = 84132$ points need to be input. Since the shrinkage has nothing to do with the loading age, it only needs to input $108 \cdot 19 = 2052$ points. After analysis in this study, it is found that if the whole bridge is analyzed only by the average V/S , that is, all segments are calculated only by using the average V/S , the composition of each deflection analysis obtained in 100 years will be very close to the exact analysis. Thus, this study suggests that the average V/S can be used in practice.



5. Conclusions

This study presents the first analysis system and fast-access cloud database for shrinkage and creep of concrete in the world, SCDT. Comparisons of the predicted results of selected models and test results in the chosen database can be generated in seconds. One example of the development of B4TW-SCC based on model B4 by using SCDT to reflect concrete characteristics in Taiwan and its implementation in bridge design is also presented in this study. The following conclusions can be drawn:

- This study builds an online real-time analysis system S.C.D.T through cloud-based databases and embedding Python into web pages created using ASP.net. Engineers and scholars around the world can use the three major functions provided by S.C.D.T without installing any software or modifying codes, including shrinkage and creep prediction, database analysis, and real-time analysis of test data upload.
- This research uses a variety of shrinkage and creep prediction models in Taiwan and abroad, including ACI 209R-92, AASHTO LRFD 2014, CEB MC90, CEB MC90, GL2000, Model B3 and Model B4TW (2020), etc., to evaluate the long-term performance of prestressed concrete bridges. From the analysis results, it can be known that if the foreign prediction model is directly applied without considering the characteristics of Taiwan concrete, the long-term deflection and prestress loss will be seriously underestimated.
- From this case, it can be found that creep deformation contributes the most to the long-term deformation of prestressed concrete bridges, and the deformation caused by it accounts for about 52% of the total deformation. Although the deformation is only 14% of the total deformation, the bridge still continues to develop when it is 100 years old, which is the main cause of the continuous deformation of the bridge.

6. References

AASHTO (2014), AASHTO LRFD bridge design specifications 7th edition, American Association of State Highway and Transportation Officials (AASHTO), Washington DC, USA.

ACI Committee 209 (1982), Prediction of creep, shrinkage and temperature effects in concrete structures, Designing for Creep and Shrinkage in Concrete Structures, A Tribute to Adrian Pauw, American Concrete Institute, Farmington Hills, MI, USA.

Bažant, Z., and Baweja, S. (1995), “Creep and shrinkage prediction model for analysis and design of concrete structures: Model B3,” *Materials and Structures*, 28, 357-365, 415-430, 488-495. <https://doi.org/10.1007/bf02486204>

Bažant, Z., Hubler, M., and Wendner, R. (2015), “Model B4 for creep, drying shrinkage and autogenous shrinkage of normal and high-strength concretes with multi-decade applicability,”

RILEM Recommendation TC-242-MDC.

CEB Bulletin (1991), Evaluation of the time dependent properties of concrete, Bulletin d'Information No. 199, Comité Européen du Béton/Fédération Internationale de la Précontrainte, Lausanne, Switzerland.

Chern, J-C., Liao, W-C., Liu, T-K., Chin, W-Y. (2018), “Development and analysis of creep and shrinkage database of concrete in Taiwan,” *Structural Engineering*, 33(1), 103-116. (in Chinese)



FIB, The International Federation for Structural Concrete (2013), Fib model code for concrete structures 2010, Berlin, Germany.

Mehta, P. K. and Monteiro, P. J., (2006). “Concrete – Microstructure, Properties, and Materials” (3rd ed.). McGraw Hill.

Wendner, R., Hubler, M. H. and Bažant, Z. P., (2015a). “Optimization method, choice of form and uncertainty quantification of Model B4 using laboratory and multi-decade bridge databases.” *Materials and Structures*, 48, 771-796.

Wendner, R., Hubler, M. H. and Bažant, Z. P., (2015b). “Statistical justification of model B4 for multi-decade concrete creep using laboratory and bridge databases and comparisons to other models.” *Materials and Structures*, 48 (4), 815-833.



A Data-Driven Method for Predicting the Temperature Response of Composite Bridges Based on Deep Learning Technology

Yanjia Wang^{1*}, Dong Yang², and Francis T.K. Au³

¹: The University of Hong Kong, Hong Kong, China; email: ansleyw@connect.hku.hk

²: Guangzhou University, Guangzhou, China; email: yangd@gzhu.edu.cn

³: The University of Hong Kong, Hong Kong, China; email: francis.au@hku.hk

*: corresponding author

Keywords: composite bridge girder; deep learning; temperature behavior

Abstract: As climate change is imminent, it is necessary to investigate the possible effects on bridges in future. Towards the end of this century, bridges may experience significant increase in thermal loading. The Structural Health Monitoring (SHM) systems installed on some bridges can provide useful data to form the basis not only for verification of the design loading, but also for estimation of the future scenarios. Recent developments in the field of Artificial Intelligence (AI) have opened up new opportunities. Compared with the traditional Finite Element (FE) Method to analyze the structural behaviour under ambient conditions, Deep Learning (DL) as a data-driven method offers an efficient alternative for simulating the temperature responses of structures based on the massive real-time SHM data available. Long Short-Term Memory Networks (LSTM) and Gate Recurrent Unit (GRU) are two typical Recurrent Neural Network (RNN) methods, which perform well in predicting the structural temperature and its effects. In this study, the nonlinear relationship between the ambient climate condition and temperature response of a bridge is predicted by the ambient condition input, with the bridge temperature sequential DL models built separately based on LSTM and GRU with monitoring data from the temperature sensors of a composite girder bridge. Comparison between the forecast structural temperature by the LSTM and GRU model with the simulated results by the traditional FE Model confirms the excellent performance of the proposed data-driven method.

1. Introduction

The impact of environmental loading on bridge structures tends to be increasingly significant due to climate change. With increasing ambient temperature, the evaluation of bridges, especially long-span bridges, becomes more important. The challenge is how to predict the temperature response of the bridge under the given climate conditions accurately. The method widely used by researchers is analysis with Finite Element (FE) models. However, most of the FE analyses rely on commercial software and are time-consuming. With the development of Machine Learning technologies, Deep Learning (DL) technology came to the stage and different kinds of DL networks are used to deal with different scenarios. Recurrent Neural Network (RNN) is a kind of Artificial Neural Network (ANN) using DL technology, which works well in solving time-dependent problems. A proper choice of DL networks would likely apply to bridge temperature response prediction. In this study, the prediction of the temperature response of a long-span

bridge is conducted using two RNNs with different structures. The efficiency and performance of the networks will be compared.

2. Bridge Monitored

The bridge studied is Ting Kau Bridge (TKB), which is a 3-tower cable-stayed bridge in Hong Kong. Fig. 1(a) shows the composite bridge deck comprising concrete slabs supported on steel plate girders. The data obtained by the Structural Health Monitoring (SHM) system of TKB covered both the structural responses and ambient air temperature data. Temperature sensors are installed on the main girders and cross girders on both sides of the symmetric deck as shown in Fig. 1(b). From heat transfer theory, the three main factors that influence the bridge temperature are the ambient air temperature, global solar radiation (GSR) I , and wind speed V . In particular, the ambient temperature includes the air temperature above the deck T_a and that below the deck T_b . In this study, these four factors will be used as input to the proposed DL model and the bridge structural temperatures are the output. The hourly monitoring data of the year 2017 are used to train and validate the model.

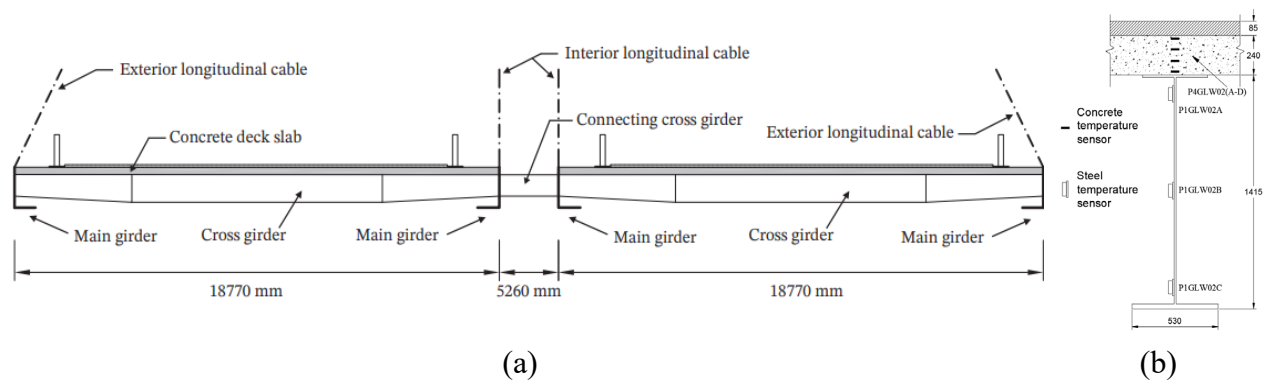


Fig. 1. (a) Layout of the TKB composite deck; (b) Temperature sensors of the cross girder.

3. Methodologies

3.1. LSTM and GRU neural network

RNN employing DL technology is commonly adopted to deal with the sequential data of time series, such as translation, natural language processing, speech recognition, etc. (Lipton, Berkowitz et al. 2015). As opposed to the basic Feedforward Neural Networks (FNN) and Convolutional Neural Networks (CNN), RNN takes information from the previous input together with the current input to calculate the current output.

Long Short-Term Memory Networks (LSTM) (Hochreiter and Schmidhuber 1997) and Gate Recurrent Units (GRU) (Chung, Gulcehre et al. 2014) are two main advanced RNNs, which can effectively solve the gradient explosion or disappearance problem of basic RNN. Fig. 2 shows that the cell structures of the LSTM and GRU networks are controlled by Gating Mechanism, and the functions with governing equations for each gate of LSTM and GRU networks are given in Table 1 and Table 2, where b 's are the bias vectors, W 's are the weight matrices, and σ is the activation function. In comparison, the structure of GRU is simpler, which uses only an update gate to balance the input information and historical information without the memory unit adopted in LSTM. Sufficient research has proved that GRU requires less training

time and less computational resources, but offers similar performance as LSTM (Fu, Zhang et al. 2016, Shewalkar, Nyavanandi et al. 2019).

Table 1. Gating mechanism of LSTM network

Gate name	Function	Governing equation
Forget Gate f_t	Determine the information to be “forgotten” from the internal state of the previous moment C_{t-1}	$f_t = \sigma(W_f \cdot [h_{t-1}, x] + b_f)$ (1)
Input Gate i_t	Determine the information to be accepted from the current candidate's internal state \tilde{C}_t	$i_t = \sigma(W_i \cdot [h_{t-1}, x] + b_i)$ (2)
		$\tilde{C}_t = \tanh(W_c \cdot [h_{t-1}, x] + b_c)$ (3)
		$C_t = f_t \cdot C_{t-1} + i_t \cdot \tilde{C}_t$ (4)
Output Gate O_t	Determine the output from the current internal state C_t to the external state h_t	$O_t = \sigma(W_o \cdot [h_{t-1}, x] + b_o)$ (5)
		$h_t = O_t \cdot \tanh(C_t)$ (6)

Table 2. Gating mechanism of GRU network

Gate name	Function	Governing equation
Update Gate z_t	Determine the information to be retained from the previous state h_{t-1} and the information to be accepted from the current candidate state \tilde{h}_t	$z_t = \sigma(W_z \cdot [h_{t-1}, x] + b_z)$ (7)
		$h_t = z_t \cdot h_{t-1} + (1 - z_t) \cdot \tilde{h}_t$ (8)
Reset Gate r_t	Determine whether the external state \tilde{h}_t should rely on the previous state h_{t-1}	$r_t = \sigma(W_r \cdot [h_{t-1}, x] + b_r)$ (9)
		$\tilde{h}_t = \tanh(W_h \cdot [h_{t-1}, r_t, x] + b_h)$ (10)

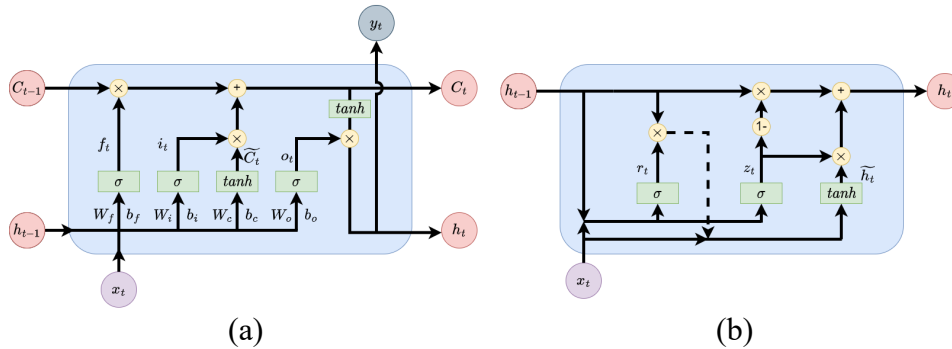


Fig. 2. Cell structure of networks: (a) LSTM; and (b) GRU

3.2. Data preparation and Deep Learning DL model

A one-year monitoring dataset of TKB is used in this study. The data from Jan 1st to October 31st are used in the training process as training sets and validation sets. The remaining two-month data from Nov 1st to Dec 30th are used as the test data to evaluate the prediction performance by comparing the forecast results with the monitoring data. To enhance the quality of training, the raw data is normalized before training. The performance of DL models is also evaluated by comparing with the simulated results by the Finite Element Analysis (FEA) using ABAQUS. For the DL models with LSTM and GRU networks, there are three hidden layers,

with 256 cells for each layer. There is a fully connected dense layer linking the last LSTM or GRU layer to the output layer. For the other hyperparameters, the Adam optimization algorithm is used and the activation function for LSTM and GRU layers are Rectified Linear Unit (*relu*). The length of the time series determining the data structure of the sequence is essential, which is set to 24 hours, implying that the prediction of current structural temperatures is based on the historical measurements of the previous 24 hours. To evaluate the performance of the proposed DL models, the Mean Absolute Error (MAE) to reflect the training loss and the accuracy indicator R^2 will be calculated in terms of the output data y_i , the predicted value \bar{y}_i , the mean of observed output \hat{y}_i , the sum of squares of residuals SS_{RES} and the total sum of squares SS_{TOT} as:

$$MAE = \frac{1}{n} \sum_{i=1}^n |y_i - \bar{y}_i| \quad (11)$$

$$R^2 = 1 - \frac{SS_{RES}}{SS_{TOT}} = 1 - \frac{\sum_i (y_i - \bar{y}_i)^2}{\sum_i (y_i - \hat{y}_i)^2} \quad (12)$$

4. Results and conclusions

4.1. DL model performance

During the training process, the performance variations of the model as shown in Fig. 3(a) indicate that the training loss and accuracy of the LSTM and GRU models are close while the GRU networks perform better in the prediction of structural temperature based on the error calculated by the test datasets in Table 3. However, the training time for GRU networks is only 70% of the training time for LSTM networks according to the average training time for 10 times as shown in Table 3, which proves that the GRU structure has higher training efficiency. Fig. 3(b) provides the statistical results of the temperature differences between the values predicted by DL models and the monitored data. By comparing the predicted bridge temperature variations by the LSTM and GRU models with the FE simulations in Fig. 3(c), the discrepancies of the predicted results of both DL models are close to the discrepancy between the FE simulation and monitored data. While it takes around 3 minutes to complete the FE analysis, the DL model only takes 1s to finish the prediction, which can effectively achieve real-time prediction.

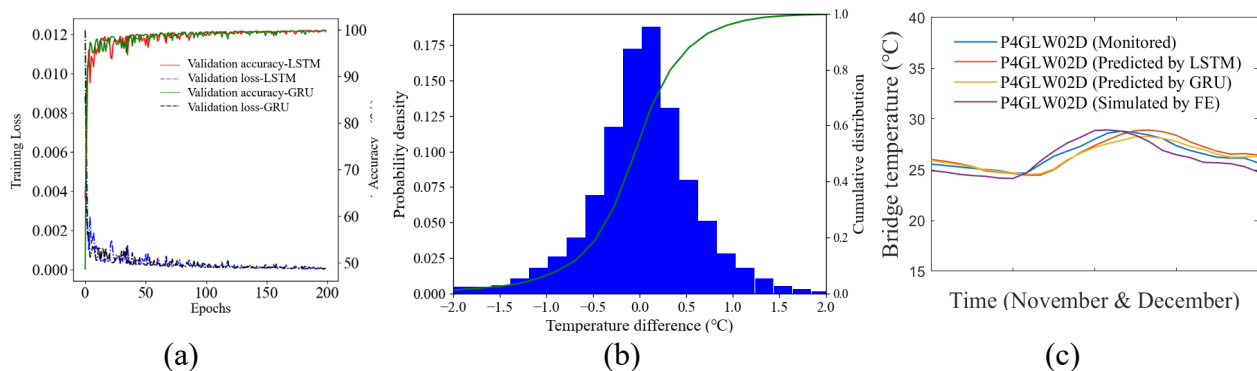


Fig. 3. (a) Loss and accuracy during training; (b) discrepancy between monitored and predicted temperatures; (c) comparison of monitored data, DL model predictions and FE simulations



Table 3. Training time and test error of LSTM and GRU networks

	LSTM	GRU
Training time (s)	2215	3346
MAE of the test sets (deg)	0.551	0.370

5. References

Chung, J., C. Gulcehre, K. Cho and Y. Bengio (2014). "Empirical evaluation of gated recurrent neural networks on sequence modeling." arXiv preprint arXiv:1412.3555.

Fu, R., Z. Zhang and L. Li (2016). Using LSTM and GRU neural network methods for traffic flow prediction. 2016 31st Youth Academic Annual Conference of Chinese Association of Automation (YAC).

Hochreiter, S. and J. Schmidhuber (1997). "Long Short-Term Memory." *Neural Computation* **9**(8): 1735-1780.

Lipton, Z. C., J. Berkowitz and C. Elkan (2015). "A critical review of recurrent neural networks for sequence learning." arXiv preprint arXiv:1506.00019.

Shewalkar, A., D. Nyavanandi and S. A. Ludwig (2019). "Performance Evaluation of Deep Neural Networks Applied to Speech Recognition: RNN, LSTM and GRU." *Journal of Artificial Intelligence and Soft Computing Research* **9**(4): 235-245.



Topology Optimization of Concrete Bridges Prestressed with Shape Memory Alloys

Minsoo Sung¹ and Bassem Andrawes^{2*}

¹: University of Illinois at Urbana-Champaign, Urbana, US; email: minsoos2@illinois.edu

²: University of Illinois at Urbana-Champaign, Urbana, US; email: andrawes@illinois.edu

*: corresponding author

Keywords: topology optimization, prestressed concrete, shape memory alloys, bridges

Abstract: Topology optimization has been widely used as a design optimization tool that distributes material at specific locations within the design domain to maximize or minimize design objectives such as stiffness and/or maximum displacement. One of the main challenges of manufacturing topology-optimized concrete structures for real-world applications is their complex geometry. Complex concrete geometries are not only difficult to build but also hard to be effectively reinforced with conventional steel reinforcement because the distribution of the tensile zones is not as simple as that of typical reinforced concrete designs. The key advantage of using shape memory alloys (SMAs) as prestressing reinforcement for topology-optimized concrete bridges is that they can prestress target regions where only tensile stresses are expected. SMAs have a unique thermo-mechanical characteristic, which allows them to recover their original configuration from an excessively deformed state once heated. Using this characteristic, SMA elements can apply prestressing forces wherever and whenever once they are triggered by heat, without any hydraulic jacking system involved. In this study, topology optimization of a two-span bridge girder prestressed with SMA reinforcement is presented to prove the feasibility of using SMAs to produce prestressed lightweight bridge members. During the topology optimization, stress constraint is used to avoid high-stress concentration either from the prestressing or the external live loads. The results of the study prove the efficacy of SMA in prestressing local regions in the topology-optimized bridge girder.

1. Introduction

Topology optimization (TO) is a powerful technique for optimizing the design of a structure by minimizing an objective function, such as compliance or maximum deflection, subject to constraints like total material volume. TO results in a truss-like structure that is lightweight, economical, and environmentally friendly. However, the implementation of TO in the real-world construction industry is impeded by the complex geometry generated by the optimization process. In particular, complex geometry in TO concrete members poses a manufacturing challenge and makes it difficult to control tensile cracks. To prevent tensile cracks in concrete bridges, the construction industry uses pre- or post-tensioning techniques using high-strength steel (HSS) reinforcements. However, with the conventional prestressing methods, it is inevitable to apply prestressing to the entire region of the bridge, even at the regions where prestressing is not necessary, such as compressive zones and end regions. The localized prestressing system using



shape memory alloys (SMAs), which could apply prestressing only at the target region, was proposed by (Sung & Andrawes, 2021) to overcome the limitations of the conventional prestressing systems. The localized prestressing system is a suitable application for the TO concrete member as it has a complex geometry with numerous localized tensile zones, which conventional prestressing system could not effectively control the tensile cracks of the bridge. In this study, the topology of the concrete and the SMA prestressing reinforcement are optimized simultaneously in a commonly used bridge girder to come up with a lightweight truss-like design.

2. Localized Prestressing System Using Shape Memory Alloys

Shape Memory Alloys (SMAs) are a family of materials exhibiting a unique thermo-mechanical characteristic called the shape memory effect (SME). The SMA wires that are extremely deformed can recover their original configuration by activating the phase transformation of the material. The phase transformation occurs when the material is subjected to sufficient stimulation energy, causing its microstructure to reorient. On a macroscopic level, if the material is heated to its phase transformation activation temperature, the excessively deformed martensitic alloy can recover its original form. However, if the material is restrained during heating, recovery stress is generated within the material, which is a source of prestressing force for SMA prestressing applications. Sung & Andrawes, 2021 proposed a localized prestressing system using SMAs that could apply the prestressing effect only at target regions where tensile cracks are expected. Pre-strained SMA reinforcements can be placed at the desired location before casting concrete, and the prestressing force can be applied by activating the SMA reinforcements once the concrete is fully cured. The new system could delay the application of prestressing force, which could significantly reduce the prestress loss from the creep and shrinkage of the early-age concrete. The new SMA-based prestressing system has the potential to reinforce complex local tensile zones within topologically optimized concrete members, eliminating the need for mechanical prestressing. To prove its feasibility, a study was conducted on a continuous-span concrete bridge girder, considering real-world loading conditions as per current design guidelines.

3. Topology Optimization of Prestressed Concrete Bridge Girder

In this study, a two-span continuous girder was selected as an application example which was designed to match the American Association of State Highway and Transportation Officials (AASHTO) Type-II girders with span lengths of 18.28m (Fig.1). The concrete was assumed to have a compressive strength of 55.17MPa. The design load was calculated based on AASHTO LRFD specifications (AASHTO, 2020) under the HL-93 live load. The maximum front and rear axle spacing of 4.27m was used for the HS-20 design truck to maximize the force effect (Fig.1). In the study, the HS-20 truck was located at 9 different locations with 1.22m of intervals as an independent load case. The live load distribution factors for multiple loaded lanes were calculated based on AASHTO LRFD specifications. The HS-20 design truckload was adjusted with a dynamic allowance factor of 33% and a multiple presence factor. The girder was modeled using a hybrid approach with concrete elements modeled as 2D continuum elements and SMA bars modeled as truss elements in MATLAB. Concrete elements were meshed with a 51mm-by-51mm grid with the section width discretized to match the configuration of AASTHTO Type-II girders (Fig.1). The width of the section was considered as the thickness of the 2D-girder model. The SMA reinforcement was placed in layers and meshed using a 102mm-by-102mm grid with diagonal elements considered (Fig.1). Both concrete and SMA elements used linear elastic

material models with SMA reinforcement made of NiTiNb alloy, which exhibits a recovery stress of 550MPa (Sung and Andrawes, 2021).

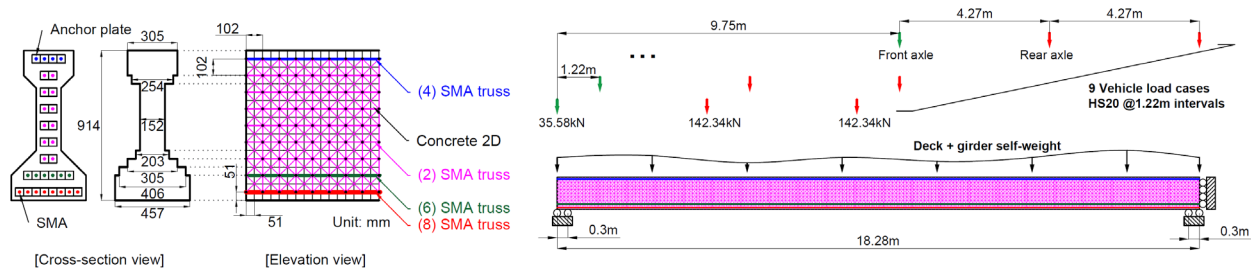


Fig. 1. Cross section and elevation view of the modeled

3.1. Topology Optimization framework

The TO framework was developed in MATLAB based on the work of Amir and Shakour, 2018 with modifications for the SMA-based prestressing system. The developed framework was comprised of two parts: FEM and Optimization module, as shown in the flowchart below (Fig.2). In the FEM module, the system was modeled based on the design variables, and the system equation is solved to get the displacement field (Fig. 2). The design variables (DVs) of the TO are densities of concrete elements (ρ_c) and SMA elements (ρ_s), which are bound from zero to one by the box constraints. The objective of the optimization was to minimize the amount of deformation that occurs in areas where multiple external loads are applied while taking into account the total volume constraints for both concrete and SMA elements. The deformation of each external load case i (ϕ_i) was calculated using the equation shown in Fig. 2, which was similar to finding the compliance of the system, where the external force vector for the load case I is \mathbf{f}_{ext_i} , and the total displacement vector is \mathbf{u}_{total} . To prevent negative values, the deformation of each load case was squared. To take the worst load case into account in objective function evaluation, the Kreisselmeier-Steinhauser (KS) function was utilized to calculate the maximum of ϕ_i for multiple load cases, as described in Fig.2. The KS function was chosen due to its differentiability, which was essential for the optimization process based on gradient descent. The DVs were filtered with density, embedding, and Heaviside filters to ensure the SMA reinforcements were embedded in the surrounding concrete and to avoid checkerboard patterns. The solid isotropic material penalization (SIMP) method was used for the elasticity moduli of the concrete and SMA elements.

The optimization module is comprised of three components: evaluating the objective function, conducting sensitivity analysis, and using the MATLAB function “fmincon” as the optimizer. The objective function is evaluated based on the solution obtained from the FEM analysis, and both the objective and constraint functions underwent sensitivity analysis. The “fmincon” optimizer updates the DVs using gradients calculated from previous iterations. The use of an augmented objective function and the method of adjoint vectors allows for efficient sensitivity analysis. The differentiation of the augmented objective function results in the calculation of the adjoint vector and sensitivity of the i -th objective function (ϕ_i) with respect to the DVs.

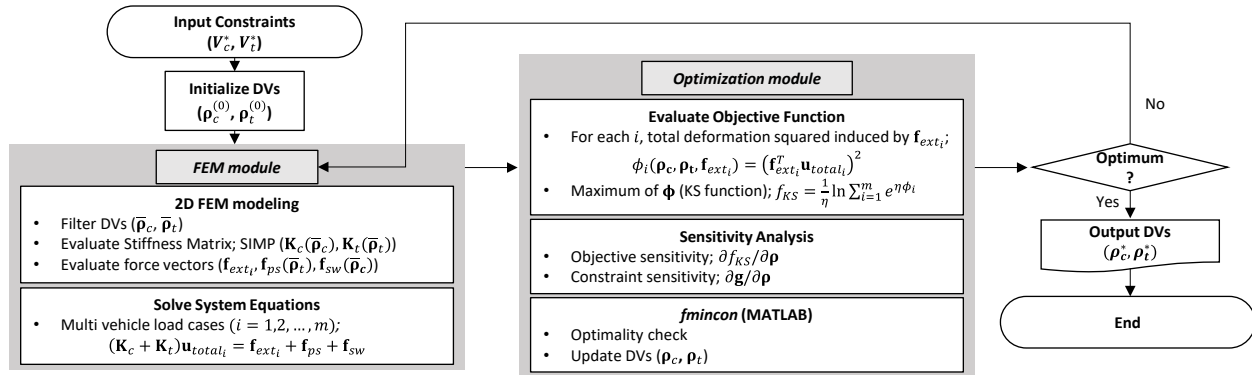


Fig. 2. Flow chart of the topology optimization framework

3.2. Optimization Results

As an example, the concrete volumetric ratio (V_c^*) of 75% and the SMA reinforcement ratio ($\rho_{SMA} = V_t^* / V_c^*$) of 0.35% case were selected to show the optimization result (Fig.3). The optimum solution showed a concrete topology and SMA reinforcement profiles which can be divided into three regions: negative moment, positive moment, and end regions. The negative moment region has SMAs located at the top chord, while the positive moment dominant region has SMAs located at the bottom chord. The end region was heavily prestressed with top reinforcements, which could contribute to uplifting the positive moment region. The optimization results showed that the diagonal reinforcements at the transitional zones near the 5m to 16m sections helped in reducing the deflection at the positive moment dominant region. The optimized girder design satisfied the stress limits as per AASHTO LRFD service I limit states.

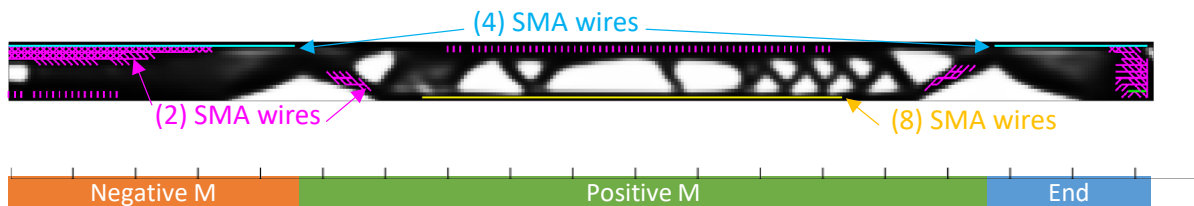


Fig. 3. A half-elevation view of the topology-optimized girder with a concrete volumetric ratio of $V_c^* = 75\%$, and 0.35%

4. Conclusion

This study presented a topology optimization framework for optimizing the design of a continuous prestressed concrete bridge girder using SMAs. The optimized design resulted in 25% reduction in concrete volume compared to conventional designs and satisfied AASHTO LRFD stress limits. The study highlights the potential of using SMAs in topology-optimized concrete structures.



5. References

Sung, M., & Andrawes, B. (2021). Innovative local prestressing system for concrete cross-ties using shape memory alloys. *Engineering Structures*, 247, 113048.

<https://doi.org/10.1016/j.engstruct.2021.113048>

Amir, O., & Shakour, E. (2018). Simultaneous shape and topology optimization of prestressed concrete beams. *Structural and Multidisciplinary Optimization*, 57(5), 1831-1843.

American Association of State Highway and Transportation Officials (AASHTO) (2020). AASHTO LRFD Bridge Design Specifications, 9th.



A Mesoscale Probabilistic Fatigue Crack Initiation Model for Steel Bridges Based on the Modified Fine and Bhat Theory

Fei Jiang^{1*}, You-Liang Ding², Kang Yang³, and Xiao-Nan Zhang⁴

1: Southeast University, Nanjing, China; email: Feijiang1995@outlook.com

2: Southeast University, Nanjing, China; email: civilchina@hotmail.com

3: Southeast University, Nanjing, China; email: 230189498@seu.edu.cn

4: Southeast University, Nanjing, China; email: nanan6677@163.com

*: corresponding author

Keywords: Steel bridges; Mesoscale modeling; Crack initiation; Non-deterministic prediction

Abstract: The safety and durability of steel bridges are strongly limited by the deterioration process of fatigue. The fatigue initiation process accounts for a large proportion of fatigue life. Therefore, performing accurate initiation life prediction can facilitate the fatigue maintenance of such structures. In this study, Fine and Bhat theory was modified to build a mesoscale small crack initiation model, which describes the crack nucleation in grains and the coalescence and propagation of microcracks. A crystal plastic finite element model was established for obtaining the plastic strain energy density parameter for the proposed model. To consider the microstructure uncertainties, the grain size variation was included through inverse transform sampling on the tested grain diameter distribution. Before prediction, the initiation model was calibrated using prescribed historical fatigue data, and Monte Carlo simulation was then conducted to predict the small crack initiation life. The proposed model was validated by performing fatigue testing on full-scale segmental orthotropic steel deck specimens with typical U-rib to diaphragm welded joints.

1. Introduction

The safety, functionality, and durability of steel bridge structures are strongly limited by fatigue deterioration problems. As the increase of external loads and service time, there is a mounting risk of bridge collapse within the designed service life. To provide a reference for the fatigue maintenance activities, it is necessary to perform accurate life predictions for fatigue-vulnerable details.

In fatigue life prediction tasks, the small crack initiation has received much attention since it takes up a large portion of the total fatigue life. Phenomenological models, such as Basquin's model (Basquin, 1910) and Manson-Coffin's model (Coffin, 1956), are still the main approaches for fatigue analysis. However, these models are based on extensive fatigue experiments, which is costly and time-consuming. Besides, macro fatigue limit, material microstructure effect, and notch effect are often sacrificed, which may introduce significant error in some circumstances (Schijve, 2009; Yuan, Zhang, Kim, & Liu, 2017).

In recent years, the mesoscale modeling of the small crack initiation stage has gained popularity. Castelluccio et al. (2014) presented a thorough review on advances in assessing

microstructure-sensitive early-stage fatigue of polycrystals and proposed that further efforts still need be paid on probabilistic methodologies to quantify uncertainty in predicting fatigue initiation life. This study proposed a mesoscale probabilistic fatigue crack initiation model, which aims to accurately predict the fatigue initiation life for steel bridges considering the material microstructure attributes and uncertainties.

2. Fatigue Experiment

An application example based on orthotropic steel deck (OSD) structures was employed to demonstrate the proposed model. The fatigue initiation at the typical U-rib to diaphragm welds was monitored by performing fatigue testing on a full-scale segmental OSD specimen. The specimen and test setup are illustrated in Fig. 1. The specimen consisted of an 18-mm-thick deck plate, two 8-mm-thick longitudinal U-ribs, and two 14-mm-thick transverse diaphragms. The global length, width, and height of the specimens were 2,900, 1,200, and 594 mm, respectively. All the steel components were made of Chinese steel type Q345. The U-rib and diaphragm were connected through fillet welds.

The OSD specimen was fixed to a testing platform by applying a cyclic pressure load with the maximum value of -20 kN, the minimum value of -260 kN, and the loading frequency of 4 Hz. A rigid load spreader was employed to transfer the concentrated actuator force into an approximate uniform area load. To avoid direct rigid contact between the spreader and the specimen, a rubber layer with dimensions of $400 \times 400 \times 54$ mm was positioned between the spreader and the deck plate to simulate a single wheel-tire contact area. During the fatigue testing, strain gauges were adopted to monitor the local fatigue stresses, and the fatigue initiation timing was recorded with the assistance of a hand-held electronic magnifier.

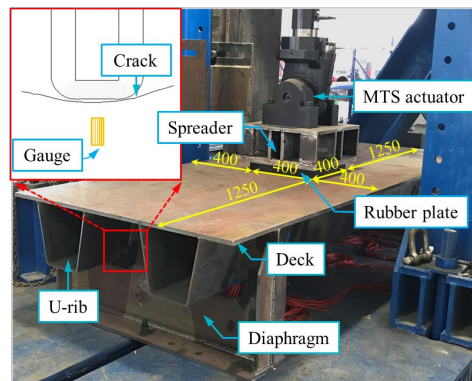


Fig. 1. Fatigue experiment on a full-scale segmental OSD specimen

3. Mesoscale Modeling of Small Crack Initiation

3.1. Modified Fine and Bhat theory

From an energy point of view, Fine and Bhat (Fine & Bhat, 2007) hold an energy barrier must be overcome for forming new surfaces during fatigue crack nucleation. It is presumed that the formation of new surfaces will result in a release of elastic energy from the applied load and accumulated lattice defects. By differentiating the change of Gibbs free energy ΔG due to crack nucleation with respect to the radius a of the half-penny-shaped virtual crack surface, the relationship between nucleation cycle N^* and the critical crack size a^* can be finally derived after designating $d\Delta G/da$ equal to zero:

$$N^* = 4 \frac{\pi E \gamma_s - 2\sigma^2 a^* (1-\nu^2)}{\pi E f^* \varpi} \quad (1)$$

where E is Young's modulus; ν is Poisson's ratio; σ is the fatigue stress range; γ_s is the surface energy of the material; $f^* = ft_m$; f is an energy efficiency factor, describing the portion of stored external work due to slip irreversibility; t_m is the maximum width of the persistent slip bands; $\varpi = \Delta\tau\Delta\gamma_p/2$ is the plastic strain energy density (PSED); $\Delta\tau$ is the shear stress range; $\Delta\gamma_p$ is the plastic shear strain range. In this study, material constants E and ν for the steel Q345 were 210 GPa and 0.3, respectively. An estimated value of 2.4 J/m² was adopted for γ_s of steel Q345 at room temperature.

However, the Fine and Bhat theory only describes the crack formation in a single grain, and it does not account for the propagation and coalescence of microcracks. In this study, the Fine and Bhat theory is modified and extended based on several presumptions to provide information about the small crack initiation life and its corresponding size. It is presumed that (1) the crack formation in every single grain follows the Fine and Bhat theory; (2) the stress concentration at grain boundaries caused by crack formation in the previous grain is the trigger for the start of slip systems in its neighboring grains; (3) the parameters γ_s and f^* remain constant for the crack formation in different grains of a given material; and (4) during cyclic loading, existing single grain cracks coalesce into a small crack, which is instantaneous and does not consume the number of cycles. Fig. 2 presents the small crack initiation process described by the modified theory. The crack surface forms first in grain 1, then in grain 2, and so on. Growth paths are set from grain 1 to the crack front of the small crack after coalescence. Therefore, the fatigue initiation life can be calculated as:

$$N_{in} = \sum_{i=1}^n 4 \frac{\pi E \gamma_s - \sigma^2 d_i (1-\nu^2)}{\pi E f^* \varpi} \quad (2)$$

where d_i corresponds to the diameter of the i th grain in the growth path. N_{in} is linearly related to the total path length $\sum d_i$ from Eq. (8), so the initiated small crack surface is half-penny-shaped, which is consistent with the current assumptions about the short crack shape for steel bridges.

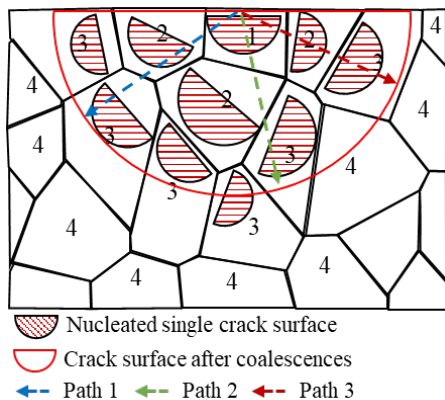


Fig. 2 Small crack initiation process described by the modified Fine and Bhat theory

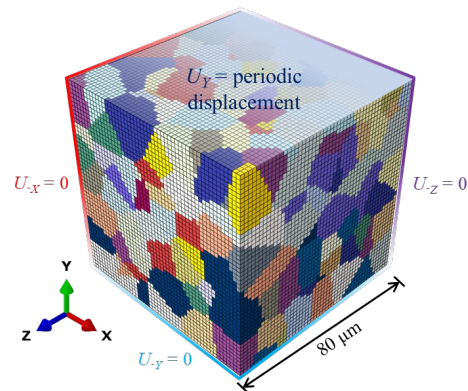


Fig. 3 Illustration of the CPFE simulation model

3.2. Crystal plasticity finite element model

To obtain the PSED $\bar{\omega}$, crystal plasticity finite element (CPFE) simulation was conducted based on the information provided by electron backscatter diffraction (EBSD) testing. A representative volume element (RVE) model for microstructure at the fatigue initiation point was established by Voronoi tessellation, as illustrated in Fig. 3. The RVE model had a length of 80 μm and contained 512 grains according to the measured average grain diameter. A periodic displacement was applied on the Y surface to realize the repetitive deformation at the crack initiation position.

4. Probabilistic Prediction of Fatigue Initiation Life

4.1. Calibration of small crack initiation model

The small crack initiation process is non-deterministic due to the microstructural uncertainties of grain size variations. To consider this, the term $\sum_{i=1}^n d_i$ was included in Eq. (2). The parameter f^* should be accordingly treated as a random variable F^* and calibrated before life prediction. Inverse transform sampling was performed on the grain diameters d along the surface crack growth path according to the EBSD testing results. During the k th sampling, a sequence of grain diameters $(\{d_i\}_{i=1}^n)_k$ was generated. This randomly sampled diameter sequence was further filtered given the constraint of the handshake small crack length, as described by the inequality (3).

$$\left| d_1 + 2 \sum_{i=2}^n d_i - a \right| \leq E_a \quad (3)$$

where a is the handshake surface crack length and equal to 0.5 mm in this study; E_a is the allowable sampling error, which was set to 1 μm . By delivering the sample $(\{d_i\}_{i=1}^n)_k$ along with historical initiation (σ, N_{in}) into Eq. (2), the k th realization f_k^* of F^* was obtained. The sampling process was repeated, and 12,451 samples were finally produced. The frequency density fitted by the lognormal distribution was obtained, as shown in Fig. 4. During the experiment, the fatigue initiation of two U-rib to diaphragm welds designated as D1 and D2 was recorded. The result ($\sigma = 298.2$ MPa, $N_{\text{in}} = 110,000$ cycles) of D2 was herein used as the historical data for the calibration, while the result ($\sigma = 340.8$ MPa, $N_{\text{in}} = 70,000$ cycles) of D1 was employed to validate the life prediction results as described below.

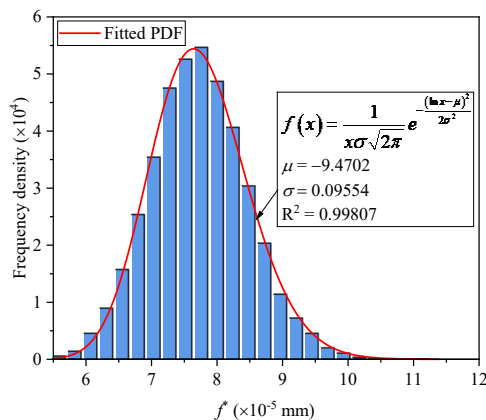


Fig. 4 Probability distribution of the calibrated F^*

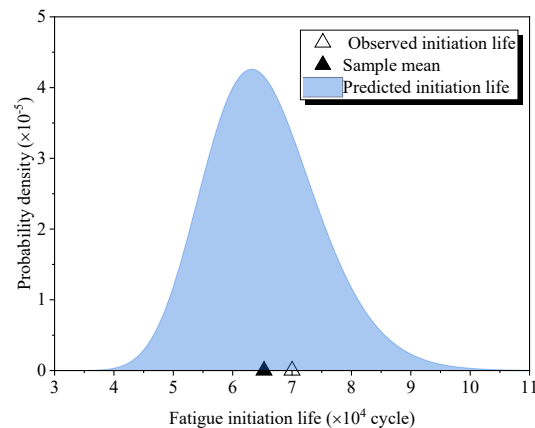


Fig. 5 Probability distribution of the predicted crack initiation life of welded joint D1

4.2. Probabilistic prediction of fatigue initiation life

After obtaining the calibrated F^* distribution, Eq. (2) was well-equipped to predict the small crack initiation life using Monte Carlo simulation (MCS). In this study, the fatigue initiation life at welded joint D1 was predicted using the proposed method. Based on processes similar to the calibration stage, a sequence of grain diameters $(\{d_i\}_{i=1}^n)_k$ and f_k^* were generated during the k th sampling. These generated parameters were submitted into Eq. (2) to output the k th sample of the predicted initiation life N_{ink} . Finally, the life distribution was obtained, as shown in Fig. 5. It can be observed that the mean of the distribution is very to the experimentally observed life result. This demonstrates the validity of the proposed method.

5. Concluding Remarks

This study proposed a novel method for mesoscale modeling of the small crack initiation life of welded joints in steel bridges. The Fine and Bhat theory was modified to further account for the microcrack propagation and coalescence during the fatigue initiation stage. Based on the modified theory, the initiated small crack surface was half-penny-shaped, which is consistent with the current assumptions about the short crack shape for steel bridges. To consider the influence of microstructure uncertainties, the model parameters were treated as random variables, and the model calibration and life prediction methods were outlined. The validity of the proposed method has been demonstrated by fatigue testing on a full-scale segmental OSD specimen.

6. References

- Basquin, O. H. 1910. The exponential law of endurance tests. American Society for Testing and Materials Proceedings, 625–630.
- Castelluccio, G. M., Musinski, W. D., and McDowell, D. L. 2014. Recent developments in assessing microstructure-sensitive early stage fatigue of polycrystals. Current Opinion in Solid State and Materials Science, 18(4), 180–187.
- Coffin, L. 1956. Design aspects of high-temperature fatigue with particular reference to thermal stresses. Transaction of the ASME, 78, 527–532.
- Fine, M. E., and Bhat, S. P. 2007. A model of fatigue crack nucleation in single crystal iron and copper. Materials Science and Engineering: A, 468–470, 64–69.
- Schijve, J. 2009. Fatigue of structures and materials (2nd ed.). Dordrecht: Springer.
- Yuan, H., Zhang, W., Kim, J., and Liu, Y. 2017. A nonlinear grain-based fatigue damage model for civil infrastructure under variable amplitude loads. International Journal of Fatigue, 104, 389–396.



Tension Estimation Method for Linked Suspenders Based on Identified Mode-shapes

Chien-Chou Chen^{1*}, Wen-Hwa Wu², and Yen-Chih Peng³

¹: National Yunlin University of Science and Technology, Douliu and Ynlin;
email: ccchen@yuntech.edu.tw

²: National Yunlin University of Science and Technology, Douliu and Ynlin;
email: wuwh@yuntech.edu.tw

³: National Yunlin University of Science and Technology, Douliu and Ynlin;
email: a0931256616@gmail.com

Keywords: tension estimation; linked suspenders; mode shape; effective vibration length

Abstract: To release the effect of complicated boundary condition on determining accurate cable force, an innovative approach based on mode shape was proposed recently by the authors. With multiple measurements to identify modal frequencies and mode-shape ratios, it has been verified numerically and then experimentally that excellent accuracy in tension estimation can be achieved with precise fitting of half-wavelength for the sinusoidal component of each chosen mode shape. This study aims to explore the feasibility of this approach in determining the tension of linked suspenders of arch bridges. It is confirmed with finite element method that the mode shapes in each segment of the linked strands still mostly follow a sinusoidal function with a variation only observable near the boundary or linkage due to the influence of hyperbolic components. The numerical analysis results show that accurate tension can be obtained with this approach. Then, the mock-up test with linked strands in laboratory is further conducted to verify the applicability of the approach in practice. The experimental results demonstrate that the errors of computed tension are pretty small. It is particularly noteworthy that the measurements together with careful mode selection and appropriate choice in covering range of measurement are all critical to hold such a superb accuracy.

1. Introduction

For efficiently tackling the difficulties associated with complicated boundary constraints, an innovative concept combining mode shape functions and modal frequencies was recently proposed by the authors to develop an accurate tension estimation method. The key of this method is to collect multiple synchronized vibration measurements on a tension member and then identify the mode shape values at different sensor locations. The corresponding effective vibration length for each considered mode can then be independently obtained by best fitting the sinusoidal component of mode shape. Previous works have indicated that the installation of sensors cannot be concentrated near one end (Chen, 2018). Otherwise, it would be difficult to obtain reasonable effective vibration lengths through optimal fitting. Such a measurement requirement, however, could greatly hinder popular applications of this method because a mobile crane is indispensable for the sensor installation close to the high end in the case of stay cable or suspender. Therefore, this research group has newly developed a novel approach for convenient

cable tension estimation simply based on local vibration measurement to fit partial mode shape. It has also been verified that excellent accuracy in tension estimation can be achieved with precise fitting of half-wavelength for the sinusoidal component of each mode shape when 1/3 or more limited coverage range is adopted (Chen, 2022).

New concept of this method is based on the consideration of the mode shape function of a tension member ignoring sag effect is the combination of a sinusoidal component and a hyperbolic sinusoidal component (Chen, 2018). When zero-crossings of the sinusoidal component are identified, the frequencies of the tension member can be explicitly expressed as Eq. (1).

$$f_k^2 = \frac{T + \frac{\pi^2 EI}{(L_k/k)^2}}{4\bar{m}(L_k/k)^2} \quad (1)$$

in which f_k represents the natural frequency of the mode with k half wavelengths in Hz, \bar{m} denotes the mass per unit length, E is the Young's modulus, I stands for the cross-sectional area moment of inertia, L_k/k is the half wavelength of the sinusoidal component and L_k is named as the effective vibration length of considered range. Eq. (1) is similar with the frequency equation of simple supported beam except that the half wavelength of the sinusoidal component is used to replace beam length. Accordingly, Eq. (1) can be applied to the tension member with more complicated boundary constraints. Nonetheless, more complicated multiple measurements are needed for identifying mode shape values to fit the sinusoidal component. To best fit the identified mode shape values at n measurement locations for each considered mode, the corresponding error function has been suggested as (Chen, 2022):

$$e_k \equiv \sum_{j=1}^n \left\{ a_k \sin \left[\frac{k\pi(x_j + d_k)}{L_k} \right] - \hat{\phi}_{jk} \right\}^2 \quad (2)$$

where a_k and d_k denote the amplitude coefficient and shifting parameter of the mode with k half wavelengths, respectively, and $\hat{\phi}_{jk}$ represents the identified mode shape value at x_j . Because there is no need to consider boundary condition, it is believed that this method could be applied to more complicated tension members in addition to single and uniform cable or suspender. Linked suspenders are, therefore, selected to be the target for the further study in this paper.

2. Numerical Exploration

The numerical analysis is performed to explore the applicability and accuracy of the method based on mode shape applied on linked-cable system. Two linked strands chosen for conducting the following mock-up test in laboratory are simulated in the finite element analysis with SAP2000 software. The analysis model is shown in Fig.1 and then the modal analysis can be executed to find the modal frequencies and mode shapes that serve as identified modal parameters. Five cases with different combinations of cable force and flexural rigidity, in which

hyperbolic sinusoidal components have different levels of contribution on mode shapes, are arranged for discovering the modal characteristics of linked-strand system. The results from the modal analysis reveal two anticipated features of modal parameters. First, different from single strand with nearly arithmetic-sequence modal frequencies, linked-strand possesses irregular modal frequencies. Second, the mode shapes in each sub-system, which is divided with the linked point, still present similar sinusoidal function except in the neighborhood of linked point and model boundary, as shown in Fig. 2, which is essential for the application of this method.

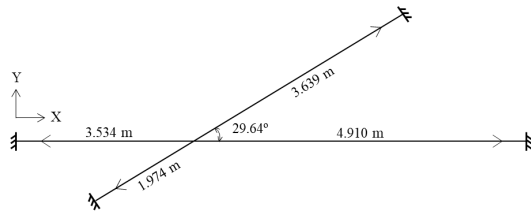


Fig. 1. Finite element analysis model

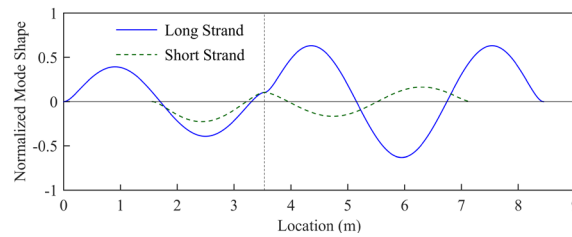


Fig. 2. Mode shape of linked system

With the prepared FE models, five sensors, either concentrated at two ends or with uniform spacing, are deployed within five considered converge ranges, $0.5l_s$, $0.6l_s$, $0.7l_s$, $0.8l_s$ and $0.9l_s$. l_s represents the length of each sub-system. For the two-end deployment, five sensors are divided into two groups, two sensors at one end and three sensors at the other ends. The numerical mode shape values corresponding to each sensor location are then optimally fitted to obtain the effective vibration length for each mode based on Eq. (2). To more systematically examine the accuracy of effective vibration length obtained from different sensor deployments, the corresponding exact solutions are attained from Eq. (1) and taken as the reference values. Due to the limitation of page number, only one mode shape from out-of-plane measurement and one mode shape from in-plane measurement of the case 1, in which two strands have same tension and flexural rigidity, are demonstrated in this paper. By comparing with the corresponding exact values solved from Eq. (1), the error percentages of the optimal effective vibration length for longer strand are computed and then plotted in Fig. 3 for in-plane measurement and Fig. 4 for out-of-plane measurement. Blue and green dots represent the error percentage of the calculated effective vibration length for uniform deployment and deployment concentrated at two ends, individually. Two red lines stand for the threshold of $\pm 0.5\%$ relative error, which can also be deemed $\pm 1.0\%$ relative error of strand tension. From Figs. 3 and 4, it is clear to observe that the error percentages from the deployment concentrated at two ends are more stable than those from the uniform deployment and increase gradually with coverage range until $0.9l_s$ where it is about 0.5% . As for uniform deployment, there is one jumped error displayed at $0.9l_s$ in Fig. 3 and one jumped error at $0.8l_s$ in Fig. 4, which are caused by the peculiar sensor deployment, all sensors near the zero crossings of mode shape. For the other four cases, similar results are also observed.

3. Experimental Verification

Referring to the analysis results of the finite element model, mock-up test with two prestressed 7-wire strands of 12.7 mm in diameter linked together and arranged as the drawing shown in Fig. 1, is conducted in laboratory for further assessing the applicability of the method based on mode shape applied on linked suspenders in practice. MENS capacity accelerometers SDI2210-002 fabricated by Silicon Design Inc. were used to measure the ambient vibration signals of

experimental linked strands. 300 seconds of duration was taken for each measurement in the experiment with a sampling rate 200Hz for longer strand and 500 Hz for shorter strand, individually. Similar to the simulation cases in numerical analysis, three cases with different strand tensions, which took the effect of hyperbolic component into account, were verified. Both in-plane and out-of-plane vibration signals were measured for each case. Five sensors concentrated at two ends of the measured strand was deployed within several chosen coverage ranges. To identify the modal frequencies and mode shape ratios of the experimental strands, discrete Fourier transform (DFT) was performed on the synchronized measurements. With the identified mode shape values, optimal process was further implemented with Eq. (2) for determining the effective vibration length of each mode. Then, the optimal value of strand tension was computed with three selected modes. Since no precise values of strand tension and flexural rigidity are available to calculate the exact effective vibration length as in the numerical examples, instead of effective vibration length, the strand tension determined from the measurements of independent strands with full coverage concentrated at two ends were adopted as the reference values in the experimental study.

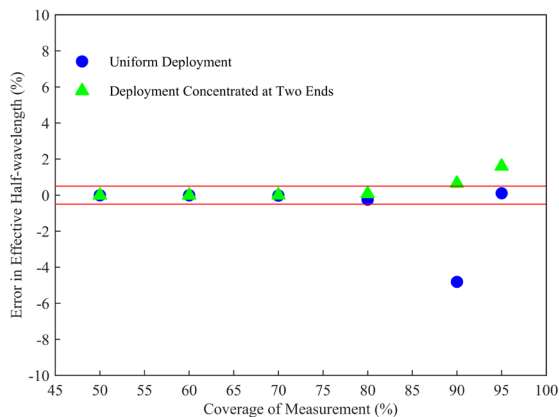


Fig. 3. Deviation of effective vibration length (out-of-plane measurement)

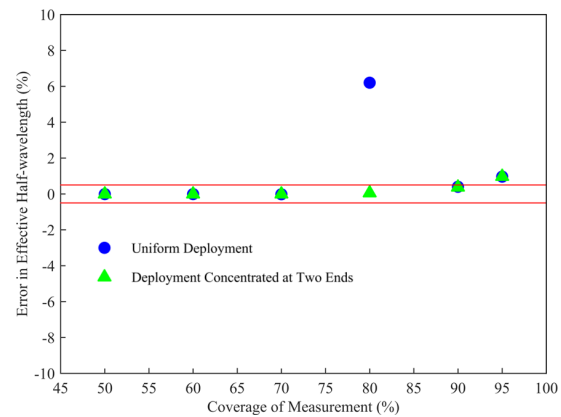


Fig. 4. Deviation of effective vibration length (in-plane measurement)

Based on the numerical investigation in the previous section, the effective vibration lengths obtained from two useless fitting curves of mode shape, coverage range less than one half wavelength or the group with two sensors located at the peak or valley of the mode shape, are not taken for the calculation of strand tension. In addition, the effective vibration length attained from the fitting mode shape with larger error is also not considered. In comparison with the reference values, two important points are observed from the analysis results of three considered cases. First, the deviation of the strand tensions calculated from in-plane measurement is much worse than that from out-of-plane measurement, that could be caused by the damping effect of the rubber pad of linkage device. Second, the largest deviation of the computed tensions of two strands is approximately 2%. Although the results from the numerical study and mock-up test validate that the method based on mode shape can estimate high accuracy tension of linked strand, it is particularly noteworthy that the measurements together with careful mode selection and appropriate choice in covering range of measurement are all critical to hold such a superb accuracy for the practical application on the linked suspender of arch bridges.



4. References

Chen, C.C., Wu, W.H., Chen, S.Y., Lai, G.L. 2018, A novel tension estimation approach for elastic cables by elimination of complex boundary condition effects employing mode shape functions, *Engineering Structures*, 166 , 152-166.

Chen, C.C., Wu, W.H., Liu, Y.T. and Lai, G.L. 2022, A Convenient Cable Tension Estimation Method Simply Based on Local Vibration Measurements to Fit Partial Mode Shapes, *Engineering Structures*, 272, Paper No. 1150081.



Research on Crack Damage Model and Size Effect of Flexible Fiber Reinforced Recycled Concrete

Yongcheng Ji¹, Yanmin Jia¹, Dayang Wang^{1*}, Yanwei Jia¹, and Zhiyang Pei¹

¹: College of Civil Engineering and Transportation, Northeast Forestry University, Harbin 150040, China; email: yongchengji@126.com

*: corresponding author

Keywords: Recycled concrete, Flexible fiber, Microscopic simulation, Compressive strength, Size effect

Abstract: A mesoscale numerical model is presented to study the fracture damage mechanism of flexible fiber-reinforced brick aggregate recycled concrete (FFF-BAC). The model considers that cement mortar matrix and flexible fiber are combined into a homogeneous material, namely flexible fiber reinforced cement mortar matrix (FF-MC), and FF-MC is combined with coarse aggregate and interfacial transition zone to form fiber reinforced recycled concrete. Combined with the experimental results of FF-MC in the research literature, the mechanical constitutive model of FF-MC is determined. The numerical model of FFF-BAC was established, and the effect of brick aggregate (BA) content and size on the mechanical properties of FFF-BAC is studied based on the new model.

1. Introduction

Many scholars use the method of mesoscopic numerical simulation to study the reinforced concrete with large stiffness fiber. Sun et al. (2019) studied the compression, splitting and bending properties of basalt fiber concrete through mesoscopic numerical simulation experiments. However, the research on the numerical simulation of flexible fiber reinforced concrete is lacking. This is because the flexible fiber itself is very thin, and millions or even tens of millions of fibers are needed in an ordinary recycled concrete test block, and it is difficult to simulate the flexible fiber reinforced recycled concrete with the current computer level.

China specification GB50242019 has stipulated the conversion factor between non-standard concrete cube and standard concrete cube. However, there are few researches on the size effect of recycled concrete. Zhang et al. (2019) studied the effect of size effect on compressive strength of recycled concrete with waste concrete aggregate with different substitution rates. The higher the replacement rate of recycled aggregate, the lower the effect of size effect. Su et al. (2022) studied the size effect of the compressive strength of recycled concrete, and found that the size effect showed an increasing trend with the increase of the replacement rate of recycled aggregate, and the size effect degree was about 1.4 times that of ordinary concrete at the replacement rate of 100% recycled aggregate. In summary, whether the size effect of recycled concrete is enhanced with the increase of recycled aggregate content. The authors believe that the inconsistent conclusions are related to the quality of recycled aggregate.

This article proposes a numerical model to study FFF-BAC, and based on this model, the size effect of FFF-BAC is studied.

2. Experimental Program

2.1. Compression constitutive of fiber reinforced cement mortar matrix

In this paper, Zhou(2015) proposed a stress-strain relationship model for FF-MC under compression. The stress-strain relationship of the ascending section can be expressed as:

$$\sigma = \begin{cases} E_0 \varepsilon & (0 < \varepsilon < \varepsilon_{0.4}) \\ E_0 \varepsilon (1 - \alpha) & (\varepsilon_{0.4} < \varepsilon < \varepsilon_0) \end{cases} \quad (1)$$

$$\alpha = \frac{a E_0 \varepsilon}{f'_{cr}} - b \quad (2)$$

Among them, a and b are 0.308 and 0.124, respectively. Considering the post-peak localization characteristic of ECC, the stress-deformation curve is introduced to describe the post-peak behavior of ECC. Bilinear curves are described as follows:

x_l and σ_l are the deformation and stress at the inflection point of the softening curve, and x_0 and f'_{cr} are the deformation and stress at the peak load. That is, the stress and deformation at the peak load, the stress and deformation at the inflection point, and the stress and deformation at any point on the curve. Statistical analysis of the test results shows that x_l and σ_l are $x_l = 1.5x_0$ and $\sigma_l = 0.5 f'_{cr}$, respectively.

$$\begin{cases} \sigma = m(x - x_0) + f'_{cr} & (x_0 < x < x_l) \\ \sigma = n(x - x_0) + f'_{cr} & (x_l < x < x_{\max}) \end{cases} \quad (3)$$

2.2. Compression constitutive of fiber reinforced cement mortar matrix

In this paper, a simplified bilinear hardening model proposed by Li (2009) is adopted. The structure consists of two stages, namely, no damage stage and stable damage stage. See equation (4) for the tension constitutive formula.

$$\sigma = \begin{cases} E_{nt} \varepsilon & (\varepsilon \leq \varepsilon_{nt}) \\ \sigma_{nt} + E_{tu} (\varepsilon - \varepsilon_{nt}) & (\varepsilon_{nt} < \varepsilon \leq \varepsilon_{tu}) \end{cases} \quad (4)$$

Where: $E_{nt} = \frac{1}{10} \times \frac{\sigma_{nt}}{\varepsilon_{nt}}$; E_{tu} is the elastic modulus of hardening stage. E_{nt} is the elastic modulus of the elastic phase. σ_{nt} is the cracking stress, ε_{nt} is the cracking strain, σ_{tu} is the ultimate stress, ε_{tu} is the ultimate strain.

2.3. Fiber reinforced cement mortar matrix

Chen conducted compressive strength test and splitting tensile strength test of PVA reinforced mortar. The detailed test process is shown in reference (Chen, 2019). The mechanical indexes of FF-MC are shown in Table 1.

Table 1. FF-MC mechanical indicators

Group	Compressive strength (MPa)	Modulus of elasticity (MPa)	Poisson's ratio	Splitting tensile strength (MPa)
FF-CM	42.36	24600	0.206	6.39

The mechanical index of Table 2 is put into formula (1) - formula (3) to draw the compression constitutive model of fiber mortar, as shown in Fig. 1(a). Bring the formula in Table 3 into formula (4) to draw the tension constitutive model of FF-MC, as shown in Fig. 1(b).

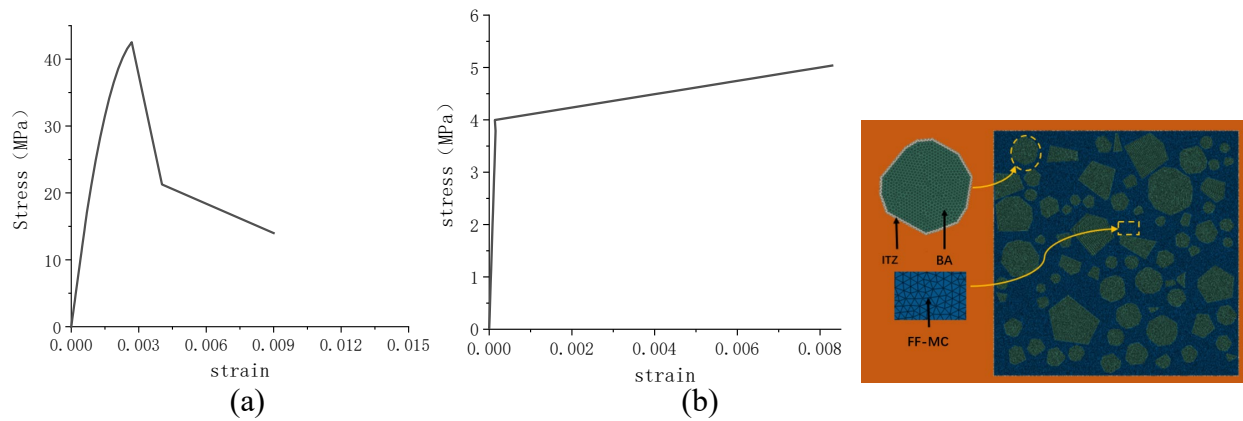


Fig. 1. (a)tension constitutive,(b) compression constitutive **Fig. 2.** Micro numerical model

3. Numerical Simulation

3.1. Numerical model of random aggregate

In this paper, ABAQUS was used to establish a random aggregate model of recycled concrete. The typical model diagram is shown in Fig. 2. The volume fraction of aggregate is about 45%. The thickness of ITZ is set to 0.5mm. The matrix of fiber and cement mortar is regarded as a homogeneous material. Three node planar stress triangle element (CPS3) is used in the grid element.

3.2. Material parameter

The mechanical behavior of cement mortar and ITZ is similar to that of concrete, so the concrete Plastic damage model (CDP model) in ABAQUS finite element software is used to describe its mechanical behavior. The mechanical parameters of each microscopic component used in this paper are shown in Table 2, and the values of each parameter are mainly taken from literature (Jayasuriya 2020).

Table 2. Material parameters

Group	Expansion Angle	Eccentricity	f_{c0}/f_{b0}	k	Modulus of elasticity	Poisson's ratio
BA(Mathew)	30	0.1	1.16	0.6667	16000	0.2
NA(Jayasuriya)	30	0.1	1.16	0.6667	70000	0.16
FF-MC	30	0.1	1.16	0.6667	28960	0.22
ITZ(Jayasuriya)	15	0.1	1.16	0.6667	26000	0.22

3.3. Numerical simulation result

Fig. 3. shows the variation law of FFF-BAC compressive strength with different BA content with section size. As mentioned above, the compressive strength decreases with the increase of brick aggregate content and decreases with the increase of specimen size. The relationship between the compressive strength of FFF-BAC and the specimen size was linearly fitted. The slope of the linear fitting line is K, which is used to represent how fast the compressive strength of the reclaimed concrete changes with the increase of the specimen size. It can be seen that with the increase of BA content, the K of FFF-BAC gradually increases, indicating that the size effect of recycled concrete is inhibited with the increase of BA content, which corresponds to the above description.

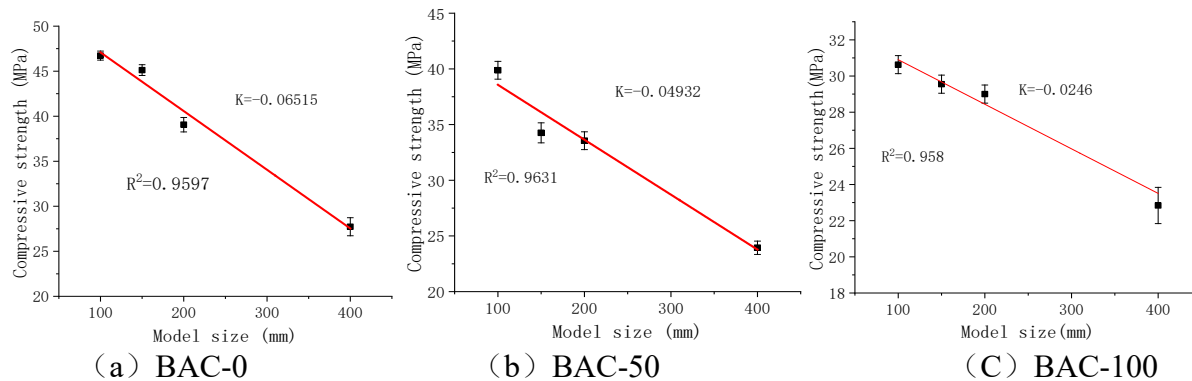


Fig. 3. FFF-BAC stress-strain curves with different BA substitution rates and different cross-section sizes

4. Conclusion

With the increase of BA content, the size effect coefficient increases, the slope K of the linear fitting line between compressive strength and cross-section size gradually increases, and the size effect of FFF-BAC is suppressed.

5. References

Sun X, Gao Z, Cao P 2019, Mechanical properties tests and multiscale numerical simulations for basalt fiber reinforced concrete, *Construction and building materials*, 202: 58-72.

Zhang Li, Yu Zhenpeng, Shen Li, Sun Xue, Xie Xinghua 2019, Study on size effect of compressive strength of recycled concrete with different replacement rates, *New Building Materials*,46(03):18-21+87.



- Su Jie, Zhu Jun, Shi Caijun, Fang Zhi 2022, Size effect on compressive strength of reclaimed concrete strengthened by silica fume, Journal of Hunan University (Natural Science Edition),49(05):174-180.
- Zhou J, Pan J, Leung C K Y 2015, Mechanical behavior of fiber-reinforced engineered cementitious composites in uniaxial compression, Journal of materials in civil engineering, 27(1): 04014111.
- Li Hedong 2009, Experimental study on Ultra-high toughness cement-based Composites , Dalian University of Technology. (in Chinese)
- Chen Yadi 2019, Study on Fiber pull-out Test and macroscopic Mechanical Properties of fiber Reinforced cement-based Materials, Hefei University of Technology.
- Mathew A A, Saibabu S, Mohan V 2021, Analysis of Strains in Brick Masonry Prism Using ABAQUS, Proceedings of SECON 2020: Structural Engineering and Construction Management Springer International Publishing, 883-897.
- Jayasuriya A, Adams M P, Bandelt M J 2020, Generation and numerical analysis of random aggregate structures in recycled concrete aggregate systems, Journal of Materials in Civil Engineering, 32(4): 04020044.
- Raj A, Borsaikia A C, Dixit U S 2020. Finite Element Modeling of Autoclave Aerated Concrete (AAC) Masonry for Estimation of Strength, Manufacturing Engineering: Select Proceedings of CPIE 2019. Springer Singapore, 511-524.



Finite Element Analysis Model of Prestressed Concrete Girder through Nonlinear Material Properties Correction of Strand

Do-Yeon Kim¹, Young-Ji Park¹, Jin-Woong Choi², Young-Jin Kim³,
Il-Young Jang¹, and Seong-Kyum Kim^{1*}

¹: Kumoh National Institute of Technology, Gumi, Korea; email: skim@kumoh.ac.kr

²: Korea Expressway Corporation Research Institute, Hwaseong, Korea; email: jchoi@ex.co.kr

³: Korea Concrete Institute Research Center, Seoul, Korea; email: kimcrete@naver.com

*: corresponding author

Keywords: FEA; PS strand; PSC girder; Nonlinear material correction; Optimization

Abstract: This paper proposes a helical strand modeling for finite element analysis of prestressed concrete structures, which is widely applied worldwide. Structural analysis using nonlinear finite element analysis is being used to evaluate the performance of structures and predict the behavior instead of structural experiments that require a lot of time and effort. For this purpose, detailed modeling of all member elements is being built, but the helical strand, one of the important members of the prestressed concrete structure, is difficult to construct a precise model because of the structural shape and material specificity such as post-tension compressive force within the elastic range. Therefore, in this study, the stress strain curve results from the tensile test results of prestressed strands used for prestressed concrete girder and tensile analysis through Abaqus were used to correct the stress strain curve for material properties containing non-linear behavior. The derived finite element model can be used as a model that shows similar mechanical properties in a shape like a round steel bar, out of the complex helical strand shape, and contributes to obtaining more efficient and accurate analysis results. In this process, the evolution algorithm used for optimization classifies objects that can approximate the objective function, determines the reaction force according to the displacement through repeated calculations through re-analysis 50 times, and corrects it in the round steel bar model to obtain the results of actual prestressed strands. Stress and properties of round steel bar model were allowed to be applied. It is expected that these results can be utilized as a model that can reflect material specificity while simplifying the model for prestressed structural analysis.

1. Introduction

PS strands are twisted strands of cold-worked steel wires after patenting and then bluing. PS strands have high strength because they are heat-treated to form a sorbite-like pearlite structure, which increases their tensile strength. However, Abaqus cannot implement the material properties of twisted steel wire after cold working because it cannot simulate the chemical composition transformation that occurs during heat treatment. If the material properties of the PS strand are used in the material properties of the steel bar, the behavioral changes due to differences in shape will not be reflected in the analysis. Therefore, the performance of the PS

strand can be obtained by applying the corrected material model derived through nonlinear material property optimization, and more accurate analysis results can be obtained when applied to prestressed concrete girders. Additionally, Modeling the strand as steel bar not only reduces penetration problems between elements, but also ensures convergence in analysis, improves analysis efficiency, and makes modeling more convenient.

2. Analysis Preparation

In this paper, a finite element analysis of the strand and steel bar was performed using the Abaqus program. The strand was composed of 7 wires, where a center wire was enclosed tightly by 6 helical wires, resulting in a total diameter of 27 mm. The steel bar was also modeled with a 27 mm diameter, and the length of both the strand and steel bar was 2000 mm. The elastic properties are shown in Table 1, and the plastic properties were set by referring to a previous study (Chueachom, K. and Sirimontree, S. 2015).

Table 1. Material properties of strand

Parameter	Value
Density, kg/m ³	7,850
Young's Modulus, Pa	2E+11
Poisson's ratio	0.3

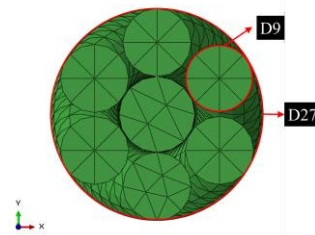


Fig. 1. Cross section of PS strand model

Due to its complex geometry, strand is more difficult to model and analyze using numerical methods than normal steel bar. The strand is a shape in which several steel bars are twisted together, and as it has many curved surfaces in contact, penetration between elements occurs in both horizontal and vertical directions, even if the aspect ratio quality of the mesh is fine. (Lin Lu et al. 2022) Therefore, we used a 10-node modified quadratic tetrahedral mesh for the strand model to effectively divide the model, and an 8-node linear hexahedral mesh for the steel bar model. The interaction between each wire in the strand was defined by the General Contact in Abaqus, and the contact properties were set as hard contact with a coefficient of friction of 0.2. To apply the load history over time and derive a result over a time increment, the analysis was conducted through the Dynamic/Explicit solver. At both ends of the strand and steel bar, 0.1 m were tied by coupling to set a reference point, with one side fixed and the other side tensioned. The tensile speed of the analysis was applied at a constant speed of 0.5 m/s.

3. Material Properties Correction

Nonlinear material property correction was performed using the optimization program Isight to correct the performance of the steel bar model by matching it to that of the prestressed concrete girder strand. The correction components were set using Abaqus and Data Matching. In Data Matching, the reaction force-displacement graph of the reference value strand was set as a target, and the objective was to minimize the sum of the absolute area differences with the simulation value of the steel bar. The technique used for correction in Isight was the Evolutionary

Optimization Algorithm (Evol). The design variables were the Young's modulus and plastic properties of the strand.

4. Results and Discussion

In Fig. 2(a), the strand and steel bar were initially stretched a total of 0.06 m at a speed of 0.5 m/s. However, it was determined that the model had fractured at the tensile point of 0.02 m after reaching the ultimate strength and necking. Furthermore, the elements were abnormally distorted after the fracture occurred. In a real experiment, if a load is applied after necking, the specimen would be fractured. However, in finite element analysis, the elements can withstand the load after necking without fracture. Since the value after fracture is meaningless in material property correction and does not need to be optimized, the analysis and optimization were conducted up to 0.02 m to avoid considering the conditions after fracture. The results are shown in Fig. 2(b).

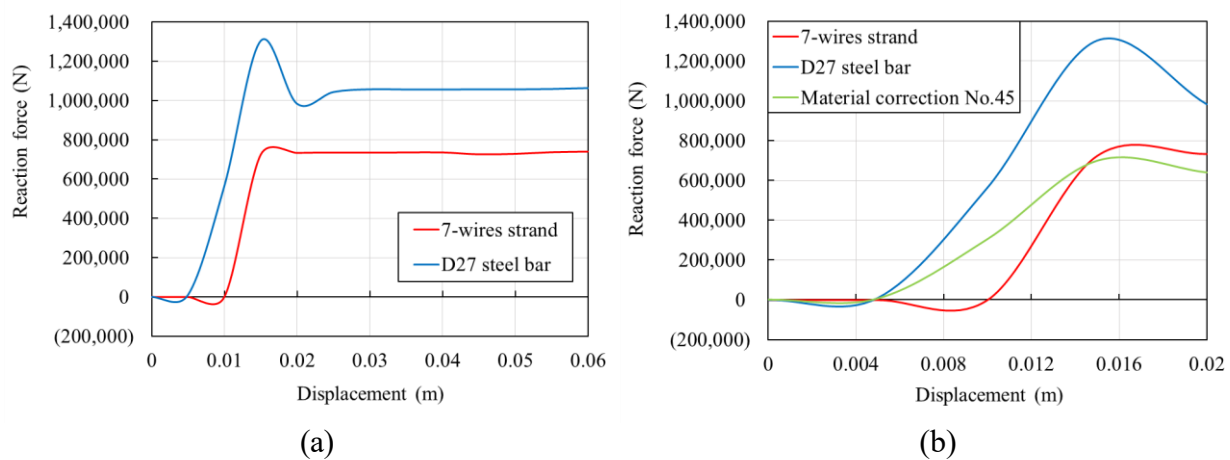


Fig. 2. Behavior of Reaction force-Displacement: (a) 0.06 m tensile behavior of 7-wires strand, D27 steel bar; (b) 0.02 m tensile behavior of 7-wires strand, D27 steel bar and Material correction No.45

In Fig. 2(b), the ultimate strength of the steel bar was 1,350 kN, which showed a 60% difference compared to the ultimate strength of the strand of 800 kN. However, after material property correction, the ultimate strength of the corrected steel bar was 700 kN, which was only 12.5% different from the target strand, and the trend of the reaction force-displacement graph became similar. In Fig. 3(a), the stress distribution according to the tension of the strand, steel bar, and corrected steel bar was confirmed. In all three models, the maximum stress occurred at the fixed end, and the corrected steel bar had a maximum stress that was 35% lower than the strand. It was observed that the strand had maximum stress occurring at the fixed end, while the steel bar had uniformly distributed maximum stress at all elements except the fixed end. However, as a result of optimizing material properties, the stress distribution of the steel bar tended to concentrate at the fixed end, similar to the strand. Out of the total 50 cases, minimized objective result was derived in the No. 45. As shown in Fig. 3(b), the tendency of the plastic curve of the corrected results was very different from the

reference. In addition to the plastic area of material properties, Young's Modulus set with variable decreased by 50% from $2e+11$ to $1.08e+11$ as a result of optimization. The reason for the significant difference in material properties and trends from previous results is thought to be due to the large difference in reaction force-displacement curves between the strand and steel bar.

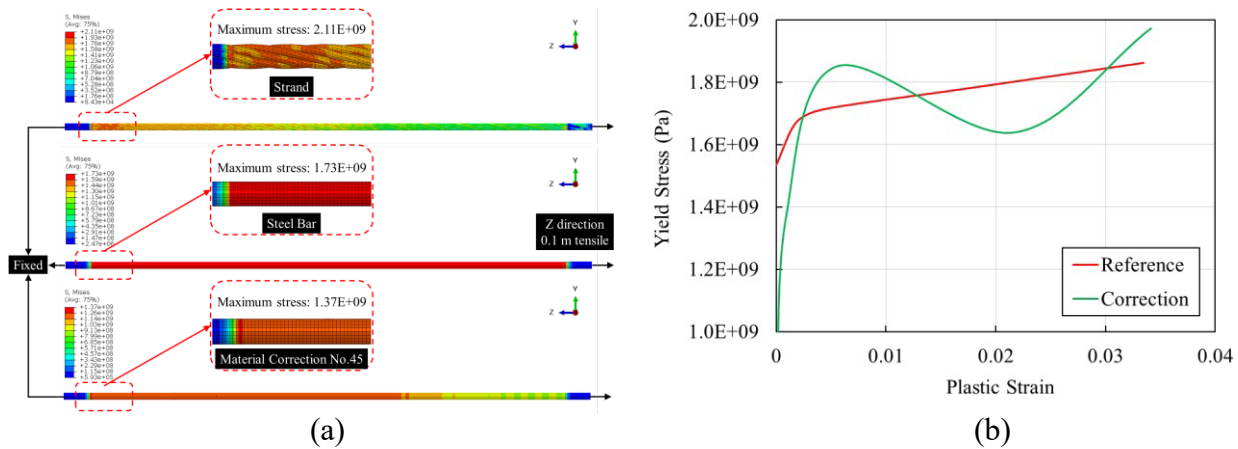


Fig. 3. (a) Stress distribution contour by tensile of the strand, steel, and corrected steel bar; (b) Comparison of plastic strain-yield stress curve between reference(Chueachom, K. and Sirimontree, S. 2015) and corrected by Isight

5. Conclusion

In this study, the performance of PS strand and steel bar of the same diameter was analyzed through finite element analysis, and a corrected material model for the steel bar was developed through nonlinear material property optimization. It was determined that the Young's modulus should be reduced and the trend change in the yield stress-plastic strain curve needed to be obtained for the performance of the PS strand of the steel bar. Therefore, the shape of the PS strand can be simplified and by increasing the number of optimization cases, a more accurate optimal material model could be derived.

6. Acknowledgment

This work was supported by the National Research Foundation of Korea(NRF) grant funded by the Korea government(MIST) (No.2021R1C1C1013130)

7. References

Chueachom, K. and Sirimontree, S. 2015. "Prediction of Flexural and Degradation Behaviors of Full Scale Prestressed Concrete Girder by Finite Element Method", American Transactions on Engineering and Applied Sciences, 4(3), 201-212.

Lin Lu et al. 2022. "The Effect of Lay Length on the Antipull Performance of Steel Cords and the Spinning Loss Based on the FEM", Advances in Materials Science and Engineering, 1-8.



Bridge Engineering Institute Conference 2023 (BEI-2023)
Rome, Italy, July 17-20, 2023



Corrosion and Durability



Visualization of the Effect of Steel Corrosion Cracks on Shear Deformation inside Mortar Using X-ray CT

Takayuki Fumoto^{1*}, Koshiro Maekawa², Shintaro Kikuchi³, and Yuta Yamada⁴

¹: Kindai University, Higashi-Osaka, JAPAN; email: fumoto@civileng.kindai.ac.jp

²: Takada kiko Co.,LTD, Osaka, JAPAN; email: k_maekawa@takadakiko.co.jp

³: Kindai University, Higashi-Osaka, JAPAN; email: 2333350511j@kindai.ac.jp

⁴: Nihon University, Tokyo JAPAN; email: yamada.yuuta@nihon-u.ac.jp

*: corresponding author

Keywords: Corrosion, Crack, Shear deformation, X-ray CT, Digital Volume, Correlation

Abstract: To evaluate the member capacity after the corrosion of steel bars, it is necessary to estimate the stress transfer mechanism based on the cracks inside the concrete induced by the corrosion of the steel bars. However, the relationship between the spatial distribution of cracks inside the concrete and the mechanism of stress transfer at those locations remains unclear. To elucidate the stress transfer mechanism, it is necessary to visualize the crack locations inside the specimen and to measure deformation under loading at those locations. Therefore, the purpose of this study is twofold: to demonstrate the effectiveness of X-ray CT images for visualizing the shear deformation near the corroding rebar and the cracks around it and to discuss the changes in the stress transfer mechanism. The X-ray CT apparatus used in this study, which combines a load testing apparatus and an X-ray CT unit, was developed by the authors. In this study, a mortar specimen with three round steel bars placed within was prepared for shear testing. The internal cracks were observed from X-ray CT images of the specimens that had been subjected to electrical corrosion. The specimens with and without electrolytic corrosion were then subjected to shear tests, and three-dimensional deformation was measured by a digital volume correlation method using X-ray CT images under different loads. After the round steel bars inside the mortar were subjected to electric corrosion, the cross-sectional images of the specimens revealed the reduction of the sectional area of the round steel bars and the formation of cracks around the round steel bars due to steel corrosion steel were observed from the cross-sectional images of the specimens. In the absence of corrosion, stress transfer in the shear plane was continuous due to adhesion. In contrast, corrosion cracking in the shear plane changed the stress transfer mechanism from adhesion to friction at relatively low loads.

1. Introduction

When assessing the performance of existing reinforced concrete structural members with corroded reinforcement, it is essential to accurately estimate the stress transfer mechanisms in the concrete. This requires information, such as surface crack widths and reinforcement distribution. The stress transfer mechanisms, such as the reduction in adhesion stress of the reinforcement and the decrease in apparent shear stress at the cracked surface, must be estimated, for example, from surface crack width and reinforcement arrangement. It is becoming increasingly clear that the relationship between the width of surface cracks and the amount of corrosion of the

reinforcement is influenced by factors such as cover thickness. However, there are still many unknowns, such as the apparent stress transfer mechanism due to corrosion cracking.

This study aims to demonstrate the effectiveness of an X-ray CT system that can capture images under loaded conditions as a method for visualizing the relationship between corrosion cracking patterns in the specimen and changes in the stress transfer mechanism in the vicinity of the reinforcement. To achieve this, we attempted to measure the shear deformation near the round steel bars with and without corrosion in the shear plane and discussed some aspects of the changes in the stress transfer mechanism.

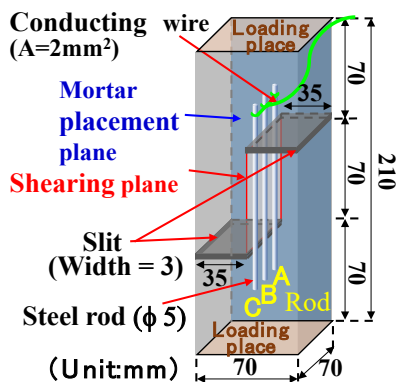
2. Specimen and Test Method

Table 1 shows the proportions of the mortar mixture, which consisted of tap water (W), early-strength Portland cement (C), crushed sand (S1), and lime sand (S2). To improve accuracy in image measurement, 30% of the fine aggregate unit volume was replaced with copper slag fine aggregate (Cu). The dimensions of the specimen, shown in Fig. 1, were 70 mm long, 70 mm wide, and 210 mm high. Two horizontal slits with a thickness of 3 mm and a depth of 35 mm created a 70 mm high, 70 mm wide shear plane (red box in Fig. 1) at the center of the height by compressive loading. Three round steel rods, denoted as Rod A, B, and C, were placed in the shear plane. Seven specimens were created, and after demolding the following day, were cured in water at a temperature of 20 °C for 14 days. Four specimens underwent an electrolytic corrosion test, in which the right side of the specimen (Fig. 1(a)) was submerged in salt water to a height of 2 cm for 30 minutes and then energized for 18 hours at a voltage of 70 V and a current of 0.41 A. The average corrosion rate after energization was 9.68%. The specimens were then cured in a room at a temperature of 20 °C and a relative humidity of 60% for 24 hours to stabilize the internal water content before subsequent tests. During the electrolytic corrosion test, the three non-corroded specimens were also immersed in tap water and adjusted to the same moisture conditions in a room under constant temperature and humidity.

Static loading tests were conducted on two specimens each without and with corrosion (Fig. 1(b)). The deformation of the specimen in the height direction was measured from the average value of two displacement transducers as the displacement of the shear plane. Characteristic points in the relationship between displacement

Table 1. Mixture proportion of mortar

W/C (%)	S/C	Unit content (kg/m ³)				
		W	C	S1	S2	Cu
68	2.4	297	438	622	430	595



(a) Specimen details



(b) Static loading test



(c) X-ray tomography with loading

Fig. 1. Specimen and testing images

and load during the static loading tests were identified as the target loads for X-ray computed tomography (CT) imaging.

Next, one specimen each without and with corrosion underwent internal imaging using an improved X-ray CT system owned by Kindai University under the target loads. The X-ray scan system was located on the inward side of the loading apparatus with a capacity of 300 kN. The imaging conditions were as follows: tube voltage 220 kV, tube current 100 μ A, frame rate 3.0 frames/s, number of projections 2000, copper plate 2 mm, and resolution 0.0615 mm per side. The X-ray CT images at 3 kN and other loads were used to measure internal deformation using Digital Volume Correlation (DVC).

3. Result and Discussion

Fig. 2(a) shows the load-displacement relationship in the static loading test. No significant difference was observed in the failure load between the corroded and uncorroded specimens. In the case without corrosion, the load and displacement were proportional, and the brittle shear failure occurred at a displacement of 0.4 mm. In the case with corrosion, the initial behavior was similar to that without corrosion, but the displacement increased rapidly from 10 kN, and the specimen failed at a displacement of 1.3 mm. The stress transfer mechanism may have been different from that of the corroded steel bars, starting at about 10 kN. Therefore, the scanning target loads were 3 kN (initial value), 10 kN, 16 kN, 21 kN, and just before failure.

Fig. 2(b) shows the load-displacement relationship during X-ray CT imaging. The arrows in the figure indicate the time intervals during which the loading plate position was held during the 11-minute imaging period. However, due to the stress relaxation caused by fixing the loading plate during the scan, the displacement of both specimens increased during re-loading after the scan, as doing the cyclic loading. As shown in Fig. 2(a), the displacement of the specimen with corrosion was greater than that of the specimen without corrosion.

Fig. 3 shows the horizontal cross-section of each specimen before and after 18 hours of energization, in which the round steel bar is displayed in white, the copper slag fine aggregate in white-gray, the mortar in gray, and the voids in dark gray. After the energization, the cross-section of the round steel bar was partially defective due to corrosion, and a yellow dotted line indicated a shadow that appeared to be a crack on the right side. The amount of corrosion of each steel bar (Rod A, Rod B, Rod C) was almost the same.

Fig. 4 shows the displacement distribution in the loading direction inside the specimen. The upper panel shows the horizontal cross-section at the center of the shear plane height (the upper panel is the driven-in surface; the lower panel is the shear plane). The left half of the image is almost fixed, and the right half moves upward (displacement is negative) due to loading from the

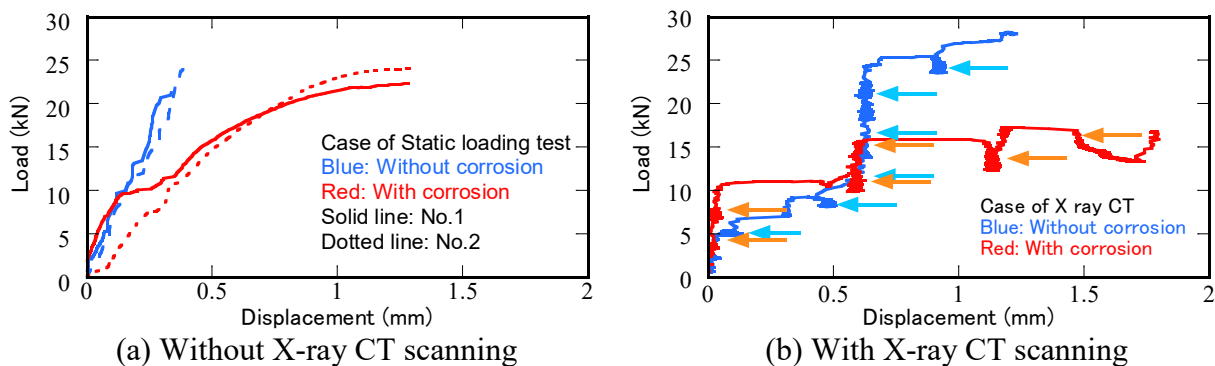
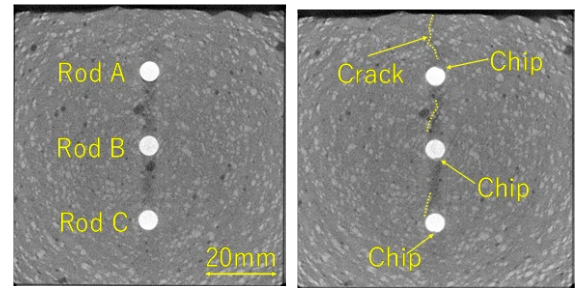


Fig. 2. Relationship between load and displacement

bottom of Fig. 1(a). In the case of no corrosion, displacement increased continuously from left to right in both horizontal and vertical sections just before failure as in the case of 10 kN loading. In other words, it is considered that stress was transmitted on the shear plane until just before failure. On the other hand, in the case of the corroded specimen, the deformation became discontinuous near the cracked area in Fig. 3 when a 10 kN load was applied, and the displacement difference became continually larger till just before failure. In other words, The X-ray CT images confirmed that the change in the load-displacement relationship due to rebar corrosion shown in Fig. 2 was caused by a change from adhesion to friction in the stress transfer mechanism induced by the corroded cracks.



(a) Before energization (b) After energization for 18h
Fig. 3. Horizontal cross-section image at the center of the height of the specimen

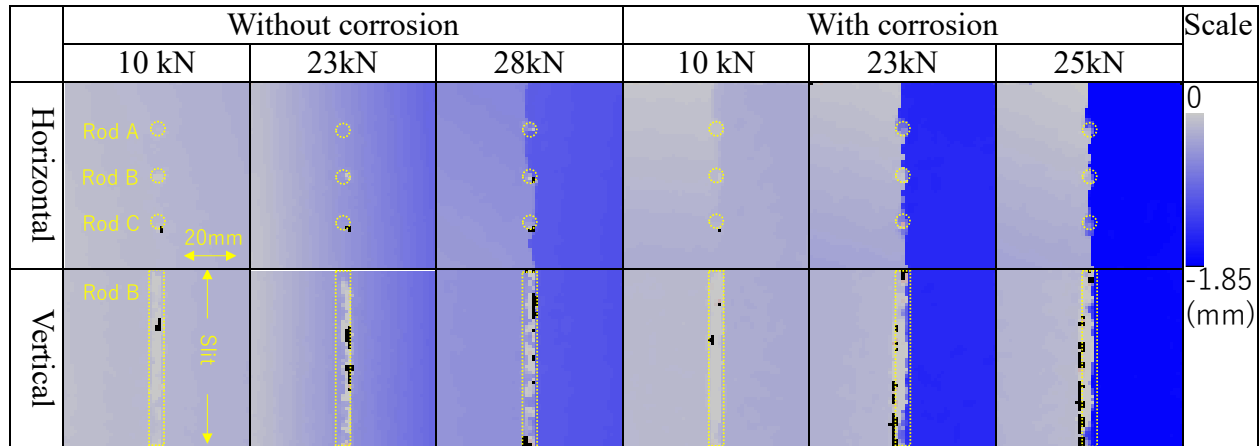


Fig. 4. Vertical displacement in the cross-section of specimen (The yellow dotted line is the bar)

4. Summary

- 1) The X-ray CT images before and after the corrosion of the rebar showed the possibility of observing the location of cross-sectional reduction due to rebar corrosion and the internal cracks around the corroded rebar.
- 2) DVC using X-ray CT images during loading confirmed that the change in the load-displacement relationship due to rebar corrosion was caused by a change in the stress transfer mechanism induced by the corrosion cracks.

In the future, changes in the stress transfer mechanism under different corrosion cracking conditions will be investigated.

References

- Fumoto, T. 2013. Development of A New Industrial X-ray CT System and Its Application to Compression Test of Polymer Concrete, Journal of Japan Society of Civil Engineers, 69(2), 182-191. (In Japanese)
- Qiao, D., Nakamura, H., Tran, K.K. Yamamoto, Y., Miura T. 2015. Experimental and analytical evaluation of concrete cover spalling behavior due to local corrosion, Journal of Structural Engineering, 61A, 707-714. (In Japanese)



A Change in the Failure Mode and Decrease in the Strength of RC Slabs Due to the Progress of Frost Damage

Hiroshi Hayashida ¹

¹ Civil Engineering Research Institute for Cold Region, Sapporo, Japan, hayashida@ceri.go.jp

Keywords: Bridge slabs; Frost Damage; Deterioration Depth; Strength; Horizontal Cracks

Abstract: In Japan, many bridges were constructed from the 1950s to the 1970s. For this reason, over the next 10 years, more than 60% of bridges will be over 50 years old. Due to this aging, damage to the bridge slabs that directly support the traffic load has become a serious problem. In particular, bridge slabs in cold regions deteriorate rapidly even with a small amount of traffic, and there are many reports of occurrence of potholes. Frost damage is the biggest factor of rapid deterioration of bridge slabs in cold regions. The deterioration progresses in the depth direction from the upper surface. In order to prevent occurrence of potholes, it is necessary to understand the relationship between the depth of deterioration due to frost damage and the decrease in strength of slabs. However, the relationship has not been clarified. In this study, to clarify the relationship between the progress of deterioration and the decrease in strength of slabs that undergo frost damage, a static loading test was conducted. The parameter for the test slab specimens was the deterioration depth. In a specimen with a deterioration depth of 1/4 of the slab thickness, the strength did not decrease; however, in a specimen with a deterioration depth of 1/2 of the slab thickness, the failure mode changed and the strength greatly decreased. The factors for the change in the failure mode were considered to be (1) the horizontal cracks from freeze-thaw cycles were already present before loading; and (2) Diagonal tensile cracks occurred because the portion of the specimen corresponding to the web of the beam deteriorated and the tensile strength decreased.

1. Introduction

In this study, to obtain the relationship between the depth of deterioration due to frost damage and slab strength, RC slab specimens whose parameter was the deterioration depth were created, and an experimental examination was done on these specimens using a static loading test.

2. Experiment Outline

2.1. Overview of the specimens

The dimensions, and reinforcing bar arrangement of the slab specimens are shown in Fig. 1. For the concrete, air-entraining agent was not used and the water cement ratio was set at 65%. The mix proportion is shown in Table 1. Data on the material properties of the concrete and the reinforcing bars are shown in Table 2. Table 3 shows the designations of the specimens and the experiment parameter. The experiment parameter is the deterioration depth from the upper surface of the slab specimen.

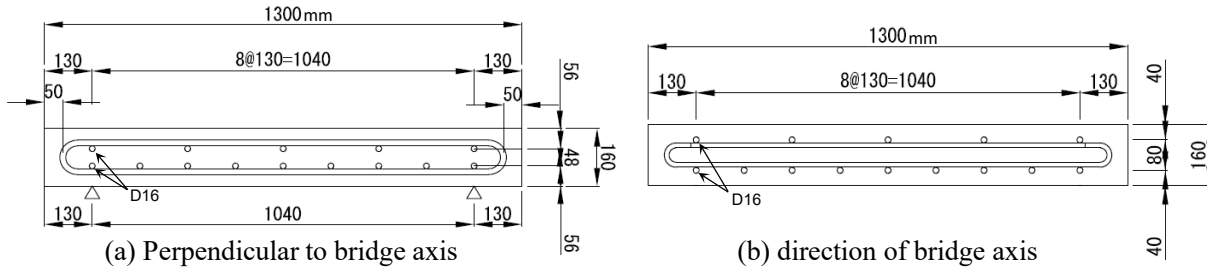


Fig. 1. The shape, dimensions and reinforcing bar arrangement of the slab specimen

Table 1. Mix proportion

W/C	Air	s/a	mix ratio (kg/m ³)			
			W	C	S	G
(%)	(%)	(%)				
65	2.0	48.6	171	263	904	947

Table 2. Material properties

Concrete	Rebar
Comp strength	Yield strength
(N/mm ²)	(N/mm ²)
25.8	362

Table 3. Experiment parameter

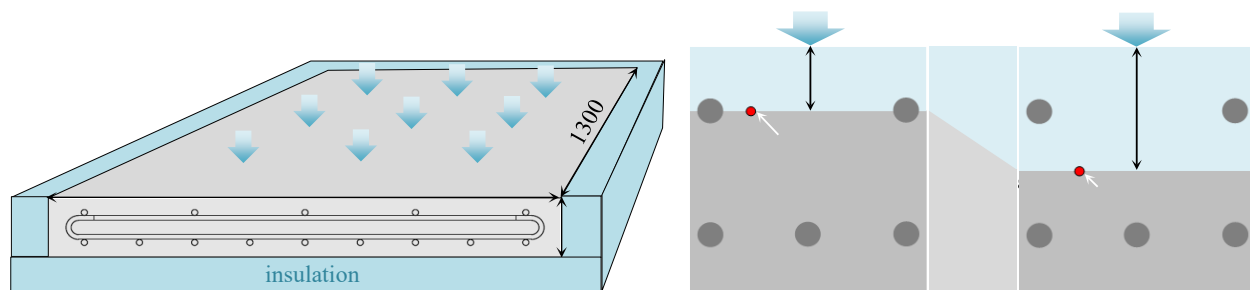
Name	Deterioration depth
N	-
H/4	40mm
H/2	80mm

2.2. Freeze-thaw test

In the freeze-thaw test, the depth of deterioration was controlled by the following two methods.

- 1) As shown in Fig. 2, thermal insulation was installed on the surfaces other than the top surface, and cooling and heating of the specimen was done only on the top surface of the specimen.
- 2) As shown in Fig. 3, freeze-thaw action was applied only to the set range of deterioration depth, and the frozen condition was maintained in the range below the set deterioration depth.

More precisely, as shown in Fig. 3, a temperature sensor was installed at a depth of 40mm for specimen H/4 and at a depth of 80mm for specimen H/2. The temperature of the specimen was adjusted between -18 and 0° C at the depth where the temperature sensor was installed in each specimen. Under these temperature conditions, the specimens were subjected to freezing in air and thawing in water 100 times for specimen H/4 and 300 times for specimen H/2.



2.3 Static loading test

The specimen was simply supported at two sides, and the span was 1040 mm. A 100mm × 100mm steel plate was used as the loading plate. Concentrated loading was done at one point at the center of the specimen.

3. Static Loading Test Results

Fig. 4 shows the load-displacement curve for each specimen. Cracks on the cut surface, which was in the direction of the span, and those on the bottom surface of the specimen are shown in Fig. 5. The following two types of cracks are seen on the cut surface.

- 1) Wide cracks that were considered to be fracture surfaces (thick lines)
- 2) Horizontal cracks caused by freeze-thaw action (thin lines)

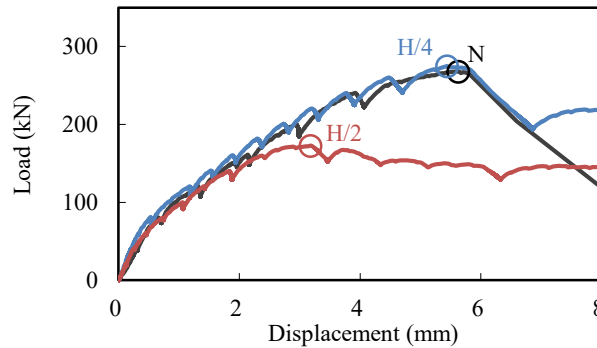


Fig. 4. Load-displacement curves

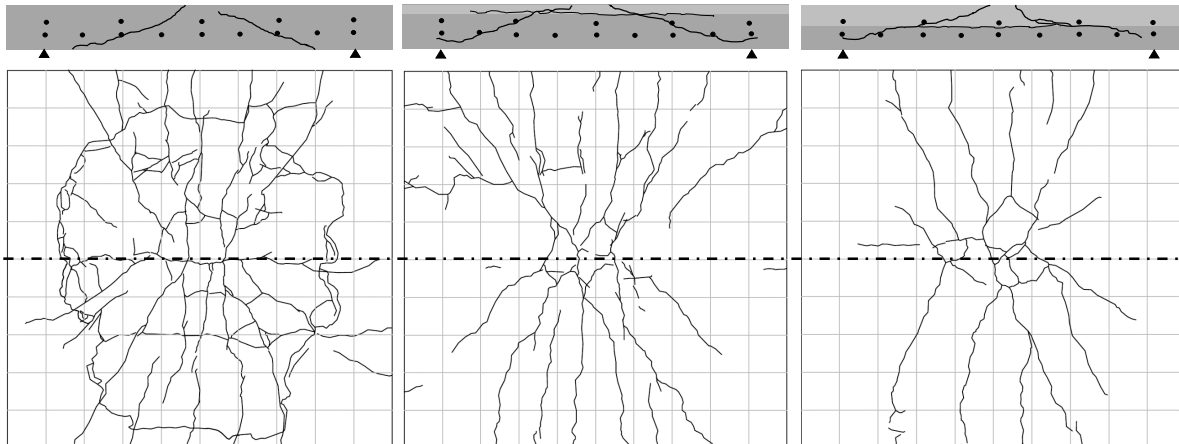


Fig. 5. Loading cracks in the cut surface and on the lower surface of the specimen

3.1. Specimen N

Specimen N reached a maximum load of 268kN at a displacement of 5.6 mm (the black line in Fig. 4). Immediately after the maximum load was reached, the displacement suddenly increased and the load suddenly dropped due to the failure. At this moment, as shown in the lower sub-figure of Fig. 5(a), cracks that form the border of the punching shear cone occurred on the bottom surface of the specimen. In addition, as shown in the upper sub-figure in Fig. 5(a), loading cracks, which connected with the cracks of the punching shear cone, were found on the cut surface.

3.2. Specimen H/4

Specimen H/4 reached a maximum load of 274kN at a displacement of 5.4mm (the blue line in Fig. 4). The maximum load and stiffness of specimen H/4 were almost the same as those of specimen N, and no drastic decrease like that seen for specimen N was observed. For specimen H/4, the load decreased and the displacement increased due to failure immediately after the maximum load was reached, which were similar to what occurred to specimen N, but the degrees of these changes were not as marked as those for specimen N. As shown in the lower sub-figure of Fig. 5(b), cracks that form the border of the punching shear cone, which occurred on the bottom surface of the specimen N, did not occur. This is consistent with the fact that the cracks on the cut surface did not reach the lower surface, as shown in the upper sub-figure in Fig. 5(b).

3.2. Specimen H/2

The load-displacement curve for specimen H/2 (the red line in Fig. 4) was completely different from those of specimens N and H/4. Specifically, the curve of specimen H/2 was as follows. As shown in Fig. 4, from the initial stage of loading to a load of 140kN (the displacement was 1.8 mm), the decrease in stiffness was negligible, and the load-displacement relationship showed almost the same trend as those for specimens N and H/4. However, when the load was further increased, the displacement suddenly increased and reached the maximum load of 172kN at a displacement of 3.2 mm. The decrease in maximum load was greater and the displacement at maximum load was smaller for specimen H/2 than for specimens N and H/4. As shown in Fig. 5(c), cracks that form the border of the punching shear cone did not occur on the bottom surface of the specimen, nor did the loading cracks on the cut surface reach the bottom surface.

4. The Reason for the Strength Decrease in Specimen H/2

It is considered that the strength decrease was greater for specimen H/2 than for specimen N due to the change in the failure mode caused by the following factors: (1) the horizontal cracks from freeze-thaw cycles were already present before loading; and (2) Diagonal tensile cracks occurred because the portion of the specimen corresponding to the web of the beam deteriorated and the tensile strength decreased. Because the specimen had no shear reinforcement against the diagonal tensile cracks and because the horizontal cracks occurred in the area without reinforcing bars, both types of cracks grew rapidly in the specimen. Therefore, it is considered that the strength decreased when the displacement suddenly increased with no considerable increase in loading, and failure occurred.

5. Conclusions

To clarify the relationship between the progress of deterioration and the decrease in strength of RC slabs that underwent frost damage, an examination based on the static loading experiment was conducted. Slab specimens in which the deterioration depth was the parameter were created for this experiment. The knowledge obtained in this study is summarized as follows.

- (1) In the slab specimen that was subjected to freeze-thaw by the cooling and heating of only the upper surface, horizontal cracks were generated throughout the upper part of the specimen.
- (2) The strength of specimen H/4, whose deterioration depth was 1/4 of the slab thickness, was almost the same as that of the sound specimen N. The strength decrease was greater for specimen H/2, whose deterioration depth was 1/2 of the slab thickness, than for sound specimen N.
- (3) It is considered that the strength decrease was greater for specimen H/2 than for specimen N due to the change in the failure mode caused by the following factors: (1) the horizontal cracks



Bridge Engineering Institute Conference 2023 (BEI-2023)
Rome, Italy, July 17-20, 2023



from freeze-thaw cycles were already present before loading; and (2) Diagonal tensile cracks occurred because the portion of the specimen corresponding to the web of the beam deteriorated and the tensile strength decreased.



Experimental Performance of Lightweight Aggregate Concrete Due to Freezing and Thawing

Sangwoo Kim^{1*}, Sardorbek Rustamov², and Jinsup Kim^{3*}

¹: Dept. of Civil Engineering, Gyeongsang National University, Jinju 52828, South Korea; email: kimsangwoo@gnu.ac.kr

²: Dept. of Civil Engineering, Gyeongsang National University, Jinju 52828, South Korea; email: sardorbek060894@gmail.com

³: Dept. of Civil Engineering, Gyeongsang National University, Jinju 52828, South Korea; email: jinsup.kim@gnu.ac.kr

*: corresponding author

Keywords: Lightweight expanded clay aggregate, Compression strength, Flexural tensile strength, Direct tensile strength

Abstract: Concrete structures are not restricted in dimensions and shape; they are inexpensive and highly capable, making them the most economical material in modern architecture. As the 21st century entered, the demand for skyscrapers increased, and concrete structures became taller. It is a desire to have long columns or beams with a large span of large structures, but there is a problem with increasing the weight of concrete as higher strength and durability are required. Due to these problems, research on the performance improvement through lightweight aggregates is being actively studied. However, there still needs to be more research on the performance change of concrete made of lightweight aggregates due to aging. Therefore, in this study, the results of experiments on concrete manufactured from expanded clay aggregates were presented under freezing and thawing conditions. Freeze and thawing were performed using the freeze and thawing in air method with reference to ASTM C666, and 150,300 cycles were performed. Compressive strength, flexural tensile strength, and direct tensile strength were experimentally evaluated. Specimens that performed freeze-thawing and specimens that did not perform freeze-thawing were experimented on the same day to compare numerical differences and analyze the effect of freeze-thawing on lightweight aggregate concrete.

1. Introduction

Concrete is a synthetic material composed of cement, water, aggregates, hybrid materials, and property improvement agents, and is the most widely used construction material by humans applied to various construction structures. Recently, science and technology are rapidly developing, and technological innovation in concrete as social infrastructure is also actively progressing. In the past, concrete only required physical performance, but as social demands have recently diversified, concrete with high performance, multifunction, and high durability, such as super concrete, has been developed and applied. In addition, as demand for high-rise buildings increases in the 21st century, we want to make long columns or beams with a large

span, but it causes problems in increasing the weight of concrete because higher strength and durability are required. Due to this problem, research on reducing the weight of concrete through weight reduction of aggregates is also being actively conducted. However, there are still few studies on the aging of concrete using lightweight aggregates. Therefore, in this study, the performance change was measured by deteriorating due to the freezing and thawing of concrete using lightweight aggregates. With reference to ASTM C 666, freeze-thawing was performed using the air freeze-thawing method, and 0,150 and 300 cycles were performed. Compression strength, flexural tensile strength, and direct tensile strength were experimentally evaluated. The specimen that performed freeze-thawing and specimens that did not perform freeze-thawing were experimented on the same day to compare numerical differences and analyze the effect of freeze-thawing on lightweight aggregate concrete.

2. Experimental Program

2.1. Materials

In this study, ordinary Portland cement (Type 1) with specific gravity 3.15 was used as a binder, in compliance with the requirement of Korean Standard KS L 52001. The physical properties of the cement are shown in Table 1. Lightweight expanded clay aggregate (LEA) was produced in firepower plant ash. The LEA was applied as coarse aggregate to manufacture the lightweight aggregate concrete. The physical properties of the LEA are indicated in Table 2. Constituents of LEA are summarized in Table 3. Tap water with a temperature of 20 ± 2 C was used to provide excellent workability. To reduce the amount of water in the concrete, a superplasticizer was applied.

Table 1. Physical property of cement

Density (g/cm ³)	Fineness (g/cm ²)	Setting time/min		Compressive strength (MPa)		
		Initial	Final	3-day	7-day	28-day
3.15	3,400	230	390	12.5	15.0	32.5

Table 2. Physical property of LEA

Density (g/cm ³)	Bulk density (kg/m ³)	Min. size of aggregate (mm)	Max. size of aggregate (mm)
1.75	250-450	3	15

Table 3. Constituents of LEA (unit: %)

SiO ₂	Al ₂ O ₃	Fe ₂ O ₃	CaO	MgO	K ₂ O	Na ₂ O	TiO ₂
66.7	18.3	4.57	1.37	0.65	1.63	1.71	0.78

2.2. Mixing Procedure

To maintain good workability and improve the concrete strength in the first step, the lightweight aggregate was cleaned and mud was totally removed from the surface of the aggregate. Furthermore, to increase the resistance to damage from freeze-thaw cycles, the aggregate was entirely saturated with water for 24 h. It was concluded by Kucharczykova (2010) that the porous aggregate (pre-saturation) has an important impact on the final strength and durability of LC when the aggregate size provides pores in the aggregate that can be filled with water in the

pre-saturation process. Afterward, the aggregate was removed from the water and dried in the air condition (sunlight and wind) fully. The surface of the aggregate was allowed to dry completely. The mixture table used was from Manu (2017). However, 15% of the cement was replaced by fly ash. The water-to-cement ratio of the concrete mixture was almost 0.35. Table 4 is the mixing table of lightweight aggregate concrete. All the procedures followed for making and curing the concrete in the laboratory, were according to the requirements of the ASTM C 192/C 192M-06 (2006) standard.

Table 4. Mixing table of lightweight aggregate concrete (unit: kg/m³)

Cement	Water	Fly Ash	Aggregate	Superplasticizer	Sand
578	205	102	696	4.1	326

2.3. Test Method

There are three kinds (Compression, Tension, Flexural) of tests to value the strength of the lightweight aggregate concrete. The cylindrical concrete specimens (100 × 200 mm) prepared for the compressive strength tests conformed with the ASTM C39/C39M-18 (2018) standard. After 28 days, the specimens were tested on a universal testing machine with a 2,000 kN maximum load capacity. The flexural tensile strength of the concrete specimens was determined using 100 × 100 × 500 mm rectangular prismatic beams with center-point loading according to ASTM C293-02 (2002). Experiments on the direct tensile strength of LC and FRLC were conducted using dog-bone specimens with dimensions of 575 × 200 × 100 mm. The experimental method for the freeze-thawing cycles involved two sets of specimens. In the first set were specimens pretreated by freezing and thawing. This first set of specimens directly after curing 28 days (0 freeze-thaw) cycle for all categories of concrete was placed into the chamber and then were subjected for (150 and 300 freeze-thaw) cycles to temperatures ranging from -18°C to +4°C. The second set was pretreated only by air drying, and these specimens were cured in the air for the same period used for the freezing and thawing cycle pretreatment. The frozen-thawed(aged) and air-dried(not aged) specimens were tested on the same day according to the selected number of freeze-thaw cycles, where 150 cycled frozen-thawed specimens were equal to 80 curing days for air-dried specimens, 300 cycled specimens equal to 130 curing days, including standard 28 curing days of frozen-thawed and air-dried specimens respectively. The difference between the strength of the frozen-thawed and air-dried (pre-treatment) specimens tested for an identical number of freeze-thaw cycles, 150 cycles (80 days) and 300 cycles (130 days) were recorded and compared.

3. Result and Conclusion

The result is summarized in Table 5. Each value represents the average value for each case. The results of specimens pretreated by freeze-thawed (aged) and air-dried (not aged) in the compressive tests are shown in Fig. 1 (a). As a result of the experiment, the not aged specimen was cured for 80 days and the strength increased. But the aged specimen did not show an increase in compression strength due to freezing-thawing of 150 cycles. After 80 days, the curing was over. The results of specimens pretreated by freeze-thawed(aged) and air-dried(not aged) in the flexural tensile tests are shown in Fig. 1 (b). As a result of the experiment, not the aged specimen was cured for 130 days and the strength increased. But the aged specimen shows a little decrease in flexural tensile strength due to freezing-thawing. The results of specimens

pretreated by freeze-thawed(aged) and air-dried(not aged) in the direct tensile tests are shown in Fig. 1 (b). As a result of the experiment, not the aged specimen was cured for 130 days and the strength increased dramatically after 80days. But the aged specimen shows a 33% decrease in flexural tensile strength due to freezing-thawing. This paper shows the influence of freezing and thawing on the lightweight aggregate concrete which is made with Lightweight expanded clay aggregate. As a result of the experiment, the compressive strength, flexural tensile strength, and direct tensile strength of lightweight aggregate concrete all increased due to curing after 28 days. However, exposure to freezing and thawing strength of concrete did not increase or rather decreased. Therefore, research is needed to improve the resistance of lightweight aggregate concrete.

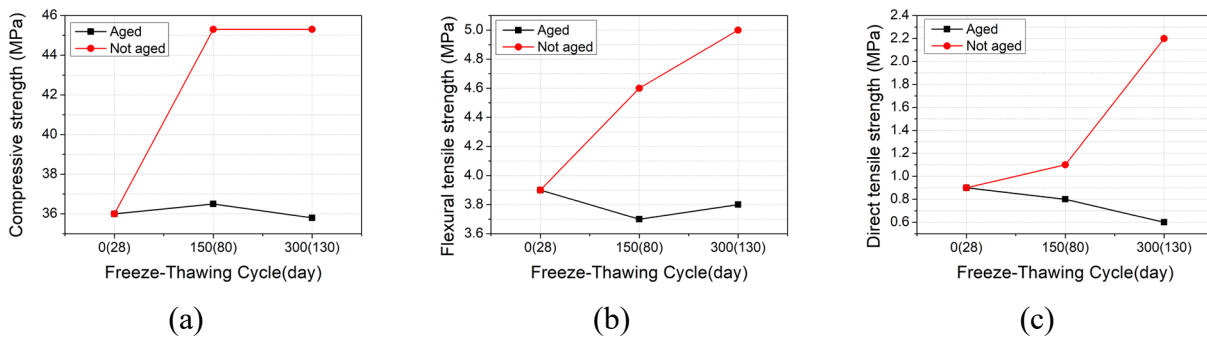


Fig. 1. Comparison of each test: (a) compressive, (b) flexural, (c) direct tensile

Table 5. Test result of all specimen (MPa)

Type of test	0cycle (28-day)	150cycle (80-day)		300cycle (130-day)	
		Aged	Not aged	Aged	Not aged
Compressive strength	36.0	36.5	45.3	35.8	45.3
Flexural tensile strength	3.9	3.7	4.6	3.8	5.0
Direct tensile strength	0.9	0.8	1.1	0.6	2.2

4. References

B. Kucharczyková, Z. Keršner, O. Pospíchal, P. Misák, and T. Vymazal 2010, Influence of Freeze-thaw cycles on fracture parameters values of lightweight concrete, *Procedia Eng.*, 2(1), 959–966

Manu S. Nadesan, and P. Dinakar 2017, Mix design and properties of fly ash waste lightweight aggregates in structural lightweight concrete, *Case Stud. Constr. Mater.*, 7, 336–347



Rust Evaluation of Weathering Steel Bridges by Optical Spectra in the Visible and Near-Infrared Regions

Ryuichi Inoue^{1*}, Rina Hasuike², Hirokazu Furuki³ and Toshihiko Aso⁴

¹: Dept. of Civil and Environmental Engineering, Yamaguchi University, Ube, Japan; email: b002wdv@yamaguchi-u.ac.jp

²: Dept. of Civil and Environmental Engineering, Yamaguchi University, Ube, Japan; email: hasuike@yamaguchi-u.ac.jp

³: Nippon Koei Co., Ltd, Tokyo, Japan; email: a5962@n-koei.co.jp

⁴: Dept. of Civil and Environmental Engineering, Yamaguchi University, Ube, Japan; email: aso@yamaguchi-u.ac.jp

*: corresponding author

Keywords: weathering steel, rust, optical spectra, dimensional reduction, random forest

Abstract: Monitoring of the rusting condition is necessary for the maintenance of weathering steel bridges. Some research has been conducted on rust condition monitoring methods that apply machine learning to digital camera images. However, to evaluate such rust conditions from digital camera images is difficult due to rust has a variety of color tones. To solve this issue, this study focuses on wavelengths other than that available under visible light and examines a rust evaluation method on weathering steel using optical spectra in visible light and near-infrared. This study attempts to classify into two classes of rust: rust with a thickness of 200-400 μm , which is considered protective rust, and rust with a thickness of 400-800 μm , which is considered non-protective rust. In this study, a hyperspectral camera (HSC) is used to measure optical spectra of weathering steel surfaces in every 1 cm square. From the first derivatives of these optical spectra, four wavelengths were selected that are valid for the two-class classification. The reflection intensities at these four wavelengths were dimensionally reduced by KPCA to produce 2D data. A classifier was constructed by applying random forest to these 2D data and tested on 128 data and the discrimination accuracy was 100 %.

1. Introduction

Weathering steel that has been used to construct bridges has a corrosion prevention property by forming protective rust layer. Thus, periodic monitoring of the rust condition is necessary to maintain the weathering steel bridges. The criteria of rust condition evaluation (JSSC, 2009) are mainly based on appearance. Therefore, the evaluation is not always quantitative, and in some cases the evaluation is not easy. To solve these challenges, some research has been conducted on rust condition easy-monitoring methods that apply machine learning to digital camera images (Sugita, 2022; Hasuike et al., 2021). However, it is sometimes difficult to evaluate the rust condition from digital camera images because rust has a variety of color tones.

In contrast, as an evaluation method which is not affected by color tone, near-infrared wavelengths have been focused on. Previous studies shows that optical spectra in near-infrared

are more effective than digital camera images in detecting rust on carbon steel, and there is a possibility to construct a rust condition evaluation classifier for carbon steel (Kerf et al., 2022; W. G. Rowley, 2018). It is thought that optical spectra in near-infrared may also be effective in evaluating rust on weathering steel, but there have been few such studies.

In this study, a rust condition evaluation method for weathering steel by measuring optical spectra in visible light and near-infrared and constructing a supervised learning classifier is investigated. This study attempts to classify into two classes of rust: rust with a thickness of 200-400 μm (Class A), which is considered protective rust, and rust with a thickness of 400-800 μm (Class B), which is considered non-protective rust.

2. Spectrum Measurement Method

Figure 1 shows the HSC (Specim IQ, Spectral Imaging) which was used to measure optical spectra. Wavelength resolution is 7 nm, and it can measure optical spectra of 204 spectral bands in the wavelength range of 400-1000 nm. The wavelength of 400-770 nm is visible light and 770-1000 nm is near-infrared. A barium sulfate plate with no specific light absorption was used as the reference plate for measuring optical spectra, and the reflected intensity was calculated by dividing the radiance value of the specimen by the radiance value of the reference plate.

Figure 2 indicates the experimental scenery. To ensure the reproducibility of the experiment, the optical spectra were measured in a room with 0 Lux illumination except for the light source. A halogen light (500 W) with a wide range of wavelengths from visible light to near-infrared was used as the light source. The HSC was placed 20-30 cm away from the specimen so that the entire specimen could be measured.

Figure 3 presents an example of the corroded weathering steel specimen. Left one has 15 cm length, 7 cm width and right one has 7 cm length, 7 cm width. It is difficult to measure rust thickness at the edges of the specimens, and the 7×15 cm specimens has a through-hole. Therefore, the measurement ranges of optical spectra were 6×11 cm and 6×6 cm, respectively. In this study, this measurement area was divided into 1 cm squares that used as one data. The rust thickness at the center of each data was measured and used as the correct data for supervised learning. There were 263 data in Class A and 265 data in Class B.



Fig. 1. HSC



Fig. 2. Experimental scenery

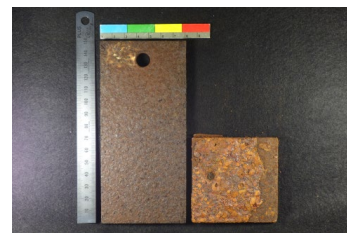


Fig. 3. Example of the specimen

3. Measured Optical Spectra, Spectral Pre-processing, and Evaluation of Rust Conditions

3.1. Optical spectra of weathering steel surfaces

Figure 4 shows examples of optical spectra and their first derivatives. For both classes, the optical spectral curves have minima at wavelengths of 516 and 896 nm, and maxima at wavelengths of 796 nm. The first derivative values at wavelengths of 569 and 694 nm are larger than that at the surrounding wavelengths. There are similar trends for all data, however, the reflection intensities at these wavelengths varied from data to data.

It is considered that the all wavelength data may have information that not need to rust condition classification. Therefore, the wavelengths effective for the two-class classification

were selected from the wavelengths shown in Fig. 4. Figure 5 shows box-and-whisker plots of the reflection intensities at wavelengths of 516 and 694 nm. The quartile ranges of reflection intensity at wavelength of 516 nm for classes A and B are indistinguishable. On the other hand, the quartile ranges of reflection intensity at wavelength of 694 nm for classes A and B are distinguishable. Similar trends were observed at the other wavelengths (569, 796 and 896 nm) shown in Fig. 4. Therefore, in this study, the wavelengths 569, 694, 796 and 896 nm are assumed to be valid wavelengths (characteristic wavelengths) for the two-class classification.

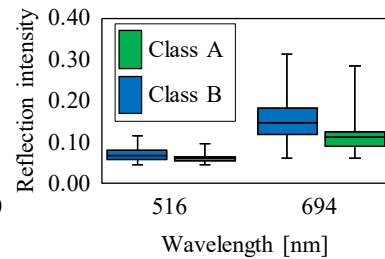
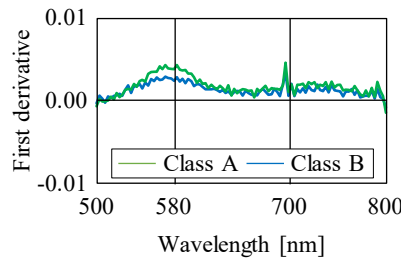
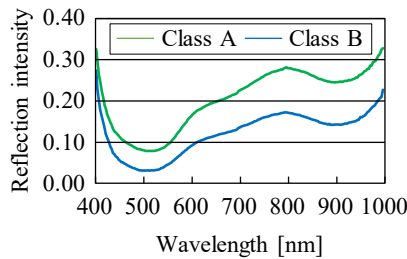


Fig. 4. Examples of optical spectra and its first derivative

Fig. 5. box plots of reflection intensities

3.2. Dimension reduction

For the optical spectra of nutrients in soil, Qi et al. reported that constructing classifier using dimension-reduced optical spectra can prevent overfitting (Qi et al., 2018). This method may also be useful in the classification of the rust condition of weathering steel. Therefore, this study used kernel principal component analysis (KPCA), a dimensionality reduction method applicable to nonlinear data to reduce the dimensionality of the measured optical spectra. Applying KPCA to the reflection intensity at each wavelength data, and the extracted first and second principal components are used to construct a classifier. To clarify the effectiveness of constructing a classifier using different number of wavelengths, following three types of classifiers are constructed and compared: classifier constructed using all wavelength data, and using near-infrared wavelengths data, and using the characteristic wavelengths data.

3.3. Classifier construction method

Classifiers are constructed using Random Forest (RF), an ensemble learning of decision trees often used as a supervised learning algorithm for the two-class classification. The training data consisted of 180 data each, the validation data consisted of 20 data each, and the remaining data (Class A: 63 data, Class B: 65 data) were used as test data.

4. Results and Discussions

Table 1 shows the discrimination accuracy. When the classifier was constructed with data obtained by applying KPCA to reflection intensities at characteristic wavelengths, discrimination accuracy was the highest (100. %). And, when the classifier was constructed with data obtained by applying KPCA to reflection intensities at all wavelengths, discrimination accuracy was the lowest (66.5 %).

Figure 6 shows the first and second principal components obtained by applying KPCA to the reflection intensities at three different wavelengths. The smaller the number of wavelengths in the optical spectra before dimensionality reduction, the less the overlaps in the data group for each class and the more clearly each class of data can be separated. As a result, classification accuracy is higher. Therefore, when constructing a classifier to evaluate the rust condition of weathering steel by optical spectra in visible light and near-infrared, it is necessary to select

wavelengths effective for classifying from the measured optical spectra and use data obtained by applying KPCA to their reflectance intensity.

Table 1. Discrimination accuracy

input data	all wavelengths	near-infrared wavelengths	characteristic wavelengths
Accuracy	64.1 %	84.4 %	100.0 %

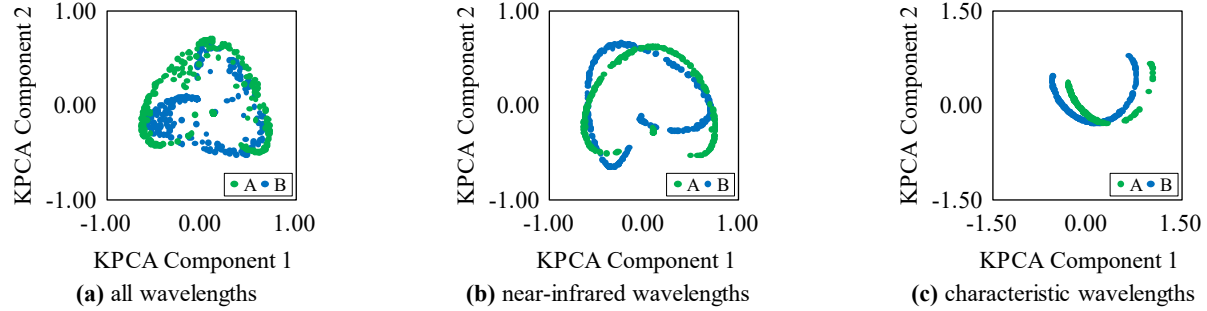


Fig. 6. Relationship between the first and second principal components

5. Conclusion

In this study, an evaluation method for the rust condition of weathering steel by constructing RF classifier using HS data in visible and near-infrared is investigated. This study focuses on the pre-processing for the HS data combining of optical spectral wavelength selection and dimensionality reduction by KPCA. As a result, the discrimination accuracy was 66.5 % when all wavelength data were used, and 83.6 % when the near-infrared wavelength data was used. On the other hand, the discrimination accuracy at four characteristic wavelengths data (569, 694, 796 and 896 nm) screened from the first derivative of the measured optical spectra was 100.0 %.

6. Acknowledgements

This work was supported by JST SPRING, Grant Number JPMJSP2111.

7. References

- H. Sugita. 2022. Development of rust appearance evaluation model for weathering steel using deep learning, *Bulletin of Hachinohe National College of Technology*, 56, 43-50. (In Japanese)
- H. Qi et al. 2018. Evaluating calibration methods for predicting soil available nutrients using hyperspectral VNIR data, *Soil and Tillage Research*, 175, 267-275.
- T. D. Kerf et al. 2022. Identification of corrosion minerals using shortwave infrared hyperspectral Imaging, *Sensors*, 22, 1.
- R. Hasuike et al. 2018. Classification of corrosion deterioration on weathering steel based on CNN, *Artificial Intelligence and Data Science*, 2, J2, 813-820. (In Japanese)
- Japanese Society of Steel Construction (JSSC). 2009. Applicability Assessment and Corrosion Prevention Maintenance of Weathering Steel Bridges, *JSSC Technical Report*, 86.
- W. G. Rowley. 2018. Hyperspectral imaging for detection of corrosion on intermediate level nuclear waste containers, University of Birmingham. (dissertation)



Effect of Measures for Inhibiting Galvanic Corrosion in an Aluminum Alloy Bridge and Guard Railings

Yoshito Itoh^{1*} and Tatsuya Kawabata²

¹: Nagoya Industrial Research Institute, Nagoya, Japan, email: itoh@civil.nagoya-u.ac.jp

²: Japan Aluminum Association, Tokyo, Japan, email: t-kawabata@alkyo.jp

*: corresponding author

Keywords: bridge railing, aluminum alloy, galvanic corrosion, stainless steel, zinc flake coating

Abstract: This paper is based on several field surveys and deals with a high durability aluminum alloy plate girder bridge “Kinkei-Bashi” built 61 years ago in Hyogo Prefecture, Japan. It focuses on the effect of measures taken against galvanic corrosion between aluminum and steel parts of the bridge, but also, secondly, between aluminum alloy joint members in bridge guard railings and their stainless steel fastenings. On-site surveys were carried out to assess the degrees of galvanic corrosion in the guard railings. In the light of the survey results, galvanic corrosion exposure tests were then performed on railing part samples over a five-year period at the Miyakojima Atmospheric Exposure Test Site in Okinawa. Two types of exposure conditions, direct and under-eave exposure, were tested for, using 250 specimens of 6000 series aluminum alloy joints. Stainless steel fasteners with a zinc flake coating were found to be the best means for inhibiting galvanic corrosion in aluminum alloy members in this kind of highly corrosive environment.

1. Introduction

Aluminum alloy is a lightweight material combining high durability with esthetic grace. Civil engineers have used it since the 1980s in structures such as bridge railings, laterally attached walkways, high-water / tsunami barriers, land locks, and lighting masts. Recently, uses have also been found for it in bridge inspection paths and work scaffolds, and the Japan Society of Civil Engineers (JSCE) is preparing design and manufacturing guidelines for its use as a main material in further types of structures such as emergency relief bridges. This paper opens with results from a survey of the present state of durability of the Kinkei Bridge (Japanese: “Kinkei-Bashi”), an aluminum alloy plate girder bridge constructed 61 years ago, and then focuses in on corrosion tests performed on samples of the fasteners used to connect 6000 series aluminum alloy joints to bridge guard railings. The object is to investigate the effects of these fastener choices on durability and to verify their suitability as resources for inhibiting corrosion.

2. The Kinkei Aluminum Alloy Plate Girder Bridge Built in 1961

2.1. A general overview and on site survey

The Kinkei Bridge is the only aluminum alloy road bridge presently existing in Japan. Its visual and schematic appearance are shown in the photographs in Fig. 1 and the drawings in Fig. 2. As seen in Fig. 2, it is a plate girder bridge of composite structure for live loads composed of four main girders, each with a span of 20.6m and a width of between 8.1m and 7.0m (the road has a

slope). It carries the “Ashiya Driveway”, a 10km stretch of toll road linking the two cities of Ashiya and Arima Onsen in Hyogo Prefecture. The bridge was completed in June 1961 and on the occasion of the 50th anniversary of this, the Durability Subcommittee of the Japan Aluminum Association (Chair: Yoshito Itoh) discussed a proposal to nominate it for the 2017 JSCE Engineering Heritage Award. The nomination was successful and the bridge was selected for inscription.

Corrosion-resistant rolled aluminum alloys plates (former JIS H 4104 A2P7-F, current equivalent A5083) were used in the girders, and members were connected by MIG welding in the factory (A54S-9/10, current A5654) and with rivets at the construction site. After the lapse of more than 60 years, the girders are still in prime condition, a testimony to the durability of aluminum alloy bridges. The main reason for choosing aluminum alloy as a material would have been the need to reduce the weight of the bridge in response to the soft clay ground in the Arima area, but one can also imagine the urge the engineers must have felt to engage in this project.



Fig. 1. The Kinkei Bridge

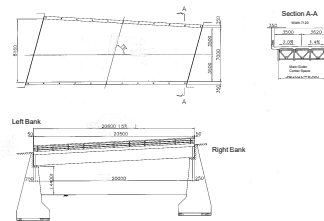


Fig.2. General drawings

Durability committee of the Japan Aluminum Association has been surveying the aluminum alloy girders of the Kinkei Bridge periodically since 1995 (34 years after the bridge’s completion). Latterly, these surveys have been at 5-year intervals, most recently in March, 2022 (61 years since completion). In addition to a visual inspection of the bridge’s appearance, items surveyed included amounts of salt deposition and depths of corrosion. As can be seen in Fig. 3, there are minor incidences of pitting corrosion on both the outer and inner surfaces of the main girders, as well as on the bracings, lateral beams, and connecting joints. This is very shallow in depth, however, (0.6mm at most) and has hardly advanced in the past ten years. As main members, the aluminum alloy girders have remained in continuous service without any need of repair, an outstanding display of endurance.



(a) Inner surface



(b) Main girder end



(c) Outer surface



(d) Bottom flange

Fig. 3. Appearance of aluminum alloy main girder

2.2. Measures against corrosion from contact with steels, and their effectiveness

As reinforced concrete floor slabs, the Kinkei Bridge uses steel dowel bars with base plate and, as shown in Fig. 4, thin plates of zinc, 1mm in thickness, are interposed between the dowel base and the upper flange surface of the girder, to which they are attached with aluminum alloy rivets. As zinc is a baser metal than aluminum alloy, a sacrificial corrosion effect is obtained from this. No significant irregularities were evident even in 2022, 61 years after completion. The same insulation methods were followed between the steel sole plate and the flange of the main girder thin zinc plates of 1mm thickness were again interposed, as shown in Fig. 5. As fasteners, aluminum alloy plate rivets and zinc plated bolts were used. Thanks to the sacrificial corrosion effect of the zinc plates, corrosion is prevented on the lower flange of the aluminum alloy main girders, very severe corrosion occurs on the cast iron bearings as iron is more noble than aluminum alloy. Indeed, after the survey the committee recommended the replacement of this particular bearing. At any rate, expedients such as interposed zinc plates can be seen as one way of guarding against galvanic corrosion in places where different kinds of metal come into contact.

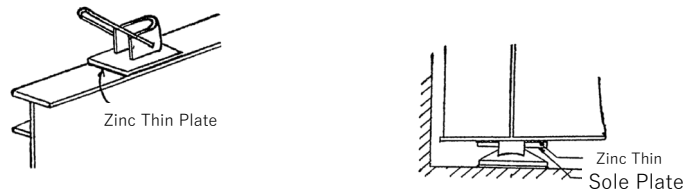


Fig. 4. Zinc plate between steel dubel and flange **Fig. 5.** Zinc plate between sole plate and flange

3. The Joints Durability Performance of Aluminum Alloy Guard Railings

Aluminum alloy parts can be joined in the factory by means of MIG or friction stir welding, but on construction sites, where welding is difficult, there is a need to use bolts. In an ordinary environment where durability is not such a strict requirement, stainless steel bolts with no special surface treatment are adequate, but in severe environments where durability is an issue, it is necessary to use stainless bolts with a zinc flake coating (“Geomet®” treatment). The need for this can be demonstrated experimentally, as argued below. Accelerated exposure tests was performed using the 4 different nut / bolt / washer (etc.) assemblies shown in Fig. 6 (Mrema et al.2018; Itoh et al. 2021). To obtain a quantitative measure of the effects of exposure, a long-term exposure test (up to 5 years) was carried out at the Miyakojima Coastal Exposure Test Site in Okinawa Prefecture. As shown in Fig. 7, two set-ups (direct exposure and eave exposure) were used for 14 types of variously shaped test pieces (250 specimens in total) representing joint members used in guard railings.

After exposure periods equivalent to 1, 3 or 5 years, the bolts were disassembled and removed and the alloy surface was minutely measured for corrosion using a laser depth meter. The values recorded were the maximal depth of corrosion CD_{max} , the corroded surface area, and the amount (mass) of corrosion loss. Fig. 8 shows the outward appearance of one set of test pieces (aluminum plates) after 5 years of exposure. Fig. 8(b) shows the plates with the bolt assemblies removed. Around the holes for bolts of type ‘A’ (stainless steel, non-coated), galvanic corrosion can be seen resulting from the contact of the aluminum alloy with the steel.

The graph in Fig. 9 shows the progression in the depths of corrosion found with non-coated ‘A’ type bolts after 1, 3, and 5 years of exposure. The maximal galvanic corrosion depth clearly increases with the length of the exposure period. Moving to Fig. 10, however, which shows corresponding results obtained with the use of zinc flake-coated bolts, no galvanic corrosion has occurred even after the lapse of 5 years. As for ‘C’ type assemblies, in which only the washer is

Painted for insulation leaving the bolt untreated, and ‘D’ type assemblies in which the bolt is surrounded by an insulating bush, both of these precautions are effective to a degree, but in both cases galvanic corrosion continues to occur locally, due to paint peeling off in the case of type ‘C’ or to deterioration in the bush material leading to a loosening of the insulation fit with type ‘D’.

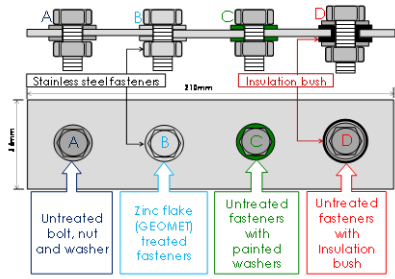


Fig. 6. Specimen concept

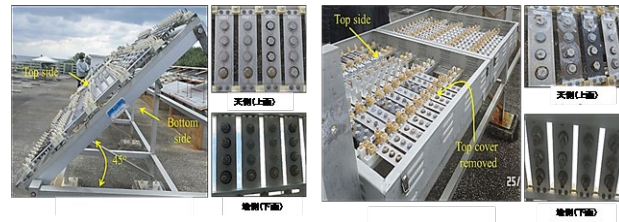
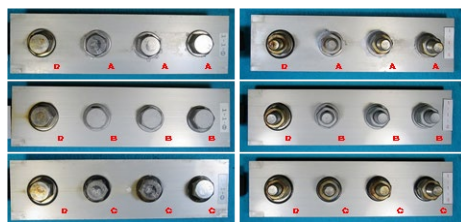
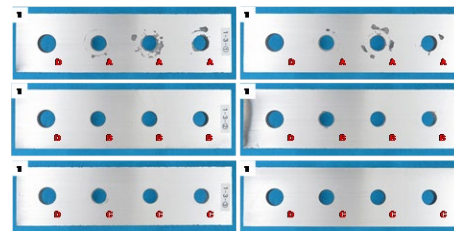


Fig. 7. Specimen set-up



(a) Specimens with bolts



(b) Aluminum alloy plates removed bolts

Fig. 8. Specimen appearances after 5 years exposure

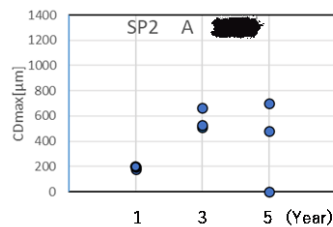


Fig. 9. Non-coated stainless steel bolt

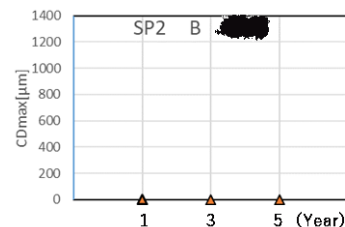


Fig. 10. Zinc flake coated stainless steel bolts

4. Conclusions

The measures taken against galvanic corrosion on the 61-year-old aluminum alloy plate girder Kinkei Bridge were found to have been effective and to have resulted in a very high durability performance. For connections between 6000 series aluminum alloy guardrails and railings, stainless steel bolts with a zinc flake coating (“Geomet”®) were tested and shown to give excellent protection against galvanic corrosion by preventing contact between the two metals.

5. References

Mrema et al. 2018. Galvanic corrosion of aluminium alloy members of bridge guiderails under severe atmospheric exposure conditions. Corrosion Engineering, Science and Technology, ISSN: 1478-422X (Print) 1743-2782 (Online), 54-2.



Bridge Engineering Institute Conference 2023 (BEI-2023)
Rome, Italy, July 17-20, 2023



Itoh et al. 2021. Durability of aluminum alloy members with fasteners using different surface treatments against galvanic corrosion. Journal of Structural Engineering (JSCE), 67A, 431-442.



Study of Water Absorption Properties in Actual Structure Concrete Based on Pore Structure.

N'da Yacoub Bouadou^{1*}, Peter Kuira Macharia², Lai Lai Mon³, and Ryo Yoshida⁴

¹: Nagoya Institute of Technology, Aichi, Japan; email: n.bouadou.525@stn.nitech.ac.jp

²: Nagoya Institute of Technology, Aichi, Japan; email: p.macharia.751@stn.nitech.ac.jp

³: Nagoya Institute of Technology, Aichi, Japan; email: l.lai.441@stn.nitech.ac.jp

⁴: Nagoya Institute of Technology, Aichi, Japan; email: yoshida.ryo@nitech.ac.jp

*: corresponding author

Keywords: Durability; Existing concrete; Carbonation; Water penetration; Pore structure.

Abstract: Concrete is one of the most important materials in public works and building construction, and because concrete is a living material, durability, and structural aging are governed by moisture content. However, it is difficult to determine the condition of reinforced concrete because concrete is permanently evolving and exposed to various environments. This paper provides an overview of design test methods in accordance with the JSCE and ASTM Standard Specification for Concrete Structures, analyzes core samples taken from existing concrete walls, and discusses future directions for new test procedures. Carbonation was observed in the collected cores and correlation between carbonation state and water infiltration depth. This is thought to be an effect of coarsening of the pore structure due to carbonation. Based on these results, the evaluation of water penetration in concrete should be based on the pore structure. Furthermore, the difference of the pore structure from the surface to the interior, of the real structures, needs to be considered in the moisture penetration prediction equation.

1. Introduction

Moisture penetration is the most significant factor in the deterioration of reinforced concrete. In the durability verification of reinforced concrete in the Japanese Society of Civil Engineers, the verification method based on moisture penetration was established in 2017. However, this verification method is tentative, and the prediction equation was developed through experiments using homogeneous concrete produced in a laboratory. Therefore, this prediction equation cannot accurately predict the depth of water penetration in concrete subjected to environmental degradation as in real structures. This is because, in the concrete of real structures, there is a difference in the denseness (pore structure) between the surface concrete and the interior concrete due to carbonation and drying, which is not considered in the prediction equation. The objective of this study is to take into account the pore structure of the real structure due to environmental effects and to accurately predict the depth of water penetration in the real concrete structure. To this end, water absorption tests (surface and immersion), carbonation tests, and Pore volume rate were conducted on cylindrical specimens cored on existing road walls. Specimens were analyzed in accordance with JSCE and ASTM standards. Based on the results of these tests, a new test method was devised by comparing the results with actual test methods and considering the distribution of densities that real concrete structures have.

2. Outline of the Experiment

2.1. Materials used and preparation of specimens

150mmx100mm ϕ concrete cores were drilled from Tokai-dori line railway track barrier walls. Visual inspection was carried done to sort out cores with open voids, cracks, and other visible defects. The suitable cores were wrapped and stored in an open container at room temperature for 100 days. Using Rilem Tubes, an initial surface water absorption test was conducted on either surface of each core to determine the effect of curing conditions and the effects of microcrack in the concrete quality within 30min(*Basheer et al.,1995*) to evaluate the quality of concrete at the cover zone under natural dominant water suction. After the surface water absorption test, the cores were dried in an oven at 80°C until the mass change in 24hrs was less than 0.1%.

Table. 1. Average of sample dimensions and mass.

Specimen Properties	JSCE	ASTM	W/C
Diameter (mm)	100	100	60%
Thickness (mm)	150	50	
Water Temperature °C	20	20	
Mass before sealing (grams)	2655.82	827.08	
Mass after sealing (grams)	2664.02	835.28	

2.2. Experimental Methods

2.2.1. JSCE-G 582-2018 Test Standard

The following method was applied to determining water penetration rate coefficients of concrete subjected to water in a short time. The concrete cores were dried in a controlled chamber at a temperature of $40 \pm 2^\circ\text{C}$ and relative humidity of $30 \pm 5\%$ until 24- hour mass change was less than 0.1% and cooled to room temperature by natural heat loss for of 1 hour and then stored in a closed container for 24 hours. The weight of each dry core was measured and a 10 mm mark from the bottom of the specimen was labelled and carefully placed 5 mm height. Tap water was used as a test solution and the specimens were split at 48 hours after immersion and sprayed with an indicator. The water penetration depth was measured at 5 points using a caliper, and the average value was taken.

2.2.1. ASTM C1585-3 Test Standard

The test method used was ASTM C1585 – 03: “Measurement of Rate of Absorption of Water by Hydraulic Cement Concrete”. This test method determines the rate of absorption (i.e. sorptivity) of water by hydraulic cement concrete by measuring the increase in the mass of a specimen resulting from absorption of water as a function of time when only one surface of the specimen is exposed to water. The disc concrete specimens of 100 ± 6 mm diameter with a length of 50 ± 3 mm were cut from the 150mm cores in order to have both internal and external disc concrete and vacuum saturated for 24 hrs, The specimen for 9 drilled cores were used were sealed with aluminum tape and later conditioned in an environmental chamber with a temperature of $50 \pm 2^\circ\text{C}$ and RH of $80 \pm 3\%$ for 3 days. Each sample was then placed in a sealed container at $23 \pm 2^\circ\text{C}$ for 15 days figure illustrative

3. Experimental Results and Discussion

3.1. Relationship between JSCE and ASTM water absorption rate

In this study, the comparison between both internal and external (side exposed to carbonation) of ASTM cores has been made with the JSCE cores in order to determine the water absorption rate (sorptivity) of both the outer and inner concrete surfaces following different conditioning methods [1]. Despite the fact that at the initial stage internal core of ASTM has a strong correlation with JSCE external, we observed a strong correlation between JSCE methods and ASTM methods Fig. 1.

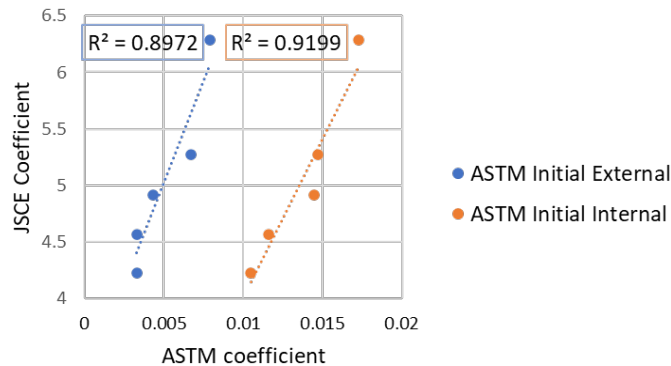


Fig. 1. Relation between JSCE and ASTM water absorption rate

3.2. Relationship between water absorption rate and carbonation depth

After slicing the JSCE cores and after checking the water infiltration depth, carbonation was determined in those cores using the phenolphthalein test method. Following the result of the mesearment and as per the previous research, a correlation was observed between water absorption and carbonation state Fig.2 .The changes in water penetration resistance due to carbonation were because of the modifications in the pore structures. It is considered that the carbonation makes the concrete pore larger and consequently affects the water infiltration rate [2] .

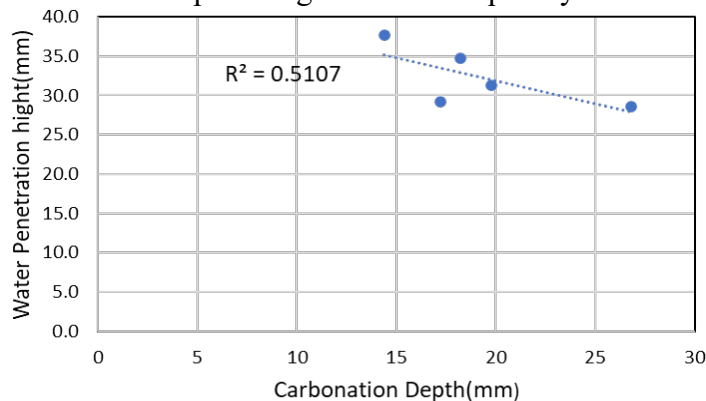


Fig. 2. Relation between absorption rate and carbonation

3.3. Relationship between JSCE water absorption rate and core slice absorption rate.

From the results of the water penetration test, it is considered that the changes in water penetration because of the porosity were calculated by Eq.1. The sample was immersed in acetone for 24 hours with mass change recording after 1min, 5, 10, 15, 30, 60mins, the mass was also recorded at an interval of one hour up to six hours.

$$w_a = \left\{ \frac{m_1 - m_2}{V} \right\} \times 100 \quad (1)$$

w_a = Absorption rate (%)

m_1 = mass in air,

m_2 = absolute dry mass (g),

v = volume of the specimen, in mm^3

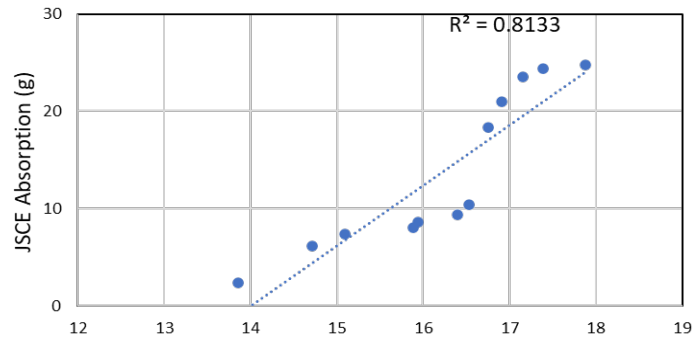


Fig. 3. Relation between absorption rate and carbonation

Based on the core slice study we observed a strong correlation between slice1-2 absorption rate and JSCE absorption rate, which can tell this slice which has a high of 30mm represents the effective water infiltration depth.

4. Conclusion

In this paper, the effect of the environment on real concrete structures has been investigated and it was confirmed that, despite the fact that ASTM and JSCE have different conditioning methods they have a good capillarity suction rate correlation. Studying the cores slices gives relevant information on the mechanism of water absorption in the existing concrete considering that real concrete is heterogenous from the surface towards the interior due to the environmental effect. Furthermore, pore structure can be considered as a durability indicator for further research on water infiltration depth prediction.

5. Acknowledgments

We would also like to thank the laboratory colleagues for their help.

6. References

- [1] R. J. Gummer son, C. Hall and and W. D. Hoff, "Water Movement in Porous Building materia;. Is --II. Hydraulic Suction and Absorptivity of brick and other Masonry Material," in *Water Movement in Porous Building Vol.15*, 1980, pp. 101 - 108.
- [2] S. Maehara, M. Suzuki and K. Hayakawa, "Effect of Carbonation Depth on Short-Term Water Penetration In Concrete," Tokyo Construction Technology Research Institute Bulletin No. 46, Tokyo, 2018.



Bridge Engineering Institute Conference 2023 (BEI-2023)
Rome, Italy, July 17-20, 2023



Performance and Evaluation



Evaluation of the National Bridge Inventory (NBI) to Predict Bridge Deterioration in Missouri, USA

Glenn Washer¹, John J. Myers^{2*}, and Mohammed Hammed¹

¹: University of Missouri - Columbia, Columbia, Missouri, USA; email: washerg@umsystem.edu

²: Missouri University of Science and Technology, Rolla, Missouri, USA; email: jmyers@mst.edu

*: corresponding author and plenary presentation

Keywords: NBI Inventory, bridge deterioration, bridge condition rating (CR), bridge service life.

Abstract: In the state of Missouri, USA, The Missouri Department of Transportation (MoDOT) is responsible for the inspection and maintenance of approximately 10,000 bridges and culverts on the state roadway system. The condition of these structures is assessed biannually to monitor deterioration that occurs as a result of environmental exposure and traffic loading. To effectively manage these important assets, MoDOT launched a research effort to develop deterioration models that would allow them to better project future preservation and rehabilitation activities and develop data-driven asset management plans.

This study developed deterioration curves for different bridge components and culverts, identified trends in deterioration patterns, and develop recommendations for cost-effective bridge types. To conduct this analysis, records from the Federal Highway Administration's (FHWA) National Bridge Inventory (NBI) were obtained for the years of 1983 - 2019. These records document the inspection results from biannual inspection through condition ratings (CR) that describe the condition of bridge components (deck, superstructure, and substructure) and culverts on a 0 - 9 numerical scale. This paper will discuss the key takeaways from the study in terms of influencing factors, rate of deterioration once certain CR's occur and future recommendations in terms of data collection.

1. Introduction

Historically, bridge inspection in the US began shortly after the collapse of the Silver Bridge on December 15, 1967. Following the collapse, requirements for the inspection and reporting of bridge conditions to the FHWA were established in 1971, with the first round of inspection on National Highway System bridges due in 1973. Inspections were completed on a component level basis that rated three primary components of a bridge (deck, superstructure, and substructure). Additional data on the characteristics and location of the structure were also recorded. In conventional component-level bridge inspection, bridge managers use inspection results to identify maintenance needs from the safety perspective to help make decisions. A subjective CR scale ranging from 0-9 is used to characterize the condition of bridge components relative to the as-built condition. Culverts receive a single CR to describe the general condition of the culvert. The CRs are recorded on a 0-9 scale where 0 is a structure in "failed condition – out of service" and 9 is a structure in "excellent condition." Structures in "good" condition have CRs of 7 or greater, structures in "poor" condition have ratings of 4 or less. Structures with CRs of 5 or 6 are considered

in “fair” condition. The results of the inspection along with other data describing a structure are submitted annually by bridge owners to the FHWA. These data are stored in the NBI. Although this data collection has been ongoing since the early 1970s, the available data from the FHWA begins in 1983.

2. Statistical Analysis Methods

Improving the understanding of the deterioration and life expectancy of bridges allows for transportation agencies to improve their planning processes and also better understand how certain bridge types perform under various environmental and physical exposure conditions. In this work, deterioration curves were developed based on Kaplan-Meier (K-M) method of survival analysis (Washer et al. 2014; Washer et al. 2018; Kaplan and Meier 1958). This methodology applies the National Bridge Inventory (NBI) Condition Rating (CR) data collected over a time interval of 37 years to calculate the probability of likelihood of a structure to transition to the next lower CR. These data were then analyzed and median service life estimates were provided for the deck, superstructure, and substructure of bridges formed from the materials of steel, reinforced concrete (RCC), and prestressed concrete (PSC). Similar curves and service life estimates were produced for concrete culverts.

Cox regression analysis was used to identify and quantify trends in the deterioration of different types of bridges MoDOT has built over the years. These data were analyzed to determine the influence of parameters such as the effect of salt application, environment, span length, traffic volume, location, and age. For the purposes of this limited paper, the authors will focus on presenting variables investigated, their general influence and data collection gaps.

3. Data for Analysis

Inspection data (records) for state-owned bridges and culverts in Missouri, USA were acquired from two different sources within the FHWA. Records from the years of 1992–2019 were obtained from the Long-Term Bridge Performance Program (LTBP) web resource called InfoBridge (see Fig. 1). In addition to these data, NBI records were acquired from 1983–1991 from the FHWA Office of Bridges and Structures. Data recorded in the NBI for the years of 1983–2019 for structures in Missouri were affected by various changes in the numbering system used for state bridges. As a result, data preparation included resolving numbering inconsistency in the records such that the historical performance of each bridge could be tracked over time. In total, 37 years of inspection data were obtained for analysis. Fig 2. Shows the years of inspection data used for bridges in Missouri, USA.

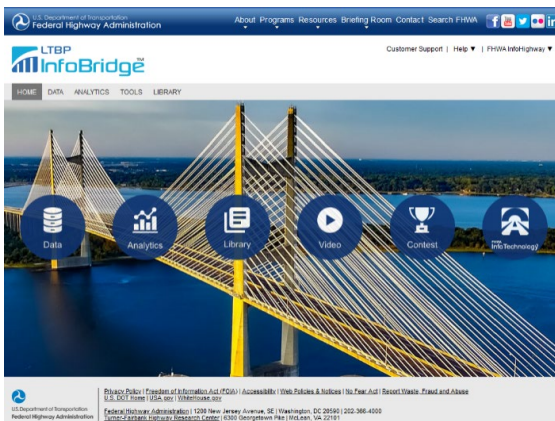


Fig. 1. FHWA InfoBridge™ Website

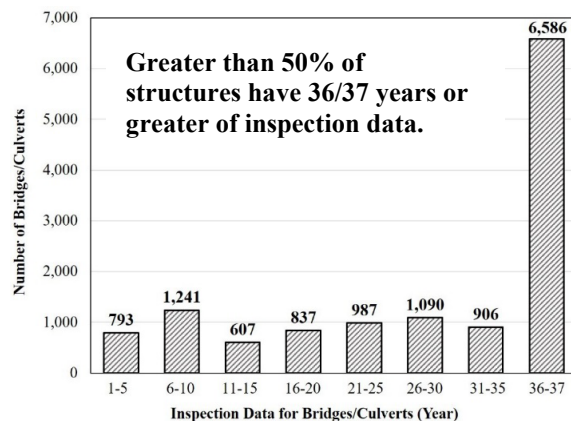


Fig. 2. Years of Inspection Data for MO Bridges

The independent variables included the age of the structure, with consideration for renovation or replacement. The structure kind, structure type, construction material (e.g., steel, reinforced concrete, prestressed concrete, etc.) and construction type (e.g., simply supported, continuous, truss, girder, etc.). There are 56 different combinations of superstructure materials and designs, including 51 different bridge combinations. In addition, structure length, span length, deck type, traffic volume (ADT and ADTT) were important parameters to examine. Other data such as climate (e.g. freeze/thaw data by district/region in the state) and salt usage by county was collected separately. Salt usage was converted to salt lanes miles in each district. The CR for decks, superstructures, substructures, and culverts are the main dependent variables used to determine the reliability of structures in the MoDOT inventory.

4. Results and Discussion

Reliability analysis for CIP decks and service life plots were developed based upon the analysis for all Missouri bridges in the database. Unlike some regions in the USA, superstructure decks in particular are most susceptible to deterioration due to heavy deicing salt usage in the winter. Fig. 3 shows the reliability of CIP decks for CR 3-8. This can be used to construct service life estimates for CIP decks based on the percentage of the CIP decks still surviving at the median value from the reliability plot. The median value is illustrated on the plot with a horizontal line at 50% reliability. Fig. 4. Shows the resulting service life for CIP decks based on medium reliability in CR 3-8.

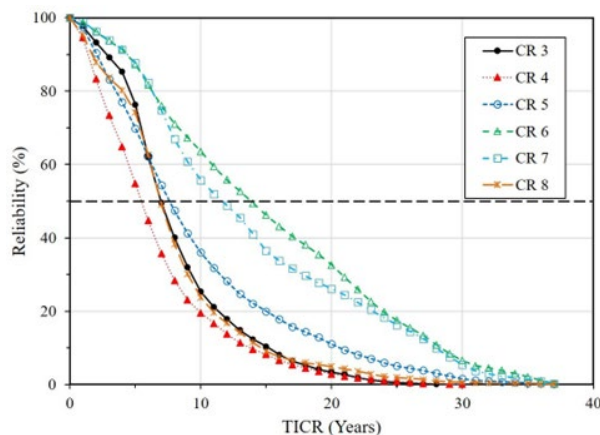


Fig. 3. K-M Curve for CIP Decks CR 3-8

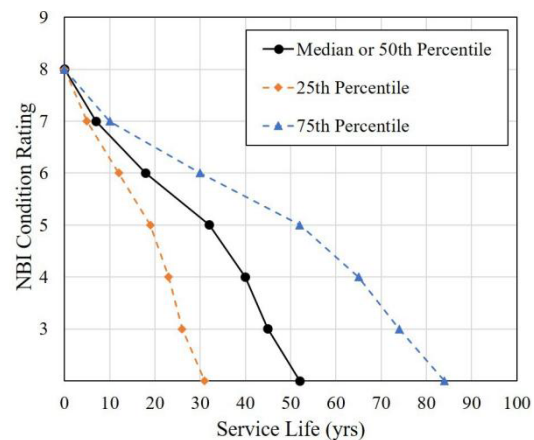


Fig. 4. Service Life for CIP Decks in CR 3-8

Table 1. Table showing maximum likelihood estimate for CIP deck covariates

Var. no.	Variables in model	-2log LL♦	Likelihood ratio	Result
0	None	242,492.64		Null model
1	Age in TICR	242,446.15	46.49	Significant
2	Structure length (ft.)	242,479.71	13.99	Significant
3	Maximum span length (ft.)	24,2435.75	56.89	Significant
4	Freeze/thaw (days/year)	242,455.34	37.30	Significant
5	Snow (days/year)	242,463.27	29.36	Significant
7	Salt (tons/lane miles)	242,419.31	73.33	Significant
8	ADT	242,492.25	0.39	Not significant
9	ADTT	242,492.41	0.23	Not significant
10	District	242,398.57	94.07	Significant
11	Region	242,442.91	49.73	Significant
12	Superstructure type	242,228.75	263.89	Significant

Table 1 indicates the maximum likelihood estimate for CIP deck covariates. The most influential factor, other than the superstructure type, which affected bridge deterioration in Missouri was the use of salt. This may seem antidotal to most bridge engineers, but confirmation of this correlation was an important finding. Fig. 5 and Fig. 6 show the Missouri district and relationship between snow days and salt usage in Missouri.

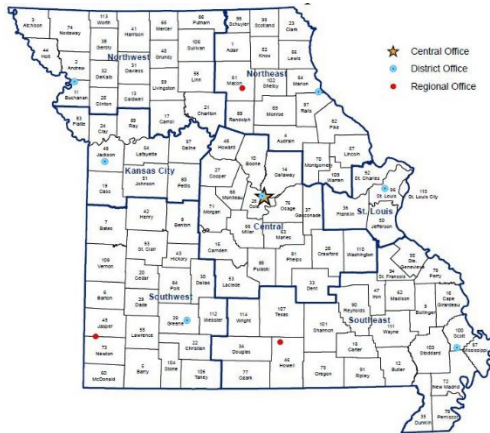


Fig. 5. Missouri's Seven Districts

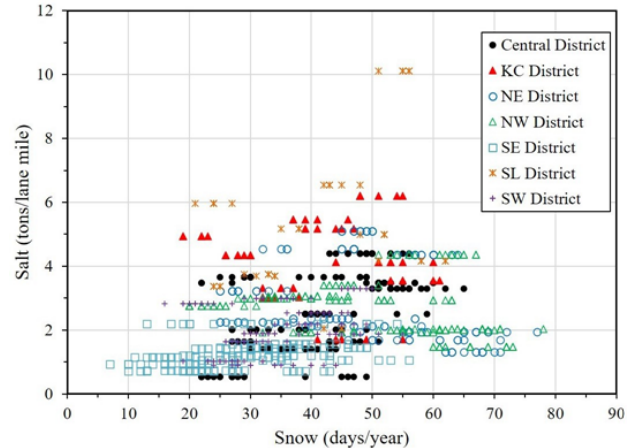


Fig. 6. MO Salt versus Snow Days for 2001-2010

Naturally the type of superstructure had an important role in the NBI condition rating and deterioration rate. Fig. 7 presents the service life plot for different types of super structures. It may be noted that Reinforced Concrete continuous (RCC) slab bridges (among the oldest in the system network) followed by Prestressed Concrete continuous (PSC) girder bridges exhibited the longest service life in the database.

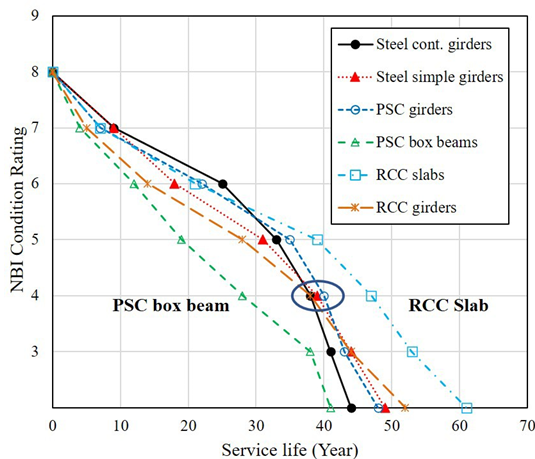


Fig. 7. Service life by Superstructure Type

The data showed that ADT and ADTT did not have a statistically significant effect on the reliability of structures. An improved understanding of the service life and major influencing factors in bridge life, will significantly assist the owner in system selection, predicting structure life and planning. The following recommendation is suggested: a more precise tracking system to track the frequency and quantity of salt application is recommended in each state in the US. This should also be integrated within the NBI data collection system.

6. References

Washer, G., et al., *Proposed Guideline for Reliability-Based Bridge Inspection Practices*. NCHRP Report 782, 2014 (Washington, D.C.).
 Washer, G., et al., *Guidelines to Improve the Quality of Element-Level Bridge Inspection Data*. 2018, NCHRP: Washington, D.C.
 Kaplan, E.L. and Meier, P., *Nonparametric Estimation from Incomplete Observations*. 1958, 53(282): p. 457-481.



Assessment of Live Load Carrying Capacity of Prestressed Concrete Bridge: a Case Study

Shin-Tai Song^{1*} and Yiching Lin²

- ¹: Associate professor, Department of Civil Engineering, National Chung-Hsing University, Taichung, Taiwan, R.O.C.; email: ssong@nchu.edu.tw
²: Professor, Department of Civil Engineering, National Chung-Hsing University, Taichung, Taiwan, R.O.C.; email: yiching@dragon.nchu.edu.tw

*: Corresponding author

Abstract: A prestressed concrete girder bridge is selected to illustrate the versatility of an approach for assessing the live load carrying capacity of the bridge span. The prestressing force on a girder is estimated using a strain relief approach. The effective flexural rigidity of the girder is assessed by conducting a truck load test for the bridge span. Determining the flexural rigidity and prestressing force will enable the construction of a finite element model of the bridge under its current condition. The extent of the allowable stress increment of the bridge span is established by comparing the stress on the girders under their current condition with the stress limit for satisfactory performance. The allowable stress increments are further used in bridge safety monitoring.

1. Introduction

The serviceability of prestressed concrete bridges is highly dependent on the stress level of their tendons. The shrinkage and creep of concrete as well as the relaxation of the prestressing tendons can cause prestress loss, resulting in the deterioration of the serviceability of a bridge. Additionally, chemicals in the environment, overweight vehicles, and unexpected natural disasters may exacerbate the deterioration of a bridge, resulting in unexpected prestress loss and the subsequent degradation of its serviceability. The actual level of prestress loss in the tendons cannot be estimated by simply observing the damage on the girders or applying theoretical calculation. Rather, the prestress loss must be determined through mechanical testing. The identification of the forces remaining on the prestressing tendons will allow for the assessment of the performance of a bridge. This study demonstrates an approach for determining the prestressing force on tendons and evaluating the live load carrying capacity of bridges with prestress loss. The primary consideration for utilizing the approach is to comprehend the behavior of a bridge with limited instrumentation. Two sets of tests are performed onsite to determine the effective flexural stiffness and prestressing force of the girders of a bridge. Knowing the effective flexural rigidity and prestressing force will enable the construction of an analytical model, which can simulate the load-deformation response of the bridge under its current condition. By comparing the stress on the girders under the current condition with the stress limit for the satisfactory performance of the prestressed concrete girders, the allowable stress increment of the bridge span can be established. The allowable stress increments are further used in bridge safety monitoring.

2. Bridge Model

A multi-span prestressed concrete I-girder bridge located on the West Coast Expressway in Taiwan is selected to illustrate the versatility of the presented approach. Routine inspection of the bridge found that several girders suffered from flexural cracks. As the bridge is located in a high-corrosion-risk region, the maintenance agency is concerned about the serviceability of the bridge and wants to assess its load carrying capacity. The bridge has 40 simply supported spans, with a span length of 40 m. Each span consists of eight prestressed concrete girders, which are connected by seven transverse diaphragms. Each girder contains six prestressing tendons, which are made of twelve 12.7-mm diameter strands. The effective prestressing force on a girder is designed to be $P_D = 7000$ kN, considering prestress loss. The ultimate tensile strength of a strand is $f_{pu} = 1870$ MPa, and the compressive strength of the concrete is $f'_c = 35$ MPa. The bridge span is modeled by a grillage model, which idealizes the superstructure as a skeletal structure consisting of interconnecting elements. The longitudinal elements simulate the response of the girders subjected to external loads, and the transverse elements simulate the load distribution effect between the girders. The grillage model of the bridge span is shown in Fig. 1. The superstructure of the bridge is simply supported, allowing each span to exhibit independent behavior when subjected to external loads. The load carrying capacity of each span can be assessed separately. For the purpose of this study, only one span is selected to illustrate the assessment process.

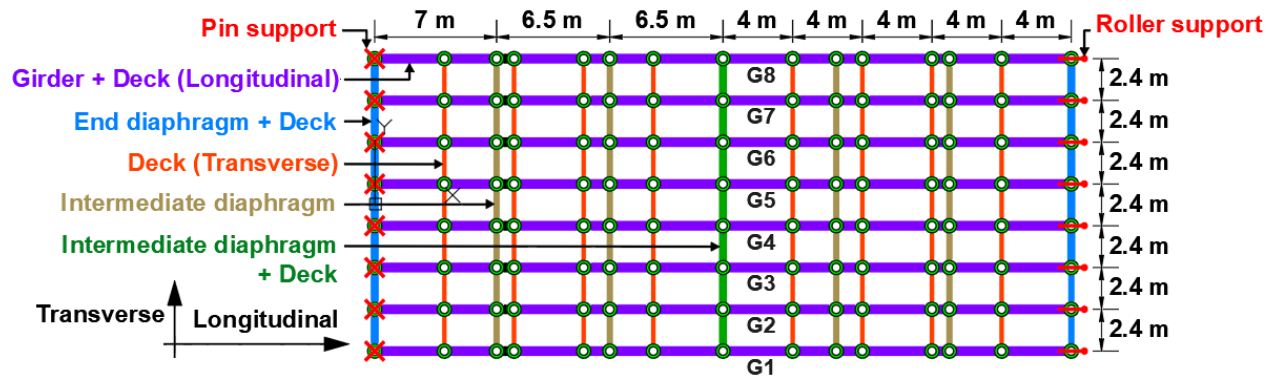


Fig. 1. Grillage model of bridge span

3. Truck Load Test and Stress Relief Test

A truck load test and stress relief test are conducted onsite to assess the flexural rigidity and prestressing force of the girders, respectively. The truck load test is conducted by slowly moving a 245 kN truck along girder 5 (G5) and briefly stopping at the midspan before proceeding to the adjacent span. Two strain gauges are installed at the midspan of G5, one mounted on the bottom of the girder and the other at 53 cm above the bottom of the girder. Fig. 2(a) shows a strain increment of $\epsilon_b = 13.49 \mu\epsilon$ at the bottom of the girder when the truck was in position. Fig. 2(b) shows that the truck caused a strain of $\epsilon_w = 7.63 \mu\epsilon$ at 53 cm above the bottom of the girder. Following the assumption of a linear strain profile under flexure, the neutral axis of the girder section is $h_n = 134$ cm from the bottom. The analytical model of the bridge span shows that when the span is subjected to a 245 kN load at the midspan of G5, the maximum bending moment of G5 is $M_{mid} = 325$ kN-m. By determining the location of neutral axis h_n , strain at the bottom of the girder ϵ_b , and associated bending moment M_{mid} , the effective flexural rigidity of the girder can be calculated by

$$EI_e = \frac{h_n}{\varepsilon_b} M_{mid} \tag{1}$$

and is equal to $EI_e = 3.23 \times 10^7 \text{ kN}\cdot\text{m}^2$. The effective flexural rigidity is 1.5 times larger than the theoretical flexural rigidity estimated by the concrete strength f'_c and section geometry. The prestressing force on the girder is assessed with a strain relief approach. The approach involves cutting two slots into the web of G5, that is, one near the top flange and another near the bottom flange. The compressive stress on the concrete will cause the edges of the slots to deform toward one another. The deformation of the edges is measured to further calculate the stress on the concrete (Jiang 2018). The top slot, which is 149 cm from the bottom of the girder, is measured as having a compressive stress of $\sigma_{ts}^{total} = 2622 \text{ kPa}$. The bottom slot is 82 cm from the bottom of the girder and has a compressive stress of $\sigma_{bs}^{total} = 2725 \text{ kPa}$. In addition to the prestressing force and self-weight, the temperature gradient across the girder section will exert stress on the concrete. This stress must be assessed to accurately evaluate the prestressing force on the girder. Figure 3 illustrates the temperature gradient measured during the strain relief test and the resulting stress induced by this gradient. The temperature gradient causes a tensile stress of $\sigma_{ts}^{temp} = 884 \text{ kPa}$ on the top slot and $\sigma_{bs}^{temp} = 345 \text{ kPa}$ on the bottom slot. By subtracting the stresses induced by temperature gradient from the results of the strain relief approach, the stresses caused by the prestressing force and self-weight are obtained as $\sigma_{ts}^{mech} = 3506 \text{ kPa}$, in compression, on the top slot and $\sigma_{bs}^{mech} = 3070 \text{ kPa}$, in compression, on the bottom slot. The stress on the bottom of the girder is estimated to be $\sigma_b^{mech} = 2530 \text{ kPa}$. Then, the prestressing force is determined to be $P_e = 5750 \text{ kN}$, which is 82% of the designed effective prestressing force.

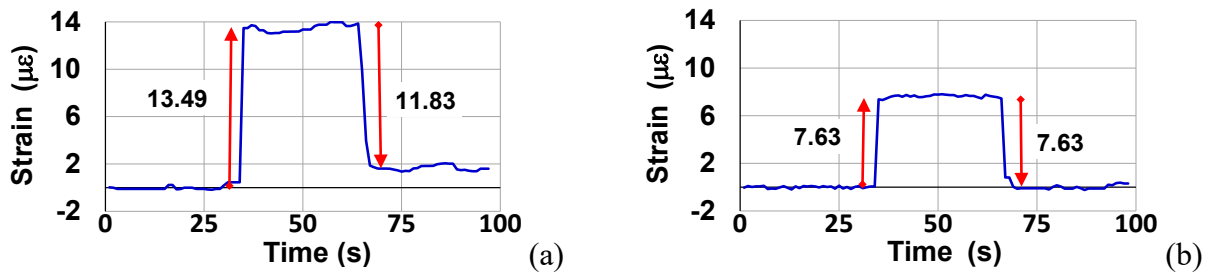


Fig. 2. Variation of the strain in truck load test

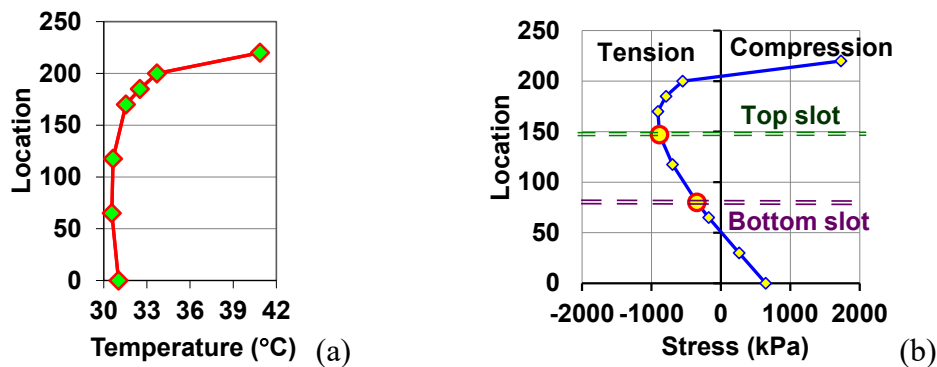


Fig. 3. (a) Temperature gradient measured in G5; (b) induced stress

4. Live Load Carrying Capacity and Strain Increment for Bridge Safety Monitoring

The effective flexural rigidity of $EI_e = 3.23 \times 10^7$ kN-m² estimated from the truck load test and prestressing force of $P_e = 5750$ kN assessed by the strain relief test are further utilized to revise the analytical model of the bridge under its current condition. The results of the stress relief test also indicate that G5 is currently under a compressive stress of $\sigma_b^{mech} = 2530$ kPa at the bottom of the girder when subjected to the self-weight of the bridge and prestressing force. For a prestressed concrete bridge located in a high-corrosion-risk region, the bridge design specification (MOTC 2020) indicates a tensile stress limit of $f_t^a = 0.249\sqrt{f'_c}$, which is 40% of the modulus of rupture of concrete and equal to $f_t^a = 1470$ kPa in the sample bridge. The difference between the compressive stress currently applied to the girder and tensile stress limit provides an allowable stress increment of 4000 kPa. The bridge was originally designed with a prestressing force of $P_D = 7000$ kN. The self-weight of the bridge and prestressing force of $P_D = 7000$ kN induce a compressive stress of $\sigma_b^{mech} = 5160$ kPa at the bottom of G5, and the allowable tensile stress increment is 6630 kPa. The comparison between the current allowable stress increment of 4000 kPa and stress increment of 6630 kPa in the original design shows that the live load carrying capacity of the bridge span is reduced to 60%. The stress increment of 4000 kPa is equivalent to an allowable tensile strain increment of $\epsilon_t^a = 97.1 \mu\epsilon$ at the midspan of G5. For the purpose of bridge safety monitoring, a strain gauge can be installed at the midspan of G5. A strain increment of $\epsilon_t^a = 97.1 \mu\epsilon$ can be applied to verify whether the traffic load caused the stress level of the girder to exceed the limit specified in the design code.

5. Conclusion

This study presents an approach for assessing the live load carrying capacity of a prestressed concrete girder bridge and establishes the allowable strain increment for bridge safety monitoring. A truck load test and strain relief test are performed onsite to determine the effective flexural stiffness and prestressing force of a bridge girder. The results of the onsite tests will enable the construction of a finite element model of the bridge under its current condition. The comparison between the stress currently applied to the girder and stress limit specified in the design code can provide the allowable stress increment for the bridge span, which is further used to evaluate the live load carrying capacity. For the bridge selected in this study to illustrate the versatility of the approach, the current live load carrying capacity is 60% of the originally designed capacity.

6. Acknowledgements

This research was sponsored by the Maintenance Agency of District-2, Directorate General of Highways, Taiwan, R.O.C. The financial support is gratefully acknowledged.

7. References

Jiang, Kuo-Ruei 2018. Numerical and experimental study of strain relief measurement method for prestressed concrete structures, Master Thesis, National Chung-Hsing University.

Ministry of Transportation and Communications (MOTC) 2020. Highway Bridge Design Specifications, Taipei, Taiwan, R.O.C.



Strategic Asset Management of Locally Owned Bridges

Mi G. Chorzepa^{1*}

^{1*}: The University of Georgia, Athens, Georgia, U.S.A.; email: chorzepa@uga.edu

*: corresponding author

Keywords: locally owned; element; bridge; maintenance; priority

Abstract: In the United States, locally county owned bridges are in relatively worse condition than state-owned bridges. To understand local counties' bridge management process and identify current practices, 50 select county maintenance personnel in the state of Georgia are interviewed. Additionally, bridge element inspection data, reports, and deficiency characteristics are analyzed. The goal of this study is to identify a strategic prioritization process in asset management of county owned bridges that are inspected by the state department of transportation. It is concluded that more resources have been allocated to address substructure elements and erosion issues as they are perceived to be more vulnerable, whereas small preventive maintenance items such as joint sealing and steel painting have been delayed. The findings indicate that county-owned steel bridges and elements are vulnerable because local governments do not generally engage in bridge painting. It is also concluded that deficiencies are consistently indicated in inspection reports over the years; however, inaction persists until counties are informed that bridges need to be posted or even worse, closed. The effect of inaction is presented with real-life examples, and the county survey and data analysis results are described with respect to a strategic prioritization process required for managing locally-owned bridges.

1. Introduction

The Georgia Department of Transportation inspects locally-owned bridges in 159 counties and sends a deficiency report to each county. However, the National Bridge Inventory Element (NBIE) data indicate that inaction is prevalent, forcing a replacement or major repair of bridges in less than 50 year of their 75-year service life.

2. Current Bridge Asset Management Practice

Currently, the Georgia Department of Transportation inspects locally-owned bridges and provides a list of maintenance items indicating deficiencies with three-tier priority ratings of A, B, and C, representing 'Immediate maintenance required-hazard to public safety', 'Schedule maintenance', and 'Preventative maintenance', respectively. While the element inspection data provide a flagging mechanism for identifying critical bridge elements in addition to the original National Bridge Inventory components (deck, superstructure, and substructure), descriptive information identifying vulnerable bridge elements is obtained in inspection reports which currently are available as pdf files, including photos taken during an inspection. Unfortunately, most local governments do not always fully review the inspection reports but mainly rely on deficiency reports, focusing on actionable maintenance items provided in a summary letter from the state agency.

2.1. Analysis of the Current Practices

Bridges in the state of Georgia are in relatively good condition in the U.S. However, once substructure concrete elements develop cracks, they rapidly develop into section loss and spalling. Thus, it is reasonable to prioritize maintenance of substructure elements, particularly those in close proximity to ocean waterways. On the other hand, joints on the deck are not always repaired when minor damage or small spalling is observed. However, signs of associated deterioration are observed in substructure components such as pile caps, columns, pier caps, and abutments due to the lack of preventive maintenance conducted on joints. Additionally, protective coating for steel beams is considered as preventive maintenance and thus has not been prioritized, resulting in corrosion and section loss and a bridge closure when no action is taken by county governments.

2.2. Three Most Vulnerable Bridge Components and Associated Elements

Table 1 shows four selected bridges for illustration, their three main components, and associated bridge elements. Approximately, 100 bridges are identified by a reliability analysis conducted using field measured vehicle weight information (Sinha et al., 2022). The change in the operating load rating shown below is determined from the NBI database, and the health indices are calculated by using nonlinear weight factors (Oyegbile et al., 2021). Finally, descriptive information in the inspection reports from years 2012 to 2022 are reviewed to search for additional details on deficiency items.

Table 1. Selected Bridge Structures, Element Health Index, and Qualitative Data.

Bridge Number Used for Illustration	Operating Rating Reduction (Year Built)	Reduction in Health Index > 5%			Areas of Concern in Inspection Reports		
		Deck & joints	Super structure	Sub structure	Deck	Super structure	Sub structure
1	72% (2016)	-	Steel Truss	RC Column, RC Pier Wall, RC Pile	Steel grating, Joints, Rail	RC beams, Steel truss	RC Pile, Column, Pier Wall, Pier Cap, and Abutment
2	63% (2009)	-	Steel Girder/ Beam	-	RC Deck deterioration	Steel girder	RC Column, Abutment, Pier Cap
3	61% (2009)	RC Top Flange	-	-	RC Deck, Approach slabs	PSC beams, RC beams	RC Abutment, RC Pier Cap, PSC Pile
4	58% (2006)	Pourable Joint	-	PSC Pile	RC Deck, Joints, Approach slabs, Guardrail	PSC beams, associated bearing	RC Pier Cap, PSC Pile, RC Abutment

3. Comparison of Quantitatively and Qualitative Information

Fig. 1 through Fig. 3 present the three most frequent deficiency types found in locally owned bridges' inspection reports, which are public information. The quantitative information provided in the bridge element data is compared with the more descriptive information available in bridge inspection reports. The deterioration on the substructure was not isolated but often initiated from deterioration of joints on bridge deck elements. The description of deficiencies presented in this paper includes the opinions of the author, not the state and county governments.



Fig. 1. Deck elements of Bridges #1-4: (a) approach (b) pourable joints (c) and (d) deck joints (GDOT, 2022).

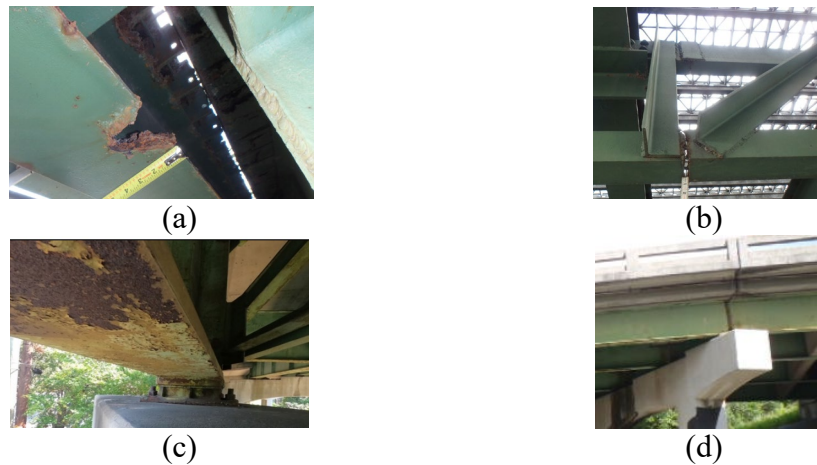


Fig. 2. Superstructure elements of Bridge #1-4: (a) steel truss section loss (b) steel truss corrosion (c) loss of protective coating (d) steel girder ends (GDOT, 2022).



Fig. 3. Substructure elements of Bridges #1-4: (a) RC pile; (b) RC pile; (c) column; (d) pile cap deteriorated (GDOT, 2022).



3.1. Analysis of Interviews with Local Governments

Only 8% of the interviewed counties reported having a written asset management plan for their bridges. Counties are heavily reliant on the state/federal support for bridge assets. Most indicate inspection reports are challenging to understand and thus rely mainly on deficiency reports and actionable maintenance items. Counties report difficulties in finding funding for themselves when it pertains to major repairs, compounded by ongoing difficulty locating competent contractors. More than 50% state that they document a record of maintenance activities on their bridges. Most common activities include brush/tree cutting, erosion control, guardrail repair, and deck repair. Structural repair of members is cited as one of the least common.

3.2. Analysis of the NBI Condition Ratings, Element States, and Inspection Reports

Most counties do not employ a civil engineer in their public works and thus find jargon which appears in bridge inspection reports difficult to understand. As shown in Table 1, the inspection reports provide additional qualitative information including the detailed description of deficiencies and interactive aspects (Oyegbile et al., 2021) of elements (e.g., joints, bearings, and substructure). Despite well documented deterioration particulars in the inspection reports, the information has not been translated to effective maintenance actions.

4. Conclusions and Future Work

A strategic prioritization process should involve budgetary planning based on prioritized maintenance actions identified through bridge inspection and thus should include a plan for preventive maintenance which extends the service life of bridges. Due to limited resources, however, most local governments focus on addressing most urgent maintenance items in their inventory. It is concluded that inspection reports provide superior qualitative information of the bridge conditions needed for maintenance whereas the quantitative element data are not as helpful in identifying preventive maintenance items that extend service life. Such relationship is in the process of being identified by means of deep learning and other decision algorithms. Additional challenges include the absence of photos showing bridge elements in good condition for a comparative analysis. A priority rating of ‘B+’ requiring a maintenance action within 12 months is currently being implemented. More importantly, the largest gap between maintenance actions and prioritized recommendation exists due to the lack of budgetary planning. A cost-benefit analysis of the actionable maintenance items is not always feasible at a local-government level, which means decision making is exclusively based on availability of funding.

5. References

GDOT, the Georgia Department of Transportation, 2022:
<https://www.dot.ga.gov/Pages/Default.aspx>

Oyegbile, O.B., Chorzepa, M.G., Durham, S.A. and Kim, S.S., 2021. Novel Prioritization Mechanism to Enhance Long-Term Performance Predictions for Bridge Asset Management. *Journal of Performance of Constructed Facilities*, 35(1), p.04020133.

Sinha, A., Chorzepa, M.G., Yang, J.J., Kim, S.S. and Durham, S., 2022. Enhancing Reliability Analysis with Multisource Data: Mitigating Adverse Selection Problems in Bridge Monitoring and Management. *Applied Sciences*, 12(20), p.10359.



Platform and Bigdata Driven Bridge Smart Maintenance Techniques

Ki-Tae Park^{1*}, Kyusan Jeong², Jaehwan Kim³, Kun-Soo Kim⁴, Byeongcheol Kim⁵, Dongwoo Seo⁶

¹: Korea Institute of Construction and Building Technology (KICT), South Korea, ktpark@kict.re.kr

²: KICT, South Korea, jungkyusan@kict.re.kr

³: KICT, South Korea, jaehwankim@kict.re.kr

⁴: KICT, South Korea, kunsookim@kict.re.kr

⁵: KICT, South Korea, bckim@kict.re.kr

⁶: KICT, South Korea, dwseo@kict.re.kr

*: corresponding author

Keywords: platform, bridge, maintenance, smart

Abstract: As of December 2021, about 37,218 bridges in Korea are currently in use, of which about 5,691 bridges are over 30 years old (15.3% of all bridges), and the number of bridges between 20 and 30 years old is 11,820 (31.8% of all bridges). By 2032, about 47% of all bridges are expected to be older than 30 years (MOLIT, 2022). Therefore, it is necessary to take preventive maintenance actions by predicting the level of damage or deterioration that may occur in the future using various data related to the current state of the bridge. Through this, the effect of reducing the huge maintenance budget that may be required in the future can be expected. In this paper, we presented a preventive maintenance technique for bridges based on the technique of accumulating more than 5 million various data related to bridge deterioration and predicting the future of bridges using the built data. Aging data includes on-site data on 100 bridges using the IoT sensor system, long-term surveyed salinity data considering environmental conditions in Korea, freezing and thawing, and frequency of use of deicing agents. In addition to the data obtained in this way, unknown data was estimated using artificial intelligence techniques for necessary but impossible data. Using the aging curve against time history, the reliability of the element technology for evaluating the aging of the bridge based on future prediction was secured. The accuracy of the future prediction-based algorithm was about 90.8%, which is expected to increase as the number of data increases. The platform under development is expected to be open after 2023, allowing users involved in bridge management to utilize it.

1. Introduction

This research aims to build more than 5 million bridge aging related data (deterioration data, environmental data, bridge behavior, long-term survey, etc.) to advance aging bridge structure maintenance technology. In addition, it includes the development of a smart maintenance platform that provides various services required for maintenance of bridge structures by user type while securing the reliability of bridge aging evaluation element technology using artificial intelligence techniques (bridge maintenance priority, budget basis for maintenance requirements, aging level etc.). And also, it is to support inspection and diagnosis-related tasks currently in progress in Korea (MOLIT, 2021).

This research started in 2021 and is scheduled to end in 2023, and data integration and algorithm updates will continue. In this paper, IoT sensor system installation, various data generation part using artificial intelligence, and platform concept design results is briefly outlined. The research results for each specific item will be presented as an additional thesis.

2. Data Integration

In this study, various data have integrated for the evaluation of aging based on the future prediction of bridges. The integrated data results are used to provide information for preventive maintenance through the data analysis process. This section summarizes bridge behavior data acquisition process using IoT sensors and data integration status of Korea's environmental condition.

2.1 IoT sensor system installation

To secure long-term data on the actual bridge behavior history, bridge aging data have integrated using an IoT sensor system. As sensors, an accelerometer, a crack gauge, an expansion joint gauge, an inclinometer, and a thermometer that can use IoT communication were applied. For three years from 2021 to 2023, it was decided to install related system for a total of 100 bridges and secure related data.

Among 954 representative bridges in Korea based on deterioration environment, it was selected first in consideration of the year of completion and the operating environment through field surveys. For sensor production and sensor installation, sensor requirements for each collection item were reviewed (basic device configuration, operating conditions, communication conditions, etc.), and IoT sensor site installation and power/communication-related equipment installation for each bridge were completed. The conceptual diagram related to data transmission and reception is shown in the figure below.

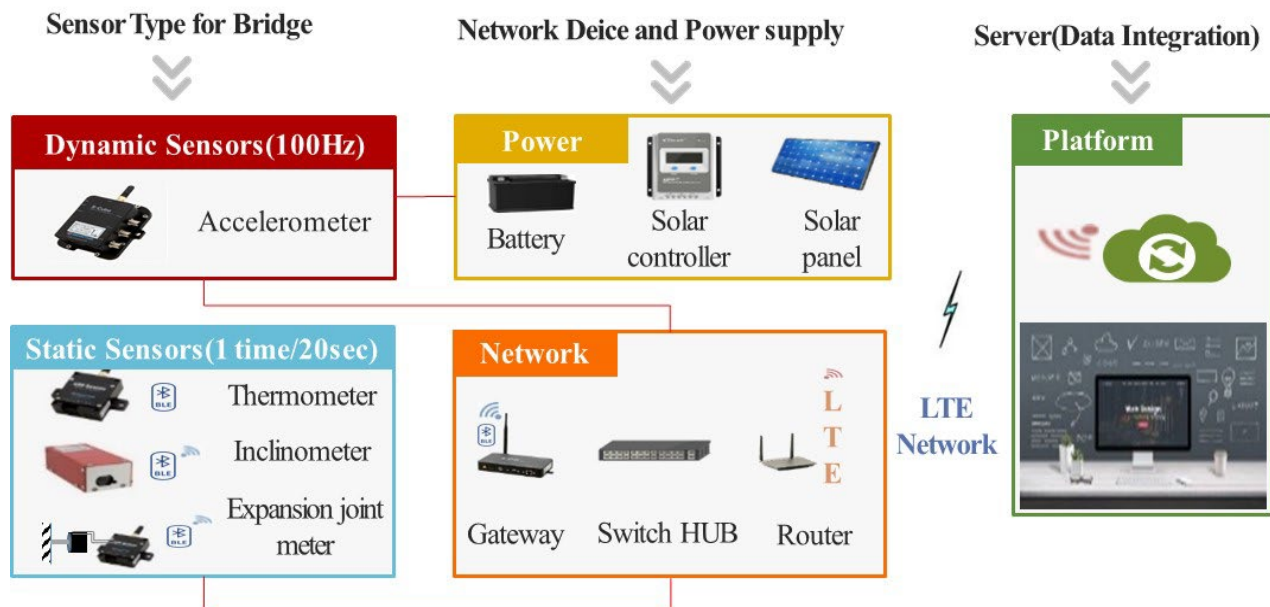
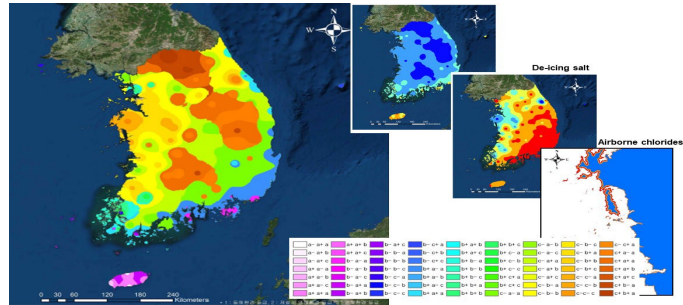


Fig. 1. IoT Sensor System Installation Concepts for Bridge

2.2 Investigation of environmental conditions in Korea

In Korea, environmental conditions vary widely according to regional conditions (JS Lee et al, 2010). Therefore, the environmental conditions were classified into a total of 108 cases by dividing into deicing agents use, freezing and thawing, and airborne salinity.

As of December 2022, 101 cumulative field survey measurement points in Korea have been selected to secure actual measurement data of the deteriorating environment. Among them, 60 points were selected to investigate the environmental conditions for airborne salinity along the coast, 26 points for the environmental for deicing agents, and 15 points for environmental surveys for



each member of the bridge. A total of 1,300 data were obtained by the end of December 2022 in relation to the survey of coastal airborne salinity deterioration environments.

Fig. 2. Environmental conditions in Korea

3. Aging Level of Bridge Evaluation by Generated Data Using Artificial Intelligence

In relation to bridge structure aging data, which is difficult to collect, a study was conducted to create a time-series degradation curve based on collected bridge aging information and artificial intelligence techniques. The previously obtained data was first classified by deterioration index in consideration of the service life of the bridge, and preprocessing work for artificial intelligence learning (classification by region and bridge type, correlation analysis, data reliability evaluation, standardization considering data characteristics etc.) was performed. And artificial intelligence learning was used to generate time series degradation curves by region/absence/deterioration index. In regions where data were not secured, data learning was performed using various degradation data (weather data and degradation environment data) of the target region to generate time-series degradation curves for each degradation index for regions where degradation data were not secured. In this research, an aging curve was created based on degradation curves by region, bridge type and member through artificial intelligence based degradation curves. As a result of applying the aging prediction algorithm to six random bridges in Seoul, Korea, the accuracy of the algorithm was calculated to be 90.8% with an error rate of 9.2% for the aging of the bridge.

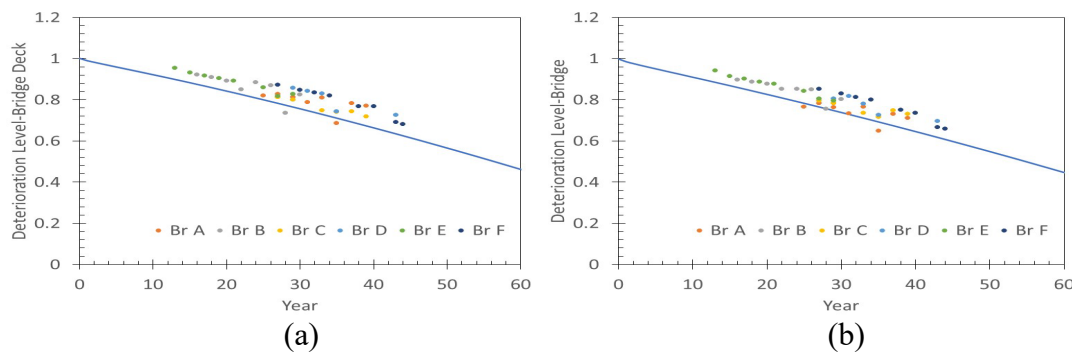


Fig. 3. Deterioration level evaluation accuracy: (a) bridge deck-91.5%; (b) bridge total accuracy-90.8%



4. Summary of Platform Function

The bridge smart maintenance platform developed in this study has the function of providing information related to bridge deterioration level evaluation and preventive maintenance methods based on future prediction. In other words, by using a platform on which bridge aging data and algorithms are built, it is possible to receive information related to the future prediction-based aging level and preventive maintenance plan for the bridge through the data analysis process. In addition, the main purpose is to provide various information related to bridge maintenance, and a methodology that can be used as a reference along with the evaluation of load capacity of bridges by conventional vibration measurement is also included (Soojin Cho et al, 2007).

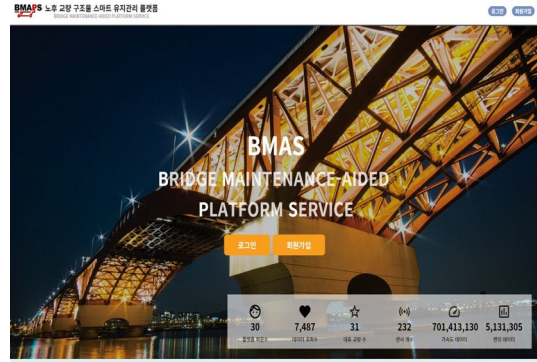


Fig. 4. Cover page of platform system

5. Conclusion

This study was conducted to secure the reliability of bridge aging evaluation core technology by using artificial intelligence to advance aging bridge structure maintenance methodologies. It is necessary to take preventive maintenance actions by predicting the level of damage or deterioration that may occur in the future using various data related to the current state of the bridge. Through this, the effect of reducing the huge maintenance budget that may be required in the future can be expected. In this paper, we presented a preventive maintenance technique for bridges based on the technique of accumulating more than 5 million various data related to bridge deterioration and predicting the future of bridges using the built data. Aging data includes on-site data on 100 bridges using the IoT sensor system, long-term surveyed salinity data considering environmental conditions in Korea, freezing and thawing, and frequency of use of deicing agents. In addition to the data obtained in this way, unknown data was estimated using artificial intelligence techniques for necessary but impossible data. Using the aging curve against time history, the reliability of the element technology for evaluating the aging of the bridge based on future prediction was secured. The accuracy of the future prediction-based algorithm was about 90.8%, which is expected to increase as the number of data increases. The platform under development is expected to be open after 2023, allowing users involved in bridge management to utilize it.

6. References

- Ministry of Land, Infrastructure and Transport. 2021. Detailed guidelines for safety and maintenance of facilities (Safety Inspection and Diagnosis). KALIS
- Ministry of Land, Infrastructure and Transport. 2022. Road Bridges and Tunnels Status Report. Road bridge and tunnel status information system.
- Jongseok Lee et al. 2010. Characteristics of airborne salinity distribution in Korea. Korean Concrete Institute, 22(6), 769-776.
- Sujin Cho et al. 2007. Evaluation of load carrying capacity of bridges by vibration measurement. Proceedings of the Korean Society of Civil Engineers, 27(1), 79-89.



The Bridge Engineering Institute
An International Technical Society

www.beibridge.org